||| 1.0

|| 2.8 || 2.5

| 3.2 || 2.2

3.6

|| 2.0

|| 1.8

||| 1.1

||| 1.25 ||| 1.4 ||| 1.6

MICROCOPY RESOLUTION TEST CHART

DEPARTMENT OF THE ARMY

OFFICE OF THE DEPUTY CHIEF OF STAFF
FOR RESEARCH, DEVELOPMENT, AND ACQUISITION
WASHINGTON, D.C. 20310

**REPLY TO
ATTENTION OF**

DAMA-ARZ-D   21 July 1980

SUBJECT: Proceedings of the 1980 Army Science Conference

SEE DISTRIBUTION

1. The twelfth in a series of Army Science Conferences was held at
the United States Military Academy, 17-20 June 1980. The conference
presented a cross section of the many significant scientific and
engineering programs carried out by the Department of the Army and
provided an opportunity for Department of the Army civilian and mili-
tary scientists and engineers to present the results of their research
and development efforts before a distinguished and critical audience.

2. These Proceedings of the 1980 Army Science Conference are a com-
pilation of all papers presented at the conference and the supplemental
papers that were submitted. The Proceedings consist of four volumes,
with Volumes I through III unclassified, and Volume IV classified.

3. Our purpose for soliciting these papers was:

   a. To stimulate the involvement of scientific and engineering
talent within the Department of the Army.

   b. To demonstrate Army competence in research and development.

   c. To provide a forum wherein Army personnel can demonstrate the
full scope and depth of their current projects.

   d. To promote the interchange of ideas among members of the Army
scientific and engineering community.

4. It is hoped that the information contained in these volumes will be
of benefit to those who attended the conference and to others interested
in Army research and development.

DONALD R. KEITH
Lieutenant General, GS
Deputy Chief of Staff for Research,
Development, and Acquisition

2

US Army Mobility Equipment Research and Development Command
  US Army Electrical Power Laboratory
US Army Natick Research and Development Command
US Army Tank-Automotive Materiel Readiness Command
US Army Tank-Automotive Research and Development Command
US Army Test and Evaluation Command
  US Army Aircraft Development Test Activity
  US Army Aberdeen Proving Ground
    Materiel Testing Directorate
  US Army Cold Regions Test Center
  US Army Dugway Proving Ground
  US Army Electronics Proving Ground
  US Army Tropic Test Center
  US Army White Sands Missile Range
    Instrumentation Directorate
    National Range Operations Directorate
  US Army Yuma Proving Ground
US Army Troop Support and Aviation Materiel Readiness Command
US Army Electronics Materiel Readiness Activity
US Army Foreign Science and Technology Center
US Army HQ TRADOC Combined Arms Test Activity
US Army Human Engineering Laboratory
US Army Logistics Center
US Army Materials and Mechanics Research Center
US Army Materiel Systems Analysis Activity
US Army Research Office
US Army Research, Development and Standardization Group (Europe)
US Army Training and Doctrine Command
US Army Concepts Analysis Agency
US Army Operational Test and Evaluation Agency
US Army Japan, Camp Zama
US Army Inst for Research in Management Info and Computer Sciences
US Army Reserve Components Personnel and Administration Center
US Army Soldier Support Center
Lawrence Livermore National Laboratory, Univ of California, Livemore
Los Alamos Scientific Laboratory
US Army Health Services Command
US Army Institute of Surgical Research
US Army Medical Research and Development Command
  US Army Medical Research Institute of Infectious Diseases
US Army Research Institute for the Behavioral and Social Sciences
US Army Research Institute of Environmental Medicine
Letterman Army Institute of Research
Walter Reed Army Institute of Research
US Army Aeromedical Research Laboratory
US Army Biomedical Laboratory
US Army Environmental Hygiene Agency
US Army Medical Bioengineering Research and Development Laboratory

3

Brooke Army Medical Center
Dwight D. Eisenhower Medical Center
Fitzsimons Army Medical Center
Madigan Army Medical Center
US Army Tripler Medical Center
Walter Reed Army Medical Center
  Armed Forces Institute of Pathology
  US Army Institute of Dental Research
US Army Coastal Engineering Research Center
US Army Cold Regions Research and Engineering Laboratory
US Army Construction Engineering Research Laboratory
US Army Engineer Topographic Laboratories
US Army Engineer Waterways Experiment Station
US Army Engineering Division, North Atlantic
PROJECT MANAGERS
  Army Tactical Data Systems (ARTADS), Fort Monmouth
  Remotely Monitored Battlefield Sensor Systems (REMBASS), Fort Monmouth
  Army Tactical Communications Systems (ATACS), Fort Monmouth
COMMANDANTS
  National Defense University
  National War College
  Industrial College of the Armed Forces
  Academy of Health Sciences
  US Army Field Artillery School
  US Army Infantry School
  US Army Intelligence Center and School
  US Army Military Police Chemical School and Training Center
  US Army Signal Center at Fort Gordon
  US Army Transportation School
SUPERINTENDENT
  US Army Military Academy, ATTN: Technical Library
  US Army Military Academy, ATTN: Acquisition Branch
COPIES FURNISHED:
  Office, Under Secretary of Defense for Research and Engineering
  Office, Deputy Director for Science and Technology, Defense Nuclear Agency
  Chairman, Defense Science Board
  Defense Advanced Research Projects Agency
  Defense Communication Agency
  Defense Communication Engineering Center
  Defense Documentation Center
  Defense Science Board
  Institute for Defense Analysis
  Deputy Chief of Staff for Logistics, HQDA
  Deputy Chief of Staff for Operations and Plans, HQDA
  Deputy Chief of Staff for Personnel, HQDA
  Assistant Chief of Staff for Automation and Communications, HQDA
  Assistant Chief of Staff for Intelligence, HQDA
  Office of the Chief of Public Affairs, HQDA

First United States Army
National Academy of Sciences
National Aeronautics and Space Administration (Code L-2)
National Bureau of Standards
National Institute for Occupational Safety and Health, HEW
National Institutes of Health
National Science Foundation
National Security Agency
Office of Personnel Management
US Army Acquisition Information Systems Agency
US Army Scientific Information Center
Air Force Institute of Technology
Air Force Office of Scientific Research
Air Force Systems Command
Naval Air Systems Command
Naval Materiel Command
Naval Research Laboratory
Naval Research Library (Code 2627)
Office of Naval Research (Code 102)
Office of Naval Research (Code 230)
HQ US Marine Corps (Code RD-1)
Science Advisor to the Commandant, US Coast Guard
Battelle Columbus Laboratories
Mathematics Research Center, Univ of Wisconsin, Madison
Southwest Research Institute

PROCEEDINGS

OF THE

1980 ARMY SCIENCE CONFERENCE

UNITED STATES MILITARY ACADEMY

WEST POINT, NEW YORK

17-20 JUNE 1980

V O L U M E   III

Principal Authors N through Z

TABLE OF CONTENTS

PROCEEDINGS OF THE 1980 ARMY SCIENCE CONFERENCE

Author	Title	Vol	Page
Aucoin, T. R. Savage, R. O. Wade, M. J. Gualtieri, J. G. Schwartz, A.	Large High Quality Single Crystal Aluminum Phosphate for Acoustic Wave Devices	1	121
Aucoin, T. R.	See Ross, R. L.	3	205
Baladi, G. Y. Rohani, B.	A Terrain-Vehicle Model for Analysis of Steerability of Tracked Vehicles	1	135
Ballato, A. Lukaszek, T.	Combat Hardened Communications: High Precision Frequency Control Using Resonators Immune to Accele- ration and Stress Fields	1	151
Ballato, A. T.	See Iafrate, G. J.	2	295
Balsara, J. P.	See Albritton, G.	1	47
Banderet, L. E. Stokes, J. W. Francesconi, R. Kowal, D.	Simulated, Sustained-Combat Oper- ations in the Field Artillery Fire Direction Center(FDC): A Model for Evaluating Biomedical Indices	1	167
Banister, G. H.	Testing of the Army's Inter- operating Network of Tactical C^3I Systems	1	183
Beatrice, E. S.	See O'Mara, P. A.	3	31
Beck, R. R.	See Hoogterp, F. B.	2	263
Beisel, W. R.	See Daniels, W. L.	1	429
Berg, N. J. Abramovitz, I. J. Lee, J. N. Casseday, M. W.	Acousto-Optic Time Integrating Correlator for Detection and Characterization of Broad Band LPI Communications	4	1
Berry, P. Keane, W. Hatfield, G. Filler, M.	The Biological Detector and Warning System, XM19/XM2	1	197

iv

vii

viii

CASE STUDY USE OF EDITSPEC,
THE CORPS OF ENGINEERS
COMPUTER AIDED SPECIFICATION PREPARATION SYSTEM (U)

*EDGAR SAMUEL NEELY, JR., DR.
CONSTRUCTION ENGINEERING RESEARCH LABORATORY
CHAMPAIGN, IL 61820

EDSOL JEROME CLARK, MR.
U.S. ARMY ENGINEERING DIVISION
HUNTSVILLE, AL 35807

INTRODUCTION. The Corps of Engineers has developed a computer-aided specification preparation system known as EDITSPEC. This system is being field tested at the Huntsville Division. Corps-wide implementation is scheduled in December 1980. EDITSPEC resides on one national computer system. Users access the system through typewriter terminals. Output is received at the typewriter terminals, local medium-speed printers, or central site high-speed printers. This paper describes the benefits expected from application of the EDITSPEC system, the guide specification process, and finally the method used to prepare project specifications. A prototype test description concludes the presentation.

BENEFITS. Several major benefits are anticipated when EDITSPEC becomes fully operational. The estimated magnitude of these benefits are listed below and will be verified during the prototype test.

1. Project specifications will be more complete, accurate, and consistent when the contract is advertised.

2. The cost of construction change orders due to specification deficiencies will be reduced 40 percent.

1

*NEELY, CLARK

3. Specification writers' production will increase 30 percent.

4. Typing production will increase 35 percent.

5. Total costs to produce project specifications will be reduced 25 percent.

A more detailed description of the areas in which EDITSPEC is expected to provide benefits is presented below.

CORPS OF ENGINEERS GUIDE SPECIFICATIONS (CEGS). Guide specifications are used as drafts when preparing project specifications. Changes to the CEGS are issued as notices.

1. Maintained in EDITSPEC by the Huntsville Division. Individual offices will no longer have to maintain the CEGS.

2. Reported errors will be corrected immediately.

3. Revisions to the guides will be available to field offices immediately. There will be no printing and mailing delays between the approval of a revision and its implementation by field offices.

PROJECT SPECIFICATIONS.

1. The writer will be provided with a posted guide specification. No resources will be required to post notices prior to application on a project.

2. Technical notes, providing instructions regarding specification preparation, will be printed directly after the text to which the note applies.

3. Writers using a guide in project specification preparation will be immediately notified of changes to the guide.

4. The writer will be provided with a project section containing all relevant guide text. No resources will be required to manually review and mark up the guide. The system will automatically pull all relevant text from the guide and place it into the project section.

5. All referenced publications will be kept current and updated automatically. No resources will be required to check the reference publications for current listings.

6. The sources of all text will be identified. Minimum management resources will be required to review and approve the project-unique text in the specification.

7. A complete, consistent, and accurate project specification is produced at bid printing. Inconsistencies are reported to the project engineer and must be corrected before the system produces the bid printing copy.

CORPS OF ENGINEERS GUIDE SPECIFICATION (CEGS) PREPARATION FOR AUTOMATION. This section describes how a guide specification is prepared for automation. Portions of the Corps of Engineers guide specification (CEGS) entitled "CEGS-07510 BUILT-UP ROOFING" have been used to illustrate the process. Guide specifications are written to cover the most frequently encountered design conditions. An actual project design would not contain all design conditions covered by a guide. The first task is to decide what design conditions the guide will cover. The writer forms the design condition list before any text is written. The list for the example guide is shown in Figure 1.

FIGURE 1. CHECKLIST--CEGS-07510--BUILT-UP ROOFING

C = Concept Design   F = Final Design

Condition Number			Design Conditions
1	C	F	Control Condition (Required)
			Built-up roofing substrate:
2	X	√	Mineral-fiber, expanded perlite or fiberboard insulation
3	X	X	Composite board, cellular glass, isocyanurate or urethane insulation
4	X	X	Cast-in-place concrete
5	X	√	Precast concrete
6			Precast gypsum
7	X	X	Cast-in-place gypsum
8	X	X	Lightweight insulating concrete
			Roof slopes:
9	√	X	All slopes 1/2" per foot or less
10	X	X	All slopes greater than 1/2" to 1" per foot
11	X	X	All slopes greater than 1" to 3" per foot

*NEELY, CLARK

12 X ✓		Combination of slopes including slopes 1/2" per foot or less
13 X X		Combination of slopes, all greater than 1/2" per foot
		Average January temperature:
14 ✓ ✓		40°F and above
15 X X		Below 40°F
16 X ✓		Gravel stops required
17 X ✓		Valleys required
18 ✓ ✓		Cants required
19 ✓ ✓		Wood walkways required
20 X ✓		Composition traffic surfaces required
21		Vertical surfaces abut sloped roof surfaces
22 X ✓		Bitumen samples required
23 X X		Light-colored aggregate is available and work is in Air Force weather condition zones A or B
24 ✓ ✓		Army or Air Force construction is not in the vicinity of warmup/operating aprons. For work that is not in the vicinity of warmup/operating aprons, the roof substrates and slopes are as follows:
25 X X		Concrete or insulation - all slopes 1/2" per foot or less
26 X X		Cast-in-place concrete - slopes greater than 1/2" per ft
27 X ✓		Precast concrete - slopes greater than 1/2" per ft
28 X ✓		Expanded perlite, fiberboard or mineral fiber insulation - slopes greater than 1/2" per ft
29 X X		Composite board, cellular glass, isocyanurate, or urethane - slopes greater than 1/2" per ft
30 ✓ ✓		Gypsum or insulating concrete - all slopes 1/2" per ft or less
31 X X		Gypsum or insulating concrete - slopes greater than 1/2" per ft
32 X X		Air Force construction is in the vicinity of AF warmup/operating aprons
		For work in the vicinity of AF warmup/operating aprons, roof substrates and slopes will be as follows:
33 X X		Concrete or insulation - all slopes 1/2" or less
34 X X		Cast-in-place concrete - slopes greater than 1/2" per ft
35 X X		Precast concrete - slopes greater than 1/2" per ft
36 X X		Expanded perlite, fiberboard or mineral fiber insulation - slopes greater than 1/2" per ft

4

37 X X	Composite board, cellular glass, isocyanurate or urethane insulation - slopes greater than 1/2" per ft
38 X X	Gypsum or insulating concrete - all slopes 1/2" per ft or less
39 X X	Gypsum or insulating concrete - slopes greater than 1/2" per ft

The second task is to form an outline. Once the outline has been established, the writer can begin to prepare the text, the third task. The fourth and one of the most important tasks is to convey the writer's ideas as to when each portion of text should be pulled from the guide and placed into a project specification. While this task may be trivial if each paragraph addresses only one design condition, it may be very complicated if each phrase in a sentence is written to address a different condition.

The writer must convey this information as quickly and efficiently as possible. For automation, this information is conveyed by marking the handwritten text. The contents of a guide can be divided into three classifications: (1) tables, (2) variable phrases, and (3) normal text. The method for marking text for each classification is presented below.

Tables - The writer must indicate under which design conditions each column and each row should be pulled from the guide and placed into the project specification. This information is indicated by writing the numbers of each design condition that would require use of the row to the left of the row. For columns, the writer indicates the design conditions by placing them above the columns. An example table is shown in Figure 2. The writer has indicated that portions of row four would be required only if the project contained one or more of design conditions 25, 26, 27, 28, or 29 and that portions of column three would be required only if the project contained design condition 1.

TABLE 1. LAPS FOR ROOFING FELTS AND ROLL ROOFING

① LAYERS OR PLIES	① LAPS IN INCHES FOR 36-INCH WIDTH	① STARTING WIDTHS IN INCHES FOR 36-INCH WIDTH
	1	4	36
㊳㊴ 2	19	18 and 36

5

1	3	24-2/3	12, 24, and 36
㉕㉖㉗	4	27-1/2	9, 18, 27 and 36
㉘㉙			

FIGURE 2. MARKING TABLES

Variable Phrases - Guides contain phrases that vary depending on the design conditions. Phrases are normally, but not necessarily, marked in the guide by the use of open and close brackets ([ ]). There is usually a fixed set of replacement phrases for each variable phrase. For automation, each variable phrase in the text is marked with a flag and each unique flag is given an identifier number. All possible choices for a flag (phrase) are defined in the order of the simplest to the most complicated. The writer marks the design conditions for each phrase to the left of the phrase definition. In the example shown in Figure 3, the unbracketed phrase "Concrete or Insulation" is marked as a variable phrase and identified as flag 7. The three choices for flag 7 are shown below the text. The writer has indicated that choice two, "Insulation," should be applied if design condition 2 or 3 is present in the project. Choice three, "Concrete or Insulation," should be applied if any of the design condition pairs 2 and 4, 2 and 5, 3 and 4, or 3 and 5 are in the project.

㉕
㉖
㉗
㉘
㉙

4.1.2 On *FL7; $ Concrete or Insulation*-Surfaces: Four plies of 15-pound asphalt-saturated felt shall be mopped in solid with hot asphalt. Felts shall be laid shingle-fashion at right angles to the direction of the roof slope and lapped in accordance with Table I/*FL8; $ and fastened in accordance with Table II, III/*-. The flashings shall be installed and the flood coat and surfacing applied.

FLAG 7

④ ⑤
②, ③
②, ④   ③ ④
②, ⑤   ③ ⑤

Choice 1 - Concrete
     2 - Insulation
     3 - Concrete or Insulation

FIGURE 3. MARKING FLAGS

6

Normal Text - When the text to be marked is several lines long, a bracket at the left margin can be used to indicate the text. The example in Figure 4 shows that the text should be pulled if design condition 1 is present in the project. When the text to be marked is only a few words long, the design condition numbers are written above the text. A slash and a dash are used to indicate the start of the phrase and a dash and a slash are used to indicate the end of the phrase. The first line of the example in Figure 4 indicates that the phrase "or coal-tar bitumen" should be pulled if the project contains either design condition 25 or 30.

2. GENERAL: Asphalt ⌐or coal-tar bitumen⌐ built-up roofing shall be applied to the roof surfaces indicated.

2.1 Storage of Materials: Felts and roll roofing shall not be exposed to any moisture before, during, or after delivery to the site. Felts and roll roofing shall be stored in an enclosed building or in a trailer, stacked on end, and maintained above 50°F for 24 hours immediately before laying. ⌐Aggregate shall be maintained surface dry as defined by ASTM D 1863⌐ ㉔

FIGURE 4. MARKING TEXT LINES

The marked-up text and the design condition list are given to an EDITSPEC operator, who enters the text and translates the markings to computer commands. The operator removes the actual text of each referenced publication and replaces it with a computer command requesting that this information be copied from the master reference publication list only when a print request is issued. This permits the master reference publication list to be maintained at one location and ensures the inclusion of the latest publication within the guide.

Since changes are made directly within the guide, eliminating the need for pages which must be posted by field personnel, changes are immediately available to all field personnel in posted form. When changes are made to a guide, the operator issues an "update message" command. The EDITSPEC system sends one update message for each project currently applying the guide. The project specification writer will receive the message as soon as he enters EDITSPEC.

Errors within a guide found by field personnel are reported by telephone to the EDITSPEC "HOT LINE." Immediate action will be taken by the HOT LINE personnel to correct the reported errors.

The commands to create the first page of guide CEGS-07510.00 are shown in Figure 5. The "NEW" command creates a document named "CEGS07510.00" on a dataset (or file) named "data." The "EDIT" command allows the document to be edited. Text is entered into the document through the "INPUT" command. Internal format commands have been embedded into the text for center (*cj---*), left (*lj---*), and right (*rj---*) justification of text during printing. Commands to skip lines (*sl*) and to perform automatic paragraph numbering and indentation (*pl*) have also been added. Reference publications are added by the "COPY TABLE NO MOVE" command. The first copy table (ct) command requests that the publication located on row 54 of the table 100 in the reference publication list named "referencepub" be copied into the guide only when a print request is given. The "ct" commands generate the "*ct*" commands shown on lines 1600 through 3100 of the listing of the text. Note that the actual text for the publication is not copied, but a request for a future copy is stored in the correct location in the guide.

<u>FIGURE 5.   GUIDE GENERATION COMMANDS</u>

```
.new (cegs07510.00); data.
.edit (cegs07510.00).
.input.
*lj DEPARTMENT OF THE ARMY*   *lg(-11) CEGS-07510* *sl*
*lj OFFICE OF THE CHIEF OF ENGINEERS*  *u* *lj(-11) July 1977*
*lj(-11) Superseding* *sl*
*lj(-11) CE-220.12* *sl*
*cj Notice 3* *sl*
*cj May 1979* *sl1*
*cj CORPS OF ENGINEERS GUIDE SPECIFICATION* *sl*
*cj MILITARY CONSTRUCTION* *sl4*
*cj SECTION *f11* * *sl1*
*cj BUILT-UP ROOFING* *sl*
*tc 1; *pl* APPLICABLE PUBLICATIONS* :  The publications listed
below form a part of this specification to the extent referenced.
The publications are referred to in the text by the basic designa-
tion only.
*p2* Federal Specifications (Fed. Spec.):  *sl1*
*tb 250*
.ct (referencepub); 100;;;54;1,2;nm.
```

```
.ct (referencepub); 100;;;78;1,2;nm.
.input.
*te*
*p2* American Society for Testing and Materials (ASTM) Publications:
*tb 250*
.ct (referencepub); 200;;;21;1,2;nm.
.ct (referencepub); 200;;;25;1,2;nm.
.ct (referencepub); 200;;;26;1,2;nm.
.ct (referencepub); 200;;;38;1,2;nm.
.ct (referencepub); 200;;;42;1,2;nm.
.ct (referencepub); 200;;;10;1,2;nm.
.ct (referencepub); 200;;;11;1,2;nm.
.ct (referencepub); 200;;;15;1,2;nm.
.ct (referencepub); 200;;;15;1,2;nm.
.ct (referencepub); 200;;;28;1,2;nm.
.ct (referencepub); 200;;;29;1,2;nm.
.input.
*te*
*tc 1; *pl* GENERAL* :  Asphalt
or coal-tar bitumen
built-up roofing shall be applied to the roof surfaces indicated.
.lt text.
100 *lj DEPARTMENT OF THE ARMY*  *lj(-11) CEGS-07510* *sl*
200 *lj OFFICE OF THE CHIEF OF ENGINEERS*   *u* *lj(-11) July 1977*
300 *lj(-11) Superseding* *sl*
400 *lj(-11) CE-220.12* *sl*
500 *cj Notice 3* *sl*
600 *cj May 1979* *sll*
700 *cj CORPS OF ENGINEERS GUIDE SPECIFICATION* *sl*
800 *cj MILITARY CONSTRUCTION* *sl4*
900 *cj SECTION *fll* *sll*
1000 *cj BUILT-UP ROOFING* *sl*
1100 *tc 1; *pl* APPLICABLE PUBLICATIONS* :  The publications listed
1200 below form a part of this specification to the extent referenced.
1300 The publications are referred to in the text by the basic
        designation only.
1400 *p2* Federal Specifications (Fed. Spec.):  *sll*
1500 *tb 250*
1600 *ct (referencepub); 1;54;1,2;100*
1700 *ct (referencepub); 2; 78;1,2;100*
1800 *toe*
1900 *p2* American Society for Testing and Materials (ASTM)
            Publications:
2000 *tb 250*
2100 *ct (referencepub); 3;21;1,2;200*
2200 *ct (referencepub); 4;25;1,2;200*
2300 *ct (referencepub); 5;26;1,2;200*
```

9

```
2400 *ct (referencepub); 6;38;1,2;200*
2500 *ct (referencepub); 7;42;1,2;200*
2600 *ct (referencepub); 8;10;1,2;200*
2700 *ct (referencepub); 9;11;1,2;200*
2800 *ct (referencepub); 10;15;1,2;200*
2900 *ct (referencepub); 11;19;1,2;200*
3000 *ct (referencepub); 12;28;1,2;200*
3100 *ct (referencepub); 13;29;1,2;200*
3200 *te*
3300 *tc 1; *pl* GENERAL* :  Asphalt
3400 or coal-tar bitumen
3500 built-up roofing shall be applied to the roof surfaces
        indicated.
.upda (cegsmastersp); (a new guide 07510.00 has been issued.)
```

OFFICE-TAILORED GUIDE SPECIFICATION PREPARATION. It is often
advantageous for a Corps office to tailor an CEGS guide or a por-
tion of the guide for local geographic and/or climate conditions.
The tailored text is applied to produce project specifications in
lieu of the original guide. When a complete guide is tailored,
it is stored in its entirety under an office guide name. For
example, if Huntsville Division (Corps office 87) tailored guide
cegs 07510.00, the name of the tailored guide would be
87GS07510.00. When only a few lines of text requires tailoring,
the tailored text is the only text stored in the document. For
example, the Huntsville Division could tailor only the paragraph
"APPLICABLE PUBLICATIONS" to read:

> APPLICABLE PUBLICATIONS: The following publications
> of the issues listed below, but referred to thereafter
> by basic designation only, form a part of this specifi-
> cation to the extent indicated by the references
> thereto:

PROJECT SPECIFICATION PREPARATION

GENERATION. Preparation of a specification begins by
obtaining the master guide specification index and marking the
index to indicate those guides that will be used for the project.
The marked index is given to an EDITSPEC operator, who enters the
selections and obtains a design condition list for each guide
specification that has been selected. This design condition list
contains all design conditions covered by the guide. The specif-
ication writer is provided with the design condition checklist
and a fully posted copy of each guide, if requested. The writer
reviews the design and marks the checklist as follows:

10

1. Checks ( ) the design conditions that are in the project.

2. Marks (X) the design conditions that are not in the project.

3. Leaves design conditions that are currently undecided unmarked.

A concept design example is shown in Figure 6. The marked checklist is given in the concept column of Figure 1.

CONCEPT DESIGN EXAMPLE

Design Criteria:
        Location: Lone Star AAP, Texarkana, Texas
        Building No. 1: 40´ x 60´ roof area
        Average roof slope of 1/4 inch per foot
        Precast gypsum roof deck
        Cants and wood walkways required
        Parapet walls and gravel stops not required

FINAL DESIGN EXAMPLE

Design Criteria: The following buildings have been added to the
        project:
        Building No. 2: 60´ x 90´ roof area
            Average roof slope of 1 inch per foot
            Steel deck with fiberboard insulation
            Parapet walls, valleys and gravel stops required
        Building No. 3: 60´ x 90´ roof area
            Average roof slope of 2 inches per foot
            Precast concrete roof deck
            Parapet walls, valleys and gravel stops required
            Composition traffic surface

FIGURE 6. CONCEPT AND FINAL DESIGN EXAMPLE

The writer decides which office-tailored guide specification sections are to be applied in lieu of and in addition to the CEGS guides and which office-tailored text is to be used instead of portions of the CEGS guide text. Handwritten notes to the EDITSPEC operator are prepared defining the required replacements. In the example, the paragraph titled "APPLICABLE

PUBLICATIONS" is to be replaced by the text of document
87GS07510.00.

Project-unique text is written to cover design conditions
not covered by the CEGS or office guides. Each segment of
project-unique text is marked as to its final location in the
project specification. The writer actually marks the location in
the guide that the project-unique text would logically appear if
it were incorporated into the guide. In the example, the para-
graph titled "GENERAL" is to be modified to read

> "GENERAL: Asphalt built-up roofing shall be applied
> to the roof surfaces indicated. Materials and their
> application to the built-up roofing system shall con-
> form to requirements of Factory Mutual and the require-
> ments specified herein to provide an approved Class I-
> 90 roof."

The EDITSPEC operator is given the completed design con-
dition checklist, the tailored office guide replacement instruc-
tions, and the project-unique text. The operator enters the com-
pleted checklist and issues the "GENERATE" command, which causes
the system to generate a new project section and add commands to
copy the required guide text to the project. These commands are
performed only when a print request is given. The operator edits
the project section and inserts the replacement request and the
project-unique text. Following a logic check command, the system
checks the text to insure that it is logically correct, complete,
and does not include extraneous material. An example generation
is shown in Figure 7.

```
.spec (87p207510.00); a; 1, -2, -3, -4, -5,
. 6, -7, -8, 9, -10, -11, -12, -13, 14,
. -15, -16, -17, 18, 19, -20, -22,
. -23, 24, -25, -26, -27, -28, -29,
. 30, -31, -32, -33, -34, -35, -36, -37, -38, -39.

.generate (87p207510.00); (cegs 07510.00); dsguo2; 1; 0.
.edit (87p207510.00).
.lt text.
100 *co (cegs07510.00); -100; 900-1000*
200 *co (cegs07510.00); -200; 1100-1300*
300 *co (cegs07510.00); -300; 1400-1500*
400 *ct (cegs07510.00); -400; 1,2;1,2*
500 *co (cegs07510.00); -900; 1800-2000*
600 *ct (cegs07510.00); -1000; 1,2,6,8,10;1,2*
700 *co (cegs07510.00); -2100; 3200-3200*
```

```
800 *co (cegs07510.00); -2200; 3300-3500*
.change 200; /co/; /cu/.
.copy (87gs07510.00);;200;10;nm.
.change 800; /co/; /cu/.
.input 800; 10.
```

```
*tc 1; *pl*
```
GENERAL*: Asphalt built-up roofing shall be applied to the roof
surfaces indicated. Materails and their application to the built-up
roofing system shall conform to requirements of Factory Mutual and
the requirements specified herein to provide an approved Class I-90
roof.

```
.lc.
.lt text.
100 *co (cegs07510.00); -100; 900-1000*
200 *cu (cegs07510.00); -200; 1100-1300*
210 *co (87gs 07510.00); 1*
300 *co (cegs07510.00); -300; 1400-1500*
400 *ct (cegs07510.00); -400; 1,2; 1,2*
500 *co (cegs07510.00); -900; 1800-2000*
600 *ct (cegs07510.00); -1000; 1,2,6,8,10; 1,2*
700 *co (cegs07510.00); -2100; 3200-3200*
800 *cu (cegs07510.00); -2200; 3300-3500*
```

810 *tc; *pl* GENERAL*: Asphalt built-up roofing shall be
applied to the roof surfaces indicated. Materials and their
application to the built-up roofing system shall conform to
requirements of Factory Mutual and the requirements specified
herein to provide an approved Class I-90 roof.

FIGURE 7. PROJECT GENERATION COMMANDS

UPDATING. Updating may be caused by a project redesign,
a more detailed design, and/or guide specification changes. The
process begins by reviewing the previous design condition check-
list and preparing an updated checklist. The project-unique text
and office guide references are reviewed and corrected if neces-
sary. All materials are given to the operator, who enters the
changes to the design condition checklist and issues the "UPDATE"
command. The system then obtains the latest copy of the guide,
the current updated project checklist, and the outdated project
specification section. The section is rewritten to comply with
the updated items automatically. The operator edits the section
changing the replacement requests and project-unique text as

13

required. A logic check command is issued to insure the project specification completeness. An example of an updated design is shown in Figure 6. The updated checklist is shown in the "final" column of Figure 1. The commands issued are shown in Figure 8. No changes to the guide references nor project-unique text is required.

A comparison of the *ct* command on line 600 of the concept and the final design project specifications shows that the publications to be copied from the reference publication document for the concept design (i.e., rows 1, 2, 6, 8, and 10) have been automatically changed to reflect the change in the final design (i.e., rows 1 through 11).

When all project sections are complete and the project is ready for printing, the operator issues the print project command (PPRO). The system will automatically obtain the latest references and latest guide text, automatically paragrpah and paginate correctly, and print complete project.

```
.spec (87p207510.00); c; 2, 5, 6, -9, 12, 14, 16, 17, 20, 21, 22,
   27, 28.
.update (87p207510.00); (cegs07510.00); dsguo2; 1; 0.
.edit (87p207510.00).
.lc.
.lt text.
100 *co (cegs07510.00); -100; 900-1000*
200 *cu (cegs07510.00); -200; 1100-1300*
210 *co (87gs 07510.00); 1*
300 *co (cegs07510.00); -300; 1400-1500*
400 *ct (cegs07510.00); -400; 1, 2; 1, 2*
500 *co (cegs07510.00); -900; 1800-2000*
600 *ct (cegs07510.00); -1000; 1,2,3,4,5,6,7,8,9,10,11; 1,2*
700 *co (cegs07510.00); -2100; 3200-3200*
800 *cu (cegs07510.00); -2200; 3300-3500*
```

810 *tc; *pl* GENERAL*: Asphalt built-up roofing shall be applied to the roof surfaces 820 indicated. Materials and their application to the built-up roofing system 830 shall conform to requirements of Factory Mutual and the requirements 840 specified herein to provide an approved Class I-90 roof.

FIGURE 8. PROJECT UPDATE COMMAND

*NEELY, CLARK

PROTOTYPE TEST PROCEDURE. All Corps Military Construc-
tion guide specifications and the master reference publications
list are loaded in the data base and EDITSPEC is being tested at
Huntsville Division. The purpose is to verify the expected bene-
fits. Detailed time and motion records will be kept on four
basic functions:

1. Updating Guide Specifications -- Huntsville maintains
the Corps guide specifications on EDITSPEC.

2. Project Specification Preparation Via MTST Machines
-- Huntsville will produce the complete project specification for
one project using their current method of specification prepara-
tion, IBM magnetic tape/selectric typewriter machines.

3. Project Specification Preparation Via EDITSPEC -
Manual System. The same project specification will be produced
using EDITSPEC as a normal text editor.

4. Project Specification Preparation Via EDITSPEC -
Automatic System -- Several sections from the same project will
be produced using the automatic generation capabilities. The
complete project specification cannot be automatically produced
since all required CEGS guides have not been coded for automa-
tion.

PROTOTYPE TEST RESULTS AND EVALUATION. Preliminary
evaluation will be conducted in June 1980. Final evaluation will
be conducted in August 1980. The Assistant Secretary of the Army
will review the prototype test results. If the test is success-
ful, field implementation will begin in December 1980.

15

A COMPARISON OF NAVIER-STOKES COMPUTATIONS WITH
EXPERIMENTAL DATA FOR A PROJECTILE SHAPE AT TRANSONIC VELOCITIES

CHARLES J. NIETUBICZ, Mr., and LYLE D. KAYSER, Mr.
U.S. Army Ballistic Research Laboratory
Aberdeen Proving Ground, Maryland 21005

I. INTRODUCTION

The in flight characteristics of an artillery shell are of
major importance to the shell designer, ballisticion and ultimately the
artillery field commander whose mission is deployment of timely and
accurate fire power. The aerodynamic properties of artillery shell,
such as pitching moment, Magnus moment and drag are critical to the
stability of shell which in turn significantly affects accuracy and
time of flight. The capability to determine the aerodynamics of shell
is required over a wide range of flight regimes since, depending on
initial launch velocities, artillery shell are subject to subsonic,
transonic, and supersonic flight. Projectile aerodynamics over these
various flight regimes have been found, in some cases, to change by an
order of magnitude. The solution techniques utilized must therefore
be capable of computing these changes.

A concentrated theoretical and experimental research program
has been ongoing at BRL in order to develop the predictive capabilities
required for determining projectile aerodynamics. Supersonic
computations using combined inviscid flow field and boundary layer
techniques have been developed by Sturek[1], et al., for cone-cylinder
and ogive-cylinder configurations. Recent results have been obtained
in supersonic flow over a typical boattailed projectile by Schiff and
Sturek[2] using modern computational techniques for solving the thin-
layer Navier-Stokes equations.

17

Inviscid transonic computational results have been obtained by Reklis[3], et al., for a secant-ogive-cylinder-boattail shape. The inviscid techniques give good results for pitch plane aerodynamic coefficients at small angle of attack. However, this technique lacks the ability to include viscous effects at transonic speeds and thus compute the Magnus effect on projectiles. Techniques which have been applied in supersonic flow for combining inviscid and boundary layer methods have not been fully established for transonic flow. These methods, which have shown good results for ogive-cylinders in supersonic flow at low angle of attack, are not accurate in modeling the severe flow expansion in the vicinity of surface discontinuities such as those that occur at the cylinder-boattail junction.

The solution of the thin-layer Navier-Stokes equations, which allows for the simultaneous computation of the inviscid and viscous regions, eliminates the need for matching two different solutions. Additionally, since all three momentum equations are retained, the ability to compute in regions of separated flow is achieved. This paper describes the governing three-dimensional thin-layer Navier-Stokes equations used for computing flow over projectile shapes at angle of attack. Secondly, the generalized axisymmetric formulation used for computations at $\alpha = 0°$ will be described. A description of the numerical algorithm and results will follow. Experimental and computational results will be presented for a secant-ogive-cylinder-boattail projectile shape at $\alpha = 0°$ and $\alpha = 2°$. Computational results will also be shown for a ring airfoil shape thus demonstrating the general geometry capability of the present numerical scheme.

II. GOVERNING EQUATIONS

The general three-dimensional thin-layer Navier-Stokes equations, used for all cases where $\alpha = 0°$, are described in Section IIa. The thin-layer generalized axisymmetric equations, which are a special case of the 3-D equations, are described in Section IIb.

a. Three-Dimensional Equations

The transformed three-dimensional thin-layer Navier-Stokes equations in non-dimensional and strong conservation law form are written as[4]

$$\partial_\tau \hat{q} + \partial_\xi \hat{E} + \partial_\eta \hat{F} + \partial_\zeta \hat{G} = Re^{-1} \partial_\zeta \hat{S} \qquad (1)$$

where general coordinate transformations

$$\xi = \xi(x,y,z,t) \quad - \quad \text{longitudinal coordinate}$$

$$\eta = \eta(x,y,z,t) \quad - \quad \text{circumferential coordinate}$$

$$\zeta = \zeta(x,y,z,t) \quad - \quad \text{near Normal coordinate}$$

$$\tau = t \quad\quad\quad\quad - \quad \text{time}$$

are used and

$$
\hat{q} = J^{-1} \begin{bmatrix} \rho \\ \rho u \\ \rho v \\ \rho w \\ e \end{bmatrix}
\qquad
\hat{E} = J^{-1} \begin{bmatrix} \rho U \\ \rho u U + \xi_x p \\ \rho v U + \xi_y p \\ \rho w U + \xi_z p \\ (e+p)U - \xi_t p \end{bmatrix}
$$

$$
\hat{F} = J^{-1} \begin{bmatrix} \rho V \\ \rho u V + \eta_x p \\ \rho v V + \eta_y p \\ \rho w V + \eta_z p \\ (e+p)V - \eta_t p \end{bmatrix}
\qquad
\hat{G} = J^{-1} \begin{bmatrix} \rho W \\ \rho u W + \zeta_x p \\ \rho v W + \zeta_y p \\ \rho w W + \zeta_z P \\ (e+p)W - \zeta_t p \end{bmatrix}
$$

$$
\hat{S} = J^{-1} \begin{bmatrix} 0 \\[4pt] \mu(\zeta_x^2+\zeta_y^2+\zeta_z^2)u_\zeta + (\mu/3)(\zeta_x u_\zeta + \zeta_y v_\zeta + \zeta_z w_\zeta)\zeta_x \\[4pt] \mu(\zeta_x^2+\zeta_y^2+\zeta_z^2)v_\zeta + (\mu/3)(\zeta_x u_\zeta + \zeta_y v_\zeta + \zeta_z w_\zeta)\zeta_y \\[4pt] \mu(\zeta_x^2+\zeta_y^2+\zeta_z^2)w_\zeta + (\mu/3)(\zeta_x u_\zeta + \zeta_y v_\zeta + \zeta_z w_\zeta)\zeta_z \\[4pt] \{ (\zeta_x^2+\zeta_y^2+\zeta_z^2)[0.5\mu(u^2+v^2+w^2)_\zeta + \kappa Pr^{-1}(\gamma-1)^{-1}(a^2)_\zeta] \\[4pt] + (\mu/3)(\zeta_x u + \zeta_y v + \zeta_z w)(\zeta_x u_\zeta + \zeta_y v_\zeta + \zeta_z w_\zeta) \} \end{bmatrix}
$$

The velocities

$$U = \xi_t + \xi_x u + \xi_y v + \xi_z w$$
$$V = \eta_t + \eta_x u + \eta_y v + \eta_z w \qquad (2)$$
$$W = \zeta_t + \zeta_x u + \zeta_y v + \zeta_z w$$

represent the contravarient velocity components.

The Cartesian velocity components (u,v,w) are retained as the dependent variables and are nondimensionalized with respect to a_∞ (the free stream speed of sound). The local pressure is determined using the relation

$$p = (\gamma - 1)(e - .5\rho(u^2 + v^2 + w^2)) \qquad (3)$$

where γ is the ratio of specific heats, density (ρ), is referenced to ρ_∞ and total energy (e) to $\rho_\infty a_\infty^2$. The additional parameters are (κ) the coefficient of thermal conductivity, (μ) the dynamic viscosity, (Re) the Reynolds number, (Pr) the Prandtl number, and (λ) which through the Stokes hypothesis is $(-2/3)\mu$.

The metric terms ξ_x, η_x and ζ_x are formed from the derivatives x_ξ, y_ξ, z_ξ, etc., and together with the Jacobian of the transformation allow for computations to be performed for variable body geometries.

The "thin-layer" approximation[4-7] used here requires that all body surfaces be mapped onto ζ = constant planes and that Re >> 1. Essentially, all the viscous terms in the coordinate directions (here taken as ξ and η) along the body surface are neglected while terms in the ζ or the near normal direction to the body are retained. This approximation is used because, due to computer speed and storage limitations, fine grid spacing can only be provided in one coordinate direction (usually taken as the near normal direction) and the grid spacing available in the other two directions is usually too coarse to resolve the viscous terms. For the type of problems currently under investigation, i.e., projectiles at low angles of attack, with no strong cross-flow separation, these approximations are considered valid.

b. Generalized Axisymmetric Equations

The thin-layer generalized-axisymmetric equations are obtained from the three-dimensional equations by making use of two restrictions: (1) all body geometries are of an axisymmetric type; (2) the state

20

variables and the contravariant velocities do not vary in the circumferential direction. In what follows, the $\partial_\eta \hat{F}$ term of Eq. (1) shall be reduced to the source term of the generalized axisymmetric equations.

A sketch of a typical axisymmetric body is shown in Figure 1a.

PROJECTILE-TYPE BODY
(a)

X = CONST. PLANE
(b)

φ = CONST. PLANE
(c)
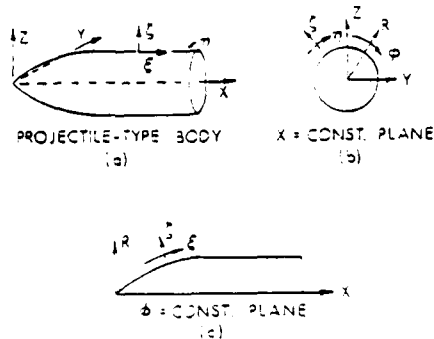
FIGURE 1   AXISYMMETRIC BODY AND COORDINATE SYSTEM

In order to determine the circumferential variation of typical flow and geometric parameters, we first establish correspondence between the inertial Cartesian coordinates (x,y,z) (to which the dependent variables are referenced), the natural inertial cylindrical coordinates (x,ϕ,R), and the transformed variables (ξ,η,ζ). The choice of the independent variables ξ, η, ζ is restricted, as shown in Figure 1c, insofar as η must vary as ϕ, i.e., $\phi = C\eta$ (where C is a constant). From the views shown in Figure 1, the relationship between the coordinate systems are observed to be

$$
\left.
\begin{aligned}
\phi &= C\eta \\
x &= x(\xi,\zeta,\tau) \\
y &= R(\xi,\zeta,\tau)\sin\phi \\
z &= R(\xi,\zeta,\tau)\cos\phi
\end{aligned}
\right\}
\tag{4}
$$

where $\phi = \phi(\tau)$ and the Cartesian and cylindrical coordinates are related in the usual way. Note that x and R are general functions of only ξ, ζ, and τ.

Evaluating the metric terms given the above assumptions and substituting in Equation (1) the resulting thin-layer generalized axisymmetric equations[5] can be written as

$$
\delta_\tau \hat{q} + \delta_\xi \hat{E} + \partial_\zeta \hat{G} + \hat{H} = Re^{-1} \partial_\zeta \hat{S}
\tag{5}
$$

where

21

$$\hat{H} = J^{-1}\phi_\eta \begin{bmatrix} 0 \\ 0 \\ \rho V[R_\xi(U-\xi_t) + R_\zeta(W-\zeta_t)] \\ -\rho VR\phi_\eta(V-\eta_t) - p/(R\phi_\eta) \\ 0 \end{bmatrix} \tag{6}$$

is the resultant source term which has replaced $\partial_\eta \hat{F}$ of Equation (1)

Equation (5) contains only two spatial derivatives but does retain all three momentum equations thus allowing a degree of generality over the standard axisymmetric equations. In particular, the circumferential velocity is not assumed to be zero allowing then computations for spinning projectiles or swirl flow to be accomplished.

The numberical algorithm used for both equations (1) and (5) is a fully implicit, approximately factored finite difference scheme as analyzed by Beam and Warming[8]. The algorithm for Equation (1) written in the delta form is

$$(1 + h\delta_\xi \hat{A}^n - \epsilon_1 J^{-1}\nabla_\xi\nabla_\xi J)(1 + h\delta_\eta \hat{B}^n - \epsilon_1 J^{-1}\nabla_\eta\nabla_\eta J)x$$

$$(1 + h\delta_\zeta \hat{C}^n - hRe^{-1}\delta_\zeta J^{-1}\hat{M}^n J - \epsilon_1 J^{-1}\nabla_\zeta\nabla_\zeta J)(\hat{q}^{n+1} - \hat{q}^n)$$

$$= -\Delta t (\delta_\xi \hat{E}^n + \delta_\eta \hat{F}^n + \delta_\zeta \hat{G}^n - Re^{-1}\delta_\zeta \hat{S}^n) \tag{7}$$

$$- \epsilon_E J^{-1}[(\nabla_\xi\nabla_\xi)^2 + (\nabla_\eta\nabla_\eta)^2 + (\nabla_\zeta\nabla_\zeta)^2]J\hat{q}^n$$

where the δ's are central difference operators, Δ and ∇ are forward or backward difference operators; $h = \Delta t$ corresponds to Euler implicit first-order and $h = \Delta t/2$ to trapezoidal second-order time accuracy. The scheme can be first or second order accurate in time and second or fourth order accurate in space. A similar algorithm can be written for Equation (5) as

22

$$(I + h\delta_\xi \hat{A}^n - \varepsilon_I J^{-1} \nabla_\xi \nabla_\xi J)(I + h\delta_\zeta \hat{C}^n - \varepsilon_I J^{-1} \nabla_\zeta \nabla_\zeta J$$

$$- hRe^{-1} \delta_\zeta J^{-1} \hat{M}^n J) \times (\hat{q}^{n+1} - \hat{q}^n) = -\Delta t(\delta_\xi \hat{E}^n + \delta_\zeta \hat{G}^n \qquad (8)$$

$$-Re^{-1}\delta_\zeta \hat{S}^n)-\Delta t \hat{H}^n - \varepsilon_E J^{-1} [(\nabla_\xi \nabla_\xi)^2] J \hat{q}^n$$

Notice that the second factored terms of Equation (7) has been reduced to the term $\Delta t \hat{H}^n$ and appears on the right hand side of Equation (8). The details of the numerical method, algorithm and boundary conditions for each formulation can be found in References (4) and (5) respectively.

III. MODEL GEOMETRY AND EXPERIMENTAL MEASUREMENTS

The ogive-cylinder boattail shape used for this study closely resembles a modern low-drag artillery projectile and can be seen in the pressure coefficient plot of Figure 2. The model has a three caliber ogive, a two caliber cylinder, and a one caliber 7-degree boattail; the model length is 343mm and the diameter is 57.2mm.

Several wind tunnel experiments have been conducted for this model geometry in order to obtain data for comparison to numerical computations. Experimental data used for comparison in this study are boundary layer profile measurements obtained at the Naval Surface Weapons Center (NSWC), White Oak Laboratory and surface pressure measurements obtained at the NASA Langley Research Center.

Boundary layer data were obtained in the NSWC Tunnel No. 2 which has an open jet test section with a nozzle exit size of 40.6 × 40.6 cm. Data were acquired at Mach = 0.908 with a supply pressure of one atmosphere and a supply temperature of approximately 320°K; these conditions give a Reynolds number of 4.5 × 10^6 based on model length. The NSWC Laser Velocimeter used to measure the boundary layer velocities is commonly referred to as a forward scatter. differential Doppler or "fringe" system and is described in Reference (9). Previous boundary layer measurements at Mach = 3.0 obtained by both laser velocimeter and by impact probe measurements showed good agreement. The present Mach = 0.908 profiles, however were not as consistently smooth and uniform as the Mach 3 profiles described in Reference (10).

Surface pressure measurements were obtained in the NASA Langley 8 ft Pressure Tunnel with supply pressures and temperatures of one atmosphere and 320°K respectively. The model was instrumented with pressure taps at 15 longitudinal stations. Data were acquired at Mach numbers of 0.91 to 1.20, angles of attack from 0 to 10 degrees, and for circumferencial positions by rolling the model in 22.5 degree increments.

IV. COMPARISONS BETWEEN COMPUTATION AND EXPERIMENT

Computations have been obtained on the same secant-ogive-cylinder boattail (SOCBT) shape used for the experiment. The 3-D Navier-Stokes equations were used for $\alpha > 0°$ and the generalized axisymmetric formulation for $\alpha = 0°$. Computational results have been obtained for a ring airfoil shape which show an interesting shock pattern being developed as a function of Mach number.

a. Secant-Ogive-Cylinder-Boattail, $\alpha = 0°$

A computational finite difference mesh of 78 longitudinal points by 50 normal points were used for these calculations. For the experimental test condition of Mach = 0.908 the surface pressure coefficient, C_p is shown as a function of axial position in Figure 2.
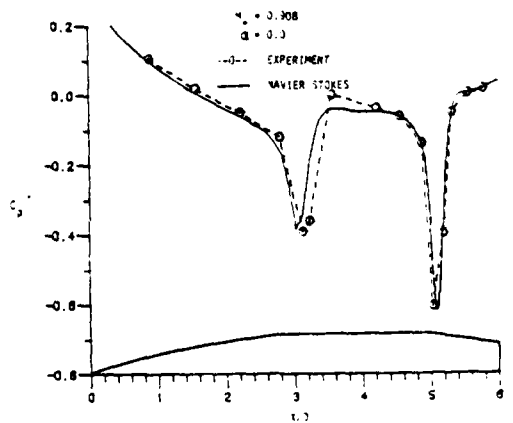
FIGURE 2. EXPERIMENTAL AND THEORETICAL COMPARISON OF SURFACE PRESSURE COEFFICIENT FOR SOCBT, M = 0.908

The computational results, indicated by the solid line are shown to be in good agreement with the experimental results. The flow expansion (decrease in C_p) and subsequent shock (increase in C_p) can be seen occurring near the nose-cylinder and cylinder-boattail junctions. An accurate computation of the pressure distribution is important since it is the integration of surface pressures which are primarily used to determine the aerodynamic coefficients.

Increasing the Mach number to M = 0.96 (Figure 3) shows the movement of shock position, which is typical of transonic flow. Again the experiment and computations show good agreement with the exception of the boattail region. This discrepancy is attributed to

24
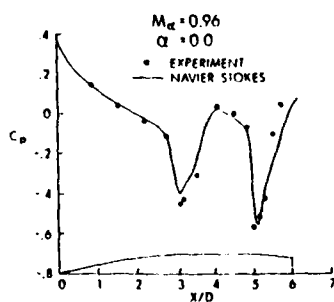
FIGURE 3. EXPERIMENTAL AND THEORETICAL COMPARISON OF SURFACE PRESSURE COEFFICIENT FOR SOCBT, M = .96
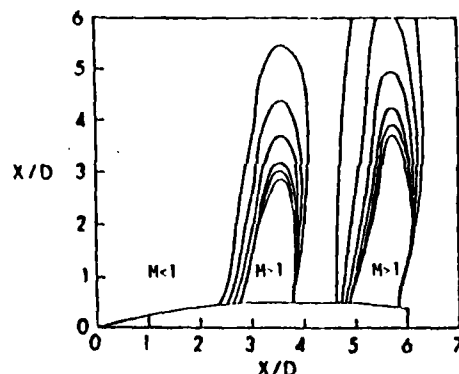
FIGURE 4. MACH CONTOURS AT M = .96 FOR SOCBT, α = 0.0

inadequate grid resolution in the vicinity of the shock. A more detailed look at the computed shock position can be seen in Figure 4 (above) where Mach contours have been plotted. The coalescence of the Mach lines represent the position of the shock and regions of subsonic and supersonic flow are identified.

The accurate determination of aerodynamic coefficients is extremely important throughout the transonic regime since the magnitude of the coefficients can change by as much as 100% in this area. A series of computations were obtained from M = 0.8 through M = 1.1 and the surface pressures were integrated to determine the aerodynamic wave drag. The results are shown in Figure 5 together with the experimental data. Excellent agreement is shown for both the drag rise and magnitude of the zero yaw drag, C_{D_o}, in the critical Mach number regime.
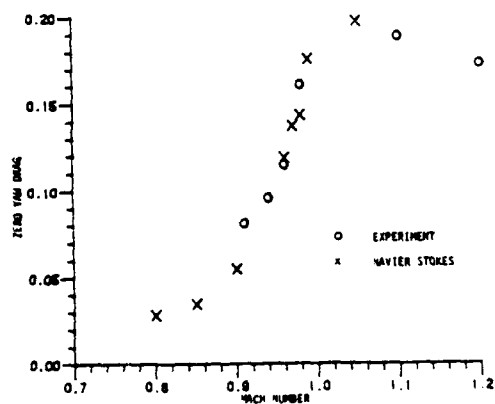
FIGURE 5. ZERO YAW DRAG FOR SOCBT, α = 0 THEORY AND EXPERIMENT

25

The dynamic stability of shell is one area of concern when designing new shell or modifying existing ones. The Magnus moment, which affects the dynamic stability, is a viscous phenomena. Therefore an accurate representation of the viscous portion of the flow field is crucial to computing the Magnus moment. As an initial attempt to look at the boundary layer in transonic flow, with its associated shock interaction, computations were performed at $M = 0.908$, $\alpha = 0°$ and comparison of computational velocity profiles with experimental profiles were made; an example of this comparison is shown in Figure 6. The Navier-Stokes result is the solid line and the circles are the experimental results. Although the computational and experimental velocity profiles are not in particularly good agreement, the shape of the computed profiles is seen to be characteristic of a turbulent boundary layer. A power law velocity profile, characteristic of turbulent flow, is included for comparison.

FIGURE 6   VELOCITY PROFILES AT X/D = 4.34

b.   Secant-Ogive Cylinder Boattail, $\alpha = 2°$

A new finite difference mesh consisting of 60 longitudinal points, 28 normal points and 20 points in the circumferential direction was designed for computations at angle of attack. Clustering of the longitudinal points was maintained in the vicinity of the expansion similar to the $\alpha = 0°$ cases. The computed leeward ($\phi = 0°$) surface pressure coefficients, as a function of longitudinal position are shown in Figure 7 compared to the experimental results. The computed results are shown to follow the same trend as the experimental data. The agreement in the vicinity of both expansions is quite good but falls off on the cylinder and boattail. A major problem in running 3-D computations is the large number of grid points required for adequate resolution. Increasing the number of longitudinal points, similar to the amount used for $\alpha = 0°$ (78 points) should result in better agreement.

26
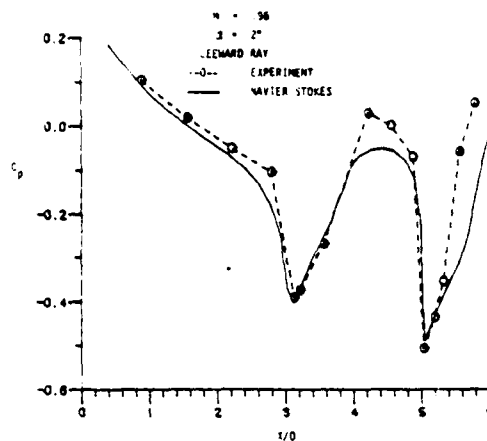
FIGURE 7. COMPARISON OF EXPERIMENTAL AND COMPUTATIONAL SURFACE PRESSURE COEFFICIENTS FOR SOCBT, $\alpha = 2°$

c. Hollow Projectile, $\alpha = 0°$

Of current interest in shell design is the utilization of hollow projectiles which have the characteristic of "flat" trajectories. A shape of this type, known as the ring airfoil, has been type classified and is currently used as an anti riot device. In order to demonstrate the general geometry capabilities of the Navier-Stokes codes, computations were performed for a ring airfoil shape at $\alpha = 0°$. A cross section of the actual shape is shown at the bottom of the C_p plot of Figure 8a. Inviscid results are presented in Figures 8a, b, c and d for M = 0.4, 0.7, 0.8 and 0.9. In all cases the pressure distribution is plotted for the internal and external surfaces using a solid line and dashed line respectively.

27
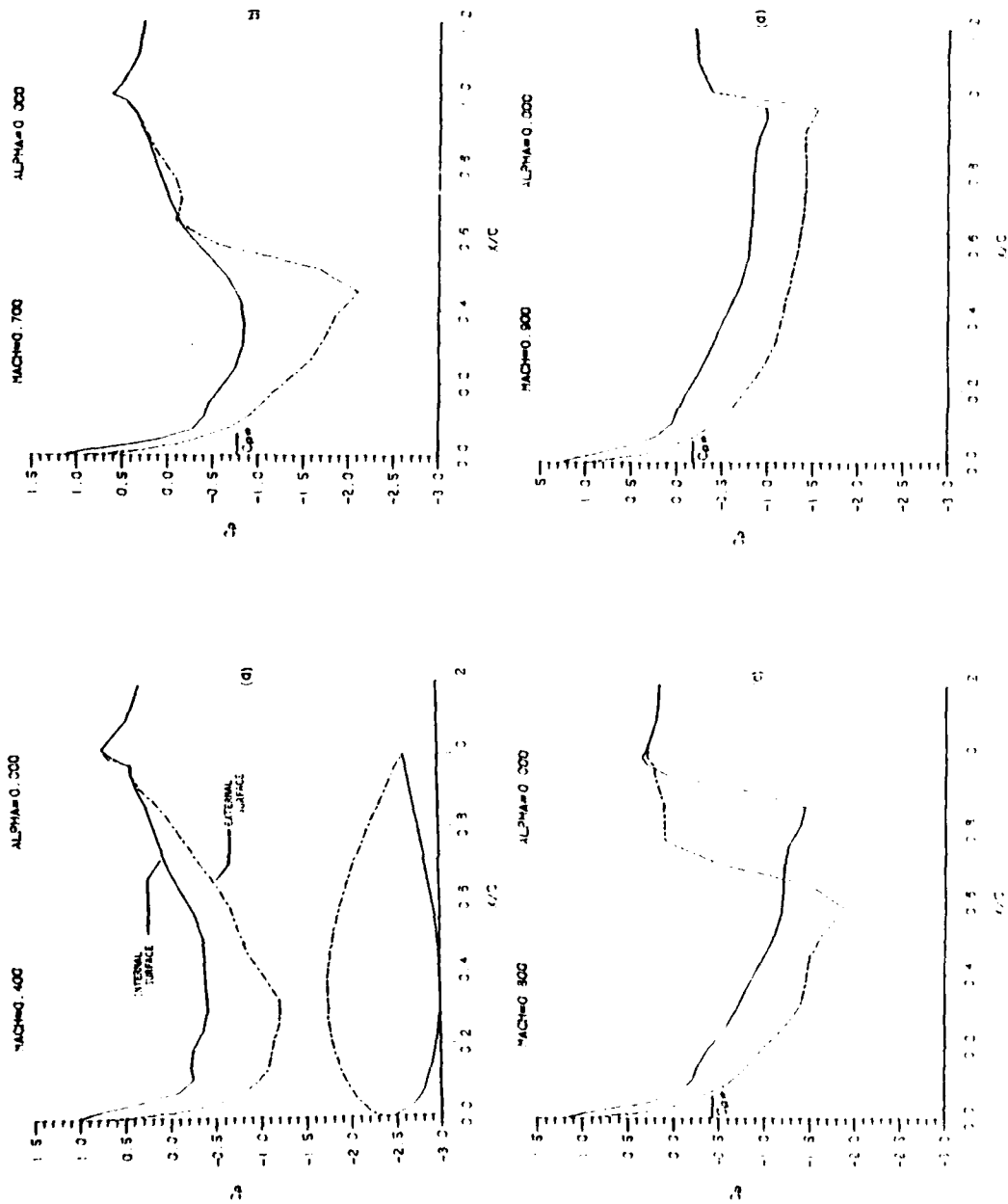
FIGURE 8. INVISCID TRANSONIC FLOW OVER A RING AIRFOIL PROJECTILE, M = .4 THRU M = .9

The critical pressure coefficient, C_p^*, is the value of the pressure coefficient at sonic velocity. The flow velocity in regions with pressure greater than C_p^* is subsonic and in regions where the pressure is less than C_p^* the flow is supersonic. For $M = 0.4$ (Figure 8a), all values of C_p are greater than C_p^* indicating the flow over both the internal and external surfaces is subsonic. However, as the Mach number is increased to 0.7, the upper surface is shown to develop supersonic flow and a shock wave while the internal flow remains subsonic. Increasing the Mach number still further to $M = 0.8$, the shock waves are now seen to exist on both the external and internal surfaces. A final solution at $M = 0.9$ shows that the shock wave has moved to the trailing edge indicating supersonic flow over most of the internal and external surfaces.

V. SUMMARY

Implicit finite difference methods have been used to solve the thin-layer Navier-Stokes equations. Both the three-dimensional and generalized axisymmetric equations have been presented and solutions of the flow field about projectile shapes have been obtained.

The computed surface pressure coefficients on the ogive-cylinder-boattail projectile were found to be in excellent agreement with the experimental data for $\alpha = 0°$. The generalized axisymmetric equations used for these computations are similar to the 2-D equations and thus have no severe limitation on the number of mesh points required for a good solution.

Computations for the same projectile shape at $\alpha = 2°$, using the 3-D equations, show good agreement with the experimental data. Computational experimentation indicate that improved agreement could be obtained with increased grid resolution.

Computations of the viscous boundary layer indicate the correct trend for a turbulent velocity profile which is critical to the determination of Magnus moment. Additional experimental velocity profiles are required to fully access the accuracy of the Navier-Stokes computations in the viscous region.

The general geometry capability of the numerical scheme was demonstrated by solving the inviscid flow field about a ring airfoil projectile. The ability to compute in regions of pure subsonic flow and mixed subsonic/supersonic flow has been demonstrated.

29

REFERENCES

1. W. B. Sturek, et al., "Computations of Magnus Effects for a Yawed, Spinning Body of Revolution", AIAA Journal, Vol. 16, No. 7, July 1978, pp. 687-692.

2. L. B. Schiff and W. B. Sturek, "Numerical Simulation of Steady Supersonic Flow Over Cone Ogive-Cylinder-Boattail Body, AIAA Paper No. 80-0066, January 14-16, 1980.

3. R. P. Reklis, W. B. Sturek and F. L. Bailey, "Computation of Transonic Flow Past Projectiles at Angle of Attack", U.S. Army ARRADCOM Technical Report, ARBRL-TR-02139, February 1979.

4. T. H. Pulliam and J. L. Steger, "On Implicit Finite-Difference Simulations of Three-Dimensional Flow", AIAA Paper No. 78-10, January 1978.

5. C. J. Nietubicz, T. H. Pulliam and J. L. Steger, "Numerical Solution of the Azimuthal-Invariant Thin-Layer Navier-Stokes Equations", AIAA Paper No. 79-0010, January 1979.

6. J. L. Steger, "Implicit Finite Difference Simulation of Flow About Arbitrary Geometrics With Application to Airfoils", AIAA Paper No. 77-665, June 1977.

7. B. S. Baldwin and H. Lomax, "Thin Layer Approximation and Algebraic Model for Separated Turbulent Flows", AIAA Paper No. 78-257, January 1978.

8. R. Beam and R. F. Warming, "An Implicit Factored Scheme for the Compressible Navier-Stokes Equations", AIAA Paper No. 77-645, June 1977.

9. W. J. Yanta and R. E. Lee, "Measurements of Mach 3 Turbulence Transport Properties on a Nozzle Wall", AIAA Journal, Vol. 14, No. 6, June 1976, pp. 725-729.

10. L. D. Kayser, W. J. Yanta and W. B. Sturek, "Measurements in the Turbulent Boundary Layer of a Yawed, Spinning Body of Revolution at Mach 3.0 with a Laser Velocimeter and Impact Probe", U.S. Army ARRADCOM Technical Report, ARBRL-TR-02074, May 1978.

LABORATORY INVESTIGATIONS OF BIOMEDICAL FACTORS
INFLUENCING LASER DESIGNATOR OPERATOR PERFORMANCE (U)

*PETER A. O'MARA, PhD, MAJ, MS
DAVID A. STAMPER, MA
EDWIN S. BEATRICE, MD, COL, MC
DAVID J. LUND, BS
LETTERMAN ARMY INSTITUTE OF RESEARCH
PRESIDIO OF SAN FRANCISCO, CA   94129

INTRODUCTION

Laser rangefinder-designators have been developed for use in various military operational environments. In a typical engagement, the rangefinder-designator is located at a known position overlooking the target coordinates. A laser-seeking missile or artillery round is fired at these coordinates. During the last several seconds of projectile flight time, the laser beam is directed to the target and the projectile is guided toward the reflected laser radiation.

In a tactical scenario, an enemy tank which is capable of sensing the laser irradiation, will turn and fire at the laser designator operator. Blast effects (flash/noise, over-pressure, dust, debris) and/or the psychological threat of the tank's response could disrupt the designator operator's performance to the extent that the missile or artillery projectile may miss its designated target. The U.S. Army is presently planning to train laser designator operators. Additional information is needed regarding environmental effects on operator performance and individual differences in performance capacities.

A field simulation laboratory has been constructed which will facilitate the controlled investigation of factors which may influence laser designator operations. The primary objectives in developing this laboratory were to obtain accurate low-cost on-line assessment of pursuit tracking performance under conditions where experimental variables could be precisely controlled. An attempt

was made to reproduce, in the laboratory, some of the conditions encountered in a field situation. The scenario which has been implemented consists of a sandbag bunker, desert terrain model, a viscous-mounted laser designator, scale-model targets, and a central control room.

Data have been collected in this simulator for comparison with normative data obtained under field conditions. During these studies, the effects of training, target angular velocity, and ambient lighting conditions were investigated. The results of these studies will be presented.

METHODS

Bunker. The sandbag bunker, which is consistent in design and construction to standard bunkers (1), is used to control the soldiers' working environment and to provide a degree of isolation from distractions occurring elsewhere in the laboratory. Light levels within the bunker are continuously adjustable by means of a solid-state controller located outside the bunker. The viewing port of the bunker opens into a large cone which restricts the view so that only the terrain model is visible from inside the bunker. The occupant's view of the terrain is further restricted to what one can see through the optics of the designator device.

The inside of the bunker is equipped with near infrared light sources and an infrared television (TV) to monitor the inside of the bunker under all lighting conditions. The bunker also contains overhead speakers which can be used to provide sound effects (e.g., blast effects of incoming projectiles). Two-way communication with the control room is provided. An instrumentation interface is provided to enable complete physiological monitoring of the occupant(s) of the bunker.

Terrain Model. The present terrain model (Fig 1) represents a desert environment but may be modified to simulate other opera-tional environments. The terrain model is 6 m wide and 4.8 m deep. The near portion of the terrain begins 1.5 m in front of the outside wall of the bunker. The platform supporting the terrain model has been elevated to a position slightly below the level of the bunker view port. An observer inside the bunker is, therefore, provided with a low-angle view of the terrain.

A dry river bed and several small hills are included as part of the natural features. The use of scaled landscape features was

32

avoided during terrain construction. Thus, targets of various scales may be employed without extensive modification of the terrain.

Figure 1. Scale model tank and simulated desert terrain.

Laser Designator. The optical tracking device was designed to reproduce the characteristics of a laser designator but does not include an active laser device. A unity power scanning scope is mounted in a fabricated metal box, which is affixed to a 500,000 centistoke viscous-damped traversing unit (Model 50 fluid head, O'Connor Engineering Laboratories). The damping character- istics of the mount can be adjusted to equal those of traversing units which are currently being considered for field deployment. Two rear-mounted handles (approximately shoulder-width apart) are used to aim the designator. The relatively close proximity of the target to the designator also requires that the mechanical response of the device be adjusted so that the effects of angular displacement

33

during tracking are matched to the simulated distances. A unique optical and mechanical compensating system was developed for this purpose. A 13-to-1 amplification of vertical and horizontal motion is obtained through use of levers which are linked to a moveable mirror located in the optical axis of the scanning scope. The line-of-sight rotates 13 times as fast as the mechanical rotation of the designator axis to simulate a 13-power optical system. This will provide the correct relationship between operator movement and displacement of the scope crosshairs on the target for any simulated engagement distance. The tracking device also contains an integral television camera. The camera line-of-sight is made colinear with the operator's line-of-sight by a dichroic mirror which reflects the far red spectrum to the camera and denies it from the operator's view. The output of the camera is used to provide a remote monitoring of the operator's field of view during tracking. These data are digitally processed to obtain tracking performance data. A strobe unit mounted in the optical train permits flash-effects studies to be performed.

Targets. The targets are scale-model tanks, available in 1/16 (Fig 1), 1/25, and 1/35 scale. Through appropriate selection of target scale and power of the designator simulator viewing optics, it has been possible to simulate various engagement ranges. The simulated range to the target is given by the expression:

$$R = \frac{Mr}{mS}$$

where,

R = range to be simulated in meters
M = power of the viewing optics of the designator to be simulated, i.e., 13 for this system
r = range to tank model in meters
m = power of the designator simulator optics
S = scale of the tank model

If one assumes that unity power optics are used in the simulator and that the target is located 5 m from the designator, then the simulated engagement distances are 1.040 km (1/16 scale), 1.625 km (1/25 scale), and 2.275 km (1/35 scale).

Control and Data Acquisition. A central control room contains the TV monitors, data acquisition and recording instruments, and computer equipment. The TV monitors are used for observing the laser designator operator, to observe the target and terrain model, and to

monitor the view obtained through the designator optics. A Heath H8 microcomputer is used to manipulate experimental conditions, to control target movement, and to provide acquisition and analysis of performance data. The H8 is equipped with a dual-drive floppy disk system, and a specially designed interface board which processes tracking performance data. Summaries of operator performance data are provided on-line by the computer and permanent records are stored on floppy disks. Statistical summaries are written to a lineprinter at the end of each tracking trial. Automation of the simulation increases system flexibility and efficiency and allows the collection and processing of large amounts of data at relatively low cost. As a result, many experiments can be conducted in a relatively short period of time.

Horizontal and vertical error amplitude data are derived from the video output of the TV camera housed within the designator. Processing of the video signal to obtain error data is simplified by providing a red light emitting diode (LED) as a point source of light on the target. This source is readily detected by the TV camera while entirely invisible to the designator operator. When the ratio of target spot to ambient illumination is sufficiently high, it is relatively easy to adjust the monitor sensitivity controls to obtain a single point corresponding to the target spot. Error amplitudes are measured as a deviation of the target spot from a point on the monitor display corresponding to the optical axis of the designator camera.

Inexpensive methods have been developed for automatically detecting high contrast targets which are present in video signal channels (2,3). In the simulator, this is accomplished by using the following procedures. First, a vertical position counter circuit is reset to zero whenever the camera vertical synchronization pulse is detected. This event corresponds to the initiation of the first of a new series of horizontal scans by the camera. Each line occupies a unique vertical position within the series of horizontal lines which make up the picture. A separate horizontal position counter is triggered whenever a horizontal synchronization pulse is encountered. This event coincides with the beginning of each left-to-right scan of the camera. Within a horizontal scan, each element of the picture is associated with a unique time delay. A threshold circuit is adjusted to switch on whenever the relatively bright target spot is detected by the camera electronics. At the same time, the cumulative vertical (line number) and horizontal (elapsed time) counts are saved for further processing. With this method, error amplitude values may be obtained at a rate of up to 60 observations per second. The resulting time series of error

observations may be subjected to statistical analysis in the time
or frequency domain. The stored horizontal and vertical counts are
algebraically compared with the predetermined values corresponding
to the optical axis of the designator in order to obtain separate
horizontal and vertical error scores. The series of aiming error
observations obtained during tracking trial are processed on-line
to obtain estimates of the mean errors, root mean square (RMS)
errors, the temporal location and magnitudes of maximum errors, and
a percent time-on-target (TOT) score. The relatively simple TOT
scores are derived by comparing the values of the pairs of vertical
and horizontal observations against boundary values stored by the
computer. The sensitivity of the TOT scores to tracking error can
be changed by reprogramming the boundary conditions. The quantita-
tively superior (4,5) RMS error scores are emphasized as the primary
criteria of tracking proficiency. The relatively less sensitive TOT
scores are mainly used to provide trial-by-trial feedback to the
operator. Within 30 sec of the end of each trial, a complete summary
of performance data is presented on the control room operator's video
terminal. Summary data are also written to a lineprinter. The
complete records of digitized horizontal and vertical aiming errors
are also recorded on floppy disk.

Validation Study

Subjects. The participants were 12 U. S. Army volunteers,
11 enlisted men and 1 officer. All volunteers received an extensive
eye examination and visual function evaluation to determine accepta-
bility. All individuals were emmetropic. The ages of the partici-
pants ranged from 22 to 38 years. None of the volunteers had
received previous training in use of a viscous-mounted laser-
designator type tracking device.

Simulator. In the present experiment, the body of an Athearn HO
model train engine was removed from the engine and frame and replaced
with a Leopard A4 1/35 plastic scale model tank chassis. This target
was mounted on a train track positioned in an arc 5.3 meters from the
laser designator mount. Power to the track was provided by three
model train transformers through a multiposition switch that allowed
for rapid change among the three velocities that were used. The
velocities were 2.5, 5.0, and 7.5 mrad/sec (at the simulated 2275 m
engagement distance these velocities were approximately equal to
11.2, 22.4, and 33.6 mph). The model was equipped with a clearly
visible aiming point, which consisted of a round black bullseye
located at the center of a square white field. The target patch,
as viewed through the designator optics, subtended a visual angle of

5.3 mrad. The corresponding traversing angle (the angular displacement of the designator when sweeping across the target) was 0.407 mrad.

The average terrain luminance, measured from the position of the designator objective lens, was 170 lm/m^2sr. The luminance reaching the eye was attenuated by the designator optics, which had a luminous transmittance of 10%. Low terrain luminance conditions were simulated by inserting a 2.5 OD neutral density attenuator in the designator optics but not in the TV camera line-of-sight. The apparent terrain luminance was thereby reduced to 0.54 lm/m^2sr. No light from the terrain passed into the bunker other than through the designator optics. The bunker light was turned off during the low-light tracking trials.

Procedure. When each soldier was asked to participate in the experiment, the nature of the research and all of the procedures were carefully explained and a volunteer consent statement was signed. An eye examination was given which included the Armed Forces Visual Acuity Test, Farnsworth Munsell 100-hue Color Vision Test, a dark adaptation test, undilated funduscopic examination, and a visual history. The color vision, acuity, and funduscopic examination were repeated after the experimental phase of the project. No test of oculomotor function was performed.

Each volunteer was given 30 training trials/day under the bright-light condition for 3 days (sessions 1, 2, and 3). During these sessions, 15 of the trials were run at 5.0 mrad/sec and 15 at 7.5 mrad/sec velocity.

Following the 90 training trials, 90 experimental trials were run (30 trials/day) that included 10 trials at each of three velocities (2.5, 5.0, and 7.5 mrad/sec). Each group of 10 trials were again divided such that 5 trials were performed under the bright-light condition and 5 under the low-light condition. The 15 trials under each light condition were combined, but the two light conditions were separated by a 10-minute rest period between trials 15 and 16. Five of the participants received the dark trials first and 7 received their light trials first. During the next two sessions, the order of the light/low-light conditions for each group was reversed from the previous day. The experimental sessions (i.e., 4, 5, and 6) were completed during the same 5-day work-week.

At the beginning of a session, the participant was seated in the bunker on sandbags which were adjusted for individual heights. If the first 15 trials were dark trials, the bunker light was turned off for 10 minutes to allow for partial dark adaptation to the

37

semi-darkened room. Following this, or if no dark adaptation was required (i.e., during the bright-light trials), at the command "ready" they would center the crosshairs of the designator on the target. At the command "go" the tank would begin an immediate right-to-left or left-to-right movement across the terrain. The total time of the track ranged from 10 to 12 seconds. Each trial was followed by a minimum delay of one minute, during which time the performance data were processed and summarized. Following this, the next trial would begin in the opposite direction.

Statistical Analyses. Separate analyses of variance (ANOVA) were computed for the analysis of the learning curve of the performance scores, including both RMS error and TOT scores, across all six sessions. For the evaluation of speed and light effects, horizontal RMS error and TOT scores for sessions 4, 5, and 6 (i.e., the experimental sessions) were also analyzed with separate ANOVA. The ANOVA were performed using Biomedical Computer Programs BMD-P2V for multifactorial mixed designs (6). The specific post hoc comparisons of significant findings were made using Newman-Keuls Tests (7). The 0.05 level was used for determining significances.

RESULTS AND DISCUSSION

Detailed summaries of the results of an evaluation of the microcomputer-controlled tracking error system, and the results of the tracking performace validation study, have been presented elsewhere (3,8). A brief summary of the results of the analyses of the horizontal RMS error data will be presented.

The effects of training on performance (Fig 2) across the three training sessions (1, 2, and 3) and the three experimental sessions (4, 5, and 6) are illustrated in Figure 2. These data were obtained during the bright-light condition only. The scores were the within session means ($\bar{X}$) of the 5.0 mrad/sec and the 7.5 mrad/sec velocity trials. The results of the ANOVA of the RMS error scores for the 5.0 and 7.5 mrad velocities indicated that there were significant repeated measure effects for both velocities. The post hoc comparisons showed, in general, a statistically significant imp ovement in performance when sessions 1 and 2 were compared with 3, 4, 5, and 6. However, with both velocities, despite the slight observable trend for continued improvement, no statistically significant differences were found when comparing the sessions subsequent to session 3. The means and standard errors of the means (SEM) of the X-axis and Y-axis RMS error data obtained during the last day of training were then compared to normative data provided by the U.S. Army Human Engineering Laboratory (9) (Fig 3). In this figure, the plotted boundary curve represents the ranges of tracking errors which would

38
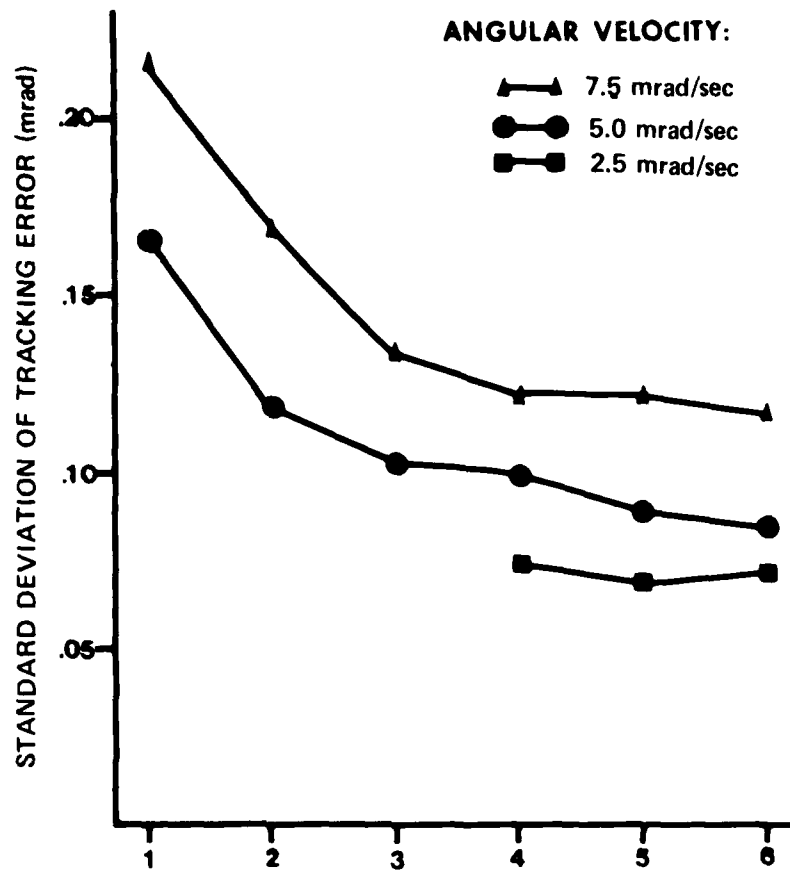
Figure 2. Horizontal error as a function of training and target velocity.

be expected when using the current generation of lightweight, viscous-damped tracking devices under field conditions. The plotted group means ± 2 SEM obtained during this study fall near the lower limits of the predicted range of tracking errors. The relatively precise tracking performance exhibited by participants in the laboratory study might be due to the less demanding environmental conditions (no wind, etc.), the degree of training received by the subjects in this study, and the mechanical characteristics of laboratory designator viscous mount.
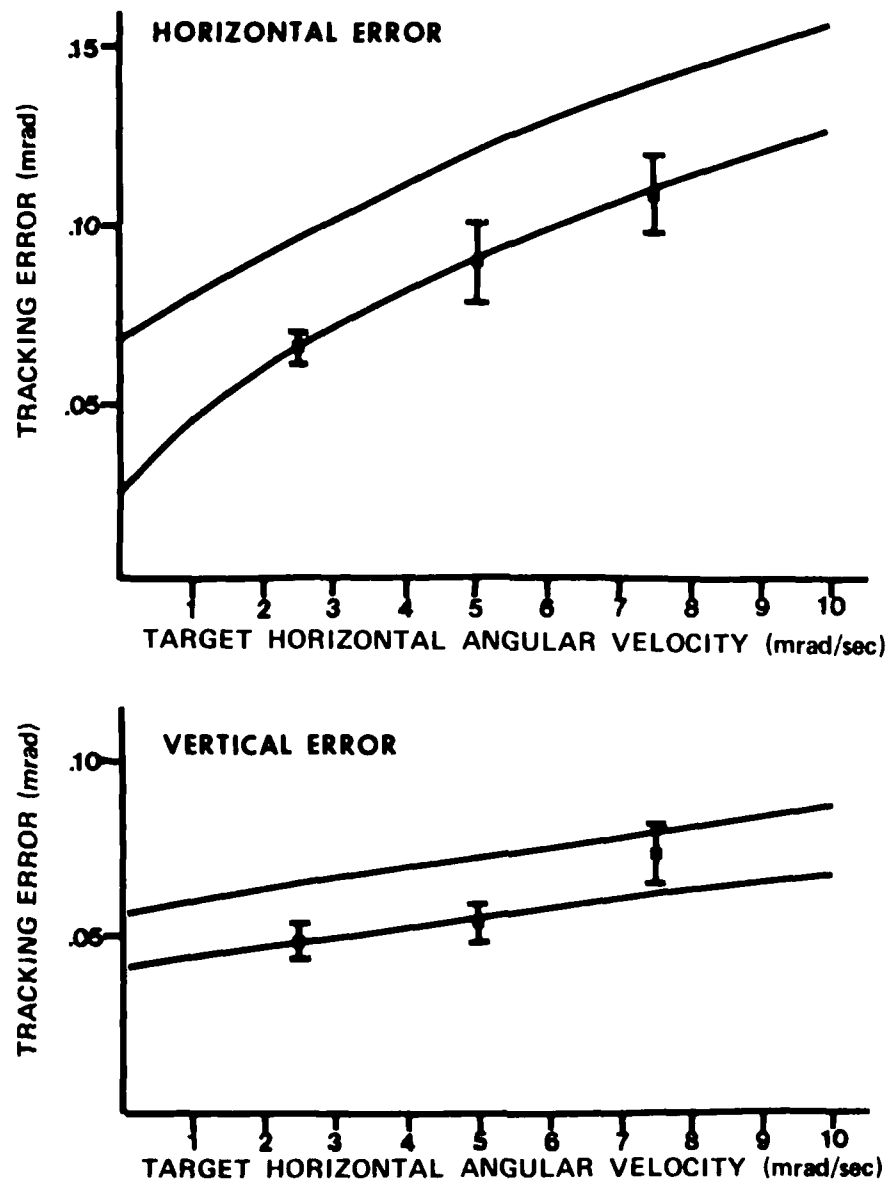
Figure 3. Predicted and observed tracking performance using the laboratory simulator.

The group mean horizontal RMS error scores obtained during sessions 4, 5, and 6 are presented in Figure 4. The results of the ANOVA of these data indicated that the effects of ambient light level, angular velocity sessions, and the interaction of angular velocity with light level were all significant. The post hoc comparisons of the differences between the bright-light and low-light conditions, at all velocities, during each session were significant. When specific comparisons of the velocity conditions were made, all 2.5 to 7.5 mrad/sec comparisons were significant. Additionally, 5 of the six 2.5 to 5.0 mrad/sec and 5.0 to 7.5 mrad/sec comparisons under the low-light condition were significant. However, under the bright-light conditions only 2 of these 6 comparisons were significant. Finally, the significant three-way interaction between sessions, light level, and target velocity can likely be attributed to changes in performance under the low-light conditions when tracking at the 2.5 and 7.5 mrad/sec velocities during these 3 sessions. The difference in horizontal RMS error between the bright-light and low-light condition was approximately 0.05 mrad at the 2.5 mrad/sec velocity, but increased to approximately 0.09 mrad for the 5.0 and 7.5 mrad/sec velocity conditions. The post hoc comparisons of these data, however, indicated that ambient light levels produced significant effects only for the 7.5 mrad/sec target velocity. The significant interaction of light level with angular velocity indicated that not only did error scores increase as velocity increased from 2.5 to 7.5 mrad/sec, but that this effect was even greater for 5.0 and 7.5 mrad/sec velocities under the low-light condition. The added difficulty of tracking under reduced illumination and the partial adaptation noted for the 7.5 mrad/sec velocity across the three experimental sessions emphasize the need to provide laser-designator operators with training under reduced illumination conditions.

PRESENT AND FUTURE RESEARCH

The simulator is now being used to study the effects of stroboscopic flashes on tracking performance. Flashes are presented alone or in combination with evasive target maneuvers while the operator tracks targets under bright or low-light viewing conditions. The results of these experiments indicate that such flashes are extremely disruptive. Future studies of countermeasures will use more complex stimuli (combined flash, noise, vibration, and target obscuration) and will include measures of the physiological response of the operator to these stressful conditions. The tracking performance of operators using various laser protective materials will also be studied in the simulation laboratory.
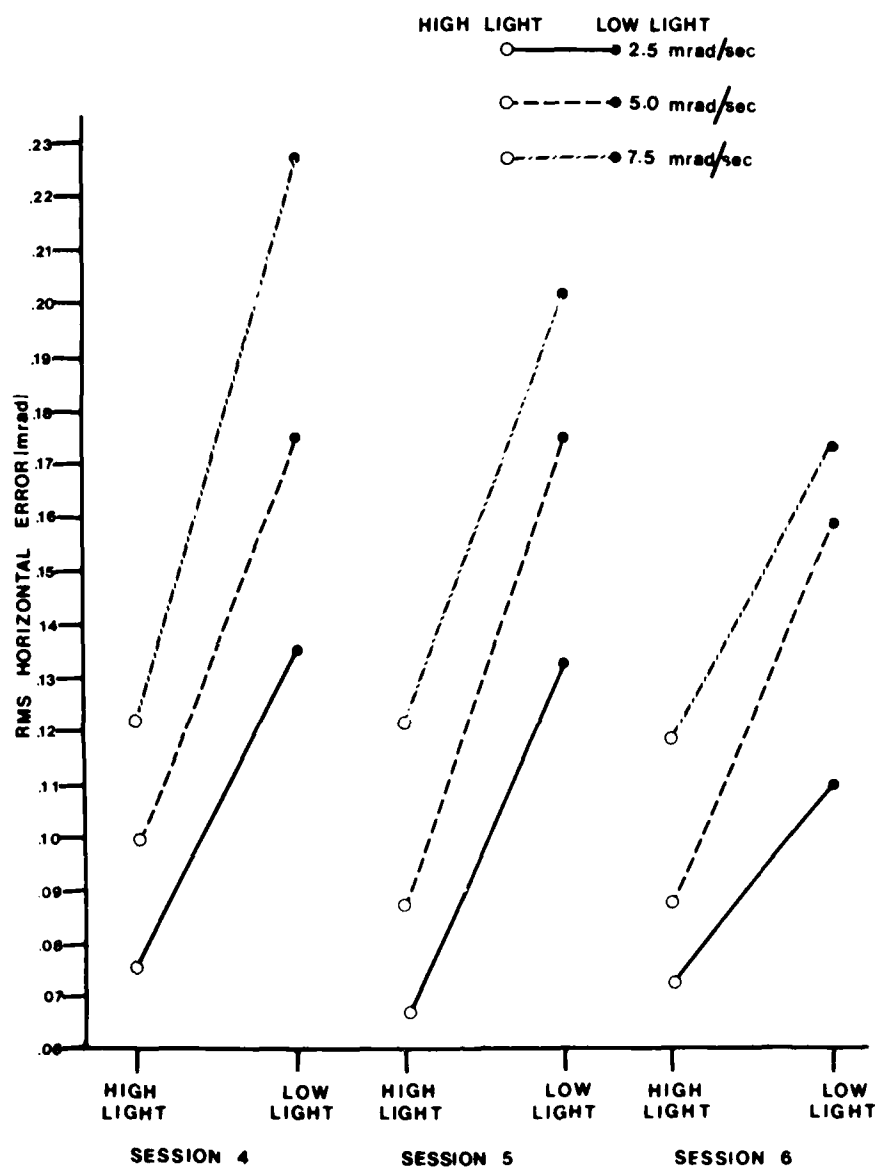
ure 4. RMS horizontal error scores for high-light and low-light trials at target velocities of 2.5, 5.0, and 7.5 mrad/sec.

CONCLUSIONS

The results of the preliminary studies indicate that the tracking performance data obtained with the use of the laboratory laser designator simulator are consistent with those obtained under field conditions in which prototype viscous-mounted laser designator devices are used. The methods and results outlined in this report demonstrate the feasibility of using relatively inexpensive microcomputer, laser, and video electronic systems to study human tracking performance in a laboratory situation where biomedical variables which influence soldier performance may be monitored under precisely controlled conditions. The data obtained through use of the simulator will be of value during the selection and training of designator operators and will provide information for use in developing means of protecting the operator from the effects of hazardous environments.

REFERENCES

1. DEPARTMENT OF THE ARMY. Field Manual, FM5-15. Field Fortifica-
   tions. Washington, DC: Headquarters, Department of the Army,
   27 June 1972

2. LUBINSKI, K.S., K.L. DICKSON, and J. CAIRNS, JR. Microprocessor-
   based interface converts video signals for object tracking. Com-
   putor Design 16:81, 1977

3. O'MARA, P.A., D.A. STAMPER, and D.J. LUND. A microcomputer-
   controlled video electronic system for measuring human pursuit
   tracking performance. (in preparation)

4. KELLEY, C.R. The measurement of tracking proficiency. Human
   Factors 11:43, 1969

5. POULTON, E.C. Tracking Skill and Manual Control. New York:
   Academic Press, 1974

6. DIXON, W.J. Biomedical Computer Programs. Los Angeles,
   California: University of California Press, 1975. pp 711-734

7. WEINER, B.J. Statistical Principles in Experimental Design.
   New York: McGraw-Hill Book Company, 1971

8. STAMPER, D.A., P.A. O'MARA, E. BEATRICE, and D.J. LUND.
   Tracking performance with a viscous-damped mount under simulated
   conditions of varied ambient light levels and target velocities.
   Institute Report No. 82. San Francisco, California: Letterman
   Army Institute of Research, January 1980

9. CHEEVER, H.L. Human tracking performance using lightweight
   viscous-damped mounts. Technical Memorandum 27-77. Aberdeen
   Proving Ground, Maryland: U.S. Army Human Engineering
   Laboratory, September, 1977

EFFECTS OF LOW POWER MICROWAVES ON THE LOCAL
CEREBRAL BLOOD FLOW OF CONSCIOUS RATS

KENNETH J. OSCAR, Ph.D.
US ARMY MOBILITY EQUIPMENT RESEARCH AND DEVELOPMENT COMMAND
FORT BELVOIR, VIRGINIA 22060

Background

Camouflage, decoy and deception techniques can play a decisive role on the modern battlefield. The rapid advance of surveillance, targeting and weapons homing sensor technology now makes every element which is detected almost assured of being destroyed. Camouflage, decoy and deception equipment and techniques are a low cost way to increase survivability and shift this balance by reducing the signature of targets (camouflage), increasing the signature level of the background (clutter), creating false targets (decoy), and distorting the perceived target value (disguise).

One decoy and deception concept presently being considered is to remotely create the perception of noise in the heads of personnel by exposing them to low power, pulsed microwaves. When people are illuminated with properly modulated low power microwaves the sensation is reported as a buzzing, clicking, or hissing which seems to originate (regardless of the person's position in the field) within or just behind the head (1). The phenomena occurs at average power densities as low as microwatts per square centimeter with carrier frequencies from 0.4 to 3.0 GHz. By proper choice of pulse characteristics, intelligible speech may be created. Before this technique may be extended and used for military applications, an understanding of the basic principles must be developed. Such an understanding is not only required to optimize the use of the concept for camouflage, decoy and deception operations but is required to properly assess safety factors of such microwave exposure.

Under MERADCOM's In-House Laboratory Independent Research (ILIR) Program an experimental effort to explore the basic interaction between microwaves and brain function has been conducted. In a joint program with MERADCOM, Stanford Research Institute (SRI) and Walter Reed Army Institute of Research (WRAIR), it was shown for the first time that lethality, seisures and behavioral performance decrements were stongiy frequency and polarization dependent (2,3). A later colaboration between MERADCOM and WRAIR demonstrated for the first time increases in the differential uptake of saccharides to water in several brain regions of rats when exposed to low power microwaves of the same characteristics which can create the perception of noise in people (4). These increases could be caused by alterations of the blood-brain barrier, brain blood volume, cerebral blood flow, or some combination of the above. In order to better define and understand these results a joint program was undertaken with MERADCOM, Naval Medical Research Institute (NMRI) and the National Institutes of Health (NIH) to measure local cerebral blood flow in conscious rats when exposed to low power, pulsed microwaves. It is these experiments which will be reported here.

Introduction

Recent experiments indicating that low power microwaves may affect brain activity and possibly alter central nervous system function have caused wide spread concern regarding the safety of such exposure. Seemingly conflicting experimental results, difficulties in extrapollating animal findings to humans, problems of dosimetry, and misunderstanding over what constitutes an effect versus a hazard have created a controversy in the area of microwave safety (5). Of particular concern have been recent reports, from several different laboratories (4, 6-9), that low power microwaves may alter the permeability of the blood-brain barrier (BBB). Several of the techniques (10,11) used to measure BBB permeability depend on constant blood flow during the experiment. We now report for the first time that microwave exposure increases local cerebral blood flow (LCBF) in the conscious rat an ' suggest that previously reported BBB permeability changes (4), may be less in magnitude than originally indicated.

Development of the in vivo ^{14}C-2- deoxyglucose technique (12, 13) as a measure of glucose consumption and the in vivo ^{14}C- iodoantipyrine technique (14) as a measure of LCBF have resulted in experiments (15) yielding convincing evidence that local blood flow is regulated by the metabolic activity of that region. Further experiments (16,17) have led to the demonstration that brain functional activity, sensory stimulation, cerebral temperature, biochemical

balance, blood volume, metabolism, BBB permeability, and blood flow
are coupled. Microwave exposure has been experimentally shown to
affect all of these parameters except LCBF. Humans and small animals
can perceive microwaves as auditory sensations (18). Microwave and
very high frequency (VHF) energy have influenced spontaneous and
conditioned electroencephalographic patterns in cats, rabbits, and
rats (19-21). Low-level pulsed and continuous wave (CW) microwaves
have altered glucose consumption in the auditory structures of rat
brain (22). Low intensity microwaves have caused thyroid suppression
and adrenomdullary activation (23). Microwaves have also been repor-
ted to affect behavior (24-28), neurotransmitter levels (29), BBB per-
meability (4,6-9) cerebral calcium efflux (30,31) and behavioral base-
lines to pharmacological agents (32). It seemed a reasonable hypo-
thesis then that microwaves would alter brain blood flow. If so, the
measurement of LCBF in the conscious animal would provide a valuable
technique to map the regional influence of microwaves and lead to a
better understanding of microwave safety factors and general brain
function.

Materials and Methods

In 1955 the first method (33,34) for quantitative determina-
tion of the rates of blood flow in discrete brain structures was
reported; the method employed the radioactive gas tracer ^{131}I-trifluo-
riodomethane along with the principles of inert gas exchange. This
radioactive gas was chosen because diffusional equilibrium between
brain and blood is established almost instantaneously when it is ad-
ministered. Two technical problems are encountered in the use of this
technique of a volatile gas tracer: short half life and difficult
assay. To overcome these problems, investigators have used ^{14}C-anti-
pyrine as a nongaseous tracer; however, it provides values of local
cerebral blood flow that are considerably below those obtained with
radioactive gases (35,26). In addition, transfer of antipyrine from
blood to brain is limited by its comparatively low diffusion at the
cerebral vasculature. Recently, a new method has been developed that
uses ^{14}C-iodoantipyrine and an audioradiographic assay (37). The ^{14}C-
iodoantipyrine has a higher oil/water partition coefficient than
^{14}C-antipyrine, is more permeable at the cerbrovasculature, and pro-
vides values of local cerebral blood flow that are comparable to those
obtained with ^{131}I-trifluoriodomethane.

The present blood flow experiments were performed with
^{14}C-iodoantipyrine measured by brain homogenization and liquid scintil-
lation counting (38). Although scintillation counting does not give
the structural resolution of audioradiography and densitometry, it is
repeatable, fast, quantitative, and technically easier. Male Wistar

rats from the Walter Reed colony were provided food and water ad libitum until they had grown to a body weight of 250-320g. All animals were prepared for the experiments by insertion of polyethylene catheters into one femoral artery and vein under sodium pentobarbital (35 mg/Kg, i.p.) anesthesia. After surgical preparation, the hindquarters were wrapped in a loose-fitting plaster cast and secured to a styrofoam block. The animals were allowed to recover from anethesia for 4 hours or more before the experiment. Conscious rats could freely move their forequarters, head and neck, and appeared comfortable.

The rats were selected randomly and individually exposed for 5, 30, or 60 minutes to sham irradiation (controls) or for 5, 15, 30, 45, or 60 minutes to pulsed microwaves of 15mW/cm^2 average power density. A microwave anechoic chamber (2m wide by 3m high by 3m long) maintained at 23 ± 2°C was used for exposure. This chamber also aided in the reduction and standardization of possible background noise stimulation. All microwave exposures were at a frequency of 2.8 gHz, a pulse rate of 500 pps, and a pulse width 2µ sec. Exposures were produced by a 40KW pulsed microwave generator (Applied Microwave Lab., PH40) coupled to a standard gain horn. The field intensity was measured with a field intensity meter (National Bureau of Standards) and an isotropic radiation monitor (Narda Model-8300). Overall accuracy of reported average power density measurements is estimated to be better than $\pm$ 25%.

Within 5 min after sham or microwave exposure, the catheter in the femoral vein was connected to a 5-ml syringe, which was mounted in a constant-flow pump (model 341, Sage Instruments) and set to deliver at a rate of 0.78 ml min^{-1}. The femoral vein was then infused for 50 s with isotonic saline containing 5µC/ml of ^{14}C-iodoantipyrine (New England Nuclear, specific activity = 50 mC/mmol). Periodically during infusion, 20µl samples of arterial blood were collected into heparinized vials. The rats were decapitated 50 seconds after infusion. Brain regions were dissected out according to the method of Chiueh et al, (39,40) placed in tared scintillation vials, and weighed. The tissue and whole blood samples were dissolved and subjected to routine liquid scintillation counting (Beckman, LS-9000).

Local cerebral blood flow, F, was calculated from the equation first derived by Kety (33,34):

$$C_{brain}(T) = mF \int_0^T C_{blood}(t) \, e^{-mF(T-t)/\lambda} dt$$

where C_{brain} (T) equals the tracer concentration (dpm/g) in the brain
parenchyma (excluding intravascular concentration) at time T; m is a
constant between 0 and 1 that represents the extent to which diffu-
sional equilibrium between the tissue and blood is reached (for
iodoantipyrine m=1); Cblood (t) equals the tracer concentration (dpm/
ml) in the arterial blood as a function of time; λ equals the steady
state, tissue: blood partition co-efficient (0.8 for iodoantipyrine);
t equals the variable time; and T equals the time from initial infu-
sion to decapitation. Cbrain (t), which represents intraparenchymal
brain concentration of tracer, was obtained by subtracting intravascu-
lar from net regional radioactivity when the former quantity was
taken as the product of regional blood volume and blood concentrate
at time T.

Results and Discussion

The results of the present study indicate that low-power
pulsed microwave exposure increases the LCBF in the conscious rat.
By 60 minutes of exposure, the blood flow in all 17 brain regions
sampled increased a minimum Of 39% with many increasing well over
100%. The calculated values of blood flow for all exposures are
presented in Table 1. The LCBF values for the control animals sub-
jected to either 5, 30 or 60 minutes of sham exposure were unchanged
and are combined in the table. In six regions both the left and
right brain structures were individually sampled. No left right
differences were observed, and after statistical testing these data
were pooled and denoted as " P " in the table. The first brain re-
gion affected, after only 5 minutes of microwave exposure, was the
inferior colliculus. The largest blood flow increases occurred after
60 minutes of microwave exposure and were in the pineal, pituitary,
temporal cortex, inferior colliculus, lateral geniculate, medial
geniculate.

The LCBF values of the control animals varied from 0.86 to
1.84 $cm^3 g^{-1} min^{-1}$ and are in close agreement with those in the recent
literature. In the conscious rat, the values of LCBF are higher in the
visual, auditory, and sensorimotor areas due to normal external stimu-
lation of these systems. The increased LCBF values after short time
microwave exposure, 5 to 30 minutes, occurred in these same sensory
regions and suggest along with experiments of Wislon et al (22) indi-
cating microwave induced glucose consumption changes in these re-
gions, that microwaves are increasing the metabolic activity through
direct or indirect excitation of brain tissue. After longer microwave
exposure, 60 minutes, all the sampled brain regions displayed large
LCBF increases of a magnitude which suggest a gross alteration of

49

Table 1 Effect of Microwave Exposure on Local Cerebral Blood Flow in the Conscious Rat

Tissue	Sham Exposure (7) 5, 30, or 60 min.	15 mW/Cm² Microwave Exposure				
		5 min(5)	15 min(8)	30 min(3)	45 min(7)	60 min(7)
Pineal	1.33+0.16	1.35+0.48	2.01+0.28	2.51+0.38≠	3.65+0.53*	5.21+0.30*
Pit	1.16+0.15	1.27+0.09	1.50+0.10+	1.75+0.33+	1.70+0.10+	2.06+0.24*
Hypo	1.40+0.18	1.28+0.09	1.41+0.08	1.61+0.05	1.54+0.07	2.00+0.08*
Temp,P	1.84+0.16	1.78+0.14	1.96+0.14	2.52+0.34+	2.92+0.20*	3.26+0.36*
Cereb	1.27+0.15	1.32+0.13	1.21+0.06	1.31+0.09	1.29+0.05	1.76+0.08≠
White	0.86+0.07	1.00+0.04	0.91+0.06	0.90+0.15	1.02+0.06	1.58+0.15*
Visual, P	1.80+0.13	1.95+0.09	2.04+0.12	2.07+0.23	2.13+0.12+	3.42+0.23*
SC,P	1.64+0.18	1.69+0.07	1.75+0.08	1.90+0.18	1.90+0.08	2.82+0.21*
IC,P	1.82+0.09	2.23+0.10*	2.43+0.16*	2.65+0.25*	2.64+0.05*	4.37+0.30*
LG,P	1.39+0.13	1.41+0.10	1.55+0.13	1.69+0.10	1.83+0.07*	3.79+0.43*
MG,P	1.47+0.15	1.35+0.09	1.75+0.11	1.68+0.10	1.84+0.09≠	3.24+0.29*

Local cerebral blood flow values are the means +S.E.M. in $cm^3g^{-1}min^{-1}$ from the measurements made on the number of animals in parenthesis. The LCBF values for the control animals subjected to either 5, 30, or 60 minutes of sham exposure were unchanged and after statistical testing are combined in the table. In several cases both left and right brain regions were individually measured yielding double the number of samples as indicated in the parenthesis. After statistical testing these data were pooled and denoted in the table as "P". Statistical significance was calculated first by brain region for all exposure conditions with a one way analysis of variance then for individual exposure conditions by a student's t-test. (Differs significantly from sham mean +p<0.05, ≠P<0.01, and *P<0.005). Pit is pituitary, Hypo is hypothalamus, temp is grey matter in the temporal region, SC is the superior colliculus, IC is the inferior colliculus, LG is Lateral geniculate, and MG is medial geniculate.

50

brain function due possibly to stress from microwave induced temperature rise, fatigue, brain stimulation, biochemical imbalance, neurotransmitter release, etc.

One area impacted by these results is the selection of techniques to quantitatively measure the affects of microwaves on BBB permeability. The dual indicator techniques of Oldendorf or Crone use either highly diffusible or relatively non diffusible internal standards and rely on constant circulatory flux during the experiment. Most previous studies reporting BBB permeability changes due to microwave exposure used protein bound markers and observation with optical, fluorescent, or electron microscopy. The one study, (4), reporting quantitative measurement of microwave induced BBB permeability increases used the Oldendorf technique with tritiated water as the internal standard. It has been subsequently found that water does not freely equilibriate in the brain, and as cerbral blood flow increases, water's diffusion is lowered, (44). Since the Oldendorf technique measures the ratio of a test substance to the internal standard, as blood flow increases and causes the brain tissue level of water to decrease, the reported ratio measurements of BBB permeability may be overly high. The small BBB permeability increases which do seem to exist from microwave exposure, as evidenced by microscopy studies, may be a secondary effect caused by microwave alterations of blood flow, blood pressure, and/or blood vessel area.

Our present experiments demonstrating microwave induced LCBF increases indicate an alteration of brain activity. The mechanism of this, and other mentioned microwave effects on brain function are unclear; direct or indirect stimulation of central or peripheral receptors by microwave induced thermal, mechanical or electrical disturbances are possibilities.

References

1. Frey, A.H., Messenger, R. and Eichert, E., National Technical Information Service, Doc. No. AD747684 (1972).

2. Hawkins, T.D., Grove, H.M., Heiple, T.W., and Schrot, J., National Technical Information Service, Doc. No. AD758136 (1973).

3. Polson, P., Jones, D.C.L., Karp, A, and Krebs, J.S., National Technical Information Service, Doc. No. AD774823 (1974).

4. Oscar, K.J. and Hawkins, T.D., Brain Research 126, 281-292 (1977).

5. Justesen, D.R., IEEE Spectrum 16, 67-68 (1979).

6. Albert, E.N., Radio Sci.14 (in the press).

7. Frey, A.H., Feld, S.R., & Frey, B. Ann.N.Y. Acad. Sci. 247, 433-439 (1975).

8. Merritt, J.H., Mitchell, J.C. & Chambers A.F. 1977 ECAC Conference on Undesirable Electromagnetic Effects, Annapolis, MD.

9. Sutton, C.H., Nunnally, R.L. & Carrol, F.B. Cytobiology 10, 513 (1973).

10. Oldendorf, W.H., Brain Res. 24, 372-375 (1970).

11. Crone, C. Acta Physiol. Scand. 58, 292-305 (1963).

12. Kennedy, C., Des Rosiers, M.H.J.W., Revich, M., Sharp, F. & Sokoloff, L., Science 187, 850-853 (1975).

13. Sokoloff, L., Revich, M. Kennedy, C., Des Rosiers, M.H., Patlak, C.S., Pettigrew, K.D., Sakurada, O., & Shinohara, M., J Neurochem 28, 897-916 (1977).

14. Sakurada, O., Kennedy, C., Jehle J., Brown I.D., Carbin G.L. & Sokoloff, L. Am. J. Physiol 243, H59-H66 (1978).

15. Reivich, N. in Brain Dysfunction in Metabolic Disorders (ed F. Plum Res. Publ. Assoc. Mev. Ment. Dis) 125-140 (Raven Press, NY, 1974).

16. Rapoport, S.I. Blood-Brain Barrier in Physiology and Medicin (Raven Press, NY 1977).

17. Blasberg, R.G. Nat'l Cancer Inst, Monogr 46, 19-27 (1977).

18. Frey, A.H. & Messenger, R. Science 181, 356-358 (1973).

19. Bawin, S.M., Gavalas-Medici, R.J. & Adey, W.R. Brain Res. 58, 365-384 (1973).

20. Goldstein, L. & Sisko, Z. in Biologic Effects and Health Hazards of Microwave Radiation (ed. Czerski, P.) 128-133 (Medical Pub. Warsaw, Poland, 1974).

21. Servantie, B., A.M. & Etienne, J. Ann.N.Y. Acad. Sci. 247, 82-86 (1975).

22. Wilson, B.S., Zook, J.M. Joines, W.T. & Casseday, J.H., Brain Res. (in the press).

23. Parker, L.N. Am. J. Physiol. 224, 1388-1390 (1973).

24. D'Andrea, J.A. Gandhi, O.P. & Lords, J.L. Radio Sci. 12, 251-256 (1977).

25. Frey, A.H., & Feld, S.R. J. Comp. Physiol. Phychol. 89, 183-188 (1975).

26. Mitchell, D.S. Switzer, W.G. & Bronaugh, E.L. Radio Sci. 12, 263-271 (1977).

27. King, N.W. Justesen, D.R., & Clarke, R.L. Science 172, 398-401 (1977).

28. Thomas, J.R., Finch, E.D., Fulk, D.W. & Burch, L.S. Ann. N.Y. Acad. Sci. 247, 425-432 (1975).

29. Merritt, J.H., Hartzell, R.H. & Frazer, J.W.. 1975 USNC/NRSI Meeting, Boulder, Colo.

30. Bawin, S.M., Kaczmarek, L.K. Adey, W.R. Ann. N.Y. Acad. Sci. 247, 74-81 (1977).

31. Blackman, C.F., Elder, J.A., Weil, C.M. Benane, S.G. & Eichinger, D.C. Radio Sci. 14, (in the press).

32. Thomas, J.R., Burch, L.S. & Yeandle, S.S. Science 203, 1357-1358 (1979).

33. Kety, S.S. Pharmacol. Rev. 3 1-41 (1951).

34. Kety, S.S. Methods Med. Res. 8, 228-236 (1960).

35. Eckman, W.W., Phair, R.D., Fenstermacher, J.D., Patlak, C.S., Kennedy, C. and Sokoloff, L., Am J. Physiol 229, 215-221 (1975).

36. Eklod, B., Lassen, N.A., Nilsson L., Norberg, K. and Siesjo, B.K. Acta. Physiol. Scand. 88, 587-589 (1973).

37. Sakurada, O., Kennedy, C., Jehle, J. Brown, J.D. Carbin, G.L., and Sokoloff, L. Am. J. Physiol. 234, H59-H66 (1978).

38. Ohno, K. Pettigrew, K.D. and Rapport, S.I. (in the press).

39. Chiueh, C.C., Sun C.L., Kopin I.J., Fredricks, W.R. & Rapoport, S.I., Stroke 10, 62-74 (1979).

40. Chiueh, C.C., Sun C.L., Kopin I.J., Fredricks, W.R. & Rapoport, S.I., Brain Res. 145, 291-301 (1978).

41. The opinions and assertions contained herein are the private ones of the writers and are not to be construed as official or reflecting the views of the Department of Defense. The experiments reported herein were conducted according to the principles set forth in the "Guide for the care and use of laboratory animals", Institute of Laboratory Resources, National Research Council, DHEW, Pub. No (NIH) 78-23.

MOLECULAR LEVEL MODELING OF THE MECHANISM OF
SHOCK INITIATION OF SOLID EXPLOSIVES (U)

F. J. OWENS, PH.D
US ARMY ARMAMENT RESEARCH & DEVELOPMENT COMMAND
LARGE CALIBER WEAPON SYSTEMS LABORATORY
ENERGETIC MATERIALS DIVISION
DOVER NJ   07801

INTRODUCTION: The ability to control the initiation of
explosives is essential to both military and civilian use of the
materials.   Control in the past has been exercised by empirical
reformulation of composition in order to adjust sensitivity.   There
is at present little fundamental understanding on the molecular level
of the phenomena of shock initiation, a situation which can only have
a detrimental effect on the possibility of attainment of finely con-
trollable insensitive high explosives.

Since explosion is a chemical reaction and because the
quantum theory has made abundantly clear that the reactive properties
of a material are determined by the vibrational and electronic struc-
ture of the constitutent molecules or atoms of the substance, under-
standing of initiation to detonation will only emerge by approaching
the problem on a fundamental molecular level.   An important objective
of such an approach would be the establishment of a relationship
between the useful properties of explosives such as sensitivity and
yield and their molecular properties.

This work represents an attempt to consider on a fundamental
level how shock or impact can cause chemical reactions in certain
solids in order to gain insight into the factors which determine sen-
sitivity to explosion.

GENERAL MODEL: A detonation is a high rate, self-sustaining
exothermic chemical reaction.   One plausible model for the process
envisions the shock pulse breaking intramolecular bonds of the con-
stituent   molecules   of   the   solid   explosive   producing   reactive

fragments such as radicals. Since this step is endothermic, the necessary exothermic reactions are viewed to be among the secondary products created by the shock pulse. Detonation is achieved when a sufficient number of these products are present in order that enough energy is liberated to cause further reaction enabling the process to become self-sustaining. The first evidence that the initial step is endothermic and requires a build up of secondary products has previously been described by this author and collaborators (1,2). Solid explosives were subjected to shock pulses less than necessary to cause initiation to detonation and examined by electron paramagnetic resonance and x-ray photoelectron spectroscopy. The results showed definitively that a preliminary build up of radicals occurred and specifically identified the bonds broken. In the case of triamino trinitrobenzene (TATB) and 1,3,5 trinitro-1,3,5 triazacyclohexane (RDX), NO_2 was severed from the ring of the molecule. In ammonium nitrate (AN) the NH_4^+ ion was observed to decompose by shock.

This paper is concerned with understanding on a molecular level how a shock pulse causes high rate chemical reactions in explosive solids. There are two general ways a shock pulse can break a bond of a molecule in a solid. One process can be characterized as thermal, where the temperature generated by shock compression of lattice is the parameter which determines the reaction. The lattice heat is transferred to the molecules of the material causing bonds of the molecules to break. More recently the idea has been considered that the chemistry is a result of mechanical processes (3). Because of abrupt changes in potential molecules are removed from their lattice site colliding with nearest neighbors causing molecules to dissociate. To some extent, as will be seen below, when specific mechanisms are considered this distinction between thermal and mechanical is artificial. Indeed examination of available macroscopic experimental data for secondary explosives suggests the chemistry induced by the shock pulse is a result of heat generated by shock compression. Inhomogeneous explosives, where the temperature rise is greater for a given shock pressure, are much more sensitive to shock than homogeneous single crystals. Also, as shown in Figure 1, there is a correlation between impact sensitivity and thermal sensitivity. Thermal intiation of explosion is generally understood in terms of the heat conduction equation

$$\rho C \frac{\partial T}{\partial t} = \tau \nabla^2 T = Q \, N \, K \qquad (1)$$

T being temperature, C the specific heat, ρ the density, τ thermal conductivity, Q heat of reaction, and K rate of reaction. The solution of the equation predicts a time delay, τ, at given temperature
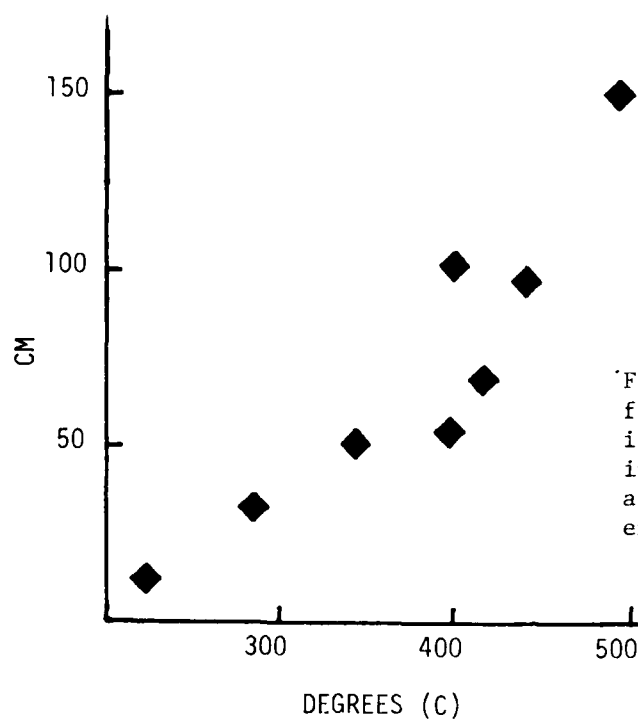
FIGURE 1. Impact height for initiation to detonation versus five second initiation temperature for a number of secondary explosives.

FIGURE 2. Schematic diagram of total ground state energy of RDX molecule versus separation between the ring and an NO_2 group.

57
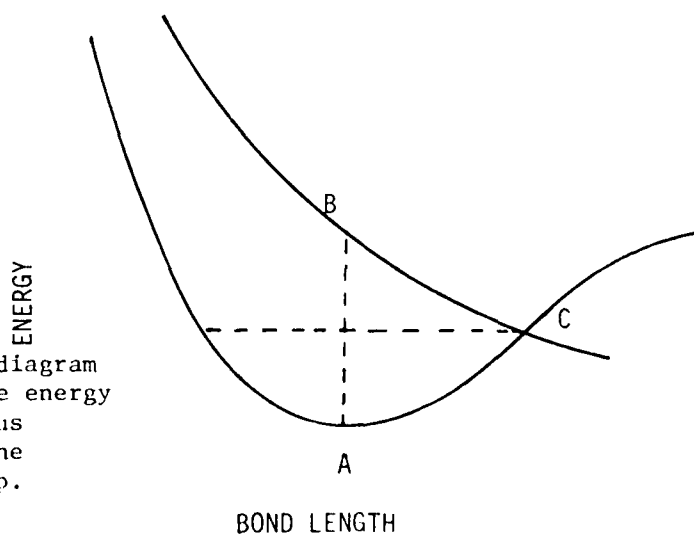
from the time the temperature is turned on to explosion. This delay time depends on temperature.

$$\tau = Ce^{-E/kT} \qquad (2)$$

Numerous measurements of delay times have been recorded and the data is described by equation (2). More recently delay times have been measured after application of shock pulses needed to detonate single crystals of RDX and PETN (4). This data is shown in Table I. These delay times after application of shock are predicted from thermal explosion theory by extrapolation of thermal delay time data described by equation (2) to the temperatures calculated at the critical shock pressure. This suggests that the reactions of shock initiation are indeed the same as thermal initiation.

Table I. Results of Measurement of Time to Detonation
After Application of Shock Pulse of Peak
Pressure Equal to Critical Pressure in
Single Crystals of Explosive Solids[*]

Explosive	Critical Pressure (Kbs)	Time to Explosion (S-1)
PETN	112	3×10^{-7}
RDX	170	1×10^{-6}
Tetryl	150	1×10^{-6}
TNT	200	7×10^{-7}

[*]Ref 4

The activation energies for thermal initiation deduced from equation (2) do not in general agree with activation energies measured from slow thermal decomposition experiments indicating that in the temperature regime of initiation different chemical reactions may be dominant than at lower temperatures. This result is also true of shock induced chemical reactions. Experiments in this laboratory which have identified the bonds broken by shock have shown that different bonds were broken in slow thermal decomposition (1,2). For example, in TNT heating to temperatues below initiation temperatures removes one oxygen of the nitro group whereas a shock pulse

appeared to alter the oxygen-hydrogen bonding on the molecule. The evidence then is that in secondary explosives the shock induced reactions are a result of heating of the lattice. However, the reactions are not necessarily the same as reactions measured at temperatures below initiation temperatures. Thus, it appears that shock induced chemical reaction is a thermal process and that the temperature generated by the shock pulse is the most important parameter in determining the reaction rate.

The work here considers possible ways a chemical reaction can occur in a crystal lattice with particular emphasis on shock induced chemical reactions. The work considers specific plausible molecular mechanisms for shock induced reactions in solids and calculates reaction rates in order to assess the feasibility of the mechanisms in initiation of detonation.

In order for an intramolecular bond to break, heat or mechanical energy of the shock pulse which is absorbed by the lattice must be transferred to the molecules. This "energization" of the molecule can occur by either an excitation of an electronic or vibrational state of the molecule. The energy states of the molecule in the short time of the shock compression are not necessarily in equilibrium with the lattice. There must be a coupling between the states of the molecule and the lattice states. The strength of this coupling could determine the sensitivity to initiation. The molecules of the lattice may also be energized by collisions with other molecules. However, because they are not as free to move as in a gas or liquid, the way these collisions occur in a solid will be quite different than in the liquid or gas phase.

In developing theoretical models for mechanisms of reaction in a shock compressed solid it is necessary to characterize the heating of the lattice due to the shock pulse. Only initiation of reaction in single crystals will be considered where the temperature rise is due to bulk heating. It will be assumed that the lattice states achieve equilibrium within a time short compared to the duration of the shock, typically 10^{-6}s. Without this assumption the concept of temperature would not be appropriate. On the other hand, it will not be assumed that the internal states of the molecule are in equilibrium with the lattice. In fact, the results of one model will justify this assumption. Therefore, in developing models for the reactive processes associated with internal states of the molecules nonequilibrium approaches will be necessary. In mechanisms involving external lattice states equilibrium theories may be appropriate.

Since temperature is a critical parameter in determining rate of reaction, modeling of reaction rates in shocked solids requires a calculation of temperature as a function of shock pressure. The calculation of shock temperature requires a knowledge of the equation of state and treats the material as a fluid characterized by only three thermodynamic variables. Examination of various approaches to calculating bulk shock temperatures indicates considerable lack of agreement in predictions suggesting that such calculations should be only regarded as estimates (5,6). Here a relatively simple method has been used where the temperature rise is given by, (7)

$$\Delta T = \frac{\Gamma T_o}{\rho C_p} \Delta P \qquad (3)$$

where Γ is volume coefficient of expansion, T_o initial temperature, ρ density, and C_p specific heat. For example, in RDX equation (3) yields a temperature of 585°K at 170 Kbs compared to 770°K calculated by Voskoboinikov (4). This is typical of the kind of agreement of various calculations.

THERMAL PROCESSES:

1. Vibrational Relaxational Processes: A shock pulse heats the solid by exciting vibrational states of the lattice. Three excited phonons are most likely to be transferred from the heated lattice to excite an internal vibration of one or more modes of the molecules which constitute the lattice. It has been shown for a Debye lattice that the rate of transfer, W_{10}, at a given temperature T to a bond of vibrational frequency ν is given by, (8)

$$W_{10} = \frac{9K^3 N^4}{16hm(4\pi M)^3} \frac{A^2 T^3}{\nu_d^7 \nu} \qquad (4)$$

where M is the mass of the molecule, m mass of atom on the molecule, ν_D is the Debye frequency of the lattice, A is a coupling constant between the lattice mode and an internal molecular vibration, K is Boltzman's constant, and h is Planck's constant.

Unimolecular breaking of the bond may occur if there is a sufficient probability for multiple excitations to a vibrational state which has energy equal to or greater than the dissociation energy of the bond. With a knowledge of W_{10}, and assuming a harmonic oscillator potential it is possible to calculate the rate of excitation to the dissociative state using a random walk stochastic theory developed by

Montroll and Shuler (9). Application of the theory to the N-N bond breaking of RDX at temperatures appropriate to 170 Kbs of shock pressure indicates there is no possibility for this kind of a process. This calculation ignored coupling between internal modes of the molecule. This coupling which has a shorter relaxation time (10^{-9}S) than the molecule-lattice relaxation time (10^{-6}S) would compete with a multiple excitation process further reducing the probability of bond breaking.

The calculated W_{10} at 170° Kbs and 770°K is 1.3×10^{-4} S^{-1} which means the relaxation time ($1/W_{10}$) for the transfer of phonons to the N-N vibration of RDX is longer than 10^{-6}S the typical pulse width used to initiate reaction. These results suggest that the internal vibrational states of the molecule do not have time to come to equilibrium within the duration of the shock pulse.

2. <u>Electronic Excitation</u>: Since it has been observed that UV light of wavelength which causes an electronic excitation can cause NO_2 to be severed from the ring of TATB and RDX, and since the same bond is broken by a shock pulse it is suggested that the first step in shock induced bond breaking is an electronic excitation. Recently French workers have indicated a correlation between the charge distribution calculated from molecular orbital theory of the excited state and impact sensitivity (10). The excited electronic structure of the RDX molecule has been elucidated by the work of Marinkas (11) and this work has shown that although there are a number of excited states, only the allowed excitations at 340 nm and shorter wavelength cause photolysis resulting in rupture on the $R-NO_2$ bond. Presumably this excited state is a dissociative state with respect to the N-N separation as schematically depicted in Figure 2. Direct thermal excitation of this level (line AB) is not probable at 770°K. However, thermal excitation to the unbound state could occur if the potential energy curve of this state as a function of N-N separation intersected the ground state potential energy (point C). Then thermal excitation of the ground state to point C would allow the possibility that the system cross over to the dissociative state leading to bond breaking. Since it is likely that this is the process for slow thermal decomposition point C the intersection point of the potential curves can be fixed at 2.0 eV for RDX which is the activation energy measured from slow decomposition studies (12). Using the formalism of equation (4) the rate at which the N-N vibration can be excited to a vibrational level 2.0 eV above the ground state which would be the 12th vibrational level can be calculated. The result is a rate again far too low compared to the rate needed to cause detonation, (10^{6} S^{-1}). This mechanism, however, could be the

61

rate controlling step in slow thermal decomposition where lower reaction rates exist, but is excluded as a mechanism for shock initiation. This conclusion is consistent with the previous analysis which showed that extrapolation of slow thermal decomposition rates to critical shock temperatures gives rates which are too low to account for the process.

The elimination of thermal excitation to the dissociative state in RDX as the first step of shock induced bond breaking assumes that the separation between the ground and excited electronic state is not greatly affected by pressure. This assumption is justified by data on the effects of high pressure on the internal vibrational frequencies of the RDX molecule which will be presented below.

The elimination of the role of any internal vibrational or electronic states in breaking the N-N bond is really a result of the fact that W_{10} is too low meaning there is not time for energy to be transferred to internal states of the molecule during the shock compression.

3. <u>Vacancy Production</u>: Another possible way the chemical reactions of explosion may start in the solid is that the thermal energy generated by the shock pulse may cause molecules to be removed from their lattice sites to interstitial positions. In these interstitial positions they may be sufficiently close to neighboring molecules to allow chemical contact and thus reaction. The rate at which a molecule can be removed from its lattice site as a function of temperature can be approximated by

$$R = v_o e^{-E/kT} \tag{5}$$

Where E is the energy needed to remove the molecule from its site to the interstitial position, and v_o is the vibrational frequency of the molecule at its lattice site. In the case of ionically bonded explosives (such as ammonium nitrate) where electrical conductivity at elevated temperatures is determined by cation diffusion, E can be estimated from studies of the temperature dependence of the electrical conductivity to be 1.17 eV (13). The translational vibrational frequencies of the NH_4^+ ion in AN have been measured by Raman spectroscopy (14). Thus equation (5) and a calculation of the lattice temperature as a function of peak shock pressure enables the rate of removal of cations from lattice sites to be calculated. At a shock pressure of 100 Kbs a reaction rate of $8 \times 10^5 s^{-1}$ is obtained which is in the order of magnitude of the rates needed to cause the initiation to detonation transition.

This analysis has not taken into account the effect of pressure on v_o or E. Raman studies of effect of pressure on lattice vibrations suggest v_o would increase by about 1/2 % per kilobar (15). Electrical conductivity decreases by an order of magnitude for a two order of magnitude increase in pressure (16). These numbers indicate that at 100 Kbs E would increase roughly by 30% which would reduce the reaction rate by about an order of magnitude from the estimate that does not take into account lattice compression. Thus vacancy production remains a possibility for the initial step which produces reaction. Indeed vacancies have been observed to be produced in solids by shock (17). Significant suppression of reaction rates in explosive solids with increasing hydrostatic pressure has not been observed (18).

4. Large Amplitude Lattice Vibrations: An examination of measured lattice mode frequencies in a number of chemically similar primary explosives indicates a correlation between certain mode frequencies and sensitivity to thermal initiation, suggesting a possible role of lattice vibrations in the initiating mechanism. In gas or liquids one of the factors that determines bimolecular reaction rates is the probability that the two reacting molecules can come into chemical contact. In a solid where the motion of the ions is constrained by the normal modes of vibration of the lattice, there will be certain modes of vibration in which two adjacent molecules of the lattice approach each other. If the amplitude of vibration is sufficiently large at elevated temperatures the two ions may get close enough to chemically react. The rate of reaction of the two adjacent ions on such a model will be given by (19)

$$R = \frac{\omega}{\pi} n e^{-KA_c^2/2kT} \qquad (6)$$

where ω is the vibrational frequency of that mode which allows the molecules to approach, K is the harmonic force constant of the mode (a harmonic potential is assumed). Ac is the amplitude of vibration at which the molecules are separated by a distance which allows them to interact. Note that because of compression of the lattice Ac will decrease with increasing shock pressure.

Because of the availability of data on the vibrational frequencies of ammonium nitrate and the relatively simple cubic structure of the high temperature phase, the model is applied to this material. The critical separation for reaction of two ammonium ions is taken as 2.92 Å which is twice the ionic radii of NH_4^+. The reaction probability is assumed to be one when the ions achieve this separation. The reaction rate can then be calculated as a function of

63

shock pressure taking into account the decrease in Ac with shock compression of the lattice. Sufficiently high reaction rates as a function of shock pressure are obtained. For example, at 100 Kbs, the model predicts a rate of $10^5 s^{-1}$. Such a mechanism could well be a possible way in which reactions are initiated in the solid state. It must be emphasized that the assumption of contact of ionic radii for critical separation is an arbitrary condition for reaction. The spirit of the calculation is to assess the feasibility of a collisional model of reaction in the solid state, particularly in a shock compressed solid. Another possibility that has been considered by other workers is that rotation of say CH_2 groups could enable hydrogen atoms and adjacent oxygen atoms of nitroamine explosives to interact (20).

MECHANICAL PROCESSES:

1. <u>Molecular Deformation</u>: As a shock pulse passes over a molecule of the lattice the molecule undergoes a time dependent compression. A mechanical breaking of the N-N bond of RDX could occur if the time dependent perturbation deforming the molecule causes a vibrational excitation to either points C in Figure 2, or directly causes an electronic excitation to B. Formal analysis of such mechanisms have been made. Assuming a Gaussian shaped shock pulse having rise time τ, the rate of excitation from the ground state to a vibrational state N=L where bond breaking can occur is obtained to be

$$K = C_{oL} \frac{h}{2} m\omega^2 \Delta^2 \pi e^{-\omega^2 \tau^2/2} \qquad (7)$$

where ω is vibrational frequency of bond, Δ the maximum deformation of bond, C_{oL} is the factor which determines probability for multiple excitations to state L, where the vibrational energy is equal to the dissociation energy. The critical parameters determining such a process are τ, the rise time of the shock, and Δ the amount of deformation of the bond. Equation (7) shows such a process is not possible unless τ is the order of magnitude of the period of vibration of molecule, (i.e. $10^{-13} s^{-1}$). It is unlikely that this is possible. Recent molecular dynamic calculations of shock propagation in inert gas solids suggest larger rise times (21). Although rise times are not presently experimentally accessible, the amount of deformation Δ of the molecular bond for a given lattice compression can be estimated from experimental data. Using Raman spectroscopy and a high pressure diamond anvil pressure cell, the internal vibrational frequencies of the RDX molecule have been measured as a function of pressure up to 30 Kbs. The data shown in Figure 3 indicates very

small changes in the vibrational frequency with pressure. For example
the frequency of the N-N vibration, the bond that is known to break by
shock only increases by 0.3 percent at 30 Kbs. From a knowledge of
the vibrational frequency of the bond and the dissociation energy a
Morse potential can be constructed to relate bond energy to N-N separation. This can be used to estimate the rate of change of frequency
with N-N separation. Coupled with the high pressure Raman data the
change in N-N separation as a function of shock pressure can be
obtained. The analysis shows that at 170 Kbs the equilibrium separation of the N-N bond would change insignificantly. Recent molecular
orbital calculations of reaction surfaces of methylnitrate indicate
that for unimolecular bond breaking to occur the molecule must be
compressed by at least 5.0%. Such a change would result in much
larger frequency shifts with pressure than have been measured in
RDX. These results suggest that unimolecular bond breaking because of
mechanical deformation of the molecule causing electronic or vibrational excitation is not possible.

2. Mechanical Vacancy Production: The abrupt mechanical
deformation experienced by the lattice under shock compression will
suddenly alter the potential that holds molecules to their lattice
site. This time dependent change in the lattice potential could cause
the molecules to be ejected from their lattice sites allowing
molecules to approach each other, thereby enhancing reaction probability. The time dependent change in the potential may cause multiple
vibrational excitations to an energy which allows the molecule to
leave its site. The rate for this kind of a process can also be
described by equation (7) where now Δ is the change in the lattice
parameter of the solid which will, of course, be much larger than the
change in the internal bond lengths of the molecule and the frequency
will now be the vibrational frequency of the molecule in the lattice,
which is an order of magnitude lower than internal molecular
vibrations. The rate at which such a perturbation can remove
a NH_4^+ ion from its lattice site in AN has been calculated as a
function of shock pressure. Sufficiently large rates were obtained to
account for a detonation process provided the rise time of the pulse
is in the order of the vibrational period of the molecule at its
lattice site. This mechanical model is really equivalent to the
thermal process of ejection of a molecule from its lattice site. The
time dependent change in the potential of the molecule at its lattice
site causes excitations of lattice vibrations which is in effect shock
heating. This mechanical model is really a fundamental explanation of
how a shock pulse heats a lattice. The distinction then between a
mechanical and thermal process for the vacancy production mechanism is
artificial, and the general agreement between the calculated rates
from the thermal approach and mechanical approach is to be expected.
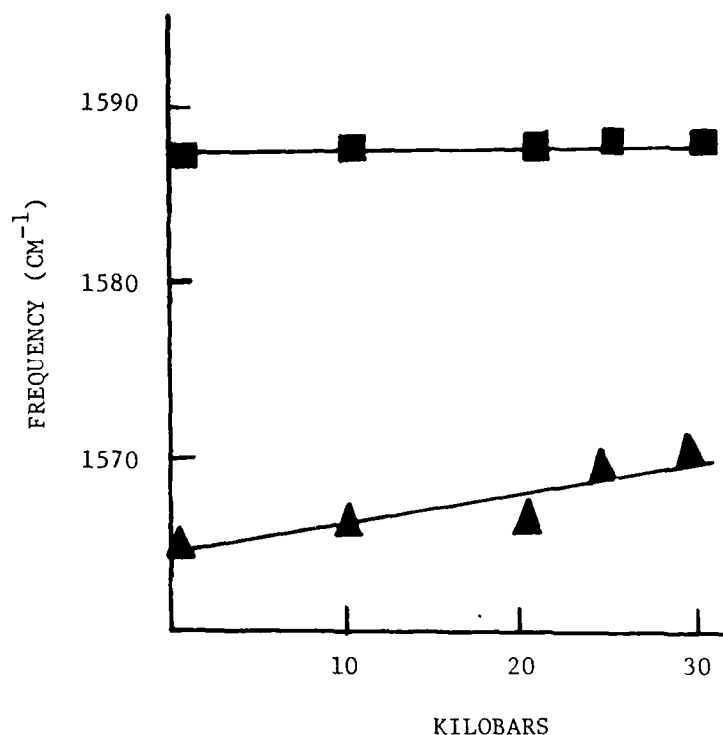
FIGURE 3. The internal vibrational frequencies of the N-N
bond of the RDX molecule as a function of hydro-
static pressure applied to the RDX lattice.

CONCLUSION:

Analysis of macroscopic shock and thermal sensitivity data
of solid explosives indicates that the chemistry caused by the shock
pulse is a result primarily of shock heating but because of the rapid
rise of temperature different reaction kinetics may occur than in
slow heating.

A number of plausible molecular mechanisms by which a shock
pulse may cause a chemical reaction in a solid were considered and
expressions for reaction rates theoretically developed. The theories

were used to calculate reaction rates as a function of shock pressure in real solid explosives. The results indicate that there is not sufficient time for energy to flow from the lattice to the internal states of the molecules of the lattice during shock compression, either due to thermal or mechanical means. In effect, the analysis shows that the internal states of the molecules are not in equilibrium with lattice states. This has two important implications. The reaction paths of slow thermal decompositon (where equilibrium is established) may not necessarily be the same as those occurring in shock heating. Also unimolecular chemical reactions are ruled out. In essence, an isolated RDX molecule should not detonate. The reactions of detonation are a result of cooperative processes between molecules of the lattice. This work indicates the most likely rate controlling process for initiation to detonation is the rate of collision between molecules of the lattice. Two possible ways in which collisions can occur in a shocked solid, large amplitude vibrations due to shock heating and removal of molecules from lattice sites where shown to be viable mechanisms.

Measurements of the effect of hydrostatic pressure on internal vibrational frequencies of the RDX molecule in the solid indicated that the deformation of the molecule is not large enough to be a mechanism of reaction. It was shown that for deformation to cause reaction, the deformation must occur in a time comparable to the vibrational period of a molecule, an unlikely situation. A summary of the probability of the various mechanisms of shock induced reaction considered is given in Table II.

The conclusion that the initial reactions leading to detonation are a result of cooperative interactions has important implications with respect to reducing sensitivity of existing formulations. To reduce sensitivity, the probability of collision of molecules in the solid must be reduced. This can be done by increasing the separation between the molecules in the solid by dispersing the molecules in chemically similar inert solids. The reaction rate should be proportional to the ratio of solvent to solute in the solid solution.

REFERENCES:

1.   J. Sharma and F.J. Owens Chem. Phys. Lett 61 200 (1979).

2.   F.J. Owens and J. Sharma J. Applied Phys. (in press).

3.   F.E. Walker and R.J. Wasley Propellants and Explosives I 73 (1976).

Table II. Summary of Results of Analysis of Possible Mechanisms of Shock Induced Chemical Reactions in Solid Explosives

Mechanism	Calculated Rate At Critical Pressure (S^{-1})	Remarks
THERMAL PROCESSES		
Vibrational Relaxation	10^4	Unlikely
Electronic Excitation	10^4	Unlikely
Ionization	0	Unlikely
Vacancy Creation	10^6	A possibility
Large Amplitude Collisions	10^5	A possibility
MECHANICAL PROCESSES		
Vibrational Relaxational	0	Not possible $(T \gg \tau)$
Vacancy Creation	10^6	possible
Electronic Excitation	0	Not possible $(T \gg \tau)$

68

4. I.M. Voskoboinikov, V.M. Bogomolov and A Ya. Apin Fizika Goreniya i Vzryva $\underline{4}$ 45 (1968).

5. R.H. Christian, Rept UCRL 4900 1957, Univ. of California.

6. L.V.A.L. Tshuler, Soviet Physics $\underline{5}$ 203 (1963).

7. P. Harris, private communication.

8. L. Lieberman J. Accoust. Soc. Am. $\underline{31}$ 1073 (1959).

9. W. Montroll and K.E. Shuler, Adv. Chem. Phys. 1, 361 (1958).

10. A. Delpuech and J. Cherville Propellants and Explosives $\underline{3}$ 169 (1978).

11. P. Marinkas, PhD Thesis Univ. Delaware, 1976.

12. B. Suryanarayana, J.R. Autera, and R.J. Graybush, Proceedings Army Science Conf. $\underline{2}$ 423 (1968).

13. R.N. Brown and A.C. McLaren, Proc. Roy. Soc. $\underline{A80}$, 329 1962.

14. H.C. Tang and B.H. Torrie, J. Phys. Chem. Solids $\underline{38}$ 125 (1976).

15. Z. Iqbal, C.W. Cristoe, and F.J. Owens, Ferroelectrics $\underline{16}$ 219 (1977).

16. C.B. Pierce , PhD Thesis Univ. Illinois, 1960.

17. W.B. Gager, M.J. Klein, and W.H. Jones, Appl. Phys. Letters $\underline{5}$ 131 (1964).

18. E.L. Lee, R.H. Sanborn, and H.D. Stromberg, Fifth Symposium on Detonation, Pasadena, CA (1970).

19. F.J. Owens, Technical Report 77041 LCWSL, ARRADCOM, Dover, NJ (1977).

20. D.J. Pastine, M.J. Kamlet, and S.J. Jacobs, Sixth Symposium on Detonation, San Diego, CA 197ʰ.

21. S. Trevino, private communication.

METHODOLOGY FOR EVALUATION OF OBSCURATION (U)

*ELLIOT G. PETERSON, Mr
LOTHAR L. SALOMON,   PhD
DUGWAY PROVING GROUND
DUGWAY, UT 84022

Since 1976, improvements in the methodology for physical and optical characterization of airborne obscurants have come about at a remarkable pace, reflecting the urgent need for objective data. Prior to that time virtually all evaluations of obscurants and associated delivery systems, and of electro-optical systems in an obscuring environment, were of the "go no-go" type. By contrast, a vast body of information is now available, much of which is based on developments at, and tests performed by Dugway Proving Ground. The purpose of this report is to describe some of the most recent advances in methodology.

A. <u>SOURCE EMISSION RATE</u>. A critical input to obscuration transport models is the source emission rate. It is defined as the fraction of mass burned as a function of time, i.e., $F_m(t)=(V_o-V(t))/V_o$ (1), where V_o is the volume of the submunition before burn, and $V(t)$ the volume at time t. The form of equation (1) was determined for five submunitions. The treatment leads to valid prediction of submunition performance, and should also be valuable in designing new submunitions.

<u>Case 1.   WP Wick Submunitions</u>. A sketch of the wick submunition is shown in Figure 1.

Figure 1.   Sketch of Wick
            Submunition
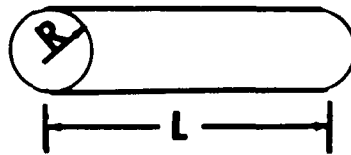
Using equation (1), the fraction of mass burned can be obtained using

$$F_m = 2\left(\frac{1}{L_o} + \frac{1}{R_o}\right)X - \left(\frac{4}{R_oL_o} + \frac{1}{R_o^2}\right)X^2 + \left(\frac{2}{R_o^2L_o}\right)X^3 \quad (2)$$

where L_O is the length before burn, R_O is the radius before burn, and X is the burn distance.

If the burn rate (dX/dt) is constant, the burn distance (X) is given by $X = X_b (t/tb)$ (3), where X_b is the burn distance at burn-out and t_b is the burn time.

Using equations (2) and (3), the fraction of mass burned becomes

$$F_m = A(t/t_b) + B(t/t_b)^2 + C(t/t_b)^3 \quad (4)$$

where $A = 2(\frac{1}{L_O} + \frac{1}{R_O}) X_b$, $B = -(\frac{4}{R_O L_O} + \frac{1}{R_O^2}) X_b^2$, and $C = (\frac{2}{R_O^2 L_O}) X_b^3$.

Table 1 is a list of theoretical constants used for three- and six-inch WP wicks.

TABLE 1. Theoretical Mass Loss Constants

Type of Wick	R_O (in)	L_O (in)	X_b (in)	A	B	C
Three-Inch	0.5	3.0	0.5	2.17	−1.34	0.17
Six-Inch	0.5	6.0	0.5	2.33	−1.66	0.33

Equation (4) was used to calculate the theoretical fraction of mass burned as a function of time. The calculations are compared with experimental results (see Figures 2 and 3) and show good agreement for these two submunitions.

Case 2. 155 M1 (HC) Canister Submunition. A sketch of the 155 M1 (HC) canister is shown in Figure 4.

Figure 4. 155 M1 (HC) Canister
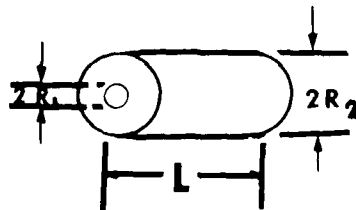
It is assumed that the only surface burning is the center cylinder ($S = 2\pi R_1 L$) and the only parameter changing is R_1. The fraction of the mass burned at any time becomes

$$F_m = (\frac{2R_{01}X_b}{R_2^2 - R_{01}^2}) (t/tb) + (\frac{X_b^2}{R_2^2 - R_{01}^2}) (t/tb)^2 \quad (5),$$ where R_{01} is the radius of R_1 before burn (0.681 in), R_2 is the outside radius (4.515 in) and the burn distance X_b is $R_2 - R_{01}$; and equation (5) then becomes

$$F_m = 0.26(t/t_b) + 0.74 (t/t_b)^2 \quad (6).$$ The comparison of equation (6) with experimental data is shown in Figure 5, and shows good agreement for the 155 M1 (HC) canister.
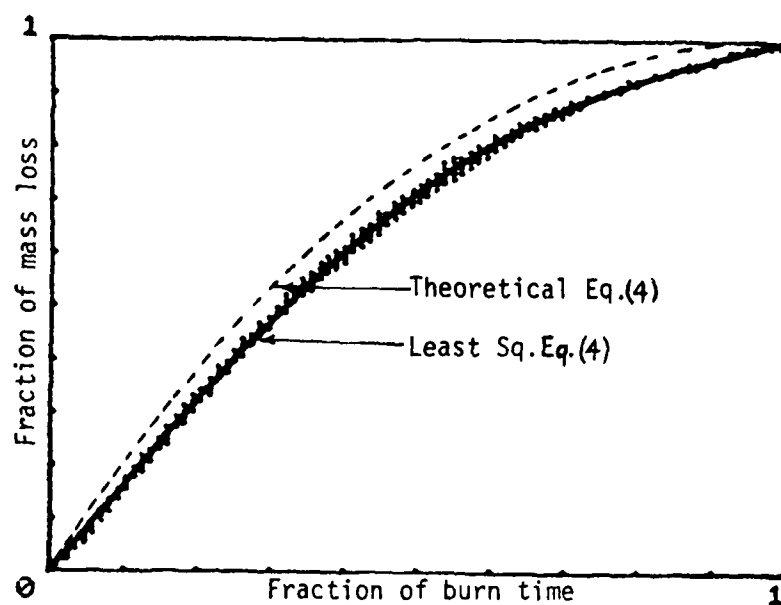
Figure 2. Three-Inch Wick (WP)
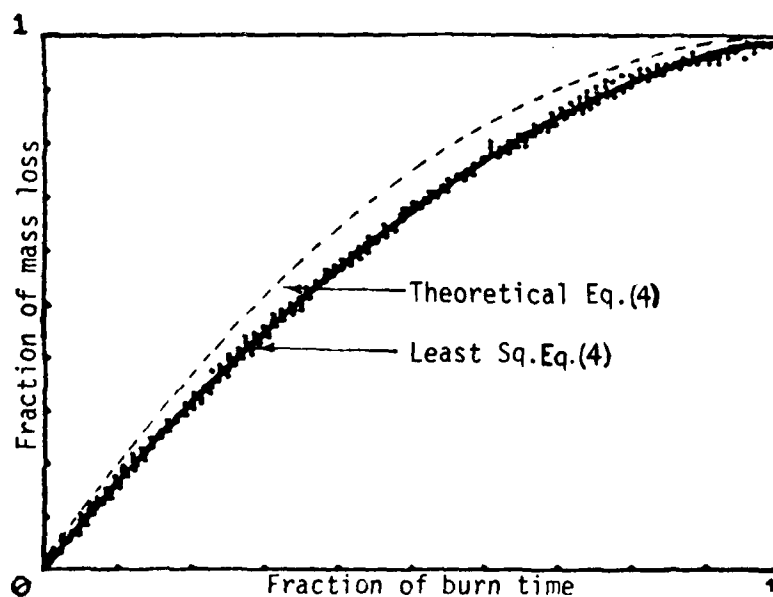
Figure 3. Six-Inch Wick (WP)

73

Figure 5.   155 mm Canister, M1, (HC)

It is assumed that all surfaces burn.   Equation (1) will then take the form of equation (4), where

$$A = 1 + \frac{W(aR_{02} + b\,R_{01})}{R_{02}^2 - R_{01}^2}, \quad B = - \frac{W[(a\,R_{02} + b\,R_{01}) + (a^2 - b^2)\frac{W}{4}]}{R_{02}^2 - R_{01}^2},$$

$$C = \frac{W^2(a^2 - b^2)}{4\,(R_{02}^2 - R_{01}^2)}, \quad a = 1 + \frac{1}{\tan(\theta/2)}, \quad b = 1 - \frac{1}{\tan(\theta/2)}, X_b = W/2$$
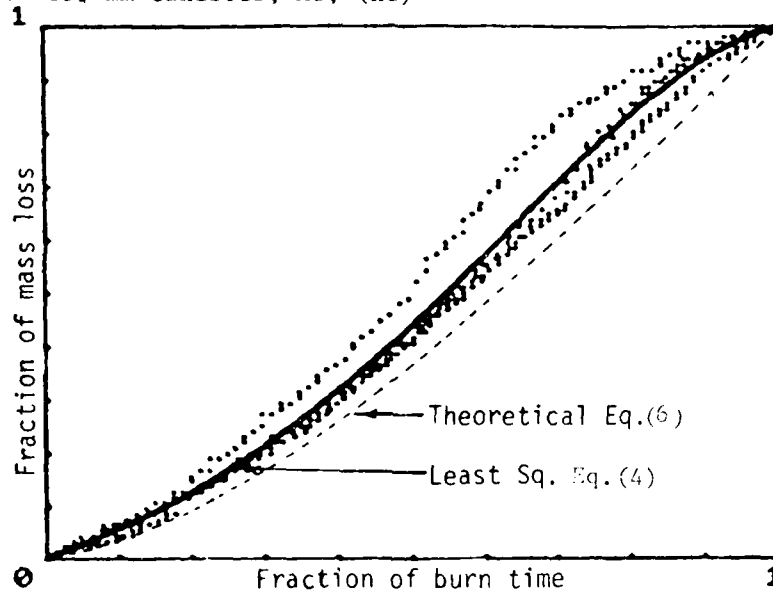
Case 3.   WP and RP Wedge Submunitions.   Six wedges form a wafer shown in Figure 6.a; the wedge itself is shown in Figure 6.b.

Figure 6.a

Figure 6.b

2 of 5

AD
A090422

1.0   2.8   2.5
           2.2

           2.0

           1.8

1.25   1.4   1.6
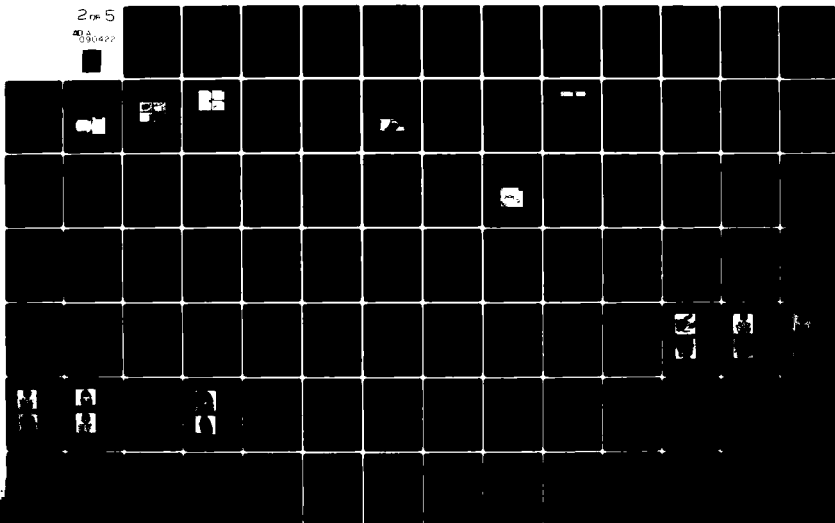
Table 2 contains a list of theoretical constants used for WP and RP wedges.

TABLE 2. Theoretical Mass Loss Constants

Type	R_{01} (in)	R_{02} (in)	W (in)	θ (deg)	a	b	A	B	C
RP	0.375	2.375	0.50	30	2.732	0.732	1.62	-1.25	0.63
WP	0.375	2.375	0.75	30	2.732	0.732	1.92	-1.10	0.18

Equation (4), along with constants in Table 2, was used to calculate the theoretical fraction of mass burned as a function of time for WP and RP wedges. The calculations compare well with experimental results (see Figures 7 and 8).

B. RELATIVE HUMIDITY (RH) AND HYGROSCOPIC OBSCURANTS. Most of the conventional smokes, including those produced by burning of phosphorus and HC, are constituted of hygroscopic particles. It has been predicted, and established by field tests, that transmittance of phosphorus and HC smokes (i.e., their light-attenuating capability) can vary considerably with RH. In the Beer-Lambert Law $T=\exp(-\alpha CL)$, both α and C are potentially dependent on RH. (Here, T is transmittance (dimensionless), α is the extinction coefficient of smoke (m^2/g), C is the concentration of smoke (g/m^3), L is the thickness of the attenuating layer (m) along the line of sight, and t is time.) Thus α cannot be relied upon as an indicator of the light-attenuating characteristics of hygroscopic smokes. Indeed, we have found that α may remain virtually unaffected by changes in RH while T varied because of changes in C. By redefining α this ambiguity can be removed.

Transmittance of free-floating (unconfined) clouds can be determined using a modified form of the Beer-Lambert Law, $T=\exp(-\alpha\int CdL)$ (7). We recommend a new procedure for calculating transmittance by defining the extinction coefficient to be ($\alpha'=Y\alpha$); equation (7) then becomes $T=\exp(-\alpha'\int C_a dL)$ (8). Values of α' over the RH range and at the wavelengths of interest can then be determined using $\alpha'=-\int \ln Tdt/\int D_a dL$ (9), where D_a is dosage ($\int C_a dt$), C_a is the concentration of smoke analyte which is independent of RH (e.g., phosporus, zinc or, in general, $C_a Y=C$ smoke, g/m^3), and Y is a dimensionless yield factor which accounts for the difference in concentration between smoke analyte and actual smoke. For the hygroscopic phosphorus and HC smokes, analytes (C_a of equation (8)) are elemental phosphorus and zinc, respectively. Plots of α' at 3.4 μm wavelength are shown in Figure 9 as an example. For a non-hygroscopic smoke, α' versus RH would be constant.

In summary, once values of α' over the RH range and at wavelengths of interest have been determined, no further efforts are needed to
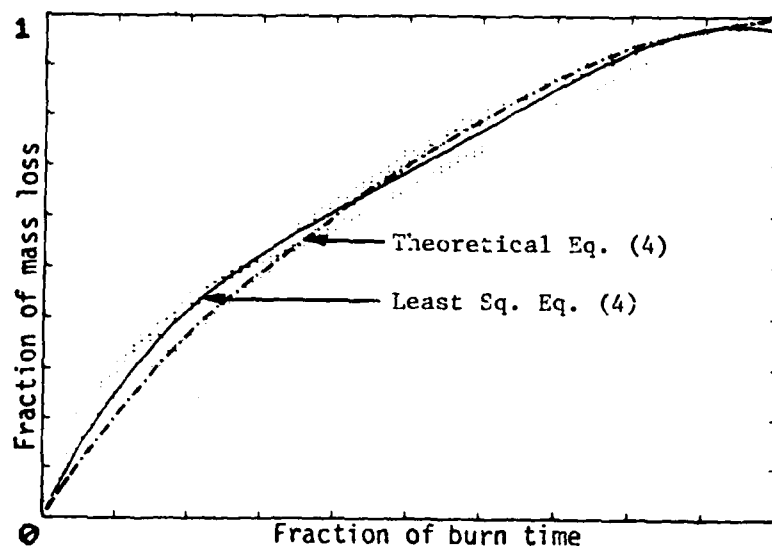
Figure 7. WP Wedge

Figure 8. RP Wedge

76
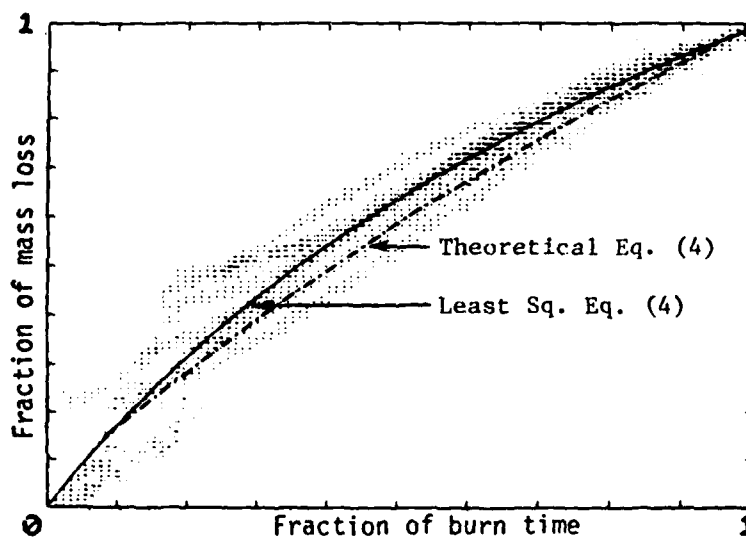
<u>ascertain yield factors, and most importantly, no assumptions are nec-</u>
<u>essary regarding the chemical nature of the obscurants.</u> (The fact
that the composition of smokes varies with environmental conditions
and, in many cases, remains uncertain, makes calculation of Y from
literature data virtually impossible.) In the present approach, mod-
ified extinction coefficients (α') become an unequivocal measure of
the light-attenuating characteristics of all types of obscurants,
whether or not they are hygroscopic. Relevant data are available from
past field tests. Furthermore, no additional burden is placed on math-
ematical modelers of obscuration since values of C_a are required in any
event, and calculations of concentration of smoke (using tenuous yield
factors) become unnecessary.
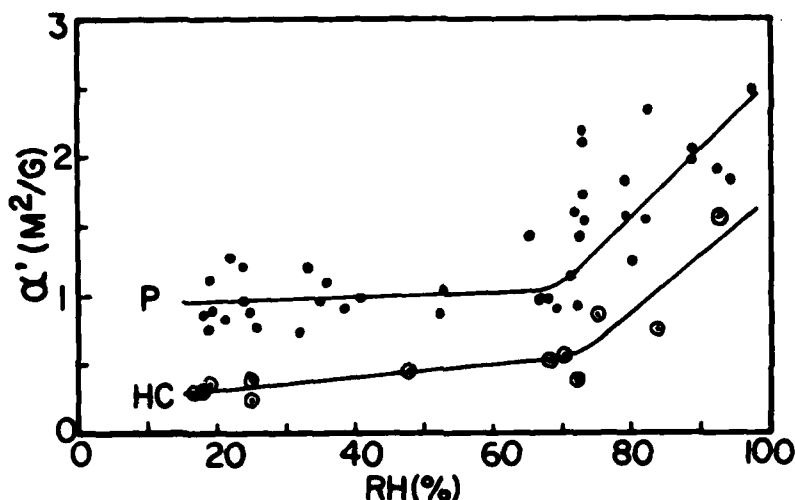
Figure 9. Extinction Coefficients α' $(\alpha Y, m^2/g)$ for Phosphorus (P) and
HC Smokes at 3.4 μm Wavelength ii m Field Data.

Coefficients vary little from about 17-70% RH: For phosphorus smokes,
$\bar{\alpha}'_{3.4} = 0.97 + 0.19$ std. dev.; for HC smoke, $\bar{\alpha}'_{3.4} = 0.38 + 0.12$. However,
beyond 70% RH, values increase rapidly. One consequence is that a re-
quired level of light attenuation can be achieved by greatly decreased
munition expenditure. (Note that increases in α' are reflected by ex-
potential decreases in transmittance.)

C. <u>CORRELATION BETWEEN HUMAN VISION AND INSTRUMENTAL MEASUREMENTS.</u>
Much emphasis is being placed on evaluating the effectiveness of modern
military electro-optical devices in obscuring environments. On the
battlefield, however, the human eye probably still is the most impor-
tant sensor. It is, therefore, a question of practical consequence
how instrumental measurements correlate with the ability of observers
to spot a target. To explore this problem, trained observers with

7-power binoculars were required to record the time during which they were unable to see a stationary M48 tank through smoke clouds at 1000m or 1500m distance. (Perception of targets in realistic situations can involve a complex set of factors; not all were tested in this study.)

In Figure 10, the time during which the target was obscured to 5 observers at each of the two distances can be correlated with transmittance (T). It is immediately evident that less light attenuation is required for obscuration at the longer distance. However, the operation of complicating factors is seen in Table 3(I), because the T threshold for obscuration varies with type of munition despite adjustment for meteorological variables. In what follows, it will be seen that contrast ratios do not suffer from this defect. The contrast ratio through time is defined as $C_R(t)=[B_T(t)-B_B]/[B_B+B_C/T(t)]$, where T(t) is the visual transmittance through time, $B_C(t)$ is the luminance (visual) of the cloud through time, B_T is the luminance of the target as determined before cloud arrival, B_B is the luminance of the background as determined before cloud arrival. $C_R(t)$ takes account not only of light attenuation, but also the relative luminance of cloud, target and background. The $C_R(t)$ curve shown in Figure 11 and $C_R(t)$ threshold values seen in Table 3(II) demonstrate good correlation between measurements and observer responses, and reproducibility independent of transitory environmental effects such as sky brightness. By comparison with T, $C_R(t)$ clearly is a superior predictor of human response.

Table 3. Threshold Values for Transmittance and Contrast Ratios.

Round	(I) Ave Transmittance for Obscuration		(II) Ave Contrast Ratio for Obscuration	
	1000m	1500m	1000m	1500m
A(RP)	.0525	.109	.0075	.018
B(WP)	.019	.058	.0070	.019
C(HC)	.012	.042	.0075	.015
Mean/Std. Dev.	.0278/.0216	.0697/.0350	.0073/.0003	.0173/.0021

If one plots $C_R(t)$ against the time a munition can maintain a stated $|C_R|$ value or less, one can determine the obscuration effectiveness of the munition and its effectiveness relative to other munitions in the visual range. This is seen in Figure 12, which represents results from 15 trials with each of three types of 155mm smoke rounds, two of which are developmental types. The time during which each of the munitions provides a cloud dense enough to preclude detection of a target, that is, the time a cloud provides contrast ratios below the threshold for the eye, is indicated.
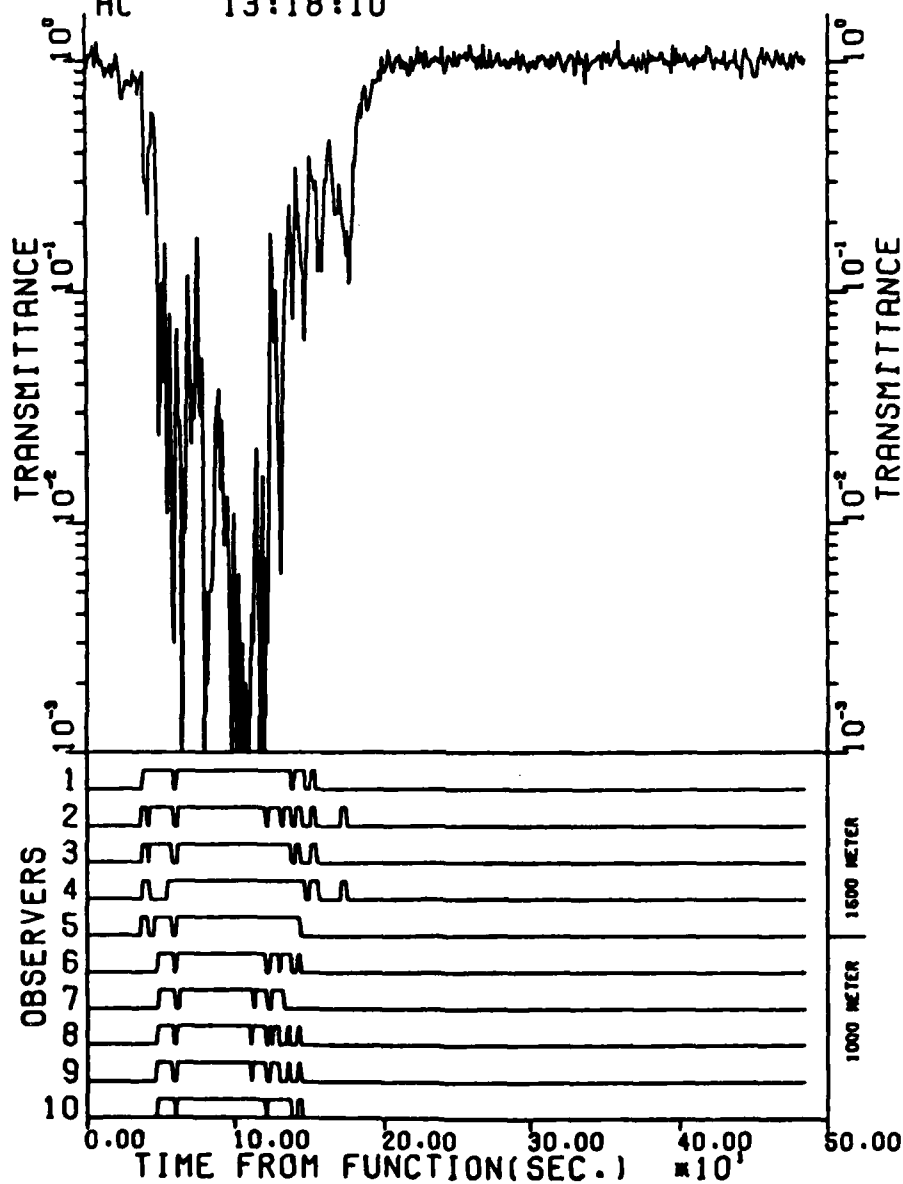
FIGURE 10. Transmittance and Observer Data Versus
Time for Wavelength 0.4-0.7

79
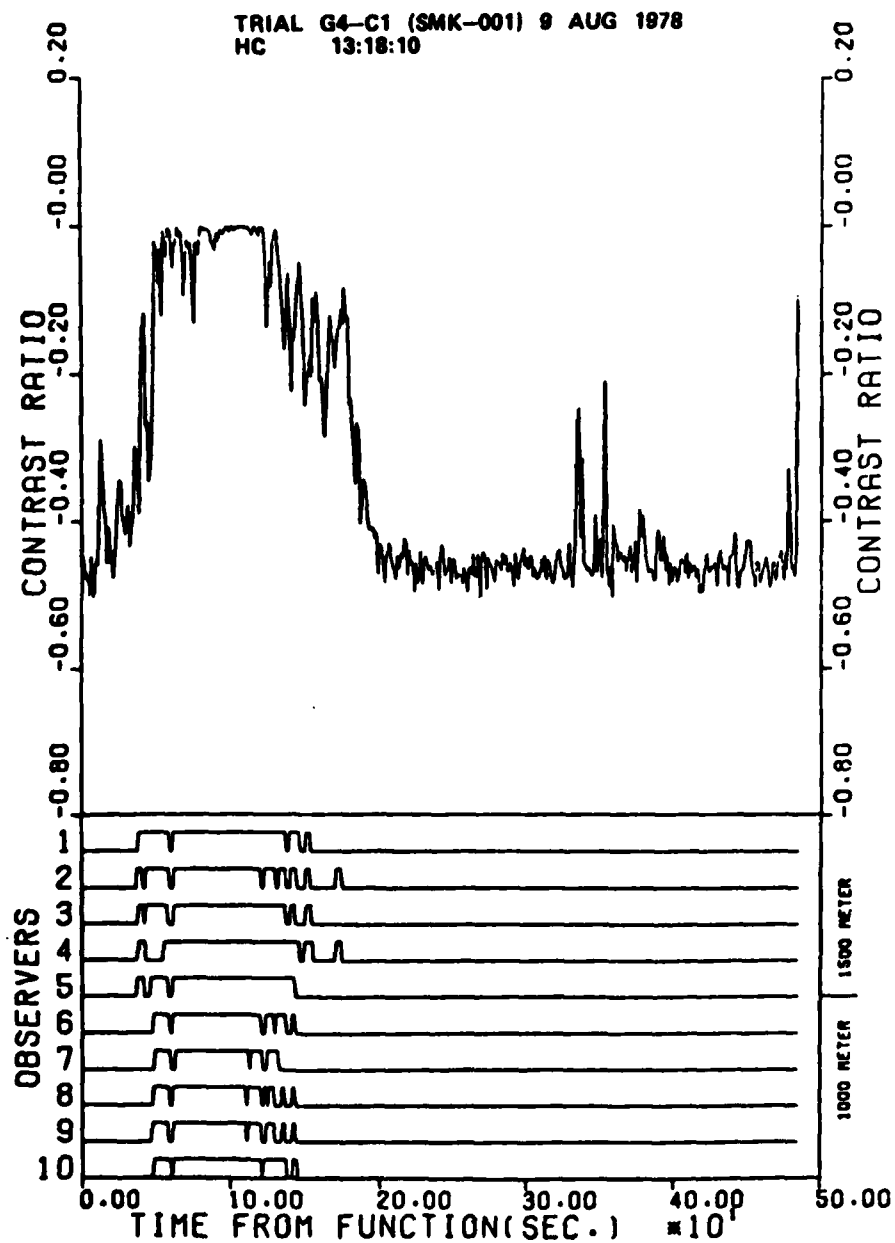
FIGURE 11.   Contrast Ratio and Observer Data Versus
Time for Wavelength 0.4-0.7

The significance of these findings is that objective instrumental measurements (a) correlate well with human responses, (b) can be used to predict the effectiveness of smoke rounds in obscuring vision, and (c) can be used in identifying munitions which provide obscuration of the required duration.
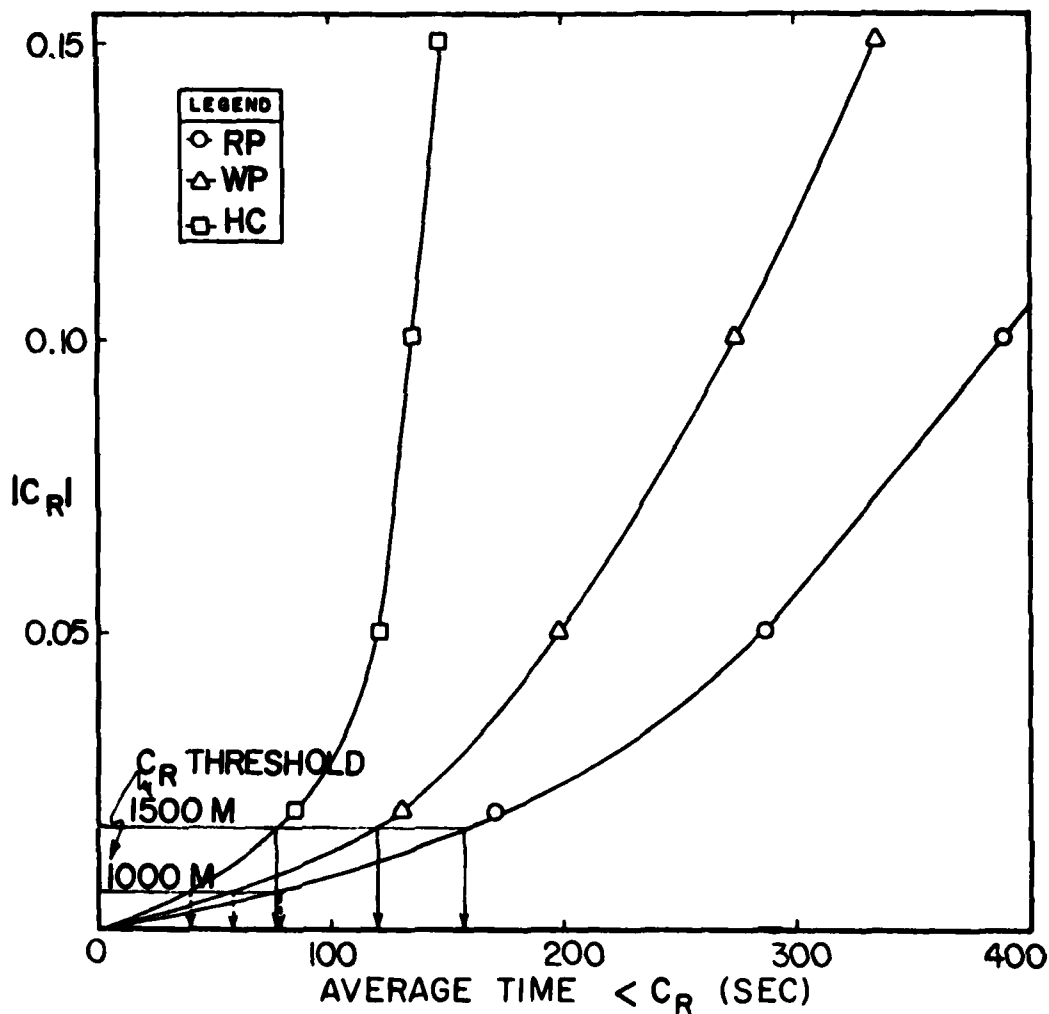
Figure 12.   Time Contrast Ratio Remains below a Stated Level.

81

D. REAL TIME CONCENTRATION (C) AND CONCENTRATION-LENGTH PRODUCT (CL)
VALUES. Aerosol photometers (APs) are routinely used by us to deter-
mine C(t) of airborne obscurants. Involved in this procedure is the
calibration of each AP using chemical impingers (CIs) which are posi-
tioned next to each AP during the field test. Since chemical analysis
of CIs is relatively time-consuming, C(t) cannot be computed until
some time after the test day. To make C(t) and CL(t) values available
in real time for test control and planning, the following automated
method was developed and employed successfully.

Analog data from aerosol photometers are digitized and recorded on
magnetic tape. In this form the data represent relative concentration
through time. CL(t) is defined as $\int C(t)dt \approx \Sigma A_i R_i(t)\Delta L_i$ (10), where A_i
is the conversion factor from millivolts (mv) to concentration for the
i-th AP, $R_i(t)$ is the reading of the aerosol photometer (mv) at time
(t) and ΔL_i is the distance between APs. From the Beer-Lambert Law,
$CL = lnT/-\alpha$ (11). Let $Y = lnT/-\alpha$ and $X = R\Delta L$. Then, in general,
$Y = A_1 X_1 + A_2 X_2 + \ldots A_n X_n$ (12), and the conversion factors (A_i) can be ob-
tained by a least square fit of equation (12) or

$$\begin{bmatrix} \Sigma\ X_1 X_1 & \Sigma X_1 X_2 & \ldots & \Sigma X_1 X_n \\ \Sigma\ X_2 X_1 & \Sigma X_2 X_2 & \ldots & \Sigma X_2 X_n \\ \vdots & \vdots & & \vdots \\ \Sigma\ X_n X_1 & \Sigma X_n X_2 & & \Sigma X_n X_n \end{bmatrix} \times \begin{bmatrix} A_1 \\ A_2 \\ \vdots \\ A_n \end{bmatrix} = \begin{bmatrix} \Sigma Y X_1 \\ \Sigma Y X_2 \\ \vdots \\ \Sigma Y X_n \end{bmatrix} \quad (12)$$

The APs are positioned along the same sampling line where the
transmittance T is measured. The inputs to the least squares equation
(12) at any given time t are $R_i(t)$, ΔL, α, T(t) and repeated through-
out time t at one-second intervals. Results of this method are shown
in Figure 13 and show good agreement between the new method and the
time-consuming method employing calibrated APs.

Figure 13.
Comparison between
Concentration Data
Obtained by Two
Methods (HC Smoke,
63 seconds after
Munition Function.)

82
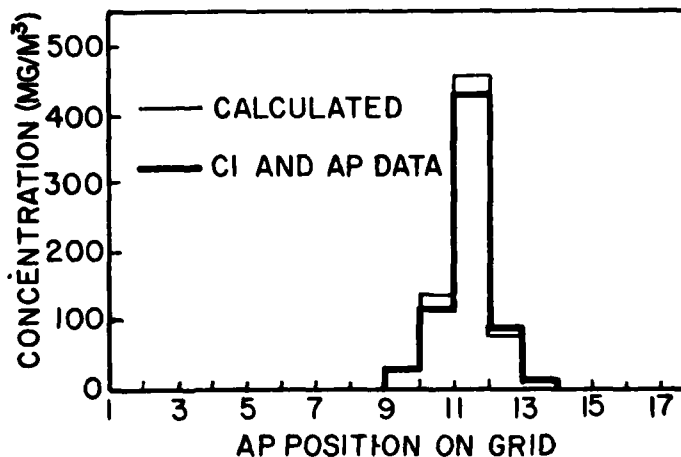
E. <u>SUMMARY</u>. In this report, we have presented descriptions and perti-
nent test data of selected methodological developments relating to eval-
uation (and, ultimately, weaponization) of obscuring systems.

It was shown that source emission rates for smoke submunitions can
be predicted with substantial validity, thus providing a critical tool
for mathematical modeling of obscuration and for the design of new sub-
munitions with specified properties.

The relationship between transmittance and relative humidity was
discussed for hydrated smokes, along with a demonstration of the drastic
effect of high relative humidity on transmittance and its bearing on
munition expenditure. A procedure was described for determination in
the field of a redefined, unambiguous extinction coefficient which
permits computation of transmittance without resort to yield factors,
and is applicable to hygroscopic and non-hygroscopic smokes.

Evidence was presented which shows that instrumental measurements
correlate well with human vision in assessing the obscuring properties
of smokes. Applications to evaluation of smoke delivery systems were
noted.

Finally, a mathematical treatment was described by means of which
it becomes possible to obtain excellent estimates of concentrations
through time, and concentration – length product time profiles, of obscur-
ing clouds in real time, i.e., by a completely automated procedure.
This is of particular value for field test control and test planning.
Heretofore, such data were contingent on completion of chemical analysis
of the contents of aerosol samplers, and thus unavailable for many hours
or days.

LASER INTERACTION WITH TBR MATERIALS

JANET S. PERKINS, Ph.D.
ARMY MATERIALS AND MECHANICS RESEARCH CENTER
WATERTOWN, MASSACHUSETTS 02172

In a number of areas the Army has need for high-temperature, heat-shielding materials that retain shape and structural integrity in severe thermal environments. Some applications are the throat of a jet engine or the interior of a rocket combustion chamber.

We have been examining the response of a number of composite materials to a high-energy-flux environment using a welding laser instead of the arc furnaces of earlier studies. A laser is a clean, well-defined energy source. If used with an air stream or an exhaust system to remove pyrolytic products and debris, we can isolate the action of energy flux from secondary effects and reduce scatter in data.

Typical of the structural forms we have tested are foams, fabric-reinforced composites and bulk graphite. Silica or carbon microballoons or fabric reinforce the newer high-temperature resins in samples we have compared with ATJ and pyrolytic graphites.

A sampling of ablation results are shown in Table I. Among these materials, two are outstanding, both as thermal barriers and in retention of structural integrity. These are pyrolytic graphite and TBR. The former is a form of bulk graphite deposited at high-temperature on a substrate from a carbonaceous gas, e.g., methane. The latter is a relatively new material fabricated from carbon cloth and a Hitco proprietary resin. Both have a laminar structure.

FABRICATION OF TBR

The class of materials known as TBR, an acronym for tungsten-bearing resins, is made by impregnating layers of carbon cloth with a resin containing tungsten atoms chemically bound within the polymer backbone. The laminate is then cured, carbonized, and fired to a graphitizing temperature producing a carbon in tungsten carbide composite. At this temperature, the tungsten carbides sinter and bond the layers of carbon fabric together.

The outstanding behavior of TBR composites has raised questions as to how and why it outperforms other composites as well

85

as bulk graphites. Our research has focused on finding answers to allow tailoring of new composites for special applications.

After analyzing the system in depth both during and after irradiation, we conclude that the excellent performance can be attributed to the following sequence of events:

(1) The 10.6-μm beam produced by the CO_2-laser caused the carbon to become incandescent, reradiate a substantial fraction of its energy, and become very hot (3300°C).

(2) The heat causes the sintered tungsten carbides to melt and coat the carbon fibers with (a) a protective layer against air erosion, (b) a reflecting and heat-conducting surface layer, and (c) a reactive layer for transport and escape of atomic carbon from the underlying carbon fabric.

This paper presents evidence for these conclusions and shows why this system is inherently able to interact with very high intensity radiation with minimal structural damage.

TABLE I.   ABLATION VALUES OF COMPOSITE MATERIALS [a]

Material	Reinforce-ment/Matrix	Density(ρ) g/cc	Exposure(t) sec	Depth of Burn(d) cm	Q^*_x kJ/g
Syntactic Foams	SiO_2-MB/ polyimide	0.38	2.5	3.8	18
	C-MB/ polyimide	0.30	2.5	3.8	23
	C-MB/ H-resin	0.78	1.9	0.5	51
Woven Fabric Laminate	SiO_2/ phenolic	1.77	3.6	1.3	17
	Nylon/ phenolic	1.02	5.5	2.6	22
	C/TBR	2.18	5.5	<0.10	>200
Bulk Carbon	Pyrolytic graphite	2.20	5.5	0.14	200

[a] Exposed to CW CO_2-laser ($I=10.5$ kW/cm^2) which was essentially mono-chromatic (10.6μm).

[b] Ablation values based on surface recession calculated by: $Q^* = \frac{It}{d\rho}$. With the exception of TBR and pyrolytic graphite, the exposure times are burn-through times.

CHARACTERIZATION OF TBR

The 1/8-inch thick material used in these experiments contained 19 layers of a satin-weave carbon cloth. It was bonded with Hitco proprietary resin, TBR-1, and fired to 2800°C.

X-ray diffraction analysis of the final product shows the broad carbon bands typical of carbon cloth (Figure 1a) underlying spectra of the three quenched high-temperature forms of tungsten carbide, W_2C, β -WC_{1-x}, and WC, (Figure 1c) as well as several of the more prominent bands of graphite. The resin alone, heated to 2800°C, gives a spectrum notable for its lack of β -WC_{1-x} and the predominance of W_2C (Figure 1b).

Examination of the phase diagram (1) for the tungsten-carbon system gives insight into the X-ray diffraction pattern of the fired resin (Figure 2). Analysis of this resin shows a large molar excess of carbon over tungsten which presumably would favor the formation of WC rather than the predominance of W_2C found. However, at 2780°C, WC melts peritectically to give solid carbon and a liquid phase rich in W from which W_2C precipitates on cooling. Absence of any of the bands of β -WC_{1-x} found in the laminate is not surprising since this is stable only above 2530°C.

Figure 1.   X-ray diffraction scans of TBR constituents and of TBR before and after CO_2- laser irradiation: (a) carbon cloth, (b) fired TBR-1 resin (2800°C), (c) TBR, as-received, (d) after 10 kW/cm^2 irradiation, (e) after 30 kW/cm^2 irradiation.
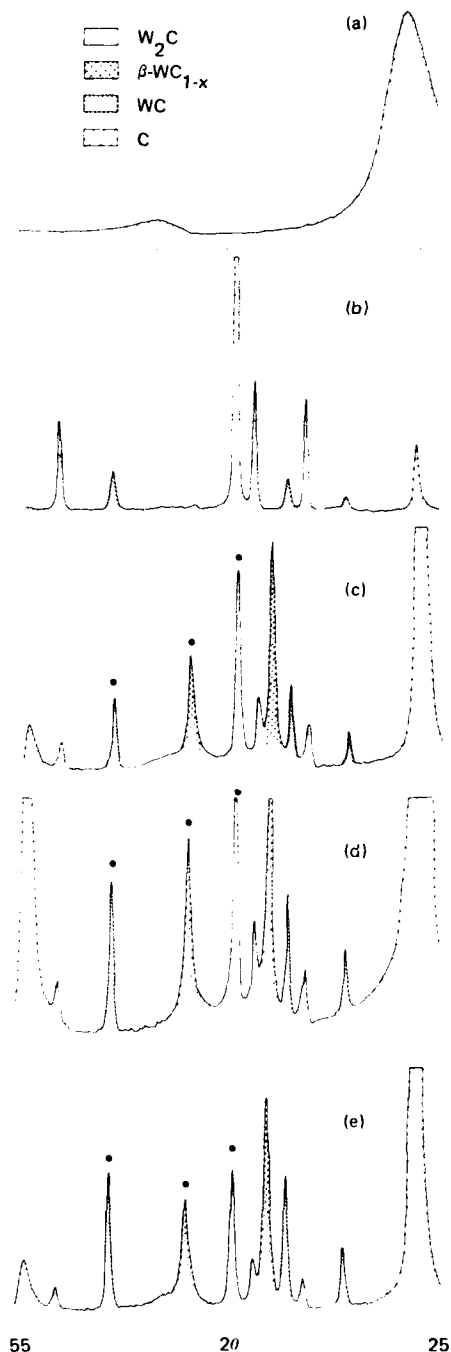
When the fired resin remains in intimate contact with the carbon-
cloth substrate at the high firing temperature for an extended period,
the three high-temperature carbides will accumulate in the steady
state and persist in the quenched product. These result from the
high-temperature reversible redox reactions:

$$W_2C \ + \ C \rightleftharpoons 2\beta\text{-}WC_{1-x} + xC \rightleftharpoons 2WC \qquad (1)$$
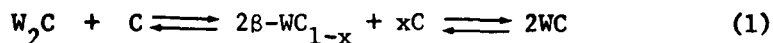
This is the evidence on which we base our description of
the starting material as carbon cloth layers held together by
sintered tungsten carbides and carbon from pyrolysis of the original
tungsten-containing polymeric system.
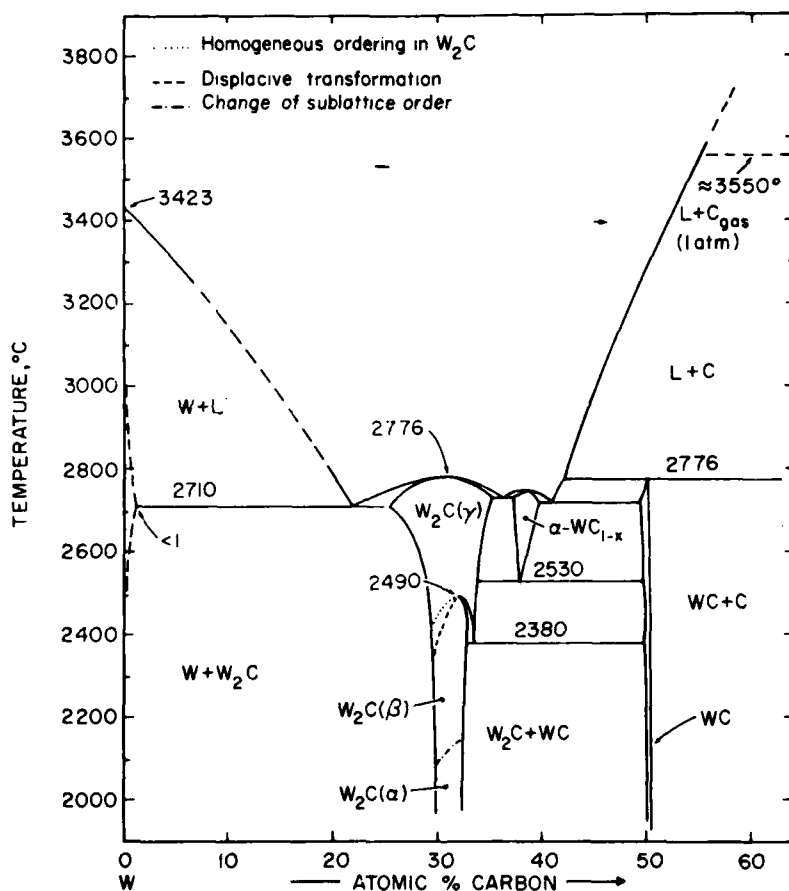
Figure 2.   Binary phase diagram of the
                 tungsten-carbon system.

EVIDENCE FOR CHEMICAL CHANGES DURING IRRADIATION

X-Ray Diffraction

The surface composition of the material irradiated by lasers (10 and 30 kW/cm^2) shows shifts in the ratios of W_2C and WC relative to $\beta\text{-WC}_{1-x}$ (Table II). There has been a shift to the right in reaction (1).

TABLE II(U). RELATIVE CHANGE IN AMOUNTS[a] OF QUENCHED
TUNGSTEN CARBIDES WITH LASER INTENSITY

	Original	10 kW/cm^2	30 kW/cm^2
W_2C	1.88	1.31	0.87
WC	0.73	0.86	1.17

[a]Ratios of W_2C and WC to $\beta\text{-WC}_{1-x}$ based on peaks (•) in Figure 1c-e.

The shift to larger concentrations of WC, the higher the laser intensity, is a reasonable effect. The increased energy flux speeds up both the escape of carbon vapor from the thin tungsten carbide surface layer as well as reaction of this hotter layer with the carbon substrate to give a net equilibrium shift toward WC.

Microscopy

At this stage in the argument, it is worthwhile to examine photomicrographs of both samples (Figure 3). The high-intensity beam

(a)   (b)
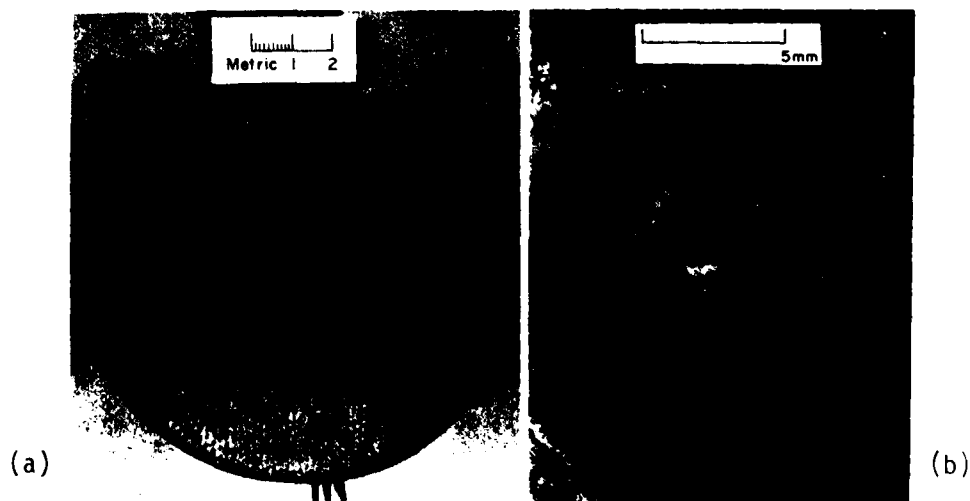
Figure 3.   (a) 10 kW/cm^2 burn on 1/8-inch disk of TBR (5.5 sec.); (b) cavity in second disk after burn-through of top 1/8-inch disk by 30 kW/cm^2 CO_2-laser (5 sec.).

cut through the upper of two stacked disks and penetrated the lower;
the low intensity beam barely penetrated the top layer of the first
disk. In the scanning electron photomicrographs, (SEM) of the low
intensity burn shown at three magnifications (Figure 4), a semiliquid
phase is just beginning to coalesce. (The tiny dot in a is enlarged
in b). The related EDAX micrograph c of the semifluid edge, enlarged
in d, shows the distribution of tungsten as white dots, indicating
great enrichment of tungsten in the semiplastic matrix though carbon
features still persist. Note the carbon fiber stubs marked by arrows
in c and d.
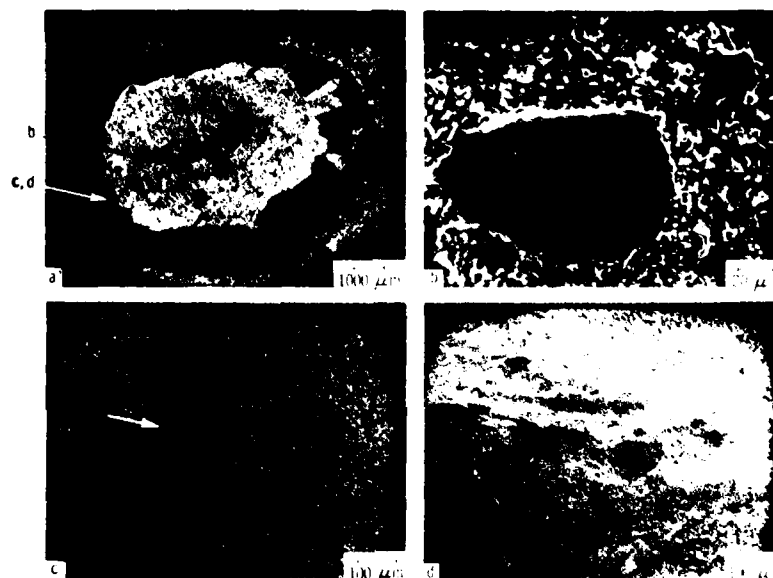
Figure 4.   Scanning electron micrographs (SEM) and energy dis-
persive analysis by X-rays (EDAX) of TBR irradiated by 10 kW/cm^2
CO_2-laser (a) SEM of burn area, (b) enlargement of microdroplet, (c)
EDAX of burn edge, (d) SEM of same area.

        The high-intensity laser cut deeply and slowly into TBR and
vaporized the carbon fabric, leaving shiny drops of molten, metallic
tungsten carbides on the walls and at the forefront of the cavity
(Figure 5). Near the mouth of the cavity, two or more phases are
clearly evident on the surface of these drops (Figure 5a and d) and
the EDAX photomicrograph showing the distribution of tungsten
(Figure 5b) verifies the enrichment of W_2C in the surface coat of WC
as C escapes.
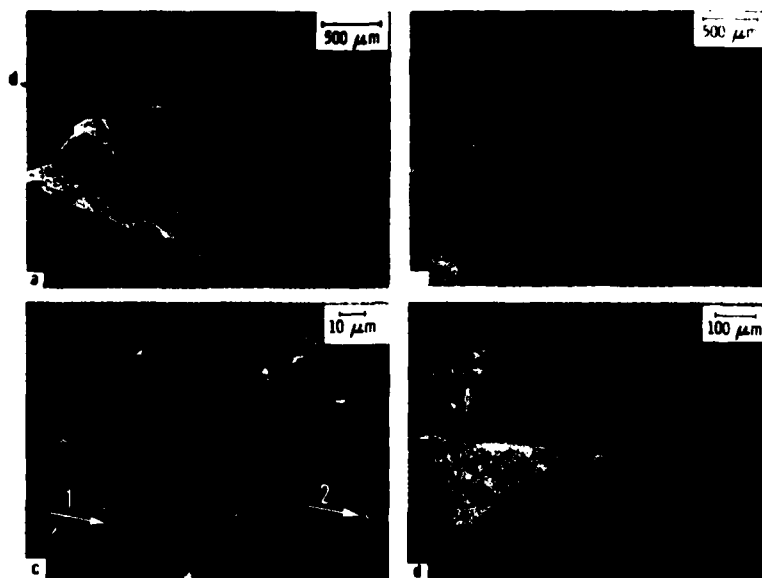
Figure 5.   Scanning electron and energy dispersive photomicrographs of TBR irradiated by 30 kW/cm^2 CO$_2$-laser: (a) SEM of mouth of burn cavity, (b) EDAX of same area, (c) fibers from midpoint of burn showing (1) redeposition of carbon, and (2) residual coating, (d) enlargement of tungsten carbide drop showing carbon deficient upper layer.

The SEM of a group of fibers from the wall area halfway down the burn (Figure 5c) has two features of interest: the bulbous growth of carbon at 1, and the residual tungsten-rich sheath at 2 which previously surrounded a fiber now eaten away. Both are evidence of the occurrence of the peritectic reaction

$$2WC \longrightarrow W_2C + C \qquad\qquad (2)$$

producing the disappearance of fiber with redeposit of some vapor in a cooler portion of the sharp thermal gradient.

LASER ENERGY ABSORPTION THROUGH CHEMICAL REACTION

The significance of these observations becomes apparent when we consider the related thermodynamic data as well as the mechanisms by which the relatively low-energy photons in a CO$_2$-laser can interact with a carbon-fiber reinforced tungsten-carbide matrix.

91

Thermodynamics

Let us first examine the thermodynamics of the proposed system. The only high-temperature data we have found gives formation enthalpies at 2800°C for W_2C and WC (2). Gupta and Seigle (3) determined the heat of formation and free energy of W_2C at 1300°C below which it is unstable. WC is the only thermodynamically stable form of tungsten carbide at room temperature.

For equilibrium or steady state conditions at 2800°C, calculated heats of reaction for solution and vaporization of carbon give a net absorption of 170 kcal/mole of C:

$$\Delta H, \text{ kcal/mole}$$

$$
\begin{array}{ll}
C(s) + W_2C \longrightarrow 2WC & -5 \\
2WC \longrightarrow W_2C + C(g) & 175 \\
\hline
C(s) \longrightarrow C(g) & 170
\end{array}
\tag{3}
$$
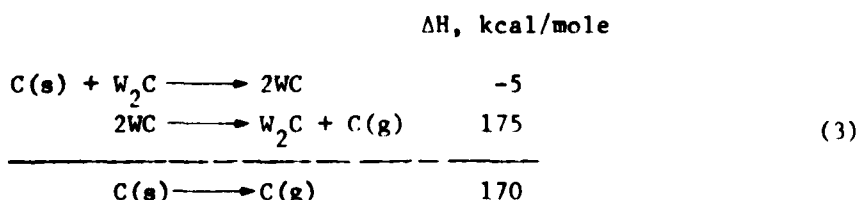
which translates to 60 kJ/g of carbon volatilized and indicates a highly endothermic system. The actual energy absorption must be greater under laser irradiation by reason of the following:

No account is taken in our energy calculations of the heat of melting the W_2C and WC (no data available).

A nonequilibrium system during irradiation corresponds to a higher energy input and a higher temperature for reaction than that measured on a system infinitesimally removed from equilibrium, i.e., conditions under which thermodynamic data are measured.

The emissivity of the tungsten carbide system is not known at the face temperature recorded (3230°C) for which the emissivity was assumed to be 0.999. The true temperature must be several hundred degrees higher, judging from emissivity measurements made in our laboratory from 700-1700°C on TBR material;* the normal spectral emissivity diminishes from 0.85 to 0.72 in this interval. The normal spectral emissivities of W_2C, WC, and pyrolytic graphite at 0.9μm, (the wavelength observed by the optical pyrometer during our experiments) are listed by Touloukian as 0.48 (2130°C), 0.59 (1530°C), and 0.79 (1780°C) (4).

*Private communication from K. J. Tauer.

Crystallography

We have assumed that monoatomic carbon is the principal volatile species from WC whereas the volatile species from graphite contain a number of polyatomic species -- C_2, C_3,...C_6, ...(5). Per gram atom, the formation of C absorbs the largest amount of energy; all bonds to neighboring atoms are broken.

With carbon release from WC, there is good reason to believe that the initial species evolved is the more highly energetic C_1 as suggested by earlier workers (6). Some aspects of carbon removal from the tungsten carbide lattice, whether solid or molten, can be deduced by examining the crystal structure of WC (Figure 6). In general, the X-ray diffraction patterns of liquids near the melting points show the same short distance order as the parent crystals (7). From two neighboring WC cells, carbon atoms are released at distances greater than the C-C bond distance in graphite (1.67Å vs 1.42A). Unless a carbon atom (or ion) rolls across the electron surface cloud to bond with another emerging C_1, C_2 should not be observed in the vapor. If present, it must be a secondary product.

Further support for this view of single carbon atom egress from the WC lattice at 2800°C or above is found in the elegant study by French of carbon atom diffusion into the tungsten body-centered cubic lattice at 1000°C (8). He photographed, by field ion microscopy, the atomic positions of W atoms in the successive layers of the tip of a carburized tungsten wire as these layers were removed one by one. This remarkable series of photomicrographs passes from the WC surface to the underlying W crystalline state. By observing the shift in the positions of the tungsten atoms, made visible by
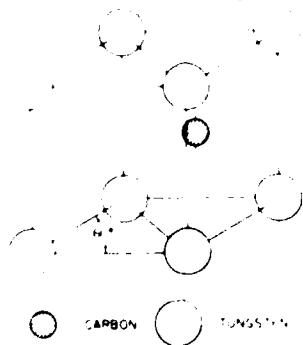
Figure 6.   Hexagonal unit cell of WC.
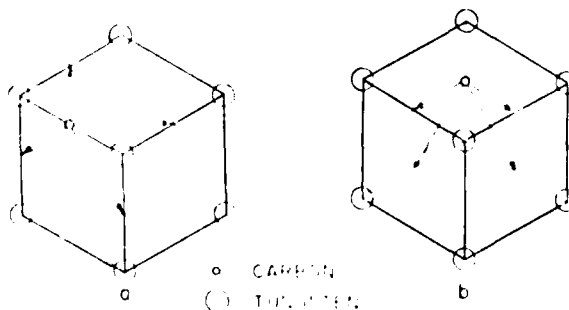
Figure 7.   Transport of carbon atoms through tungsten body-centered cubic lattice [after French (8)].

this technique, he concluded that the diffusion of carbon into and through the tungsten lattice proceeded by single atoms entering either the edge or the face of the unit cells on the surface, followed by passage within the cells from edge to inner edge or from face to inner face (Figure 7).

The phenomenon that we have trapped in the thin skin of tungsten carbides overlaying the carbon fibers corresponds to the reversal of carbon diffusion -- from carbon fiber, in this case, through the thin tungsten-carbide skin to the surface.

Let us consider the fate of the released single carbon atoms. Those emerging with sufficient energy to escape from the surface can be oxidized or can redeposit downstream either to build pyrolytic graphite or amorphous soot. Those with lesser energy can travel across the surface to a cooler area where a well-crystallized graphite ring is forming. We have evidence for both. In either case, the net energy required to produce these single carbon atoms from the underlying graphite fibers must be greater than the thermo-dynamic value to atomize graphite given in Equation 3.

As is clearly visible in Figure 8, the high-energy laser burn is surrounded by a border of pyrolytic carbon in well-formed graphite layers. Low-intensity laser burns also are surrounded by pyrolytic carbon. The movies of samples during irradiation show

Figure 8.   (a) SEM of portion of carbon ridge around 30 kW/cm^2 burn and (b) polished metallographic mount of burn cavity cross section showing solid- and open-layered structure of ridge, and large drop of tungsten carbides at lower right.

94

intense incandescence of these rings as the atomic building blocks release their energy. By contrast, the centers of these burns appear relatively cool.

When a block of pyrolytic carbon is irradiated, the entire burn area and the overlaying plume become incandescent due to poly-atomic species. These seem to be absent when TBR is irradiated.

From these observations and arguments, it may be concluded that the energy required to release carbon must exceed that required to separate the original carbon lattice into atoms.

UNIQUE FEATURES OF TBR

Stability of Carbide Matrix: 3000° Liquid Phase

Physical Constants

At this point in the argument, some observations on stability are in order. Among all elements, carbon has the highest melting point (3652 or 3870°C) and a very high boiling point (4200°C) (9). These signify the strongest interatomic bonds between atoms of any element as well as strong lattice bonding. Tungsten, with the next highest melting point (3400°C) and somewhat weaker lattice bonding, has a higher boiling point (5530 or 5900°C) (9) and shows very strong interatomic bonding.

Most significant, however, are the melting and boiling points of the binary tungsten carbides. The three high-temperature crystallographic phases all melt within 30 ± 12 degrees and the three associated eutectic compositions within the 40-degree interval below this. This means that the tungsten carbides melt sharply at about $2750\pm30°C$, nearly 1000 degrees below the melting point of carbon and 600°C below that of tungsten (Figure 2). The boiling point of the tungsten-carbon "alloy" is listed as greater than 6000°C, higher than that of any other compound. What is particularly significant about this 3000°C liquid range is the relative permanence of the liquid state as the solid substrate vaporizes through it. Also indicated is the stabilizing effect of carbon atoms intermingled with tungsten in the liquid phase; the liquid phase remains well above the boiling points of either constituent.

Wetting of Fibers

A second significant property of the tungsten-carbon "alloy" that we have observed, is that once molten, it wets the carbon fibers of the cloth very well. Silvery bundles of fibers were separated from the sawdust of the sample irradiated with the higher intensity laser, which was sawed in half before mounting. These came from the

cylindrical area near to and surrounding the burn-hole to which the molten, reactive matrix had been driven. The molten coating (a) improved the contact of the $C-W_2C$ reactants, (b) protected the hot carbon fabric from reactive gases such as CO, CO_2, or O_2, and (c) on solidifying, "mechanically hardened" the structure. The mechanical hardness of tungsten carbides is well known.

What we observe, then, in the interaction of the high-intensity $10.6\mu m$ laser and TBR is a highly endothermic "redox" reaction of liquid tungsten carbides with solid carbon, initially supplied by the pyrolyzed resin, then by the reinforcing fabric itself. There is also a fluid flow inward of the reacting matrix to give a permanent hard bond on cooling. Additionally, some of the released carbon redeposits as pyrolytic carbon around the periphery of the burn; this also increases the mechanical strength of the damaged piece.

Laminar Structure

Radial Energy Dissipation

There are further aspects of the burn residues shown in the polished metallographic section in Figure 8 that elaborate this mechanism. The only two to which reference will be made are the following:

> Because of the very low volatility of tungsten carbide even as carbon is diffusing through it, the atoms of tungsten remains in or near the burn area. The laser energy is chiefly dissipated by vaporizing monatomic carbon.

> Because of the laminar structure of the TBR material tested (as is also true of the pyrolytic graphite similarly irradiated in our tests), penetration of energy normal to the surface is minimal; energy not absorbed by the reaction or by reradiation is dissipated laterally by conduction within the upper layers only.

Skin Effect

Another unusual aspect of TBR may be called a "skin effect." This was observed in monitoring both TBR and pyrolytic graphite samples during irradiation. We believe this effect accounts for the peculiar patterns of soot deposited on these surfaces and certain anomalies in the surface-temperature records made during laser irradiation. It appears to contribute significantly to the barrier action of TBR.

(a)   (b)

Figure 9.   Five-second 10 kW/cm^2 burns on (a) TBR
and (b) pyrolytic graphite (0.1 Mach wind tunnel).

Figure 9 shows burns of both TBR and pyrolytic graphite
which were mounted in a 0.1-Mach wind tunnel and irradiated with a
10 kW/cm^2 laser beam. The similarity in soot patterns is striking.
Both patterns appear to originate at or near the edge of the molten
or plastic face of the burn area. These figures verify that the soot
source is at the edge of what high-speed movies indicate is a lifting
of a cohesive but plastic surface due to carbon vapor build-up below
as well as above the upper-most laminae. Trapped below this blister,
the carbon vapor has a chance to coalesce into soot mixed with other
condensed carbon fragments until the vapor pressure becomes great
enough to slit the blister or tear the edge in the weakest area and
release the trapped mixture.

With pyrolytic graphite in two successive runs, the
breaking of the plastic "skin" was quite visible on the video scan
monitor as well as in the movies. A white incandescent bulge
appeared, tore at the right edge, lifted up and burned back from the
reactive broken edge exposing a much cooler, black underlayer which,
in turn, became incandescent, lifted, and similarly disappeared. In
one run, this occurred twice; in the other, three times. The rise and
fall of the recorded front surface temperatures, twice and three
times, verifies the observations. The front face temperature
recorded with TBR was considerably lower and has a shallow wave form
consistent with the more fluid or plastic top laminate during
irradiation.

Multiphoton Absorption: Initially by Carbon

This discussion would be incomplete without some remarks
about the initial stages of irradiation. Each mole of photons in the
10.6μm laser beam carries only 2.7 kcal (0.9 kJ) of equally distri-
buted energy. This energy is only sufficient to initiate restricted,
rotational motion of one C-C bond per photon absorbed. Each bond
must absorb many quanta of this energy to approach the energies for
bond vibrations, for electronic transitions resulting in light
emission, and ultimately for bond breaking or the initiation and
support of an energy-absorbing chemical reaction.

97

One observation from the high-speed movie record of a sample of TBR is that the first frame showing a visible change occurred 1.41 seconds after the start of laser action and showed the cross-hatch appearance of the incandescent carbon fabric just as the matrix melted. In the next frame, this was obliterated in the over-all incandescence of the fabric and matrix. This supports the belief that carbon, rather than the tungsten carbides, is capable of absorbing significant amounts of radiation at 10.6μm. This is a requirement for interaction of photons with matter.

From these data and observations, we conclude that the sequence of reactions is the following:

- Multiphoton absorption of 10.6μm radiation by carbon to raise it to incandescence and a sufficiently high temperature to soften the tungsten-carbide/carbon matrix.

- Initiation of rapid carbon migration from solid carbon through the tungsten carbide matrix to the liquid-vapor phase boundary in a highly endothermic process.

- Escape of hot atomic (or ionic) carbon either from this surface as vapor or across this surface to produce an incandescent pyrolytic graphite ring.

- As a concomitant reaction, lifting of the top layer of the laminate intermittently to release clouds of soot and vapor which have cushioned lower layers from direct conductive heat transfer.

SUMMARY

To recapitulate and add some corollaries, the damage-limiting mechanisms provided by TBR under CO_2-laser irradiation include:

- reradiation of higher energy photons by multiphoton-activated carbon;

- reflection of substantial fractions of laser energy as the tungsten carbide both on and under the surface laminate becomes molten;

- protection of carbon fabric from air erosion by the molten matrix;

- lateral energy transfer through molten carbide-coated carbon fabric layers;

- limitation of energy transfer from layer to layer by protective blister formation;

- intermittent detachment of radiating reacting layers from the substructure;

- the highly endothermic, renewable reaction system of tungsten carbides and carbon which facilitates a smooth, relatively slow burn;

- mechanical strengthening of the burn area in this laminar material by transport and resolidification of the molten matrix and deposit of pyrolytic graphite in the vicinity of the laser burn.

We submit that this analysis defines the major sequence of events that occur when TBR is irradiated by a CO_2-laser and that it provides a reasonable model to explain the outstanding thermal response of this material.

REFERENCES

1. E. Rudy, "Ternary Phase Equilibria in Transition Metal-Boron-Carbon-Silicon Systems," Part V, AFML-TR-65-2, Air Force Materials Laboratory, June 1969, p. 192.

2. H. L. Schick, "Thermodynamics of Certain Refractory Compounds," Vol 2, Academic Press, New York, 1966, pp. 83, 85.

3. D. A. Gupta and L. L. Seigle, Metall. Trans., 6A, 1939 (1975).

4. Y. S. Touloukian and D. P. DeWitt, "Thermophysical Properties of Matter," Vol 8, IFI/Plenum, New York, 1970, p. 830.

5. H. B. Palmer and M. Shelef, "Vaporization of Carbon," Chemistry and Physics of Carbon, Vol 4, Marcel Dekker, Inc., New York, 1968, p. 129.

6. E. K. Storms, "The Refractory Carbides," Academic Press, New York, 1961, p. 154.

7. M. A. Omar, "Elementary Solid State Physics," Addison-Wesley Publishing Co., Reading, MA, 1978, pp. 21-23.

8. R. D. French, PhD Thesis, Brown University, Providence, RI, 1967.

9. G. V. Samsonov, "High-Temperature Materials: Properties Index," Plenum Press, New York, 1964, pp. 96, 100-01.

*PINNICK, JENNINGS and
 CHÝLEK

RELATIONSHIPS BETWEEN EXTINCTION AND MASS
CONTENT OF ATMOSPHERIC FOG AND MILITARY SMOKES (U)

RONALD G. PINNICK, PhD
S. GERARD JENNINGS, PhD
ATMOSPHERIC SCIENCES LABORATORY
WHITE SANDS MISSILE RANGE, NEW MEXICO 88002

PETR CHÝLEK, PhD
CENTER FOR EARTH AND PLANETARY PHYSICS, HARVARD UNIVERSITY
CAMBRIDGE, MA 02138

INTRODUCTION:

A possible relation between the extinction (or atmospheric visibility) and particle mass content of fogs and aerosols has been a subject of interest to many scientists since the beginning of the century.[26,1,8,13,25,3,17,19,18,2] If such a relation exists, it would be of considerable practical interest since then remote sensing extinction measurements would yield information concerning the fog or aerosol mass content, and vice versa, from mass content measurements (which are more easily done at various meteorological stations) one could deduce the extinction properties of fogs and aerosols--at least at definite wavelengths.

All previous attempts to relate the extinction (or visibility) to the mass content of fogs and aerosols were only partially successful since all derived relations also turned out to be functions of the particle size distribution, and thus the derived relation varied from one case to another.

We will show that at definite wavelengths, which are determined primarily by the size of the largest particles present in a given polydispersion of fog or smoke aerosol particles, there exists an unambiguous relation between the extinction and mass content which is independent of the form of the particle size distribution.

101

*PINNICK, JENNINGS and
CHÝLEK

EXTINCTION AND MASS CONTENT OF FOG AND SMOKE AEROSOL:

Consider a polydispersion of spherical aerosol particles characterized by a size distribution $n(r)$ and refractive index m. We want to derive relationships between the aerosol extinction coefficient σ_e and the aerosol mass content M given by

$$\sigma_e = \int \pi r^2 Q_e(m,x) n(r) dr \qquad (1)$$

$$M = \rho \int \frac{4}{3} \pi r^3 n(r) dr \qquad (2)$$

where $Q_e(m,x)$ is the Mie efficiency factor for extinction for a particle with refractive index m and size parameter $x = 2\pi r/\lambda$ at the radiation wavelength λ and ρ is the aerosol density.

It can be seen from the integrals in equations (1) and (2) that for the extinction coefficient σ_e and mass content M to be uniquely related for arbitrary particle size distributions $n(r)$, we must be able to approximate the Mie extinction efficiency factor $Q_e(m,x)$ by a linear function of particle radius $Q_e \sim r$ [or equivalently, let us say $Q_e(x) = cx$ as suggested by Chýlek].[4,5] Then the right-hand side of equation (1) contains the integral $\int r^3 n(r) dr$ and combining equations (1) and (2) yields

$$\sigma_e = \frac{3\pi c}{2\lambda\rho} M \; . \qquad (3)$$

Unfortunately, the task of finding a wavelength for which the $Q_e = cx$ approximation is a good one is formidable because in general the extinction efficiency is a rather complicated function of particle size, refractive index, and wavelength. Nonetheless, examination of the form of the Mie efficiency function $Q_e(x)$ for fog droplets, phosphoric acid droplets, HC, and carbon smoke particles for wavelengths ranging from the visible through the middle infrared reveals that at particular wavelengths the $Q_e(x) = cx$ approximation is acceptable.

An example of such a wavelength for fog droplets is shown in figure 1 where the Mie extinction efficiency function at $\lambda = 11\mu m$ is well approximated by $Q_e = cx$, up to a maximum value $x_m \cong 8$

*PINNICK, JENNINGS and
CHÝLEK

(corresponding to a maximum radius $r_m \cong 14 \mu m$). Therefore, under the constraint that fog droplets have radii not exceeding $r_m = 14 \mu m$ (which is not unrealistic for radiation and most advection fogs), we expect a linear relation between extinction at $\lambda = 11 \mu m$ and liquid water content of fog according to equation (3).
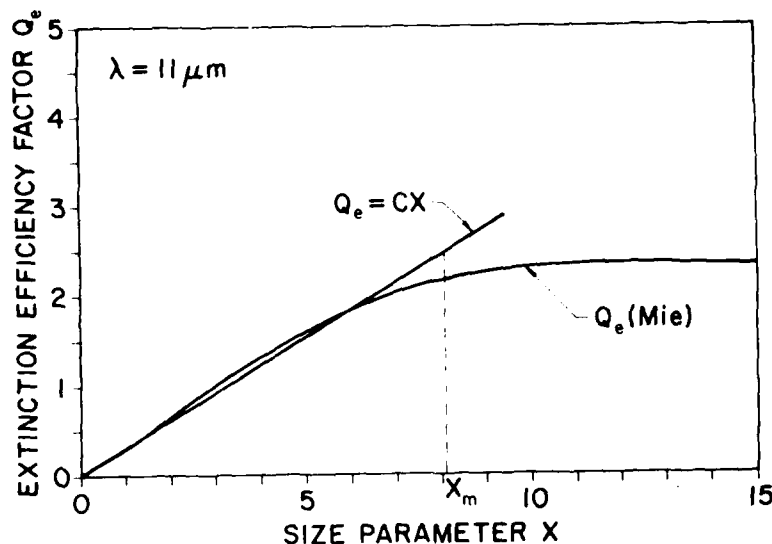
Figure 1. The efficiency factor for extinction Q_e for water droplets versus size parameter x at a wavelength λ = $11 \mu m$ (index of refraction m = 1.153 - 0.0968i). The efficiency factor can be approximated by a straight line Q_e = cx providing $x \leq x_m$. The approximation overestimates the exact value of Q_e for some some size parameters, but underestimates it for others (still with $x \leq x_m$). These two errors tend to cancel, leading to the extinction coefficient being linearly related to the liquid water content of fogs according to equation (3).

We should point out that this linear approximation of the Mie extinction efficiency is distinctly different than a Rayleigh approximation, which requires the particle size (with respect to wavelength) and phase shift be small ($|m - 1|$ x << 1). Clearly, this Rayleigh condition is not satisfied for size parameters as large as x = 8 as in figure 1.

*PINNICK, JENNINGS and
CHÝLEK

In the next sections we apply this approximation procedure and the resulting extinction-mass content prediction (3) to polydispersions of particles having widely different optical properties: atmospheric fog, phosphoric acid, HC, and carbon smokes. The success achieved with relation (3) attests to its simplifying impact on the gamut of radiative transfer problems in which atmospheric fog or aerosols play a role. Thus, our relation (3) connecting particulate extinction to particulate mass content should prove useful in such diverse research areas as earth climate, remote sensing, and electro-optical communications.

APPLICATION TO ATMOSPHERIC FOG:

Before we can have confidence in applying the linear relation (3) between extinction and liquid water content of fog we should test its validity with existing measurements that are available. Since simultaneous infrared extinction and liquid water content measurements in fog do not yet exist, we calculated the volume extinction coefficient σ_e using Mie theory and the liquid water content M for 341 measured size distributions of fog droplets reported in the literature.[9,10,22,13,14,21] The fog measurements were chosen to represent a wide range of meteorological conditions ranging from maritime and continental advection fogs[13,14,9] to inland radiation fogs.[9,10,22,21]

The results of these calculations together with the derived approximation equation (3) at $\lambda = 11\mu m$ are shown in figure 2. Points showing the results of the Mie calculations are always within a factor 2 of the straight line showing the equation (3) approximation ($\sigma_e = 128W$) even though the extinction coefficient and liquid water content ranges over almost four orders of magnitude with the considered size distributions. In view of the fact that the $\sigma_e = 128W$ relation is not a result of any fit to experimental points, but rather an absolute calculation (by absolute we mean that no free fitting parameter is involved) using equation (3), we consider the agreement to be acceptable.

On the other hand, we do not expect a unique extinction-liquid content relationship at all wavelengths. To demonstrate this point, we present Mie calculations for the same 341 droplet distributions at $\lambda = 4\mu m$ in figure 3. For a given liquid water content, the extinction coefficient varies by more than an order of magnitude as a function of the size distribution.
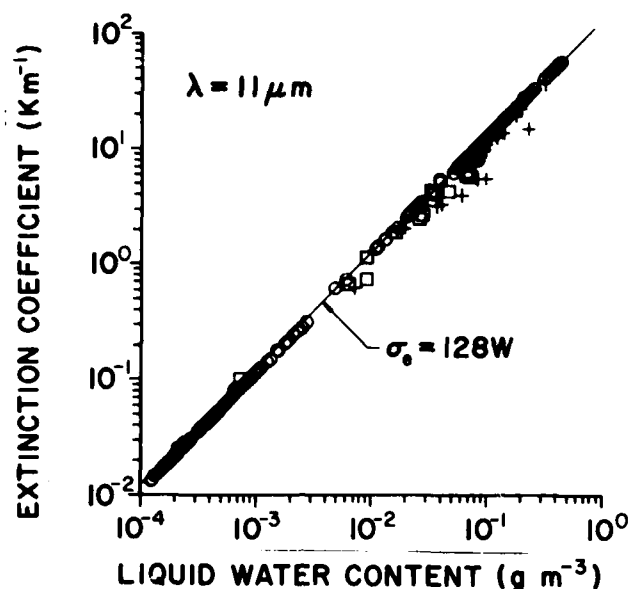
Figure 2. Variation of particulate extinction coefficient (at λ =
11μm) with liquid water content W. The points were
determined from 341 size distribution measurements of
atmospheric fog and haze made at different geographic
locales and under a variety of meteorological
conditions [open circles denote measurements of
Pinnick,[21] plus symbols of Garland and Roach[9,10,22],
square symbols of Kumai,[13] and solid circle symbols of
Kunkel[14]]; the straight line labeled σ_e = 128W was
determined from equation (3).

APPLICATION TO PHOSPHORIC ACID AND RP SMOKE:

Phosphoric acid smoke differs from atmospheric fog in two
important respects. First, smoke particles are much smaller than
fog droplets; and second, they are generally strongly absorbing at
infrared wavelengths. These two characteristics result in Mie
efficiency factors Q_e being well approximated by Q_e = cx for most
infrared wavelengths, and consequently, we expect the extinction-
mass relation (3) should be applicable throughout the infrared.

*PINNICK, JENNINGS and
CHÝLEK
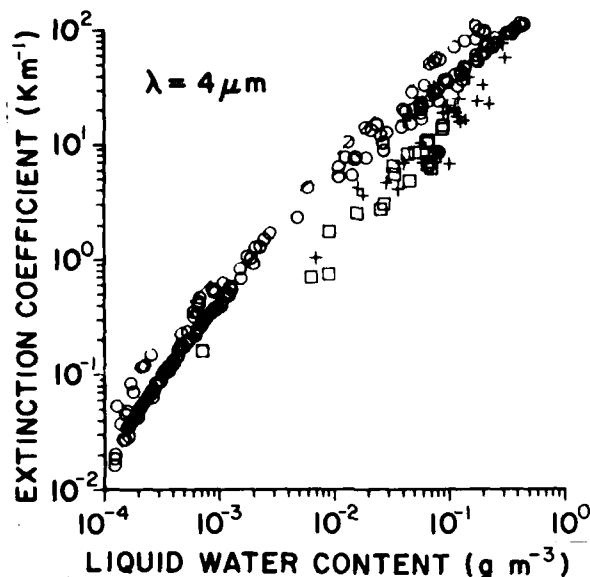
Figure 3. Variation of particulate extinction coefficient (at λ = 4 μm) with liquid water content for the 341 size distributions of fog and haze considered in figure 2.

To test this contention we have compared the ratio of the extinction coefficient to mass content σ_e/M predicted according to our size-distribution-independent relation (3) to values of σ_e/M determined from the transmission and mass content measurements of Milham.[15]* The results, which are seen in figures 4 and 5, show

*The extinction coefficients σ_e were derived from transmission measurements for which forward scattering corrections[7] and multiple scattering corrections should be considered. Forward scattering corrections arise from singly scattered photons that enter the detector along with the unscattered (direct) radiation due to the finite angular aperture of the detector. Similarly, multiple scattering corrections arise from signal contributed by multiply-scattered photons. Both these effects cause increased detector signal and hence result in a smaller inferred extinction coefficient if they are not considered. We estimate the forward scatter corrections for the experimental setup used by Milham[15] to be not more than 3 perce; and have neglected them; however, no attempt was made to make quantitative estimates of multiple scatter corrections.

106

*PINNICK, JENNINGS and
CHÝLEK

agreement of predicted and measured σ_e/M values to within 30 percent throughout the 3mm to 5μm and 8μm to 12μm atmospheric window spectral regions suggesting the validity of relation (3) for phosphoric acid smoke. The extinction-mass measurements in figures 4 and 5 can only suggest (and not prove) the validity of relation (3), as the measurements are for only one particular size distribution of phosphoric acid particles.
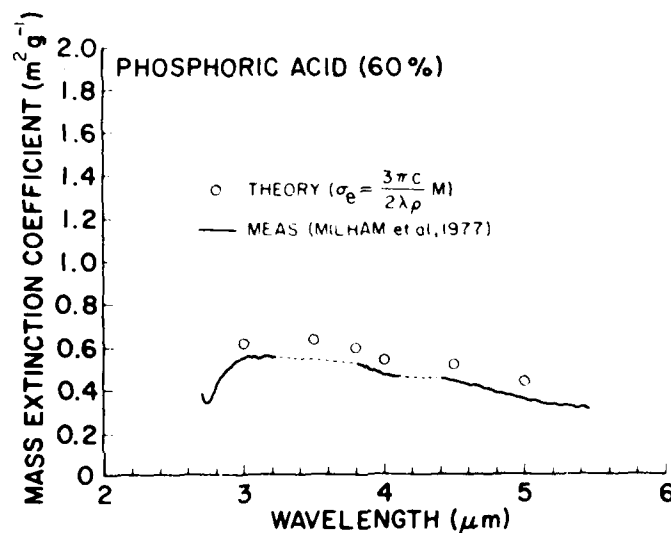
Figure 4. Values of the ratio of aerosol extinction coefficient to aerosol mass content (σ_e/M in m^2g^{-1}) predicted according to the size-distribution-independent linear relation (3) (open circles), and measured by Milham[15] (smooth curve) for 60 percent phosphoric acid aerosol. Good agreement between prediction and measurement is obtained throughout the $3\mu m \leq \lambda \leq 5\mu m$ spectral region.

In contrast to the phosphoric acid results, comparison of the relation (3) to Milham's[15] measurements on RP smoke (figure 6) show relatively poor agreement in the 8μm to 12μm spectral region. The reason for the poor agreement is that the burning of RP/WP smokes apparently results in production of an unknown chemical species[16] whose refractive indexes cannot be approximated by those of phosphoric acid [which was assumed in determination of $c(\lambda)$ in relation (3)].

*PINNICK, JENNINGS and
CHYLEK
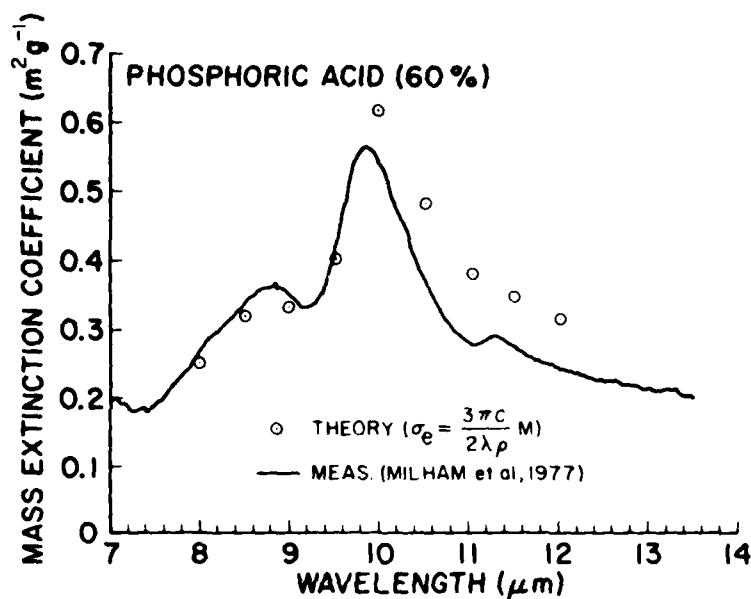
Figure 5. Same as figure 4 except for the $8\,\mu m \leq \lambda \leq 12\,\mu m$ spectral
region.

APPLICATION TO HC SMOKE:

Like phosphoric acid and RP smoke particles, HC smoke
particles are much smaller than fog droplets. However, they are
much weaker absorbers than these other smokes at most infrared
wavelengths, and as a result the Q_e = cx approximation is less
accurate.

This inaccuracy is reflected in the comparison of σ_e/M
values predicted according to equation (3) with measurements of
Milham[13] in figures 7 and 8. For some wavelengths in the $3\,\mu m$ to
$5\,\mu m$ and $8\,\mu m$ to $12\,\mu m$ spectral regions the disagreement between
prediction and measurement is as much as a factor 2.5. Thus,
although we expect relation (3) to be successful throughout the
infrared for strongly absorbing phosphoric acid smoke, for weakly
absorbing HC smoke our relation (3) should only he applied for
wavelengths around $\lambda = 4\,\mu m$ and $\lambda = 11\,\mu m$.

*PINNICK, JENNINGS and
CHÝLEK
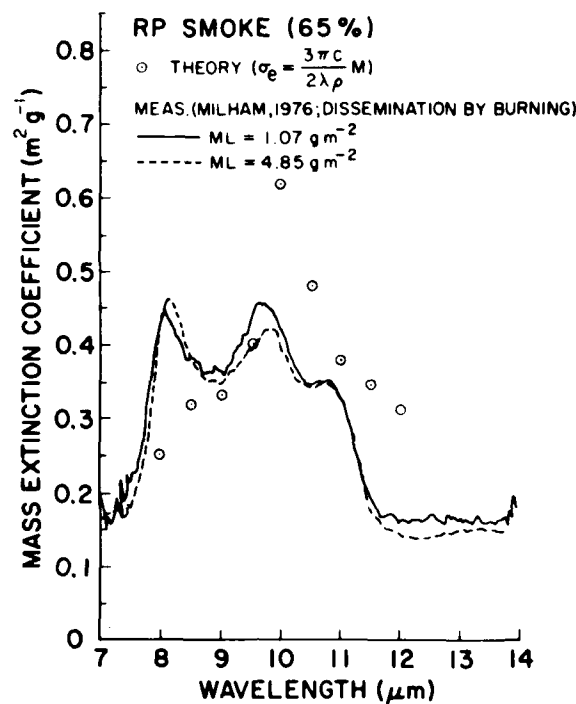
Figure 6. Same as figure 5 except for RP smoke rather than phos-
phoric acid. In this case, measurements are shown for
two different aerosol mass loadings (M is the aerosol
mass content and L the transmission chamber path
length).

APPLICATION TO CARBON SMOKE:

Caution must be exercised in applying the aerosol extinc-
tion coefficient-mass content relation (3) to carbon smoke because
in general the particles are irregular in shape and the derivation
of equation (3) requires the assumption of spherical homogeneous
particles. We know from extinction and scattering measurements on
slightly irregular particles by Greenberg,[11] Zerull,[27] and
Pinnick,[20] that providing their equivalent size parameters are
less than $x = 3$, they scatter like spheres. If carbon smoke
particles were only slightly irregular and if they had size param-
eters less than $x = 3$, we might expect that our neglect of irreg-
ular particle effects in the application of equation (3) to these

*PINNICK, JENNINGS and
CHÝLEK

particles might be of little consequence. However, some carbon smoke particles, for example those measured by Roessler and Faxvog,[23] consist of long extended chains of small ($\sim$0.05μm diameter) spheres (figure 9). For these particles, we are probably not justified in approximating their extinction efficiency by some equivalent sphere extinction efficiency [as is done in determination of the parameter c in equation (3)].

Keeping in mind reservations concerning particle shape effects, we have proceeded to compare the extinction coefficient-mass relation (3) to transmission measurements made through carbon smokes from several different sources. We chose measurements reported by Hurley and Bailey[12] on a hand-fired Lancashire boiler operating at full load, by Conner and Hodkinson[6] on an experimental smoke stack, by Roessler and Faxvog[23] on acetylene smoke, and from the Handbook of the Society of Automotive Engineers (SAE),[24] for diesel engine smoke emissions.
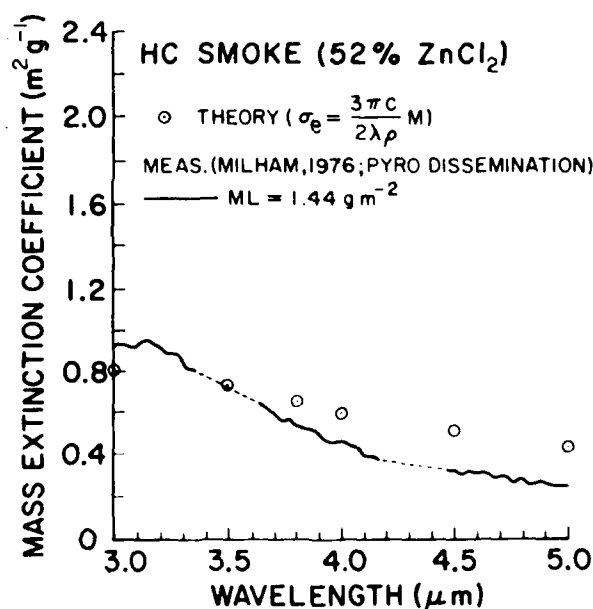
Figure 7. Values of the ratio of aerosol extinction coefficient to aerosol mass content (σ_e/M in $m^2 g^{-1}$) predicted according to the size-distribution-independent relation (3) (open circles), and measured by Milham[15] (smooth curve) for HC smoke.
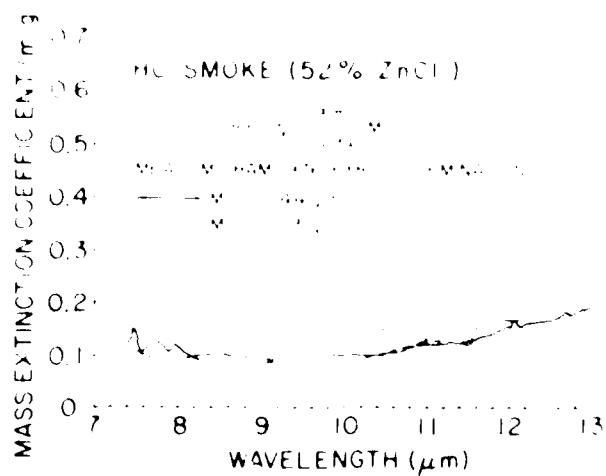
MASS EXTINCTION COEFFICIENT m²/g

0.7
0.6
0.5
0.4
0.3
0.2
0.1
0

HC SMOKE (52% ZnCl)

WAVELENGTH (µm)

7   8   9   10   11   12   13

Figure 8. ...

0.2 µm

Figure 9. ...

*PINNICK, JENNINGS and
CHYLEK

The results of the comparison are shown in table 1 where
the values of σ_e/M predicted on the basis of equation (3) are
generally within 20 percent of those determined from the measure-
ments on various types of carbon smokes. Thus, even for quite
nonspherical smoke particles, the relation (3) correctly predicts
a relation between extinction and mass content, at least for
visible wavelengths.

CONCLUSIONS:

We have shown that a linear size-distribution-independent
relation should exist between the volume extinction *coefficient*
and particulate mass content of atmospheric fog, phosphoric acid
smoke, HC smoke, and carbonaceous smokes—but only at particular
wavelengths. The suitable wavelengths are $\lambda \cong 11 \mu m$ for fog, $\lambda \cong$
$3 \mu m$ to $5 \mu m$, $8 \mu m$ to $12 \mu m$ for phosphoric acid, $\lambda \cong 4 \mu m$, $11 \mu m$ for HC,
and $\lambda \cong 0.55 \mu m$ for carbon smoke. These relations can be used to
uniquely connect the transmission across a path in a fog or smoke
cloud to the path-integrated particulate mass content, providing
forward scattering and multiple scattering corrections can be
neglected.

112

*PINNICK, JENNINGS and
 CHYLEK

TABLE 1

Comparison of measured and predicted values of the ratio of aerosol volume extinction coefficient to mass concentration σ_e/M for carbonaceous smoke particles. The measured values of σ_e were determined from visible transmissometer measurements under the assumption that forwardscatter and multiple scatter corrections to the inferred extinction coefficient are negligible. The measured values of smoke mass concentration M were determined from filter sampling. Also given are values of the smoke path length L and the transmissometer wavelength λ. The predicted values of σ_e/M were obtained from the size-distribution-independent relation (3) under the assumption of a particle density $\rho = 2$ g cm^{-3}.

Reference	Mass Concentration $M(g\ m^{-3})$	Path Length $L(m)$	Wavelength $\lambda(\mu m)$	σ_e/M $(m^2 g^{-1})$	Predicted [(from equation (3)] $\sigma_e/M = 3\pi c/2\lambda\rho$ $(m^2 g^{-1})$
Black Smoke	0.29	0.305	0.55	8.04	9.5
(coal stoker)	1.05	0.305	0.55	8.38	
Hurley and	1.40	0.305	0.55	9.0	
Bailey (1958)					
Black Smoke	0.16	0.10	0.56	8.78	9.3
(oil fired	0.55	0.10	0.56	9.61	
smoke stack)	1.0	0.10	0.56	9.52	
Conner and					
Hodkinson (1967)					
Acetylene smoke	0.0155	1.835	0.514	9.93	10.2
Roessler and	0.0527	0.10	0.514	9.96	
Faxvog (1979)	0.120	1.835	0.514	9.68	
	0.165	0.10	0.514	9.60	
	0.321	0.10	0.514	10.1	
Diesel Engine	1.0	0.10	0.55	6.79	9.5
Emission					
SAE handbook					
(1977)					

113

*PINNICK, JENNINGS and
 CHÝLEK

REFERENCES

1. Barteneva, O. D., and E. A. Polyakova, 1965, "A Study of
Attenuation and Scattering of Light in a Natural Fog Due to its
Microphysical Properties," Izv Atmospheric Oceanic Phys, 1:193-207.
2. Box, M. A., and B. H. J. McKellar, 1978, "Direct Evaluation of
Aerosol Mass Loadings from Multispectral Extinction Data," Quart J Roy
Meteorol Soc, 104:755-781.
3. Charlson, R. J., N. C. Ahlquist, and H. Horvath, 1968, "On the
Generality of Correlation of Atmospheric Mass Concentration and Light
Scatter," Atmospheric Environ, 2:455-464.
4. Chýlek, Petr, 1978, "Extinction and Liquid Water Content of Fogs,"
J Atmospheric Sci, 35:296-300.
5. Chýlek, Petr, J. T. Kiehl, and M. K. W. Ko, 1979, "Infrared
Extinction and the Mass Concentration of Atmospheric Aerosols,"
Atmospheric Environ, 13:169-173.
6. Conner, W. D., and J. R. Hodkinson, 1967, "Optical Properties and
Visual Effects of Smoke-Stack Plumes," US Department of Health,
Education, and Welfare, Public Health Service Publication, 999-AP-30.
7. Deepak, A., and M. A. Box, 1978, "Forwardscattering Corrections
for Optical Extinction Measurements in Aerosol Media. 1:
Monodispersions," Appl Opt, 17:2900-2908.
8. Eldridge, R. G., 1971, "The Relationship Between Visibility and
Liquid Water Content in Fog," J Atmospheric Sci, 1183-1186.
9. Garland, J. A., 1971, "Some Fog Droplet Size Distributions
Obtained by an Impaction Method," Quart J Roy Meteorol Soc,
97:483-494.
10. Garland, J. R., and I. C. Cox, 1973, "A Study of tne Contribution
of Pollution to Visibility in a Radiation Fog," Atmospheric Environ,
7:1079-1092.
11. Greenberg, J. M., 1972, "Absorption and Emission of Radiation by
Nonspherical Particles," J Coll and Inter Sci, 39:513-519.
12. Hurley, T. F., and P. L. Bailey, 1958, "The Correlation of
Optical Density with the Concentration and Composition of the Smoke
Emitted from a Lancashire Boiler," J Inst Fuel, 31:534-540.
13. Kumai, M., 1973, "Arctic Fog Droplet Size Distribution and Its
Effect on Light Attenuation," J Atmospheric Sci, 30:635-643.
14. Kunkel, B. A., 1971, "Fog Drop-Size Distributions Measured with a
Laser Hologram Camera," J Appl Meteorol, 10:482-486.
15. Milham, M. E., 1976, "A Catalog of Optical Extinction Data for
Various Aerosols/Smokes," Report ED-SP-77002, Edgewood Arsenal,
Aberdeen Proving Ground, MD.

16. Milham, M. E., D. H. Anderson, R. H. Frickel, and T. L. Tarnove, 1977, "New Findings on the Nature of WP/RP Smokes," Technical Report ARCSL-TR-77067, US Army ARADCOM, Chemical Systems Laboratory, Aberdeen Proving Ground, MD.

17. Noll, K. E., P. K. Mueller, and M. Imada, 1968, "Visibility and Aerosol Concentration in Urban Air," Atmospheric Environ, 2:465-475.

18. Patterson, E. M., and D. A. Gillette, 1977, "Measurements of Visibility vs Mass-Concentration for Airborne Soil Particles," Atmospheric Environ, 11:193-196.

19. Pilat, M. J., and D. S. Ensor, 1970, "Plume Opacity and Particulate Mass Concentration," Atmospheric Environ, 4:163-173.

20. Pinnick, R. G., D. E. Carroll, and D. J. Hoffman, 1976, "Polarized Light-Scattered from Monodisperse Randomly Oriented Nonspherical Aerosol Particles: Measurements," Applied Optics, 15:384-393.

21. Pinnick, R. G., D. L. Hoihjelle, G. Fernandez, E. B. Stenmark, J. D. Lindberg, S. G. Jennings, and G. B. Hoidale, 1978, "Vertical Structure in Atmospheric Fog and Haze and Its Effects on IR and Visible Extinction," J Atmospheric Sci, 35:2020-2032.

22. Roach, W. T., R. Brown, S. J. Caughly, J. A. Garland, and C. J. Readings, 1976, "The Physics of Radiation Fog: I - A Field Study," Quart J Roy Meteorol Soc, 102:313-333.

23. Roessler, D. M., and F. R. Faxvog, 1979, "Optical Properties of Acetylene Smoke at 0.5145μm and 10.6μm Wavelengths," submitted for publication in J Opt Soc Am.

24. SAE Handbook, 1977, "Diesel Engine Smoke Measurement (Steady State)," SAE J255, SAE Information Report, 871-877.

25. Tomasi, C., and F. Tampieri, 1976, "Features of the Proportionality Coefficient in the Relationship Between Visibility and Liquid Water Content in Haze and Fog," Atmosphere, 14:61-76.

26. Trabert W., 1901, "Die Extinction des Lichtes in einem truben Medium," Meteorol Z, 18:518-525.

27. Zerull, R. H., 1976, "Scattering Measurements of Dielectric and Absorbing Nonspherical Particles," Beitr Phys Atmosphere, 49:168-188.

STATUS OF IMPROVED AUTOROTATIVE
LANDING CAPABILITY RESEARCH

WILLIAM A. PLEASANTS, III
G. THOMAS WHITE, III
APPLIED TECHNOLOGY LABORATORY
FORT EUSTIS, VA   23604

Introduction

Current Army helicopter flight tactics require frequent operation at
low level and low speed conditions ordinarily restricted by flight
safety. While this nap-of-the-earth (NOE) flight does reduce proba-
bility of detection, it necessitates that the helicopter be operated
within the envelope shown in Figure 1. Within this envelope the
unique autorotative landing capability of the helicopter, which is an
inherent safety characteristic heavily relied upon during in-flight
power loss and other emergencies, is severely diminished or eliminated.

While the frequency of all emergency autorotative landings (i.e.,
rate per 100,000 flight hours) has decreased over the past several
years for Army single-engine fleet helicopters, the percentage of
unsuccessful landings resulting from emergency autorotations has
remained relatively high. United States Army Safety Center accident
statistics reveal that at least 30 percent of all emergency auto-
rotative landings involving AH-1, UH-1, OH-58, and OH-6A helicopters
result in some degree of vehicle damage or personnel injury. These
statistics further indicate that the probability of each of these
helicopters experiencing at least one emergency autorotation accident
during an assumed 10,000-hour service life is as follows:

OH-6	94.0%
AH-1	77.5%
OH-58	76.3%
UH-1	63.3%

117

(NOTE: "Emergency autorotation accidents" include damage classifications ranging from "precautionary landings" to "major damage".)

These autorotation accident statistics, coupled with the current emphasis on NOE operation, the potential high threat environment of the modern mid-intensity battlefield, the high cost of aircraft and their mission equipment, and the value of highly skilled crews, command renewed attention to engine-out survivability. Recent design studies and supplementary research of previously documented findings indicate that it is possible to significantly improve helicopter autorotation capability and reduce demands on pilot skill through helicopter rotor energy augmenting concepts. This paper discusses results of current studies as well as an outline for future in-depth research which will define optimum approaches and answer detailed design questions which are beyond the scope of current efforts.

Notation

AE	Auxiliary energy for concepts other than high energy rotor
$\overline{C_L}_{max}$	Maximum rotor average lift coefficient
C_T	Thrust coefficient $= T/(\pi R^2 \rho (\Omega R)^2)$
DL	Disk loading $= W/\pi R^2$
EE	Engine energy during autorotation, HP-sec
E req	Total energy required in autorotation
E^o req	Total energy required in autorotation at disk loading $=3$, Sea Level Standard (SLS)
h	Height above ground level, ft
KE	Helicopter kinetic energy due to horizontal velocity, HP-sec
K	Empirical constant relating initial hover power to average power
I_b	Rotor inertia per blade, slug-ft^2

I_R Total rotor inertia, slug-ft^2

PE   Potential energy, HP-sec $= Wh/550$

P(t)   Engine power available during autorotation, horsepower $(SHP-SHP_f) \, \bar{e}^t + SHP_f$

R   Rotor radius, ft

RE   Rotor energy, HP-sec $= I_R \dfrac{(\Omega_o^2 - \Omega_{min}^2)}{1100 \; SHP}$

SHP   Initial hover power, HP

SHP_f Minimum engine power, HP

$SHP_{hover_{oge}}$ Hover shaft horsepower out of ground effect

t   Flight time, sec

t_d Collective time delay, sec

(t/k)   Autorotation index, sec

V_{v_D} Autorotation vertical touchdown velocity, ft/sec

W   Helicopter flight weight, lb

W_{rs} Rotor group weight

W_{rs}^o Rotor group weight at disk loading $= 3$, SLS

Ω_o Normal rotor rotational speed, rad/sec

Ω_{min} Minimum rotor rotational speed, rad/sec

δ Average blade profile drag coefficient

η Overall helicopter efficiency factor

ρ Density

σ Rotor solidity

Autorotation Accident Statistics

The rationale supporting the need for the initiation of the investigation reported in this paper lies in the simple analysis of real-world autorotation accident data. Based on data supplied by the US Army Safety Center (USASC), an attempt was made to define first order critical or troublesome parameters that either affect individual helicopters or carry a common thread among all of the subject helicopters (i.e., UH-1, AH-1, OH-58, and OH-6).

The USASC data was instrumental in identifying overall causes of emergency autorotations and accident frequency of occurrence trends for the subject helicopters. The major categories of "cause-related factors" or factors which precipitated the emergency autorotation and subsequent accident are summarized in Figure 2. As might be expected, engine failure contributes the highest single "cause-related factor", with human error being second. In an attempt to define abnormal accident rates within the normal operating ranges of such parameters as airspeed, height above ground level (AGL), gross weight and mission, a relation to actual operational time spent by the subject helicopters at each flight condition or in each mission segment was formulated. Southeast Asia (SEA) Operational Flight Loads Investigation data was available for the AH-1G, OH-6A, and UH-1H helicopters based on an approximately 200-flight-hour operational survey conducted for each aircraft consecutively from 1968 through 1972.

The surveyed flight hour trends were in concert with the accident rates in all areas in which comparisons could be made. Unfortunately, the operational survey summary reports did not include data adequate to define the exact AGL height for the recorded mission flight hours, and thus the operational AGL height trends could not be directly compared with USASC accident statistics. It is estimated, however, that based on recorded average density altitudes and outside air temperatures, the AH-1G, OH-6 and UH-1H aircraft spent 30 to 50 percent of their mission time at heights of 1000 feet or lower. This estimate agrees with accident statistics which indicate that just over 50 percent of the emergency autorotational accidents (due to noncombat causes) were initiated from within this height band. For all four of the subject helicopter types the trend of unsuccessful autorotations at constant gross weight increases with decreasing height, as shown in Figure 3. The height below which most accidents occur ($\leq$ 500 ft) encompasses nap-of-the-earth (NOE), contour, and low-level flying currently in vogue for modern battlefield tactics.

Recent Experimental Work - High Energy Rotor System (HERS)

The Bell Helicopter Textron High Energy Rotor System (HERS) discussed in References 1 and 2 has demonstrated the ability to increase rotor inertia to eliminate or reduce the low speed portion of the H-V curve. An OH-58A helicopter was used as a test bed with blades modified by adding tip weights and structural strengthening. Bell Helicopter built the test hardware and conducted preliminary tests to expand the flight envelope. The HERS was then extensively tested under a contract with the Army Applied Technology Laboratory with investigative emphasis on the effect rotor inertia has on flight safety, performance, agility and control. The benefits and some of the penalties of high inertia rotors are discussed in detail in Reference 2. This paper will discuss only the impact of increased inertia on the low speed H-V avoid area.

The HERS concept uses the stored energy resulting from increased rotor inertia to reduce the H-V avoid region. The flight test rotor allowed testing of high (I_b = 672), mid (I_b = 500), and low (I_b = 323) rotor inertia configurations. Testing indicated that as rotor inertia increased, the H-V curve collapsed to a critical condition of hover at a height equal to that at the "knee" of the normal rotor curve (approximately 100 ft). This condition has been used as the design point for sizing auxiliary rotor energy concepts discussed later in this paper.

The essential summary results of the extensive H-V autorotation testing are compared in Figure 4 to the standard OH-58A results from earlier Army Engineering Flight Activity (AEFA) qualification flight tests. Three significant factors may be seen from this figure: the effect of increased inertia on the H-V curve, the difference between the operational and maximum performance H-V curves, and the apparent difference between the standard OH-58A and the HERS low inertia H-V curves.

The HERS and standard OH-58A maximum performance H-V curves represent the maximum autorotational performance demonstrated by the test pilots. The operational curve is adjusted for average pilot technique by allowing a 2-second collective delay. In determining the maximum performance curves, the test pilot immediately adjusted collective when power was reduced.

The OH-58A and the HERS low inertia configuration are nearly equivalent aircraft but demonstrated significantly different H-V curves. For the HERS low inertia configuration, the high-hover point was

lowered and the low-hover point raised. A more effective flare, thought due to the slightly wider chord blades of the HERS configuration, is suggested as being responsible for the two hover point improvements. The slight worsening of the "knee" of the HERS "deadman's" curve is possibly due to the aerodynamically dirty blades as a consequence of upper and lower surface strengthening doublers along the blade radius from root to tip. The differences between these curves may also be attributed, at least in part, to a difference in technique rather than a true difference in the H-V curves. Subsequent calculations indicate that for similar technique, the OH-58A and the HERS low inertia F-V curves would have been nearly identical.

Analytical Methodology - Autorotation Maneuver Program (AMP)

The development of the autorotation methodology discussed herein stemmed from both the lack of an economical and accurate prediction tool for in-house autorotation analysis and the obvious need to investigate potential autorotation improvements, as evidenced by the USASC accident statistics. Available analyses proved insufficient for various reasons. Through competitive procurement a contract was subsequently awarded to Sikorsky Aircraft to develop and correlate a computer program capable of simulating not only typical autorotation maneuvers but also the nonstandard helicopter autorotation profiles with various types of auxiliary rotor energy devices. The method of analysis is basically an energy and force balance procedure and is outlined in Figure 5. This Autorotation Maneuver Program (AMP) is capable of generating height-distance-time relationships for any of three different flight regimes: (1) takeoff, (2) landing, (3) autorotation, or any combination of the three.

To accommodate emergency conditions, the program provided for evaluation of auxiliary power units, rotor tip rockets, Jet Assist Takeoff (JATO), flywheels, drag brakes, and dropping of external loads. Provisions have also been made for calculating the minimum H-V envelope for user-specified constraint criteria. The details of the formulation and initial correlation efforts are contained in draft form in References 3 and 4. The analysis is currently viewed as developmental and has achieved mixed success to date. The fundamental analysis is viewed as basically sound, as demonstrated by the parametric sensitivity trends of Table A, which have been corroborated by other findings, and the H-V curves of Figure 6, which compare moderately well with both flight test and operator handbook sources. However, an internal, automated method of determining the minimum H-V curve has proved unreliable in evaluating the impact of high energy systems on the H-V curve as shown in Figure 7. The curves for the OH-6A in Figure 7 illustrate the anticipated reduction of the H-V

envelope with increased rotor inertia. The AH-1G, on the other hand, seems to indicate an insensitivity to inertia. This insensitivity is considered to be due (at least in part) to the "typical autorotation" control algorithm "hard-wired" into the AMP automated procedure. Subsequent computations with the AMP in the "you-fly-it" mode produced more realistic results.

The extensive time history data obtained during the HERS flight test was used to provide additional validation of the basic AMP analysis. The data from several flights was extracted from Reference 2 and duplicated using the AMP manual "you-fly-it" mode. Exact duplication of the flight path is not practical with the current program, although it may be closely approximated. Rotor energy at any point in time is directly porportional to rotor speed (RPM), and in general, the prediction of the rotor RPM bleed appears adequate for initial studies. Improved program flexibility to better model specific flight time histories and further improve the basic energy formulation could be expected to improve correlation. To obtain satisfactory correlation with the HERS data, it was necessary to model the engine power time history. A typical breakdown illustrating the relative importance of the various sources of energy in HERS autorotative landing tests is shown in Figure 8. During these tests a large amount of residual engine power remained, decreasing exponentially with time to idle following throttle chop. Actual engine failure time histories may vary considerably from the throttle chop time histories shown in the HERS flight test. The very limited amount of existing data indicates that actual emergency engine power loss may vary between instantaneous failure to a slow failure over 30 to 90 seconds. The worst case of power loss, that is, instantaneous failure of the engine, was used as the design condition for most of the auxiliary energy concept designs presented later in this paper.

In order to better evaluate the AMP automated H-V curve procedure, the operational curves (based on t_d=2 sec, V_{v_D} = 5 ft/sec, and instantaneous power loss) were calculated using the automated "minimization" scheme (Figures 9 through 12). The AH-1G and OH-58 operational H-V curves were reasonably approximated by the program. Manual mode calculations for the UH-60 indicated no H-V avoid area for the one-engine-inoperative (OEI) condition studied for vertical touchdown velocities on the order of 8 ft/sec, in contrast to Figure 11. The operator's manual claims no low speed avoid area for the UH-60 at 16,000 pounds gross weight, SLS. (Note the scaling of Figure 11 and that of the other H-V curves for an indication of the relative influence of OEI and power-off effects.) The Advanced Scout Helicopter (ASH) projected H-V curve was expected to have autorotation characteristics similar to the AH-1. Manual mode calculations indicate

123

that the AMP "minimization" generated curve shown in Figure 12 is not representative of the ASH design's true characteristics. Subsequent computations with slight alterations to the input limits for minimum touchdown rpm and maximum rotor thrust (C_T/σ) produced more realistic H-V envelopes (very similar to the AH-1G results in Figure 9). In summary, the automated method appears to give only a starting point for analysis. The program manual mode must be used to accurately determine the H-V avoid region.

Predesign Autorotation Criteria

A number of autorotation indices have been developed which allow comparative evaluation of a helicopter's autorotational performance without resorting to a detailed time history calculation. References 1 and 5 review a number of these indices. The equation

$$(t/k) = I_R \frac{(\Omega o^2 - \Omega^2 min)}{1100 \; SHP_{hover \; OGE}} \qquad seconds \qquad (1)$$

is typical of these indices. The minimum rotor speed can be related to maximum rotor lift capability by

$$\frac{\Omega^2 min}{\Omega_c^2} = \frac{C_T/\sigma}{\dfrac{K1(\overline{C_{L_{max}}})}{6}} \qquad (2)$$

where $K1 = .8$ and $\overline{C_{L_{max}}} = 1.0$ to 1.2

The primary limitation of indices such as (1) is that extrapolation to a new design is difficult or impossible if the required information on a similar design is not available. Estimation of actual power required, the effect of all energy terms, the effect of vertical touchdown velocity, and the variation of the index with the H-V curve must be treated to accurately study the elimination of the "deadman's" curve.

An empirical index for analysis of helicopter autorotational performance has been developed based on the data contained in References 2 and 6. This index relates the time of flight to the ratio of total energy available to average power required and is given as

$$t = \frac{PE + KE + RE + EE + AE}{K \; SHP} \qquad (3)$$

124

The flight time, t, has been empirically related to the initial hover height as shown in Figure 13. The crosshatched area of Figure 13 represents primarily the data from References 2 and 6 but also includes data from References 7 through 11. The majority of the data for current helicopters was found to be well represented by

$$t = (h/1.75)^{0.5} \tag{4}$$

Equations 3 and 4 define the minimum acceptable initial energy level required to land with zero touchdown velocity from any height. The power required, however, varies considerably during an autorotative descent. This variation in power is primarily a function of main rotor thrust, rate of descent, tail rotor thrust, and ground effect. The average power during autorotation for the lower hover point (100 ft or less) was found to be about 83 percent (K = .83). Time histories generated with the AMP indicate that K decreases with increasing height. As the primary emphasis of this study was the elimination of the H-V curve, no attempt was made to generalize K with height or initial velocity. The relation for t shown in Figure 13 was derived for maximum autorotative performance (t_d = 0) and a vertical touchdown velocity of zero. Equation 4 was modified to include estimates of the effects of touchdown velocity and time delays such that

$$t = \frac{-.38V_{v_D} + \sqrt{(.38V_{v_D})^2 + 7h}}{3.5} + t_d \tag{5}$$

Equation 5 was derived based on an idealized model of a typical auto-rotation acceleration-deceleration time history. This approximation has shown reasonable agreement with AMP calculations, but should be regarded as an area requiring additional study.

Equations 3 and 5 may be combined and solved for the desired unknown. Typically, height would be specified and the desired quantity (i.e., inertia for a high energy rotor) may be determined as given in equation 6.

$$I_R = \frac{1100}{\Omega_o^2 - \Omega^2} \left[t(K)(SHP) - PE - EE - KE \right] \tag{6}$$

In general, it was found that the kinetic energy was negligible for an initial hover condition at 100 feet or less.

Auxiliary Rotor Energy Concepts for Autorotation

The approach of a related Independent Laboratory In-House Research
(ILIR) investigation currently underway is to examine the autoro-
tative performance benefits of several devices that have the effect
of augmenting helicopter main rotor energy.

Simply stated, this performance objective is to provide adequate
emergency power to the main rotor, by either torque-free or torque-
generating concepts in conditions of partial power or zero power from
the primary propulsion system, to significantly reduce the baseline
vehicle H-V envelope. The ILIR investigation is concentrating on six
emergency power concepts gleaned from the fairly comprehensive list
of candidate systems in Table B. The investigators felt that these
concepts -- high inertia rotor, flywheel(s), tip rockets (solid and
liquid propellant), rocket turbine or auxiliary propulsion unit (APU),
and hybrid propulsion system -- offered the highest potential for
meeting the auxiliary rotor energy performance objective. An as-yet-
unpublished Applied Technology Laboratory report will detail the
efforts of this ILIR investigation and describe the selected concepts
and the associated pros and cons. This paper presents some initial
estimates of the cost (in terms of energy and weight) of two of the
above systems as well as some of the design options available and the
expected payoff of a successful system.

The autorotation criteria given by equation 3 were used to para-
metrically investigate the total energy required to eliminate the H-V
avoid region of the subject helicopters with both the high inertia
rotor and the solid propellant tip rocket auxiliary energy concepts.
This required energy is primarily a function of power required, which
is given as:

$$\text{SHP} = \left[\frac{(C_T)^{1.5}}{\sqrt{2}} + \frac{\sigma \delta}{8} \right] \left(\frac{T}{C_T} \quad \frac{\Omega R}{8} \right) \frac{T}{C_T} \frac{\Omega R}{550} \frac{1}{\eta} \tag{7}$$

Energy required increases with disk loading, design altitude, and
temperature as shown in Figure 14. These trends were essentially
independent of gross weight or auxiliary energy concept.

The relative rotor weight penalty to eliminate the H-V curve with a
high inertia rotor is shown in Figure 15. The weight penalty is
strongly dependent on the rotor disk loading and the engine failure
time history. The relative weight penalty was insensitive to gross
weight. The baseline rotor group weight at all disk loadings was
predicted using statistical trend relations for advanced structural

126

technology. The baseline rotor group weight was then adjusted to a
constant autorotative performance (i.e., same H-V curve) typical of
current helicopters. A significant portion of the blade weight
savings attributed to advanced structural technology was lost when
the baseline cases were adjusted to have the same H-V curve.

The OH-58A (3050 lb), the UH-60 (18000 lb), and a single-engine ASH
(5108 lb, DL=6) were selected along with the high inertia rotor and
the solid propellant tip rockets for point designs which would eliminate
the H-V curve at SLS conditions. The results of this study are given
in Table C. The weight penalty required to eliminate the H-V curve
for complete engine failure and a collective control time delay of 2
seconds is very large for the high inertia rotor concept. Tip rockets
appear to offer a far more weight-efficient system, but pose many
unanswered questions pertaining to rocket design, systems dynamics,
and reliability. The RPM decay of the rotor for the OH-58A with the
two systems was generated with the AMP and is shown in Figure 16.
The difference in response is primarily due to the fact that the high
inertia rotor has no activation time delay and provides over the whole
flight, while the tip rocket has a finite activation time delay and a
limited time during which it provides energy to the system.

The influence of touchdown velocity on a high inertia rotor system
for an ASH design is also shown in Table C. Significant weight
reductions are possible through use of the landing gear and fuselage
to dissipate the energy of high touchdown velocities without injury
to the crew.

The twin-engine UH-60 was used to study the effect of both the power-off
and the one-engine-inoperative (OEI) conditions. The rotor energy of
the UH-60 is lower than that of most single-engine helicopters. The
design experiences a large weight penalty for an auxiliary energy
concept capable of eliminating the H-V curve for failure of both
engines. For the loss of only one engine and moderate touchdown
velocities (on the order of 8 ft/sec), calculations predicated no H-V
avoid region for a gross weight of 18,000 pounds at SLS. The weight
of either a high inertia rotor or a tip rocket system sufficient to
allow a zero touchdown velocity for the OEI condition was not
prohibitive.

Beyond the obvious safety aspects of having an on-board energy
augmentation source, the economical benefits could be substantial.
The data presented in Figure 2 indicates that 71 percent of all
emergency autorotation accidents were initiated by failures in either
the fuel system or the engine. Approximately 17 percent of these

categories of accidents resulted in minor to major damage. Based on the assumption that 67 percent of these fuel system and engine related accidents would be preventable or at least attenuated with an auxiliary energy device, the estimated value of the preventable damage was $37,700,000 for a recent 7-year period.

Concluding Remarks

Areas in which significant progress has been made in providing an improved autorotative landing capability include:

- The successful reduction or elimination of the "deadman's" curve by the HERS. Excessive weight penalties (30 to 90 percent of useful load) for complete elimination of the H-V curve (which implies total power loss) make the HERS concept unattractive for all single-engine vehicles.

- The development of an analytical tool capable of evaluating new auxiliary energy concepts. Current efforts have identified the need to refine the basic AMP analysis, with particular emphasis on the determination of optimum H-V curves.

- The development of new predesign criteria that may be used to make preliminary estimates of the impact of auxiliary energy concepts.

- The identification of a number of feasible approaches toward providing high energy systems to eliminate the low speed H-V avoid region. The use of the landing gear to absorb the energy of high touchdown velocities can result in large reductions (up to 50 percent) in the weight required for an auxiliary energy concept. Even with the use of the landing gear capability, single-engine helicopters will require concepts with a high energy per unit weight (tip rockets for example) if the H-V avoid curve is to be eliminated at reasonable weight penalty. The OEI case for twin-engine helicopters greatly reduces the H-V curve compared to single engine designs. Hence, energy augmenting concepts like the HERS, which are unattractive for single-engine designs, may provide the best approach for twin-engine configurations.

Areas of ongoing work include:

- A detailed definition of the optimum approach and technology necessary to improve helicopter autorotation without seriously degrading vehicle agility and maneuverability.

- An improved analytical methodology that will encompass pilot control techniques, touchdown dynamics, greater flexibility to determine the optimun H-V curve, and improved overall accuracy.

- A definition of Army autorotation requirements.

Areas in which additional effort is planned or desired include:

- Improved accident statistics to allow determination of the critical factors in unsuccessful autorotations.

- Flight simulator investigation of integrated pilot technique with autorotation assist concepts, pilot in-the-loop training, and electronic cockpit displays and/or automatic descent controllers.

- Experimental and full-scale investigations to update technology contained in much of today's analysis methodology and to design, fabricate, and flight test helicopter energy augmentation concepts for effectiveness, control technique verification, and operational suitability.

References

1. Wood, T. L., "High Energy Rotor System", presented at the 32nd Annual National V/STOL Forum of the American Helicopter Society, May 1976.

2. Dooley, L. W., and Yeary, R. D., "Flight Test Evaluation of the High Inertia Rotor System", USARTL-TR-79-9, June 1979.

3. Studwell, R. E., "Helicopter Dynamic Performance Program, Volume I - Engineer's Manual", Draft AVRADCOM TR, SER-510011, February 1980.

4. Studwell, R. E., "Helicopter Dynamic Performance Program, Volume II - User's Manual", Draft AVRADCOM TR, February 1980.

5. Engineering Design Handbook, "Helicopter Engineering, Part One, Preliminary Design", AMCP706-201, August 1974.

6. Wood, T. L., Interim Technical Report, "High Energy Rotor Flight Test Data", Volumes I and II, June 1977.

7. "Height-Velocity Test, OH-58A Helicopter", Final Report, USAASTA Project No. 69-16, June 1971.

8. "Height-Velocity Test, AH-1G Helicopter", Final Report, USAASTA Project No. 69-13, February 1971.

9. "Government Competitive Test, Utility Tactical Transport System, Sikorsky YUH-60A", Final Report, USAAEFA Project No. 74-06-1, November 1976.

10. "A Flight Research Investigation of Autorotational Performance and Height-Velocity Testing of a Single Main Rotor Single Engine Helicopter", Final Report, USAAEFA Project 68-25.

11. Pegg, R. J., "An Investigation of the Helicopter Height-Velocity Diagram Showing Effects of Density Altitude and Gross Weight," NASA TN D-4536, May 1968.

12. Hanley, W. J., and DeVore, G., "An Analysis of the Helicopter Height-Velocity Diagram Including a Practical Method for Its Determination," FAA Technical Report ADS-67-23, October 1967.

TABLE A

AUTOROTATIONAL PARAMETER SENSITIVITY TRENDS

PARAMETER	EFFECT ON H-V	
	OH-6A	AH-1G
DISC LOADING (INCREASE)	DEGRADES	DEGRADES
ALTITUDE (INCREASE)	DEGRADES	DEGRADES
CG (MOVING AFT)	DEGRADES	DEGRADES
ROTOR INERTIA (INCREASE)	IMPROVES	IMPROVES
ALLOWABLE FLARE ANGLE (DECREASE)	DEGRADES	DEGRADES
AIRFOIL (DECREASE DRAG)	IMPROVES	IMPROVES
TIME DELAY (INCREASE)	DEGRADES	DEGRADES
INITIAL N_R (INCREASE)	IMPROVES	IMPROVES
AIRFRAME DRAG (INCREASE)	DEGRADES	DEGRADES
AIRFRAME STATIC STABILITY (DECREASE)	NO CHANGE NOTED	NO CHANGE NOTED
VERTICAL IMPACT SPEED (INCREASE)	IMPROVES	IMPROVES
BODY ALTITUDE AT TOUCHDOWN (DECREASE)	DEGRADES	DEGRADES
MAX. ALLOWABLE C_T/σ (DECREASE)	DEGRADES	DEGRADES

TABLE B

CANDIDATE AUTOROTATION DEVICES

ACTIVE ENERGY ADDITION

TIP PULSE JET
TIP TURBO JET
TIP RAM JET
TIP ROCKET (LIQUID)
TIP ROCKET (SOLID)
ROCKET TURBINE GAS GENERATOR
AUGMENTED ENGINE GAS
  GENERATOR
AUXILIARY POWER UNIT
DUAL STANDBY ENGINE
PRESSURIZED GAS EJECTION
HYBRID (AUXILIARY TURBINE GAS
  EJECTION AND SHAFT DRIVE)
COMPRESSED AIR EJECTION
WET OEI BOOST
DRY OEI BOOST

ENERGY ABSORPTION

PARACHUTE
AIRBAGS
LANDING GEAR

PASSIVE STORED ENERGY

HIGH INERTIA MAIN ROTOR
MOVABLE BLADE WEIGHT
MECHANICALLY DRIVEN GYRO
  OR FLYWHEEL
HYDRAULICALLY DRIVEN GYRO
ELECTRICALLY DRIVEN GYRO
PNEUMATICALLY DRIVEN GYRO

LIFT AUGMENTATION

LIFT JET
LIFT ROCKET (SOLID)
LIFT ROCKET (LIQUID)

OTHER

ROTOR OVERSPEED
ROTOR BL CONTROL
ROTOR FLAPS AND/OR SLATS
JET FLAPS
AUTOMATIC POWER MANAGEMENT
JETTISONABLE COMPONENTS
VARIABLE ROTOR GEOMETRY

131

TABLE C

WEIGHT AND ENERGY REQUIREMENTS

FOR TWO AUXILIARY ENERGY CONCEPTS

AIRCRAFT	CONCEPT		V_{V_D} (ft/sec)	t_d (sec)	ENERGY (HP-sec)	W (lbs)
OH-58A	A	(1)	0	0	77	67
OH-58A	A		0	0	696	210
OH-58A	A		0	2	1119	337
OH-58A	B		0	2	1119	26
ASH	A	(1)	0	0	1160	424
ASH	A		0	2	3156	1155
ASH	A		20	2	2223	814
ASH	A		42	2	1511	553
ASH	B		0	2	3156	80
UH-60	A		0	2	11567	2418
UH-60	A	(2)	0	2	453	95
UH-60	A	(2)	8	2	0	0
UH-60	B		0	2	11567	227
UH-60	B	(2)	0	2	453	9

Concept A - High Inertia Rotor
Concept B - Solid Propellant Tip Rockets
(1) Engine power time history typical of HERS flight test throttle chop
(2) One Engine Inoperative (OEI)
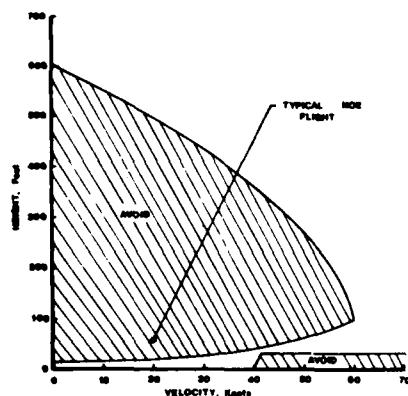
FIGURE 1. TYPICAL HEIGHT-VELOCITY ENVELOPE
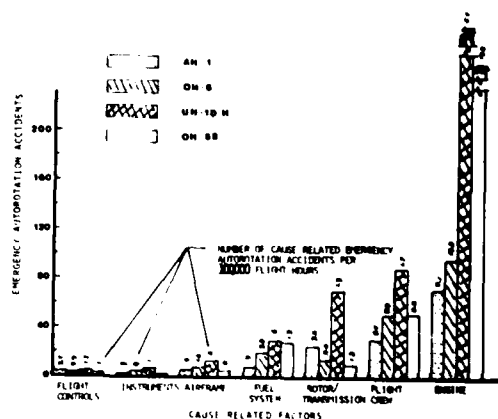
FIGURE 2. EMERGENCY AUTOROTATION CAUSE RELATED FACTORS

HEIGHT AT TIME OF EMERGENCY (ABOVE GROUND LEVEL), FT
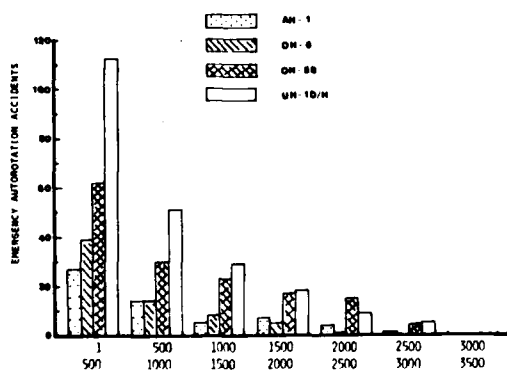
FIGURE 3. AUTOROTATION ACCIDENTS WITH HEIGHT (AGL)
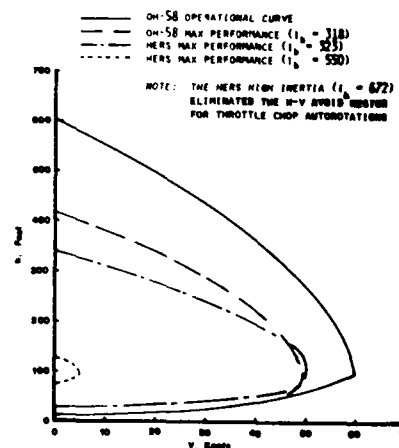
FIGURE 4. A COMPARISON OF THE HERS AND OH-58a
HEIGHT VELOCITY TESTING

133
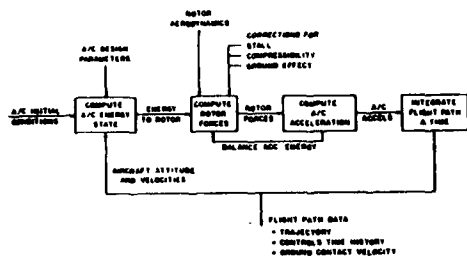
FIGURE 5. BASIC PROGRAM FLOW CHART

FIGURE 6. EFFECT OF DISC LOADING
ON H-V ENVELOPE

FIGURE 7. EFFECT OF ROTOR INERTIA ON H-V
ENVELOPE
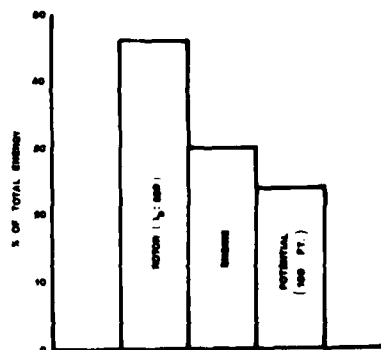
FIGURE 8. TYPICAL ENERGY BREAKDOWN FOR THE BELL HERS
FLIGHT TEST (100 FT HOVER INITIAL CONDITION)
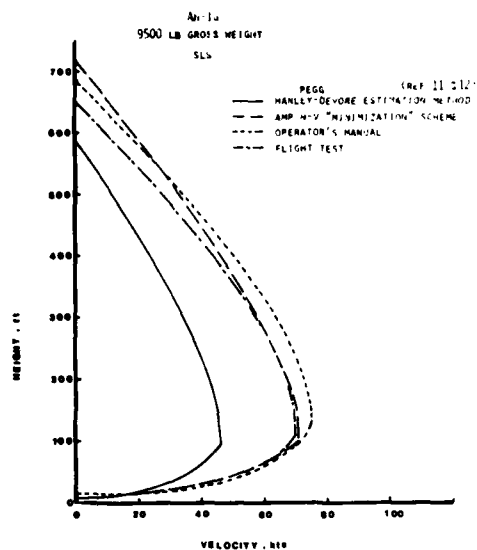
134

FIGURE 9. AH-1G HEIGHT-VELOCITY ENVELOPE

FIGURE 10. OH-58A HEIGHT-VELOCITY ENVELOPE
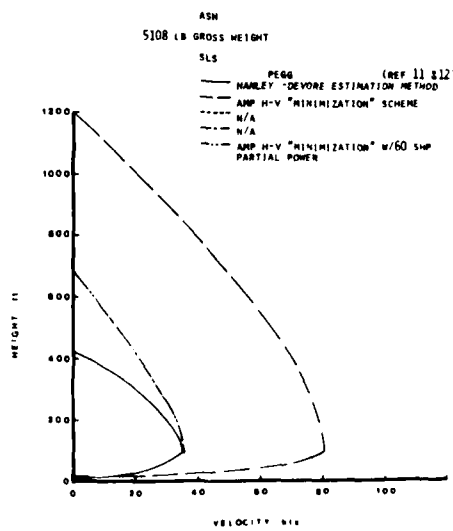
135
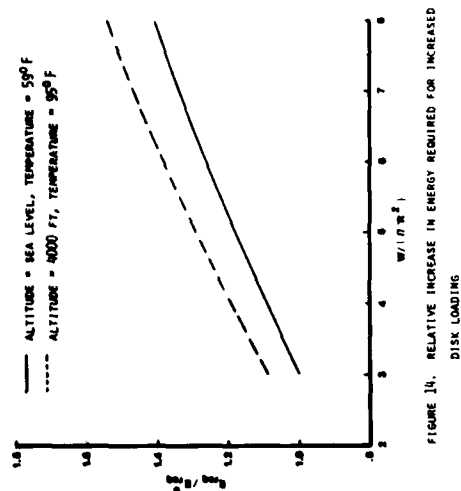
FIGURE 14. RELATIVE INCREASE IN ENERGY REQUIRED FOR INCREASED DISK LOADING
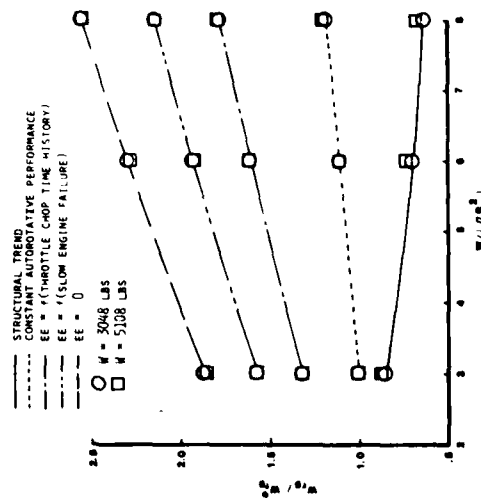
FIGURE 15. EFFECT OF DISK LOADING, GROSS WEIGHT, AND RESIDUAL ENGINE POWER ON ROTOR GROUP WEIGHT REQUIRED TO ELIMINATE THE H-V AVOID AREA
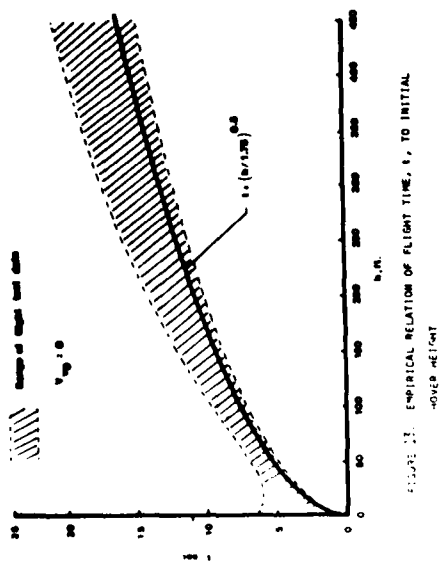
FIGURE 13. EMPIRICAL RELATION OF FLIGHT TIME, t, TO INITIAL HOVER HEIGHT
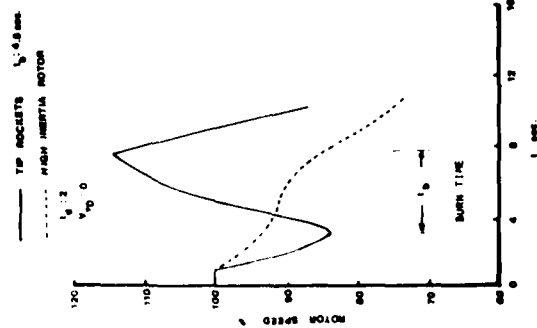
FIGURE 16. CALCULATED RPM DECAY FOR TIP ROCKET AND HIGH INERTIA ROTOR SYSTEMS CAPABLE OF ELIMINATING THE OH-58A H-V AVOID AREA

136

THE EFFECTS OF HIGH VELOCITY VARIABLE MASS
PROJECTILES ON THE MAXILLOFACIAL COMPLEX (U)

*WILLIAM R. POSEY, COL, DC
DUANE E. CUTRIGHT, COL, DC, EMERY A. RUSSELL, JR., COL, DC
JOHN F. NELSON, COL, DC
U. S. ARMY INSTITUTE OF DENTAL RESEARCH
WASHINGTON, D. C. 20012
V. ROBERT CLARE, et al*
CHEMICAL SYSTEMS LABORATORY
ABERDEEN PROVING GROUND, MARYLAND 21010

Introduction
    The weaponry used against the United States Soldiers in the
Vietnam conflict produced wounds which required modification of numer-
ous accepted conventional treatment methods and also resulted in new
methods of treatment. However today with the scenarios predicting
the appearance of new small high velocity missiles, these treatment
methods may be outmoded. Therefore, if surgical treatment capabili-
ties and doctrine are to keep pace with these new advances in combat
arms, new baseline data must be found through controlled studies to
determine the morphology of wounds caused by such projectiles and to
establish and disseminate treatment data which will provide optimum
treatment to the soldier.
    The inventories of fielded weapons of many nations include
anti-personnel weapons and devices with the capability of hurling pro-
jectiles of varying sizes (2-25 grains) at peak velocities which ex-
ceed 8,000 feet per second (fps). Due to the extremely high energies
and small sizes of these missiles, they produce entirely different
wounding patterns as compared to the so called "conventional" weapons,
such as used in Vietnam, which imparted speeds usually not exceeding
3500 fps. Due to this lack of knowledge concerning wound production
and morphology, morbidity and mortality, it is imperative to generate
baseline data on such wounds for the combat casualty management teams.
Such information will enable these teams to establish methods and

doctrine for casualty management usable in future conflicts.

The maxillofacial complex is the only vital area of the body totally unprotected during combat and therefore highly subject to injury by high velocity missiles in any conflict.

History of Combat Maxillofacial Wounds

A review of the literature suggests that most advances in the surgical treatment of wounds have historically ocurred during periods of combat or armed conflict. Although gun-powder-propelled missiles have been used in combat for hundreds of years, it was not until the Napoleanic Wars in the late eighteenth century that wide debridement of wounds was initiated (Schwartz, 1944). This debridement was probably quite crude because, as far as can be ascertained from the literature, it was not until the Crimean War (Mid-19th Century) that recorded observations are available concerning a very important principle of debridement. That is, the extensive vascular supply to the maxillofacial region makes debridement of this region basically different from that of other areas (Macleod, 1862). This principle, obviously, is just as valid today as it was then.

As one would suspect of trench warfare, World War 1 produced a high number of severe maxillofacial injuries; the trench protected the body, the helmet protected the head, and the face was the major point of exposure (Converse, 1942). He further attributed the severity of these wounds to machine gun bullets and bomb fragments hitting and penetrating the tissues of the face. His observations were substantiated by data from the Army Surgeon General. In 8,000 facial injuries to the American Expeditionary Forces, 3,000 proved to be fatal (Blair, 1943). This high incidence of facial wounds was probably the driving force behind the sudden surge in the development of new maxillofacial treatment techniques. According to Kelly, 1977, (a), "This was the first time in recorded history that a universal attempt had been made to accomplish reconstructive surgery in patients who had sustained maxillofacial battle injuries."

There is a paucity of reports concerning the development of new and better diagnostic procedures, surgical techniques, and other methods for improved care of patients with maxillofacial injuries resulting from conventional missiles from World War I (WWI) to World War II (WWII). In fact, in sp•ie of the advances made in the management of maxillofacial wounds during WWI, the importance of debridement was again overlooked at the beginning of WWII; however, this serious error in the proper surgical management of the conventional maxillofacial injury was soon corrected (Kelly, 1977 [b]).

A review of 2600 KIA's in Vietnam revealed that 46.6% had head and neck wounds. In Maughon's (1970) discussion, he stated "...the large number of head and neck wounds (46.6%) was impressive, especially those where a single wound or small fragment was the only

138

apparent injury." When surgical treatment requirements are considered for the combat environment, the other statistics of wound categories are equally significant. Of the 303,469 war related injuries during the period 1 January 1965 through 31 March 1973, 10-15% were of the maxillofacial complex (Tinder, et al., 1969).

The importance of information concerning combat casualty management of maxillofacial injuries becomes even more significant when the following quotes from Emergency War Surgery NATO Handbook (1975) (a,b) are considered.

"The number of high-velocity missile wounds has been increasing in succeeding wars of modern times; the increase resulted from the use of high-velocity small arms and automatic weapons together with reintroduction of the Claymore mine which, upon detonation, emits numerous small spherical missiles at high velocity... Artillery, mortar, grenade and mine fragments are irregular and vary not only in size and shape but also in velocity. Both bullets and fragments are considered to be primary missiles. Secondary missiles include shell wadding, clothing, building material, rocks, and other objects which are converted into wounding missiles by the effects of the primary missile." In the maxillofacial area secondary missiles also must include tooth fragments such as enamel, dentin and bone. "The type of wound which results from a missile may be a simple contusion or a penetrating or perforating wound. In a penetrating wound the kinetic energy is dissipated wholly into the tissues. In a perforating wound, the amount of energy imparted to the tissues is the difference between the kinetic energy remaining at the point of exit and that present at the wound of entrance. The density of the tissues struck determines the nature of the wounds as described above. Kocher demonstrated in 1876 that tissues which contained large quantitites of water (body fluids) were most severely damaged , and Daniel, in 1944, correlated the severity of high-velocity wounds with the specific gravity of the tissue involved. Muscle is severely damaged because of its relatively high homogenous density. In contrast, the lung sustains less extensive local destruction because of its low density, resulting in absorption of less energy and a small temporary cavity. Tissues of varying density, such as fascia or bone, may divert the direction of the missile, resulting in bizarre wound tracts." This quote is particularly applicable to the maxillofacial area with its increased blood supply, covering muscle and bony framework.

Large projectiles are not necessary to produce incapacitation. Small projectiles at higher velocities can create as much or more incapacitation, the controlling factors being variations of velocity and projectile size. Recent data concerning foreign anti-personnel combat arms reveals that hand grenades, mines and other weapons are carefully designed and fabricated to deliver the largest numbers of small fragments in the 2 to 50 grain size at very high velocities.

In an excellent study utilizing gelatin blocks, different sized spheres, and velocities up to 2.09 Km/second (Charters and Charters, 1976), it was noted that "smaller projectiles will give up their energy during penetration in a shorter distance than will larger projectiles of equal energy." To gain a better appreciation of the development of a specific wound morphology, one of their observations is quoted as follows: "The tissue moves spherically away from the projectile, opening up a temporary wound cavity that is characteristic of high-velocity gunshot wounds. After the cavity reaches its maximum volume, the tissue rebounds, collapsing into the cavity, leaving a narrow residual wound track. The magnitude of the temporary wound cavity is dependent upon the energy imparted by the projectile during penetration of the tissue, since the energy decreased exponentially with the distance penetrated."

When wounds of hard and soft tissues are evaluated (as opposed to soft tissue only), major implications and complications arise (Clemedson, 1973; Kabkob and Slepchenko, 1979). The striking or wounding projectile may be the primary injuring missile, but it may be only one of many contributors to the morphology of the wound. High velocity projectiles, striking bone and/or teeth, produce numerous secondary missiles, all of which have the potential of high velocity movement within the tissue. Obviously, any or all of these secondary missiles can produce extensive and distant damage in addition to the damage of the positive and negative pressures resulting from the high velocity of the primary missile. It is the combination of the effects of the primary and the secondary missiles that are responsible for the different wound morphology produced by high velocity missiles. It is also this myriad of presentations in the maxillofacial region that tests the surgeons diagnostic acumen, surgical knowledge and techniques. How critical rapid accurate diagnosis and subsequent surgical management of maxillofacial wounds becomes is evident when one considers the close proximity to the maxillofacial complex of numerous vital structures, such as sight, smell, hearing, taste, airway, vascular networks, and the brain. The implications of future social stigma due to facial injuries must also be considered by the military combat casualty management team at the earliest opportunity.

Purpose of Study

This study, using controlled conditions, was designed to provide new data on potential wound morphology from high velocity projectiles of varying sizes by using simulants for human maxillofacial hard and soft tissues. The validity of studying wound morphology in gelatin blocks has again recently been substantiated by Dubin who in 1974 showed that there were remarkable similarities between gelatin and freshly excised pig tissues. The data generated in this study will answer the following questions and provide a more meaningful base on which to improve and develop effective diagnostic procedures,

surgical techniques, and enhance total patient care:

What are the effects of high velocity variable size projectiles
on the human maxillofacial complex? What is the morphology of
wounds created at these very high energy levels? Are current
diagnostic and surgical techniques adequate to provide optimum
care for injuries caused by varying sized projectiles impacted
at speeds in excess of 1,750 m/s (5250 fps)? Will the induced
morphology necessitate modifications of existing surgical tech-
niques or must new ones be developed?

A final justification of this study can be found in the
following quote from "Emergency War Surgery NATO Handbook" (c):   "From
the medical standpoint, the surgeon must know the wounding capacity of
the weapons to assist in evaluating the extent of injury to achieve
the most effective therapy".

Methods and Materials

In order to study tissue changes resulting from the impaction
of high velocity missiles it was necessary to fabricate tissue simu-
lants for the high velocity study. These simulants were composed of
human skulls, purchased from Wards Natural Scientific Establishment,
Inc., P.O. Box 1712, Rochester, New York 14603, infiltrated by and
imbedded in Pharmagel "A" type gelatin to simulate the soft tissues
of the head. These tissue simulants in block form were then carved
to closely approximate the human facial conturs (see Figure #8).

Impact velocities were achieved via a precisely fabricated
launching device utilizing large capacity brass powder cases in high
pressure steel chambers threaded to long barrels to gain velocities of
5000 feet per second (fps) or higher, utilizing 2, 7, 16 and 55 grain
missiles. These missiles were fabricated in both spherical and cylin-
drical shapes from high carbon steel rods or special bronze alloys.
These missiles and the actual firings were carried out in a special
room in Chemical Systems Laboratory facilities at Aberdeen Proving
Ground, Maryland.

This study consisted of a total of sixteen (16) firings
with the following missile sizes:

55 grain	3 shots
16 grain	3 shots
7 grain	6 shots
2 grain	4 shots

Muzzle to target distance varied from 4.2 meters to 4.47 meters.
Muzzle velocities varied from a low of 5637 fps to a high of 7340 fps.

Each firing and impact was recorded by high speed cinema-
photography at 3,000 and/or 30,000 frames per second to study the dis-
placement, deformity and extent of tissue alteration during impaction,

141

penetration or perforation.

Immediately post-impaction, the gelatin-impregnated skulls and any fragments were assembled, studied and photographed in order to assess tissue damage.

Findings

The following descriptions of selected firings are representative examples of the types of wound morphology found in this study.

Fifty-five grain missile at 6144 fps - impacted into a gelatin block measuring 5"X6"X15" and weighing 17 pounds.

The block was split into 3 pieces along nearly its entire length. As the imparted energy of the missile was expended, the cavity in the gelatin block opened to approximately 1½ times its original size. This created a negative pressure which pulled fragments of the timing grid and other nearby debris into the wound, figure 1.

Fifty-five grain bronze cylinder fired at 6,104 fps impacted into the right ramus of the mandible.

The right and left bodies of the mandible were completely avulsed. Numerous small fragments of bone and teeth were scattered throughout the gelatin block, figure 2. Both the right and left zygomatic arches were separated at the suture lines. Much of the maxillary tooth bearing bone was also avulsed, although the anterior maxillary process was displaced but still present in the block. The extent of involvement of the facial skeleton was only fully revealed after partial removal of the gelatin, figure 2. After removal over 180 bone and tooth fragments were found scattered throughout the oral cavity and soft tissue, figure 3.

Sixteen grain missile impacted at the midline (symphysis) of the mandible at 5746 fps.

The entire anterior mandible was avulsed. Also all of the maxillary teeth and part of the maxilla were avulsed. The entire anterior maxilla was displaced and the floor and wall of the orbit were similiarly fractured and loosened, figure 4. Careful removal of the gelatin revealed many secondary missiles had spread into the foramen magnum and across the base of the skull, figure 5.

Sixteen grain missile impacted at 7340 fps on the right Zygomatic Complex. Exit was at angle of left mandible.

The entire maxillofacial complex and base of skull were fractured and displaced. The entire mandible and much of the maxillary tooth bearing bone were missing, figures 6 and 7.

Seven grains impacted at 5637 fps into the zygomatic arch.

The zygoma, wall of the orbit and right condyle were all fractured, figure 8. The wound tract (figure 9) traversed through the oral cavity to the left mandible ramus where the missile stopped. The left mandible was not fractured. The extent of damage was not easily ascertained until the gelatin was removed. This revealed multiple fragmentation of both the maxilla and mandible, figure 10. Many small

Figure 1: Fifty-five grain missile impacted at 6144 fps.
The block was split into 3 pieces and the resulting cavity and negative pressure sucked in surrounding debris. Arrows.

Figure 2: Fifty-five grain bronze cylinder impacted into symphysis of the mandible at 6109 fps.
Anterior view showing avulsion of anterior mandible and much of the maxilla. Hundreds of secondary missiles of various sizes can be seen A. Suture separations are visible at B.

Figure 3: Fifty-five grain bronze cylinder impacted into symphysis of the mandible at 6109 fps. Composite of bone and tooth fragments found when the gelatin was removed. Fragments smaller than 2-3 millimeters are not included.
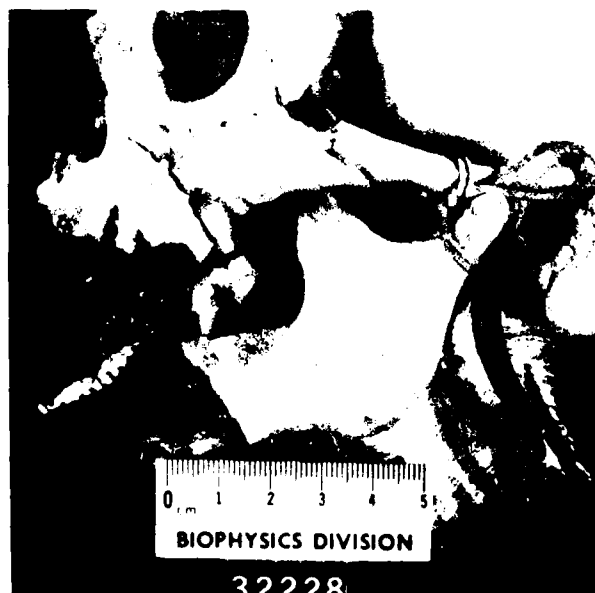
Figure 4: Sixteen grain sphere at 5746 fps impacted at mandibular symphysis, lateral view. Avulsion of anterior mandible and fractures of maxilla and maxillary molars are seen at A. Zygomatic and orbital fractures are shown in B. Fragment of target grid is shown at C.
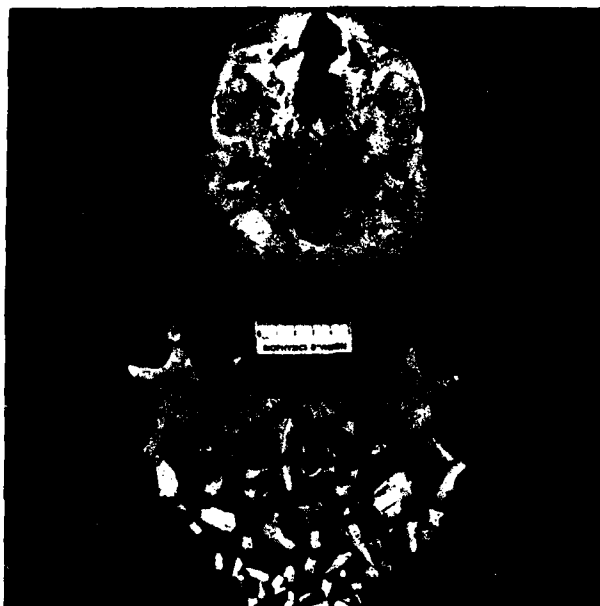
Figure 5: Sixteen grain sphere at 5746 fps impacted at symphysis of the mandible. Composite view. Secondary fragments of bone and teeth can be seen in the Foramen Magnum and across base of skull. (Arrows).
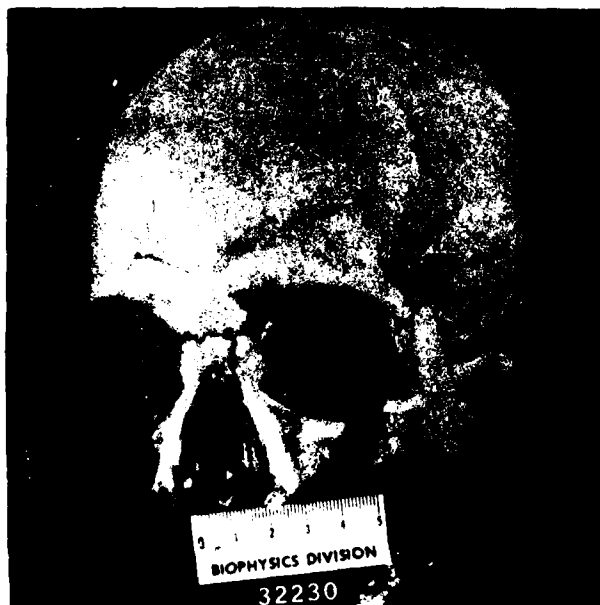
Figure 6: Sixteen grain sphere impacted at 7340 fps into right zygomatic complex.
Gross fracture and displacement is evident throughout the maxillo-facial complex.

Figure 7: Sixteen grain sphere impacted at 7340 fps into right zygomatic complex.
The fractures and displacement across the base of the skull are clearly evident. The multiple fragments and secondary missiles consisting of bone and teeth are at bottom.

Figure 8: Seven grain sphere impacted into the right Zygoma at 5637 fps. Fractures of the zygoma, condyle and orbit are clearly seen.
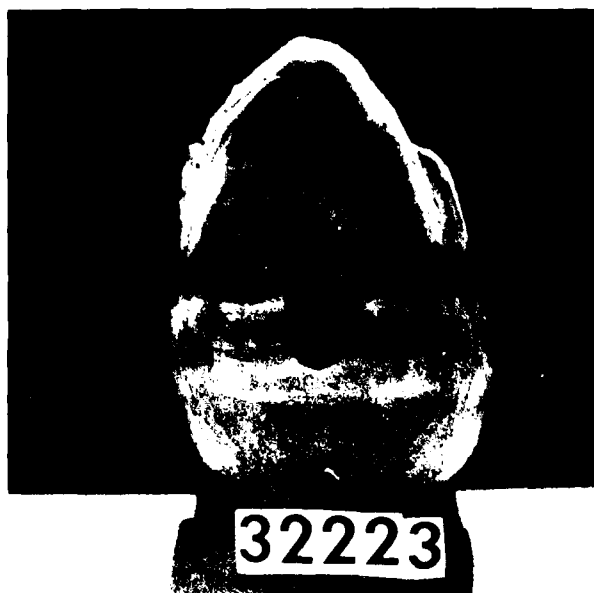
Figure 9: Seven grain
sphere impacted into the
right Zygoma at 5637 fps.
Fracture of the Zygoma is
evident at upper left.
Wound tract (arrow) is vis-
ible traversing across oral
cavity to left mandible.

Figure 10: Seven grain
sphere impacted into the
right Zygoma at 5637 fps.
Composite view.
Multiple fragments includ-
ing many small fragments
within the right orbit
(arrow) are clearly evident.

fragments were found across the base of the skull and within the right orbit.

Two grains impacted into the right zygoma at 5637 fps.

The right zygoma, coronoid process and articular emminence were fractured with formation of multiple small fragments, figure 11. The 2 grain missile penetrated into the oral cavity, lodging in the gelatin approximately 3 cm. lingual to the coronoid process, figure 12.

Discussion

The gelatin block firings demonstrate the soft tissue wound morphology which could result from a 55 grain bullet or missile with a speed of 6144 fps. The tremendous cavitation produces a wound and distant tissue damage much greater than that experienced with conventional speeds of 3500 fps or lower. In this study similiar mass/velocity impacts into the skull/mandible demonstrated avulsion of tissue, fractures and a large number of secondary missiles. There were at least 180 major secondary fragments of bone and teeth. The wound pathways of these secondary missiles, the cavitation due to the high velocity and the primary missile wound tract would combine to form a wound which would, in most cases, be fatal. This wound extension and contamination would be greater and encompass more tissues, contain more foreign debris and require much more complex and dedicated treatment than those produced by lower speed missiles.

The reduction of mass/velocity to 16 grains at 5746 fps still produced significant avulsion of the bony facial skeleton and caused significant radiating non-displaced fractures of the frontal bone. Again secondary missiles and contamination would have caused extensive local and distant damage to various structures and the movement of secondary missiles, especially tooth fragments, would markedly enlarge the wound size and increase the complexity and scope of treatment.

The effects of increased velocity with a constant mass (16 grains at 7340 fps) produced only slightly less tissue destruction, bone fractures and wound size as seen with the 55 grain missile at 6144 feet per second. Again, this type of wound would, in most cases, prove to be fatal.

In contrast reducing the mass/velocity figures to 7 grains and 5637 fps changed the wound morphology significantly. There was no gross tissue avulsion, although several fractures of the maxillofacial skeleton occured with minimal displacement of fragments. These large bony fragments were maintained within reasonable anatomic approximation. Small fragments did penetrate through several different structures including the foramen magnum. At this energy level and penetration site, the missile did not exit the tissue but remained against the mandible opposite the entry site. This wound, although incapacitating and possibly life threatening, would most likely allow for successful treatment. However, the success or failure might well depend upon the surgeons knowledge of the differences in morphology

Figure 11: Two grain sphere impacted at 5637 fps into the right Zygoma. Fractures of the coronoid process, Zygoma and articular eminence are clearly evident. Multiple small fragments can be seen in the area of the temporo-mandibular joint and infra-temporal space.

Figure 12: Two grain sphere impacted at 5637 fps into the right Zygoma.
Green stick fracture of the mandible is seen at A and the missile is identified at B.

produced by high velocity missiles.

When mass/velocity figures were reduced to 2 grains at 5637 fps, there was a marked decrease in the severity of damage with minimal fractures and few secondary fragments. Again, this small missile did not exit.

The findings of this study indicate that an increased velocity produces greater cavitation in soft tissue with an expected increase in the amount of contamination from protective gear, clothing, soil, etc. This factor would be expected to cause an increase in wound size, more distant disruptions along tissue planes, greater vascular damage, increased damage to the central nervous system and increase the number of secondary infections in comparison to conventional weaponry. A second important finding of the study is the increased numbers of secondary missiles produced by the impact of fast moving missiles on bone and teeth. This increased fragmentation would be expected to cause larger total wound size, injury to more surrounding and more distant structures, greater incapacitation and increased secondary infections. This is especially true of hits shattering the hard enamel of teeth.

These findings tend to re-emphasize the work of Mcleod who stated that debridement around the maxillofacial area requires a different approach. Similiarly, this statement from the Emergency War Surgery NATO Handbook needs restating, "From the Medical standpoint, the surgeon must know the wounding capacity of the weapons to assist in evaluating the extent of injury to achieve the most effective therapy."

In summary, this study has shown that the morphology of wounds produced by weapons systems which produce ultra-fragmentation into very small size particles delivered at very high velocities is different from conventional speed missiles and that presently accepted treatment modalities may well require alteration in order to produce optimum treatment results. This is especially true in a small compact area such as the maxillofacial complex which contains the very organs responsible for sight, smell, hearing, taste and life itself.

References
1. Blair, V.P.: Relation of The Early Care to the Final Outcome of Major Face Wounds in War Surgery. Mil Surg 92:12-17, 1943.

2. Charters, A. Crane, and Charters, Alexander C.: Wounding Mechanism of Very High Velocity Projectiles. J. of Trauma 16:464-470, June 1976.

3. Clemedson, C.J. et al: Head Injuries Caused by Small-Caliber High Velocity Bullets, an Experimental Study. Z. Rechtsmedizin 73:103-114, 1973.

4. Converse, J.M.: War Injuries of the Face. Trans Am Acad Ophthalmol(1941) 46:250-255, May-June, 1942.

5. Dubin, H.C.: A Cavitation Model for Kinetic Energy Projectiles Penetrating Gelatin. Bal. Res. Lab Memo. Rept. 2423, 1974.

6. Kabakob, B.D. and Slepchenko, M.A.:Organization of Specialized Care for Maxillofacial Wounds. Moscow Military Medical Journal. Number 3, 19-21, 1979, pp.(a) 17, (b) 8,9.

7. Kelly, J.F. (ed).: Management of War Injuries to the Jaws and Related Structures. Washington, D.C., U.S. Govt. Printing Office, 1977, pp (a) 7, (b) 8,9.

8. MacLeod, G.H.B.: Notes on Surgery of War in Crimea. Philadelphia, J. B. Lippincott and Company, 1862, pp 198-201.

9. Maughon, J.S.: An Inquiry Into the Nature of Wounds Resulting in Killed in Action in Vietnam. Mil Med 135:8, 1970.

10.NATO Handbook, Emergency War Surgery, US Revision,Washington, D.C. U.S. Govt. Printing Office, 1975, pp (a) 10, (b) 13, and (c) 9.

11.Schwartz, L.L.: The Development and the Treatment of Jaw Fractures. J. Oral Surg. 2:193-221, 1944.

12.Tinder, L.E., Osbon, D.B., Lilly, G.E., Salem, J.E., and Cutcher, J.L.: Maxillofacial Injuries Sustained in the Vietnam Conflict Mil Med. 134:668, 1969.

NONDESTRUCTIVE TESTING OF ARMAMENT-SYSTEM COMPONENTS
BY MEANS OF NEUTRON DIFFRACTION (U)

*HENRY J. PRASK, DR.[+]
CHANG S. CHOI, DR.
SAMUEL F. TREVINO, DR.
ENERGETIC MATERIALS DIV., LCWSL
U.S. ARMY ARMAMENT RESEARCH AND DEVELOPMENT COMMAND
DOVER, NEW JERSEY   07801

I.   INTRODUCTION

In recent years, increasing emphasis has been placed on
nondestructive testing (NDT) techniques for quality control in a large
variety of applications. Progress in this area has considerable
importance for DOD because of the increasing complexity and cost of
armament systems and the inherent limitations of quality control by
means of traditional, destructive test methods. This is dramatically
illustrated by the on-going, multi-billion dollar DA plant moderniza-
tion project within which incorporation of state-of-the art NDT
methods is an essential part.

Various NDT techniques in which x-rays are employed (e.g.
radiography, diffraction) are already well established as quality
control methods. The use of neutrons which complements and parallels
x-ray techniques has been -- except for neutron radiography -- ne-
glected for NDT, primarily because their use is generally limited to
a laboratory environment (e.g. a research reactor). Despite this
current limitation, there has been a renewed interest in utilizing
neutron scattering for certain technological applications. In

---

particular, sizeable programs have been completed at European reactor facilities and begun in the U.S. to construct sophisticated instruments for small-angle neutron scattering.

In the present paper we describe the utilization of wide-angle neutron diffraction for the nondestructive characterizatioi of two properties of importance in metallurgical systems: texture (i.e. preferred grain orientation) and residual stress. The complementary nature of neutron diffraction relative to x-ray diffraction is illustrated by a detailed description of texture measurements for shaped-charge liners and tungsten-alloy kinetic-energy penetrators. The potential of small-angle neutron scattering for nondestructive characterization of precipitates and voids in metals is also discussed.

II. BACKGROUND

A. General (1)

Thermal neutrons from a reactor beam tube are employed for diffraction experiments; typically, neutron velocities of 2 km/sec with an energy of 0.02eV and a wavelength, λ, of 2 A are in the useful range. In contrast to x-rays, thermal neutrons have both energy and wave-vector ($2\pi/\lambda$) in a regime characteristic of lattice vibrations or phonons. Extremely important results relating to interatomic forces have come out of the use of this property in inelastic neutron scattering studies of condensed matter. Microstructural properties, such as texture and residual stress, are probed by elastic scattering (2), to which inelastic scattering contributes only a relatively small background.

Neutron scattering processes can be described by approximating the nucleus as a hard sphere of radius 10^{-12} cm. With x-rays, the atomic scattering factor is a function of scattering angle and is proportional to atomic number. This results from the fact that with x-rays the electrons are the scatterers so that the atom has a finite dimension relative to the x-ray wavelength. This is not the case for elastic scattering of neutrons by the nucleus so that the nuclear scattering power, called scattering length, b, is not angularly dependent (except in the case of magnetic scattering which is outside the scope of the present discussion).

Formally, the intensity measured in a diffraction experiment is proportional to the square of the structure factor $F(\vec{Q})$ where

$$F(\vec{Q}) = \int_V \rho(\vec{r})e^{i\vec{Q}\cdot\vec{r}}d\vec{r}. \qquad (1)$$

In Eqn. (1), $\rho(\vec{r})$ is the "scattering density", $\vec{Q} = \vec{k}_i - \vec{k}_f$ is the wave-vector transfer, $k_i = 2\pi/\lambda = k_f$, and the integration is taken over the sample volume.[1] In the neutron scattering case

$$\rho(\vec{r}) = \sum_i b_i \delta(\vec{r}-\vec{r}_j) \qquad (2)$$

where b_i is the scattering length of each nucleus in the sample and δ is the Dirac delta function. From Eqns. (1) and (2)

$$F(\vec{Q}) = \sum_i b_i e^{i\vec{Q}\cdot\vec{r}_i} \qquad (3)$$

which gives rise to maxima in the intensity when the Bragg reflection conditions are fulfilled, i.e. when

$$n\lambda = 2d \sin(\theta/2) \qquad (4)$$

where d is the plane spacing, θ the scattering angle and n is an integer.

Two important differences between x-ray and neutron scattering processes make the use of neutrons essential for certain applications. As mentioned above, scattering density in the x-ray case varies continuously with atomic number. Scattering density in the neutron case varies discontinuously with atomic number and, in fact, differs for different isotopes of the same element.* In addition, both types of radiation may be absorbed by the scatterers. Typical absorption coefficients, μ, for neutrons and x-rays are on the order of 0.3 and 1000 cm^{-1}, respectively, where intensity after absorption is $I = I_o \exp(-\mu x)$, with I_o the initial intensity and x the sample thickness. For metallurgical samples, neutrons are, in general, on the order of 1000 times more penetrating than x-rays of the same wavelength. In Figure 1, the use of the penetrating power of neutrons for wide-angle diffraction studies of bulk properties in NDT applications is shown schematically.

---

*Dramatic illustration of this is found in structural studies of metal hydrides where hydrogen locations are invisible to x-ray but not to neutron diffraction; substitution of deuterium for hydrogen further enhances the sensitivity of the neutron method.
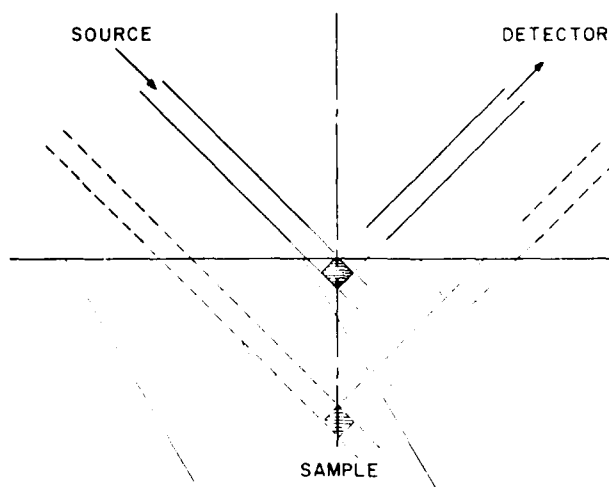
Figure 1. Schematic drawing of stress or texture vs. depth measurement. Heavier dashed and solid lines represent collimators. Lighter lines represent neutron beam path. For single scattering, neutrons reaching the detector can only come from the regions indicated by cross-hatching.
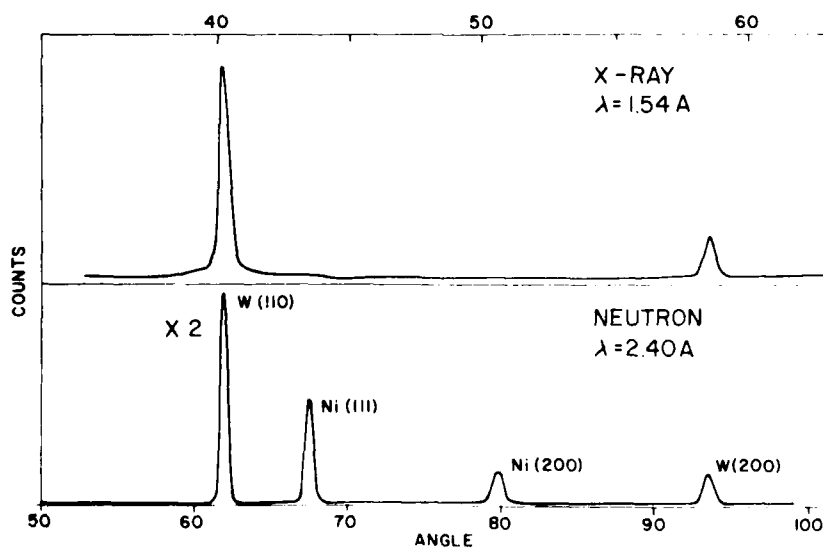
Figure 2. Partial diffraction patterns for a .97 tungsten - .018 nickel - .012 iron (by weight) KE penetrator sample.

B. Metallurgical properties (3)

1. General: Metal end-items are composed of individual crystallites or grains, the diameters of which may range from 1.00 mm (ASTM No. -3) to 0.006 mm (ASTM No. 12). Although the intrinsic properties of individual grains (e.g. elastic moduli, number and orientation of slip planes) are important in determining the mechanical characteristics of a specimen, the polycrystallinity introduces properties which are often dominant. For example, grain size, intra- and inter-grain boundaries, preferred grain orientation (or texture), dispersion of precipitate particles and residual stresses are inter-active (to varying degrees) and affect mechanical properties. In the following subsections three of these properties for which neutron scattering studies have been made are considered in greater detail.

2. Texture: A metal which has undergone severe deforma-tion, as in rolling or swaging, will develop an overall preferred crystallographic orientation or texture. That is, the individual grains tend to orient themselves in a preferred manner with respect to the direction of maximum strain. This arises from the tendency of slip planes in single crystals to rotate parallel to the axis of principal strain. Individual grains are anisotropic but their random aggregation leads to isotropy with respect to mechanical properties. However, preferred alignment of grains introduces anisotropy in mechanical properties which leads to uneven response of the material during forming and fabrication processes and in use.

3. Residual stress: A body which has undergone nonuniform plastic deformation can retain a system of stresses within the body after the external forces have been removed. Macro residual stresses vary continuously through the volume of the body over regions which are large compared with atomic dimensions. They are produced by virtually all forming operations, welding, nonuniform cooling of ingots and electroplating. The important point to be made is that the response of a body in a particular application includes the super-position of the external stress system and the residual stresses. For example, a compressive residual stress (as produced by autofrettage of gun tubes) will reduce the effectiveness of an applied tensile stress in producing fatigue failure, while residual tensile stresses will increase the ease with which failure occurs.

Another type of residual stress, microstress or textural stress, should also be mentioned. These stresses act over dimensions as small as several crystallographic unit cells but may extend throughout a grain. Stress developed around a second-phase precipitate

157

is an example of this. Nitriding and carburizing are processes in
which microstresses around each particle produce a macro residual
stress on the treated surface.

4. Second-phase hardening: Most commercial alloys contain
a heterogeneous microstructure consisting of two or more metallurgical
phases. The strengthening produced by a fully dispersed insoluble
second phase in a metallic matrix is known as dispersion hardening.
Precipitation hardening, which also produces strengthening, is
achieved by solution treating and quenching an alloy in which a
phase in solid solution at elevated temperatures precipitates upon
quenching and aging at a lower temperature. Many of the factors which
affect strengthening, such as size, shape and number of the second
phase particles, have been very difficult to measure with any degree
of precision.

The following section describes armament components in which
texture, residual stress and precipitation hardening are known to be
important for optimizing performance, and the use of neutrons for
characterizing these properties.

III. RESULTS AND DISCUSSION

A. Texture

1. Tungsten-alloy KE penetrators: Kinetic-energy penetra-
tor rounds represent a major part of the Army's armor-defeating
weapons. With continual improvements in fielded armor, increased
penetration is necessary, preferably without increases in size or
weight of the rounds. In this subsection we examine one property of
state-of-the art tungsten-alloy penetrators: the anisotropy of
texture produced by various types of cold working.

The samples are composed of tungsten, nickel and iron in a
wt % ratio of 97/1.8/1.2. Sample preparation - which involves iso-
static pressing, sintering, heat treatment and cold working - leads to
a system consisting of a "tungsten" phase (96.5 wt %) and a "matrix"
phase (3.5 wt %). The approximate compositions by weight of the two
phases are 99.7W - 0.1Ni - 0.2Fe and 55Ni - 23Fe - 22W, respectively.
The potential of neutron diffraction for studies of this type of
sample can be inferred from Figure 2 in which partial x-ray and
neutron diffraction patterns which cover the same range in lattice
spacing are shown. The full diffraction patterns show that the
tungsten phase can be indexed according to the bcc tungsten structure
with $\underline{a}$ = 3.160(1) A, and the matrix phase can be indexed according to
a fcc nickel structure with $\underline{a}$ = 3.586(1) A. For alloys of these
compositions and relative concentrations, the matrix phase is

W(110)   W(200)   Ni(III)

5904 B

5903 B

5905 J
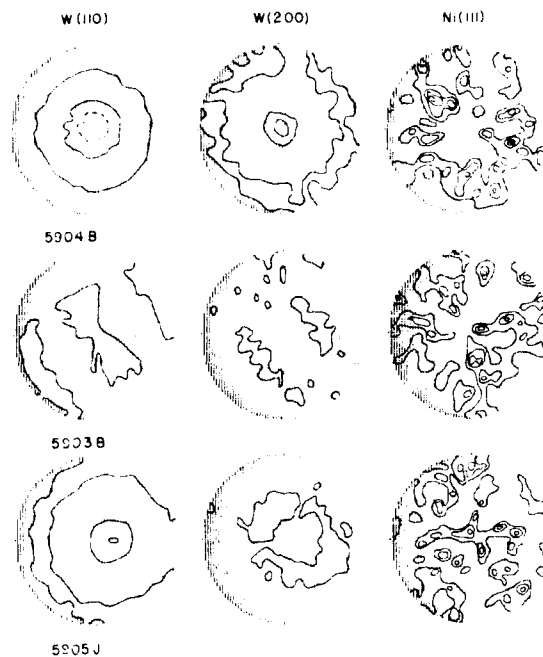
Figure 3. Texture distributions for the three 8% cold-worked
tungsten-alloy penetrator samples described in the text. The
center of each figure corresponds to the cylinder-axis direc-
tion; the periphery of each figure corresponds to a 70% tilt
with respect to the cylinder axis. Angular displacement around
the periphery corresponds to rotations of the sample about its
own axis. Contour lines show "random" and 15% increases in
orientation with respect to random (dashed contour = decrease).
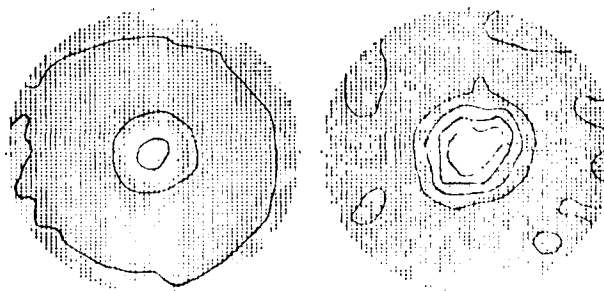
Figure 4. W(110)-on left-and Ni(111) textures for a 16% R.A.
swaged sample.

virtually invisible to x-rays. In contrast, two matrix-phase peaks are clearly visible in the neutron pattern which makes possible texture studies and, in principal, residual stress studies of the matrix phase.

Texture resulting from various types of cold working have been measured for these types of alloys. In Figure 3 are shown pole-figure patterns for one matrix-phase and two tungsten-phase reflections. These were obtained for a 1 cm region at the leading or front end of the 0.7 cm diameter, 10 cm long small-scale penetrators. The three sets of pole figures correspond to samples which have been cold worked by "upsetting" with an 8% increase in cross-section (5904), and swaged with an 8% reduction in area (5903 and 5905). Cold working of the latter pair was performed at two different fabrication facilities. As one would expect, the fiber textures of the "upset" and swaged samples are different. On the other hand, the pattern of sample 5903 is essentially untextured, whereas that of 5904 shows definite texture in the tungsten phase for nominally, the same cold working. The matrix phase (111) pattern shows little if any clear texture.*

In contrast to the above results, samples which have been swaged to a 16% reduction in area show very pronounced tungsten and matrix phase textures (Figure 4). The high degree of axial orientation of the (111) slip planes in the 16% R. A. penetrators relative to the 8% cold-worked samples suggests the possibility of quite a different response to axial stresses in the two types. Although much less pronounced, there is some indication of differences in (111) slip plane texture among the three 8% cold-worked samples. Since the matrix phase is the binder which provides cohesion and strength to the penetrators, test-firing of inspected penetrators -- which is possible because the neutron measurements are truly nondestructive -- is imperative to further test these possibilities.

2. Metallurgically-compensated shaped-charge liners: The second major type of armor-defeating round employed by the Army utilizes the shaped-charge principle. A typical shaped-charge missile has a steel body fitted at the forward end with a cone-shaped metal liner (as shown in Figure 5) whose apex extends backward into the body cavity. On impact, the detonation wave of the charge collapes the

---

*A pole figure is a map of the orientational distribution of the normal direction to a specific crystallographic plane (2). The diffractometer geometry is fixed to observe scattered radiation for the Bragg reflection of interest, and the sample rotated - over as large an angular range as possible - about two mutually perpendicular axes. The pole figure is a two-dimensional map of intensity maxima and minima as a function of sample orientation.
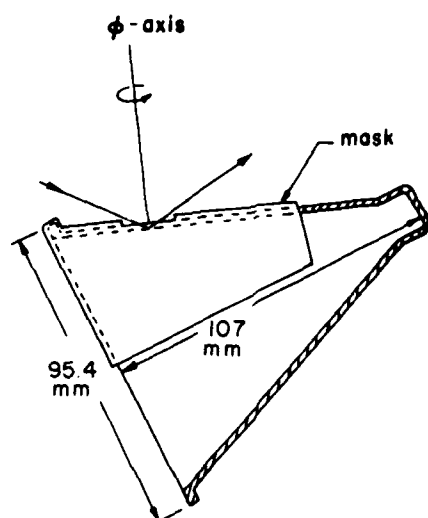
Figure 5.   Shaped-charge liner and scattering geometry for neutron diffraction texture measurement.
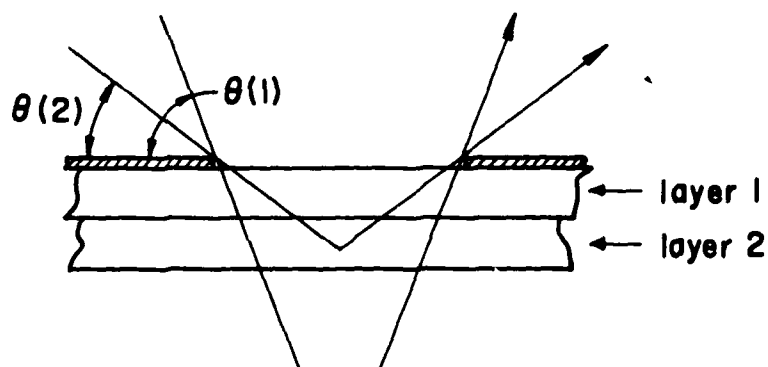
Figure 6   Schematic illustration of sample volume vs. Bragg angle for two-layer, thin sample.

161

cone from apex to base sequentially and produces a long narrow jet of cone material traveling along the cone axis with extremely high speed. This jet, which is solely responsible for producing the deep hole in armor, breaks up prematurely when the projectile is rotating about its axis at impact. "Spin compensation" is the term applied to methods employed to counteract degradation of the jet because of rotation.

Spin compensation can be achieved when the cone-shaped metal liner is manufactured by the rotary extrusion process. It has been shown by x-ray diffraction (5) that the critical parameters in this case are related to the alignment of slip planes and slip directions in the cone. However, a quantitative correlation between these metallurgical properties and spin compensation (or performance) has never been established because of the lack of a nondestructive technique for determination of texture.

At the 1976 Army Science Conference we demonstrated that neutron diffraction could be used to nondestructively determine the average texture within the liner wall (6). However, the desired non-destructive determination of texture as a function of depth in the liner wall did not appear possible (by, for example, the technique shown in Figure 1) because the wall was too thin relative to minimal neutron beam dimensions.

Since then we have conceived and tested an approach by which the needed measurement becomes feasible (7). The method makes use of the fact that for an appropriately masked sample, as shown in Figure 6, different depths are probed for a given set of crystallographic planes by changing the Bragg angle. With reference to Eqn. (4), this is achieved either by changing wavelength (which is continuously variable in the neutron case) or by examining higher orders of a given reflection (e.g. 220 or 330 and 110). For a two layer sample, as shown in Figure 6, in the $\theta(2)$ Bragg-angle configuration a volume is examined which is almost entirely layer 1; the $\theta(1)$ configuration includes layer 1 and layer 2 almost equally. Since the overall geometry can be measured to very high precision, appropriately weighted differences of scattered intensities allow separation of the layer 1 and layer 2 textures. The method has been tested with striking success for a two-plate, flat Cu sample (7). The (200) plane texture for each 0.8 mm thick plate was extracted from (200) and (400) texture distributions of the two plates together.

The method has now also been applied to the principal problem of interest: texture as a function of depth for a metallurgically compensated 105 mm HEAT-T liner. Measurements were made employing a diffractometer with fixed wavelength (1.26 A) so that only limited characterization was possible. Nevertheless, at a position 25.4 mm above the base (see Figure 5), the average orientation of the (111) slip planes within two layers was obtained. In Figure 7 texture distributions are shown for (111) and (100) reflections for the total

162

200 BULK   **400 BULK**   **111 BULK**   **222 BULK**

100 TOP   **100 BOTTOM**   **111 TOP**   **111 BOTTOM**
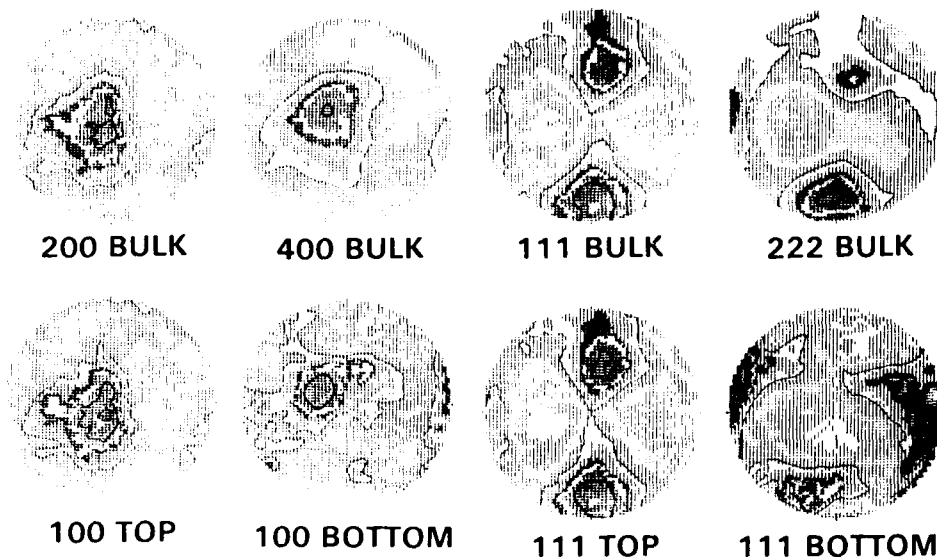
Figure 7. Textures for shaped-charge liner obtained as described
in the text. The center of each figure corresponds to the
normal direction to the cone surface. The cone-apex direction
is toward the top of the page. Other details as in caption,
Figure 3.
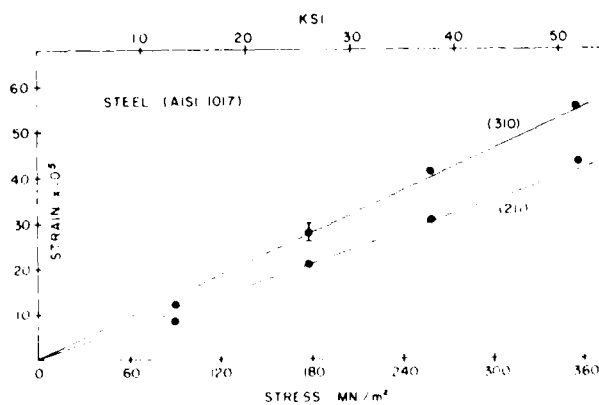
Figure 8. Radial strain vs. stress for a 1.59 cm diameter steel
rod in tension.

163

thickness and the extracted average textures for the 0.5 mm thick "surface" layer and the 2.3 mm thick lower layer. As one would expect, the rotary extrusion fabrication process produces a texture gradient across the thickness of the liner. Our technique and measurements are the first nondestructive characterization of these texture gradients which, when pursued under optimized conditions, have the potential for providing the first texture gradient vs. performance correlation for metallurgically compensated shaped-charge munitions.

B. Residual Stress

Macro residual stresses have long been recognized to be of great importance in determining the lifetime and performance of armament-system components in the field. Programs to measure residual stresses in such diverse items as helicopter rotor blades and hubs, high performance gears, gun tubes, tank track pins and torsion bars, KE penetrators, shaped-charge liners, shell-casings and the general category of weldments are, or have recently been, active. Micro-stresses are believed to be of less importance than macro residual stresses in hardware and will not be considered here explicitly.

Among nondestructive techniques for measurement of residual stress, x-ray diffraction and ultrasonic methods have received the greatest attention. The former has, in fact, been developed to the point where portable equipment for in-field inspection is available. Because of the limited penetration of x-rays in the energy range suitable for diffraction, this technique is truly nondestructive only for surface measurements. Ultrasonic methods show great promise for characterization of residual stress gradients in the bulk of metallurgical samples. However, the presence of internal interfaces, preferred grain orientation and other inhomogeneities introduce large uncertainties into the measurements.

In principal, neutron diffraction techniques -- as in the case of texture -- exactly parallel x-ray methods for residual stress measurement. The enormously greater penetration of neutrons makes them potentially useful for nondestructive determination of residual stress gradients in the bulk, following the approach illustrated in Figure 1. However, the measurement of residual stress by diffraction methods is much more difficult than texture measurements. The determination consists of measuring strain resulting from residual stress as manifested by the changes in d-spacing and angle of Bragg reflection (see Eqn. 4). Depending on the lattice planes examined and the radiation wavelength, the change in $\theta/2$ is on the order of $0.05°$ in going from unstrained sample to the yield point. Neutron diffraction measurements benefit from the fact that lineshapes of diffracted peaks are Gaussian, which is a considerable aid in analysis. On the other hand, intensities available at even the best of research reactors is less by

orders-of-magnitude than that of analagous x-ray diffraction instruments. This limitation makes the counting time necessary for the measurement of subtle shifts in peak positions impractically long with current "standard" neutron diffractometers. The introduction of focused beams and position-sensitive area detectors would alleviate this difficulty. We have, therefore, concentrated on the more fundamental questions related to the determination of residual stress by neutron diffraction.

Studies which have been completed have established that: 1) no competing effects (e.g. multiple scattering) distort the peak position obtained in the subsurface type of measurement illustrated in Figure 1; 2) the two-dimensional (x-ray) formalism for extraction of stresses from measured strains can be extended to three-dimensions; and 3) because of the Gaussian peak shape the Bragg peak centroid can be determined to on the order of thousandths of a degree even though the resolution is on the order of a degree. The confirmation of the last point is illustrated in Figure 8 in which measured radial strain vs. applied stress is shown for a steel rod in axial tension. The results for two crystallographic planes are shown and the ratio of elastic modulus to Poisson's ratio extracted from the measured slopes are in excellent quantitative agreement with theoretical values for polycrystalline samples reported in the literature (8).

Current work in this area is directed toward the determination of three-dimensional stress gradients in a prototype sample employing a well-collimated beam. Armament components of simple geometry such as KE penetrators would follow.

C. Second-phase Hardening

Small-angle x-ray scattering (SAXS) has been used to study small-concentration precipitates in alloys for decades (9). This approach also makes use of Bragg scattering (Eqn. 4), but in this case scattering which takes place within a few degrees reveals structural properties in the 10 to 1000 Å range. With the development of area detectors and new high flux reactors, small-angle neutron scattering (SANS) has in the last few years also been brought to bear on the study of this area of physical metallurgy. Because of the great penetration of the neutron and the different scattering selectivity relative to x-rays, previously unexplorable problem areas now may be amenable to solution, some of them in the context of NDT.

To date, the most interesting SANS work in the area of technological alloys has been done by a group from the FIAT Co. One example of their efforts is the study of the evolution as a function of service time of the γ' precipitate in nickel-base, superalloy UDIMET-710 in turbine blades (10). They clearly observe the accelerated growth of the γ' particles prior to failure.

At the NBS reactor a state-of-the art SANS instrument is nearing completion. An interim facility has been operating with which a variety of problems have been studied in a preliminary way. In the metallurgical area, SANS has been used to study creep-induced voids in iron (10). Fe-0.2% Ti subjected to a σ = 35 ksi, ϵ = 1.2% stress at 500°C showed voids of 360 A average diameter with SANS but not with SEM. These results illustrate the relative ease by which SANS can characterize metallurgically important defects in the nucleation stage nondestructively.

Upon completion of the new facility, second-phase hardening studies for armament related alloys will be pursued. Among these, the effect of cold work and heat treatment on precipitates in new, tungsten-based, KE penetrator alloys requires immediate characterization.

IV. SUMMARY AND CONCLUSIONS

In the present work we have described the limitations and advantages of neutron diffraction for nondestructive determination of certain properties in metallurgical samples. In the area of residual stress, several necessary tests of the neutron diffraction method have been made and it has been shown for the first time that the technique has the potential for determination of three-dimensional stress gradients in the bulk.

In the area of texture or preferred grain orientation determination, both neutron selectivity and penetration have been used for specific armament system applications. We have conceived and tested a method by which texture can be characterized nondestructively in samples which are thin relative to typical neutron diffraction beam dimensions. The method has been applied to the long-standing problem of texture determination in metallurgically compensated shaped-charge liners, and the first - though not yet complete - nondestructive measurement of texture as a function of depth in a shaped-charge liner has been achieved.

The neutron diffraction technique has also been employed for the first time to determine nondestructively, textural anisotropy in the matrix phase of tungsten-alloy KE penetrators. Because of the enormously greater x-ray scattering from tungsten relative to nickel or iron, this type of information is unobtainable either destructively or nondestructively except by means of neutrons.

Results obtained by means of small-angle neutron scattering have been outlined which demonstrate a capability which will be employed in the area of second-phase precipitates.

In summary, although neutron diffraction techniques for NDT are limited to laboratory environments, there are numerous examples where needed information cannot be obtained by any other means. In

these cases the neutron techniques – since they are nondestructive –
are seen as a means by which property/performance correlations can be
determined and specifications established for routine inspection by
other, more portable methods.

V.   ACKNOWLEDGMENTS

REFERENCES

1. G. E. Bacon, Neutron Diffraction, 3d. ed. (Oxford Press, London,
1977).

2. H. P. Klug and L. E. Alexander, X-ray Diffraction Procedures for
Polycrystalline and Amorphous Materials, 2d. ed. (John Wiley & Sons,
New York, 1974).

3. G. E. Dieter, Jr., Mechanical Metallurgy, (McGraw-Hill, New York,
1961).

4. E. M. Pugh, R. J. Eichelberger and N. Rostoker, J. Appl. Phys. 23,
532 (1952).

5. F. Witt, FATR-75001 (1975), and references cited therein.

6. Z. Iqbal et al., Army Sci. Conf., West Point, NY (1976).

7. C. S. Choi, H. J. Prask and S. F. Trevino, J. Appl. Crys. 12, 327
(1979).

8.   E. Kroner, Z Physik 151, 504 (1958); F. Bolenrath et al.,
Z. Metallkde. 58, 76 (1967).

9.   A. Guinier and G. Fournet, Small Angle Scattering of X-rays,
(John Wiley & Sons, New York, 1955).

10. Choi, Prask, Trevino, Alperin, Fatemi, and Rath, Proc. 27th DOD
Conf. on NDT, p. 324, (1978).

CHEMILUMINESCENCE IMMUNOREACTIVE ASSAY (CLIA):
A RAPID METHOD FOR THE DETECTION OF BACTERIAL AND VIRAL AGENTS -
FRANCISELLA TULARENSIS, LIVE VACCINE STRAIN (LVS) AND VENEZUELAN
EQUINE ENCEPHALOMYELITIS VACCINE STRAIN (VEE TC-83) (U)

*DOUGLAS W. REICHARD, MAJ, MSC, ROBERT J. MILLER, JR., 1LT(P), MSC
U.S. ARMY MEDICAL RESEARCH INSTITUTE OF INFECTIOUS DISEASES
FORT DETRICK, FREDERICK, MARYLAND 21701

The ability to detect rapidly, small numbers of microorganisms is of great military importance. In the case of a biological warfare attack, it is imperative that field commanders be informed as rapidly as possible as to the nature and consequences of the causative agents. Currently, there are no methods for rapid identification of potential BW agents during military operations. We describe efforts to develop a rapid diagnostic procedure for the specific detection and identification of microorganisms of military importance using a chemiluminescent immunoreactive assay (CLIA).

Chemiluminescent reactions have been used to determine picomoles of hematin compounds (1-3), as well as direct estimation of bacterial concentration (4). Combination of the solid-phase enzyme-linked immunoassay (ELISA) and CLIA (5) has resulted in ultrasensitive determinations of bacteria (6), viruses (7), and enterotoxin (8) concentrations. As previously reported (9), a polystyrene solid-phase, peroxidase-labeled antibody immunoassay based on the luminol-H_2O_2 reaction was used to measure 10^1 to 10^2 bacteria.

Part I of this paper describes the use of antibody covalently bound to polyacrylamide beads (10) for the determination of virion concentrations using a luminol CLIA. Part II describes work on a CLIA for determination of bacteria utilizing passively adsorbed antibody on polystyrene beads.

169

Part I. Venezuelan Equine Encephalomyelitis (VEE) TC-83 Assay

Robert J. Miller, Jr.

MATERIALS AND METHODS

Apparatus: The chemiluminescent (CL) luminol analyses were per-
formed using a Chem-Glow Photometer (Aminco, Rockville, MD) and peak
flash heights measured on a potentiometric recorder, 50 mV setting
(Aminco). Radioimmunoassay samples (RIA) were counted on a Searle (Des
Plaines, IL) Mark III liquid scintillation counter. Centrifugations
were carried out in an IEC PR-6000 (Damon/IEC Division, Needham
Heights, MA) (2500 x g, 4°C, 15 min, unless otherwise noted). All test
tubes and reaction cuvettes (6 x 50 mm) were of borosilicate glass
(Kimble Products, Toledo, OH).

Reagents: All buffers and assay reagents were made up in dis-
tilled water which had been passed through Barnstead ultra-pure mixed
bed and combination cartridge demineralizers.

Sera: Hyperimmune monkey anti-VEE serum was kindly provided by
Animal Assessment Division (USAMRIID). A crude immunoglobulin frac-
tion was prepared from a 40% (w/v) $(NH_4)_2SO_4$ precipitation which was
dialyzed exhaustively against 0.01 M potassium phosphate buffered sa-
line, pH 7.4 (KPBS). Crude immunoglubulin (10 mg) was then applied to
a 0.9 x 10 cm column of protein A-Sepharose 4B-CL (5 mg, Pharmacia
Fine Chemicals, Piscataway, NJ) which had been pre-equilibrated with
KPBS, pH 7.4, containing 0.1% azide as preservative. The column was
then eluted with buffer until the absorbance at 280 nm was negligible.
Bound IgG was eluted with 0.1 M acetic acid-0.15 M saline (11); peak
tubes were pooled and dialyzed exhaustively against KPBS. The monkey
IgG anti-VEE (MaVEE) fraction was stored at 4°C as a stock solution of
2.7 mg/ml, with a titer of 1:1024 as determined by protein A-radioimmu-
noassay (12). Purity of the fraction was determined by crossed immuno-
electrophoresis which indicated only one precipitin band, corresponding
to IgG.

Conjugate: Horseradish peroxidase (HRPO)-conjugated rabbit anti-
monkey IgG (RaMP) was obtained commercially from Cappel Laboratories,
Inc. (Cochranville, PA), or prepared using the method of Nakane et al.
(13), using HRPO type VI, from Sigma Chemical Co. (St. Louis, MO) and
rabbit anti-monkey IgG from Cappel Laboratories. Both types of peroxi-
dase conjugates were further purified by protein A column chromato-
graphy as previously described. RaMP with a HRPO:IgG molar ratio of
3:1 was stored at 4°C in KPBS, pH 7.4 with 0.1% NaN_3. Horseradish per-

oxidase concentration was determined by the luminol H_2O_2 chemiluminescent reaction (1,2).

Chemiluminescent Reagents: The Chemical Systems Laboratory (Aberdeen Proving Grounds, MD) kindly supplied a stock solution of 1.5 mM luminol containing 0.1 N NaOH, and 1% ethylenediamine tetraacetate (EDTA) in deionized H_2O. Fresh 3% H_2O_2 in 1% EDTA, deionized H_2O was prepared from stock 30% H_2O_2 (J. T. Baker Chemical Co., Phillipsburg, NJ) prior to each assay.

Solid-Phase Support: MaVEE was covalently linked to polyacrylamide beads (Immunobeads, Bio-Rad Laboratories, Rockville Centre, NY) following manufacturer's recommended procedure. One-ml samples of 1 mg/ml MaVEE-beads (untreated as well as 4% BSA-treated) were stored at 4°C in KPBS, pH 7.4, with 0.1% NaN_3.

Virus Preparation: Serial log dilutions of sucrose gradient purified TC-83 (graciously supplied by Dr. Jahrling, Virology Division, USAMRIID) were prepared in 1% BSA-KPBS, pH 7.4. Serial dilutions of reconstituted live attenuated VEE vaccine (NDBR 102, National Drug Company, Philadelphia, PA) were prepared in deionized H_2O or 0.05% Tween 20 (Sigma).

Chemiluminescent Immunoassay (CLIA) Procedure: One ml of each virus dilution was reacted with 100 µl of MaVEE-bead in 10 x 75 mm borosilicate glass test tubes and incubated from 4 to 6 h at 37°C with mild agitation. Antibody bead-virus complex was centrifuged at 2,500 x g for 30 min at 4°C. The pellet was then washed once with 3.0 ml KPBS, vortexed, and recentrifuged. Next, the supernatants were gently decanted, and the pellets resuspended with 1 ml RaMP (60 µg/ml). Following an incubation of 2 h at 37°C, the mixture was again centrifuged and the supernatant and pellet assayed by the luminol-H_2O_2 chemiluminescent reaction described below.

Supernatant Assay: To each 6 x 50 mm reaction cuvette were added 100 µl of supernatant and 100 µl of 30 µM luminol reagent. After mixing and a 5 to 10 min incubation at room temperature, the reaction cuvette was placed in the reaction chamber of the photomultiplier microphotometer and 100 µl of fresh 3% H_2O_2 injected. The chemiluminescent peak flash height was measured and recorded as relative light intensity in millivolts.

Pellet Assay: Pellets were resuspended in KPBS and centrifuged for 10 min. This washing procedure was repeated three times. Following the final wash, pellets were resuspended by vortexing in 1 ml 0.1 N NaOH 1% EDTA reagent. After allowing the mixture to stand for

10 to 15 min, 100 µl aliquots were assayed by the luminol-H_2O_2 method described above. (A minimum of five replicates was assayed for each supernatant or pellet of virus dilution tested.)

Radioimmunoassay (RIA) Procedure: To 12 x 75 mm borosilicate glass test tubes were added 50 µl of 1 mg/ml antibody bead, 50 µl tritiated TC-83 (10^9 PFU/ml) supplied by Dr. Jahrling and 1.0 ml of virus preparation. Following an incubation period of 18 to 66 h at 37°C, the tubes were centrifuged and supernatants and pellets were assayed as follows: 200-µl samples of supernatant were mixed with 6 ml of scintillation cocktail and counted for 10 min; pellets were washed once with KPBS, centrifuged, and resuspended with 0.5 ml 0.05% Tween 20. The resuspended samples were transferred to scintillation vials, 6 ml of cocktail added, and counted for 2 min.

RESULTS

As shown in Figure 1, various ranges of viral concentrations were detectable by varying the concentration of antibody bead. The maximum chemiluminescent response (CL) is directly proportional to the maximum binding of labeled second antibody. Bound second antibody is indirectly proportional to the concentration of bound virus. As the concentration of virus increases per antibody bead concentration, the binding of labeled second antibody decreases, which results in a decrease in the measured CL response. Therefore, as the concentration of virus approaches saturation of the antibody bead, the CL response approaches background (endogenous) chemiluminescence.
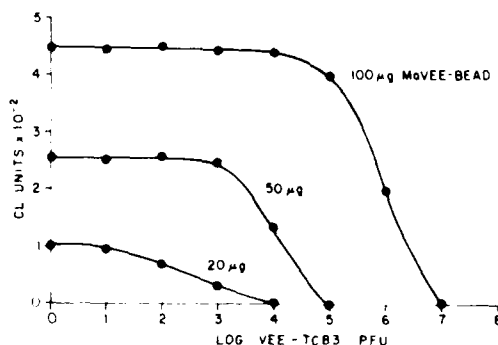
Figure 1. Chemiluminescent Analyses. 100, 50, and 20 µl of stock MaVEE-bead (1 mg/ml) incubated 4 h with sucrose gradient purified TC-83 followed by a 1 h incubation with 1 ml RaMP (60 µg/ml).

172

In order to confirm the CLIA results, a RIA competitive antigen binding assay was examined using tritiated TC-83 in competition with sucrose gradient purified TC-83 and live attenuated VEE vaccine. Both BSA-treated and untreated antibody beads were used in the assay. The RIA results of a 66-h incubation with sucrose gradient purified TC-83 are shown in Figure 2. Figure 3 shows the results of an 18-h incubation with live attenuated VEE vaccine. In both cases the same degree of sensitivity and detection limits were achieved with a 6-h CLIA.
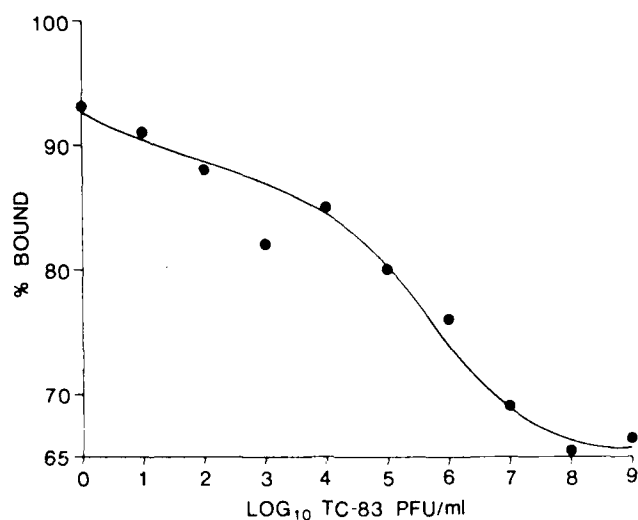
Figure 2. RIA Pellet Analysis of Sucrose Gradient Purified TC-83. 50 μl MaVEE-bead (1 mg/ml), 50 μl-tritiated TC-83 PFU/ml), and 1.0 ml TC-83 dilution, incubated for 66 h.
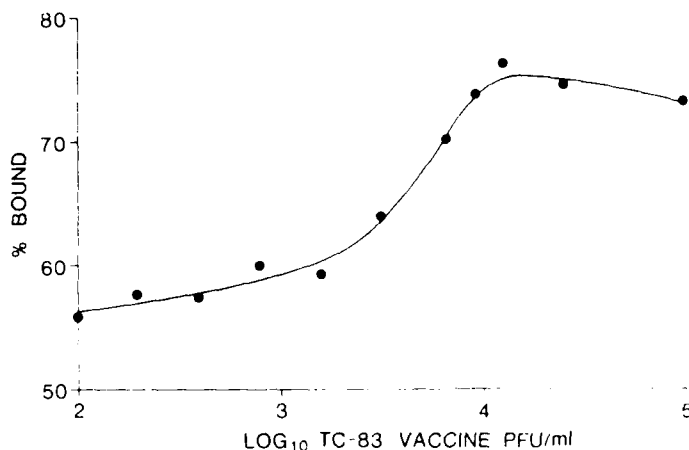
Figure 3. RIA Supernatant Analysis of Live
Attenuated VEE Vaccine.   50 µl MaVEE-bead
(1 mg/ml), 50 µl tritiated TC-83 (10^9 PFU/ml),
and 1.0 ml vaccine dilution, incubated for 18 h.

DISCUSSION

The use of RIA and ELISA for determinations of antibody and anti-
gen concentrations is well-documented (14-18). As described in this
paper, a CLIA method has been developed which parallels the reported
sensitivity of RIA and ELISA, but offers several advantages. CLIA
uses a covalently bound antibody-solid phase system, which eliminates
the problems of desorption of antibody that occur during washing in
the ELISA system (19,20). The CLIA-luminol system does not require
the use of radioactive materials as does RIA, and therefore is not de-
pendent upon radioactive half-lives in reagent shelf life, as well as
the hazards associated with radioactivity. The luminol based assay
also does not require an enzymatically active label as does ELISA.
The chemiluminescent response in the CLIA-luminol system is dependent
on heme concentration (1,2,4) present in the conjugate.

Finally, the viral CLIA system described requires only 6 h to de-
tect 10^2 PFU of virus; standard RIA and ELISA procedures (11,12,14,15,
17) require 18 to 48 h for detection, while other luminescent proce-
dures (7) indicate detection limits of 10^6 PFU.

Currently, other group A arboviruses are being tested for specifi-
city and possible cross-reactivity. The CLIA system will also be exa-
mined for detection of other potential BW viral agents.

174

PART II. Francisella tularensis Live Vaccine Strain (LVS) Assay

Douglas W. Reichard

MATERIALS AND METHODS

Apparatus: Equipment and reagents were identical to those described in Part I.

Sera: Hyperimmune anti-Francisella tularensis serum was obtained from rabbits inoculated in the foot pads with 10^{10} (0.5 ml total) F. tularensis live vaccine strain (LVS) and followed 28 days later by intramuscular inoculation of 10^{10} LVS. Rabbits were exsanguinated on day 46; serum was separated. A crude immunoglobulin fraction was prepared from a 40% (w/v) $(NH_4)_2SO_4$ precipitation which was dialyzed against 0.01 M KPBS, pH 7.0. Crude immunoglobulin was further purified on protein A-Sepharose as described in Part I. Rabbit anti-F. tularensis (RaFT) was stored at 4°C in 0.01 M KPBS with 0.1% azide.

Conjugate: Horseradish peroxidase conjugated goat anti-rabbit IgG (GARP) was obtained commercially (Miles Laboratories, Inc., Elkhart, IN). Peroxidase conjugates could be further purified on protein A-Sepharose.

Chemiluminescent Reagents: The luminol and hydrogen peroxide reagents were as described in Part I.

Solid Phase Support: RaFT (1.2 mg) was passively adsorbed to 400 frosted 1/8-in diameter, polystyrene beads (Clifton Plastics, Clifton Heights, PA) in 25 ml of 0.1 M Na_2CO_3 pH 9.0, for 4 h at room temperature and overnight at 4°C (15). The antibody-coated beads were washed two times with KPBS and stored at 4°C in KPBS containing 0.1% NaN_3.

Bacteria Preparation: Serial log dilutions of 10^9 LVS obtained from Bacteriology Division, USAMRIID, were prepared in normal saline.

Chemiluminescent Immunoassay (CLIA) Procedure: Bacterial dilutions were incubated and mildly agitated at 37°C for 2 h with antibody-coated polystyrene beads (1 ml/bead/tube). The supernatant was then aspirated and discarded; the beads were washed two times with KPBS. One ml of labeled second antibody (GARP) diluted 1:250 with 0.01 M Na_2CO_3 with 0.1% BSA, pH 8.5, was added to each tube and the beads incubated for 2 h at 37°C with mild agitation. Following incubation, the GARP solutions were removed by aspiration and the beads washed several times with KPBS. The beads were then transferred to 6 x

1.0

2.8   2.5

3.2   2.2

2.0

1.1

1.8

1.25   1.4   1.6

MICROCOPY RESOLUTION TEST CHART
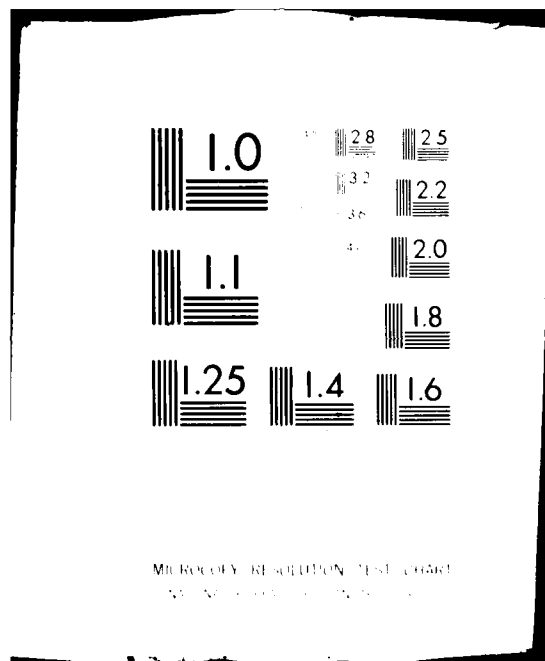
50 mm reaction cuvettes and 100 μl of luminol solution were added. After allowing the beads to sit for 5 min, the tubes were placed in the reaction chamber and 100 μl of 3% H_2O_2 were injected to produce the chemiluminescence. The light values were measured on a potentiometric recorder and expressed as relative light intensity.

RESULTS

Since a labeled species-specific second antibody was employed in this assay, the amount of light produced should be directly proportional to the amount of HRPO present (1,2) and, therefore, inversely proportional to the amount of bacteria in the original solution.

As can be seen in Figure 4, our data show an increase in chemiluminescence with increasing bacterial concenrations with a cut-off in detection at approximately 10^2 bacteria/ml.
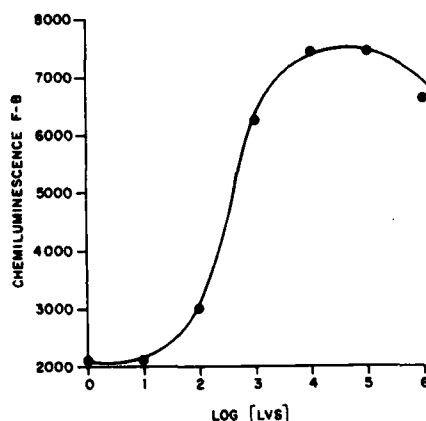
Figure 4. Chemiluminescent Analysis. Antibody-coated polystyrene beads incubated with serial log dilutions of bacteria for 2 h at 37°C followed by incubation with labeled second antibody for 2 h at 37°C. Chemiluminescence values were calculated by subtracting background from peak height responses.

The chemiluminescence response of our data is opposite to that which was theoretically anticipated; several hypotheses were proposed as possible explanations: (a) labeled second antibody bound non-specifically to antigen, (b) free HRPO bound nonspecifically to polystyrene beads, (c) chemiluminescence was due to bound bacteria (4), and (d) antibody-binding was similar to that observed in quantitative

precipitin reactions.

In various experiments designed to test these hypotheses, it was found that GARP does not bind to LVS antigen (hypothesis a). Less than 10% free HRPO does bind, but this amount is not enough to influence the chemiluminescence observed during the assay (hypothesis b). The chemiluminescence from bound bacteria is not detectable until the bacterial concentration reaches 10^7 to 10^8/ml (hypothesis c). To test hypothesis d, beads were coated with varying concentrations of first antibody. If precipitin-type binding parameters were involved, at high concentrations of first antibody, an increase in chemiluminescence should be observed due to matrix formations. At low concentrations of first antibody, a decrease in chemiluminescence should appear as matrix formation becomes less probable. At high concentration of antibody (1:400 dilution), an increase in light emission was observed while a decrease in light emission was noted at a low concentration (1:400 dilution). It is, therefore, suggested that the observed chemiluminescent response in the assay is probably due to the antibody-binding parameters described.

DISCUSSION

Passive adsorption of antibody to plastic as a practical assay procedure was first described by Catt and Tregear (19). Since then, this method has been utilized to develop RIA and ELISA tests for many antigens (16). The preferred plastic for these tests has been polystyrene in test tube and microtiter plate form.

However, an inherent problem of antibody desorption during multiple washing and incubating steps has been observed with these regular polystyrene solid supports (20,21). Recently, the use of polystyrene beads with a milled textured finish has been reported (22). The use of these frosted beads suggested that desorption might be limited, compared to the aforementioned polystyrene support mediums. The use of polystyrene beads, while providing good adsorptive properties, still suffers from the problem of antibody desorption during washing. Multiple wash steps are necessary to insure that no contaminating substances (i.e., heme-containing compounds and divalent cations) are present to produce extraneous chemiluminescence.)

As with all immunoassays, the affinity and homogeneity of the primary antibody determines the specificity and degree of cross-reactivity of the assay method. Typically, F. tularensis does not produce high titer IgG antibodies, usually only 1:64 at 3.5 mg/ml. Higher titer IgM antibodies can be obtained, but they do not adsorb to polystyrene (20). As shown in Part I, the VEE antibody titer was more than 10 times

177

greater than the F. tularensis titer. Further studies are in progress in an attempt to produce higher titer F. tularensis antibodies.

CONCLUSIONS

The results presented show that a rapid procedure for the detection and identification of viral and bacterial antigens is possible with chemiluminescent immunoassays. Chemiluminescent immunoassays appear to offer the sensitivity and simplicity required for rapid identification of potential BW agents during military operations. Further research is underway to explore new approaches which may yield even more applications of this new technology.

1. Neufeld, H. A., C. J. Conklin, and R. D. Towner. 1965. Chemiluminescence of luminol in the presence of hematin compounds. Anal. Biochem. 12:303-309.
2. Ewetz, L., and A. Thore. 1976. Factors affecting the specificity of the luminol reaction with hematin compounds. Anal. Biochem. 71:564-570.
3. Puget, K., A. M. Michelson, and S. Avrameas. 1977. Light emission techniques for the microestimation of femtogram levels of peroxidase. Anal. Biochem. 79:447-456.
4. Neufeld, H. A., L. T. Carleton, and S. Witz. 1966. Chemiluminescence as a tool for biodetection. Army Science Conference Proceedings 2:157-168.
5. Olsson, T., G. Brunius, H. E. Carlsson, and A. Thore. 1979. Luminescence immunoassay (LIA): a solid-phase immunoassay monitored by chemiluminescence. J. Immunol. Methods 25:127-135.
6. Halmann, M., B. Velan, and T. Sery. 1977. Rapid identification and quantitation of small numbers of microorganisms by a chemiluminescence immunoreaction. Appl. Environ. Microbiol. 34:473-477.
7. Velan, B., H. Schupper, T. Sery, and M. Halmann. 1979. Solid phase chemiluminescent immunoassay. In International Symposium on Analytical Applications of Bioluminescence and Chemiluminescence Proceedings 1978, vol. 1. State Printing & Publishing Co., Westlake Village, CA, pp. 431-437.
8. Velan, B., and M. Halmann. 1977. Chemiluminescence immunoassay; a new sensitive method for the determination of antigens. Immunochemistry 15:331-333.
9. Reichard, D. W., and R. J. Miller. 1979. Chemiluminescent immunoreactive assay for rapid detection of Francisella tularensis. Fed. Proc. 38:1013 (abstract).
10. Inman, J. K., and H. M. Dintzis. 1969. The derivatization of cross-linked polyacrylamide beads. Controlled introduction of functional groups for the preparation of special-purpose, biochemical adsorbents. Biochemistry 8:4074-4082.

11. Goding, J. W. 1976. Conjugation of antibodies with fluoro-chromes: modification to the standard methods. J. Immunol. Methods 13:215-226.
12. Jahrling, P. B., R. A. Hesse, and J. F. Metzger. 1978. Radioim-munoassay for quantitation of antibodies to alphaviruses with staphylococcal protein A. J. Clin. Microbiol. 8:54-60.
13. Nakane, P. K., and A. Kawaoi. 1974. Peroxidase-labeled antibody. A new method of conjugation. J. Histochem. Cytochem. 22:1084-1091.
14. Drow, D. L., D. G. Maki, and D. D. Manning. 1979. Indirect sand-wich enzyme-linked immunosorbent assay for the rapid detection of Haemophilus influenzae type b infection. J. Clin. Microbiol. 10: 442-450.
15. Ruitenberg, E. J., P. A. Steerenberg, B. J. M. Brosi, and J. Buys. 1974. Serodiagnosis of Trichinella spiralis infections in pigs by enzyme-linked immunosorbent assays. Bull. W.H.O. 51:108-109.
16. Voller, A. 1978. The enzyme linked immunosorbent assay (ELISA). Diagnostic Horizons 2:1-7.
17. Miranda, O. R., G. D. Bailey, A. S. Fraser, and H. J. Tenosa. 1977. Solid-phase enzyme immunoassay for herpes simplex virus. J. Infect. Dis. 136:S304-S310.
18. Wolters, G., L. P. Kuijpers, J. Kacaki, and H. W. M. Schuurs. 1977. Enzyme-linked immunosorbent assay for hepatitis B surface antigen. J. Infect. Dis. 136:S311-S317.
19. Catt, K., and G. W. Tregear. 1967. Solid-phase radioimmunoassay in antibody-coated tubes. Science 158:1570-1572.
20. Herrmann, J. E., and M. F. Collins. 1976. Quantitation of immu-noglobulin adsorption to plastics. J. Immunol. Methods 10:363-366.
21. Kalimo, K. 1977. Solid-phase radioimmunoassay of antiviral IgG and IgM class antibodies. Academic Dissertation, Department of Virology, Medical Microbiology and Dermatology, University of Turku, Turku, Finland.
22. Ziola, B. R., M.-T. Matikainen, and A. Salmi. 1977. Polystyrene balls as the solid-phase of double-antibody radioimmunoassay for human serum albumin. J. Immunol. Methods 17:309-317.

A NEW TECHNIQUE FOR DOPPLER FREQUENCY
ANALYSIS OF RADAR SIGNALS

*OTTO E. RITTENBACH
US ARMY COMBAT SURVEILLANCE &
TARGET ACQUISITION LABORATORY
FORT MONMOUTH, NJ 07703

1. BACKGROUND

A longstanding performance goal for Army ground surveil-
lance radars is the automatic classification of moving ground targets
on the battlefield. Limited classification has been achieved by
splitting the radar doppler spectrum into lower and higher frequency
bands, thus distinguishing between targets having different radial
velocities. While this is an important feature, since only certain
targets (vehicles) are capable of obtaining high radial speeds, it
does not provide a distinction between a moving man and vehicles
having low radial speed components.

That there are distinct differences in the doppler signa-
tures between man and vehicle is easily established by listening to
typical doppler return signals. One can clearly distinguish the step
modulation of a walking man from the relatively constant or slowly
changing tone of a vehicle. As to be expected, a spectrogram of a
walking man (Figure 1) shows this repetitive behavior. Most obvious
is a sinewave like frequency modulation at the step frequency of the
main body return power appearing as a black band near 100 Hertz.

181

This oscillatory temporal characteristic in the doppler shifted frequency is practically never seen in vehicular return and is the discriminant chosen for automatic classification.

Figure 1: Doppler Spectrum of Walking Man

This paper describes efforts at the Combat Surveillance and Target Acquisition Laboratory at Fort Monmouth, NJ to develop an automatic classifier for moving personnel using a novel frequency locked loop to detect the modulation present in radar echos. After developing the theory, experiments are described and recommendations for further work are given.

2. THEORY

A coherent radar transceiver is used to obtain the doppler signal from a moving target. This signal is fed in a frequency locked loop using a frequency modulation discriminator to transform the momentary doppler frequency in a voltage. After the frequency loop locks on the target, the voltage proportional to the doppler frequency is analyzed for frequency modulation inafast fourier transform.

Its detector supplies signals to the display indicating the echo area, the radial speed and the step frequency (if any) of the target. Emphasis is placed on evaluation of different frequency locked loop variations of a novel discriminator.

For an uncluttered presentation, only the essential building blocks of the classifier are discussed. Also only the parameters relevant to the classification techniques described are included. When not essential, attenuation, phase and time delays are omitted or set to zero, oscillator signals have unit magnitude, multipliers have a multiplication constant of two and rectifiers give the magnitude of the input sinewave. Angular frequencies are used throughout. The main parts of the radar system are Transceiver, Frequency Modulation Transformer, Detector and Display.

| TARGET | ⟷ | TRANSCEIV | → | FM-TRANSF | → | DETECTOR | → | DISPLAY |
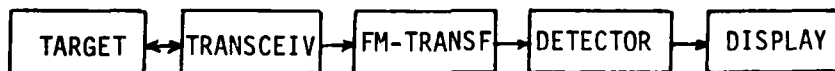
Figure 2. Radar System for Automatic Identification

2a. <u>RADAR TRANSCEIVERS</u>: The doppler signal out of a radar is described by a magnitude m_d which is proportional to the target backscatter strength and the doppler frequency shift a_d. The output depends on the radar design and can be represented as $m_d\cos(a_o+a_d)t$, a sideband of an offset frequency a_o where a_o represents either the radio frequency, the intermediate frequency, or a natural number multiple of the pulse repetition frequency. In the homodyne transceiver case, both the inphase component $m_d\cos(a_o+a_d)t$ and the quadrature component $m_d\sin(a_o+a_d)t$ are needed to derive information on radial direction.

2b. FREQUENCY MODULATION TRANSFORMER: The frequency modulation of the doppler return from a walking man is transformed into an amplitude modulation for further processing. The transformation is described in three steps: Frequency Sensitive Elements, Discriminator, and Frequency Locked Loop.

2b1. FREQUENCY SENSITIVE ELEMENT: Resonant circuits and R-C circuits are discussed.

2bIA. RESONANT CIRCUIT: Consider a tuned circuit of resonant frequency a and quality factor Q consisting of inductance L and a capacitance C in parallel ($a = 1/\sqrt{L.C}$), followed with a resistor R in series (normalized frequency $n = Q(a_S/a - a/a_S)$ with $Q = RaC = R/aL$), fed from a constant voltage source. For this configuration, the capacitances of the connecting lead and the load can be compensated by a corresponding reduction of capacitance C (figure 2bI). If the magnitude of the source signal is m_S and its frequency is a_S, the input voltage is $m_S \cos a_S t$. The output i across the tuned circuit is $o_i = (m_S/\sqrt{1+n^2})\cos(a_S t - \tan^{-1} n)$ and the output q across the resistor is $o_q = (m_S/\sqrt{1+1/n^2})\cos(a_S t + \cot^{-1} n)$. Since both output connections for o_q are floating, it is sometimes desirable to use the circuit of figure 2bIA where one output connection is grounded.
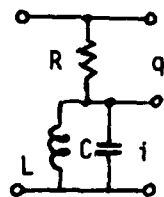
Fig. 2bI.
Frequency
Splitter
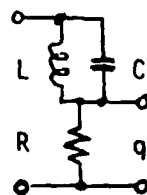
Fig. 2bIA.
Frequency
Stop

2bIB. R-C CIRCUIT: Since inductors are usually the largest, lossiest and most expensive tuned circuit elements, inductorless designs are included. The above formulas are then simplified by letting $L \rightarrow \infty$, resulting in resonant frequency $a = 0$, quality $Q = 0$ and the normalized frequency $n = RCa_S$.

2bII: <u>DISCRIMINATOR</u>: A conventional and a novel discriminator are treated.

2bIIA. <u>CONVENTIONAL DISCRIMINATOR:</u> After bandpass filtering the source signal with frequency a_s is fed with magnitudes m_- and m_+ to the filters Frequency Pass - and + (figure 2bIIA) whose resonant frequencies are a_- and a_+ (figure 2bI). Designating the inductances as L_- and L_+, the capacities as C_- and C_+, the resistances as R_- and R_+, the qualities of the tuned circuits as Q_- and Q_+, the normalized frequencies as n_+ and n_{-1}, the output signals as o_- and o_+, the outputs feed the twoway linear rectifiers + and -. The rectifier outputs o_+ and o_- feed the Subtractor, whose output $|o_+| - |o_-|$ is smoothed in the <u>Lowpass</u> filter, making its output $\overline{|o_+| - |o_-|} =$ $m_+/\sqrt{1+n_+^2} - m_-/\sqrt{1+n_-^2}$. The amplitude versus frequency slope is $s_+ - s_-$ with $s = d(m/\sqrt{1+n^2})/d(a_s/a_m) = mnn'/(1+n^2)^3$ and $n' = dn/d$ (a_s/a_m), where $a_m = \sqrt{a_- a_+}$, the geometrical mean of the resonant frequencies.
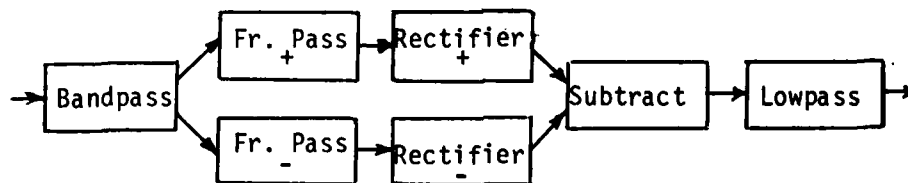
Figure 2bIIA: Conventional Discriminator

For the special case of equal signal magnitudes $m_- = m_+ = m_s$ and equal quality $Q_- = Q_+ = Q$, the output is $m_s \cdot (1/\sqrt{1+n_+^2} - 1/\sqrt{1+n_-^2})$. For large normalized frequencies this approximates $2m_s(a_m-1)/(Qa_s/a_m)$. The slope at the a_m becomes then $2m_s Q^2(a_m^2 - 1/a_m^2)/\{\sqrt{1+[Q(a_m-1/a_m)]^2}\}^3$ Figure 2bII shows the lowpass output and its contributions from Frequency Pass - and + for unit source signal magnitude $m_- = m_+ = m = 1$,

185
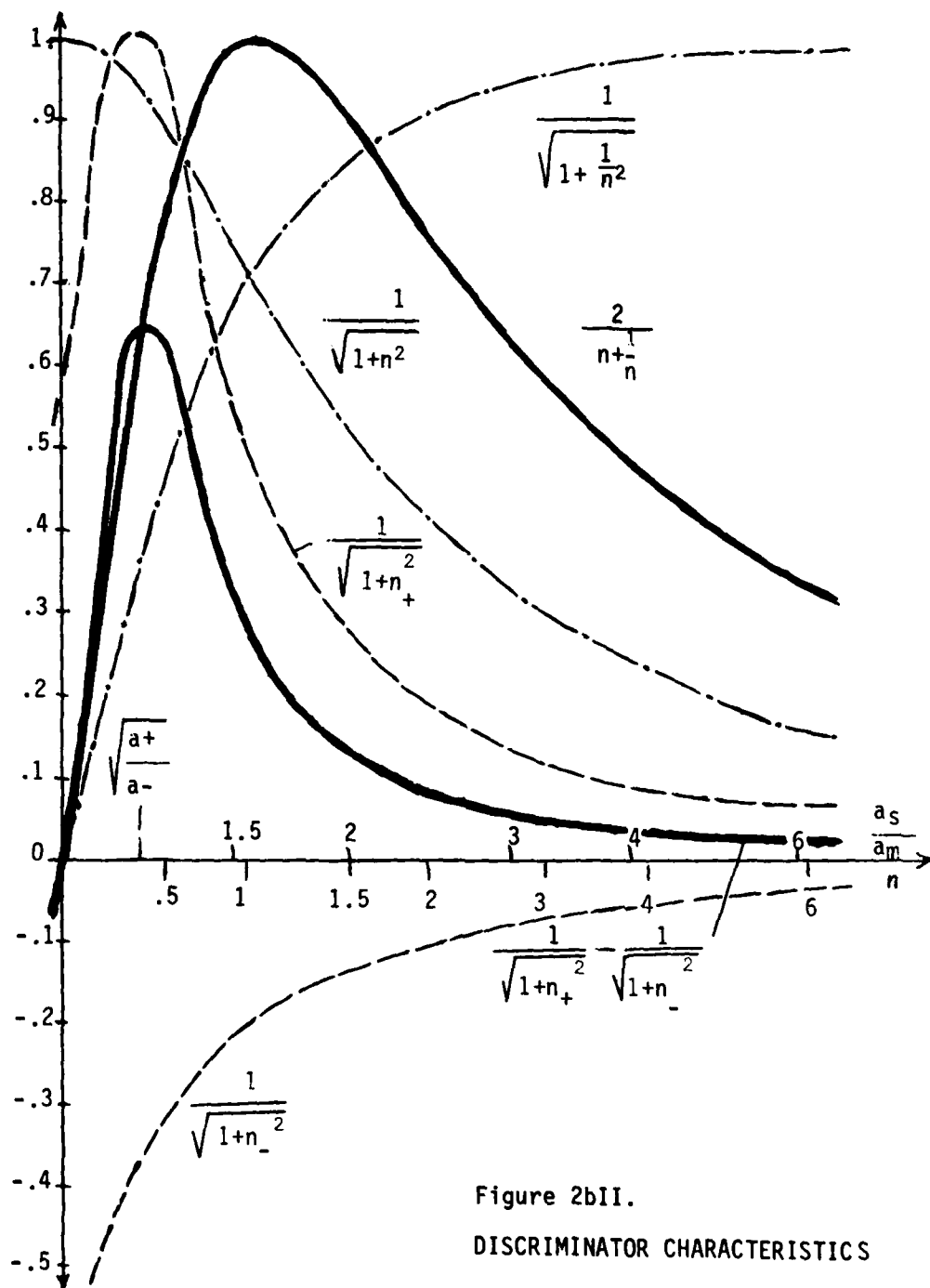
Figure 2bII.

DISCRIMINATOR CHARACTERISTICS

Quality $Q_- = Q_+ = 12$ and resonance frequency ratio $a_+/a_- = 1.44$. The slope for $a_s = a_m$ is 4.2354 at the origin.

      2bIIB. <u>NOVEL DISCRIMINATOR</u>: The preferred characteristic of a discriminator has odd symmetry response with respect to a center frequency. The susceptance of a lossless tuned circuit $j(aC-1/aL)$ has this property, but approaches infinity for frequencies nearing zero or infinity. A response which decreases at the extreme frequencies as with the conventional discriminator, can be achieved by correlation using resonant or R-C circuits.

      2bIIB1. <u>RESONANT CIRCUIT CASE</u>: A source signal $m_s \cos a_s t$ is fed into the Pass filter for rejection of undesired frequencies. The Frequency Splitter (figure 2BIIB1) outputs i and q are fed into Phaseshifters i and q with phaseshifts p_i and $p_q = p_i + 90^o$ to supply cosine signals with magnitudes $m_s \sqrt{1+n^2}$ and $m_s/\sqrt{1+1/n^2}$, and phase $|a_s|t + p_i - \tan^{-1} n$ to the Multiplier with constant M, whose output $[Mm_s^2/2(n+1/n)][1-\cos 2(|a_s|t + p_i - \tan^{-1} n)]$ is fed to the Lowpass, which removes the alternating part, leaving $Mm_s^2/2(n+1/n)$. For small and large normalized frequencies, this can be approximated by $Mm_s^2 n/2$ and $Mm_s^2/2n$. At the origin of Figure 2bII $n = o$ and the slope, $Mm_s^2(n-1/n)/2n(n+1/n)^2$, becomes $Mm_s^2/2$ giving an output of $Mm_s^2 n/2$. The slope vanishes for $n = \pm 1$, where the outputs become the extremes $\pm Mm_s^2/4$. For large n the output is about $\pm Mm_s^2/2n$.
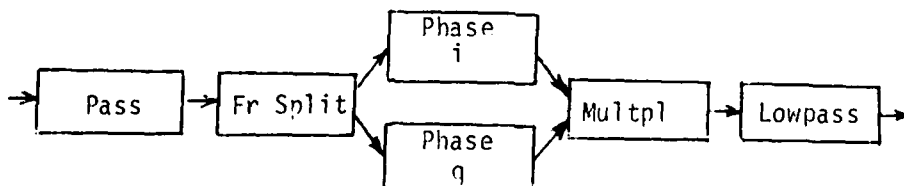
Figure 2bIIBI: NOVEL DISCRIMINATOR
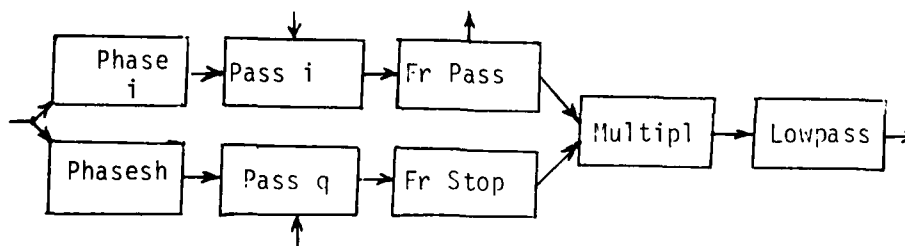
Figure 2bIIB2:   NOVEL DISCRIMINATOR

For comparison of both types of discriminators it is assumed that their noise outputs are equal as well as the dynamic range of their nonlinear elements, the rectifiers and multipler. Setting the maximum input voltage to unity for both should make the output of the nonlinear element equal at the extremes. Since this was set to unity for the conventional discriminator, the multipler contant becomes $M = 4$. In addition, the slope of both discriminators shall be equal at the origin. Since the slope for the conventional discriminator was given in units of source over resonant frequency, the slope for the Novel Discriminator with respect to the normalized frequency has to be multiplied with the derivative of the normalized frequency to source over resonant frequency: $(Mm_S^2/2)(d\ n/d\ a_S/a) = (4.1^2/2)[d\ Q.(a_S/a-a/a_S)]$ $/(d\ a_S/a) = 2Q[1+(a/a_S)^2] = 4Q$, since at the origins source and resonant frequency coincide. Setting both slopes equal gives $4.2354 = 4Q$ or $Q = 1.0594$ (figure 2bII). For this case, the outputs for large normalized frequencies are about 16 times larger for the Novel Discriminator.

An equivalent circuit to figure 2bIIB1 is shown in figure 2bIIB2. The phaseshifters have been shifted to the input, requiring

the Pass function to be performed by Pass i and Pass q and the Frequency Splitter function by Frequency Pass and Frequency Stop.

If the source signal consist of two sinusodial signals with magnitudes m_1 and m_2 and with frequencies a_1 and a_2, the series of Frequency Splitter and Phaseshifter i and q gives outputs (figure 2bIIB1) of: $(m_1/\sqrt{1+n_1{}^2})\cos(|a_1|t+p_1-\tan^{-1}n_1)+(m_2/\sqrt{1+n_2{}^2}).\cos(|a_2|t+p_2$ $-\tan^{-1}n_2)$ and $(m_1/\sqrt{1+1/n_1{}^2})\cos(|a_1|\ t+p_1-\tan^{-1}n_2)+(m_2/\sqrt{1+1/n_2}$ $\cos(|a_2|t+p_2-\tan^{-1}n_2)$. Both are fed into the Multipler, that forms 4 products equivalent to 8 frequency components. The Lowpass rejects all alternating parts, leaving $M[m_1{}^2/(n_1+1/n_1)+m_2{}^2/(n_2+1/n_2)]$. For the case of equal magnitudes $m_1 = m_2 = m$ and about equal frequencies, the output can be approximated by $Mm^2(n_1+1/n_2)/2$.

2bIIB2. <u>R-C CIRCUIT CASE</u>: The inductances are left out of the tuned circuit $(L\rightarrow\infty)$. The Pass or Pass i and q are now low-passes. If the signal is applied as shown in figures 2bIIB2, only positive output values corresponding to positive n in figure 2bII are achievable, since one input frequency is all times assumed to be positive. But if two out-of-phase source frequencies are available as from a quadrature homodyne receiver and they are applied to the inputs of the Pass i and q of figure 2bIIB2, the full output range can be covered (including negative values). The lowpass output is now $(|a_S|/a_S)Mm_S{}^2(RCa_S+1/RCa_S)$.

2bIIC. <u>USE OF DISCRIMINATOR</u>: Despite its lower dynamic range, the conventional discriminator with its many variable parameters has potential for a larger linear range near the origin than the Novel Discriminator. But using a discriminator directly as in frequency modulation broadcast receivers is not desirable, since the radar echo from walking man changes in amplitude and is mixed with noise and sometimes other doppler signals from different speed targets and windblown clutter. Clipping before discriminating will erase amp-

189

litude modulation, but is a far cry from matched filtering, since it gives equal emphasis to small and large returns, thereby increasing the nonsignal contributions.

2c. **FREQUENCY LOCKED LOOP:** The disadvantages of clipping can not only be avoided by using a frequency locked loop but an additional increase in signal-to-noise-ratio is possible by having an increased gain of the discriminator circuit near its axis of asymetry, where the correction signal for the control voltage most of the time will appear. Outside this narrow band the gain should be lower but stay above a certain minimum level for timely aquisition of a newly appearing target echoe at any frequency of the selected doppler band.

The output of the conventional discriminator increases proportional to the input magnitude, while the novel discriminator follows a square law response. If the Lowpass has a long storage time, the outputs for changing inputs are averaged. But a square law response gives heavier emphasis to times with higher input signals and therefore higher signal-to-noise ratio. For these reasons, only the Novel Discriminator will be considered further on. Signal bands being centered and onesided to an offset frequency a_0 are being treated.

2cI. **SIGNAL BAND CENTERED AT OFFSET FREQUENCY:** The direct doppler return is used or its conversion to an intermediate frequency by either an intermediate receiver or by a pulse quadrature receiver. Frequency locked loops using discriminator with resonant and R-C circuits are treated.

2cIA. **USING DISCRIMINATORS WITH RESONANT CIRCUITS:** After filtering in Pass 1, the signal supplied by the radar receiver $m_d \cos(a_0 + a_d)t$ is multiplied with an oscillator signal, at frequency a_c having a unit amplitude, $\cos a_c t$, in Multipler 1 (figure 2c), providing a signal $m_d[\cos(a_0 + a_d - a_c)t + \cos(a_0 + a_d + a_c)t]$ to the discriminator, whose Pass (figure 2bIIB1) rejects the sum frequency. The difference frequency becomes the source frequency $a_s = a_0 + a_d - a_c$ with

190

a magnitude of $m_S = m_d$. For zero doppler shift, both source and resonant angular frequency should be equal $a_S = a_1$ while the normalized angular frequency and the output signal vanish: $n = Mm_d^2/2(n+1/n) = 0$, making the oscillator frequency to a_0-a. Approximating the oscillator behavior by a linear characteristic with a slope F gives therefore $a_c = a_0$-a+$FMm_d^2/2(n+1/n)$. This equation does not yield a simple solution. But after frequency lock is achieved, only the discriminator characteristic part near the origin is used, where the slope is MQm_d^2, so that $a_c = a_0$-a+$FMQm_d^2(a_S$-a$)/a$. This gives the discriminator output as $a_d/(F+a/MQ \cdot m_d^2)$, which approaches for large signal magnitudes a_d/F.
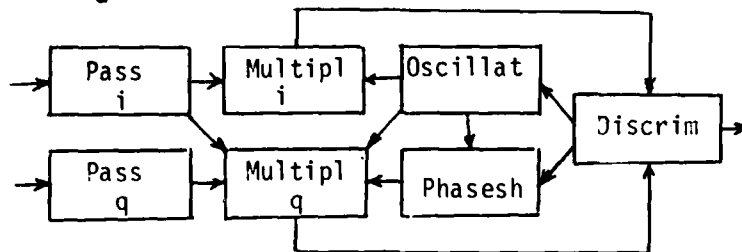
Figure 2c: Frequency Locked Loop

2cIB. USING R-C CIRCUITS: The signal $m_d\cos(a_0+a_d)t$ is let through Pass i for Multipliers i and q, whose other inputs are cos $a_c t$ from the Oscillator and sin $a_c t$ from the Phaseshifter, whose input is also supplied from the Oscillator (figure 2c). The Multiplier i and q outputs $m_d \cdot [-\cos(a_0+a_d-a_c)t + \cos(a_0+a_d+a_c)t]$ and m_d $[-\sin(a_0+a_d-a_c)t+\sin(a_0+a_d+a_c)t]$ are fed to discriminator Pass i and q (figure 2bIIB2), which reject the sum frequencies signals. The difference frequency acts as source frequency $a_S = a_0+a_d-a_c$ as before. But since the slope at the origin is now $Mm_S^2RC/2$ and the resonant frequency vanishes a=0, the oscillator angular frequency is approximated as $a_c = a_0+FMm_d^2RCa_S/2$, giving the output of the Discriminator as $a_d/(F+2/RCMm_d^2)$, which again approaches a_d/F for large magnitudes.

2cII. ONESIDED SIGNAL BANDS : To preserve information of

radial direction, two quadrature inputs at the same frequency band
are needed. Only the discriminator using R-C circuits is suited.
Signal with and without offset frequencies are treated.

2cIIA. <u>NON-BASEBAND SIGNALS</u>: From a quadrature pulse re-
ceiver both lower or both upper sidebands of a integral multiple
greater than zero of the pulse repetition frequency are suitable. The
signals $m_d\cos(a_0+a_d)t$ and $m_d\sin(a_0+a_d)t$ are fed through Pass i and q
(figure 2c) to Multiplers i and q, whose other inputs $\cos a_c t$ are sup-
plied by the Oscillator. The Multiplier i and q outputs
$m_d[\cos(a_0+a_d-a_c)t + \cos(a_0+a_d+a_c)t]$ and
$m_d[-\sin(a_0+a_d-a_c)t+\sin(a_0+a_d+a_c)t]$ are fed to discriminator Pass i and
q (figure 2bIIB2) which rejects the signals with sum frequencies. The
leftover signal at the source frequency of the discriminator $(a_0+a_d-a_c$
$= a_s)$ is centered around an frequency $a_0+a_M-a_c$ (where the middle fre-
quency of the doppler band is symbolized as a_M), which should be zero
for optimum discriminator performance. This makes the oscillator fre-
quency equal to a_0+a_m for zero input and in general $a_c = a_0+a_M+FMRCm_d^2$
$a_S/2$. This yields a discriminator output of $(a_d-a_M)/(F+2/MRCm_d^2)$,
which approaches $(a_d-a_M)/F$ for large magnitudes.

2cIIB. <u>BASEBAND SIGNALS</u>: This includes doppler signals
from quadrature homodyne receivers and the baseband signals of quad-
rature pulse receivers. The signals $m_d\cos a_d t$ and $m_d\sin a_d t$ are fed
through Pass i and q (figure 2c) to Multiplers i and q, whose other
inputs are $\cos a_c t$ from the oscillator and $\pm\cos a_c t$ from the phase-
shifter. The Multiplier i and q outputs $m_d[\cos(a_d-a_c)t+\cos(a_d+a_c)t]$
and $m_d[-\sin)(a_d\pm sa_c)t + \sin(a_d\pm a_c)t]$ are fed to discriminator Pass i
and q (figure 2bIIB2), which attenuates the sum frequency signals
only if their frequency exceed the cut off frequency of the Passes i
and q. In this case, the further processing is the same as in 2cIIA,
but with an offset frequency $a_0 = 0$.

But if the sum frequency does not exceed the cut off frequency of the Passes i and q, the difference as well as the sum frequencies are sent to the Frequency Pass and Stop. After track is acquired, doppler and oscillator frequencies are about the same and the output of the lowpass can then be approximated by $Mm_d^2(n_1+1/n_2)/2$ with $n_1 = RC(a_d+a_c)$ and $n_2 = RC(a_d+a_c)$. Without input, the oscillator frequency is equal to the middle frequency, therefore $a_c=a_M+FMm_d^2(n_1+ 1/n_2)/2$. By approximating the sum frequency by two times the doppler $a_d+a_c=2a_d$, the discriminator output is $(a_d-a_M+1/2a_d)/(F+2/MRCm_d^2)$. For large magnitudes, the discriminator output is $(a_d-a_M+1/2a_d)/F$. Whenever the output of the discriminator has a negative value sufficient to drive the oscillator below the lowest expected absolute doppler frequency, it forces the Phaseshifter to change the polarity of its output, thus both incoming and outgoing targets can be tracked.

2d. DETECTOR AND DISPLAY: The signal at the Frequency Splitter i or Frequency Pass output is rectified and monitored by a threshold. If a preset level is exceeded an analog-to-digital converter digitizes the echo magnitude for display (figure 2d). Also, the discriminator lowpass signal is fed in a Fast Fourier Transformer, and detected. Outputs exceeding a minimum level are converted and displayed, including the d.c. output giving the average doppler frequency. Since the modulation frequency even for running man is only a few Hertz, the Fast Fourier Transformer and A/D Converter can be time shared by many channels.

Rectifier → Threshold → A/D Conv ← Detector ← FFT
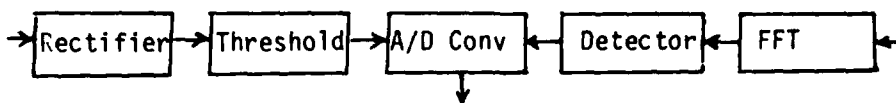
Figure 2d: Detector for Frequency Locked Loop

EXPERIMENTS

A frequency locked loop using the Novel Discriminator with R-C circuit was built. An endless loop with the recording of a radially walking man using the base channel of a simple pulse radar supplied the input voltage to both phaseshifters i and q (figure 2bIIB2). The discriminator output was monitored with a digital voltmeter and a recording real time spectrum analyzer. The signal fora walking man presented clearly the doppler speed and the step frequency. It was also observed, that the power of the doppler signal has a small spectral component at the step frequency.

CONCLUSION AND RECOMMENDATIONS

While the limited experiments proved the feasibility of automatic classification of a walking man, a wide range of experiments should be conducted to determine the influence of speed and angle towards the radar of different single and multiple targets, noise, moving clutter, antenna modulation and observation time. Also the replacement of multipliers by modulators should be investigated to minimize power consumption.

The Novel Discriminator should have a wide range of applications in systems benefiting from frequency locked loops.

REFERENCES

1. Doppler Discrimination as a Solution to the "Radar Angle Problem", W. Vander Meer, 1970 Tri-Service Symposium, Colorado Springs, CO

2. "Vehicle Discriminator", O.E. Rittenbach, 1973, Tri-Service Symposium, Colorado Springs, CO

3. "Lightweight Combat Surveillance Correlation Radar", O.E. Rittenbach, 1965, Radar Symposium, Ft Monmouth, NJ

PULSE CODE MODULATION OF CO_2 TEA LASER PULSE

*ROBERT S. ROHDE, DR. AND RUDOLF G. BUSER, DR.
US ARMY NIGHT VISION AND ELECTRO-OPTICS LABORATORY
LASER DIVISION, FT. BELVOIR, VA 22060

NEAL T. NOMIYAMA, MR.
SCIENCE APPLICATIONS, INC., McLEAN, VA 22102

Introduction

The CO_2 TEA laser pulse is characterized by a gain-switched spike followed by a slow decaying tail. As a ranging waveform, the tail with its slow fall time does not contribute to the device's accuracy in ranging measurements. Elimination of this tail, with resulting increased energy in the spike, by optimization of the gas ratios, has been sought after.[1] On the other hand, utilization of the entire pulse to include the tail, leads to the concept of multifunctional applications such as range finding and Cooperative Battlefield Identification Friend or Foe (CBIFF). Application to CBIFF requirements would utilize the modulated tail by transferring coded telegrams to the target being interrogated.

The tail portion of the CO_2 TEA laser waveform is approximately 2 to $4\,\mu$ sec long. Depending on the achievable bandwidths for the modulator and receiver system, 10 to 100 bits of information can possibly be transmitted on a single CO_2 TEA laser pulse. A number of applications besides CBIFF can be explored including communication between two vehicles, data transmission, and precision ranging to name a few. In this report, the CO_2 TEA laser pulse tail is electro-optically (EO) modulated with a polarization sensitive switch capable of 5 MHz repetition rate and 100 nanosecond pulsewidths. With this capability, three operational modes can be realized; namely, 1) pulse shaping/sharpening of the gain-switched spike for precision ranging, 2) information transfer via modulation of tail, or 3) combining (1) and (2) on the same laser pulse. Mode #2 has been demonstrated and will be presented in this report.

195

Experiment

Linearly polarized light in the plane of incidence passes through an uncoated ZnSe beam splitter placed at Brewster's angle (Fig. 1). Zero reflection for the plane polarized beam is observed while maximum reflection for the perpendicular polarized beam takes place. The polarizing angle ℓ_p is defined by Brewster's Law[2]

$$\tan \ell_p = n \tag{1}$$

where n is the index of refraction for the beam splitter material (n = 2.40 for ZnSe).

The Pockels Cell (II-VI, Inc.) is an electrically-induced birefringent material whose index of refraction changes proportionally to the applied electric field. In a transverse-applied electric field configuration, the electro-optic retardation causes the polarized light to rotate its polarization about the optical axis such that one orthogonal component (say, Z' component) grows as it propagates along the propagation axis at the expense of the other orthogonal component (say, Y'). For CdTe, the electric field is applied along the cube diagonal <111> direction perpendicular to the propagation axis. The phase retardation experienced by the polarized light passing through the crystal with an applied voltage V is given below:

$$\Gamma = \frac{(\sqrt{3}\pi) \; n_o^3 r_{41}}{\lambda_o} \; \frac{V \; \ell}{d} \tag{2}$$

where n_o = index of refraction
r_{41} = electro-optic coefficient
λ_o = vacuum wavelength of laser beam
ℓ = crystal length
d = crystal width across which electric field is applied.

Using the following parameter values provided by Yariv,[3] $n_o^3 r_{41}$ =120 x 10^{-12} m/V, and λ_o = 10.6 x 10^{-6} m, and crystal dimensions d = 3 mm, ℓ = 6 cm, the calculated half-wave voltage (Γ = $180°$) is 2554 volts. The approximate half-wave voltage measured by the manufacturer is 2650 volts. The quarter-wave voltage for CdTe is, therefore, 1325 volts (based on manufacturer's estimate).
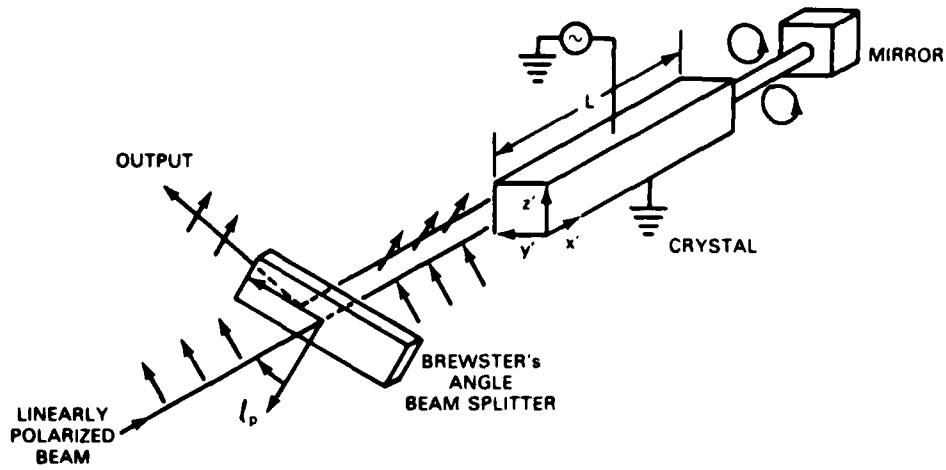
A. THREE DIMENSIONAL SCHEMATIC
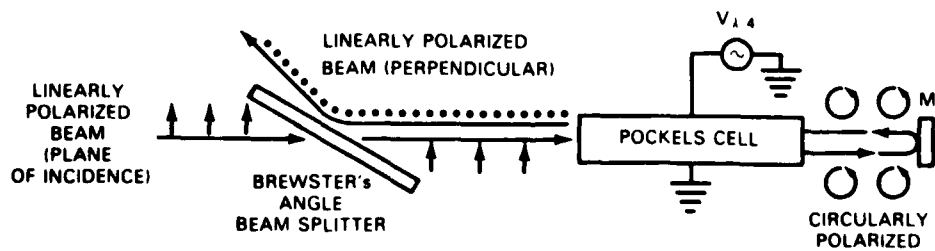
B. TWO DIMENSIONAL SCHEMATIC

Figure 1.   Double Pass Pockels Cell
            Modulator

197

A diagram of the experiment is shown in Fig. 2. In a double-pass configuration, the plane-polarized beam passes through the energized Pockels Cell and is converted into two orthogonal components of equal amplitude and 90° relative phase difference. The electric field vector is now circularly polarized. When the circularly polarized light is reflected back through the energized Pockels Cell, it undergoes another 90° phase shift and is transformed back to linearly polarized light, but now perpendicular to the plane of incidence. This polarized beam is reflected off the beam splitter (placed at its polarizing angle) and propagated to the receiver.

Results

The linearly polarized CO_2 TEA laser produces an average of 22 mJ per pulse with an optimum gas mixture. Increasing the laser energy by an order of magnitude will not damage these EO modulator units as they have been reported to operate reliably with 300 mJ CO_2 TEA laser pulses. For pulse code modulation (PCM), a long tapered tail is desirable, and hence a nitrogen-rich mixture is used (CO_2:N_2:He = 6:18:76). The resulting waveform is shown in Fig. 3. A telescope is used to reduce the beam to fit through the crystal. A Ge crystal polarizer is used to further increase the linear polarization of the partially polarized laser beam. Detector #1 is the timing detector (HgCdTe) which triggers the modulator electronics. A pulse generator produces a 2 microsecond gate during which a 5 MHz square waveform is generated. This signal drives the high voltage power supply which drives the crystal cell producing an optical signal 100 nanoseconds wide at 5 MHz repetition rate (see Fig. 4 for power supply voltage). The high voltage power supply was manufactured by Cober Electronics and was designed specifically for this application using vacuum tube technology. The modulation optical signal is detected by a reverse-biased HgCdTe PV detector with a frequency response greater than 10 MHz. The received signal is shown in Fig. 5 with two resolutions. Within a 2 microsecond gate, ten 100 nanosecond pulses are created. The finite rise time of approximately 30 nanoseconds is limited by the frequency response of the power supply. A possible alternative to the vacuum tube design that would improve the rise time and hence increase the repetition rate of the modulator might be using an avalanche transistor design for the power supply. The rise time of the CdTe crystal is less than a nanosecond (500 MHz frequency capability) and should not limit the overall frequency response.

Pulse code modulation can be achieved by transmitting a sequence of pulses at 5 MHz; if a pulse is present, a one is indicated, and if a pulse is absent, a zero is indicated. To demonstrate PCM, the repetition rate was changed to 2.5 MHz, or every other pulse was deleted from the pulse train logic. An oscilloscope trace of this particular telegram is shown in
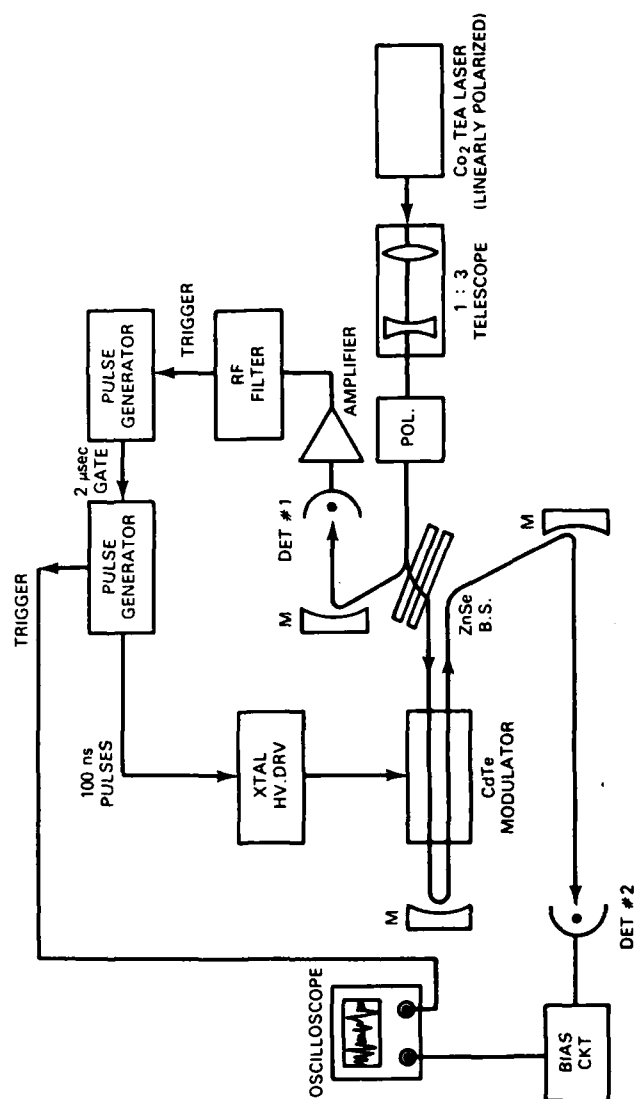
Figure 2. Experiment for PCM of
CO$_2$ TEA Laser

199
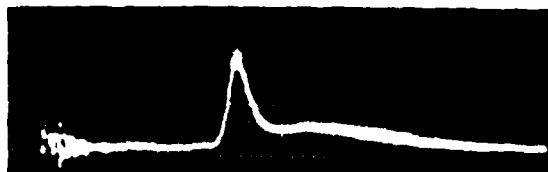
Figure 3. Unmodulated CO_2 TEA Laser
Pulse with N_2 Rich Gas
Mixture (500 ns/DIV)

Figure 4. Output Signal of High
Voltage Power Supply for
CdTe Crystal Modulator
(500 V/DIV, 500 ns/DIV)
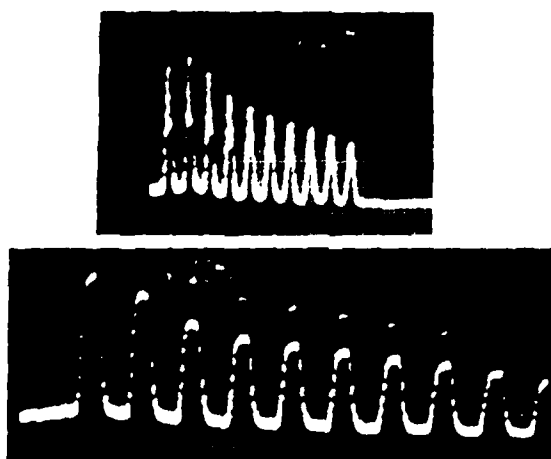
Figure 5. Receiver Signal from Pulse
Code Modulation of CO_2 TEA Laser
Pulse (Top trace: 500 ns/DIV,
10 mV/DIV; Lower trace: 200 ns/DIV,
10 mV/DIV) Logic: 1111111111

Fig. 6. Note that the initial pulse is the unmodulated gain-switched spike that has leaked through the polarizers.

In fact, the extinction level of the modulator will depend on this polarization leak-through. Measurement of the zero level of modulation was obtained indirectly by comparing the unmodulated signal due to polarization leak-through and the modulated signal at its zero level. By examining Figs. 7 A and B, which are sequential shots of the unmodulated and modulated signal, the extinction appears to be 100%. When averaged over several oscilloscope traces, the zero level coincided with the unmodulated signal level indicating 100% extinction. The issue of signal extinction is important to CBIFF if confidence in the transmitted signal is to be maintained. In a dynamic atmospheric environment such as fog, rain, dust, and smoke, the detection threshold is required to be set at the minimum allowable level so as to obtain the largest dynamic detection range possible. By insuring a 100% extinction of the signal, the threshold can be set as low as possible.

Beam quality was determined by measuring the horizontal intensity profile of the output beam with and without the crystal modulator in the optical train. Ten independent pulses were averaged for each position across the beam in increments of 0.9 milliradians. The average signal normalized to the peak average signal is plotted in Fig. 8 with and without the effects of the crystal. The results indicate substantial beam degradation initially from the beam splitters due to multiple reflections, and some further degradation by the CdTe crystal. Beam degradation by multiple reflections can be minimized by using a single, wedged beam splitter instead of parallel surface beam splitters such that the internal reflections produce highly diverging wavefronts. The calculated beam divergence for a Gaussian beam is given by the following equation:

$$\theta = \frac{4}{\pi} \frac{\lambda}{D} \tag{3}$$

Using the aperture of the Pockels Cell unit as the limiting case, D = 3 mm, the beam divergence ($\theta/2$) is 2.75 mrad, much less than what was observed in Fig. 8. The additional beam spread can be attributed to multiple reflection. Beam quality after the telescope was not measured although burn patterns indicate a symmetric beam unlike that measured after the beam splitters.

Conclusion

In conclusion, we have demonstrated pulse code modulation of the tail of the CO_2 TEA laser pulse at a 5 MHz repetition rate with a 100% depth of modulation using an external double-pass Pockels Cell modulator. Each
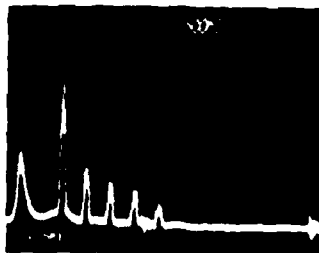
Figure 6. Pulse Code Modulation
            Logic: 1010101010
            (500 ns/DIV)
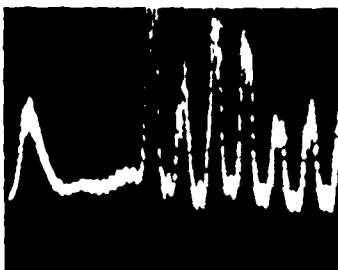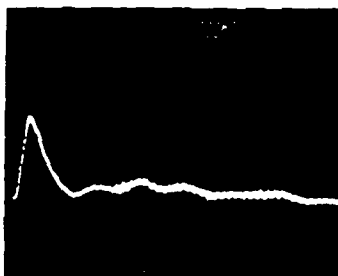
Figure 7. Extinction Level Measure-
           ment. Two Sequential Oscilliscope
           Traces (Top trace: unmodulated,
           200 ns/DIV; Lower trace: modulated,
           200 ns/DIV)

202
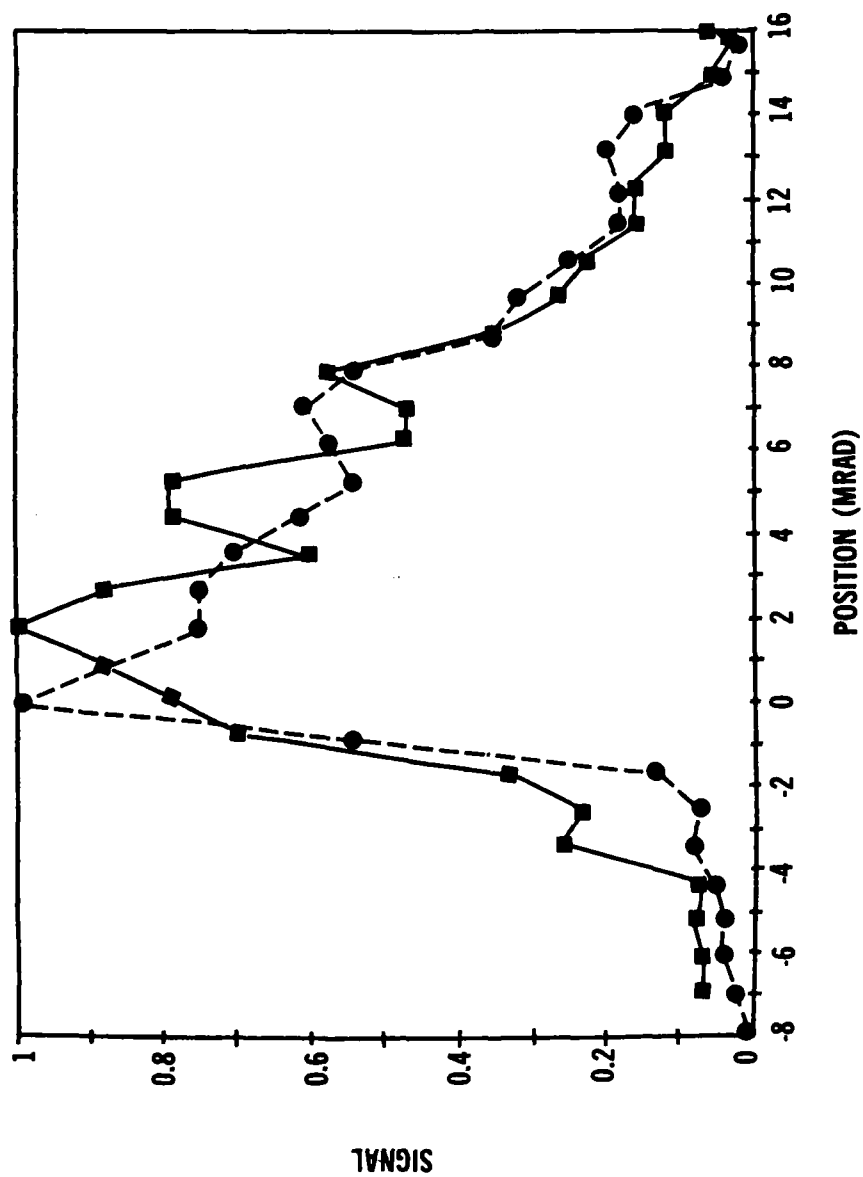
Figure 8. Horizontal Beam Profile of
Pulse Code Modulator. Squares
represent output with the Pockels
Cell, and dots are without the cell.

pulse is approximately 100 nanoseconds wide with a rise and fall time of approximately 30 nanoseconds. With a 100% depth of modulation, a high false alarm rate under dynamic battlefield induced transmission conditions is prevented.

This device can extend the capabilities of a CO_2 TEA laser rangefinder to CBIFF applications by using the tail for sending encoded telegrams to the target and shaping the gain-switched spike to improve ranging accuracy. Therefore, a multifunctional device has been conceptually demonstrated to provide both precision range finding and information transfer from the transmitter to the receiver. The multifunctional device concept can be applied to all EO devices to provide a cost effective method to improve and extend performance capabilities.

References

1. R. I. Rudko, J. W. Barnie, E. Barsack, "10.6 Micron Target Designator", IEEE   J. Quan. Electr., Vol QR-13, No. 9, p 390.

2. Longhurst, R. S., "Geometrical and Physical Optics", Longman, (1973).

3. Yariv, A., "Introduction to Optical Electronics", 2nd Edition, Holt, Rinehart   & Winston, (1976).

SEMI-INSULATING GALLIUM ARSENIDE FOR MILLIMETER
WAVE AND HIGH SPEED IC DEVICE APPLICATIONS

*RAYMOND L. ROSS, MR.,   THOMAS R. AUCOIN, MR.,
ROBERT O. SAVAGE, MR.,   JOHN J. WINTER, MR.,
and ROGER J. MALIK, MR.
U.S. ARMY ELECTRONICS TECHNOLOGY AND DEVICES LABORATORY (ERADCOM)
FORT MONMOUTH, NEW JERSEY   07703

INTRODUCTION

A wide variety of semiconductor devices utilizing gallium arsenide (GaAs) is currently under development by the military for use in advanced communication, surveillance, and target acquisition systems. GaAs, a compound semiconductor exhibiting a large energy bandgap, is characterized by a high intrinsic electron mobility (8600 $cm^2V^{-1}sec^{-1}$ @ $300^{\circ}K$) and resistivity (> 10^8 ohm-cm). The low-field electron mobility of GaAs is one of its greatest attributes and offers high frequency operation in devices such as the field effect transistor (FET). Coupled with the material's high peak velocity and low threshold field, GaAs integrated circuit (IC) devices offer a two to six time speed improvement over their silicon counterparts. When compared with standard silicon IC technology, the process steps for GaAs ICs are relatively simple and few in number. As a result of these advantages, the technology of manufacturing high performance GaAs devices is maturing at a rapid rate. Thus, it is not surprising to find these devices experiencing a greatly expanding role in oscillator, mixer, logic element, power amplification, and low noise/high gain application. However, the full potential and low-cost manufacture of GaAs devices has yet to be realized, partly due to material problems experienced by substrate suppliers and device manufacturers.

It is commonly held by major GaAs device manufacturers that the quality of semi-insulating substrates is one of the barriers to obtaining reliable, reproducible, high-performance devices. In addition, because the quality of commercially available semi-insulating GaAs substrates is highly variable, extensive material

qualification tests are required before substrates are accepted for device fabrication. It has been shown that chromium (Cr), which is used to compensate native impurities and produce high resistivity in GaAs, redistributes during thermal processing (1-3), whether during a subsequent epitaxial process or a high temperature ion-implantation anneal procedure. Typically, the Cr depletes from a region one or two microns deep and migrates to the surface where it occupies a region about $400°$ Å thick. The most serious consequence of this distribution is that the depletion of Cr can uncompensate some of the native donor impurities existing in the n-depleted region, resulting in excess uncontrolled n-type activation and significant changes in device characteristics and reliability. In addition to this "surface conversion" problem, fast diffusing deep-level acceptors, carbon-arsenic vacancy complexes and diffusing deep-level impurities are still observed as a result of process-induced substituents.

In order to minimize the effect of substrate imperfections on devices fabricated by epitaxy, one usually grows a high quality buffer layer to isolate the device from the substrate. However, the epitaxial approach has two major drawbacks; cost and difficulty in achieving the required thickness and uniformity. Although ion-implantation reduces the cost of active layer fabrication, the important properties of the implanted layers, such as mobility and doping profile, can be significantly affected by substrate characteristics. In addition, inter-device leakage becomes a problem if Cr redistribution causes a thin conducting layer to form on the GaAs surface during the high temperature implant annel procedure.

The alternative solution to these problems is to improve the quality of substrate material through the reduction of impurity and defect levels and/or the elimination of charge compersators such as Cr. Such is the objective of our research program.

CRYSTAL GROWTH

The technology involved in the growth of GaAs is considerably more complicated than that employed for silicon, for one is dealing with more complicated binary phase equilibria and a highly volatile compenent, arsenic. Precise control of the As vapor pressure in the chosen growth system is required in order to maintain exact stoichiometry of the GaAs compound during the growth process so as to achieve high mobility and crystal perfection.

The bulk compound is normally formed by the reaction of As vapor with Ga metal at elevated temperatures in sealed quartz ampoules as shown in Fig. 1. Typically, an As reservoir contained at one end of
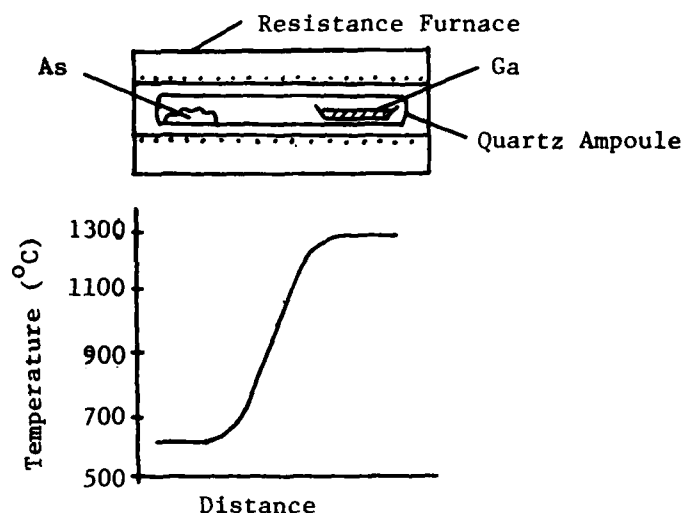
Fig. 1. Typical furnace and temperature profile for
compounding GaAs in quartz.

the ampoule is heated to 600°C. This generates approximately 1 atm
of As vapor pressure in the system, a prerequisite for obtaining
stoichiometric GaAs (4). The As vapor reacts with the Ga metal
maintained at approximately 1260°C and located at the other end of
the ampoule in a quartz boat. After the Ga has been completely
reacted, single crystal growth may be initiated by programmed
cooling (gradient freeze) or by physically moving either the ampoule
or furnace to provide proper temperature gradients for growth. This
process is commonly referred to as the "horizontal Bridgeman"
technique and is the method used by all major commercial GaAs material
suppliers to date. Crystals prepared by this technique have a "half
moon" cross-section and, therefore, result in considerable waste in
IC processing where the required shape is a circular disk.

Another approach to the commercial production of bulk GaAs which
is gaining favor is the liquid encapsulated Czochralski technique
(LEC CZ). Metz et al (5) first described the use of an encapsulant
to suppress the loss of a volatile component from a melt. Mullin et
al (6) used this method for the growth of InAs and GaAs from stoich-
iometric melts. In this method, shown in Fig. 2, the vaporization
of As from molten GaAs is inhibited by placing a layer of a non-
reactive encapsulant (e.g., B_2O_3) on the melt surface. An inert gas
pressure which is higher than the As vapor pressure is then main-
tained over the molten B_2O_3 layer. A rotating seed crystal con-
tacting the molten GaAs is then slowly withdrawn through the liquid

207
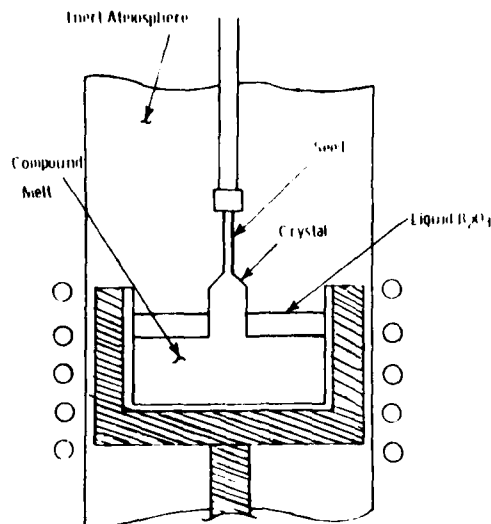
Fig. 2. Liquid encapsulated Czochralski pulling technique.

encapsulant while the temperature is regulated to obtain the desired
diameter crystal. The advantage of the LRC CZ technique is the
ability to prepare large diameter crystals in a relatively short
period to time. However, the GaAs polycrystalline source material
used in this technique and from which the crystal is pulled, is
normally compounded in quartz ampoules. The use of quartz as a
container for Ga, As, and molten GaAs, or as a reaction vessel can
lead to appreciable silicon contamination (7). Since silicon can act
as a shallow donor or acceptor in GaAs (8), chromium, a deep-level
acceptor and/or oxygen, a deep-level donor, must be deliber tely
added in order to compensate the GaAs, thereby making it semi-
insulating (> 10^8 ohm-cm).

A second drawback to the convential LEC CZ technique is its
separate two step process - compounding and subsequent crystal
growth. Because of this increased handling, more impurities can be
introduced than those obtained in the horizontal Bridgeman process.
The in-situ LEC compounding/Czochralski growth process we describe
for growing semi-insulating GaAs incorporates, for the first time,
both steps and eliminates all dependance on quartz components,
thereby, reducing or eliminating the requirement for chromium com-
pensation. This is accomplished by reacting elemental gallium and
arsenic under a molten encapsulant in pyrolytic boron nitride (PBN)
crucibles at nitrogen pressures to 100 atm. A specially designed

208

high pressure Czochralski crystal pulling system, Varian model
HPCZ, was used for maintaining the nitrogen gas ambient and for growth
of the bulk GaAs (see Fig. 3). This system contains provision for
the following: rotation of the crystal and/or crucible; raising and
lowering of the crystal and/or crucible; remote control of tempera-
ture, gas flow, pulling and rotation rates; TV process monitoring;
cryo fore-pumping; vac-ion pumping to 10^{-5} torr; hydraulic lifting
of the chamber; and is designed for operation at pressures to 135 atm
with neutral, oxidizing or reducing ambients.

The in-situ LEC compounding and Czochralski growth of GaAs was
carried out in the following manner. The PBN crucibles were etched
in HCl, rinsed with de-ionized water following by methonal and then
vacuum dried overnight at $200^{\circ}C$. The crucibles were then loaded with
stoichiometric quantities of high-purity gallium and arsenic. A
dehydrated pellet of boron oxide encapsulant was placed on top of the
charge and the entire assembly centered within a tantalum or graphite
susceptor in the Czochralski pulling chamber as shown in Fig. 4.

It was found that if the boron oxide encapsulant contained an
excessive amount of moisture, bubbles continuously formed at the melt/
encapsulant interface. These bubbles subsequently rose to the surface
releasing arsenic which, in turn, led to nonstoichiometric melts and
resultant twinning of the crystals. An oil-free, high-vacuum baking
system was constructed to further dehydrate the pellets. Heating the
boron oxide to approximately $1000^{\circ}C$ at 10^{-7} torr in induction heated
platinum/gold crucibles was found to give satisfactory results.

After the growth station was established (susceptor, crucible,
gallium, arsenic, boron oxide, etc.) and the chamber closed, the
system was evacuated to 10^{-5} torr. The charge was then slowly heated
to $325^{\circ}C$ to remove residual moisture and volatile gallium/arsenic
oxides. If the temperature exceeded $325^{\circ}C$, significant amounts of
arsenic were lost by volatilization prior to compounding. After
several hours, the system was then backfilled with high-purity
nitrogen gas to 3.0 atm and the temperature increased to $450^{\circ}C$.
During this step, the boron oxide melted and flowed into the voids.
The pressure in the pulling chamber was then increased to 60 atm.
As the temperature was slowly increased, the compounding reaction
could be observed on the TV monitor being accompanied by a rapid
temperature rise as the crucible approached $700^{\circ}C$.

Single crystals of GaAs were grown from the in-situ compounded
material by the LEC CZ technique as previously shown in Fig. 2. All
crystals were grown in the <111>-B direction with nitrogen gas
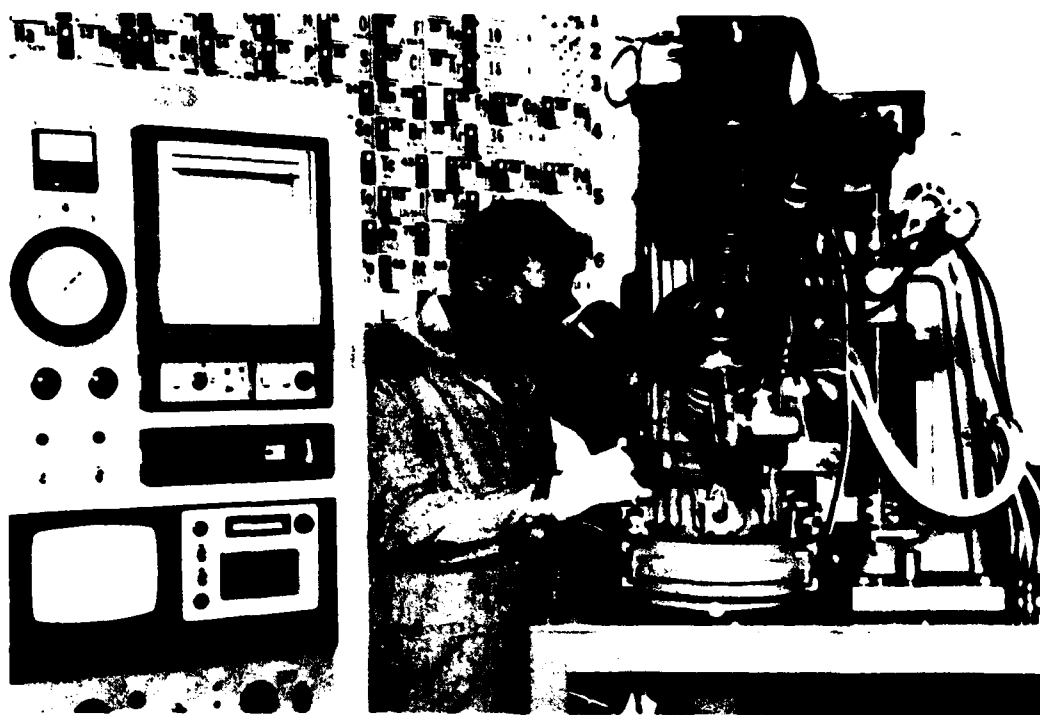
Fig. 3. High pressure Czochralski crystal pulling system.
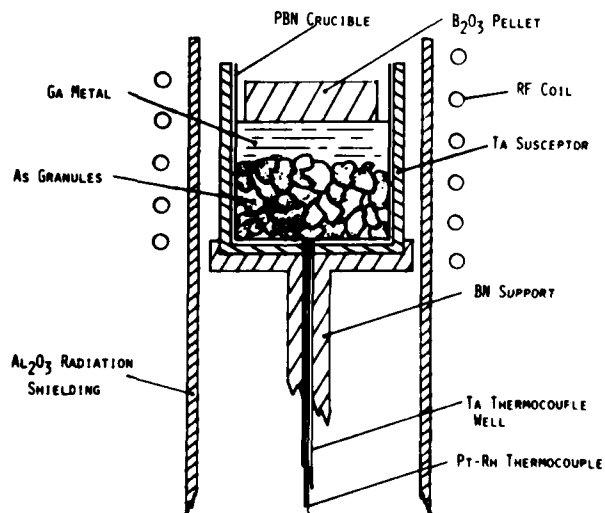
Fig. 4. Arrangement for liquid encapsulated compounding of GaAs.

210

pressures of 1.0 to 20.0 atm. and pulling rates of 1.0 to 2.0 cm/hr. Both concurrent and countercurrent rotation of crucible and crystal were used at rates of 5 and 15 rpm respectively; the concurrent rotation producing a more convex interface.

ELECTRICAL MEASUREMENTS

The measurements of resistivity, Hall mobility and Hall co-efficient were performed using the van der Pauw method (9). This technique has the advantage in that only four contacts are required and only the sample thickness need be known. In this work, the conventional "clover-shaped" sample geometry is replaced by an equivalent "Greek-cross" structure (10) (see Fig. 5). The actual GaAs structures are produced using an ultra-sonic milling machine.

The resistivity, ρ, in ohm-cm is given by

$$\rho = \frac{\pi t}{\ln 2} \left[\frac{R_{AB,CD} + R_{BC,DA}}{2} \right] F$$

where $R_{AB,CD} = V_{AB}/I_{CD}$

and $R_{BC,DA} = V_{BC}/I_{DA}$

Fig. 5. Sample geometry.

are in units of ohms, t is the sample thickness in centimeters and F is the van der Pauw factor which is a dimensionless quantity dependent only upon the ratio of $R_{AB,CD}/R_{BC,DA}$ and is defined by the transcendental equation

$$\cosh \left[\frac{\ln 2}{F} \cdot \frac{R_{AB,CD}/R_{BC,DA} - 1}{R_{AB,CD}/R_{BC,DA} + 1} \right] = \tfrac{1}{2} e^{\ln 2/F} \quad .$$

The Hall mobility, μ_H, in $cm^2 volt^{-1} sec^{-1}$ is given by

$$\mu_H = 10^8 \frac{t}{B\rho} \Delta R_{AC,BD}$$

where B is the applied magnetic field in gauss and $\Delta R_{AC,BD}$ is the change in resistance when the magnetic field is applied perpendicular to the sample. The Hall coefficient, R_H, in cm^3/coulomb is calculated from

$$R_H = \rho \mu_H .$$

The disadvantage of the van der Pauw method is that two resistances ($R_{AB,CD}$ and $R_{BC,DA}$) must be measured requiring that voltage and current leads be switched. In addition, good experimental practice dictates that current leads be reversed and switched in order to

ROSS, AUCOIN, SAVAGE
WINTER and MALIK

eliminate contact resistances and potentials, rectifying effects and
thermal emfs. Thus, in the collection of van der Pauw transport data,
eight configurations are used for resistivity measurement (Fig. 6.
(a)-(h)) and eight for mobility measurement (Fig. 6. (i)-(p)).
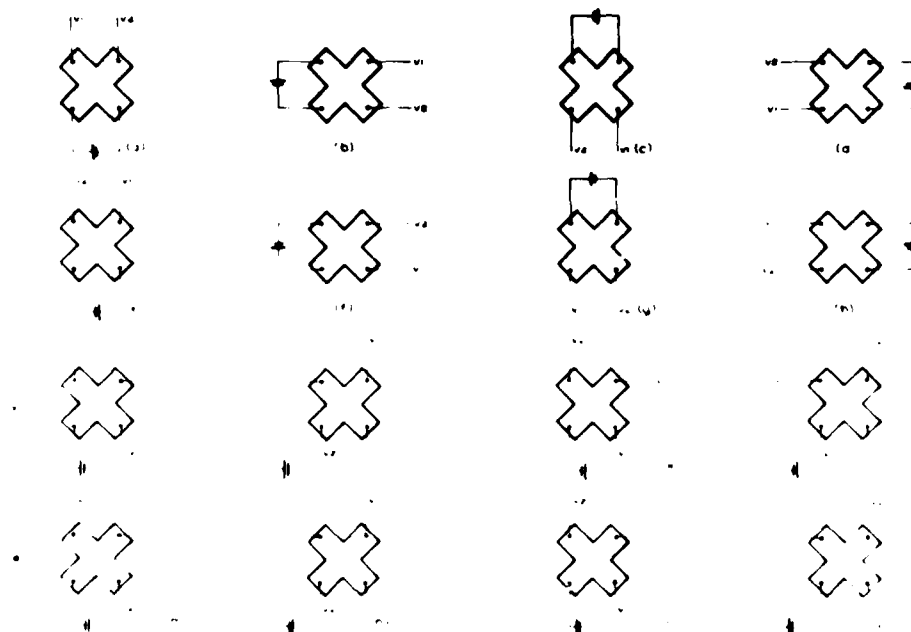
Fig. 6. **SAMPLE CONFIGURATION FOR VAN DER PAUW TRANSPORT DATA**
        (a)-(h) RESISTIVITY
        (i)-(p) MOBILITY

The switching of current and voltage leads and the reversing
thereof is accomplished by the arrangement shown in Fig. 7. The
sample is contained in a fully shielded and evacuated chamber (Fig.
8.) and is connected to four electrometers by triaxial cable, the
inner shield of which is driven by the output of each electrometer.
Shielded coaxial reed relays provide the required lead switching to
generate the various circuit configurations of Fig. 6. The result is
a fully guarded system capable of measuring samples having up to 10^{12}
ohms resistance with a minimum of noise and settleling time.

Beacause of the large number of measurements necessary and the
large number of samples investigated, the guarded van der Pauw system
of Fig. 7. was automated whereby all switching of leads and electro-

212
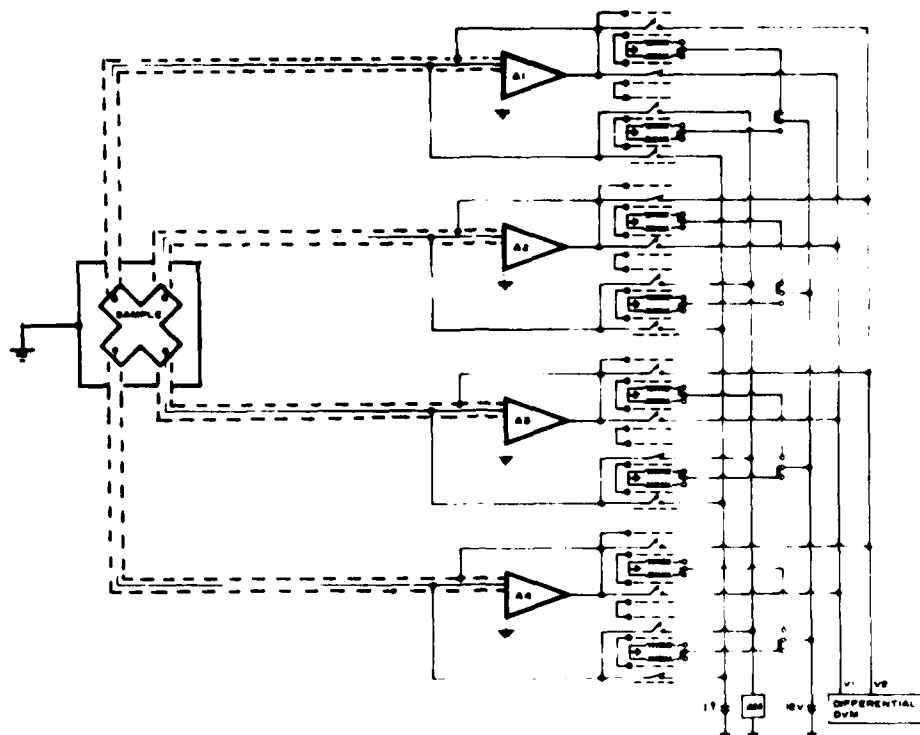
Fig. 7. GUARDED VAN DER PAUW SYSTEM

Fig. 8. Sample chamber.

213
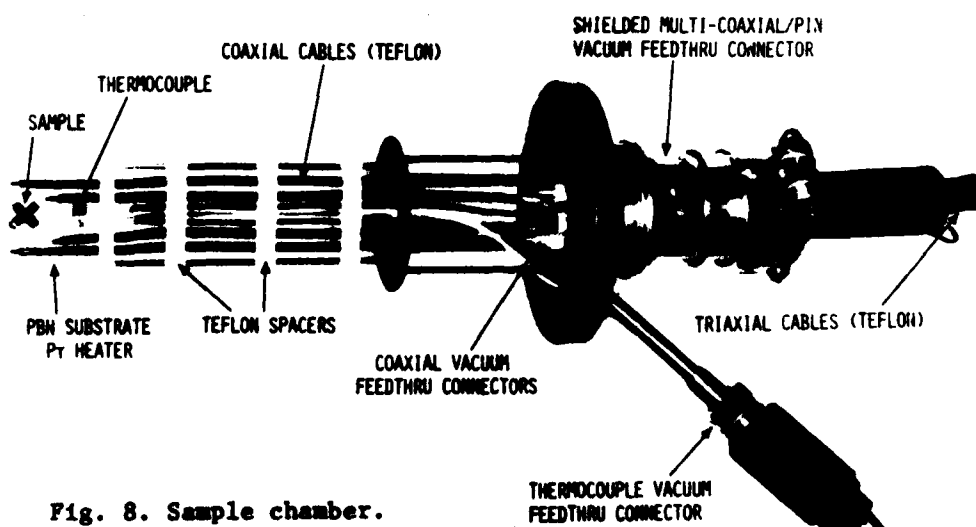
meters, measurement of current and voltage and calculation of param-
eters is accomplished under the control of a programmable calculator
(Fig. 9.). The system is presently under expansion to provide for
automatic magnetic field selection and temperature control.
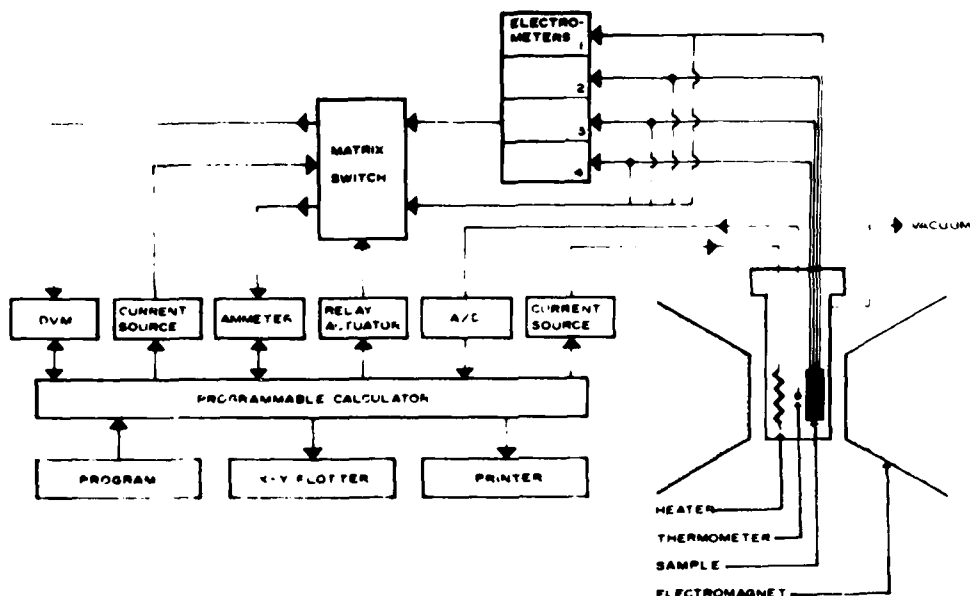
Fig. 9.

AUTOMATED VAN DER PAUW HALL AND RESISTIVITY SYSTEM

MIXED CONDUCTION ANALYSIS

When one carrier type dominates the conduction process, simple
Hall coefficient and resistivity measurements at low magnetic fields
provides values of carrier concentration and mobility. Semi-insula-
ting GaAs, however, exhibits mixed conduction; i.e., conduction by
both holes and electrons. This complication requires additional
information, in particular, the magnetic field dependence of both Hall
coefficient and resistivity, in order to permit resolution of the
independent carrier properties.

The total Hall coefficient is given by

$$R = \frac{R_n \sigma_n^2 + R_p \sigma_p^2 + R_n R_p \sigma_n^2 \sigma_p^2 (R_n + R_p) B^2}{(\sigma_n + \sigma_p)^2 + \sigma_n \sigma_p (R_n + R_p)^2 B^2} \qquad (1)$$

214

ROSS, AUCOIN, SAVAGE
WINTER and MALIK

and the total conductivity by

$$\sigma = \frac{(\sigma_n + \sigma_p)^2 + \sigma_n^2\sigma_p^2 (R_n + R_p)^2 B^2}{\sigma_n(1 + R_p^2\sigma_p^2 B^2) + \sigma_p(1 + R_n^2\sigma_n^2 B^2)} \tag{2}$$

where the subscripts n and p indicate the contribution due to electrons and holes, respectively, and B is the magnetic field (11). Using the intermediate functions X, Y, and Z (12), equations (1) and (2) can be rewritten as

$$R = R_o\left[1 + \frac{Y + Z}{X} \cdot \frac{\Delta\rho}{\rho_o}\right] \tag{3}$$

$$\frac{1}{B^2} + \mu_n^2 Y = \mu_n^2 X \frac{\rho_o}{\Delta\rho} \tag{4}$$

where ρ_o is the resistivity at zero magnetic field, $\Delta\rho = \rho(B) - \rho_o$ and is called the magneto-resistivity and R_o is the Hall coefficient, equation (1), at zero magnetic field. Varying the magnetic field from 0 to 18kG and plotting equations (3) and (4) yields curves (a) and (b) as shown.
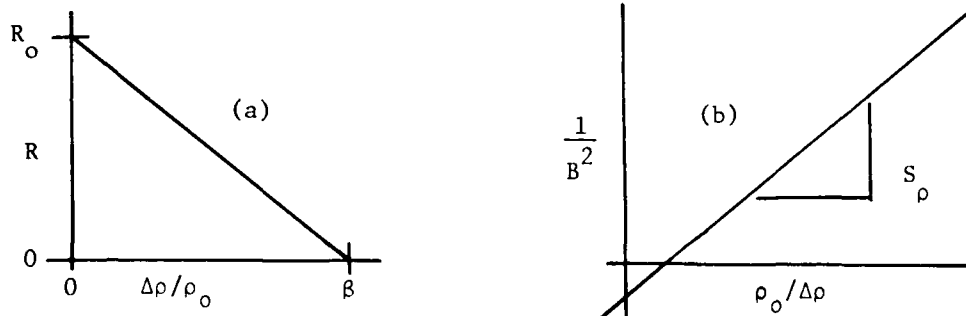
Curve (a) gives R_o and $\beta = X/Y+Z$ whereas curve (b) yields the slope $S_\rho = -\mu_n^2 X$. Letting:

$$T = (R_o\sigma_o)^2/S_\rho, \qquad A = [2 + T(1 + \beta^{-2})]/(1 + T/\beta)$$

$$b = [A + (A^2 - 4)^{1/2}]/2\alpha, \qquad c = (1+\alpha b\beta)/[b(\alpha b + \beta)]$$

where $\alpha = r_n/r_p$ and is the ratio of scattering factors and assumed to be unity, then the individual carrier properties can be calculated from:

215

ROSS, AUCOIN, SAVAGE
WINTER and MALIK

$$\text{electron mobility} = \mu_n = \frac{1 - \beta^{-1}}{\alpha - b^{-1}} \cdot \frac{(-R_0)\sigma_0}{r_p} \quad cm^2 volt^{-1} sec^{-1},$$

$$\text{hole mobility} = \mu_p = \mu_n/b \quad cm^2 volt^{-1} sec^{-1},$$

$$\text{hole concentration} = p = \frac{\sigma_0}{q\mu_n} \cdot \frac{1}{c + b^{-1}} \quad cm^{-3},$$

$$\text{electron concentration} = n = cp \quad cm^{-3},$$

$$\text{intrinsic carrier concentration} = n_i = (np)^{\frac{1}{2}} \quad cm^{-3}.$$

In addition, the Fermi level can be calculated from

$$E_c - E_F = kTln(N_c/n),$$

where N_c is the effective density of states in the conduction band.

An indication of the accuracy of this mixed conduction analysis is given by the linearity of equations (3) and (4) and the similarity of the calculated value of n_i to its theoretical value of 1.5×10^6 (12).

Table 1. compares the electrical properties of undoped GaAs grown by the ET&DL process to chromium doped substrates from other sources. Although the resistivity is slightly lower, the ET&DL material has one of the highest electron mobilities, nearly equal carrier concentrations and a Fermi energy level nearly intrinsic. Recent growths have resulted in material with resistivities of 0.8×10^9 ohm-cm. In addition, thermal conversion analysis indicates the material is stable to $700^\circ C$ for 30 minutes in H_2, ultimately converting to p-type at $1000^\circ C$.

SUMMARY

The physical and electrical properties of GaAs show it to be an important semiconductor material for use in advanced military electronic systems. However, millimeter wave and high speed IC device development has been slowed due, in part, to poor and unpredictable quality semi-insulating substrate material. A new modification of the liquid encapsulated Czochralski pressure-assisted growth process has been developed which employs in-situ compounding of GaAs from its elements. This process, first demonstrated in the U.S. by ET&DL, consistently yields high resistivity (to 10^9 ohm-cm) GaAs without the intentional addition of charge compensators. Transport property

216

	ρ_o	$-R_o$	μ_n	μ_p	n	p	n_i	E_c-E_F
	$\times 10^9$	$\times 10^3$	$\times 10^3$	$\times 10^2$	$\times 10^6$	$\times 10^6$	$\times 10^6$	
	ohm cm	cm^3/coul	cm^2/Vsec	cm^2/Vsec	cm^{-3}	cm^{-3}	cm^{-3}	eV
HP	1.21	2.25	3.41	8.44	.963	2.23	2.76	.684
NRL	.697	1.95	5.85	8.42	.832	5.94	2.22	.688
Laser Diodes	.733	1.80	2.94	4.90	2.48	2.48	2.48	.660
Monsanto	.0645	.370	5.74	..	16.9	..	..	.611
Morgan	.843	.647	4.73	5.55	.392	10.0	1.98	.707
Crystal Specialties	.897	2.48	4.43	5.19	1.04	4.50	2.16	.682
Sumitomo	.961	1.14	4.40	4.21	.492	10.2	2.25	.701
ET&DL*	.420	1.67	5.37	9.89	2.16	3.33	2.68	.664

*non-Cr doped $\quad n_i$(theoretical) $= 1.5 \times 10^6$ cm^{-3}

$\qquad\qquad\qquad E_c - E_F$(theoretical) $= 0.675$ eV

Table 1. Comparison of electrical properties of undoped GaAs (ET&DL) to chromium doped substrates from other sources.

determinations by mixed conduction analysis indicates the material has electron mobilites higher than Cr-doped material and Fermi levels which are nearly intrinsic.

The one step technique for "in-situ" liquid encapsulated compounding and Czochralski growth of GaAs is believed to be the best approach to solving the current problems associated with semi-insulating substrate fabrication. Various semiconductor material and device manufactures such as Varian Assocites, Westinghouse, Hughes, Rockwell, Microwave Associates and Metals Research are in the process of acquiring, or have purchased equipment to grow semi-insulating GaAs by this technique. Indeed, this approach is now becoming the basis for U.S. volume production of large diameter, high quality, semi-insulating GaAs material.

ACKNOWLEDGMENTS

ROSS, AUCOIN, SAVAGE
WINTER and MALIK

REFERENCES

1. B. Tuck, G.A. Adegoboyega, P.R. Jay and M.J. Cardwell, "Out Diffusion of Chromium from GaAs Substrates," Proceedings of the 7th International Symposium on GaAs, St. Louis, Mo., September 1978.

2. R.G. Wilson, "Ion-Implanted Chromium Profiles and Redistribution in GaAs," presented at the IEEE GaAs Symposium, Lake Tahoe, Nevada, September 1979.

3. R.G. Wilson, "Cr Concentrations, Depth Distributions and Diffusion Coefficient in Bulk and Epitaxial GaAs and in Si," Appl. Phys. Letts. 36, 215 (1980).

4. L.R. Weisburg, F.D. Rosi and P.G. Herkart, "Properties of Elemental and Compound Semiconductors," Interscience Publishers, New York, 1959, p.31.

5. E.P.A. Metz, R.C. Miller and R. Mazelsky, "A Technique for Pulling Single Crystals of Volatile Materials," J. Appl. Phys. 33, 2016 (1962).

6. J.B. Mullin, B.W. Straughen and W.S. Brickwell, "Liquid Encapsulation Techniques: The Use of an Inert Liquid in Suppressing Dissociation During the Melt-Growth of InAs and GaAs Crystals," J. Phys. Chem. Solids 26, 782 (1965).

7. J.W. Harrison, "A Survey of Single Crystal Growth Methods for Gallium Arsenide," Solid State Technology 16, 48 (1973).

8. S.M. Sze and J.C. Irvin, "Resistivity, Mobility and Impurity Levels in GaAs, Ge and Si at 300°K," Solid State Elec. 11, 599 (1968).

9. L.J.van der Pauw, "A Method of Measuring Specific Resistivity and Hall Effect of Discs of Arbitrary Shape," Philips Research Reports 13, 1 (1958).

10. J.M. David and M.G. Buehler, "A Numerical Analysis of Various Cross Sheet Resistor Test Structures," Solid State Elec. 20, 539 (1977).

11. E.H. Putley, "The Hall Effect and Semiconductor Physics," Dover Publications, New York, 1968, p.88.

12. D.C. Look, "Mixed Conduction in Cr-Doped GaAs," J. Phys. Chem. Solids 36, 1311 (1975).

13. Private communications.

PERFORMANCE EVALUATION FOR DIRECT FIRE SYSTEMS   (U)

RICHARD C. SCUNGIO, JULIAN A. CHERNICK
US ARMY MATERIEL SYSTEMS ANALYSIS ACTIVITY
ABERDEEN PROVING GROUND, MD   21005

Historically, the item level performance of a weapon system has been expressed in terms of the firepower characteristics of the weapon. The weapon characteristics normally included in the computation of firepower were range, accuracy, lethality, and rate of fire. With the introduction of more sophisticated weapons, an awareness of the need to include additional factors in the assessment of a weapon's performance has emerged at both the decision and research and development levels.

This awareness has resulted in the development of a methodology permitting better understanding of the operational performance of a weapon system, especially concentrating on the battlefield environment and its possibly degrading effects. The methodology is patterned after a model which was originally developed to evaluate the performance of the 155mm laser-guided COPPERHEAD artillery projectile. Analyses performed with this method are identified as being "COPE" type analyses and are primarily designed to evaluate the performance of systems requiring uninterrupted line-of-sight between the attacker and the target.

The operational performance of direct fire systems is affected by many factors which can combine in one manner or another and influence the utility of the system on the battlefield. The methodology developed requires the identification of the influence of each factor on the employment or performance of the particular weapon system being evaluated. Initially an employment concept must be available to permit identification of the location of the weapon on the battlefield, especially related to the anticipated enemy advancement.

From this information, the anticipated ranges of engagement and the corresponding periods of target unmask can be identified. Weapon or projectile performance characteristics usually in the form of engagement ranges, accuracies, and lethalities are needed; if pertinent, these data should be correlated to weather condition. The effects of terrain, as it influences target movement and intervisibility, is included. The presence of vegetation and its effect on intervisibility is also reflected in the methodology. For a system such as COPPERHEAD, communications, command, and control and the problems inherent in a designator operator's fire request being answered in a timely manner to engage moving targets is portrayed. For other systems such as tanks or anti-tank guided missiles, this factor is not pertinent and therefore, not included. Enemy fire and counter fire and its obscuration and lethal effects are also considered when assessing operational performance. These factors combine to reflect what is a realistic environment for the analysis of a weapons system's operational performance.

A COPE type analysis exhibits certain characteristics. It is basically one-sided. Provisions are included in the methodology to evaluate the effects of enemy direct and indirect fire and their obscuration and lethal effects, however, it is not two-sided in the sense of a force-on-force model. The model uses probability density functions as input, reflecting the frequency of occurrence of the many factors influencing performance. As such, it is stochastic in its approach. All performance factors are combined in the methodology resulting in a tool which is very easy to test the sensitivity of total performance to variations in one or more factors. However, the most noteworthy characteristic of the methodology is its simplicity. The output is quite transparent, giving results which are easy to understand and interpret.

The events influencing the performance of a weapon system are interwoven within the methodology, producing estimates of the chance of successfully surmounting each factor. Four critical events, selected for their tactical significance, aid in applying the output of the model. These critical events are:

1. The occurrence of an occasion,

2. The attempt to engage a target,

3. The actual engagement of the target, and

4. The end of the mission.

The methodology assumes that an occasion occurs once a target breaks terrain shielding. Once this occurs, the conditions for success

must be satisfactory for seven factors before an engagement is attempted. These factors constitute a set of conditions within which the observer has survived, is able to detect the target, and the target is within the employment range of the weapon system. Once the designator operator requests fire, he must establish communications and line-of-sight must exist before a round is fired. If the methodology determines that these two factors are satisfactorily met, one or more rounds are fired and seven additional factors are evaluated prior to the determination of a target kill.

The last critical event, the end of the mission, occurs when all rounds have been fired or at the cessation of available target vehicles due to their passing out of line-of-sight or attrition.

To interpret the results of the model, four measures of performance are developed. These measures are:

1. The probability of attempting an engagement given an occasion occurs,

2. The probability of firing a shot given an engagement is attempted,

3. The probability of killing a vehicle given a shot is fired, and

4. An overall measure of operational utility which combines the effects of all the performance factors.

The methodology has produced quantitative estimates of the degrading effects of environmental factors which previously have been treated mostly qualitatively. In general, it has been found that the most serious degrading factor influencing the utility of a direct fire weapon system when engaging moving vehicles is the obscuration effects of smoke and dust raised by supportive fires. Given that the decision is made to engage a target, a shot usually follows, however, the probability of killing a target is usually lower than fire power estimates would have estimated. The most serious degrading factor influencing the weapons kill probability given a shot is fired, has been found to be the loss of line-of-sight to the target during the flight of the missile or projectile.

Comparisons have been made of the relative performance of COPPERHEAD, tanks, TOW and HELLFIRE when engaging targets in relatively open and close terrain.

221

Due to their relatively shorter ranges, tank and TOW do not attempt as many engagements as COPPERHEAD and HELLFIRE, however, due to their shorter reaction time, they are more likely to get a shot off once the decision is made to engage. The longer engagement ranges also affect the $P_{K/SHOT}$ for tanks and TOWs as they fall below the other systems with this measure. The measure of operational utility shows that HELLFIRE outperforms all systems in the open terrain case, with tanks and TOW being the least preferred. One factor has been omitted from the HELLFIRE evlauation to date, which probably produces a favorable estimate of performance, that is, the likelihood of a helicopter being available and properly located for the engagement. Current evaluations assume that an AAH is on station and assesses performance from that point.

For terrain which can be classified as being close, thereby affording short periods of intervisibility at short ranges, tanks outperform TOW and COPPERHEAD.

The methodology is such that it produces results which are intuitively appealing and permit the direct comparison of various weapon systems. However, its greatest value and the way that it has been most used to date, is to analyze the operational performance of a system, especially reflecting the environment and its effects on performance. Used in this way, the model enables the assessment of the most serious factors affecting performance, identifying which ones, given improvement, could most increase performance. The model also has a tendency to identify conceptual improvements which offer little or no improvement in performance once combined with all the other potentially degrading factors. This can be a most valuable analytical tool, most valuable indeed.

NUCLEAR RADIATION EFFECTS IN FIBER-OPTIC WAVEGUIDES (U)

*STEWART SHARE, Ph.D., AND JOHN WASILIK, Ph.D.
U.S. ARMY ELECTRONICS RESEARCH AND DEVELOPMENT COMMAND
HARRY DIAMOND LABORATORIES
ADELPHI, MARYLAND   20783

I.   Introduction

        Fiber-optic communication systems, now under development by the U.S. Army, will be a prime factor in satisfying the Army's communication needs of the 1980's. An important issue for any communication system is survivability: in particular, survivability on the tactical nuclear battlefield. One of the important advantages gained by using fiber optics is their immunity to electromagnetic pulse effects, which are frequently damaging to conventional communication systems operating in tactical nuclear environments. However, glasses in general, and optical fibers in particular, are susceptible to the darkening effects of ionizing radiation found in tactical nuclear weapon environments. This problem is especially serious for Army applications because of the long lengths of cables used in communication systems. Long-haul fiber-optic communication systems are planned by the Army with unrepeatered lengths up to 8 km and data rates of 20 Mb/s(1). Previous fiber radiation data indicate that the use of optical waveguides involving long lengths may be severely affected in nuclear environments. The solution to this problem is an optical waveguide with minimal sensitivity to nuclear radiation.

        The purpose of this paper is to identify an optical wave-guide which has a good chance for meeting the Army's requirements for a radiation-hardened fiber-optic communication system. To accomplish this goal we have carried out an experimental research program on a wide variety of commercially available optical wave-guides and research prototypes. Glass-clad, high-silica fibers, suitable for long-length telecommunications applications, were

studied. The first step consisted of evaluating the ionizing radiation sensitivity of commercially available glass-clad fibers as a function of fabrication procedure and dopants. Then, after the least radiation-sensitive fiber composition and fabrication procedure was chosen, additional investigations were carried out, primarily on research fibers, to further reduce the ionizing-radiation-induced losses. This was accomplished by selecting a dopant concentration which we judged to have a significant probability of decreasing the fiber's radiation sensitivity.

Our investigation has shown that the radiation losses induced in optical fibers can be greatly reduced by a judicious choice of dopants, by the use of a particular fabrication procedure, and by the wavelength of operation. Recognizing the system requirements and radiation environments, we have chosen a fiber which has a good chance of surviving the nuclear ionizing radiation environment.

II.   Fiber-Optic Waveguides

Fiber-optic waveguides are composed of a core material surrounded by a cladding material. The refractive index of the core is always greater than the cladding. Transmission of the optical signal is achieved through light guided in the core because of internal reflections at the core-cladding interface. Current glass-clad fibers are made from silica (SiO_2), whose index of refraction may be raised or lowered by doping with various impurities. Typical index raising dopants include germanium, phosphorus and cesium, and are found in the core. Index lowering dopants include boron and fluorine and are found in the cladding. Several fabrication procedures have been devised to fabricate doped-silica optical fibers with low losses. These include the inside vapor oxidation process or modified chemical vapor deposition (MCVD) process, the outside vapor deposition process, the modified rod-in-tube (MRT) process, the plasma-activated process, and the phase-separable process. The signal bandwidth of a fiber may be controlled by adjusting the index of refraction profile through a gradation of the core and cladding dopants. Before discussing the ionizing radiation response of optical waveguides, we describe the radiation simulation and measurement techniques.

III.   Radiation Simulation

The nuclear ionizing radiation was simulated using a ^{60}Co air source (located at the Harry Diamond Laboratories). The losses induced in the fiber were measured during irradiation (i.e., in

situ) when the source was brought out of the pool. The annealing of the losses was continuously monitored following the irradiation. Measurements of the losses were carried out over a temperature range from -77 to 100°C; this temperature range includes the military operating range. Measurements were made at wavelengths of 0.8 to 1.3 μm , which includes the range under consideration for operation of fiber-optic communication systems. The radiation dose was obtained using CaF_2 thermoluminescent dosimeters. The radiation effects data obtained on a wide variety of optical waveguides is discussed in the next section.

IV.   Fiber Radiation Data

Fabrication Technique and Dopant Dependence

The losses induced at 0.8 μm in a low-loss, commerically available, Corning Glass Works (CGW) fiber from in-situ ^{60}Co radiation are shown in figure 1, as a function of ionizing dose and temperature. The fiber was fabricated by the standard outside process; the core was doped with germanium and boron, and the cladding with boron. As can be seen, the losses induced increase dramatically as the temperature is lowered: the induced losses are more than a factor of 20 smaller at room temperature then at low temperatures (-50°C). The temperature dependence of these curves can be described by a thermally activated diffusion process with an activation energy of 0.55 eV (2). Previous experimenters concerned themselves with measuring the room-temperature radiation response (3,4). Figure 1 shows that at -50°C the losses for a dose of 200 rad(SiO_2) are in excess of 400 dB/km; at room temperature, the induced loss is less than 20 dB/km. These data point out the importance of measuring fiber radiation response over the entire military temperature range. The annealing of the induced losses in this fiber is shown in figure 2. The radiation dose was 2000 rad(SiO_2). Again, the losses increase as the temperature is decreased. At 1000 s after ^{60}Co irradiation, the losses are in excess of 200 dB/km at -50°C; at 22°C the losses decrease to less than 10 dB/km. These data illustrate that if optical communication systems are to be operational at low temperatures typically found in military applications, as well as in radiation environments, a means must be found to reduce the large losses that occur below room temperature.

Figure 3 shows the losses induced from in-situ ^{60}Co irradiation as a function of ionizing dose in a CGW fiber doped with germanium, boron, and phosphorus in the core and fabricated by the standard inside process. Here it is seen that the temperature

225

dependence of the losses at low temperatures ($<-30°C$) is reduced compared to the previous fiber (in Fig. 1): this is attributed to the addition of the phosphorus. The losses at 2000 $rad(SiO_2)$ are approximately 300 dB/km at $-50°C$ and are about six times smaller than in the previous Ge-B-doped fiber fabricated by the outside process. The annealing of the induced losses is shown in figure 4. A similar temperature independence is observed here as in the in-situ radiation experiments.

These results demonstrate that the radiation response of fiber-optic waveguides over the miliary temperature range depends on dopant composition and waveguide fabrication techniques. For this reason similar radiation measurements were performed on other commercially available optical waveguides, having a wide range of dopants and standard industry fabrication procedures (5). The fibers are listed in Table I, along with vendor, core dopant, cladding dopant, and fabrication procedure; the intrinsic loss and bandwidth are listed in Table II. The CGW fibers have been discussed. The International Telephone and Telegraph (ITT) fiber contained phosphorus and germanium in the core and was fabricated by the inside process. The Times Wire and Cable (TWC) fiber, Valtec (VAL) fiber* and the Dainichi-Nippon Cables (DNC) fiber have silica cores with boron and/or fluorine in the cladding. They are fabricated by the outside, plasma-activated, and modified rod-in-tube (MRT) process respectively. Also listed is a Canstar (CAN) fiber fabricated by the phase-separable technique. Several research fibers (BTL and HRL) are listed and will be discussed later.

Figures 5 and 6 show the losses induced at 0.8 µm in the commercially available fibers from $200-rad(SiO_2)$ in-situ ^{60}Co irradiation and at 1000 s following a $2000-rad(SiO_2)$ ^{60}Co irradiation as a function of temperature. The CGW and TWC fibers, both fabricated by the outside process, show large losses at low temperatures for both measurement conditions. The losses induced in the fibers containing F (i.e., Valtec and Dainichi-Nippon) showed large losses at low temperatures in the 1000 s recovery experiment. The phase-separable Canstar fiber has losses nearly similar to the P-doped ITT fiber at 1000 s following the ^{60}Co radiation, but the in-situ ^{60}Co induced losses are considerably lower in the ITT fiber than in the Canstar fiber.

*The F-doped Valtec fiber was manufactured from a Hereaus-Amersil, Inc. preform.
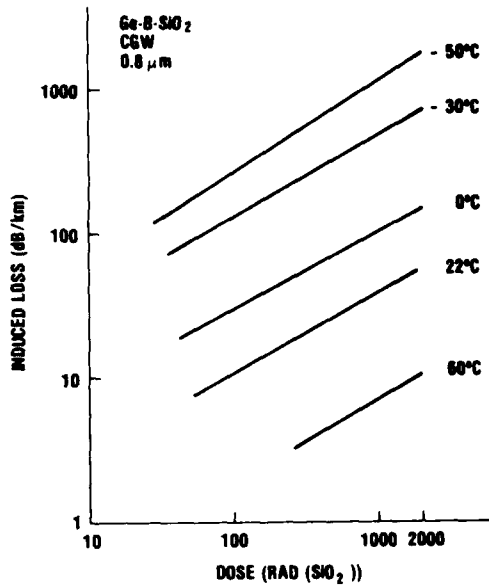
Figure 1. Induced loss at 0.8 μm in CGW Ge-B-SiO$_2$ fiber from in-situ ^{60}Co irradiation at various temperatures. The ^{60}Co dose rate was 95 rad(SiO$_2$)/s.
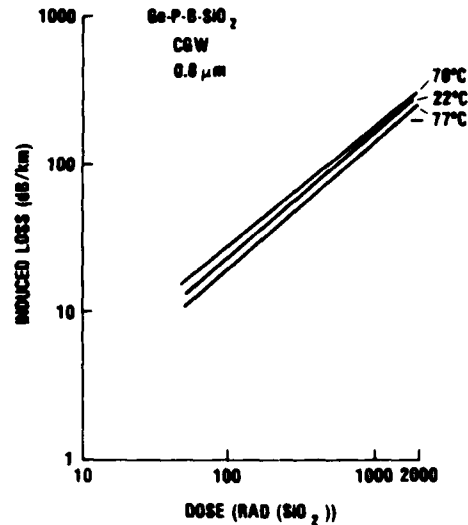
Figure 3. Induced loss at 0.8 μm in CGW Ge-P-B-SiO$_2$ fiber from in-situ ^{60}Co irradiation at various temperatures. The ^{60}Co dose rate was 95 rad(SiO$_2$)/s.
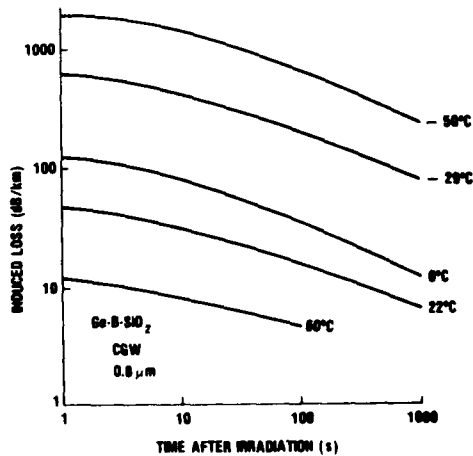
Figure 2. Induced loss at 0.8 μm in CGW Ge-B-SiO$_2$ fiber versus time after 2000 rad(SiO$_2$) ^{60}Co irradiation at various temperatures.
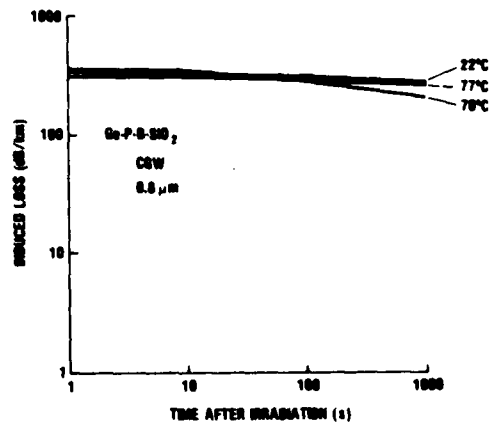
Figure 4. Induced loss at 0.8 μm in CGW Ge-P-B-SiO$_2$ fiber versus time after 2000 rad(SiO$_2$) ^{60}Co irradiation at various temperatures.

227

Table I. Fiber Composition and Fabrication Procedure

| Vendor | Composition | | Fabrication |
	Core	Cladding	Procedure
CGW	Ge-B-SiO$_2$	B-SiO$_2$	Outside
CGW	Ge-P-B-SiO$_2$	B-SiO$_2$	Inside
ITT	Ge-P-SiO$_2$	B-SiO$_2$	Inside
DNC	SiO$_2$	B-F-SiO$_2$	MRT
TWC	SiO$_2$	B-SiO$_2$	Outside
VAL	SiO$_2$	F-SiO$_2$	Plasma-Act.
CAN	Ca-SiO$_2$	doped-SiO$_2$	Phase-Sep.
BTL	Ge-P-SiO$_2$	B-SiO$_2$	Inside
HRL	Ge-P-SiO$_2$	B-SiO$_2$	Inside

Table II. Optical Characteristics of Fibers

Vendor	Intrinsic loss at 0.82 μm (dB/km)	Bandwidth (3dB) for 1 km length (MHz)
CGW	5	270
CGW	4	220
ITT	~5	150
DNC	~3	800**
TWC	~4	200
VAL	~3.5	45
CAN	~17*	15
BTL	~6	--
HRL	~10	--

*at 0.89 μm
**6 dB

228
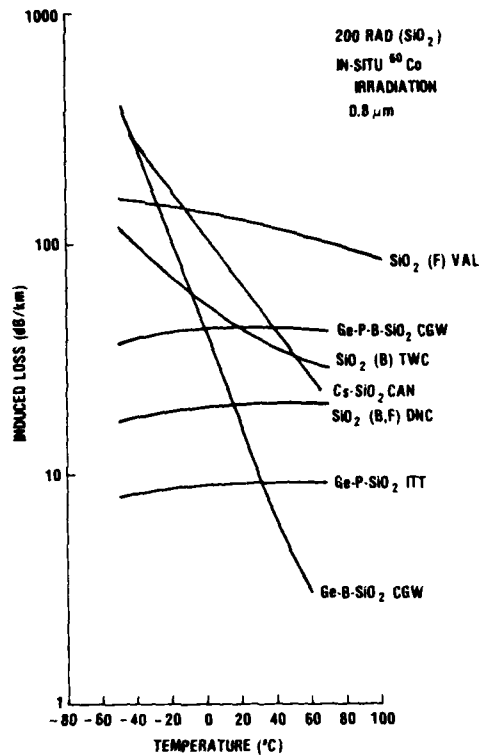
Figure 5. Induced loss at 0.8 μm in several fibers from 200 rad(SiO$_2$) in-situ ^{60}Co irradiation at various temperatures. The elements in parentheses are cladding dopants.
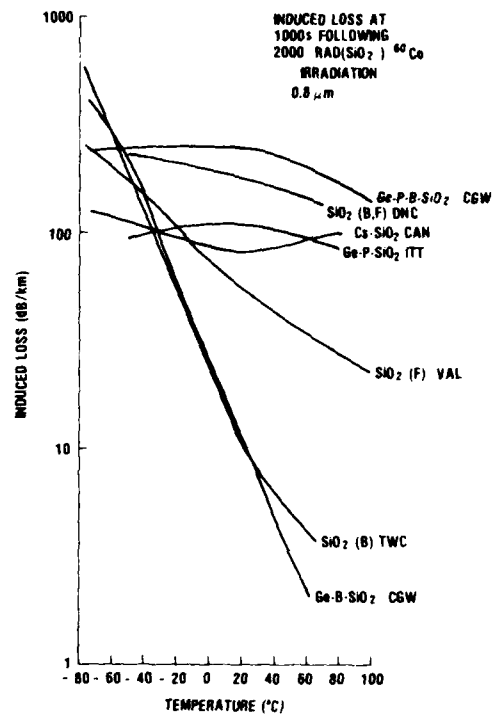
Figure 6. Induced loss at 0.8 μm in several fibers at 1000 s following 2000 rad(SiO$_2$) irradiation at various temperatures. The elements in parentheses are cladding dopants.

These results suggest that a Ge-doped fiber containing phosphorus and fabricated by the MCVD process (inside process) could yield a fiber with a low radiation sensitivity. To further explore this, several Ge-doped fibers with different phosphorus content were examined. Figures 7 and 8 compare the losses induced at 0.8 μm in several P-doped fibers from 200-rad(SiO$_2$) in-situ ^{60}Co irradiation and at 1000 s following a 2000-rad(SiO$_2$) irradiation. The Bell Telephone Laboratories (BTL) and Hughes Research Laboratories (HRL) fibers are research fibers; the ITT fiber was shown previously (in Fig. 5 and 6). These fibers were all fabricated by
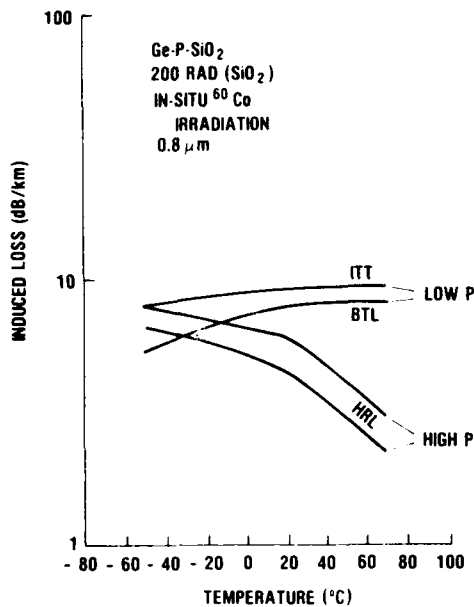
Figure 7. Induced loss at 0.8 μm in Ge–P–SiO$_2$ fibers from 200 rad(SiO$_2$) in situ ^{60}Co irradiation at various temperatures.
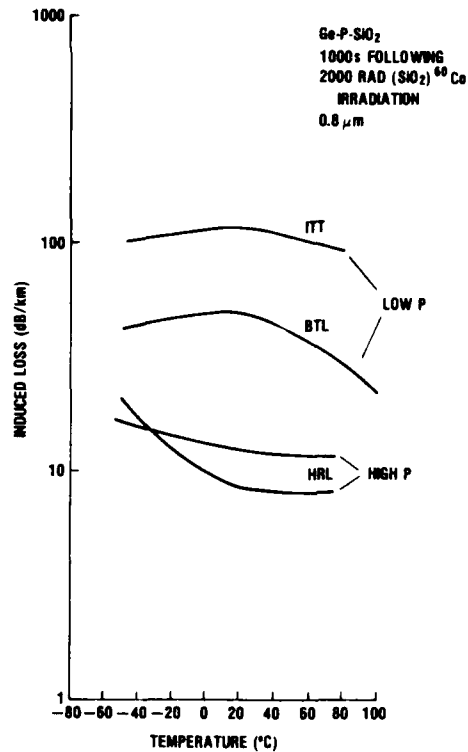
Figure 8. Induced loss at 0.8 μm in Ge–P–SiO$_2$ fibers following 2000 rad(SiO$_2$) ^{60}Co irradiation at various temperatures.

the MCVD technique, and had different phosphorus content in the core. The ITT and BTL fibers had low phosphorus concentration; the HRL fibers had high phosphorus concentration. All the fibers had similar germanium content in the core except the BTL fiber which had somewhat more. The cladding of these fibers was all doped with boron. The intrinsic losses (at 0.8 μm) of the BTL and HRL fibers were 6 and 10 dB/km; the ITT fiber was 5 dB/km. The bandwidth of the HRL fibers was probably less than that of BTL and ITT fibers because the HRL fibers have a layered index profile (e.g. step or W)(6) while the ITT and BTL fibers have graded index profiles. From figure 8, we can see that the HRL fibers show much lower induced losses at 1000 s following ^{60}Co irradiation than the ITT and BTL fibers: the losses induced in the HRL fibers were more than a factor of five less than those observed in the ITT fiber

230

over the temperature range of the measurements. The losses measured during 200-rad(SiO_2) ^{60}Co irradiation (in Fig. 7) show the reduced sensitivity of HRL fibers compared with the ITT fiber. This becomes more apparent as the temperature is increased.

These data show that a Ge-doped fiber with a high phosphorus content has an improved radiation response, especially in recovery from the induced losses following irradiation, compared with low-phosphorus-content fibers. However, these fibers also have different index profiles. Whether this plays a role in the radiation response of these fibers is under investigation. At any rate Ge-doped fibers manufactured by the MCVD process and with a high phosphorus content show the lowest radiation sensitivity of the fibers evaluated.

Wavelength Dependence

In general, the radiation response of glass and optical waveguides depends on wavelength. The spectral dependence of the radiation losses induced in the low P BTL fiber and the high P HRL fiber is shown in figure 9. The losses are given relative to 0.8 μm in the wavelength range from 0.8 to 1.06 μm. The radiation dose was 2000 rad(SiO_2); the radiation temperature was 22°C. As seen, the induced losses tend to decrease as the wavelength increases from 0.8 to 1.06 μm. Similar results were observed at other temperatures. Data taken at longer wavelengths (1.3 μm) on the high-phosphorus content Ge-doped fiber revealed that losses increased beyond 1.06 μm and were similar to those observed at 0.9 μm. Considering only the fiber, these results indicate that the most desirable wavelength for operation in a radiation environment is at 1.06 μm. However, consideration must be given to other system characteristics (sec. V).

Figure 9. Spectral dependence of induced loss for Ge-P-SiO_2 fibers. The radiation dose was 2000 rad(SiO_2); the radiation temperature was 22°C.

231

V.   Discussion

The fiber-optic response data shows that a high-phosphorus-content Ge-doped waveguide fabricated by the MCVD technique gives the lowest radiation response of the fibers measured. Selection of the optimum operating wavelength depends not only on the fiber radiation response but also on other system parameters. These include emitter output, receiver sensitivity, component degradation, and the intrinsic preirradiation losses of the fiber. From the spectral dependence of the radiation response data in figure 9, it appears that operation at long wavelengths, especially at 1.06 μm, would be beneficial. However, the emitter and detector performance must be considered. It is desirable to use an emitter with as high an output power as possible. Currently GaAlAs lasers operating from 0.8 to 0.89 μm yield the highest output power. For wavelengths beyond 0.9 μm to 1.06 μm, light-emitting diodes (LED's) are used primarily because lasers operating in this regime at present have short lifetimes. Approximately 15 dB more power can be coupled into a fiber with a 0.8 to 0.89 μm laser emitter than with an LED emitter at 1.06 μm. The sensitivity of silicon photodiode detectors used in optical receivers also decreases at longer wavelengths. Even though the 1.06-μm fiber radiation losses are less than those occurring at shorter wavelengths, the reduction is not enough to offset the superior performance of the 0.8 to 0.89 μm emitter and receiver components. Therefore, within current emitter and detector technology, and taking into account that the fiber radiation response decreases as the wavelength increases, operation near 0.9 μm with an injection laser would be preferred in a radiation environment.

It was noted that the losses induced in the high-phosphorus fiber increase for wavelengths greater than 1.06 μm: the 1.3 μm radiation losses were similar to the 0.9 μm losses. However, because of the low sensitivity of the receivers currently used at 1.3 μm and the smaller emitter output compared with those used in the 0.8 to 0.89 μm region, operation near 0.9 μm appears to be advantageous where radiation survivability is desired. If research now being conducted to improve device performance at 1.3 μm should yield suitable detectors and emitters, then operation at 1.3 μm may become more desirable, especially since intrinsic fiber losses are minimal at this wavelength.

To assess fiber survivabilility, it is useful to determine the total loss which might be induced in a given length of fiber when exposed to a particular radiation environment. As an example

232

two cases will be considered: (1) the losses induced in a length of fiber following nonuniform irradiation from a point source and (2) the losses induced during irradiation in a fiber uniformly exposed over its length. The first case could apply to an initial nuclear weapon environment, the second to a residual radiation (fallout) environment. The length of fiber we considered is that typically found in long haul communication applications, 4 km. If we choose a high-phosphorus-content Ge-doped fiber operating in the 0.85 to 0.9 μm wavelength region, the losses remaining at 1000 s following a nonuniform irradiation from a point source are 12 to 15 dB throughout the military temperature range. We choose the peak radiation dose in the center of the fiber to be 2000 rad(SiO_2). The magnitude of the losses are determined by the low-temperature (-50°C) fiber response. Extending the length of fiber does not significantly increase the losses because the radiation field of a point source decreases rapidly with distance. In the second case if we choose a uniform exposure of 200 rad(SiO_2) over the high-phosphorus-content fiber operating in the 0.85 to 0.9 μm range, the induced losses range from 9 to 12 dB for a 4 km length. Increasing the length of fiber in this case increases the losses.

The overall losses that can be sustained by the system from irradiation are determined by many system parameters: pre-irradiation cabled fiber loss, receiver sensitivity, connector losses, component degradation, bandwidth, and emitter output power, to name a few. Also, consideration must be given to the radiation degradation of other components, such as receivers, in determining the loss margin that should be allotted to radiation losses in the fiber. Using system parameters for present commercially available fiber-optic technology, the margin that could be allowed for radiation effects in a 4 km system operating at 20 Mb/s is 16 to 18 dB over the 0.85 to 0.9 μm wavelength range. The losses induced in the high-phosphorus research prototype fiber by the two radiation environments discussed above have similar values. This result points to the possibility that a fiber may be found that could be used in a long haul radiation environment. We would like to point out that more work is needed, but compared to the situation that existed two years ago (at the outset of this study) where fiber radiation losses (see fig. 1 to 4) were around several hundred dB/km, things are greatly improved; said in another way, the nuclear-radiation-survivable length of fiber has increased by more than a factor of 20. Additional work is needed to improve the intrinsic loss and bandwidth of the high-phosphorus Ge-doped fiber so that it can meet system performance parameters. Also the radiation effects in the receiver must be considered in the total system response.

VI.   Summary

An investigation was made of the response of optical wave-guides to ionizing radiation for different fiber compositions, fiber fabrication techniques, and wavelengths. Our research has shown that large radiation-induced losses occurring in commercially available fibers could be greatly reduced using research fibers fabricated by the MCVD process and doped with germanium and and a large concentration of phosphorus. Analysis shows that a 4 km length of this type of fiber exposed to a nuclear radiation environment produces losses in the fiber at 0.85 to 0.9 μm which are within operating expectations of systems now under development. With additional work to reduce the intrinsic losses and to increase the bandwidth, an MCVD Ge-doped fiber containing phosphorus has a good chance of satisfying the Army's need for a radiation-hardened fiber.

Acknowledgement

Literature cited

1. L. U. Dworkin and J. R. Christian, IEEE Trans. Communications, COM-26, No. 7, 999 (1978).

2. S. Share and R. McCracken, IEEE Trans. Nucl. Sci. NS-25, No. 6, 1288 (1978).

3. R. D. Maurer, E. J. Schiel, S. Kronenberg and R. A. Lux, Appl. Opt. 12, 2023 (1973).

4. E. J. Friebele, R. E. Jaeger, G. H. Sigel, Jr., and M. E. Gingerich, Appl. Phys. Lett. 32, 95 (1978).

5. "Optical Fiber Telecommunications" Stewart E. Miller and Alan G. Chynoweth, eds., Academic Press Inc., p. 233 (1979).

6. Op. cit., p. 18

ACOUSTIC EMISSION AS A NDE TECHNIQUE FOR
DETERMINING COMPOSITE ROTOR BLADE RELIABILITY

RICHARD J. SHUFORD
*WILLIAM W. HOUGHTON
ARMY MATERIALS AND MECHANICS RESEARCH CENTER
WATERTOWN, MA   02172

I.   INTRODUCTION

Fiber-reinforced composite rotor blades are being intro-
duced into the Army inventory to replace conventional metal blades.
An all-composite blade offers the advantages of lower cost, increased
aerodynamic performance, improved ballistic tolerance and a greatly
increased service life.

Nondestructive evaluation of these structures is extremely
important, as they are susceptible to fabrication errors, service
damage and environmental degradation. Due to the complex design
and fabrication of these blades, adequate nondestructive evaluation
(NDE) techniques have not been developed.

This paper will discuss the progress made in an ongoing
program to investigate the use of acoustic emission (AE) to deter-
mine the structural integrity of a composite main rotor blade. The
blade is constructed primarily of S glass/epoxy and aramid/epoxy.
Figure 1 shows the blade structure, which is composed of a multiple-
cell filament-wound spar, an aramid trailing edge and a filament-
wound blade skin supported by an aramid fiber paper honeycomb core.
The design and manufacture of these blades have been presented else-
where (1). A total of four blades are being tested, two blades with
known areas of delamination and two blades without these defects.
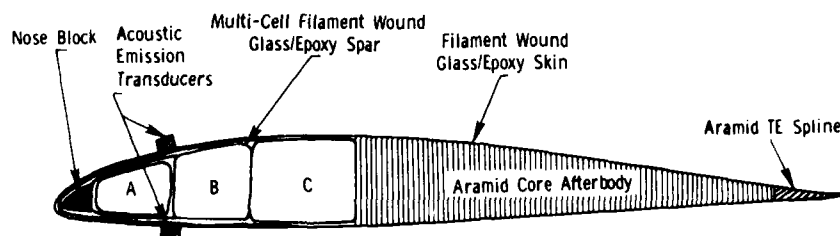
Figure 1. BLADE CROSS SECTION SHOWING PLACEMENT OF TRANSDUCERS

The Applied Technology Laboratory (ATL) at Ft. Eustis and the Army Materials and Mechanics Research Center (AMMRC) are presently investigating the propagation characteristics of flaws in this rotor blade. An AE proof test, a novel NDE technique, is being used to monitor flaw initiation and growth in the blades as a result of fatigue testing. The acoustic emission results will be correlated with mechanical property and other NDE data (ultrasonic, thermography, and radiography) and used to determine the structural integrity of the rotor blade. It is expected that these techniques will be readily adaptable to new product certification and in-service inspection of nonmetallic rotor blades.

II. EXPERIMENTAL

The blades are being fatigue tested by the Structures Laboratory of ATL in a 200K-2-108 fatigue test machine. The blade is mounted in the machine at the tip using a doubler arrangement (shown in Figure 2) and at the root end through an adapter to a hub yoke. The fatigue loading spectrum of alternating flap, chord and torsion bending moments used is representative of actual flight loads (2). A steady axial load is applied through the centrifugal force (Cf) loading system. This tensile load approximates the centrifugal force exerted on the blade during flight. Test frequency is approximately 13 Hz. Flight spectrum loading continues for 28 million cycles, which is equivalent to 1440 hours (4 years) of flight time. If no void growth occurs after 28 million cycles of spectrum loading, the fatigue loads will be increased. AE proof tests will occur prior to the spectrum loading, at 10 and 20 million cycles and at the completion of the first phase of testing (28 million cycles). AE proof tests will be performed more frequently during the higher amplitude loading. Thermographic analysis of heat patterns generated during spectral loading are being performed at periodic intervals by Virginia Polytechnic Institute and State University (VPI) under contract DAAG29-76-D-0100. Ultrasonic, X-ray and borescope inspections are also being conducted by personnel at ATL.

236

Figure 2. TIP END CONFIGURATION (SHOWN DURING FLAPWISE
BENDING PROOF TEST)

III. ACOUSTIC EMISSION

A. Theory

Research on acoustic emission (AE) from reinforced plastics
began in the aerospace industry in the early 1960's. The most
significant observation was that the AE count activity began at
a repeatable load and increased as the sample was stressed to
failure. Since then, the study of acoustic emission has accelerated
along with the expanded use of reinforced plastics in structural
applications. In the mid 1970's two more basic observations were
made: the first related the amplitude of the AE event to the actual
failure mechanism (3), and the second documented a deviation from
the well-known Kaiser effect (4).

Recently, several application areas have emerged which
utilize the ability of AE to assess the structural integrity of
reinforced plastic components. In the chemical industry AE has
been used to certify hundreds of new and in-service reinforced
plastic storage tanks (5,6). The test procedure is presently being
modified to include pressure piping and pressure vessels. Numerous

237

aerial manlift device (cherry picker) booms have been examined (7).
The booms, used primarily by utility companies, were a major
inspection problem. AE has proven to be a reliable and cost-
effective solution to this safety problem. The automotive industry
is investigating AE as a quality assurance tool for the growing
number of reinforced plastic automotive components (8,9).

When a material is significantly stressed, it emits
mechanical stress waves. These stress waves are known as acoustic
emissions. The observed acoustic emission event (Figure 3) from
a reinforced plastic material under stress can be described as
an exponentially decaying sinusoid. Though various characteristics
of the event can be measured, the number of events, amplitude of
the event, number of counts (threshold crossings) and rms measurements
are particularly significant.

As a reinforced plastic material is loaded to failure,
the event characteristics change significantly. The AE during low
stress levels are low amplitude signals, and are usually related
to cracking of the matrix material or delamination. At higher
stress levels higher amplitude signals are observed, which have
been associated with fiber failure. Amplitude results are usually
displayed in a histogram fashion (Figure 4), known as an amplitude
distribution. On the X-axis is the amplitude in decibels (dB)
(relative to 1 μV at output of preamp), and on the Y-axis is the
number of events. Figure 4 depicts the triple-peaked amplitude
distribution first reported by Wadin (3). Though this has not
been fully explored, it is widely accepted that each amplitude
cluster is associated with a specific failure mechanism. In this
example the lowest amplitude events are the result of matrix crazing.
The intermediate amplitude cluster is due to delamination and the
highest amplitude events are the result of fiber fracture.

The acoustic emission count activity (Figure 5) also
provides a characteristic curve as composite samples are loaded
to failure. Counts begin at 25 to 50 percent of the failure load.
There is very little variation in the onset of emission or in the
shape of the "knee" during tests of identical samples.

The Kaiser effect is the "absence of acoustic emission
activity until previously applied stress levels are exceeded." The
phenomenon can be observed in reinforced plastics at low load levels.
At high loads, repeated stress to the same level will result in
additional emission. As illustrated in Figure 5 the deviation from
the Kaiser effect can be quantified and is often referred to as the
Felicity ratio. It is widely believed that the Felicity ratio is a
measure of the amount of previous damage to the material.

238
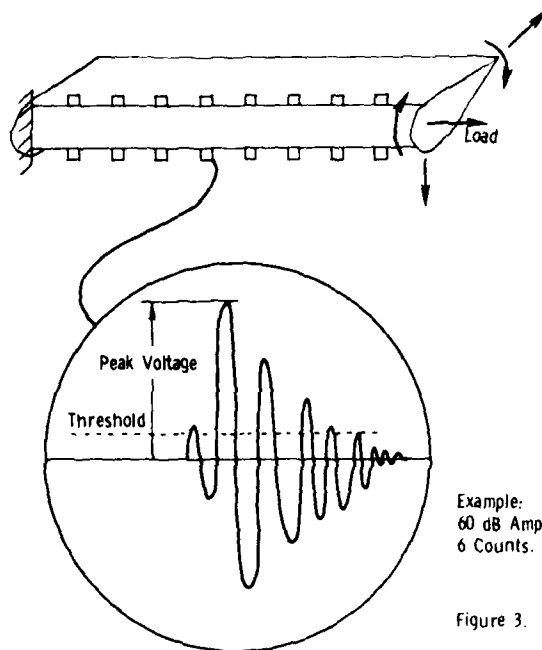
Figure 3. TYPICAL ACOUSTIC EMISSION EVENT
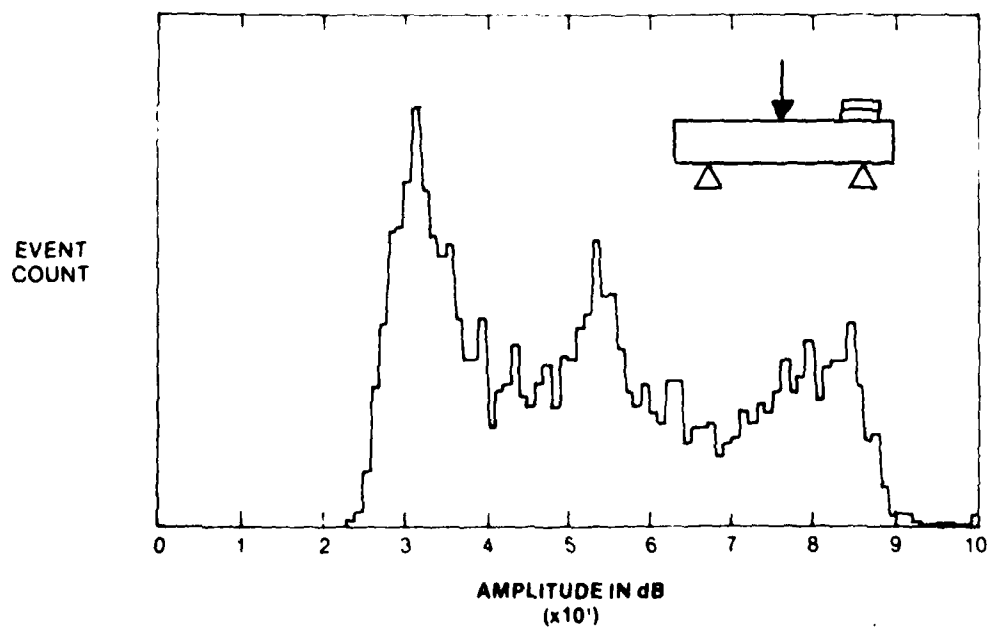
Figure 4. AMPLITUDE DISTRIBUTION (AFTER WADIN, REF. 3)
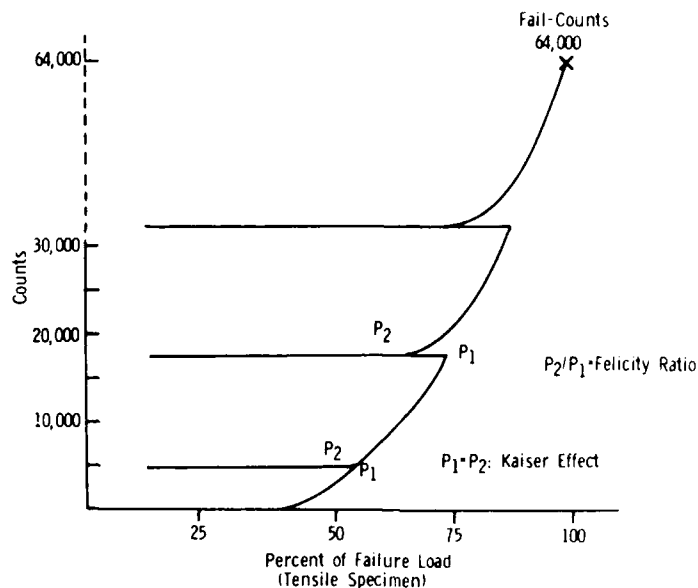
Figure 5. AE COUNT ACTIVITY (AFTER FOWLER. REF 5)

In order to study the degradation of a material due to cyclic loading an acoustic emission proof test can be used. If a material is loaded to a proof load and this load is in the region where the Kaiser effect applies, we can reload to this level and no emission will occur. Also, no emission will be heard during a hold period. However, as fatigue damage starts to occur, an increase in AE activity will be evident during each proof load, and emission will occur during hold periods. This change in the AE behavior can be used as a measure of the residual strength and of the remaining fatigue life.

As the acoustic emission stress wave travels through a material it loses energy by attenuation and dispersion. Figure 6 illustrates attentuation along the length of an actual rotor blade. An electronic device was used to simulate AE events at various distances from a sensor. In one case (lower curve) the simulator was set to output a small signal similar to that of matrix crazing, and in the second case (upper curve) the signal was similar that of fiber fracture. Naturally, the larger signal can be detected over a greater distance.

We can take advantage of the fact that AE signals travel only short distances in composite materials. As illustrated in Figure 7 an event of 60 dB (matrix crazing) would be detected by

240

Pulser: S140B
Reciever: S140HS(S9204)
170 KHz Bandpass Filter
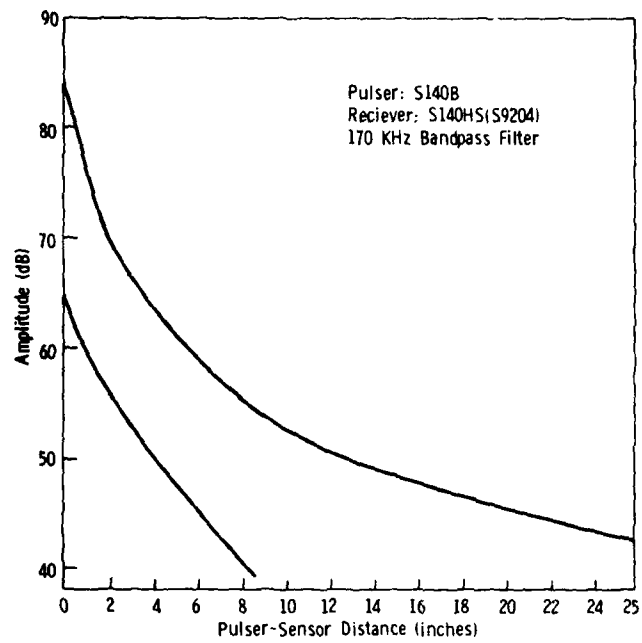
Figure 6.   ATTENUATION PLOT
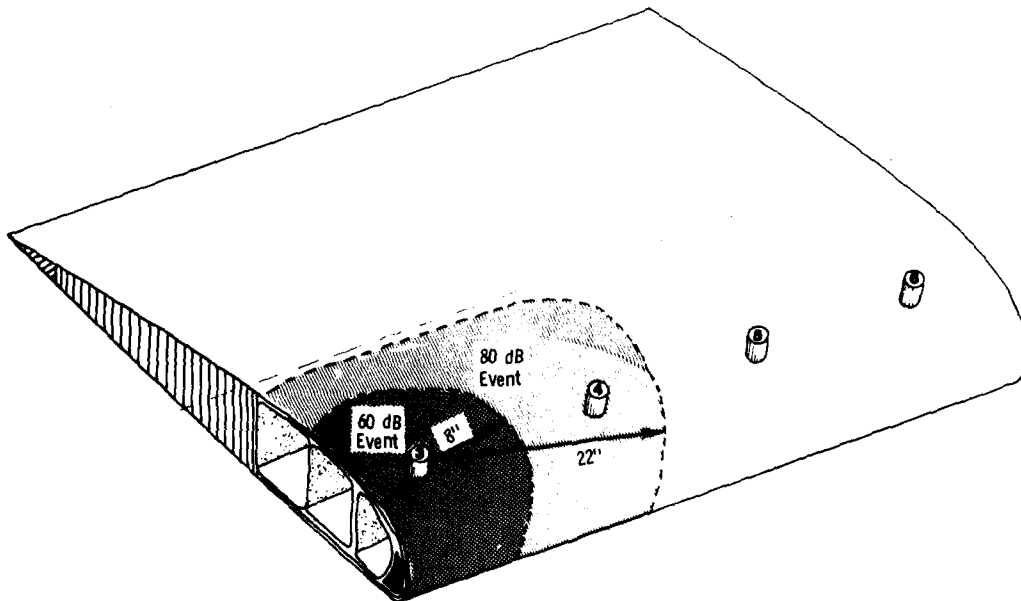
Figure 7.   ZONE LOCATION

241

sensor number 3 only if it occurred within the dashed line marked
60 dB event. There is no possibility that a 60 dB event occurring
close to sensor number 3 could be detected at sensor number 5.
Thus, an operator noting activity from only sensor number 3 would
be aware that the source is close by. However, a large event,
of perhaps 80 dB (fiber fracture), will travel a much greater dis-
tance, and several sensors would be affected. An operator noting
several simultaneously active sensors could assume that a large
event had occurred in the center of the group. To further simplify
the location of large events an electronic gate can be used. The
gate allows only the first sensor hit to record the event. The
philosophy of locating events in this manner is known as zone
location.

B. Procedure

The acoustic emission system used to monitor the rotor
blade proof loads is illustrated in Figure 8. It is an 8-channel,
mixer-based, noncomputerized unit manufactured by Dunegan/Endevco
Corporation. The system accepts signals into eight independent
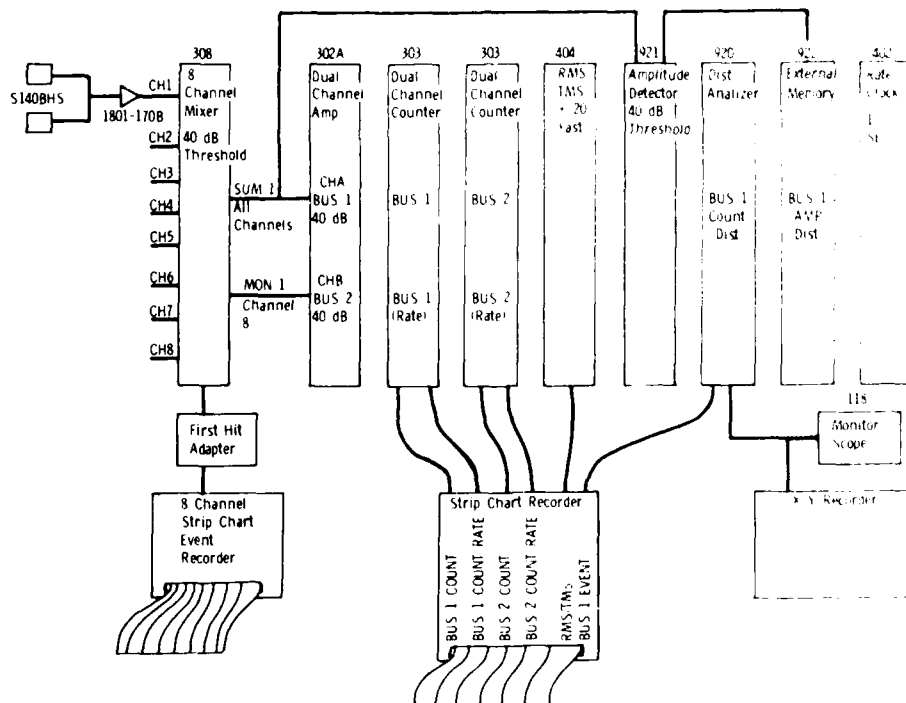
Figure 8   MODULAR DIAGRAM OF ACOUSTIC EMISSION APPARATUS

channels. Each channel consists of two sensors teed into one pre-amplifier. Four output devices are utilized: an 8-channel event recorder indicating which sensors are closest to the source, a 6-pen strip chart recorder indicating count, event and rms data, a real-time monitor oscilloscope displaying count and amplitude distributions, and an X-Y recorder to plot the count and amplitude distributions. The equipment is shown in Figure 9.
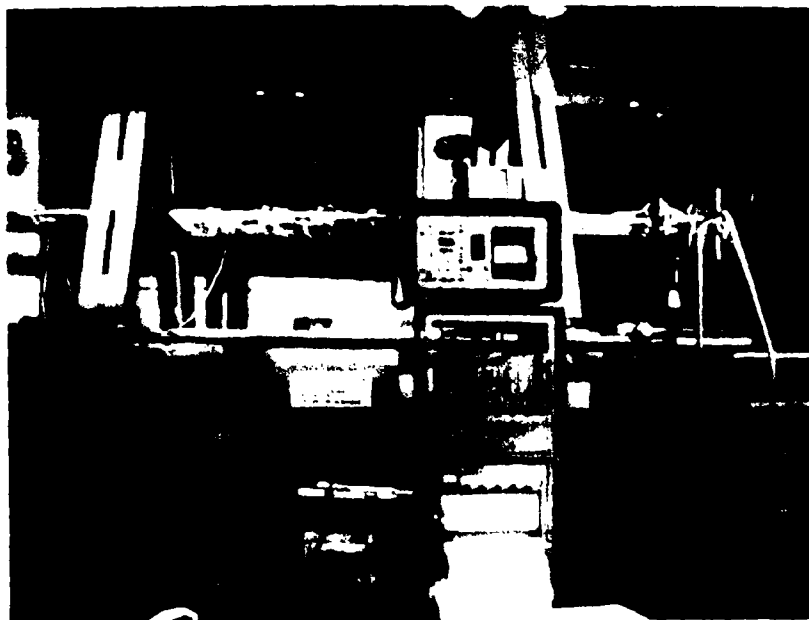
Figure 9. ACOUSTIC EMISSION EQUIPMENT

Dunegan/Endevco S140B/HS (S9204) transducers were selected for this test because of their high sensitivity and good frequency response at 100 to 120 kHz. Prior to attaching the transducer, the blade was lightly sanded and cleaned with acetone. The transducers were then mounted on the blade with silicone rubber adhesive (GE RTV 102). Figure 10 shows the spanwise transducer location and spacing (approximately 14.5 inches apart). The chordwise transducer location is at the junction between cells A and B as shown in Figure 1. This spacing will pick up a 60 dB event at a distance of 8 inches, and an 80 dB event at a distance of 22 inches (see Figure 7). The operation of each sensor is checked at the beginning of each test with a hand-held pulser.

243
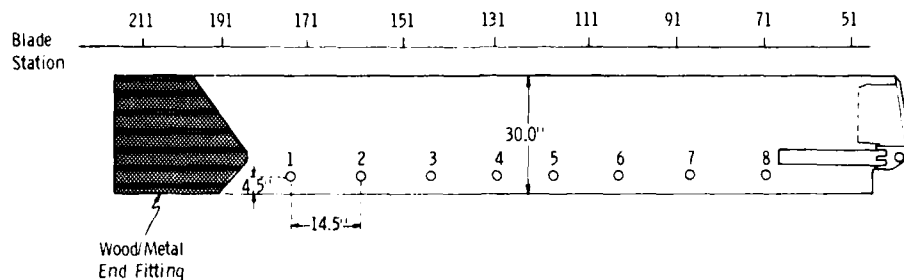
Figure 10. AE TRANSDUCER LOCATION

The blade is proof tested in increments to a load approximately 10 percent higher than the load achieved during spectrum loading. The blade is proofed separately in each loading mode in the following order:

a. Flapwise bending
b. Chordwise bending
c. Cf (tension)
d. Torsion
   minimum Cf
   varying Cf

C. Results and Discussion

The acoustic emission tests have been only partially completed, but some of the preliminary results are presented here. The initial (prior to spectrum loading) proof loads resulted in negligible acoustic emission in bending (chordwise and flapwise) and torsion, but a large activity in the Cf loading. During the Cf loading, 21,273 counts and 1481 events were accumulated, with amplitudes primarily in the 40 to 70 dB range. The second proof load, applied at approximately 10 million cycles, again resulted in very little emission in all modes except the Cf loads. The Cf load resulted in emission from sensor pairs 5 and 8. A total of 752 counts and 144 events were measured, and the amplitudes ranged from 40 to 60 db. The AE was primarily coming from the area of sensor pair 5 (station 115) with sensor pair 8 (root end) one quarter as active. Figure 11 shows the data points obtained, as well as the projected AE results based on the periodic overload technique. As fatigue damage occurs, the ultimate strength of

the composite structures will decrease. When this value decreases
to approximately twice the proof stress, an upswing in the event
curve is anticipated.
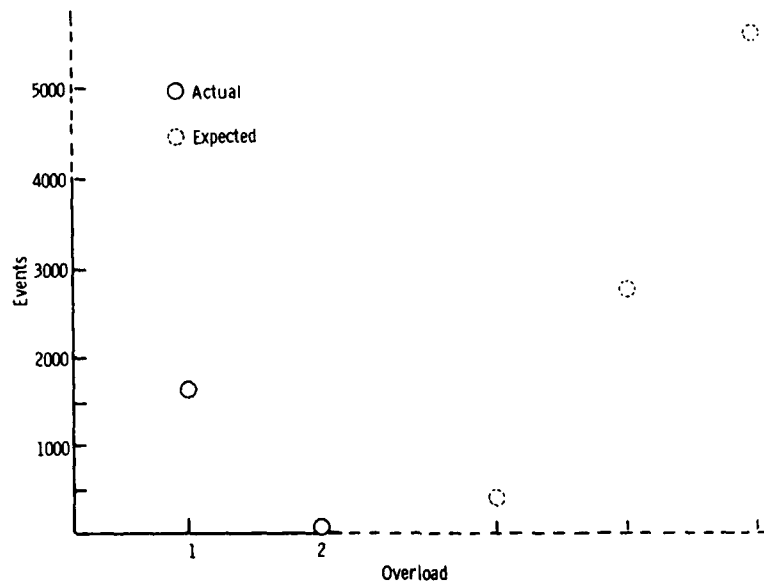
Figure 11. DETECTED EVENTS PER OVERLOAD

The acoustic emission results have been as expected—
an initially "noisy" proof load, and a second, much quieter, proof
load. The amplitudes resulting from both tests were in the range
expected from matrix crazing and delamination. There is also the
possibility that some of the emission is due to rubbing of surfaces
in the delaminated areas. Upon examination of the pulse-echo
ultrasonic results, it was seen that the area near sensor pair
5 was the site of a large delamination. This indicates that the
instrumentation could be picking up some growth in the delaminated
area. Pulse-echo ultrasonic examination subsequent to the second
proof test (10 million cycles) showed no measurable change in void
dimensions, leading to the conclusion that the AE resulted from
either very small void growth or rubbing of the void surfaces or
a combination of the two. However, the amplitudes of the emissions
were low enough to conclude that no significant damage occurred
during either the fatigue loading or the proof tests.

IV. OTHER NDE TECHNIQUES

A. Thermography

There is preliminary evidence that "trouble spots" can
be located during cyclic testing by a nondestructive technique
called vibrothermography, originated in 1974 by Reifsnider (10),
et al. Vibrothermography uses a real-time heat imaging device
such as a video-thermographic camera to observe the heat patterns
generated by hysteresis dissipation during cyclic excitation of
the specimen under test. The heat patterns generated in this way
are directly related through their intensity and distribution to
the mechanical response of the test piece and to the collective
effect of any and all defects which disrupt the integrity of the
material and thereby disrupt the internal distributions of stress.
Figure 12 shows such a heat pattern which was observed during spec-
tral loading of the subject rotor blade after about 4.7 million
cycles. The image of the blade extends from the bottom left to
the top right of the figure; other details in the figure are back-
ground images. Just to the lower left of center in the figure

Figure 12. HEAT PATTERN GENERATED
DURING FATIGUE TEST

there is a distinct contour pattern which was formed by different shades of color in the display of the thermographic camera. Each of these is an isotherm separated by 0.5°C. Another contour pattern, somewhat less distinct, is visible in the top right corner of the figure. These two "hot spots" showed an elevation of from 2 to 2.5°C in temperature compared to the remainder of the blade which was essentially uniform in temperature. The pattern was distinct, unchanged in pattern when observed from day to day, and reproducible in the sense that when cyclic loading ceased, it faded out slowly but reappeared upon the resumption of cyclic excitation. These indications are very promising, and they support earlier findings which suggest that vibrothermography may be an excellent quantitative method for locating, characterizing, and understanding defect development and growth during the cyclic loading of composite laminates and structures (11).

B. **Ultrasonic Inspection**

A pulse-echo ultrasonic technique to monitor defect growth during the test was developed and is being used throughout the program. The initial test, which covered the entire spar, nose cap, and trailing edge surfaces, was found to be in good agreement with the original C-scan results. Nine specific areas are being monitored by the periodic tests. A complete pulse-echo ultrasonic test, similar to the one run prior to the initiation of the fatigue test program was run at 10 million cycles. There was no measureable change in the flaw size during any of these ultrasonic tests. This is in agreement with the other results, which indicate very little fatigue damage to the blade.

C. **X-Radiography and Borescope Inspection**

The test blade was X-rayed prior to the start of the fatigue test. Initial radiographic analysis of the nose cap showed random minor separation in the unidirectional fibers. The blade trailing edge radiographs showed areas of varying density which have been attributed to resin content variations.

The internal condition of individual spar tubes is monitored by using a borescope. Initial inspection detected damage in the middle spar tube between stations 150 and 165. The damage, which was probably caused by withdrawal of the mandrel, extended from the tube floor forward to the wall and continued to the tube ceiling. Photographs were taken of the area to document this condition and provide data for reference purposes. Inspection of the spar tubes

after 10 million cycles showed some additional tearing away of the loose fibers with some now extending to the aft wall of the tube.

V. SUMMARY

This paper has been a presentation of progress made in a continuing project to evaluate the usefulness of several NDE techniques for monitoring flaw initiation and growth in composite helicopter rotor blades.

The acoustic emission results indicate minor fatigue damage, and lead us to believe that it is possible to project an AE failure curve based on the emissions from periodic proof overloads. The vibrothermography results suggest that it may be an excellent method for locating, characterizing, and understanding defect development and growth during cyclic loading of composite structures. Preliminary indications suggest that these two novel and complementary NDE techniques can be used to determine problem areas, and these areas can be further investigated using conventional NDE techniques.

The AE technique could have wide application in new product certification and in-service inspection of composite rotor blades. The blades could actually be proof loaded while in the field, and the acoustic emission results would give an accurate estimate of the remaining service life. This technique could be adapted to determine the structural integrity of many composite structures.

ACKNOWLEDGMENTS

SHUFORD and HOUGHTON

REFERENCES

1. White, Mark L., "Filament Wound Main Rotor Blade - The Army's New Production Blade for the AH-1," Preprint number 78-36, 34th Annual National Forum of the American Helicopter Society, May 1978.

2. Orleano, Drew. Test Plan: The Evaluation of the Effect of Voids in Composite Rotor Blades. Internal Report, Applied Technology Laboratory, Ft. Eustis, VA. January 1980.

3. Wadin, James R., "Listening to Composite Materials," Dunegan Endevco Publication, LT4, August 1978.

4. Fowler, T. J., "Acoustic Emission Testing of Fiber Reinforced Plastics," Preprint 3092, ASCE Fall Convention, San Francisco, CA October 1977.

5. Fowler, T. J., Gray, E., "Development of an Acoustic Emission Test for FRP Equipment," Preprint 3583, ASCE Convention and Exposition, Boston, April 1979.

6. Mitchell, James R., "Fundamentals of Acoustic Emission and Application as an NDT Tool for FRP," 34th Annual Technocal Conference, Reinforced Plastics/Composites Institute, the Society of the Plastics Industry, Inc., New Orleans, January 1979.

7. Pollock, A. A., and Cook, W. J., "Acoustic Emission Testing of Aerial Devices," Southeastern Electric Exchange, Engineering and Operations Division, Annual Conference, New Orleans, April 1976.

8. Djiauw, Lie, J. Fesko, Donald G., "Fatigue Life Prediction in FRP by Acoustic Emission Analysis," Ford Motor Company, Plastics Development and Applications Office.

9. Brown, Thomas, S., and Mitchell, James, R., "Acoustic Emission Evaluation of Automotive Hybrid Composites and Attachments," 35th Annual Technical Conference, Reinforced Plastics/Composites Institute, The Society of the Plastics Industries, Inc., New Orleans, February 1980.

10. K. L. Reifsnider and W. W. Stinchcomb, "Investigation of Dynamic Heat Emission Patterns in Mechanical and Chemical Systems," Proc. of 2nd Biennial Infrared Information Exchange, AGA Corp., St. Louis, MO, pp. 45-58 (1974).

11. E. G. Henneke II, K. L. Reifsnider, and W. W. Stinchcomb, "Thermography - An NDI Method for Damage Detection," Journal of Metals, Vol. 31, pp. 11-15 (1979).

CORRELATION AND PREDICTION OF PROPAGATION
TIME-DELAYS ALONG EARTH-SPACE LINKS (U)

HAIM SOICHER, Ph.D.
COMMUNICATIONS SYSTEMS CENTER
US ARMY COMMUNICATIONS RESEARCH & DEVELOPMENT COMMAND
FORT MONMOUTH, NJ 07703

INTRODUCTION

High precision in radar detection, in earth-satellite orbit
determination, and in satellite navigation necessitates that the
signal data used be corrected for the errors imposed by the
ionosphere.[1] Signal time-delays, or equivalently range errors, are
always encountered in transionospheric measurements because the
electromagnetic propagation velocity in the medium is slightly less
than the free-space velocity. For frequencies at VHF and above, an
excess time delay is inversely proportional to the square of the
frequency and is directly proportional to the integrated electron
density along the propagation path (i.e., total electron content (TEC)
measured in units of el/m^2). Thus, if TEC is known, or is measured
in real time, a perfect correction to ranging can be performed. The
TEC may be measured in real time, provided the user has dual-frequency
capabilities. Since the ionosphere is a dispersive medium, the
relative time delays (or phase differences) between the two frequen-
cies may be used to eliminate the error introduced by the TEC.
However, substantial simplification in user equipment could be
realized if only one frequency were utilized. Time delays would then
be determined by forecasting techniques based on media models.
Because of the spatial and temporal variability of the ionospheric
electron density, the time-delay errors vary with geographic location,
target (or source) altitude, and time. For improved accuracy, the
forecasting techniques should be supported by periodic updating of
data (preferably in real-time) at specified locations. The question
arises as to the extent of the geographic area, surrounding a station
having real-time TEC-determination capabilities, within which TEC
values could be interpolated with acceptable accuracy. In ether

251

words, could TEC be determined at location A if a real-time measurement were taken at a different location B, and what would be the geographic constraints on A and B.

To this end, a specific investigation designed to determine the correlation (based on linear regression analysis) between TEC values at Fort Monmouth, NJ (40.18°N, 74.06°W) and at Richmond, FL (25.60°N 80.40°W), and between TEC values at Richmond, FL, and Anchorage, AK (61.04°N, 149.75°W) was undertaken. Beacon transmissions from geostationary satellites were used to determine the TEC at the stations by means of the Faraday rotation technique.

The subionospheric points for the Richmond-Fort Monmouth stations (i.e., the geographic locations where the ray paths to the ATS-6 Satellite [2,3] (located at 94°W) intersect a "mean" altitude of 420 km) were 36.5°N, 76.6°W and 23.6°N, 81.6°W, respectively. Thus, the "representative" TEC for the two stations was separated by $\sim 13^\circ$ in latitude and by $\sim 5^\circ$ in longitude (corresponding to a 20-minute difference in local time). The subionospheric points for the Richmond-Anchorage stations (monitoring the SMSI Satellite (located at 105°W), and the ATS-6 (located at 140°W),respectively) were 22.5°N, 82.7°W and 54.3°N, 147.3°W respectively. The "representative" TEC was separated by $\sim 31.8^\circ$ in latitude and $\sim 63.8^\circ$ in longitude (corresponding to a 4 hour 15 minute difference in local time).

THE DATA

The daily variations of vertical TEC measured by the Faraday technique for the representative month of February 1975 at Fort Monmouth and at Richmond are shown in Fig. 1. The equivalent ionospheric signal delay times normalized to a frequency of 1.6 GHz (in the satellite navigation frequency band) are also indicated in this figure. The normal diurnal variation of TEC is evident, as is its day-to-day variability.

Figure 2 indicates the variation of the maximum daily correlation of the Fort Monmouth-Richmond data pairs for September 1974 and January, February, March, April, and May 1975. These were arrived at by comparing the TEC daily data sets at Fort Monmouth and Richmond. At first, the correlation coefficient was calculated for identical UT times. Then, the Richmond data was shifted in time with respect to the Fort Monmouth data at 15-minute intervals in the forward (+) direction and in the backward (-) direction. Correlation coefficients are calculated for up to ten shifts in the forward and backward direction. The maximum correlation coefficient as well as the number of shifts for which the maximum correlation coefficient is attained
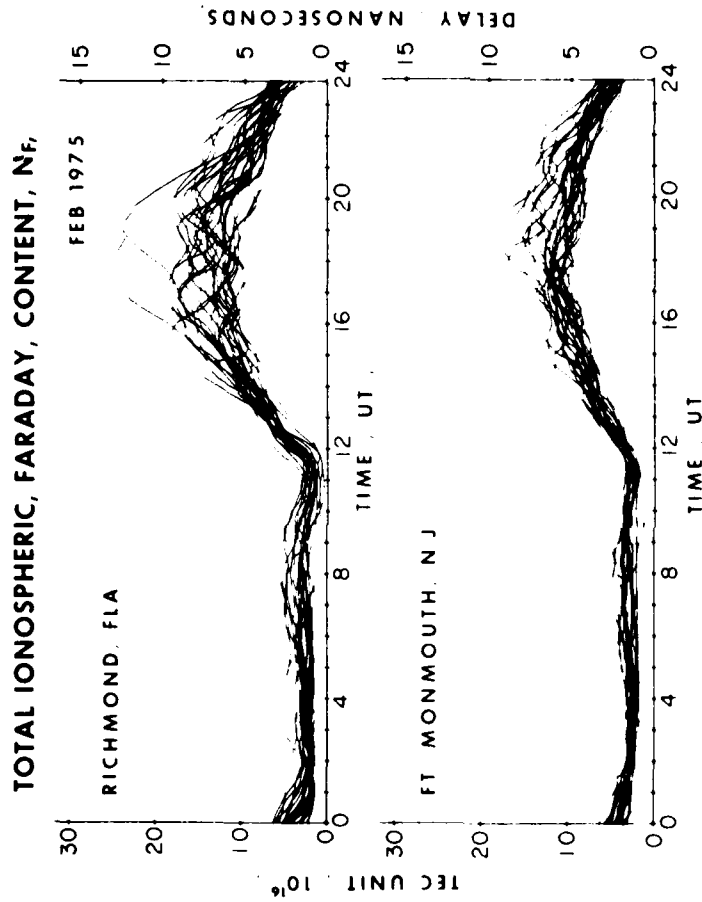
Figure 1: Total ionospheric (Faraday) electron content (N_F) at Fort Monmouth,NJ, and Richmond,FL, February 1975 (left ordinate: 1 TEC unit = 10^{16} el/m^2; right ordinate: time delay normalized to 1.6 GHz).
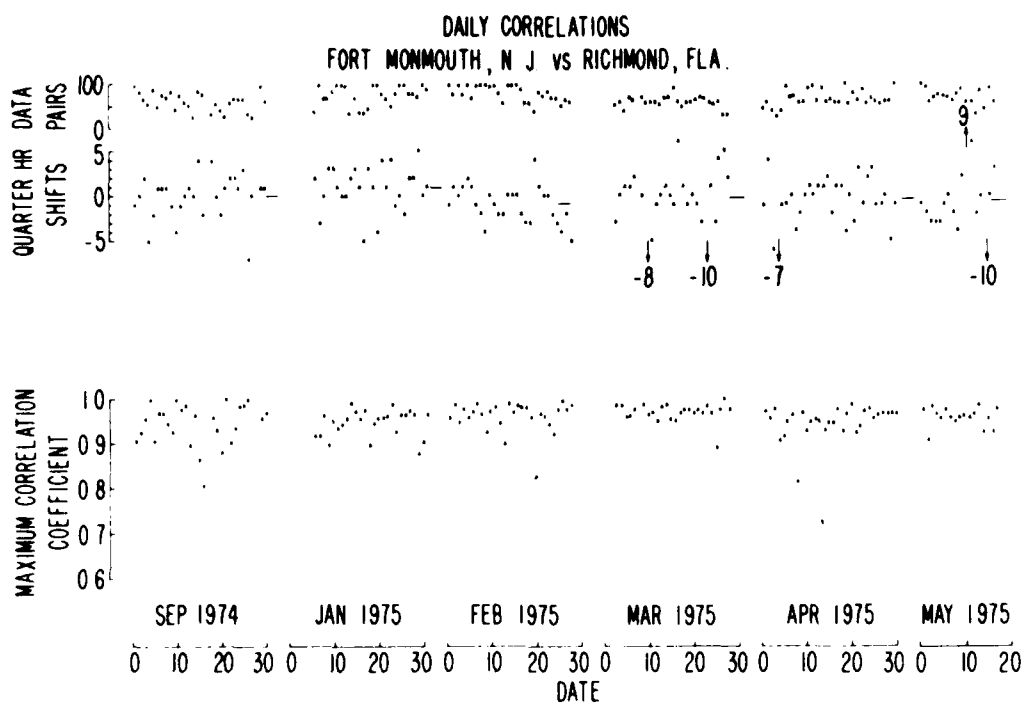
Figure 2: Variations of the maximum correlation coefficients of
the Fort Monmouth, NJ, and Richmond, FL, daily data sets.
Also indicated are the time shifts for which these were
attained, their averages (-), and the number of
data pairs used in analysis.

are indicated in the figure, as are the shifts' monthly averages. In addition, the number of data pairs available for the correlation analysis for each day (maximum of 96 data pairs, since the data is available at 15-minute intervals) is also shown in the figure.

In general, the correlation coefficients ranged between $\sim$ 0.9 and $\sim$ 1.0 with relatively few falling below 0.9. The lower values of the coefficients did not necessarily coincide with the sparsity of the available data. On the average, the coefficient was maximum for no shifts in September, for $\sim$ 1 shift in January, and for $>$ (-1) shift for the other months. While most maximum coefficients occurred for $\pm$1 hour shifting ($\pm$ 4 fifteen-minute shifts), shifts of two hours and more were observed occasionally.

Figure 3 indicates the variation of the maximum daily correlation coefficients of the Richmond-Anchorage data pairs for October, November and December 1976, arrived at in a similar manner as above except that the data sets were moved to correspond in local time (i.e., zero shifts correspond to identical local time).

In general, the coefficients ranged from $\sim$ 0.8 and $\sim$ 1.0 with relatively few falling below 0.8. The bulk of the coefficients was above 0.9, which was the range of the Richmond-Fort Monmouth data. The correlation coefficient was, on the average, higher in October, declined in November, and declined further in December. This was undoubtedly due to the sunrise and sunset times at both locales. In mid-October the sunrise and sunset times (at 400 Km) at the sub-ionospheric points differed by about 15 minutes, while in mid-December they differed by about 45 minutes. Thus, in December the shape of the diurnal variation was considerably different for the two locales than in October. The result is a decrease in the magnitude of the correlation coefficients. On the average, the coefficients were maxima at $\sim$ -5 shifts in October, no shifts for November, and $\sim$ -2 shifts for December.

The next phase of the investigation was the effort to determine whether it is possible to accurately predict TEC at one locale from TEC at the other, using average regression lines obtained for the corresponding data sets. The technique employed was as follows: Average monthly regression lines were computed. In one case, average slopes as well as average intercepts of the regression lines at monthly intervals were computed. In a second case, average slopes were computed while the intercepts were forced to pass through a common data point for the two sets at a specific predawn time for each day. Having determined the average regression lines, TEC at one locale was calculated for a given TEC at the corresponding other

255

DAILY CORRELATIONS
RICHMOND, FLA VS ANCHORAGE, AK
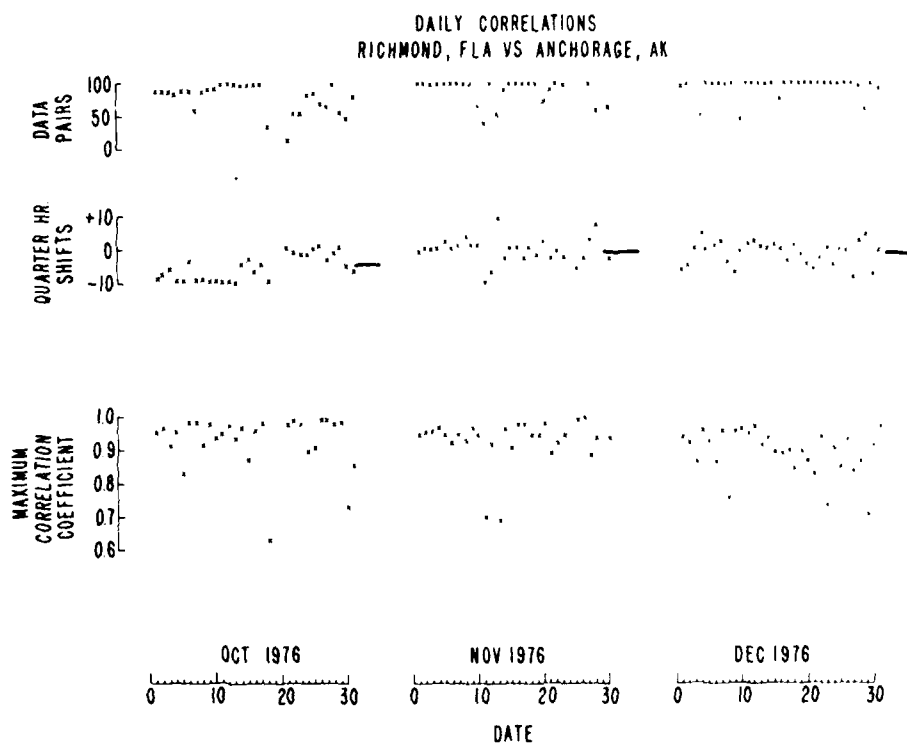
Figure 3: Variations of the maximum correlation coefficients
of the Richmond, FL, and Anchorage, AK, daily data
sets. Also indicated are the time shifts for which
these were attained, their averages (-), and the
number of data pairs used in analysis.

256

locale. The deviation (D_i) of the calculated TEC from its actual value at a particular time is then determined. This deviation, D_i, is then divided by σ_i, the monthly TEC standard deviation value at the same time. The average absolute value of this ratio, i.e., $|D|/\sigma$ was then computed for each day.

The results for the Fort Monmouth-Richmond data sets (i.e., predicting TEC at Richmond from TEC at Fort Monmouth) using average slopes and intercepts of the monthly regression lines are shown in Fig. 4. Also shown in the figure is the number of data pairs available for the analysis for each day (data is available at 15-minute intervals; ninety-six data points signify a full days data availability. Data is sometimes missing, due to turn-off of the satellite's beacons). The results using average slopes and intercepts of the monthly regression lines, but for the time period 1500-2100 UT, when the maximum diurnal TEC values occur are shown in Figure 5.

The results for the Richmond-Anchorage data sets (i.e., predicting TEC at Anchorage from TEC at Richmond for the same local time) using average slopes and intercepts of the monthly regression lines are shown in Fig. 6. The results using average slopes and intercepts of the monthly regression lines, but the time period 1500-2100 UT (for Richmond and the correspondingly shifted time for Anchorage), when the maximum diurnal TEC values occur are shown in Fig. 7.

DISCUSSION

As Fig. 4 indicates, the daily average of the ratios $\frac{|D|}{\sigma} = \frac{1}{N} \sum_{i=1}^{N} \frac{|D_i|}{\sigma_i}$ for Richmond is, for the most part, smaller than one, (i.e., on the average, the deviation of the computed Richmond TEC values from Fort Monmouth TEC values, is, in general, within the monthly standard deviation of the Richmond data). The diurnal behavior of the ratio is such that the ratio is higher during the night (when σ is small) than during the day. Some of the high values of this ratio are attributable to ionospheric effects during magnetically active periods, e.g., on September 15 and 18, 1974, large enhancement of TEC were observed in response to magnetic sudden commencements; on March 11, the K_p index ranged from 4^0 to 7^-. The results of the figure also indicate that the ratio appears larger during the equinoctial period (September, March) than during the winter and spring months. This is observed despite the fact that the standard deviation during the equinoctial months was considerably higher than during the other months. Calculations using the average slopes of the regression lines and forcing the lines to pass through actual common points at 0200 UT indicate that the ratio, in general, does not

257
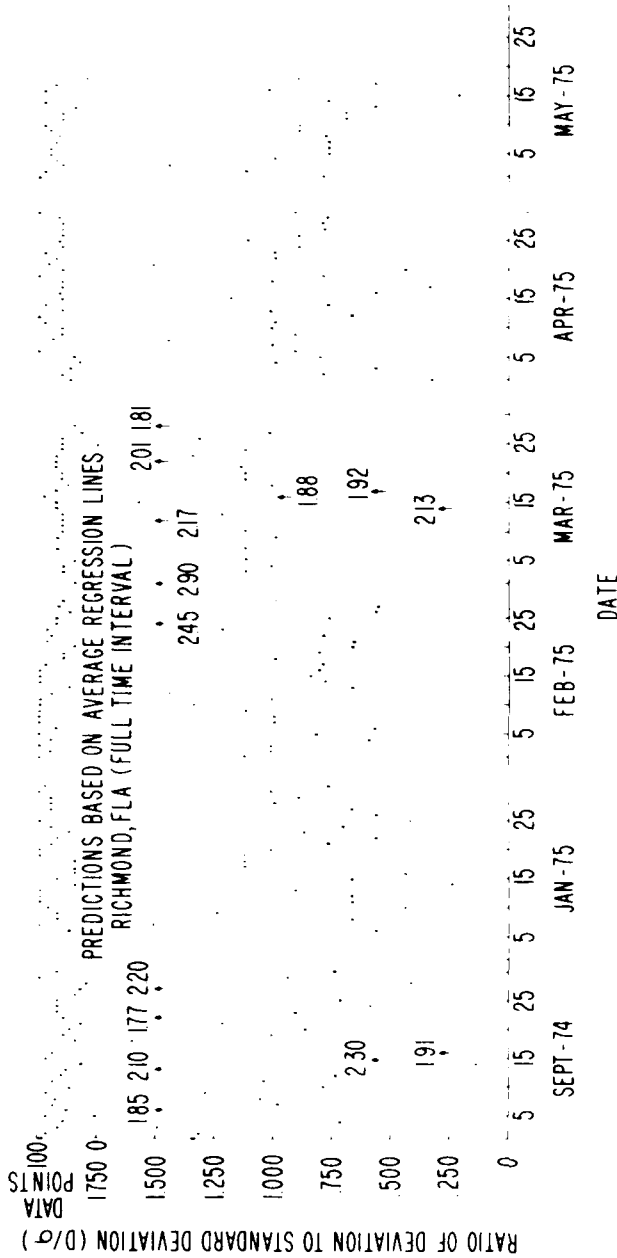
Figure 4: The variation of the ratio $|D|/\sigma$ for Richmond, FL, for the time period September 1974, and January 1975-May 1975 calculated for full diurnal periods by average regression lines obtained by Fort Monmouth,NJ-Richmond, FL, data sets. ($|D| \equiv$ diurnal average of the deviations of the computed TEC values from observed ones; $\sigma \equiv$ monthly standard deviation of the Richmond data). The arrows and the corresponding numerical values are for those values of the ratio which exceed the scale of the Figure. Also indicated in the upper portion of the Figure are the number of TEC data pairs at 15-minute intervals used in the analysis.

258
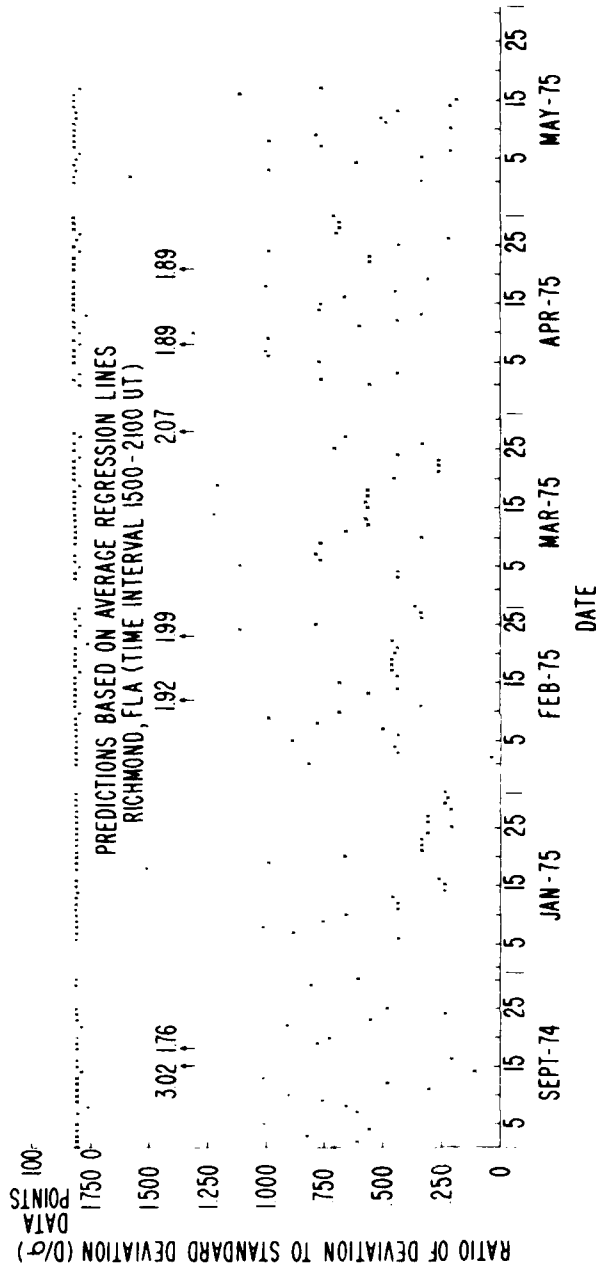
Figure 5: Same as 4, except that the ratios are computed only for the time period 1500-2100 UT.

259

PREDICTIONS BASED ON AVERAGE REGRESSION LINES

ANCHORAGE, ALASKA (FULL TIME INTERVAL)
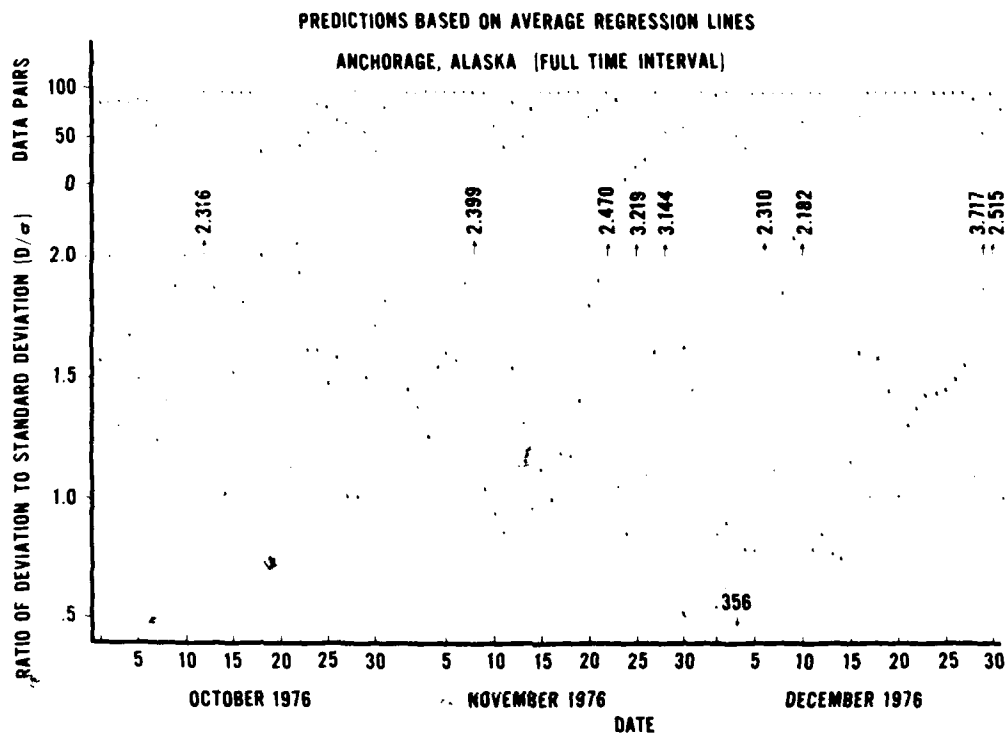
Figure 6: The variation of the ratio |D| /σ for Anchorage, AK, for the time period October 1976-December 1976, calculated for full diurnal periods by average regression lines obtained by Richmond, FL-Anchorage, AK data sets. (|D| = diurnal average of the deviations of the computed TEC values from observed ones; σ ≡ monthly standard deviations of the Anchorage data). The arrows and the corresponding numerical values are for those values of the ratio which exceed the scale of the Figure. Also indicated in the upper portion of the Figure are the number of TEC data pairs ι. 15-minute intervals used in the analysis.

Figure 7: Same as Figure 6, except that the ratios are computed only for the time period 1500-2100 UT (Richmond), and the correspondingly shifted Anchorage time period.

change substantially (as compared to the above case).

As Fig. 6 indicates, the daily average of the ratios $|D|$ /σ for Anchorage is for the most part, smaller than two, (i.e., on the average, the deviation of the computed Anchorage TEC values from the corresponding Richmond TEC values is, in general, within two standard deviations of the Anchorage data). As in the Fort Monmouth-Richmond data sets the diurnal behavior of the ratio is such that the ratio is higher during the night than during the day. In addition the figure indicates that the ratio is larger, on the average, in October than in the following two months. This occurs despite the fact that the coefficient was, on the average, higher in October, declined in November and declined further in December (due to changes in TEC diurnal shapes associated with changing separation in sunrise and sunset times at the two locales). As with the Fort Monmouth-Richmond case, the ratio here does not change substantially (as compared to the above case) when the average regression lines are forced to pass through the actual data points at the two locations at 0200 UT Richmond time (and the correspondingly shifted Anchorage time). The disadvantage of using this technique for possible operational application is, of course, the inavailability of any data points at the locale where the predictions are to be made.

Since the total signal time-delays are largest during the day and thus, introduce significant errors in navigation and radar systems, it is appropriate to examine the ratio $|D|$ /σ during the time when TEC is diurnally larger, i.e., between 1500 and 2100 UT (Richmond, Fort Monmouth times and corresponding Anchorage time).

For the Fort Monmouth-Richmond case Figure 5 indicates that the ratio $|D|$ /σ , obtained by average regression line for the day period, are substantially lower than the corresponding ratios for the full diurnal periods (Figure 4). This happens despite the fact that D is smaller during the night (although σ is also small compared to its day values). The fact that the bulk of the data indicates that the ratio falls below 1 is encouraging since both correlation methods yield "predicted" TEC values that fall within the monthly standard deviation of the data during the time period when the presence of TEC poses the source of largest error.

For the Richmond-Anchorage case a similar statement cannot be made. On the average, the ratio is not markedly different for the full time interval and for the time interval for maximum value of TEC.

CONCLUSIONS

The high correlation of signal time delay variation at two sets of locale separations, one widely separated by latitude, and the other widely separated by latitude and longitude (and hence by local time), prompted the examination as to whether time-delay data at one locale may be "predicted" if continuous corresponding data were available at the other locale. The correlation is high, in part, due to the 24 hour periodicity of the data. It is precisely this periodicity, however, that gives the "prediction" technique employed here its accuracy. The <u>variation</u> of the time delay is the highly correlatable quantity, and thus, the whole data set – if available – should be used in the prediction scheme.

Monthly average regression lines were used in the analysis. The slopes of the average monthly regression lines were within $\pm$ 20% from their average for the whole period. The intercepts of the monthly lines of regression were considerably more scattered.

For the two locales separated mainly in latitude (Fort Monmouth-Richmond) the deviation of the "predicted" data from the observed data was for the most part, within one standard deviation of the monthly data set. For daytime period, when the error introduced by the time-delay is greatest, the ratio $|D|/\sigma$ was even lower. When an average regression line for the entire period considered was calculated (i.e., the average of six monthly averages), the bulk of the "predicted" data was still within one standard deviation of the monthly data set. The ratio is often high during time periods characterized by ionospheric disturbances.

For the two locales widely separated by latitude and longitude (Richmond-Anchorage), the deviation of the "predicted" data from the observed data was, for the most part, within two standard deviations of the monthly data set. When an average regression line for the entire period was used, the bulk of the "predicted" data was still within the two standard deviations of the monthly data sets.

Since the monthly value of the standard deviation is $\sim$25% of the absolute value of the time delay, the method of prediction outlined here appears to have the capability of correcting the time delay due to the ionosphere to within $\sim$25% for stations separated in latitude, and $\sim$50% for stations widely separated in latitude and longitude.

REFERENCES

(1) H. Soicher, "Ionospheric and Plasmaspheric Effects in
     Satellite Navigation Systems", IEEE Trans. Antennas &
     Propagation, Vol. Ap-25, No. 5, Sep 77.

(2) K. Davies, R. B. Fritz, and T. B. Gray, "Measurement of
     Columnar Electron Contents of the Ionosphere and Plasmasphere",
     J. Geophysical Research, Vol. 81, p.16, June 1, 1976.

(3) H. Soicher, "The ATS-6 Radio Beacon Experiment", Nature,
     Vol. 253, pp.252-254, January 24, 1975.

RECENT RESEARCH ON PHOSPHORUS SMOKE (U)

EDWARD W. STUEBING, Ph.D.
ROBERT H. FRICKEL
GLENN O. RUBEL
CHEMICAL SYSTEMS LABORATORY, USAARRADCOM
ABERDEEN PROVING GROUND, MD   21010

I. INTRODUCTION

The optical extinction coefficients of phosphorus smokes in various regions of the spectrum are expected to depend on relative humidity due to the hygroscopic nature of the aerosol. They also depend on the amount of smoke (C-ℓ product) present. These are important problems for systems analysts who model the effectiveness of smoke munitions, and for scientists conducting field tests on smokes who measure the transmission through smoke clouds and use assumed extinction coefficients to calculate the amount of smoke present from Beer's law. The growth of smoke particles with increasing relative humidity changes their size distribution and their refractive indices, both of which alter the extinction cross sections (m^2/particle). In addition, the density of droplet material changes which causes further variation in the aerosol extinction coefficient (m^2/gram). This paper presents the results of a study of the dependence of visible, mid-IR, and far-IR extinction coefficients on relative humidity and includes consideration of non-Beer's law behavior of these extinction coefficients with (concentration) x (pathlength) product. The model used for relative humidity dependence assumes that the aerosol is composed of phosphoric acid for optical (refractive index) properties. The adequacy of this assumption is examined by comparison with experimental data on phosphorus smokes. The examination of deviations from Beer's law is based on actual phosphorus smoke extinction data and results in extinction coefficients for use in mid and far IR regions which should be satisfactory at relative humidities below 70%.

II. RELATIVE HUMIDITY CONTROLLED GROWTH OF PHOSPHORUS SMOKE

A model for the growth of phosphoric acid droplets due to dilution by condensation of water vapor as relative hujidity increases has been developed by Rubel[1], and its implications for relative humidity dependence of the optical properties of phosphoric acid aerosols have been examined by Frickel, et. al.[2]. The application of the results to phosphorus smoke is questionable because there exists conclusive evidence[3] that phosphorus smoke particles are not composed of pure phosphoric acid, and because the description used for the water vapor pressure over phosphoric acid solution was accurate for the relative humidity range 0.10-0.90, whereas the principle growth effects occurred at relative humidities above 0.90. Rubel has recently completed a new droplet growth model[4] which incorporates a modified description of droplet water vapor pressure (water activity) accurate to relative humidities of 0.99, and has treated the acid concentration as an unspecified mixture of acids (e.g. pyrophosphoric, metaphosphoric, and orthophosphoric acids) characterized by an association parameter, a, which reduces the concentration of solute ions available compared to a solution of orthophosphoric acid having the same acid weight fraction. By comparison to various experimental data Rubel[4] has found that values of a between 1.3 and 1.5 seem appropriate to phosphorus smoke particles. The value a=1.5 is used here because it represents the greatest variation from the previous[2] pure orthophosphoric acid (a = 1.0) model and therefore provides a "worst case" test of the errors in the simpler model of reference[2].

An analysis of the kinetics of the particle growth process[4] shows that for relative humidities below 95% the particles very rapidly reach equilibrium with their environment so that these results would be expected to apply to a real smoke in the open atmosphere. This model predicts that all particles in a polydispersion change size by a common factor when relative humidity changes. Consequently, if a log-normal aerosol size distribution characterized by a mass median diameter (MMD) and geometric standard deviation (σg) is subjected to a change in relative humidity, the new size distribution will remain log-normal and will have the same σg; however, the MMD will be shifted according to the common size change factor. In particular, the radius (r) of a particle at any relative humidity (Ψ) can be predicted from its size at $\Psi = 0$ (denoted r_0). This size shift is given by

$$r = f^{1/3}(\Psi) \; r_0 \tag{1}$$

where

$$f(\Psi) = \frac{a\rho_1 M_2 + x(M_1\rho_2 - a\rho_1 M_2)}{a \; \rho_1 M_2 (1-x)} \tag{2}$$

with

$$x = \begin{cases} \dfrac{2.152 - (0.655 - 0.632\Psi)^{\frac{1}{2}}}{2} & 0.75 \le \Psi \le 0.995 \\[12pt] 0.632 \cdot \cos\left[\dfrac{\cos^{-1}(1.175 - 1.928\Psi)}{3} + 240\right] + 0.803 & \\ \text{(degrees)} & 0.10 \le \Psi \le 0.75 \end{cases} \tag{3}$$

where ρ is density, M is molecular weight, and the subscripts are 1 for water and 2 for H_3PO_4: $M_1=18$; $M_2=98$, $\rho_1=1.0$, $\rho_2=1.87$. The parameter a describes the average degree of combination of the phosphate moiety in the acid mixture: a=1 corresponds to pure orthophosphoric acid, a=4 would apply to pure tetrametaphosphoric acid[4]. For this study the value a=1.5 was used as discussed above. The dilution of the drop with increasing relative humidity is given by

$$F = \frac{\rho_1\rho_2\left[M_1 x + aM_2(1-x)\right]}{a\rho_1 M_2 + x(M_1\rho_2 - aM_2\rho_1)} \tag{4}$$

where F is the weight fraction of acid in the drop. For calculations involving density of the smoke droplets, tabulated values[5] of the specific gravity of aqeous phosphoric acid solutions corresponding to acid weight fraction given by equation (4) were used, see Table I.

TABLE I. ACID CONCENTRATIONS WITH THEIR
CORRESPONDING RELATIVE HUMIDITIES FOR a=1.5,
AND SOLUTION DENSITY.

Weight Fraction Acid	Relative Humidity (a=1.5)	Density (g/cc)
0.05	1.00	1.025
0.10	0.99	1.053
0.20	0.97	1.112
0.40	0.90	1.254
0.50	0.82	1.335
0.65	0.64	1.475
0.75	0.44	1.570
0.95	0.16	1.630

Experiments have shown that log-normal distributions provide reasonable descriptions for phosphorus smokes. Therefore, once a size

267

distribution is established for pure acid drops* produced by the smoke munition, called hereafter the "primitive acid nucleus" distribution, then the actual aerosol size distribution achieved at relative humidity Ψ will be given by

$$\frac{d\ M}{Md\ln(d)} \quad (2\pi\ln(\sigma g))^{-\frac{1}{2}} \exp\left\{-[(\ln(d)) - \ln(f^{1/3}(\Psi)d_0)]^2/2\ln^2\sigma g\right\} \quad (5)$$

where M is the mass distribution function, d_0 is the mass median diameter of the distribution of primitive acid nuclei and σg is the geometric standard deviation of the distribution of primitive acid nuclei (and also of all distributions derived from it by hydration). The size distribution of smokes at various relative humidities then can be predicted provided d_0 and σg are determined from data taken at a time when significant distribution disturbing processes (e.g. coagulation, sedimentation) are absent.

III. SIZE DISTRIBUTION OF PRIMITIVE ACID NUCLEI PRODUCED BY PHORPHORUS MUNITIONS

Given size distribution data (d, σg) on any phosphorus smoke cloud and the relative humidity at which it was determined, equations (1)-(5) can be used to extrapolate back to the primitive acid nucleus distirbution for that cloud. If all phosphorus-based munitions produced identical smokes, then all such extrapolations would produce the same parameters d_0 and σg. A number of experimental measurements made on a variety of white phosphorus and red phosphorus munitions[6] are shown in Table II along with the extrapolated primitive acid nucleus distribution from each for a = 1.5.

The particle size measurements were made using an Anderson Impactor, and relative humidity was determined either by dew point hygrometer or gravimetric determination of water vapor collected on magnesium perchlorate. The data was selected from chamber experiments which met the following three conditions:

(1) Smoke concentrations were relatively low (<1.0 gm/m^3) to help insure that size distributions would not be pushed toward larger sizes by coagulation effects in smokes denser than expected in the field.

*These are conceptually the drops that would be formed if there was just enough water in the atmosphere to react chemically with the P_2O_5 to produce H_3PO_4 but no additional water for hydration or dilution. These drops probably do not exist physically; they merely provide a mathematical basis for calculating the size changes of true size distributions at relative humidities in the range of 10-99.5%.

TABLE II. EXPERIMENTALLY MEASURED PARTICLE SIZE
DISTRIBUTIONS FOR PHOSPHORUS SMOKES AND
THEIR PRIMITIVE ACID NUCLEUS DISTRIBUTIONS

| Case | EXPERIMENTAL DATA | | | Acid Nucleus* |
	MMD (μm)	σ_g	Relative Humidity	MMD (μm) $a=1.5$
1	0.72	1.44	0.37	0.62
2	0.69	1.48	0.23	0.62
3	0.69	1.40	0.16	0.63
4	0.75	1.44	0.34	0.65
5	0.77	1.47	0.12	0.71
6	0.86	1.51	0.51	0.71
7	0.87	1.43	0.22	0.78
8	0.91	1.46	0.20	0.82
9	0.93	1.44	0.17	0.85
10	1.02	1.45	0.19	0.92

*See text. The acid nucleus distribution has the same σ_g as the experimental data.

(2) The σg was in the vicinity of 1.4, a value known theoretically[7] to typify a "mature" log-normal distribution (in the sense that coagulation processes carry any log-normal distribution of $\sigma g \neq 1.4$ toward a distribution with $\sigma g = 1.4$).

(3) The relative humidity was not established artificially in the chamber by introducing water vapor. Therefore, the humidity in the laboratory matched closely that within the chamber for the selected experiments so there is no problem with size distribution data being distorted due to any sample changes on being removed for gravimetric analysis from a cloud of one humidity into a laboratory at a different humidity.

The results tabulated in Table II suggest that a σg slightly higher than 1.4 typifies phosphorus smokes; therefore, the value $\sigma g = 1.45$ was selected for this study. Because the mass median diameters for the primitive acid nucleus distributions appear to vary too widely to accept a single number as typical of phosphorus smoke, calculations were performed for three values: $d_0 = 0.60, 0.75, 0.90$.

IV. REFRACTIVE INDICES FOR PHOSPHORIC ACID

Refractive indices for phosphoric acid in the 3-5.5 μm and 7-12 μm regions of the infrared have been measured for a number of acid concentrations[8]. These were used for Mie calculations in which at each relative humidity the acid concentration of the drop is given by equation (4) and the size distribution by equation (9). The refractive

index in the visible was taken to be constant with respect to wave-length, and its variation with acid concentration was estimated from[9].

$$n = 1.333077 + 0.001999 \ w^{\frac{1}{2}} + 0.07155w + 0.0868841 \ w^{3/2}$$
$$- 0.2375104 \ w^2 + 0.3625678 \ w^{5/2} - 0.1669960 \ w^3 \tag{6}$$

where w is the weight fraction concentration of H_3PO_4 over the range $0 < w < 0.90$.

V. LIMITATIONS OF THE PHOSPHORUS SMOKE MODEL

Inaccuracies due to errors in the size distribution derived from Table II and in the visible refractive index from equation (6) have been examined by parametric calculations. The size distribution was varied over the full range of MMD's observed in Table II in the course of our calculations. It has a significant effect on the extinction coefficient and is therefore shown explicitly in the results section as an inherent range of variation in the extinction by phosphorus smoke. Exploratory calculations on the effects of varying σg were performed. The resulting variation in extinction is somewhat less significant than the MMD variation; hence the variation plotted in our results is a reasonable estimate of optical variation due to MMD and σg variation. The real part of the visible refractive index was varied about the value given in equation (6), which applies at the wavelength 0.546 μm, by a proportion similar to the variation with respect to wavelength in the visible of the refractive index of water. In addition, the effects of adding a complex component up to 10^4 times that of water was examined. The range of resulting uncertainty in the properties of phosphorus smoke was less than $\pm 1.0\%$. However, there remains a more fundamental limitation on the application of the model used here to phosphorus smokes. It is known[3] that during the period of tactical significance (say, 20 minutes after generation) that phosphorus smoke is not composed of phosphoric acid. The model used here relies on phosphoric acid data (e.g., H_2O vapor pressure vs solution concentration adjusted for combination of phosphates in the pyro and meta components of the mixture) for the growth properties of droplets and for the optical properties (refractive indices). The growth model has not yet been tested against phosphorus smoke, although such studies are presently underway[4]. For this study, sensitivity to errors in the growth model is reduced by using the same equations to extrapolate back to the primitive acid nucleus distribution from actual phosphorus smoke size distribution data as are used in running the distribution forward with increasing humidity, and by considering a fairly wide range of primitive size distributions. The optical model

has been examined in the infrared[3]; it gives a reasonably accurate
spectral curve in the 3-5.5 μm region, but is quite inadequate in the
7-12 μm region. Therefore, predicting the relative-humidity dependent
phosphorus smoke extinction at individual wavelengths from this study
would be perilous, particularly in the 7-12 μm region. Integrating
over wavelength to produce an overall extinction coefficient for the
region may produce a somewhat closer representation of the behavior of
phsophorus smoke; however, it is probably better to pay more attention
to the predicted trend in 7-12 μm extinction with relative humidity
than to its absolute value. As an aid to making an empirical ad-
justment by scaling the phosphoric acid extinction to the level of
phosphorus smoke extinction, the results of this model have been
compared with measurements made on phosphorus smoke at low relative
humidities. This comparison is discussed in Section 8.

VI. DEFINITION OF OVERALL EXTINCTION COEFFICIENTS FOR THE VISIBLE, MID-IR, AND FAR-IR

The problem of defining an overall extinction coefficient for
a smoke in each spectral region has been previously discussed with
respect to deviations from Beer's law[10]. The results showed that
effective extinction coefficients in a wavelength region $\Delta\lambda$, $\alpha_{eff}(\Delta\lambda)$,
were often dependent on the (concentration) x (pathlength) product.
This is especially true for phosphorus smokes in the 7-12 μm region.

The calculations used here follow those of reference[10]; they
have been extended to include the visible region. The measurement of
light transmission (T) through a smoke cloud is often used in field
experiments to infer the amount ($C \cdot \ell$ product) of the smoke in the
optical path. This inference is made using Beer's law:

$$T(\lambda) = \frac{I(\lambda)}{I_o(\lambda)} = e^{-\alpha(\lambda)C\ell} \tag{7}$$

where $I_o(\lambda)$ = the light intensity at wavelength λ measured by the
detector with no smoke in the path.

$I(\lambda)$ = the light intensity at wavelength λ measured by the
detector with smoke in the path.

$\alpha(\lambda)$ = the extinction coefficient (commonly m^2/gm) at
wavelength λ.

C = concentration (commonly gm/m^3).

ℓ = path length (commonly m).

271

The inference is generally valid provided the measurement is made at a single wavelength (e.g. a laser transmissometer) and the value of α is known for that wavelength, or if the transmission mwasurement is made over a wavelength band $(\Delta\lambda)$ provided that $\alpha(\lambda)$ is constant over the region $\Delta\lambda$. These conditions are usually well satisfied in the narrow band pass of a spectrophotometer. However, in some field measurements, broadband radiometers (e.g. 3-5.5 μm or 7-12 μm) are used for the transmission measurement. Beer's law does not generally apply in these cases with a single effective α (e.g. α_{eff} (7-12 μm)). Should one attempt to define such an effective α from the equation

$$T(\Delta\lambda) = e^{-\alpha_{eff}(\Delta\lambda) \, C\ell} \tag{8}$$

by measuring T under conditions of known $C\ell$ and solving for $\alpha_{eff}(\Delta\lambda)$, different values of $\alpha_{eff}(\Delta\lambda)$ would be found for different values of $C\ell$. This effect is most prominent in cases where $\alpha(\lambda)$ varies strongly over the region $\Delta\lambda$, and disappears as $\alpha(\lambda)$ becomes constant over the region $\Delta\lambda$.

The treatment of broadband transmission behavior in the infrared may be made analagously to the photometric treatment of broadband transmission in the visible with the following definitions: luminance, $L(\Delta\lambda)$, is the apparent brightness of the target; transmittance, $Tr(\Delta\lambda)$, is the ratio of luminance with smoke in the path to luminance without smoke and corresponds to the transmission in Beer's law. The governing equation is then:

$$Tr(\Delta\lambda) = \frac{L(\Delta\lambda)}{L_o(\Delta\lambda)} = \frac{\int_{\lambda_1}^{\lambda_2} S(\lambda) \, e^{-\alpha(\lambda)C\ell} D(\lambda) \, d\lambda}{\int_{\lambda_1}^{\lambda_2} S(\lambda) \, D(\lambda) \, d\lambda} \tag{9}$$

where $S(\lambda)$ = source signature as a function of wavelength.
       $D(\lambda)$ = the detector response curve as function of wavelength.

The denominator of equation (9), $L_o(\Delta\lambda)$, gives the original apparent brightness of the source as seen by the detector; the numerator, $L(\Delta\lambda)$, gives the reduced apparent brightness when a smoke characterized by $\alpha(\lambda)$, C, and ℓ intervenes. For the purpose of calculating $Tr(\Delta\lambda)$, it is only necessary to have relative curves for the source and detector.

The source functions, $S(\lambda)$, in the 3-5.5 and 7-12 μm regions are taken to be $300°$K blackbodies[10]; the visible source is the standard CIE-C (artificial daylight) function[11]. The detector response functions, $D(\lambda)$, in the 3-5.5 and 7-12 μm regions are those of typical

InSb and HgCdTe detectors[10]; the visible detector is the standard photopic observer[11].

VII. RESULTS

The particle growth model is shown in Figure 1 where the growth curves of the mass median diameters of each of the three primitive nuclei distributions is given. The acid concentrations for which refractive index data were available; and their corresponding relative humidities are shown in Table I. The computed extinction coefficients are unchanged from those previously reported[2]; however they are associated with changed values of relative humidity because the mixed-acids model requires somewhat higher relative humidities than does pure phosphoric acid in order to produce the same degree of droplet dilution, c.f. Table I.

Integrated extinction coefficients will depend on $C \cdot \ell$ product as well as relative humidity. For the visible and mid-IR, the $C \cdot \ell$ dependence is weak. In only a very few of the cases examined did the reduction in α_{eff} exceed 2% over the range $0.1 < C \cdot \ell < 20$. In the visible and mid-IR, the variation in α_{eff} due to uncertainty in the primitive acid nucleus size distribution far outweighs effects due to $C \cdot \ell$. However, in the far-IR there is a significant decrease in α_{eff} (7-12) with increasing $C \cdot \ell$ product at low and moderate relative humidities, which is significant in comparison with the effect of the uncertain size distributions. This is shown for three relative humidities in Figure 2.

Because of the Beer's law deviation problem with integrated extinction coefficients, in order to examine the effect of relative humidity on integrated extinction coefficients it is necessary to choose a value of $C \cdot \ell$ product. From the above discussion, it makes little difference in the visible and mid-IR which $C \cdot \ell$ is used. Therefore, the $C \cdot \ell$ for this study was selected to be one of interest to measurements in the far-IR. From Figure 2, the values of the $C \cdot \ell$ dependent α_{eff}'s are in the range 0.25-0.30; therefore a $C \cdot \ell = 5.0$ was chosen as this provides sufficient smoke to reduce transmission in the far-IR to 20-30%. The results for each spectral region are shown in Figures 3-5. The extinction coefficients in these figures are in the conventional units of m^2 per gram of aerosol material suspended. It is also of interest to examine the extinction coefficient in terms of mass of elemental phosphorus delivered by the munition and its dependence on relative humidity, Figures 6-8. These data are of value to systems analysts modeling smoke effects as they include the humidity dependence of the "yield factor". It can be seen from Figures 3-8 that although the extinction coefficient per unit mass of smoke

1.0

2.8   2.5

3.2   2.2

.30   2.0

1.1   1.8

1.25   1.4   1.6
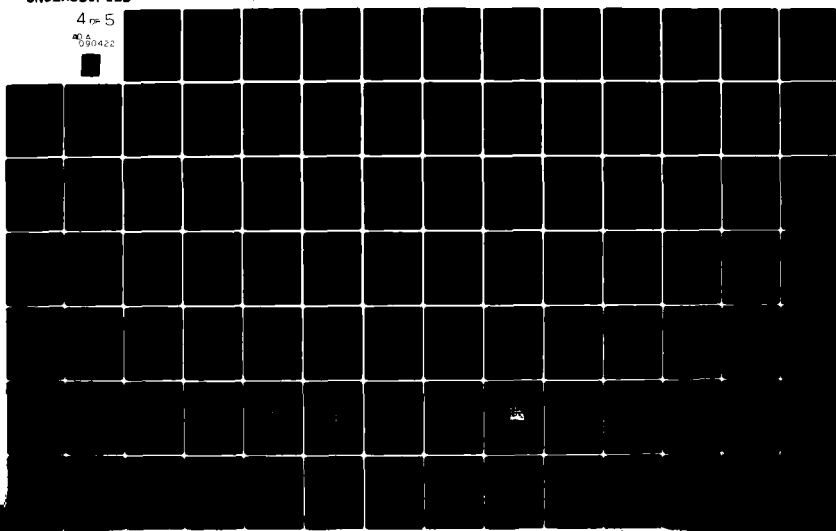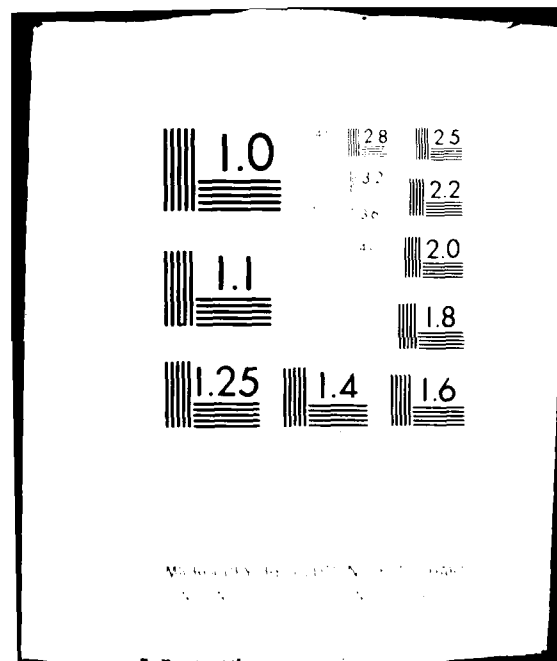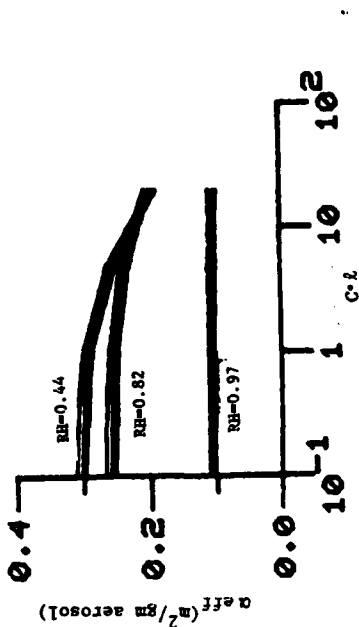
Figure 2. Variation of Far-IR Extinction Coefficient with C·ℓ Product for Phosphoric Acid Aerosol. At each relative humidity the region between the lines represents the expected range of variation due to particle size variations typical of phosphorus smokes (see text).
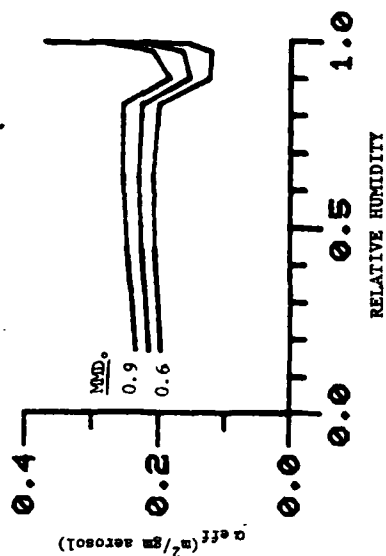
Figure 4. Mid-IR Extinction Coefficient for Phosphoric Acid Aerosol. The region between the lines represents the expected range of variation due to particle size variations typical of phosphorus smokes (see text).
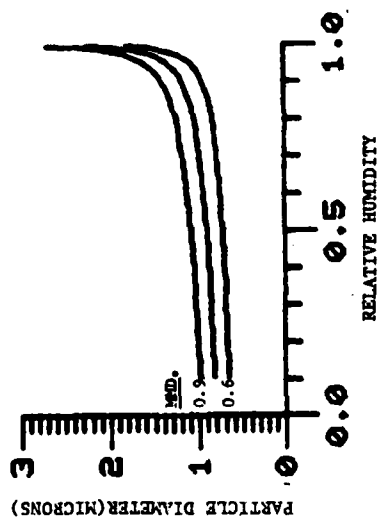
Figure 1. Growth of Mass Median Diameter (MMD) with increasing Relative Humidity for Primitive Acid Nuclei Distributions Having Initial MMD's (MMD$_o$) of 0.6, 0.75, and 0.90, using association parameter a = 1.5.
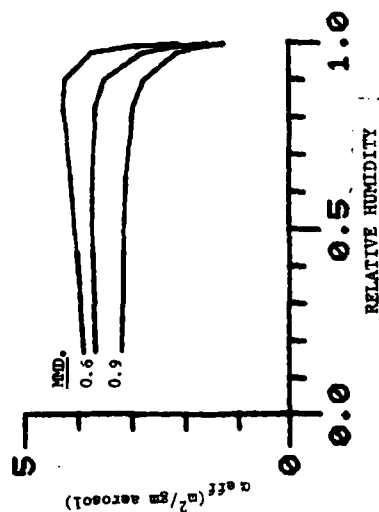
Figure 3. Visible Extinction Coefficient for Phosphoric Acid Aerosol. The region between the lines represents the expected range of variation due to particle size variations typical of phosphorus smokes (see text).

274
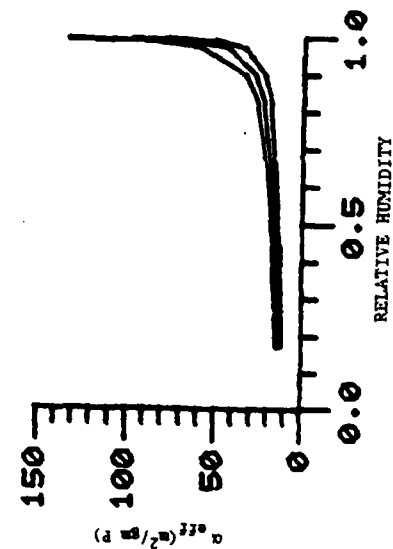
Figure 6. Visible Extinction Referred to Mass of Phosphorus in the Aerosol (c.f. fig. 3).

Figure 8. Far-IR Extinction Referred to Mass of Phosphorus in the Smoke (c.f. figure 5).

Figure 5. Far-IR Extinction Coefficient for Phosphoric Acid Aerosol. The region between the lines represents the expected range of variation due to particle size variations typical of phosphorus smokes (see text).
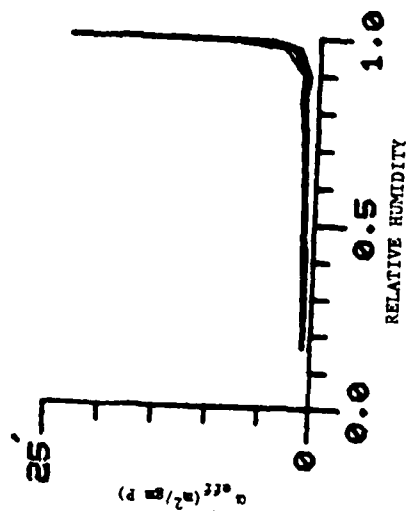
Figure 7. Mid-IR Extinction Referred to Mass of Phosphorus in the Aerosol (c.f. figure 4).

275

decreases with dilution (at about 80% relative humidity) the increase
of mass due to extraction of water from the atmosphere tends to
compensate for this, so that extinction per unit mass of airborne
phosphorus is relatively constant over most of the relative humidity
range, and increases dramatically for relative humidity greater than
0.9.

VIII. COMPARISON WITH PHOSPHORUS SMOKE DATA

Integrated extinction coefficients in the mid-IR and far-IR have
been computed from actual phosphorus smoke spectra[10]. The spectral
data used was averaged over several experiments conducted at different
relative humidities, all of which were below 70%. The present model
predicts little change in extinction coefficient for relative humidi-
ties between 10 and 70%; therefore, it is reasonable to use an α_{eff}
computed from spectra averaged over several relative humidities in
this range for comparison purposes. In the mid-IR the phosphorus
smoke data[10] give $\alpha_{eff}=0.25$, which is at the very top of the range
predicted by the present model in Figure 4. In the far-IR the phos-
phorus smoke data[10] gives $\alpha_{eff}=0.32$ for the $C \cdot \ell$ product value 5.0
used in Figure 5, which is approximately 20% higher than the value
given by the phosphoric acid optical model.

Systems analysts modeling smoke effects and scientists conducting
smoke field tests need working values for integrated extinction co-
efficients for phosphorus smoke. The results so far suggest that
Beer's law deviations are relatively important only in the far IR (7-
12 μm) region, and then only at low and moderate relative humidities,
c.f. Figure 2; over most of this range, relative humidity has
little effect, c.f. Figure 5. The experimental spectra of phosphorus
smokes for relative humidities below 70% have been used to examine
the $C \cdot \ell$ dependence of the far infrared extinction coefficient[10].
Data on smokes produced by both white phosphorus and red phosphorus
have been examined and are very nearly identical. Both may be treated
by the results given here, which are shown in Figure 9. If this change
in broadband extinction coefficient with $C \cdot \ell$ product is ignored for
phosphorus smokes in the 7-12μm window, quite serious errors could
occur. For example, with measured transmittance of 5% and the low $C \cdot \ell$
limit of $\alpha(\lambda)=0.37$ chosen as $\alpha_{eff}(\Delta\lambda)$, the $C \cdot \ell$ calculated in a field
experiment is in error by 30%.

In order to provide a means for correcting for these errors, equa-
tion (9) has been used to calculate the transmittance expected from
various $C \cdot \ell$ values and the results tabulated in Table III. The tables
cover transmittance down to 0.1% as the lower limit likely to be
achieved by a broadband transmissometer. The table can be entered

TABLE III. TRANSMITTANCE, $C \cdot l$ (gm/m²), AND ALPHA (m²/gm) VALUES FOR PHOSPHORUS SMOKE AGAINST A 300°K BLACKBODY TARGET IN THE 7 - 12 µM WINDOW

Trans	$C \cdot l$	Alpha	Trans	$C \cdot l$	Alpha	Trans	$C \cdot l$	Alpha
0.964	0.1	0.37	0.123	7.0	0.30	0.008	22.0	0.22
0.929	0.2	0.37	0.098	8.0	0.29	0.007	23.0	0.22
0.896	0.3	0.37	0.078	9.0	0.28	0.006	24.0	0.21
0.864	0.4	0.37	0.064	10.0	0.28	0.005	25.0	0.21
0.434	0.5	0.36	0.052	11.0	0.27	0.005	26.0	0.21
0.804	0.6	0.36	0.043	12.0	0.26	0.004	27.0	0.21
0.776	0.7	0.36	0.036	13.0	0.26	0.003	28.0	0.20
0.749	0.8	0.36	0.030	14.0	0.25	0.003	29.0	0.20
0.723	0.9	0.36	0.025	15.0	0.24	0.003	30.0	0.20
0.698	1.0	0.36	0.021	16.0	0.24	0.002	31.0	0.20
0.498	2.0	0.35	0.018	17.0	0.24	0.002	32.0	0.20
0.362	3.0	0.34	0.015	18.0	0.23	0.002	33.0	0.19
0.269	4.0	0.33	0.013	19.0	0.23	0.001	34.0	0.19
0.204	5.0	0.32	0.011	20.0	0.22	0.001	35.0	0.19
0.157	6.0	0.31	0.010	21.0	0.21	0.001	36.0	0.19

TABLE IV. EFFECTIVE EXTINCTION COEFFICIENTS FOR PHOSPHORUS SMOKES

Window Region	α_{eff}		Applicable Range	
		$C \cdot l$ (gm/m²)	Transmittance in Window	
1-5.5	0.25	0-30	0.001 - 1.0	
7-12	0.35	0-2	0.5 - 1.0	
	0.32	2-8	0.1 - 0.5	
	0.25	8-20	0.01 - 0.1	
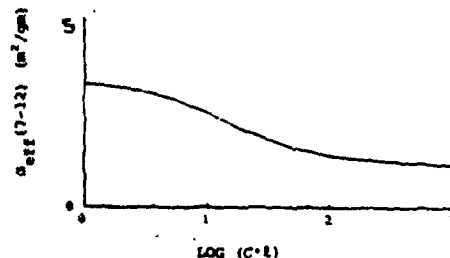
Figure 9. Variation in Effective Extinction Coefficient with $C \cdot l$ Product in the Far-IR for Phosphorus Smoke.

with the observed transmittance and the corresponding $C \cdot l$ product read out. The numerical values of the "effective α's" are also tabulated. Although the detector response curves are quite generally typical, as are the smoke extinction curves, the source curves used in generating these tables are for a 300°K blackbody. In some experiments sources of quite different spectral characteristics are employed, in which cases these calculations should be repeated.

IX. CONCLUSIONS

1. A model for the expected range of particle size distribution expected in phosphorus smokes and their variation with relative humidity has been proposed: Figure 1.

2. Using these size distributions and optical constants for appropriate dilutions of phosphoric acid, estimates of the integrated extinction coefficients in the visible, mid-IR, and far-IR were computed as functions of relative humidity: Figures 3-5.

3. These estimates were tested against a small amount of phosphorus smoke data in the mid- and far-IR. They appear reasonably close in the mid-IR and low by 20-25% in the far-IR where phosphoric acid optical constants are known to poorly represent phosphorus smoke[3]. The smoke data used for comparison did not address variation with relative humidity.

4. The model predicts trends in α_{eff} with relative humidity in each

spectral region. The extinction coefficients remain relatively constant in each region for relative humidities below 70%. The trends above 70% in each region could serve in the design of experiments on phosphorus smokes. The trends in extinction coefficients shown in Figures 3-5 all indicate a decrease above 80% relative humidity; it should be kept in mind that the suspended mass of the particles increases due to extraction of additional water from the atmosphere so that any given cloud does not become significantly less opaque with increasing relative humidity and increases greatly in opaqueness at humidities above 90%, as shown in Figures 6-8.

5. Although Beer's law does not apply generally for broadband extinction effects, it is often a reasonably good approximation. In such cases an effective extinction coefficient, $\alpha_{eff}(\Delta\lambda)$, can be defined for a given window region. For phosphorus smoke these values and the $C \cdot \ell$ range over which they can be reasonably used are shown in Table IV.

REFERENCES

1. G. O. Rubel, An Aerosol Kinetic Model for the Condensational Growth of a Phosphorus Smoke (U), Proceedings of the Smoke/Obscurants Symposium III, Vol. II, Techncial Report DRCPM-SMK-T-002-79, APG, MD, pg 729 (1979). CONFIDENTIAL

2. R. H. Frickel, G. O. Rubel, and E. W. Stuebing: Relative Humidity Dependence of the Infrared Extinction by Aerosol Clouds of Phosphoric Acid (U) , Proceedings of Smoke/Obscurants Symposium III, Vol. II, Technical Report DRCPM-SMK-T-002-79 , APG, MD, pg 517 (1979). CONFIDENTIAL.

3. M. E. Milham, D. H. Anderson, R. H. Frickel, and T. L. Tarnove, New Findings on the Nature of WP/RP Smokes , ARCSL-TR-77067, Chemical Systems Laboratory, APG, MD (1977). ADB-020554.

4. G. O. Rubel, Droplet Growth in a Phosphorus Smoke, CSL Technical Report, APG, MD (1980).

5. Chemical Rubber Company, Handbook of Chemistry and Physics.

6. D. Anderson, Chemical Systems Laboratory, APG, MD. Private Communication.

7. G. C. Lindauer, and A. W. Castleman. Initial Size Distribution of Aerosols, Nucl. Sci and Eng. 43, 212 (1971). E. R. Cohen and E. U. Vaughn, Approximate Solution to the Equations for Aerosol Agglomeration, J. Coll. and Interface Sci. 35, 612 (1971).

8. M. R. Querry and I. L. Tyler, Complex Refractive Indices in the Infrared for H_3PO_4 in Water, J. Opt. Soc. Am. 68, 1404 (1978).

9. O. W. Edwards, R. L. Dunn, and J. D. Hatfield, Refractive Index of Phosphoric Acid Solutions at $25^{\circ}C$, J. of Chem. and Engr. Data I, 508 (1964).

10. E. W. Stuebing, Deviations from Beer's Law Which Sometimes Prevent Defining a Single Overall Extinction Coefficient for a Smoke in Each Atmospheric Window, Proceedings of the Smoke Symposium II, DRCPM-SMK-T-004-78, Office of the Project Manager for Smoke/Obscurants, Aberdeen Proving Ground, MD (1978).

11. L. A. Riggs, "Light as a Stimulus for Vision", in Vision and Visual Perception, C. H. Graham, ed., John Wiley & Sons, Inc, N.Y., NY (1965).

COMPUTATIONAL PARAMETRIC STUDY OF THE AERODYNAMICS OF SPINNING SLENDER BODIES AT SUPERSONIC SPEEDS

WALTER B. STUREK, PhD, DONALD C. MYLIN, Mr.,
and CLARENCE C. BUSH, Mr.
U.S. Army Ballistic Research Laboratory
Aberdeen Proving Ground, Maryland 21005

I. INTRODUCTION

Recent trends in projectile design have led to shapes with greater length and more slender ogives. Unexpected flight stability problems have been encountered due to decreased aerodynamic stability of these new shapes. Clearly, conventional aerodynamic predictive capabilities were not adequate. In an effort to avoid these problems in the future, the Ballistic Research Laboratory has been developing advanced numerical computational techniques for computing projectile aerodynamic characteristics to improve shell design technology.

Substantial progress has been made in the past 10 years in the development of aerodynamic computational techniques and in the availability of high speed digital computers. This progress has made it possible to begin to use advanced finite-difference computational techniques to perform parametric aerodynamic studies for evaluation of proposed design concepts.

The use of advanced numerical computational techniques for a parametric study is difficult to justify to compute only static aerodynamic parameters since cheaper, less complex techniques such as Ref. (1), (2) and (3) are available. However, if dynamic derivatives such as Magnus and pitch damping are considered important and if viscous drag is of interest, then the advanced computation techniques are justified and, in fact, must be used. This paper reports the initial results of an ongoing research effort at BRL to form an advanced aerodynamic computation capability that will provide the shell designer with a complete package of static and dynamic aerodynamic coefficients for use in design studies.

281

II. COMPUTATIONAL TECHNIQUES

Scope of Effort

Three dimensional finite-difference flow field computational techniques for inviscid and turbulent viscous flow have been applied to generate a comprehensive set of aerodynamic coefficients for cone-cylinder (CC), tangent-ogive-cylinder (TOC), and secant-ogive-cylinder (SOC) body configurations. The model geometries considered in this study are shown in Figure 1. Body lengths up to seven calibers and ogive lengths of two, three, and four calibers have been considered. The aerodynamic coefficients computed are pitching moment, normal force, center of pressure, Magnus moment, Magnus force, Magnus center of pressure, form and viscous drag, roll damping and pitch damping. The sign convention for the pitch plane and Magnus forces is shown in Figure 2. All aerodynamic coefficients are computed in a conceptually exact manner. The only empirical input is that required for the modeling of turbulent eddy viscosity.

Figure 1. Model Geometries

The computations have been carried out for a Mach number range of $1.75 \leqslant M \leqslant 5$. These computations were all performed for an angle of attack of $1°$, a nondimensional spin rate (PD/V) of 0.19, and for sea level atmospheric free-stream conditions. Specific comparisons to wind tunnel data were made for the tunnel operating conditions.
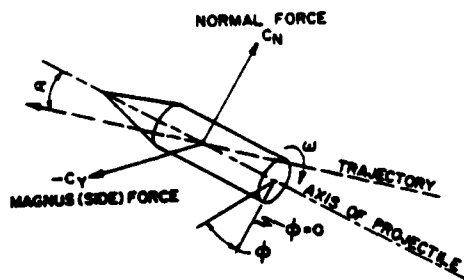
Figure 2. Magnus and Normal Forces on Spinning Projectile

282

Coupled Inviscid-Viscous Computations

The sequence of computations which are run in order to compute the static aerodynamic parameters, including turbulent viscous effects, is shown in Figure 3. Each block represents a separate computer code. These codes have been combined using the overlay technique on the BRL Cyber computer. The two main codes are those which compute three dimensional turbulent boundary layer development and three dimensional inviscid flow.

The computation of the effects of viscosity is of crucial importance when such parameters as roll damping, Magnus, and drag are of interest. The technique employed here is a fully implicit, finite difference numerical scheme developed by Dwyer[4]. This technique takes into consideration the changes in direction of the cross-flow velocity that occur on the side of the shell where the inviscid cross-flow opposes the surface spin.

The equations solved are the basic equations defining the three-dimensional compressible, turbulent boundary-layer flow over a body of revolution described by the relation $r = r(x)$. The coordinate system is shown in Figure 4.

Figure 3. Sequence of Computations
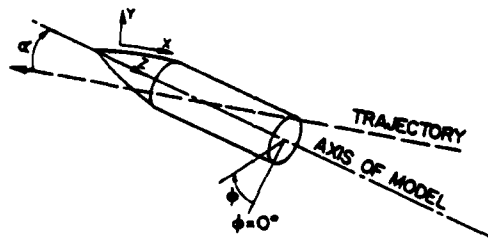
Figure 4. Coordinate System

283

Continuity

$$\frac{\partial}{\partial x} (r\bar{\rho}\bar{u}) + \frac{\partial}{\partial y} (r\bar{\rho}v) + \frac{\partial}{\partial \phi} (\bar{\rho}\bar{w}) = 0 \tag{1}$$

x momentum

$$\bar{\rho}\left[\bar{u}\frac{\partial \bar{u}}{\partial x} + \hat{v}\frac{\partial \bar{u}}{\partial y} + \frac{\bar{w}}{r}\frac{\partial \bar{u}}{\partial \phi} - \frac{\bar{w}^2}{r}\frac{\partial r}{\partial x}\right] = -\frac{\partial \bar{p}_e}{\partial x} + \frac{\partial}{\partial y}\left[\mu\frac{\partial \bar{u}}{\partial y} - \overline{\rho u'v'}\right] \tag{2}$$

ϕ momentum

$$\bar{\rho}\left[\bar{u}\frac{\partial \bar{w}}{\partial x} + \hat{v}\frac{\partial \bar{w}}{\partial y} + \frac{\bar{w}}{r}\frac{\partial \bar{w}}{\partial \phi} + \frac{\bar{u}\bar{w}}{r}\frac{\partial r}{\partial x}\right] = -\frac{1}{r}\frac{\partial \bar{p}_e}{\partial \phi} + \frac{\partial}{\partial y}\left[\mu\frac{\partial \bar{w}}{\partial y} - \overline{\rho v'w'}\right] \tag{3}$$

Energy

$$\bar{\rho}\left[\bar{u}\frac{\partial \bar{h}}{\partial x} + \hat{v}\frac{\partial \bar{h}}{\partial y} + \frac{\bar{w}}{r}\frac{\partial \bar{h}}{\partial \phi}\right] = \bar{u}\frac{\partial \bar{p}_e}{\partial x} + \frac{\bar{w}}{r}\frac{\partial \bar{p}_e}{\partial \phi} + \mu\left[\left(\frac{\partial \bar{u}}{\partial y}\right)^2 + \left(\frac{\partial \bar{w}}{\partial y}\right)^2\right]$$
$$- \overline{\rho u'v'}\frac{\partial \bar{u}}{\partial y} - \overline{\rho v'w'}\frac{\partial \bar{w}}{\partial y} + \frac{\partial}{\partial y}\left[\frac{\mu}{Pr}\frac{\partial \bar{h}}{\partial y} - \overline{\rho v'h'}\right] \tag{4}$$

where $\hat{v} = \bar{v} + \overline{\rho'v'}/\bar{\rho}$ and the bar indicates a time-averaged quantity.

In order to obtain closure of this system of equations, the following models of the turbulence terms have been introduced:

Turbulent shear stress

$$- \overline{\rho u'v'} = - \overline{\rho v'w'} = \bar{\rho}\ell^2\left[\left(\frac{\partial \bar{u}}{\partial y}\right)^2 + \left(\frac{\partial \bar{w}}{\partial y}\right)^2\right] = \epsilon\left[\left(\frac{\partial \bar{u}}{\partial y}\right)^2 + \left(\frac{\partial \bar{w}}{\partial y}\right)^2\right]^{\frac{1}{2}}$$

where ϵ is introduced as the turbulent viscosity and the mixing length, $\ell = 0.09 \, \delta\tanh[(0.4/0.09)(y/\delta)]$. Van Driest damping is used to account for the effect of the laminar sublayer.

Turbulent heat transfer

$$- \overline{\rho v'h'} = \frac{k_t}{c_p}\frac{\partial \bar{h}}{\partial y}$$

The turbulent Prandtl number is introduced as

$$Pr_t = c_p\epsilon/k_t = 0.90$$

The three-dimensional displacement surface is not merely the vector sum of the longitudinal and circumferential components of the boundary-layer displacement thickness. Instead, the differential equation derived by Moore[5]:

$$\frac{\partial}{\partial x} \left[\rho_e u_e r (\delta^*_{3\text{-}D} - \delta^*_x) \right] + \frac{\partial}{\partial \phi} \left[\rho_e w_e (\delta^*_{3\text{-}D} - \delta^*_\phi) \right] = 0 \tag{5}$$

must be solved for $\delta^*_{3\text{-}D}$, the three-dimensional boundary-layer displacement thickness where

$$\delta^*_x = \int_0^\delta \left(1 - \frac{\rho u}{\rho_e u_e} \right) dy \qquad\qquad \delta^*_\phi = \int_0^\delta \left(1 - \frac{\rho w}{\rho_e w_e} \right) dy$$

With a body fixed coordinate system, the gas dynamic equations for inviscid flow can be written as

$$E_z + F_r + G_\phi + H = 0 \tag{6}$$

where the flux vectors E, F, G, and H are

$$E = \begin{bmatrix} \rho u \\ \rho u^2 + p \\ \rho uv \\ \rho uw \end{bmatrix} \qquad F = \begin{bmatrix} \rho v \\ \rho uv \\ \rho v^2 + p \\ \rho vw \end{bmatrix} \qquad G = \frac{1}{r} \begin{bmatrix} \rho w \\ \rho uw \\ \rho vw \\ \rho w^2 + p \end{bmatrix} \qquad H = \begin{bmatrix} \rho v \\ \rho uv \\ \rho(v^2 - w^2) \\ 2\rho vw \end{bmatrix}$$

These equations are solved using MacCormack's[6] two-step, predictor-corrector finite difference scheme. The unique feature of the program used here, which was developed by Sanders[7] for the Magnus problem, is that the flow field is computed about an axisymmetric model plus displacement surface. Due to the distortion of the viscous layer caused by interaction of the surface spin, the effective aerodynamic shape has no plane of symmetry.

The flow field variables resulting from these computation steps have been developed to yield the following aerodynamic coefficients--pitching moment, normal force, center of pressure, Magnus force, Magnus moment, Magnus center of pressure, form drag, viscous drag, and roll damping. The computational time for a single body configuration and flow field condition is approximately ten minutes on a CDC 7600 computer.

285

Coning Motion Computations

In order to compute the effective pitch damping, the technique developed by Schiff[8] is used. This computational technique relates the side force on a body undergoing a coning motion about the CG location to the pitch damping $(C_{M_q} + C_{M_{\dot\alpha}})$, see Figure 5.
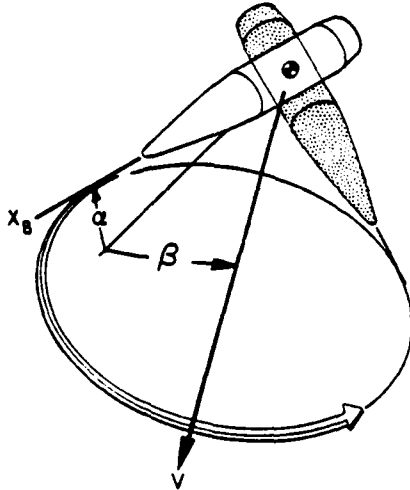
The numerical technique is MacCormack's[6] predictor-corrector, explicit marching scheme. This computation involves the solution of the Euler equations including terms for Coriolis $(2\rho\times\bar\Omega\times\bar v)$ and centrifugal $[\rho\bar\Omega\times(\bar\Omega\times\bar r)]$ forces in a body fixed coordinate system. For this case, the H vector in equation 6 becomes

Figure 5. Coning Motion About Center of Gravity

$$
H = \frac{1}{r}
\begin{bmatrix}
\rho v \\
\rho uv + \rho r[2(\omega_2 w - \omega_3 v) + \omega_1 \omega_2 r - x(\omega_2^2 + \omega_3^2)] \\
\rho(v^2 - w^2) + \rho r[2(\omega_3 u - \omega_1 w) + \omega_1 \omega_2 x - r(\omega_1^2 + \omega_3^2)] \\
2\rho vw + \rho r[2(\omega_1 v - \omega_2 u) + \omega_3(\omega_2 r + \omega_1 s)]
\end{bmatrix}
$$

where ω_1, ω_2, and ω_3 are the components of the angular velocity vector $\dot\theta$ resolved in the z, r, and ϕ directions, respectively.

For the case of a steady coning motion, the flow field is time-invariant in the body-fixed coordinate system. The effective pitch damping $(C_{M_q} + C_{M_{\dot\alpha}})$ is determined using the relation

$$C_{Y_{\dot{\theta}}} \approx \sin\sigma (C_{M_q} + C_{M_{\dot{\alpha}}}) \tag{7}$$

where $C_{Y_{\dot{\theta}}}$ = side force at coning rate $\dot{\theta}$ and effective angle of attack σ, which is valid for small values of σ and $\dot{\theta}$. Thus a dynamic aerodynamic parameter is determined using a steady flow field computation. This is a potentially very useful tool for the exterior ballistician. The computation time is approximately 90 seconds on a CDC 7600 computer for the body configurations in this study.

III. RESULTS

Comparisons to Experiment

Detailed comparisons of the computations to experimental data for turbulent boundary layer profile characteristics, wall pressure measurements and Magnus force are reported in Ref. (9). Comparisons shown here will be limited to the aerodynamic coefficients of interest.

Examples of comparisons of the computed results to experimental data are presented in Figures 6 through 10. The comparisons for pitch plane static parameters shown in Figures 6, 7 and 8 indicate excellent agreement. The limited comparison for Magnus in Figure 9 indicates acceptable agreement if allowance is made for the small magnitude of the Magnus effect and the variance between the wind tunnel and range experimental measurements. A comparison between computation and experiment for pitch damping is shown in Figure 10. The experimental point, which is for an L/D of 5.12 and cone angle of 9.52°, shows excellent agreement with the trend of the computed results. In general, it is felt that the numerical computations do provide an accuracy for the aerodynamic coefficients that is within the uncertainty of our ability to determine these coefficients experimentally. However, it is felt that a broader scope of comparison for the aerodynamic coefficients between experiment and computation is of interest and increased effort to accomplish this is underway.

SOC LN = 2
C.G. AT 0.6L BEHIND NOSE

⊙ W.T. (L/D = 5)
☐ W.T. (L/D = 7)
△ RANGE (L/D = 5)
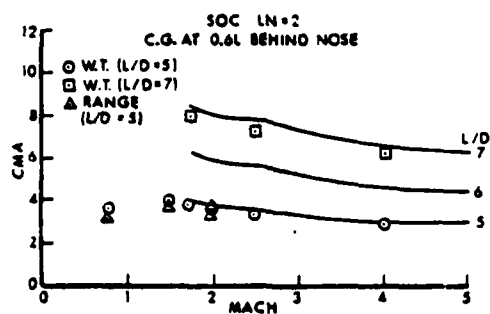
Figure 6. Pitching Moment, Comparison with Experiment

SOC, LN = 2
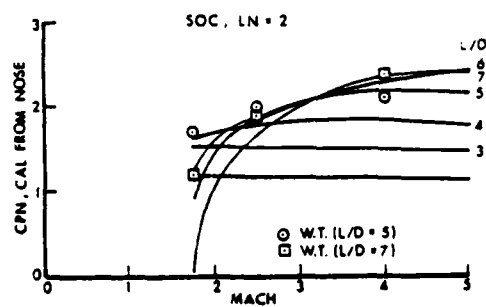
Figure 7. Center of Pressure, Comparison with Experiment

⊙ W.T. (L/D = 5)
☐ W.T. (L/D = 7)

SOC, LN = 2

⊙ W.T. (L/D = 5)
☐ W.T. (L/D = 7)
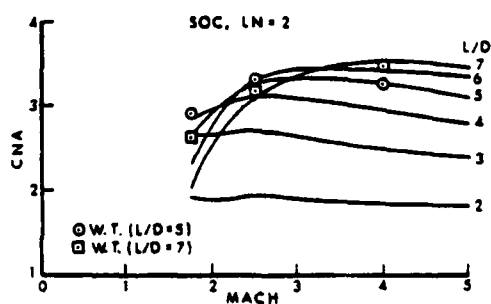
Figure 8. Normal Force, Comparison with Experiment

SOC, L/D = 5
C.G. AT 0.6L BEHIND NOSE

+ W.T (LN = 2)
⊙ RANGE (LN = 2)
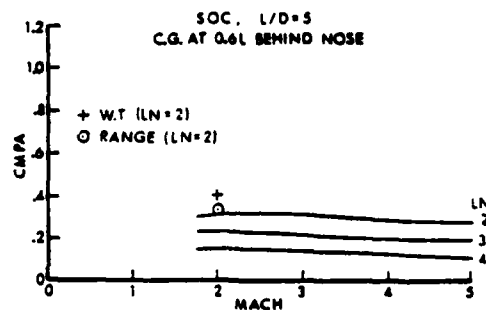
Figure 9. Magnus Moment, Comparison with Experiment

10°CC, LN = 2.84
C.G. AT 0.6L BEHIND NOSE

⊙ RANGE (L/D = 5)
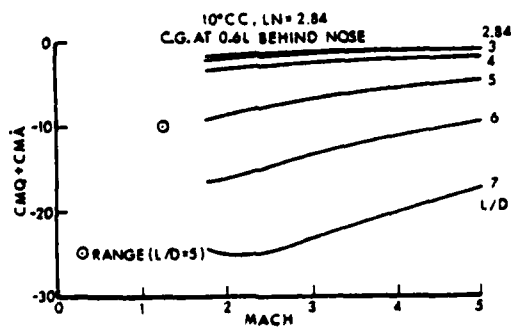
Figure 10. Pitch Damping, Comparison with Experiment

288

Parametric Comparisons

Examples illustrating the parametric results are shown in
Figures 11 through 26. The series of comparisons shown in Figures 11
through 20 illustrates an example for each aerodynamic coefficient
computed in this study. The case chosen is the SOC model for a total
length of six calibers and for ogive lengths of two, three, and four
calibers. The aerodynamic coefficients are plotted versus Mach number
for atmospheric free stream launch conditions assuming an adiabatic
wall temperature boundary condition. These comparisons show, for a
fixed body length, that configurations with long slender ogives have
reduced pitch damping, less drag, and a reduced Magnus moment compared
to bodies with shorter ogive lengths.
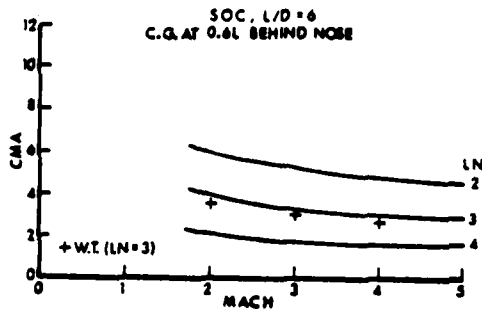
Figure 11. Pitching Moment, Parametric
Comparison, SOC, L/D = 6
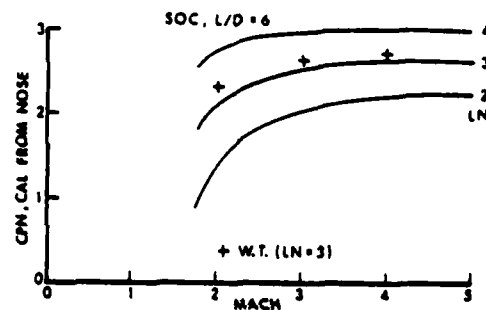
Figure 12. Center of Pressure, Parametric
Comparison, SOC, L/D = 6
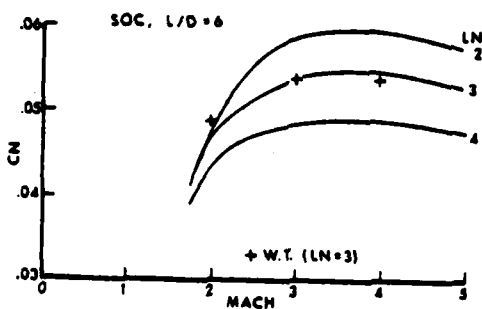
Figure 13. Normal Force, Parametric
Comparison, SOC, L/D = 6
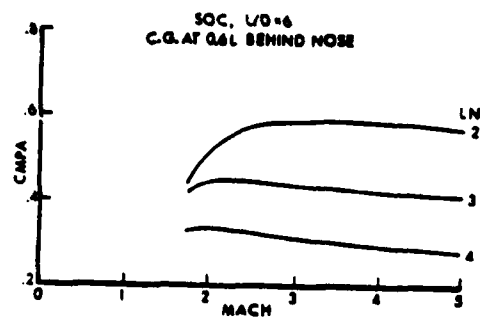
Figure 14. Magnus Moment, Parametric
Comparison, SOC, L/D = 6

289
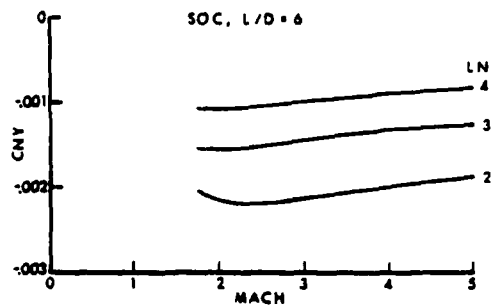
Figure 15. Magnus Force, Parametric Comparison, SOC, L/D = 6
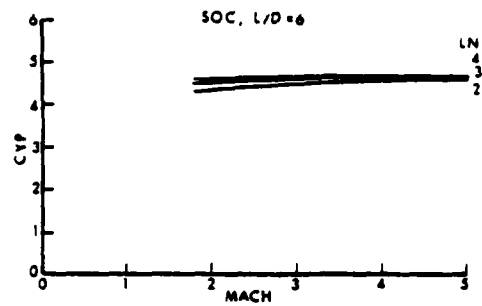
Figure 16. Magnus Center of Pressure, Parametric Comparison, SOC, L/D = 6
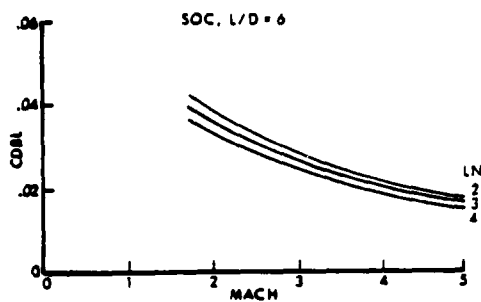
Figure 17. Viscous Drag, Parametric Comparison, SOC, L/D = 6
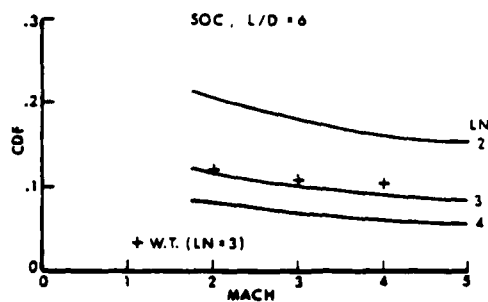
Figure 18. Form Drag Plus Viscous Drag Parametric Comparison, SOC, L/D = 6
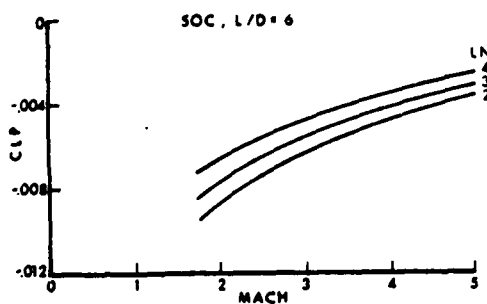
Figure 19. Roll Damping, Parametric Comparison, SOC, L/D = 6
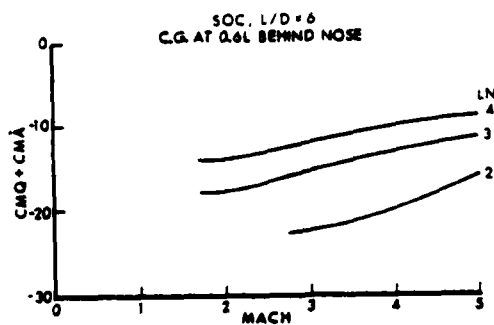
Figure 20. Pitch Damping, Parametric Comparison, SOC, L/D = 6

Examples are shown in Figures 21 through 23 illustrating the effects of variations in ogive shape for fixed forebody and total projectile lengths. These comparisons show that pitching moment, Magnus moment, and pitch damping are increased as ogive bluntness is increased.
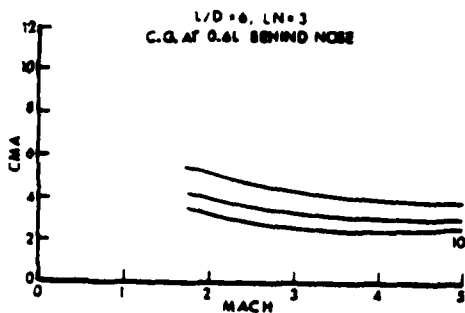
Figure 21. Pitching Moment, Parametric Comparison, $L/D = 6$, $L_N = 3$
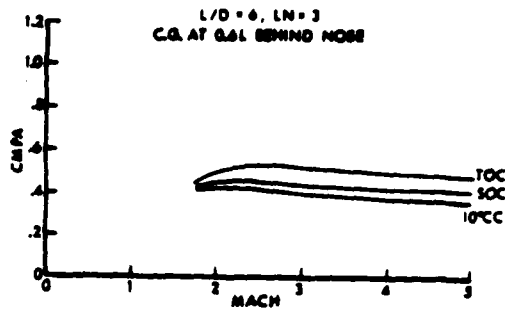
Figure 22. Magnus Moment, Parametric Comparison, $L/D = 6$, $L_N = 3$
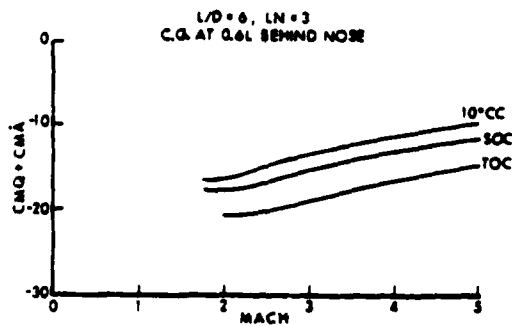
Figure 23. Pitch Damping, Parametric Comparison, $L/D = 6$, $L_N = 3$

The final sequence of parametric comparisons is shown in Figures 24 through 26 where the effect of varying the body length is shown for a fixed ogive shape. These figures show that pitching moment, Magnus moment, and pitch damping are all increased as the body length is increased.
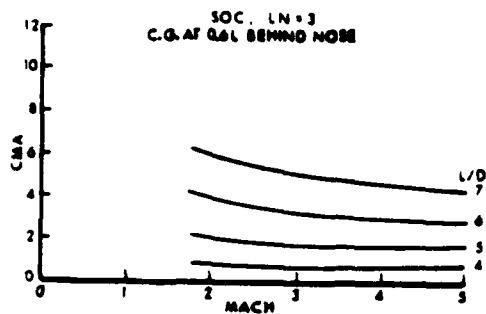
Figure 24. Pitching Moment, Parametric Comparison, SOC, $L_N = 3$
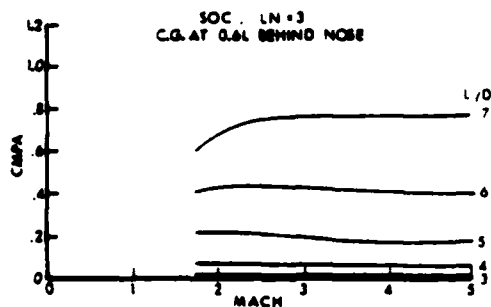
Figure 25. Magnus Moment, Parametric Comparison, SOC, $L_N = 3$
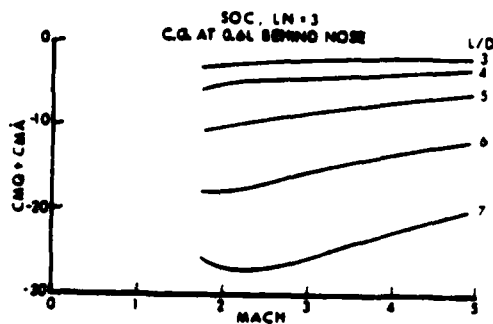
Figure 26. Pitch Damping, Parametric Comparison, SOC, $L_N = 3$

292

The comparisons shown represent a small fraction of the potential comparisons possible from the total data base generated. The intent here has been to illustrate the capability of the computation techniques rather than develop any conclusion as to the relative superiority of any particular configuration. This study is part of a continuing effort that is being expanded to include boattail configurations and a wider Mach number range--transonic velocities are of particular interest.

IV. SUMMARY

A computational aerodynamics parametric study has been described in which advanced numerical techniques for computing three-dimensional inviscid and turbulent viscous supersonic flow fields have been used. A comprehensive data base has been generated for cone-cylinder, tangent-ogive-cylinder, and secant-ogive-cylinder configurations. Comparisons between the computed results and experiment have provided verification of the computational techniques. Comparisons of the computed results for differing body configurations have established the ability of the computation techniques to distinquish the effects of body configuration on the aerodynamic coefficients.

The comparisons for this study represent the first comprehensive use of advanced flow field computation techniques to develop a parametric aerodynamic analysis which includes turbulent viscous effects. Of particular interest are the computations of Magnus effects, which are accomplished in a conceptually exact manner, and the computations of pitch damping. Although the technique of computing pitch damping from a steady coning motion has been available for several years, this study is the first known comprehensive application of this technique to ogive-cylinder bodies.

REFERENCES

1. R. H. Whyte, "Spinner- A Computer Program for Predicting the Aerodynamic Coefficients of Spin Stabilized Projectiles", General Electric Class 2 Reports, 1969.

2. F. G. Moore and C. W. McKerley, "Aerodynamics of Guided and Unguided Weapons; Part II-Computer Program and Usage", NWL TR-3036, 1974.

3. F. G. Moore and Roy C. Swanson, "Aerodynamics of Tactical Weapons to Mach Number 3 and Angle of Attack 15°, Part I- Theory and Application", NSWC/DL TR-3584, February 1977.

4. H. A. Dwyer and B. R. Sanders, "Magnus Forces on Spinning Supersonic Cones. Part I: The Boundary Layer", AIAA Journal, Vol. 14, April 1976, pp. 498-504.

5. F. N. Moore, "Displacement Effect of a Three-Dimensional Boundary Layer", NACA TN 2722. June 1952.

6. R. W. MacCormack, "The Effect of Viscosity in Hypervelocity Impact Cratering", AIAA Paper 69-364, 1969.

7. B. R. Sanders and H. A. Dwyer, "Magnus Forces on Spinning Supersonic Cones. Part II: The Inviscid Flow", AIAA Journal, Vol. 14, May 1976, pp. 576-582.

8. L. B. Schiff, "Nonlinear Aerodynamics of Bodies in Coning Motion", AIAA Journal, Vol. 10, No. 11, November 1972, pp. 1517-1522.

9. W. B. Sturek, et al, "Computations of Magnus Effects for a Yawed", Spinning Body of Revolution", AIAA Journal, Vol. 16, No. 7, July 1978, pp. 687-692.

NOMENCLATURE

A = reference area = $\pi D^2/4$

$CDBL$ = viscous drag = $(\iint \tau_x \cos\theta_B dS)/qA$

CDF = total drag = $(\iint p_w \sin\theta_B dS)/qA + CDBL$

CLP = roll damping = $(\iint r\tau_\phi dS)/(qAD\ PD/V)$

CM = pitching moment = $(\iint z p_w \cos\phi \cos\theta_B dS)/qAD$

CMA = pitching moment coefficient = CM/α

$CMPA$ = Magnus moment coefficient = $CMY/(PD/V/\alpha)$

CMY = Magnus moment = $[\iint (z p_w \sin\phi \cos\theta_B + z\tau_\phi \cos\phi \cos\theta_B + z\Delta p \sin\phi \cos\theta_B + z\tau_x \sin\phi \sin\theta_B) dS]/(qAD)$

CN, C_N = normal force = $(\iint p_w \cos\phi \cos\theta_B dS)/qA$

$CMQ + CMA$ = pitch damping = $C_{n\dot\theta}/\sin\sigma$

CNY, C_Y = Magnus force = $[\iint (p_w \sin\phi \cos\theta_B + \tau_\phi \cos\phi \cos\theta_B + \Delta p \sin\phi \cos\theta_B + \tau_x \sin\phi \sin\theta_B) dS]/qA$

$C_{Y_{\dot{\theta}}}$ = side force in coning motion = $(\iint p_w \sin\phi \cos\theta_B dS)/(qA\dot{\theta})$

CPN = center of pressure = CM/CN

CPY = Magnus center of pressure = CMY/CNY

D = diameter of model

P = spin rate, rad/s

q = free stream dynamic pressure = $(\rho_\infty V_\infty^2)/2$

r = local radius of model

Re_ℓ = Reynolds number based on model length

S = surface area

u, v, w = velocities in boundary-layer coordinates

V = velocity along model trajectory

x = surface coordinate in longitudinal direction

y, Y = coordinate perpendicular to local surface

z = cylindrical coordinate along model axis

Δp = centrifugal pressure gradient contribution to side force

σ = effective angle of attack for coning motion

τ_x = longitudinal velocity wall shear

τ_ϕ = circumferential velocity wall shear

θ_B = local slope of body surface

$\dot{\theta}$ = coning rate

NOISE PERFORMANCE OF A NEW TYPE
OF LOW NOISE FM DETECTOR

DR. ALLAN B. TARBELL
OFFICE OF THE PROJECT MANAGER, SOTAS
FORT MONMOUTH, N. J.   07703

The development of the wideband quasi-coherent detector described in this paper resulted from the need for a low noise, very low delay FM detector for use in power line protection systems. At NTC-1975, Klapper and Kratt described the new detector and presented the results of their analyses of output distortion and performance in the presence of sine wave interference. Recently they have published a more detailed analysis [1]. These previous authors showed that under usual operating conditions the detector output contains distortion components that are relatively small. They also found that in the presence of weak sine wave interference their detector performed approximately the same as the limiter discriminator. However, with a strong interfering carrier the Klapper-Kratt detector performed much better than did the limiter discriminator. The detector's performance in the presence of strong interference led to the inquiry whether the new detector might possibly provide threshold extension.

The detector (without limiter) has now been analyzed with noise and found to perform identically to the limiter discriminator above threshold. However, threshold occurs at a higher CNR than that of the conventional limiter discriminator. The results of this analysis were confirmed experimentally by assembling and testing a version of the new detector family. It was also verified experimentally that the Klapper-Kratt detector preceded by a limiter performs identically to the limiter discriminator.

Noise Analysis

There are several forms of the Klapper-Kratt detector. In

297

this paper, the version shown in Figure 1 was chosen to be analyzed in detail. The primary reason for this choice was determined by the lack of an integrator in the demodulator portion of the detector. With no integrators, the potential integrator initial condition problem previously described[1] is nonexistent resulting in a detector with true wideband performance.
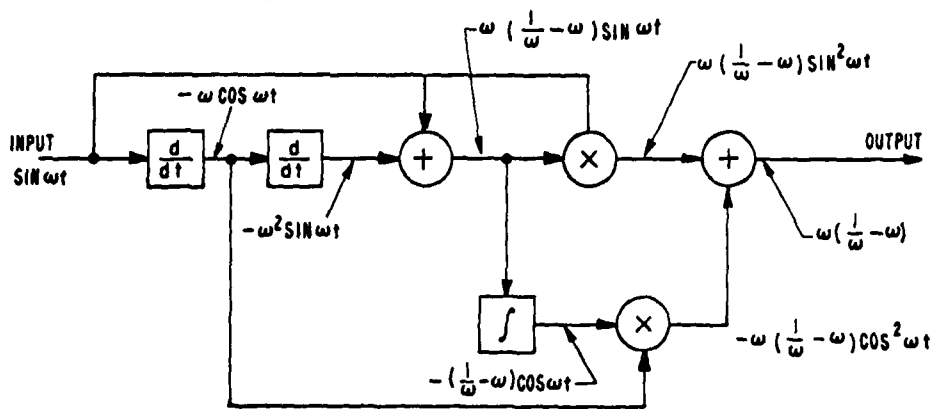
Figure 1. Dual Differentiator Version of The New FM Detector

The operation of the detector may be understood as follows. The input signal is applied to the first differentiator input. The output of the second differentiator is 180° out of phase with the input signal, and the amplitude varies as the square of the instantaneous input frequency. The time constant of each differentiator is selected to give unity gain at some radian frequency, ω_b . Thus, at this center frequency, the output of the summer vanishes. Above and below this frequency, the output of the summer has an amplitude which increases as the frequency of the input signal moves away from ω_c . Coherent detection is performed by the first multiplier. The output of this multiplier is a signal containing the demodulated output plus a component at the second harmonic of the detector input signal.

The RF canceller portion of the detector has been added to remove the second harmonic of the input signal with theoretically zero delay. The canceller circuit generates a term proportional to $\sin^2 \omega_c t$ which, when added to the first multiplier output, cancels the second harmonic present in the demodulator output.

A brief description of the derivation of the SNR-CNR relationship will now be presented. The demodulator portion of the detector is redrawn in Figure 2.

298

TARBELL
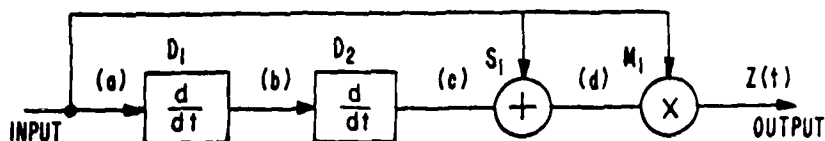
Figure 2. Demodulator Portion of FM Detector

The input signal is assumed to consist of a carrier plus additive narrowband Gaussian noise, or

$$\text{INPUT} = A \sin \omega_0 t + \underbrace{x(t) \cos \omega_c t - y(t) \sin \omega_0 t}_{\text{NOISE}} \tag{1}$$

where ω_c is the center frequency.

Passing this signal through the demodulator and completing the indicated mathematical operations results in

$$Z(t) = -\frac{A \dot{x}(t)}{\omega_0} - \frac{A \ddot{y}(t)}{2 \omega_c^2} + \frac{y(t) \dot{x}(t)}{\omega_c} + \frac{y(t) \ddot{y}(t)}{2 \omega_0^2} \tag{2}$$
$$+ \frac{x(t) \ddot{x}(t)}{2 \omega_c^2} - \frac{x(t) \dot{y}(t)}{\omega_c} .$$

Assuming that $\omega_c^2 \gg \omega_0$ Equation 2 reduces to Equation 3,

$$Z(t) = -\frac{A \dot{x}(t)}{\omega_c} + \frac{y(t) \dot{x}(t)}{\omega_0} - \frac{x(t) \dot{y}(t)}{\omega_0} . \tag{3}$$

299

Next, the autocorrelation of z(t), defined by Equation 4, is determined.

$$R_{zz}(\tau) \triangleq E\left\{ z(t)\, z(t+\tau) \right\} \tag{4}$$

$$R_{zz}(\tau) = E\left\{ \left[-\frac{A\dot{x}(t)}{\omega_o} + \frac{y(t)\,\dot{x}(t)}{\omega_o} - \frac{x(t)\,\dot{y}(t)}{\omega_o} \right] \right.$$

$$\left. \left[-\frac{A\dot{x}(t+\tau)}{\omega_c} + \frac{y(t+\tau)\,\dot{x}(t+\tau)}{\omega_o} - \frac{x(t+\tau)\,\dot{y}(t+\tau)}{\omega_o} \right] \right\} \tag{5}$$

By rewriting Equation 5 as the sum of expected values and simplifying, the autocorrelation becomes

$$R_{zz}(\tau) = \frac{A^2}{\omega_o^2}\, \frac{d^2 R_{xx}(\tau)}{d\tau^2} + \frac{2}{\omega_c^2}\, R_{yy}(\tau)\, R_{\dot{x}\dot{x}}(\tau) - \frac{2}{\omega_o^2}\left[\frac{dR_{xx}(\tau)}{d\tau} \right]^2 \tag{6}$$

The Fourier transform of $R_{zz}(\tau)$ will produce the output power spectral density (PSD), or,

$$R_{zz}(\tau) \Longleftrightarrow S_{zz}(f) \text{ WATTS}/_{Hz} \tag{7}$$

$$S_{zz}(\omega) = \frac{A^2}{\omega_o^2}\left[\omega^2 S(\omega) \right] + \frac{2}{\omega_o^2}\left\{ \mathcal{f}\left[R_{yy}(\tau)\, R_{\dot{x}\dot{x}}(\tau) \right] \right\}$$

$$- \frac{2}{\omega_o^2}\, \mathcal{f}\left\{ \left[\frac{dR_{xx}(\tau)}{d\tau} \right]^2 \right\}, \tag{8}$$

300

where $S(\omega)$ is as shown in Figure 3a.
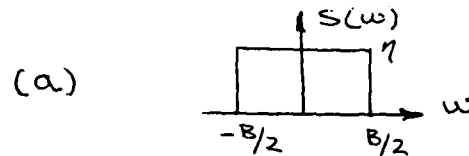
Figure 3a. PSD of x(t) and y(t)

(b)
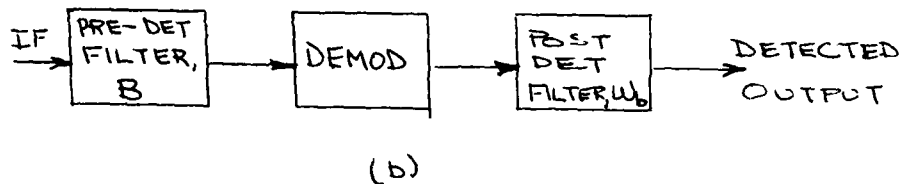
Figure 3b. Complete Detector

The second and third terms of Equation 8 may be evaluated using convolution techniques. After extensive manipulation, the output PSD becomes

$$S_{zz}(\omega) = \frac{A^2}{\omega_0^2}\left[\omega^2 S(\omega)\right]$$

$$+ \frac{1}{\pi\omega_0^2}\begin{bmatrix} \eta^2/3\left[(\omega+\frac{B}{2})^3 + (\frac{B}{2})^3\right], & -B \le \omega < 0 \\ \eta^2/3\left[(-\omega+\frac{B}{2})^3 + (\frac{B}{2})^3\right], & 0 \le \omega \le B \end{bmatrix} \quad (9)$$

$$+ \frac{1}{\pi\omega_0^2}\begin{bmatrix} \eta^2\left[\frac{2}{3}(\frac{B}{2})^3 + (\frac{B}{2})^2\omega - \frac{\omega^3}{6}\right], & -B \le \omega \le -\frac{B}{2} \\ \eta^2\left[\frac{\omega^3}{2} - 2\frac{(\frac{B}{2})^3}{3} - (\frac{B}{2})^2\omega\right], & -\frac{B}{2} \le \omega \le 0 \\ \text{(SYMMETRIC IN POSITIVE HALF PLANE)} \end{bmatrix}.$$

301

where B is the predetection bandwidth (Figure 3b).

The output noise power is determined by integrating Equation 9 over the post detection bandwidth (Equation 10).

$$\text{NOISE POWER} = \frac{1}{\pi} \int_{-\omega_b}^{\omega_b} S_{zz}(\omega)\, d\omega \qquad (10)$$

where ω_b is the post detection bandwidth.

Completing the integration results in Equation 11.

$$\text{NOISE POWER} = \frac{A^2 \eta \omega_b^3}{3\pi \omega_c^2} + \frac{\eta^2 \omega_b^4}{24\pi^2 \omega_c^2} + \frac{\eta^2 \omega_b^3 B}{6\pi^2 \omega_c^2}$$

$$- \frac{\eta^2 \omega_b^2 B^2}{4\pi^2 \omega_c^2} + \frac{\eta^2 \omega_b B^3}{6\pi^2 \omega_c^2}. \qquad (11)$$

In order to obtain the output signal to noise ratio, the signal output power from the demodulator must also be obtained. Single tone modulation is a common standard of comparison. Assuming single tone modulation, the input signal can be written as

$$\text{Input Signal} = A\cos(\omega_0 t + \beta \sin \omega_m t), \qquad (12)$$

where β = modulation index

and ω_m = frequency of modulating signal.

Passing this signal through the demodulator yields

$$\text{Output Signal Power (RMS)} = \frac{A^4 \beta^2 \omega_M^2}{2 \omega_0^2} \qquad (13)$$

The SNR at the detector output is simply the ratio of Equations 11 and 13, or, (assuming signal and noise can be taken additively)

$$SNR = \cfrac{\dfrac{3}{2} (CNR) B \beta^2 \dfrac{\omega_M^2}{\omega_b^3}}{1 + \dfrac{\omega_b}{8B(CNR)} + \dfrac{1}{2(CNR)} - \dfrac{3B}{4\omega_b(CNR)} + \dfrac{B^2}{2\omega_b^2(CNR)}} \qquad (14)$$

This result is exceedingly simple. It is valid above threshold, at threshold, and below threshold. Only three assumptions were made in this derivation:

(1) $\quad \omega_0^2 >> \omega_0$

(2) The signal and noise are additive.

(3) $\quad \omega_b < \dfrac{B}{2}$

Special Case—High CNR

For the high CNR case the last four terms in the denominator of Equation 14 become negligible. Hence,

$$SNR(\text{For High CNR}) = \frac{3}{2}(CNR) B \beta^2 \frac{\omega_M^2}{\omega_b^3} . \qquad (15)$$

Setting $\omega_M = \omega_b$ and recalling that

303

$$CNR_{AM} = CNR \ (B/2 \, \omega_b \ ),$$

Equation 15 may be reduced to

$$SNR \ (H_igh \ CNR) = 3 \, \beta^2 \, CNR_{AM}$$

Equation 17 describes the SNR improvement expected in the linear improvement region. This expression is identical to the well known expression for the conventional limiter discriminator above threshold. [2]Hence, the performance of the Klapper-Kratt detector above threshold is identical to that of the limiter discriminator above threshold, without the use of a limiter. A conventional discriminator, however, has a highly degraded performance without a limiter.

Threshold

Equation 14 may be used to determine threshold occurence for a specified ω_b and B. This equation has been evaluated for various values of the ratio $B/2\omega_b$, and the result is plotted in Figure 4.
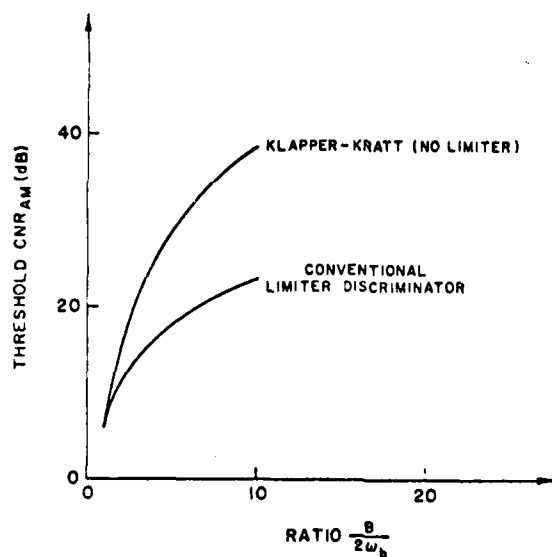
FIGURE 4 THRESHOLD CNR_{AM} VS IF TO BASE BAND RATIO

Comparing this curve with that of the limiter discriminator shows no apparent threshold improvement as was previously thought. However, the new detector, without the additional complexity of a limiter, will

TARBELL

perform nearly as well as the limiter discriminator for low modulation indices.

RF Cancelling

Up to this point of the analysis the RF cancelling portion of the detector has been ignored. It has been assumed that the canceller simply eliminates the undesired high frequency products of detection, and has no effect on the output signal to noise ratio. This assumption is, in fact, true as can be demonstrated by following the signal plus noise through the canceller. This derivation will not be included in this paper. It is straight-forward, but lengthy.

Experimental Verification

The demodulator portion of the dual differentiator version of the Klapper-Kratt detector has been built and tested. Data taken with this demodulator is presented for comparison with the analytical results of the preceding paragraphs.

The circuitry, assembled with silicon monolithic integrated circuits, is shown in Figure 5.
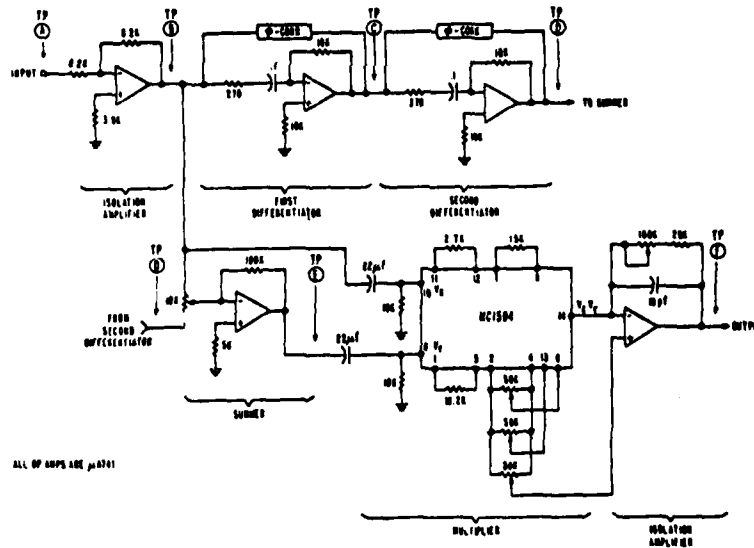
FIGURE 5 DEMODULATOR CIRCUIT DIAGRAM

305

A center frequency of 1000 Hz. was chosen for convenience. Adjustable, active, electronic filters were used to establish pre- and post-detection filtering. The predetection filter bandwidth was set to 165 Hz., while the post-detection filter was adjusted to a bandwidth of 32 Hs. A 25 Hz. baseband modulating signal was used to deviate the carrier $\pm$ 75 Hz. A plot of the measured SNR versus CNR characteristic for the Klapper-Kratt demodulator is shown in Figure 6.
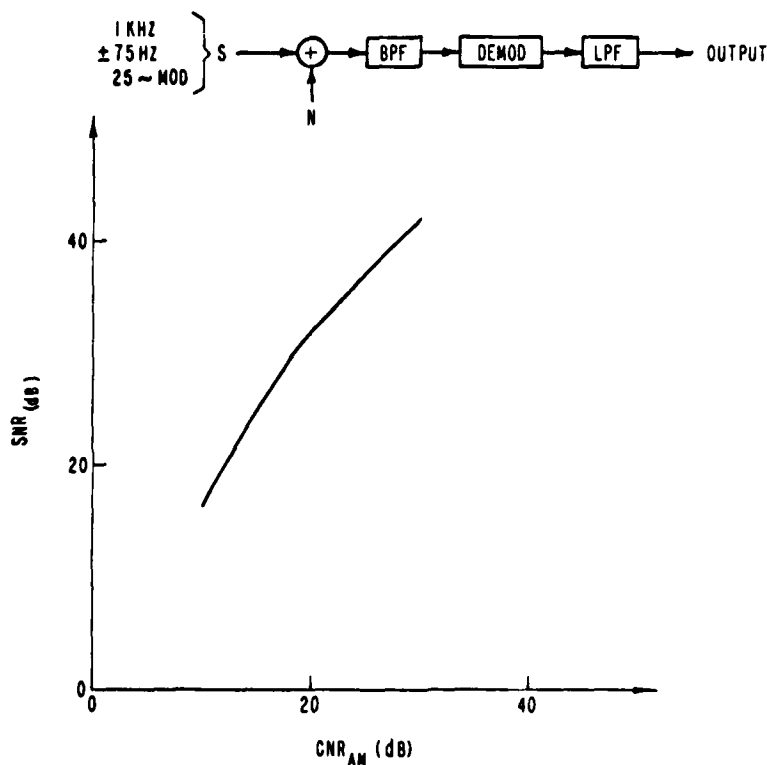
FIGURE 6.   EXPERIMENTAL PERFORMANCE OF KLAPPER-
KRATT DEMODULATOR WITHOUT LIMITER

Figure 7 is an expanded portion of Figure 6. Figure 7 shows threshold occurring at $CNR_{AM} = 16.9$ dB; the SNR improvement above threshold is 12.3 dB. A conventional limiter discriminator was assembled and evaluated for comparison.
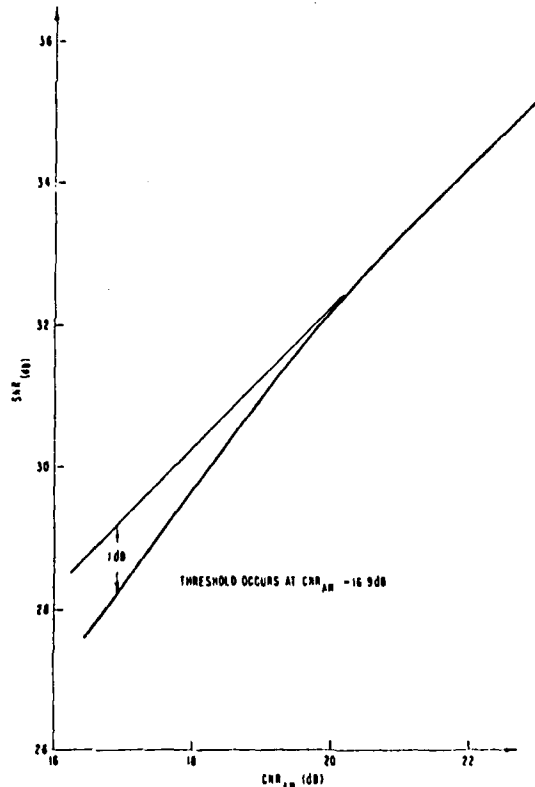
FIGURE 7-8   EXPERIMENTAL PERFORMANCE OF KLAPPER-KRATT
DEMODULATOR WITHOUT LIMITER (EXPANDED SCALE)

Figure 8 and Table I present a comparison of the experimental and analytical data gathered in this investigation of the noise performance of the Klapper-Kratt detector. The graphical comparison shows excellent agreement above and below threshold. These curves, while not coincident, are quite similar in the vicinity of threshold. The small ($<$ 1.0 dB) differences between the measured and analytical SNRs produce the 3.0 dB difference in the experimental versus analytical threshold CNRs. From Figure 8 it is clear that the Klapper-Kratt detector (no limiter) performs the same as the limiter discriminator above threshold. Threshold in the Klapper-Kratt detector, however, occurs at a higher CNR than that of the limiter discriminator. This result led to the experimental investigation of the Klapper-Kratt

307

detector with the addition of a limiter.
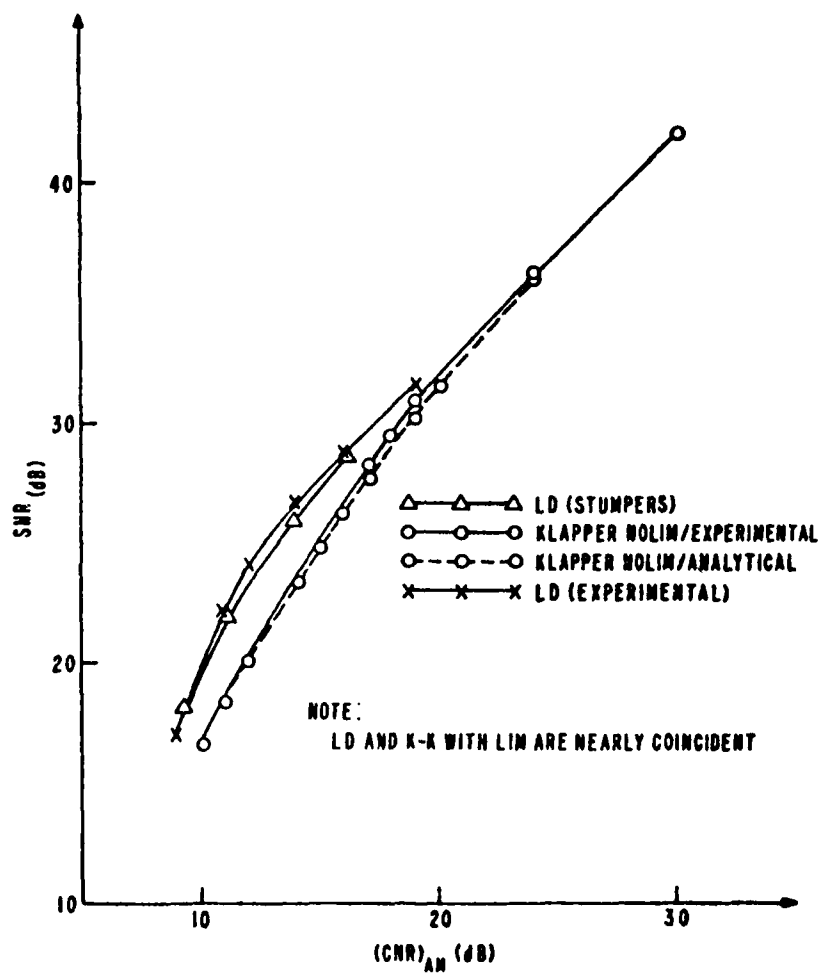
CNR$_{AM}$ (dB)		ANALYTICAL		EXPERIMENTAL	
		Improve.	Threshold	Improve.	Threshold
LIMITER DISCRIMINATOR		12.2	12.5	12.6	11.5
KLAPPER KRATT	NO LIMITER	12.2	19.9	12.3	16.9
	WITH LIMITER	---	---	12.6	11.2

TABLE I. COMPARISON OF THE LIMITER DISCRIMINATOR WITH
THE KLAPPER-KRATT DEMODULATOR

Results of this investigation are shown in Figure 9.
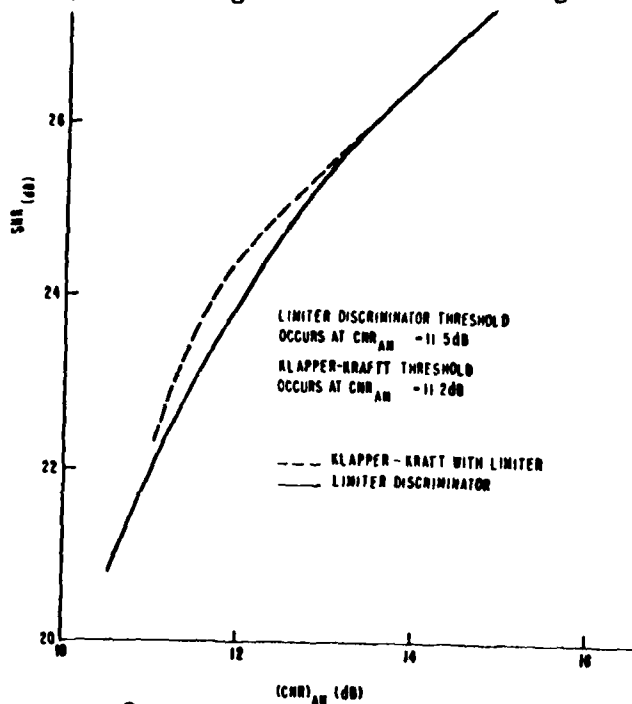
FIGURE 9.   COMPARISON OF KLAPPER-KRATT DEMODULATOR
(WITH LIMITER) AND LIMITER DISCRIMINATOR

The performance of the Klapper-Kratt detector (with limiter) is virtu-
ally identical to that of the conventional limiter discriminator.

Conclusions

In the above threshold region the Klapper-Kratt detector per-
forms identically to the limiter discriminator. Threshold in the
Klapper-Kratt detector occurs at a higher CNR than that of the limiter
discriminator. For small or moderate modulation indices this differ-
ence in threshold performance is quite small. Small enough, in fact,
that in applications where a limiter is undesirable the Klapper-Kratt
detector would likely be a preferred alternative to the conventional
limiter discriminator. The primary application for this demodulator
is where delay must be minimized.

The equation describing the performance of the new demodulator
is very simple. This result is valid in the linear improvement region,
at threshold, and in a region below threshold.

TARBELL

REFERENCES:

1. J. Klapper & E. Kratt, "A New Family of Low Delay FM
    Detectors" , IEEE Transactions on Communications, February, 1979.

2. J. Klapper & J. Frankle, Phase-Locked and Frequency-Feedback
    Systems, Ch. 3, Academic Press, 1972.

3. L. Stumpers, "Theory of Frequency Modulation Noise" ,
    Proc. IRE, Vol 36, No 9, p.1081-92, September, 1948.

*VOGEL, WRIGHT & PATTON

DEVELOPMENT OF NEW GENDER-FREE
PHYSICAL FITNESS STANDARDS
FOR THE ARMY

JAMES A. VOGEL, Ph.D., JAMES E. WRIGHT, CPT, MS, Ph.D.
JOHN F. PATTON III, Ph.D.
US ARMY RESEARCH INSTITUTE OF
ENVIRONMENTAL MEDICINE
NATICK, MA   01760

I. Introduction

The General Accounting Office recommended to the Armed
Services in May 1976 that they --"develop standards for measuring the
ability of personnel to satisfy strength, stamina and operational
performance requirements for specialties where such attributes are
factors in effective performance". This action was in response to
the arbitrary closure to women of many military occupational special-
ties (MOS) presumed to be too physically demanding.

With the need to utilize increasing numbers of women in non-
traditional MOSs as well as to respond to affirmative action policies,
it became apparent that the Army must qualify and assign new entrants
by matching individual qualifications with specific MOS physical re-
quirements, regardless of gender. Arbitrarily barring all women from
a physically demanding MOS, because it is beyond the capacity of the
average woman, is wasteful of manpower, if not, unjustifiable. Thus,
in July 1977, the Army Vice Chief of Staff directed that research
begin to establish gender-free occupationally related physical fitness
standards which could be used for MOS selection and assignment. This
paper presents the process by which this has been accomplished.

II. Background

The process was based on the following series of assumptions.

Assumption No. 1: Standards should be

313

established for two separate components
of physical fitness - aerobic fitness and
muscle strength fitness.

Physical fitness can best be defined in terms of the various
capacities of the body to carry out physical activity. These capaci-
ties are best described by the sources or processes of energy genera-
tion for muscular exertion. These energy sources are physiologically
quite distinct and therefore no single capacity or fitness measure is
adequate to encompass physical fitness in the terms necessary to
define the variety of Army MOSs.

Physiologically there are three distinct energy sources and
thus three physical fitness components. These are illustrated in
Figure 1. Energy for brief muscular activity, such as the lifting of

MUSCLE ENERGY SOURCE	STORED	ANAEROBIC METABOLISM	AEROBIC METABOLISM
EXAMPLE OF ACTIVITY	LIFTING	SPRINTING	RUNNING
CAPACITY MEASURED AS	MAXIMAL CONTRACTION FORCE	ENDURANCE TIME AT HIGH INTENSITY	MAXIMAL O_2 UPTAKE
TERMINOLOGY	MUSCULAR STRENGTH	ANAEROBIC POWER — MUSCULAR ENDURANCE	AEROBIC POWER — STAMINA

Figure 1.   Components of physical fitness
in terms of energy sources

314

boxes or artillery rounds, is predominantly provided from energy
(in the form of phosphate compounds) stored in the muscle cells. On
the opposite end of the spectrum, energy to sustain long term dynamic
movement, such as running or repetitive light lifting, is provided
from metabolic pathways which utilize oxygen to convert substrates
into useable energy. The third energy source which plays an inter-
mediate role between stored and aerobically derived energy is that
derived from anaerobic metabolic pathways. In this latter system,
conversion of substrate to energy does not require oxygen. This
source is utilized when stored energy is depleted and the demand rate
exceeds the velocity and capacity of the aerobic system.

Most physical exertion is in fact a combination of these fit-
ness components. While strength and aerobic fitness are relatively
easy to isolate and identifiable, anaerobic fitness overlaps exten-
sively with the other two and is quite difficult to separate and
measure. It is for this reason, as well as simplicity, that in estab-
lishing occupationally related standards, it was decided to operation-
ally use only two components of fitness, muscular strength and aerobic
fitness.

> Assumption No. 2: Standards should be
> based on objectively determined physical
> demands of MOSs.

The capability exists to actually measure the aerobic energy
costs and calculate the forces exerted in individual tasks performed
in the field. Thus, standards based objectively on actual physiologi-
cal demands are preferable to subjective determinations of task de-
mands, i.e., impressions, perceptions, estimations or judgements.

> Assumption No. 3: Standards should be
> established for groups or clusters of
> MOSs having apparently similar fitness
> requirements.

There are approximately 350 enlisted Army MOSs. Many have
similar, if not identical, physical tasks and therefore physical fit-
ness requirements. For this reason as well as simplicity and ease of
administration, the smallest number of different fitness standards
would be desirable. Thus, MOSs having apparent similar physical
demands would be grouped together so as to reduce to the minimum the
number of established standards.

Assumption No. 4: Standards should be
based on the most demanding tasks found
within each MOS grouping.

Since a soldier must perform every task within his MOS, it
was decided to establish standards based on the most demanding tasks
within that MOS grouping. This process was selected instead of using
the average demand of all tasks.

Assumption No. 5: The resolution or
sensitivity of the scale of standards
should be commensurate with operational
needs.

The application or administration of fitness standards in the
field must be simplified as much as possible if they are to be
accepted at all. This is due to the magnitude and diversity of Army
personnel and their locations. A scale of standards with many gradu-
ations would defeat the purpose intended. Sufficient resolution
however, should be established which separates any differences in
aerobic and muscular strength demands which are meaningful in terms
of job performance.

III. Methodology

A summary of the steps developed to derive gender-free,
occupationally related physical fitness standards is shown in
Figure 2.

Step No. 1. The initial step of this process was to assemble
a list of all physically demanding tasks for each MOS. Each Army
service school provided a detailed description of the physically
demanding tasks of MOSs for which they are the proponent. Provision
of insufficient information or unrealistic descriptions were re-
checked and verified until the investigators were satisfied that
the information was accurate.

Step No. 2. The next step was to visually inspect these
physical task lists and group MOSs into clusters with similar fitness
demands by using a set of objective criteria. These clustering

```
┌─────────────────────────────────┐
│ FORMULATE PHYSICAL TASK         │
│ LIST FOR EACH MOS               │
└─────────────────────────────────┘
                │
                ▼
┌─────────────────────────────────┐
│ GROUP MOSs BY INSPECTION        │
│ INTO CLUSTERS WITH SIMILAR      │
│ FITNESS DEMANDS                 │
└─────────────────────────────────┘
                │
                ▼
┌─────────────────────────────────┐
│ IDENTIFY MOST DEMANDING TASKS   │
│ TO REPRESENT EACH CLUSTER       │
└─────────────────────────────────┘
                │
                ▼
┌─────────────────────────────────┐
│ MEASURE FORCE/ENERGY DEMANDS    │
│ OF REPRESENTATIVE TASKS         │
└─────────────────────────────────┘
                │
                ▼
┌─────────────────────────────────┐
│ ADJUST FOR DURATION             │
│ AND CONVERT INTO                │
│ CAPACITY STANDARD               │
└─────────────────────────────────┘
                │
                ▼
┌─────────────────────────────────┐
│ CONVERT STANDARD FROM           │
│ PHYSIOLOGICAL UNITS             │
│ INTO PF TEST SCORES OR          │
│ TRAINING LEVEL INTENSITIES      │
└─────────────────────────────────┘
```

Figure 2.   Sequence of steps taken
to develop occupationally
related fitness standards.

criteria are shown in Table 1. These criteria, one for muscular
strength and one for aerobic power demand, were derived by plotting
the full range of individual task values observed in the task list
and then establishing three levels which divided the total range into
approximately equal parts by taking into account natural concentra-
tions of points. This process is illustrated in Figure 3.

317

TABLE 1. MOS Clustering Criteria

Intensity Rating	Strength Demand (kg weight lifted to waist height)	Aerobic Demand (energy cost in kcal/min)
Low	<30	<7.5
Medium	30-40	7.5-11.25
High	>40	>11.25

STAMINA
(ENERGY DEMAND RATE)

MUSCLE STRENGTH
(WEIGHT LIFTED)
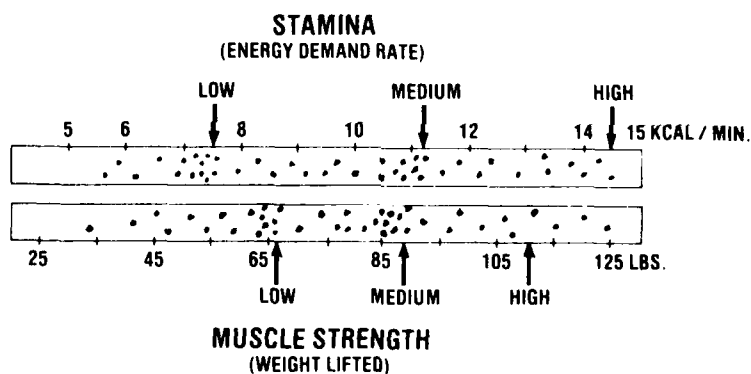
Figure 3. A representation of how objective criteria were chosen for MOS clustering.

Step No. 3. Once the grouping had been completed and clusters of MOSs with like demands were formed, the task lists of each cluster were again examined to select those to be the most demanding. Four to six of the most demanding tasks in each cluster in terms of aerobic power were selected for detailed physiological analysis. These selections were made by evaluating weights lifted, heights to which lifted, distances carried and estimated caloric expenditure of the task. The latter was based on previously published energy costs of both civilian and military tasks (1-3).

Step No. 4. The next step consisted of actually measuring the energy costs and verifying the weights lifted and distances moved for the representative (most demanding) tasks. Soldiers from the Training Center, Ft. Jackson, SC and the 24th Infantry Division, Ft. Stewart, GA were utilized for hese measurements.

Caloric costs of tasks were determined by measuring oxygen consumption with the Kofranyi-Michaelis portable respiratory gas Meter (3). The subject inspired through a mouthpiece and valve so that the expired air was delivered to the meter carried as a back pack (weight of 3.8 kg). The meter directly measured expired ventilation and produced an aliquot of gas for separate fractional analysis of oxygen and carbon dioxide. These two gas concentrations plus expired minute ventilation were used to calculate the oxygen consumed each minute. This was converted to kilocalories using the conversion ratio of 5 kcal per liter of oxygen consumed.

Step No. 5. The energy cost of the tasks selected in Steps No. 3 and 4 was measured over a period of time (10-20 minutes) sufficient to produce a stable period of oxygen consumption. This period did not necessarily have to equal the actual length of the task as described but only long enough to accurately ascertain the average energy expenditure rate of the task being performed at the prescribed intensity. Most tasks were considered as being performed on a sustained basis (short rest to work period ratios) and therefore the measured rate was utilized as the eight hour average sustained rate.

The next step was the crucial one of converting the eight hour sustained energy cost rate into the necessary aerobic capacity for an individual to perform at that level of intensity. A number of reports (4-6) have suggested that average energy expenditure rates for an 8 hour work day should not exceed 35 to 50% of one's aerobic capacity in order to prevent an inordinate amount of fatigue from which one could not recover overnight. Thus, using a 45% figure,

319

if the highest energy cost of a representative task was found to be 8 kcal per minute, then a person would be required to possess an aerobic capacity of not less than 18 kcal per minute or a maximal oxygen consumption of 3.6 liters per minute. We employed the percentage figure of 45% which will be discussed later. At this point, the requirement or standard was established in terms of physiological units (kcal or liters of oxygen) for aerobic demand and physical units (weight and distance) for strength demand.

Step No. 6. The final step was to convert these physiological and physical units of capacity into two sets of physical fitness test scores, one to be applied at the time of entrance qualification and the other on-the-job within the MOS (Figure 4). The differences between these two tests are in the mode of testing and the test score

FITNESS DEMANDS

RATING	WEIGHT	CAL / MIN.
LOW	66	7.5
MEDIUM	88	11.25
HIGH	110	14.5

ENTRANCE FITNESS STANDARDS

RATING	STRENGTH INDEX	STAMINA INDEX
LOW	X	X
MEDIUM	X	X
HIGH	X	X

PLUS TRAINING

MOS FITNESS STANDARDS

POINTS

RATING	STRENGTH	STAMINA
LOW	60	60
MEDIUM	100	100
HIGH	120	120
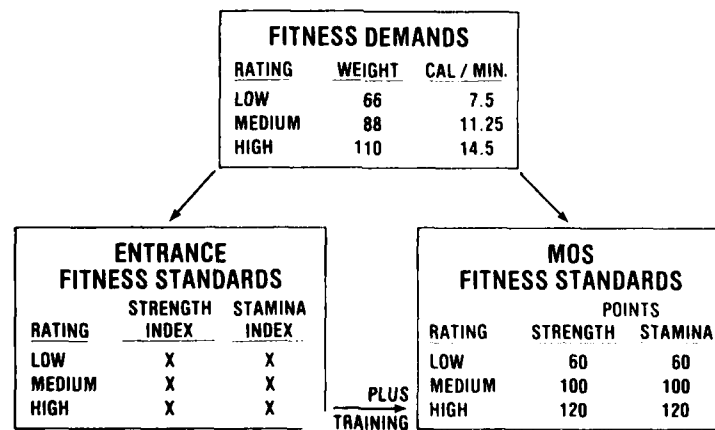
Figure 4.   Scheme for Converting MOS Demands into Entrance as Well as On-The-Job Standards.

standard. The entrance test would be administered at the Armed Forces Examining and Entrance Stations (AFEES) where laboratory type equipment and procedures can be utilized to yield relatively precise

measures of aerobic and strength capacity. In the "field", on-the-job, we are limited to the use of performance tests such as running, push-ups, etc. The other difference is that the entrance standard will be less than the "on-the-job" standard by an amount equal to the average expected gain during basic and advanced individual training. The test measures presently being considered are listed in Table 2.

Table 2

Physical Fitness Test Measures for
Entrance and On-the-Job

Component	Entrance (AFEES)	On-the-Job
Aerobic	Heart rate during step test plus % body fat.	2 mile run
Muscle strength	Isometric upright pull at 38 cm.	Push-ups Sit-ups

Capacities from Step No. 5 are then converted into equivalent scores on these two sets of tests through the means of regression analysis. The aerobic capacity and two mile run relationship is illustrated in Figure 5 and the muscle strength-isometric pull relationship is illustrated in Figure 6.

IV. Results

A. Physical Task List

Based on information provided by the service schools, the physical tasks of 349 enlisted MOSs were compiled. An example of a task write-up is given below:

MOS 12E, task-1: Backpack an ADM.

Condition: given an XM120E1 in the H-911 bay secured to the backpack, cross-country route, under daylight conditions.

321

Standard:

    i.   lift a 30 kg XM120El
    ii.   backpack ADM 1 km
    iii. perform task in 20 minutes
    iv.   perform task 2 times per day
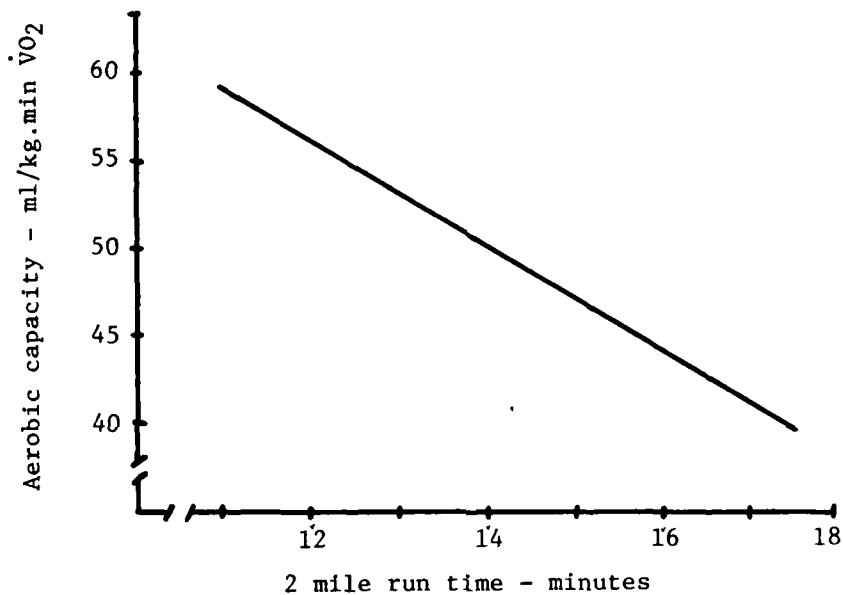
Figure 5. Relationship between aerobic
capacity and 2 mile run time.

B. Clustering of MOSs by Fitness Demand

Using the procedure of judging task demand in two categories at three levels of intensity (Table 1), five clusters resulted out of a possible nine combinations (Table 3). Table 4 presents the five clusters in terms of distribution of MOSs and personnel.
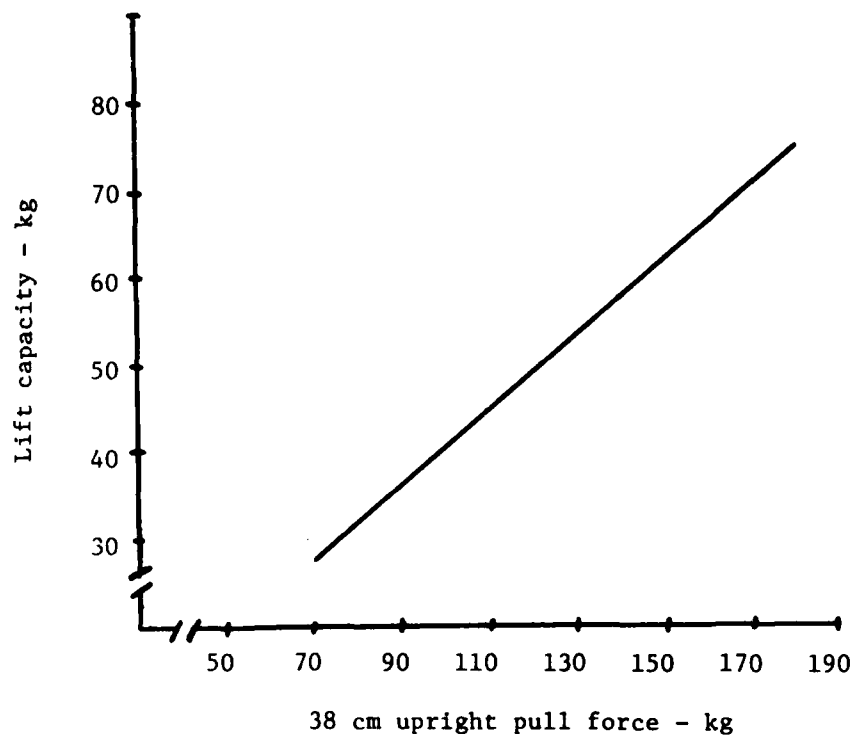
Figure 6. Relationship between maximum
lift capacity and isometric
upright pull test.

Table 3

MOS Clusters

| Level of Demand | | Cluster |
Strength	Aerobic	Designation
High	High	Alpha
High	Medium	Bravo
High	Low	Charlie
Medium	Low	Delta
Low	Low	Echo

Table 4

MOS Cluster Distribution

Cluster	Number of MOSs	% of Total MOS	% of total Personnel
Alpha	10	3	19
Bravo	39	11	13
Charlie	63	18	21
Delta	53	15	21
Echo	184	53	26
	349		

C. Representative Most-Demanding Tasks

Table 5 presents an example of representative tasks selected for each cluster to be used for cost measurements. Special note should be taken of the Echo cluster tasks. Echo cluster includes all MOSs which have no, or only minimal, physically demanding tasks within their job description. Thus, there were no physical tasks upon which to base a fitness standard. It was therefore decided by HQ-Training and Doctrine Command that a group of tasks would be formulated which would be used to derive the fitness standard. These tasks, referred to as "common soldiering tasks", were selected by a committee at the US Army Infantry School to represent those tasks which all soldiers must be able to perform, at a minimum, in a wartime defensive situation. These are also tasks which are to be accomplished by the end of Basic Initial Entry Training.

D. Measurement of Energy Cost

Table 6 presents examples of mean energy costs of a representative task from each cluster.

E. Convert Cost into Capacity and Test Standards

Demand for muscular strength was expressed in terms of weight lifted to a height of 132 cm. Thus, the greatest lifting demands identified in the cluster representative tasks were converted into this unit (adjusted for height lifted) and expressed as the required absolute strength capacity. For aerobic capacity, 8 hour energy demands were set not to exceed 45% of capacity and aerobic capacities thereby calculated.

324

Table 5

Examples of Cluster Representative Tasks

Alpha
"Carry 45 kg CWIE bag 1000 m in 20 minutes."

Bravo
"Lift and carry 41 kg ammo box 6.7 m 32 times
per hour."

Charlie
"Lift 132 cm and carry 25 kg projectile 15 m,
50 times per hour."

Delta
"Lift and carry 27 kg container 15 m, 40 times
per hour."

Echo (complete list)
1. "8 km march in 120 minutes."
2. "Dig one-man emplacement in 45 min."
3. "Lift and carry 23 kg, 50 m, 8 times in
     10 min."
4. "Rush 75 m in 25 sec."
5. "Low and high crawl 75 m in 90 sec."

The conversion of these physical and physiological units into
field test event scores or AFEES measurement scores is then carried
out by regression analyses as described earlier. The purpose of this
paper is to present the process used to derive these standards and
therefore the actual computed standards are not presented but will
be published elsewhere.

IV. Discussion

This paper outlines the rationale and step-by-step process
taken to develop new gender-free physical fitness standards for the
Army based solely on occupational (MOS) physical demands. It estab-
lishes an objective basis for minimum physical standards for MOSs so
that individuals can be selected and assigned to MOSs based on the

physical demands of the MOS. It is recognized that a number of assumptions must be made during this process, some of them based on inprecise data. However, it is felt that the precision achieved is appropriate to the resolution desired.

Table 6

Examples of task energy cost
from each cluster

Cluster	Task	Cost $1/\text{min } \dot{V}O_2$
Alpha	Carry 50 43 kg bags 20 ft in one hr.	0.96
Bravo	Lift 45 kg projectile to 132 cm and carry 20 m, 100 times per day.	0.89
Charlie	Lift and carry 25 kg projectile 15 m, 50 times per hr.	0.75
Delta	Lift and carry 27 kg container 15 m, 40 times per hr.	0.73

Occupationally based fitness standards are not meant to be either the ultimate or sole physical fitness standards. They are intended to serve as a requirement upon which to base MOS assignment qualification at the time of enlistment into the Army and secondly as the minimal standard that must be met to retain qualification in a particular MOS or for retention in the service. It is envisioned that, particularly in operational units, these MOS-based standards would be exceeded in order to achieve the additional goals of improved health, appearance, morale and overall military performance. These additional or supplemental standards would be determined by unit commanders to meet the needs of their personnel and their unit mission.

In conclusion, this research has resulted in a process by which physical fitness demands of all enlisted MOSs can be represented by 5 sets of standards, representing three levels of demand in two separate categories of fitness. This categorization was accomplished by applying objective criteria to MOS tasks, including the weight lifted and rates of energy expended. This system establishes a basis by which physically demanding occupations can be assigned on a gender free basis which will be both legally and scientifically defensible.

It should lead to more cost effective matching of individual capabilities to occupational demands.

VI.   References

1.   Passmore, R. and J.V.G.A. Durnin.   Human energy expenditure. Physiol. Reviews 35:801-840, 1955.

2.   Goldman, R.F.   Energy expenditure of soldiers performing combat type tasks.   Ergonomics 8:321-327, 1965.

3.   Consolazio, C.F.   Energy expenditure studies in military populations using Kofranyi-Michaelis respirometers.   Am J. Clin. Nutrition 24:1431-1437, 1971.

4.   Bink, B.   The physical working capacity in relation to working time and age.   Ergonomics 5:25-28, 1962.

5.   Bonjer, F.H.   Actual energy expenditure in relation to the physical working capacity.   Ergonomics 5:29-31, 1962.

6.   Müller, E.A.   Occupational work capacity.   Ergonomics 5:445-452, 1962.

STUDIES IN THE IDENTIFICATION
OF HYDROCARBON PRODUCTS IN WASTEWATER

*RAYMOND S. VOGEL, MR.
ROBERT J. FILECCIA, MR.
WALTER J. MIKUCKI, MR.
RICHARD G. LAMPO, MR.
U.S. ARMY CONSTRUCTION ENGINEERING RESEARCH LABORATORY
CHAMPAIGN, ILLINOIS 61820

INTRODUCTION

At Army installations, operations essential to the maintenance, servicing, and cleaning of wheel- and track-type vehicles produce large volumes of wastewater which may contain variable concentrations of hydrocarbon products used in the servicing and cleaning operations. Federal regulations require the monitoring of hydrocarbon concentrations in effluents discharged into waterways; and regulatory agencies such as the Environmental Protection Agency are vested with authority to assess liabilities for restoration costs in cases of environmental pollution by outfalls exceeding established concentration limits.

Methods of quantification of "total hydrocarbons" have been developed and approved by EPA and provide the basis for the monitoring of this class of environmental pollutant (1,2). However, while these methods provide essential data on hydrocarbon concentrations in effluent samples, they do not provide information needed for identification of the specific hydrocarbon products present in the effluent to aid in tracing a given hydrocarbon pollutant to its source for preventative action.

Extensive R&D efforts by other agencies and independent groups have been directed to the identification and classification of petroleum oils. A variety of analytical techniques have been employed, including infrared spectroscopy, absorption and fluorescence

329

spectrophotometry, gas and liquid chromatography, and trace-elemental analyses. Reviews and investigations of applications of these techniques are reported by Adlard (3), Bentz (4), Brown et al. (5), Gruenfeld (6), Kawahara (7), and Wilson et al. (8). A comprehensive current review of the state of the art in oil-spill identification, including remote-sensing methods, was presented by Bentz (9).

The general focus of the reported research has been on identification ("fingerprinting") for forensic purposes of a crude oil or petroleum derivative occurring as a single component in an accidental or clandestine marine spill. Former studies have not been concerned with identifying specific hydrocarbon products occurring as multiple components of complex mixtures as would be found in wastewater effluents.

OBJECTIVE

The objective of this study was to develop a readily usable analytical method for the identification of specific hydrocarbon products in wastewater from vehicular service and wash-rack areas at Army installations.

The hydrocarbon products to be included for identification in this study were to be limited to the following MIL-Spec products employed in the servicing and maintenance of military vehicles: Motor Oil, Diesel Fuel, Hydraulic Fluid, Brake Fluid, and Solvent Type II.

APPLICATION OF INFRARED SPECTROSCOPY
TO OIL IDENTIFICATION

For more than three decades, infrared spectroscopy (IR) has been used extensively to characterize the composition of petroleum constituents. In the early development of methods for the "fingerprinting" of oil-spill samples, IR provided a direct means for identification through visual comparison of the IR spectrum of a recovered oil spill sample with a library of reference spectra of oils of known origin.

The advent of commercially available IR spectrophotometers with digitizing capability, and the application of computer interfacing has opened the way for the use of statistical methods of data reduction to replace the earlier, subjective visual-comparison techniques.

In the pattern-recognition method developed by Lynch and Brown (10), log-ratios of absorptivities of an unknown oil sample to a reference oil, at each of 21 selected absorption peaks, are used to obtain a single numerical value which is a measure of the overall difference between the unknown sample and the reference oil. The multivariate statistical approach to the fingerprinting of oils developed by Mattson et al. (11,12) has introduced statistical probability functions in describing the extent of match or mismatch between the IR spectrum from the oil spill sample with a computer file of reference spectra of petroleum oils of known origin.

In another computer-oriented fingerprinting method described by Killeen et al. (13), a digitized IR spectrum is treated as a vector in n-dimensional space; and the closeness of fit to the hyperplanes generated by an unknown oil and a reference oil is a measure of overall difference.

THE ANALYTICAL PROBLEM DEFINED

The analytical objectives and associated problems in fingerprinting oil-spill samples are distinctly different from those in identifying the presence of specific hydrocarbon products as components in a mixture of hydrocarbons. Fingerprinting a given oil sample involves the use of a set of variables (absorption bands in IR spectroscopy) to test whether the spectrum of an oil-spill sample corresponds, at a high statistical confidence level, to one in a computer file of reference oils of known origin. Differences between the infrared spectra may be very subtle, and small variations in intensity ratios between a myriad of peaks must be determined with high precision and accuracy.

Identification of hydrocarbon products in a mixture of petroleum-derived hydrocarbon products (each of which is a mixture of hydrocarbons) involves the use of an appropriately selected set of absorption bands to test for the presence (above a given discriminator value) of specific hydrocarbon products on the basis of the reference spectra of the individual products. The absorption spectrum of the mixture to be analyzed is a summation of the absorption spectra of the individual hydrocarbon products present; and the analytical problem consists of "unscrambling," or differentiating the integrated signals to the extent that individual hydrocarbon products in the mixture can be identified.

331

*VOGEL, FILECCIA, MIKUCKI, and LAMPO

DEVELOPMENT OF THE ANALYTICAL METHOD

In a system in which five specific hydrocarbon products in an effluent are to be identified but not quantified, analytical requirements might be met through the use of a simple binary information format based on the presence or absence of absorption peaks unique to each hydrocarbon product--if an adequate number of such peaks for each product could be found that are analytically suitable.

On that supposition, scans of absorption spectra of the five hydrocarbon products were made on a computer-interfaced Perkin-Elmer 283B spectrophotometer (Figures 1 through 5). Digitized spectral information of each product was simultaneously stored on magnetic discs. Peak tables listing the wavenumber of each absorption peak with the corresponding absorbance value were computer generated for each of the five referenced hydrocarbon products; and a compilation of the wavenumbers of the recorded peaks for the five hydrocarbon products was assembled.

Since the hydrocarbon products were all of petroleum origin, the major and secondary absorption bands were in common to all five products. Absorption bands that were not in common to the five products were relatively weak--some barely above background noise. The intensities of the very weak peaks were then computer enhanced by accumulating and averaging five successive spectral scans. This process significantly improved the signal-to-noise ratio of these peaks because baseline noise, being random, tends to average to zero, whereas true absorption signals occur in only a positive direction.

Peaks in common with more than two hydrocarbon products were eliminated from further consideration; the wavenumber values of the remaining peaks and the corresponding hydrocarbon products represented by each peak are listed in Table 1. A tabulation from Table 1 of the number of absorption bands unique to each hydrocarbon product, and of the number of bands shared between two products, gave the following scores:

Product	Bands Unique to One Product	Bands Shared Between Two Products
30W Motor Oil	4	5
Diesel Fuel	6	5
Hydraulic Fluid	8	2
Brake Fluid	4	6
Solvent Type II	0	4

TABLE 1

INFRARED ABSORPTION BANDS UNIQUE TO TWO OR LESS HYDROCARBON PRODUCTS

Absorption Band (cm^{-1})	30W Oil	Diesel Fuel	Hydraulic Fluid	Brake Fluid	Solvent Type II	Frequency of Occurrence
1952				x		1
1775	x					1
1734			x			1
1717		x				1
1706	x					1
1690		x				1
1325				x	x	2
1297				x		1
1269			x		x	2
1248				x		1
1240			x			1
1227	x					1
1207	x					1
1157		x			x	2
1150			x			1
1115				x		1
1092		x				1
1077	x	x				2
1070				x	x	2
1064			x			1
1031	x	x				2
1014	x		x			2
945	x	x				2
865	x	x				2
851			x			1
805		x				1
775			x			1
747			x			1
739		x				1
699		x				1
634			x			1

Figure 1. Infrared Spectrum of 30W Motor Oil
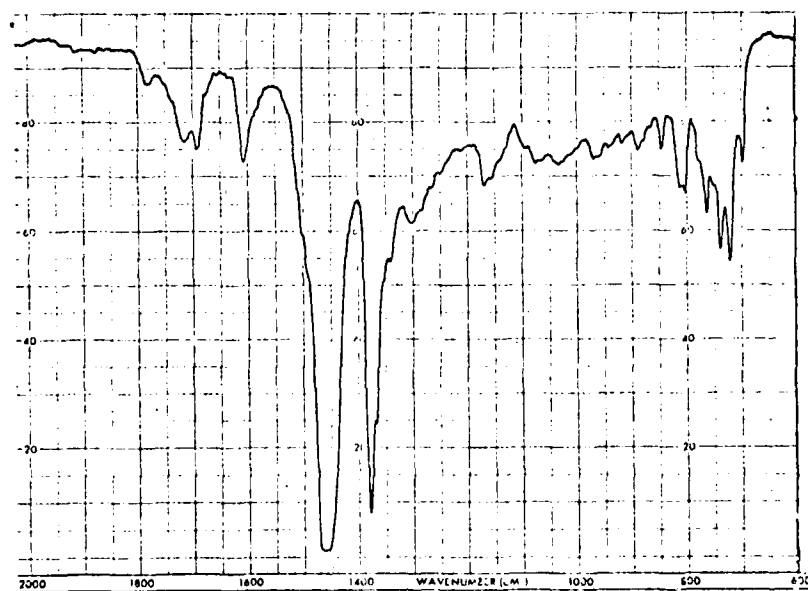
Figure 2. Infrared Spectrum of Diesel Fuel
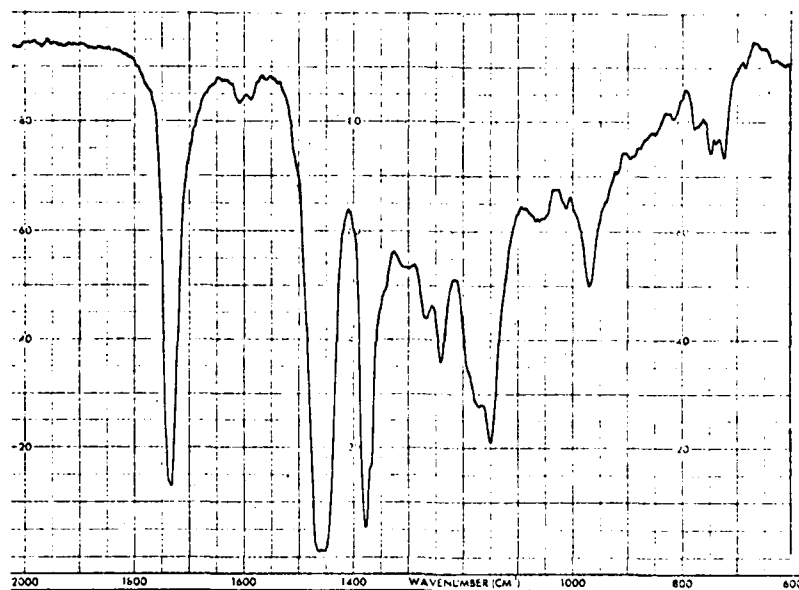
Figure 3.   Infrared Spectrum of Hydraulic Fluid
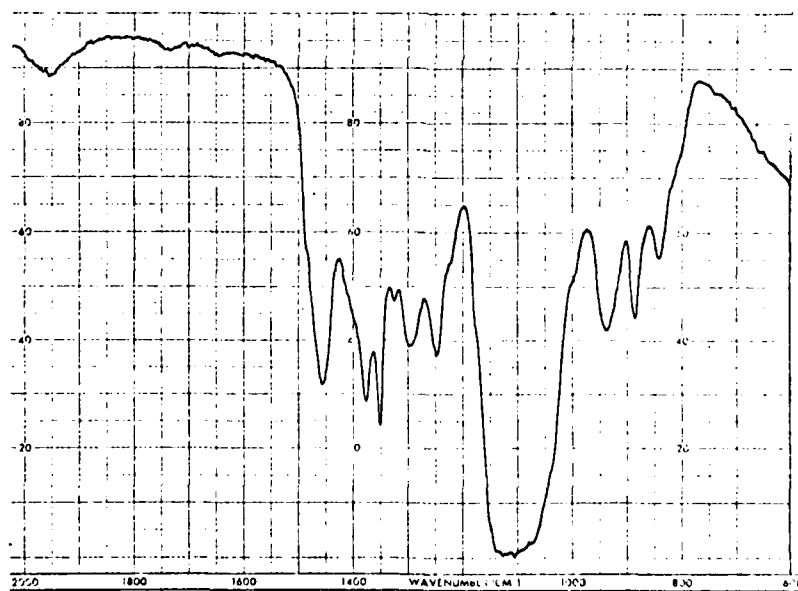
Figure 4.   Infrared Spectrum of Brake Fluid

335
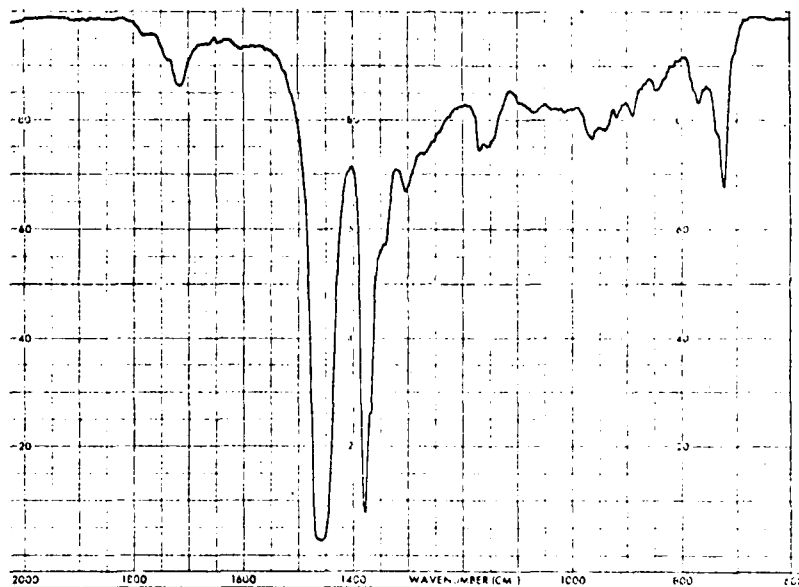
Figure 5. Infrared Spectrum of Solvent Type II

DEVELOPMENT OF THE ANALYTICAL METHOD (continued)

On the basis of the scores, and of the peak intensities, "recognition power" for Diesel Fuel, Hydraulic Fluid, and Brake Fluid was acceptable; for Motor Oil was marginal; and for Solvent Type II was poor. The poor recognition power for Solvent Type II by the absence of unique peaks was further diminished in that the five shared peaks were respectively present in the remaining four products, as shown in Table 1. Consequently, under the procedural conditions used, Solvent Type II would not be identifiable by infrared spectroscopy in a mixture in which the four other hydrocarbon products are present.

This deficiency was remedied by the auxiliary use of gas-liquid chromatography, which has the inherent capability for differentiating between hydrocarbons having similar molecular structure, but differing in some other property.

336

Application of Gas-Liquid Chromatography (GLC)

Motor Oil, Diesel Fuel, and Solvent Type II are all related to each other in being fractions obtained from the distillation of petroleum. Petroleum crudes have a predominant component of n-paraffin hydrocarbons in a homologous series of carbon numbers to C_{40} or more. The chromatogram of a typical petroleum sample is characterized by a periodic sequence of peaks representing unit increments in carbon numbers of the n-paraffin series. Through application of the carbon-number criterion in GLC, differentiation of the lower molecular-weight n-paraffin fractions, which characterize Solvent Type II and Diesel Fuel, from the higher molecular-weight fractions, which constitute motor lubricating oils, can readily be made. The chromatograms subsequently run on Solvent Type II, Diesel Fuel, and 30W Oil (Figure 6) clearly show this differentiation.

Thus, th gh the complementary capabilities of GLC with IR spectroscopy, recognition of each of the five specific hydrocarbon products in the presence of each other was made possible.

INSTRUMENTAL PROCEDURES

Infrared Spectroscopy

Infrared spectra of reference materials and samples were obtained using a double-beam, optical-null type, microprocessor-controlled infrared spectrophotometer (Perkin Elmer 283B) with operating parameters selected for a nominal resolution of 1 cm^{-1} in the range between 2000 and 600 wavenumbers. Absorption cells were of the sealed, demountable type, with KBr windows and cell path-lengths of 0.01 and 0.05 mm, dependent on sample type. Replicate transmission spectra were digitally recorded over the range between 2000 and 600 cm^{-1} at 1-wavenumber sampling intervals through a computer-interfacing system (Perkin-Elmer Data Station). The spectral scans were averaged, and stored on magnetic discs. The retrieved spectra were smoothed with a 13-point quartic smooth (14) prior to generating peak files formatted to print the wavenumber and transmittance (or absorbance) of each peak occurring above a given threshold value. The signal-averaged spectra were viewed on a video display by which the necessary transformation of transmittance/absorbance, or accumulation techniques to enhance peak intensity, could be observed. The resulting spectra were then computer plotted on formatted strip charts or on variable computer-generated grids.

337

Figure 6. Gas-Liquid Chromatograms of (A)Solvent Type II,(B)Diesel Fuel,(C)30W Motor Oil
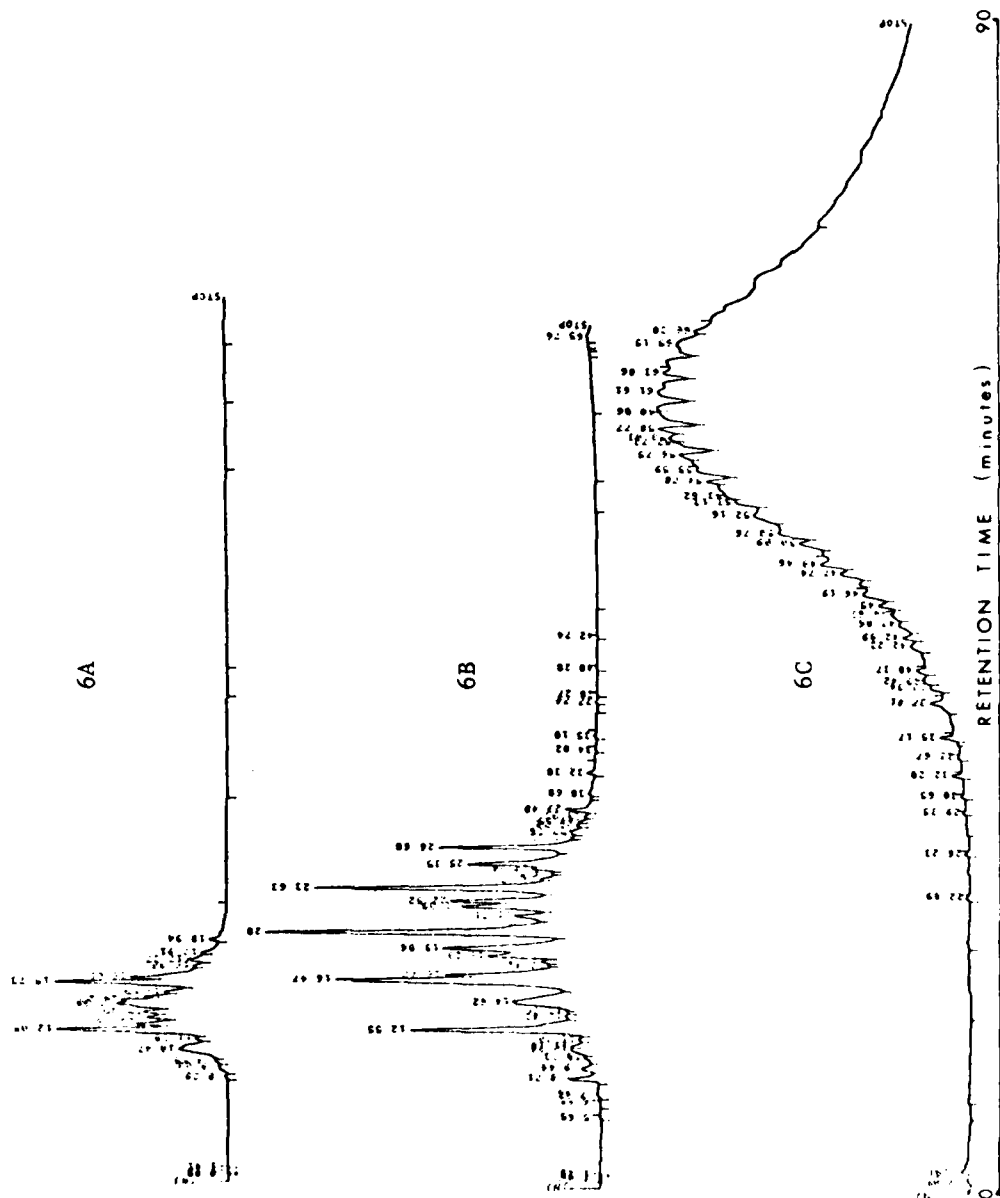
Gas-Liquid Chromatography

Equipment used in the GLC measurements consisted of a Hewlett-Packard Model 5754 Gas-Liquid Chromatograph equipped with temperature programming and a flame ionization detector. A 6-foot 3.2 mm stainless-steel column was packed with 6% Dexcil 300 on 80/100-mesh Chromasorb WHP. Column temperature was programmed through a linear range between 90° and $325^\circ C$ at a rate of $4^\circ C$ per minute. Sample volumes were typically between one and four microliters, depending on sample type. Output signals were processed through a Hewlett-Packard 3380A recording integrator which plotted the chromatogram with retention times indicated at each recorded peak, and also printed a table of the respective peak areas as percent of the total.

Sample Preparation

Reference samples of the hydrocarbon products included in the study were MIL-Spec materials obtained from the Ft. Lewis stores. Hydrocarbon samples received from the field were typically skim samples consisting of an oily phase containing solid debris and occluded water overlaying an aqueous phase. Since water even in trace amounts presents strong spectral interference in the infrared region and etches alkali-halide cell windows, complete separation of the organic phase from the aqueous phase was necessary. This was accomplished on a physical basis by centrifugation of appropriate portions of the sample in 20-ml centrifuge tubes at a temperature of approximately $30^\circ C$. A portion of the supernatant organic layer was then carefully drawn off with a Pasteur pipette and transferred to another tube. The cycle was repeated until a clear organic phase was obtained. The separated organic phase was filtered through anhydrous magnesium sulfate, which reduced the remaining traces of water to levels not detected in the recorded spectra.

Conventionally employed solvent extraction of the organics from field samples, followed by evaporation of the solvent, was avoided because of the inevitable addition of interfering solvent peaks if evaporation is performed at low temperatures, and the variable loss of relatively volatile fractions of the sample if the solvent evaporation is conducted at higher temperatures.

WEATHERING EFFECTS

When oils or other hydrocarbons are discharged in an aqueous effluent and are exposed to the atmosphere as emulsions or films overlaying an aqueous phase, changes in molecular structure occur on a time-related basis from the effects of solar irradiation, temperature, agitation, adsorption on solids, bacterial action, and by chemical interaction with other compounds in the effluent. These changes are reflected in the IR spectra and chromatograms of the materials. This so-called "weathering" must be taken into account in using "off the shelf" standard reference samples of the hydrocarbon products for identification of the same products in a recovered sample that has undergone environmental exposure. The changes that occur in weathered hydrocarbons are reflected in the emergence or increases of the oxidation-related carbonyl bands around 1700 cm^{-1}, increases in some aromatic-related bands, and in a general increase in baseline level in the 600 to 1500 cm^{-1} region.

Numerous techniques to simulate environmental weathering have been developed. The U.S. Coast Guard, the Department of the Interior, the Environmental Protection Agency, and others concerned with the fingerprinting of crude oil and petroleum products in marine and terrestrial environments have devoted considerable R&D effort in studies of the compositional changes due to weathering, and to the development of techniques for simulated weathering of reference samples that takes into account or compensates for the environmental effect (15,16). It has been shown in the reported references that the reliability of analytical fingerprinting methods is improved when synthetically weathered standards are employed in the identification of a recovered crude oil or petroleum product.

Methods developed and adopted by ERDA and ASTM for the synthetic weathering of crude oil involves a distillation under reduced pressure of the suspect and recovered oil samples, and collection of the +275°C (atm) fraction which is used in the subsequent analysis (16,17). The distillation technique for synthetic weathering of crude oils results in the rejection of the light fractions having n-paraffin carbon numbers of 15 or less. The rejection of the low carbon-number fraction does not affect analytical methods for the fingerprinting of crude oils which usually contain a n-paraffin series extending to C_{40} or more. However, such synthetic weathering methods are unsuited for the synthetic

weathering of effluent samples containing diesel fuel, solvent, and other light hydrocarbon fractions. Synthetic weathering by long-wavelength ultraviolet irradiation and aeration at temperatures below 40°, as used by Anderson et al. (18), offer more appropriate alternatives.

In the weathering procedure adopted for this study, a 10-ml volume of a given MIL-Spec reference hydrocarbon material was added to approximately 30 ml of water contained in a 100-ml beaker, forming a supernatant organic layer of approximately 5 mm overlaying the aqueous layer. The beakers containing the five hydrocarbon products were irradiated by sunlight-simulating fluorescent tubes placed approximately 10 cm above the liquid level in an Atlas UVCON atmospheric weathering chamber for a period of 48 hours at a temperature of 31°C. The percent change in weight of the reference materials after weathering was calculated.

As would be expected, significant weight losses by evaporation occurred in the light-distillate petroleum materials such as Diesel Fuel (37%) and Solvent Type II (54%). Weight losses from Hydraulic and Brake Fluids were moderate (6-8%), and the 30W Motor Oil showed an insignificant weight loss (less than 0.2%).

A comparison of the infrared spectra of the weathered vs not weathered reference materials showed neither emergence of new peaks nor disappearance of existing ones. Spectral changes were limited to slight increases in background absorption in the 1300 to 600 cm^{-1} region; an increase in peak heights of oxidation-related bands around 1700 cm^{-1}, and changes in the peak ratios of the Diesel Fuel absorption bands in the 750 cm^{-1} spectral region. Thus, for the specific hydrocarbon products included in this study, artificial weathering of reference materials did not change the "recognition power" of the selected infrared absorption bands.

Since the weathering of light fractions of the hydrocarbons which constitute Solvent Type II and Diesel Fuel results in significant loss of lower-boiling components, this loss is reflected in attenuation or absence of the lower carbon-number peaks in gas-liquid chromatograms. In GLC techniques, weathering effects must be taken into account in the interpretation of chromatographic data. Reference materials should be artificially weathered before chromatographic comparisons are made with field samples.

RESULTS

The utility of the tentative infrared/gas-liquid chromato-graphic analytical method was shown by its ability to successfully identify hydrocarbon products in "known unknowns" prepared from the five hydrocarbon reference materials. In a field sample of waste-water from the Flora Road outfall, Ft. Lewis, Washington, hydrocarbon products identified in the organic phase included motor oil, diesel fuel, and hydraulic fluid. The complementary "recognition powers" of IR and GLC were clearly evident--the marginal capability of IR to recognize motor oil in the presence of the other specified hydrocar-bon products was effectively augmented by the strong recognition power of GLC for this material. Diesel fuel was identified by both IR and GLC; hydraulic fluid was readily identified by IR.

CONCLUSIONS

At this stage in the development of a method to identify specified hydrocarbon products in wastewater from vehicular service areas on Army installations, neither infrared spectroscopy nor gas-liquid chromatography, when used alone, completely establishes the identity of all the products in the presence of each other. However, when used in combination, IR/GLC can be the basis of an effective analytical method.

Although a method involving only one analytical discipline would have obvious advantages over one involving, as in this case, both IR and GLC, the advantages would be real only if the total pro-cedural details and instrumentation required in the application of the single discipline would be less complex than through the use of two disciplines in combination. The tentative method described for this specific and limited purpose is relatively simple, and could be used with instrumentation and by personnel typical of the well-equipped analytical laboratory.

ACKNOWLEDGMENT

REFERENCES

1. Gruenfeld, M., Environ. Sci. and Technology, July (1973).

2. "Oil and Grease, Total Recoverable," EPA STORET No. 00560.

3. Adlard, E.R., J. Inst. Petrol., 58, 63-74 (1972).

4. Bentz, A.P., "Oil Spill Identification," Anal. Chem. Rev., 48, 6, 455A-470A (1976).

5. Brown, C.W., Lynch, F.P., and Ahmadjian, M., Appl. Spectros. Rev., 9, 223 (1975).

6. Gruenfeld, M., "Proceedings of the Joint Conference on Prevention and Control of Oil Spills," Amer. Petrol. Inst. (1973).

7. Kawahara, F.K., J. Chromatogr. Sci., 10, 629-636 (1972).

8. Wilson, C.A., Ferrero, C.P., and Coleman, H.J., "Crude Oil Spills Research," U.S. Bureau of Mines, RI8024 (1975).

9. Bentz, A.P., "Oil Spill Identification and Remote Sensing." Presented at Division of Petroleum Chemistry, ACS Meeting, Sept. 1978.

10. Lynch, P.F., and Brown, C.W., Environ. Sci. and Technology, 7, 1123 (1973).

11. Mattson, J.S., Anal. Chem., 43, 1872 (1971).

12. Mattson, J.S., Mattson, C.S., Spencer, M.J., and Starks, S.A., Anal. Chem., 49, 297 (1977).

13. Killeen, T.J., Eastwood, D., and Hendrick, M.S., "Oil Matching Using a Simple Vector Model," 1978 Pittsburgh Conf., Paper 397.

14. Savitsky, A., and Goloy, M., Anal. Chem., 36, 1627 (1964).

15. Brown, C.W., Ahmadjian, M., Baer, C.D., Lynch, P.F., Environ. Sci. and Technology, 10, 777 (1976).

16. Grizzle, P.L., and Coleman, H.J., ERDA, BERC/RI-77/12 (1977).

17. ASTM Method D-3415-75T, "Practices for Identification of Waterborne Oils," Annual Book of ASTM Standards, Part 31 (1978).

18. Anderson, C.P., Killeen, T.J., Taft, J.B., and Bentz, A.P., 1979 Pittsburgh Conference, Paper 527.

THE EFFECTS OF CATHEPTIC ENZYMES ON MUSCLE PROTEINS

*JOHN E. WALKER, JR., FREDERICK M. ROBBINS AND SAMUEL H. COHEN
FOOD SCIENCES LABORATORY
US ARMY NATICK RESEARCH AND DEVELOPMENT COMMAND
NATICK, MASSACHUSETTS 01760

It is well recognized that two structural components-collagen of the connective tissue and the actomysin complex of the contractile apparatus determine the tenderness of meat. Muscle collagen is comprised of three genetically distinct types, each stabilized by lysine derived cross-links. As the animal matures the degree of cross-linkage increases relating to the textural alteration in the meat from older animals. Textural changes not related to the age of the animal occur postmortem (after slaughter) in which the meat goes through a cycle of toughening (rigor) and tenderization. The natural tenderization following rigor occurs after 4 or 5 days postmortem and involves primarily changes in the interaction of two major elements of the contractile apparatus; myosin (the thick filament) and actin (the thin filament). Examination of the changes in the ultrastructure of the muscle during the natural tenderization process include: loss of the "Z" band (a structure occuring periodically along the muscle fiber to which it is believed attaches thin filaments to each other), and changes in the distances between the thick and thin filaments. In 1973 Eino and Stanley (1) showed that a group of proteases in muscle produced structural alterations in muscle resembling those which occured during postmortem tenderization. These enzymes were released maximally after 5 days postmortem. The group of enzymes are known to be acid hydrolases called cathepsins and are found within special organalles in the muscle called lysosomes. In 1976 Robbins and Cohen (2) of the Food Sciences Laboratory of NARADCOM, reported that muscle when treated with an extract of bovine spleen could be considered as an exogenous tenderizer which would simulate the natural aging process that occurs postmortem.

345

The work that I will report on today is the progress since the 1976 paper. This work gives biochemical, ultrastructural and technological evidence for the use of spleen enzymes (cathepsins) as exogenous tenderizing agents. We have recently published these findings (3).

The extraction of the active enzyme fraction is shown in figure 1. The release of the catheptic enzymes from the lysosomes occurs when the pH is lowered to 3.5. The subsequent lyophilate is rehydrated prior to its application. The catheptic enzymes found in the spleen extract are given in figure 2. Our attention has been focused on cathepsin D and B. As a model system of meat in order to examine the effect of these catheptic enzymes we chose bovine myofibrils. Myofibrils contain thick (myosin) and thin (actin) filaments as well as the regulatory proteins (tropomyosin and the troponins). In addition the myofibril contains a protein (actinin) which many consider the main component of the "Z" band. The effect of the action of the spleen enzymes was followed by electrophoretic analyses of the treated myofibrils. In these experiments the enzyme extract was added to a solution of myofibrils and after the specified incubation time the myofibrils were solubilized in a phosphate buffer containing urea, sodium dodecylsulfate, and dithiothreitol (a reducing agent). The electrophoresis was performed on polyacrylamide gels and the individual proteins were visualized by staining with coumassie blue dye. The results of the reaction with the spleen extract is shown in figure 3, where A is the control myofibril untreated, B and C are myofibrils treated with spleen enzyme (cathepsin D) and with cathepsin D (isolated from muscle) respectively. The most dramatic change is seen in the myosin which has decreased in molecular weight from 200,000 daltons to 145,000 daltons, other changes occured in the regulatory proteins especially troponin I and troponin C. Changes in myosin might be expected to weaken the structure of the muscle fiber and lead to an alteration in tensile strength (a tenderization. We compared the action of the spleen enzyme to a commercial meat tenderizer, papain which is derived from plants and goes under the trade name of "Adolph's Tenderizer". The myofibrils were treated with papain in a similar manner as the spleen enzyme and analyzed by gel electrophoresis. The results are shown in figure 4. The control (untreated) myofibril is A and the papain treated, B. The action of papain leads to a complete hydrolysis of the myofibrilar proteins. Such an extensive proteolysis may be the cause of the over tenderizing action observed in the indiscriminate use of commercial meat tenderizers. In order to examine the extent to which the organization of the myofibril is disrupted on the molecular level during the reaction with the spleen enzymes, a series of experiments involving electron spin resonance were performed. In these experiments low molecular weight organic compounds which posses an unpaired electron in one region of their structure was covalently

attached to the myofibril through a functional group in another region
of their structure. The two organic compounds we used in our studies
are shown in figure 5A. They attached themselves primarily to one
region of the myosin (thick filament). The attached organic free radi-
cals acted as reporter groups in the myofibril since their electropar-
amagnetic resonance spectra (figure 5B) would be altered in shape if
there were structural alterations occuring near to them. In figure 6
is shown the effect of 4 commercial meat tenderizers A,B,C, and D on
myofibrils containing the free radical reporter groups. Their effect
is compared to the action of the spleen enzymes (E and F). The para-
meter "R" on the ordinate scale represents the degree of structureal
alteration in the area near the reporter groups. We noted that each
of the commercial tenderizers bring about rapid structural disorder
while the spleen enzyme treated samples showed no such effect. Ultra-
structural examination on the spleen enzyme treated myofibrils was
made by scanning electron microscopy. After treatment with the spleen
enzyme the myofibrils were washed and fixed in glutaraldehyde. Fol-
lowing a dehydration procedure, the samples were critically point
dried with CO_2, mounted and coated with gold-palladium. The prepared
specimens were examined in a Coates and Welter Model 100-Z Field
Emission Scanning Electron Microscope. Figure 7 shows the S.E.M.
micrographs of the untreated (A) and the enzyme treated myofibril (B
and C). The structural alterations seen in the enzyme treated myo-
fibrils are; a loss of the "Z" band structure (refer to the arrow in
the figure), and a shortening of the lengths of the sarcomeres (the
region of the myofibril bounded by each "Z" band). Loss of the "Z"
band is the commonly observed ultrastructural change that postmortem
meat undergoes during the natural tenderization process. In the
natural tenderization process this "Z" band loss occurs after 4 to 5
days whereas the spleen enzyme extract brings this about after one
hour.

Although our biochemical and ultrastructural experiments had
shown that the changes brought about by the spleen enzymes were very
similar to those reported during natural tenderization, a technologi-
cal experiment was needed to prove its potential usefulness for the
Army;s Food Program. In this experiment, precooked freeze-dehydrated
beef slices were placed in vacuum sealed cans and stored at room tem-
perature. At periods of 3,6,9, and 12 months dehydrated beef slices
were rehydrated in water with and without the spleen enzyme extract.
Figure 8 shows a textural measurement on the rehydrated meat slices
performed on a Instron Universal Testing Instrument. At all times
during the storage experiment the effect of the spleen enzyme was to
increase the tenderness of the beef slices.

The work of the Food Sciences Laboratory of NARADCOM has thus
shown that extracts from bovine spleen, highly active in catheptic
enzymes have an excellent potential for use as exogenous meat

*WALKER, ROBBINS & COHEN

tenderizers because of their selectivity of action and ready avail-
ability from bovine spleen which is a cheap by-product of the meat
industry.

REFERENCES:

1. Eino, M.F. and Stanley, D.W. 1973. Catheptic activity, textural
    properties and surface ultrastructure of postmortem beef muscle.
    J. Food Sci. 38:45.

2. Robbins, F.M. and Cohen, S.H. 1976. Effects of Catheptic enzymes
    from spleen on the microstructure of bovine semimembranosus
    muscle. J. Text. Stud. 7:137.

3. Robbins, F.M., Walker, J.R., Cohen, S.H., and Chatterjee, S. 1979.
    Action of proteolytic enzymes on bovine myofibrils. J. Food
    Sci. 44:1672.

Spleen
 | 1. Grind
 | 2. Extract with Acetone
 | 3. Dried in air, 4°

Acetone Powder
 | 1. Extract with distilled water (cold)
 | 2. Filter and adjust pH to 3.5 with
 | HCL
 | 3. Centrifuge

Supernatant   Residue
 | 1. Adjust pH   Discard
 | to 6.5
 | 2. Centrifuge
 | 3. Concentrate supernatant
 | by membrane ultrafil-
 | tration
 | 4. Lyophilize

Spleen Enzyme Lyophilate

FIGURE 1

LYSOSOMAL CATHEPTIC ENZYMES

1. Cathepsin A - Carboxypeptidase, has little action on protein itself, but acts synergistically with endo- peptidases

2. Cathepsin B - Endopeptidase with broad specificity similar to papain

3. Cathepsin C - Exopeptidase capable of sequentially split- ting dipeptides from the amino terminals of polypeptide chains.

4. Cathepsin D - Endopeptidase that resembles pepsin in its specificity

FIGURE 2
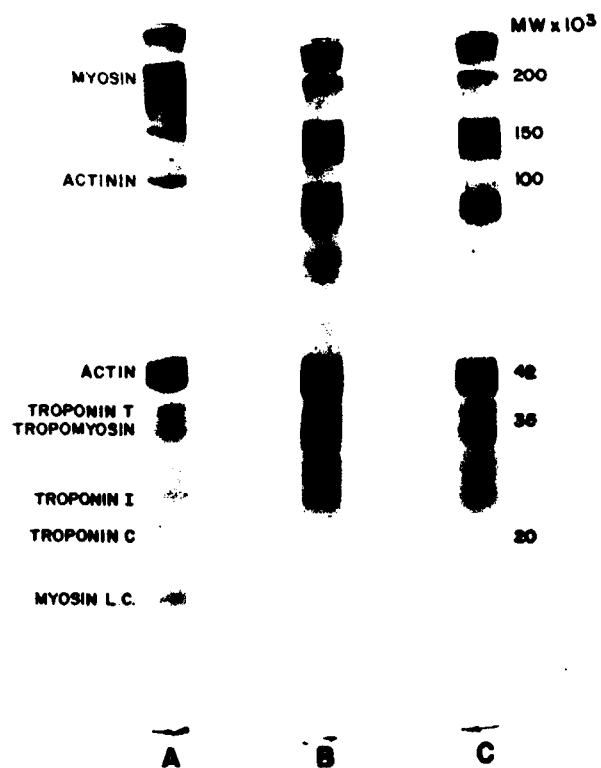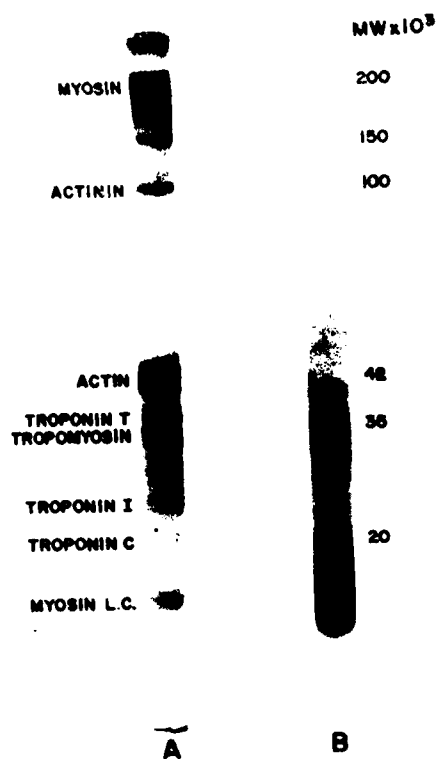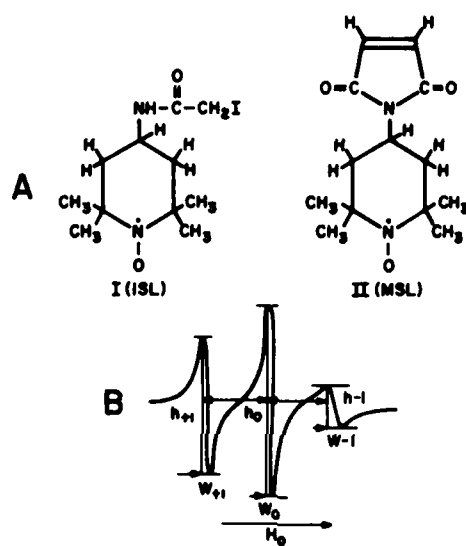
FIGURE 3

FIGURE 4

352
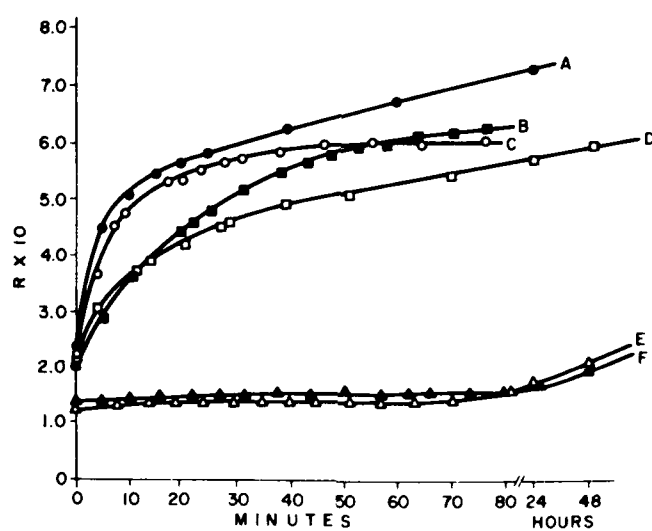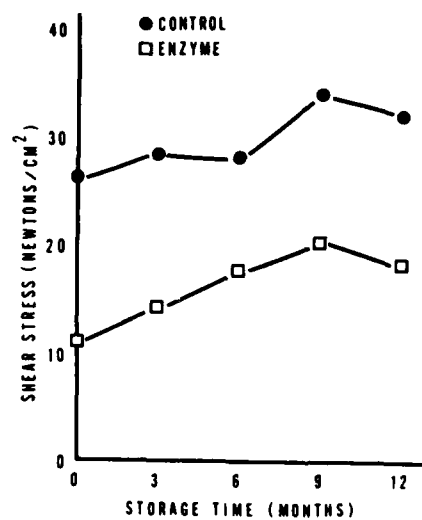
FIGURE 5

FIGURE 6

FIGURE 7

FIGURE 8

HEAT CONDUCTION IN FINITE CYLINDERS AND THE COMPUTER-AIDED
CALCULATION OF BACTERIA SURVIVAL IN HEAT STERILIZATION

*CHIA PING WANG, DR.
ARI BRYNJOLFSSON, DR.
US ARMY NATICK RESEARCH AND DEVELOPMENT COMMAND
NATICK, MASSACHUSETTS 01760

1. INTRODUCTION

The temperature distribution $T(x,y,z,t)$ in a specimen during heating and cooling of its outer surface is determined by solving the heat diffusion equation for given boundary conditions. Solutions are often obtained for special forms, such as infinite cylinders or infinite slabs, of the specimen, and for some simplified boundary conditions, such as abrupt initial temperature change at the surface of the sample. In practical problems, the solutions are often approximated by simple forms of the time temperature relations. For instance, in the case of retorting of food, the center temperature in the can is usually approximated by a zero order Bessel function valid for very large values of time. Such approximations, while valuable, are inadequate for exact studies. Using modern computers, we were able to calculate $T(x,y,z,t)$ very accurately for any practical size cylinder and for different boundary conditions corresponding to Nusselt numbers between 0 and 5000. The high accuracy and the rapid calculations make the method very useful in many fields of thermal engineering. In the present paper, we apply this method to exact integral calculations of the survival fraction of bacteria during heat sterilization process.

2. HEAT DIFFUSION EQUATION FOR A FINITE CYLINDER

The conduction of heat in a cylinder is given by a second order differential equation. In cylindrical coordinates it is:

$$\frac{\partial T(r,\theta,z,t)}{\partial t} = \kappa \nabla^2 T(r,\theta,z,t) \qquad (1)$$

where $T(r, \theta, z, t)$ is the temperature at point $P(r, \theta, z)$ and at time t, and κ is the thermal diffusivity of the material of the solid

$$\kappa = \frac{\lambda}{\rho \cdot c} = \frac{\text{thermal conductivity}}{\text{density} \cdot \text{specific heat}} \tag{2}$$

We will consider heating a cylindrical specimen from an initial temperature T_i with a constant temperature T_h on the outside of the surface. Then the temperature $T(r, \theta, z, t)$ at any point in the specimen at any time t will be given by Eq. (1), together with the boundary conditions. To simplify the equations, we introduce a new temperature variable:

$$T = T - T_h \tag{3}$$

Eq. (1) becomes

$$\frac{\partial T}{\partial t} = \kappa \, \nabla^2 T \text{ for } r \leq a, \; |z| \leq \ell \tag{4}$$

where a is the radius, and ℓ the half-length of the cylinder. The initial value of T at any point of the specimen is:

$$T_i = T_i - T_h, \text{ for } t \leq o \tag{5}$$

We will consider here the case of convective heating outside the cylinder. At the boundary there will be an interface or transition layer in which the temperature is changing from T_h to the actual temperature of the specimen at the surface. We then obtain the following boundary conditions by equating the heat flowing through the transition layer and the heat flowing through the outermost layer of the specimen.

$$\frac{\partial T}{\partial r} + \frac{h}{\lambda} \, T = o \text{ at } r = a \tag{6}$$

$$\frac{\partial T}{\partial z} + \frac{h}{\lambda} \, T = o \text{ at } z = \ell \tag{7}$$

$$\frac{-\partial T}{\partial z} + \frac{h}{\lambda} \, T = o \text{ at } z = -\ell \tag{8}$$

where λ is conductivity of the specimen, and $h = \lambda gas/\delta gas$, the conductivity of the gas (air) divided by the thickness of the gas (air) film, is the coefficient of heat transfer due to the gas film only.

358

Due to radiation at the surface, h actually would be equal to $\lambda_{gas}/\delta_{gas}$ plus some constant. Also, in the case of a meat sample with casing, we have two transition layers instead of one at the surface, the solid casing material and the gas film adhered onto it. All these three factors can be combined into a single coefficient in front of T in Eqs. (6), (7) and (8). Henceforth, h/λ in Eqs. (6), (7) and (8) will stand for this effective coefficient.

Eq. (4) with boundary conditions Eqs. (6) - (8), i.e., $\partial T/\partial r$ being proportional to T, can be solved with the usual technique of the separation of variables.[1,2] The solution for the temperature distribution in a finite cylinder, in our case, takes the following form:

$$T = \sum_j \sum_n A_{j,n} \cdot \cos(\lambda_j z) \cdot J_c(\alpha_n r) \cdot e^{-\kappa(\lambda_j^2 + \alpha_n^2)t} \tag{9}$$

where $A_{j,n}$ are the coefficients of expansion and where $x_n = a \cdot \alpha_n$ are the roots of the following equation (J_0 and J_1 being Bessel functions of order zero and one respectively),

$$x_n \cdot J_1(x_n) = \frac{h}{\lambda} a \cdot J_0(x_n) \tag{10}$$

and $y_j = \lambda_j \ell$ are the roots of

$$\frac{h\ell}{\lambda} \cos y_j - y_j \sin y_j = 0 \tag{11}$$

We have deduced from the boundary conditions the coefficients of expansion $A_{j,n}$ in Eq. (9). After some lengthy calculation, $A_{j,n}$ are found to be

$$A_{j,n} = 2T_i \frac{1}{x_n\left[\left(\frac{x_n}{\nu}\right)^2 + 1\right] \cdot J_1(x_n)} \cdot \frac{4 \sin y_j}{\sin(2 y_j) + 2 y_j} \tag{12}$$

The temperature $T = T(r, \theta, z, t)$ of the specimen is then

$$T - T_h = 2(T_i - T_h) \sum_{j=1}^{\infty} \sum_{n=1}^{\infty} \frac{1}{x_n\left[\left(\frac{x_n}{\nu}\right)^2 + 1\right] \cdot J_1(x_n)} \cdot$$

$$J_0(\alpha_n r) \cdot \frac{4 \sin y_j}{\sin(2 y_j) + 2 y_j} \cdot \cos \lambda_j z \cdot e^{-\kappa(\lambda_j^2 + \alpha_n^2)t} \tag{13}$$

359

where

$$\nu = \frac{h}{\lambda} \cdot a = \text{effective conduction Nusselt Number,}$$
or Biot Number[3] $\quad\quad\quad\quad$ (14)

and x_n and y_i are roots of Eqs. (10) and (11).

3. CALCULATIONS OF THE TEMPERATURE DISTRIBUTION

The temperature distribution $T(r, \theta, z, t)$ can be computed for any point $P(r, \theta, z)$ inside the cylinder and any time t provided the roots x_n of Eq. (1) for a given ν, and the roots y_i of Eq. (11) for a given value of $h\ell/\lambda$ are known.

Our task then is to devise first some means to compute rapidly these roots with any practical values of ν and $h\ell/\lambda$.

We have written computer programs which enable us to compute the first 36 roots of Eqs. (10) and (11), for $\nu = 0$ to 5000 and $h\ell/\lambda = 0$ to 10,000, with rapid convergence.

Likewise, the double summation of Eq. (13) has been carried out with the computer. This double summation in principle could be carried out to as many terms as we wish, so long as the values of the roots x_n and y_i are available.

We have also used a temperature variable Ψ, the "relative excess temperature", which is independent of the actual initial and heating temperature,

$$\Psi = \frac{T - T_h}{T_i - T_h} \quad\quad\quad\quad (15)$$

It is seen from Eq. (13) that Ψ is equal to twice the double summation of that equation, and is independent of T_i and T_h. Thus, the actual temperature distributions $T(r, \theta, z, t)$, due to different initial and heating temperatures, can be directly compared or derived from one another.

The temperature distribution $T(r, \theta, z, t)$ in specimens during heating and cooling has often been obtained by some approximations for the heat diffusion equation or its solution. In the present paper we deduced, on the other hand, the exact analytical solution to the heat diffusion equation for finite cylinders in convective heating. The truncation of the two series in Eq. (13) to 36 terms in each of

360

the summations results in a very accurate form, allowing $T(r, \theta, z, t)$ to be calculated for any practical size finite cylinders and for Nusselt (Biot) number extending from 0 to 5000. The method developed should have great applicability in thermal engineering industry. Tables I – II give the relative excess temperature Ψ on the cross sections at $z/\ell = 0$, and 0.6 respectively, at $r/a = 0$, 0.2, 0.4,—1.0 and times $t = 5$, 10, 15,---240 minutes, for a specimen of radius $a = 5$ cm, half-length $\ell = 2.5$ cm, with $\kappa = 1.35 \times 10^{-3}$ cm^2s^{-1} and $\nu = 6.0$. Similar tables for Ψ on the cross sections $z/\ell = 0.2$, 0.4, 0.8, and 1.0, are available from the authors.

The last columns of these tables give the survival fraction calculations of bacteria during sterilization to be discussed in later sections.

Figs. 1a–1f are the computer plots of these tables.

4. CALCULATION OF BACTERIA SURVIVAL IN HEAT STERILIZATION

We now apply the above calculations of heat diffusion to thermal killing of bacteria in finite cylindrical specimens. The microbial kill is described quantitatively by the survival fraction N/N_0 where N is the number of bacteria survived at time t and N_0 is the initial value of N. For a large class of microorganisms, N/N_0 during thermal sterilization at a given constant temperature T follows closely the following equation [1,5,6]:

$$\ln \frac{N}{N_0} = -C \cdot \left[\exp (-E_a'RT) \right] \cdot t \qquad (16)$$

where

E_a = the Arrhenius activation energy in $kcal-mol^{-1}$ for inactivating a unit or a molecule that is essential for the survival of a bacterium

R = the universal gas constant in $J \cdot mol^{-1}$

T = sterilization temperature in Kelvin

t = sterilization time in s

C = a constant

361

TABLES I & II- RELATIVE TEMPERATURE DIFFERENCES, ψ = (T-T$_h$)/(T$_i$-T$_h$) IN TWO CROSS SECTIONS AT Z/ℓ=0 AND 0.6. THE FIRST COLUMN GIVES THE TIME, THE COLUMNS 2-7 GIVE ψ FOR DIFFERENT DISTANCES r/a = 0, 0.2, 0.4, 0.6, 0.8, 1.0 AND COLUMN 8 GIVES THE SURVIVAL FRACTION FOR Cl. BOTULINUM SPORES AT r/a=0.

TABLE I

A = 5.0 C+ NU = 6.0 L = K1 = 2.5 CM 1.35-03 CM SQ/S

TIME MIN	0.0	0.2	0.4	0.6	0.8	1.0 (Z/L = .0)	S.F. AT AXIS
	DISTANCE FROM AXIS						
5	.9973	.9973	.9970	.9876	.8853	.4809	1.000+00
10	.9627	.9618	.9528	.9015	.7252	.3632	1.000+00
15	.8972	.8921	.8656	.7814	.5906	.2855	1.000+00
20	.8163	.8059	.7644	.6649	.4833	.2298	1.000+00
25	.7297	.7154	.6652	.5628	.3984	.1863	1.000+00
30	.6436	.6274	.5744	.4761	.3307	.1533	1.000+00
35	.5623	.5457	.4937	.4031	.2763	.1272	9.999-01
40	.4879	.4719	.4233	.3417	.2319	.1062	9.999-01
45	.4212	.4064	.3622	.2900	.1953	.0892	9.991-01
50	.3628	.3499	.3096	.2463	.1650	.0752	9.951-01
55	.3109	.2991	.2643	.2094	.1397	.0635	9.789-01
60	.2663	.2559	.2256	.1781	.1185	.0538	9.260-01
65	.2277	.2187	.1924	.1516	.1006	.0456	7.908-01
70	.1944	.1860	.1641	.1290	.0855	.0387	5.576-01
75	.1661	.1598	.1399	.1099	.0727	.0329	2.665-01
80	.1417	.1364	.1193	.0936	.0619	.0280	6.851-03
85	.1209	.1159	.1016	.0797	.0527	.0238	1.936-04
90	.1031	.0989	.0866	.0679	.0448	.0203	1.090-06
95	.0879	.0843	.0738	.0578	.0382	.0173	9.060-10
100	.0749	.0718	.0629	.0493	.0325	.0147	8.467-14
105	.0639	.0612	.0536	.0420	.0277	.0125	7.410-19
110	.0544	.0522	.0457	.0358	.0236	.0107	5.456-25
115	.0464	.0444	.0389	.0305	.0201	.0091	3.249-32
120	.0395	.0379	.0332	.0259	.0171	.0077	0.000
125	.0337	.0323	.0283	.0221	.0146	.0066	0.000
130	.0287	.0275	.0241	.0188	.0124	.0056	0.000
135	.0244	.0234	.0205	.0160	.0106	.0048	0.000
140	.0208	.0199	.0175	.0137	.0090	.0041	0.000
145	.0177	.0170	.0149	.0116	.0077	.0035	0.000
150	.0151	.0145	.0127	.0099	.0065	.0030	0.000
155	.0129	.0123	.0108	.0085	.0056	.0025	0.000
160	.0110	.0105	.0092	.0072	.0048	.0021	0.000
165	.0094	.0090	.0078	.0061	.0040	.0018	0.000
170	.0080	.0076	.0067	.0052	.0034	.0016	0.000
175	.0068	.0065	.0057	.0045	.0029	.0013	0.000
180	.0058	.0055	.0049	.0038	.0025	.0011	0.000
185	.0049	.0047	.0041	.0032	.0021	.0010	0.000
190	.0042	.0040	.0035	.0028	.0018	.0008	0.000
195	.0036	.0034	.0030	.0023	.0015	.0007	0.000
200	.0030	.0029	.0026	.0020	.0013	.0006	0.000
205	.0026	.0025	.0022	.0017	.0011	.0005	0.000
210	.0022	.0021	.0019	.0015	.0010	.0004	0.000
215	.0019	.0018	.0016	.0012	.0008	.0004	0.000
220	.0016	.0015	.0013	.0011	.0007	.0003	0.000
225	.0013	.0013	.0011	.0009	.0006	.0003	0.000
230	.0012	.0011	.0010	.0008	.0005	.0002	0.000
235	.0010	.0010	.0008	.0007	.0004	.0002	0.000
240	.0008	.0008	.0007	.0006	.0004	.0002	0.000

TABLE II

A = 5.0 C+ NU = 6.0 L = K1 = 2.5 CM 1.35-03 CM SQ/S

TIME MIN	0.0	0.2	0.4	0.6	0.8	1.0 (Z/L = .6)	S.F. AT AXIS
	DISTANCE FROM AXIS						
5	.9027	.9027	.9024	.8939	.8013	.4353	1.000+00
10	.7681	.7674	.7600	.7380	.5937	.2974	1.000+00
15	.7013	.6973	.6766	.6107	.4616	.2232	1.000+00
20	.6255	.6175	.5856	.5594	.3703	.1754	1.000+00
25	.5543	.5434	.5053	.4275	.3026	.1415	1.000+00
30	.4871	.4748	.4347	.3603	.2503	.1160	9.999-01
35	.4249	.4124	.3731	.3046	.2088	.0961	9.991-01
40	.3685	.3564	.3196	.2580	.1751	.0802	9.957-01
45	.3180	.3068	.2734	.2189	.1475	.0673	9.820-01
50	.2735	.2635	.2337	.1859	.1246	.0567	9.382-01
55	.2347	.2258	.1995	.1581	.1055	.0479	8.264-01
60	.2010	.1932	.1703	.1345	.0894	.0406	6.098-01
65	.1719	.1651	.1453	.1144	.0759	.0344	3.217-01
70	.1469	.1410	.1239	.0974	.0645	.0292	9.662-02
75	.1254	.1203	.1056	.0829	.0549	.0249	1.236-02
80	.1070	.1026	.0900	.0766	.0467	.0211	4.101-04
85	.0913	.0875	.0767	.0601	.0397	.0180	5.482-06
90	.0778	.0746	.0654	.0512	.0338	.0153	6.767-13
95	.0663	.0636	.0557	.0436	.0288	.0130	1.376-17
100	.0565	.0542	.0475	.0372	.0245	.0111	1.848-23
105	.0482	.0462	.0405	.0317	.0209	.0095	2.618-30
110	.0411	.0394	.0345	.0270	.0178	.0080	1.817-38
115	.0350	.0335	.0294	.0230	.0152	.0067	0.000
120	.0298	.0286	.0250	.0196	.0129	.0058	0.000
125	.0254	.0244	.0213	.0167	.0110	.0050	0.000
130	.0217	.0208	.0182	.0142	.0094	.0042	0.000
135	.0184	.0177	.0155	.0121	.0080	.0036	0.000
140	.0157	.0151	.0132	.0103	.0068	.0031	0.000
145	.0134	.0128	.0112	.0088	.0058	.0026	0.000
150	.0114	.0109	.0096	.0075	.0049	.0022	0.000
155	.0097	.0093	.0082	.0064	.0042	.0019	0.000
160	.0083	.0079	.0070	.0054	.0036	.0016	0.000
165	.0071	.0068	.0059	.0046	.0031	.0014	0.000
170	.0060	.0058	.0050	.0040	.0026	.0012	0.000
175	.0051	.0049	.0043	.0034	.0022	.0010	0.000
180	.0044	.0042	.0037	.0029	.0019	.0009	0.000
185	.0037	.0036	.0031	.0024	.0016	.0007	0.000
190	.0032	.0030	.0027	.0021	.0014	.0006	0.000
195	.0027	.0026	.0023	.0018	.0012	.0005	0.000
200	.0023	.0022	.0019	.0015	.0010	.0005	0.000
205	.0020	.0019	.0016	.0013	.0008	.0004	0.000
210	.0017	.0016	.0014	.0011	.0007	.0003	0.000
215	.0014	.0014	.0012	.0009	.0006	.0003	0.000
220	.0012	.0012	.0010	.0008	.0005	.0002	0.000
225	.0010	.0010	.0009	.0007	.0004	.0002	0.000
230	.0009	.0008	.0007	.0006	.0004	.0002	0.000
235	.0007	.0007	.0006	.0005	.0003	.0001	0.000
240	.0006	.0006	.0005	.0004	.0003	.0001	0.000

FIGS. 1a-1f-THE ORDINATE SHOWS THE RELATIVE TEMPERATURE DIFFERENCES, $\psi = (T-T_B) / (T_1-T_B)$, IN A FINITE CYLINDER FOR VARIOUS CROSS SECTIONS AT Z/ℓ EQUAL 0, 0.2, 0.4, 0.6, 0.8, 1.0. THE ABSCISSA SHOWS THE HEATING TIME t.

363

In this case where T is constant, we obtain by differentiation of Eq. (16), that the kill rate function (dN/dt)/N is the exponential exp $(-E_a/RT)$, that is:

$$\frac{dN}{dt} \cdot \frac{1}{N} = -C \cdot [\exp(-E_a/RT)] = -C \cdot F(T(t), t) \qquad (17)$$

In some experiments it is found that the semi-logarithmic plot of the survival fraction has a "shoulder". This may be represented by the function

$$F(T(t),t) = 1 - [1-\exp(-E_a/RT(t))]^n \qquad (18)$$

which for n = 1 reduces to the form in Eq. (17), the frequently used Arrhenius function:

$$F(T(t), t) = \exp[-E_a/RT(t)] \qquad (19)$$

We now show that for the general case where the kill rate function assumes a general form $F(T(t), t)$, with the temperature $T(t)$ varying with time t, the survival fraction is given by the following time integral:

$$\ln \frac{N}{N_0} = -C \int_0^t F(T(t), t) \, dt \qquad (20)$$

From the emperical law Eq. (16) for constant T,

$$\ln \frac{N}{N_0} = -C \cdot [\exp(-E_a/RT)] \cdot T \qquad (16)$$

we obtain the following differential form in terms of the kill rate

$$\frac{dN}{dt} = -C \cdot [\exp(-E_a/RT)] \cdot N \qquad (21)$$

Now we generalize Eq. (21) to include the case where T varies with t. By integrating Eq. (21) for this temperature varying case, we have the following time integral for the logarithmic survival fraction

$$\ln \frac{N}{N_0} = -C \int_0^t \exp(-E_a/RT) \, dt \qquad (22)$$

Next, we generalize Eqs. (21) for the general kill rate function $F(T(t), t)$,

$$\frac{dN}{dt} = -C \cdot F(T(t), t) \cdot N \tag{21a}$$

the logarithmic survival fraction is then

$$\log \frac{N}{N_O} = -C \int_o^t F(T(t), t) \, dt \tag{22a}$$

which is Eq. (20).

5. CALCULATIONS OF BACTERIAL SURVIVAL EQUATION

We now put our function $T(t)$ of Eq. (13) into the "bacterial survival integral" of Eqs. (22) or (22a) to calculate the survival fraction N/N_O of the bacterium. In this paper, we carried out the calculations for Cl. botulinum spores for which we assume the kill rate function to be given by the exponential function $\exp(-E_a/RT)$ rather than the general function $F(T(t), t)$ which may represent any empirical function or other theoretical function such as Eyring's.

The calculations for other microorganisms will be exactly the same.

The integrand of Eq. (22) after substituting T from Eq. (13) looks quite complicated. We have written computer programs to carry out the computation. But, before we carry out the computation, the two constants, which characterize the bacterium being considered, C and E_a in Eqs. (16) and (22), have to be determined.

6. DETERMINATION OF E_a

We show in some details below the relationship between the so-called z-value in the terminology used by the microbiologist, the temperature T, and the Arrhenius activation energy E_a.

The reaction rate equation, Eq. (21a),

$$\frac{dN}{dt} = -kN = -C \cdot \left[\exp(-E_a/RT)\right] \cdot N \tag{21}$$

means that the temperature dependence of k is through T in the exponential function $\exp(-E_a/RT)$ only where E_a is a constant independent of T. Otherwise, k will have to be expressed by the general function

$F(T(t), t)$. Thus, at temperatures T_1 and T_2, we have

$$(\frac{dN}{dt})_1 = -C \cdot [\exp(-E_a/RT_1)] \cdot N \qquad (23)$$

$$(\frac{dN}{dt})_2 = -C \cdot [\exp(-E_a/RT_2)] \cdot N \qquad (24)$$

From Eqs. (23) and (24),

$$\frac{(dN/dt)_1}{(dN/dt)_2} = \exp\left[-\frac{E_a}{R} \frac{T_2 - T_1}{T_1 T_2}\right] \qquad (25)$$

Now if we choose the temperature T_2 such that the rate of inactivation is changed by a factor of 10 from that at T_1, that is:

$$\frac{(dN/dt)_1}{(dN/dt)_2} = 10 \qquad (26)$$

whence, using Eq. (25) it follows that:

$$E_a = \frac{(\ln 10) \cdot R\, T_1 T_2}{T_1 - T_2} \doteq \frac{(\ln 10) \cdot R\, T_1 T_2}{z} \qquad (27)$$

where, by definition, $T_1 - T_2$, the temperature change as specified, is the z-value.

In case of <u>Cl. botulinum</u> spores, representative values for z are in the range $z = 10.4 \pm 0.8°$ at $121.1°C$[4]. From Eq. (27), we have then for <u>Cl. botulinum</u> spores,

$$E_a = \frac{(\ln 10) \cdot 394.26 \cdot 384.26 \cdot 1.987 \cdot 10^{-3}}{10.4}$$

$$= 66.6 \pm 5.4 \text{ kcal. mol}^{-1} \qquad (28)$$

7. DETERMINATION OF THE CONSTANT C

For <u>Cl. botulinum</u> spores, we will use for 12D (i.e., reduction of the spore number to 10^{-12} of the initial number) the conservative F_0-value of 3.5 min for non-acid and non-cured meats, which means that heating at $121.1°C$ for 17.5 sec. ($= 3.5 \times 60/12$) reduces

the number N by one order of magnitude. Thus, from Eq. (16), for Cl. botulinum spores,

$$[C \cdot \exp(-E_a/RT)] \cdot 17.5 = \ln 10$$

giving

$$C = \frac{2.3026}{17.5} \cdot e^{85.076}$$

$$= 1.17 \cdot 10^{36} s^{-1}$$

Calculations are made rather simply with the computer of Eq. (22) as a function of time. The last columns of Tables I and II give the values of the survival fraction N/N_0 at the axis thus computed. Fig. 2 is the plot of these "integral" survival curves for Cl. botulinum spores at the center of the cross-sectional planes $z/\ell = 0$, 0.4, 0.6, 0.3 and 1.0, of the cylinder with a = 5 cm, $\nu = 6$ and $\kappa = 1.35 \times 10^{-3}$ cm^{2}s^{-1}. The heating and the initial temperatures T_h and T_i, are 121.1°C and 21°C respectively.

It is seen from the survival curve for $z = o$ that in order to reduce the survival fraction of Cl. botulinum spores to 10^{-12} of the initial spore number, about 1-1/2 hours heating is needed for a beef roll of radius = 5 cm and 5 cm long.
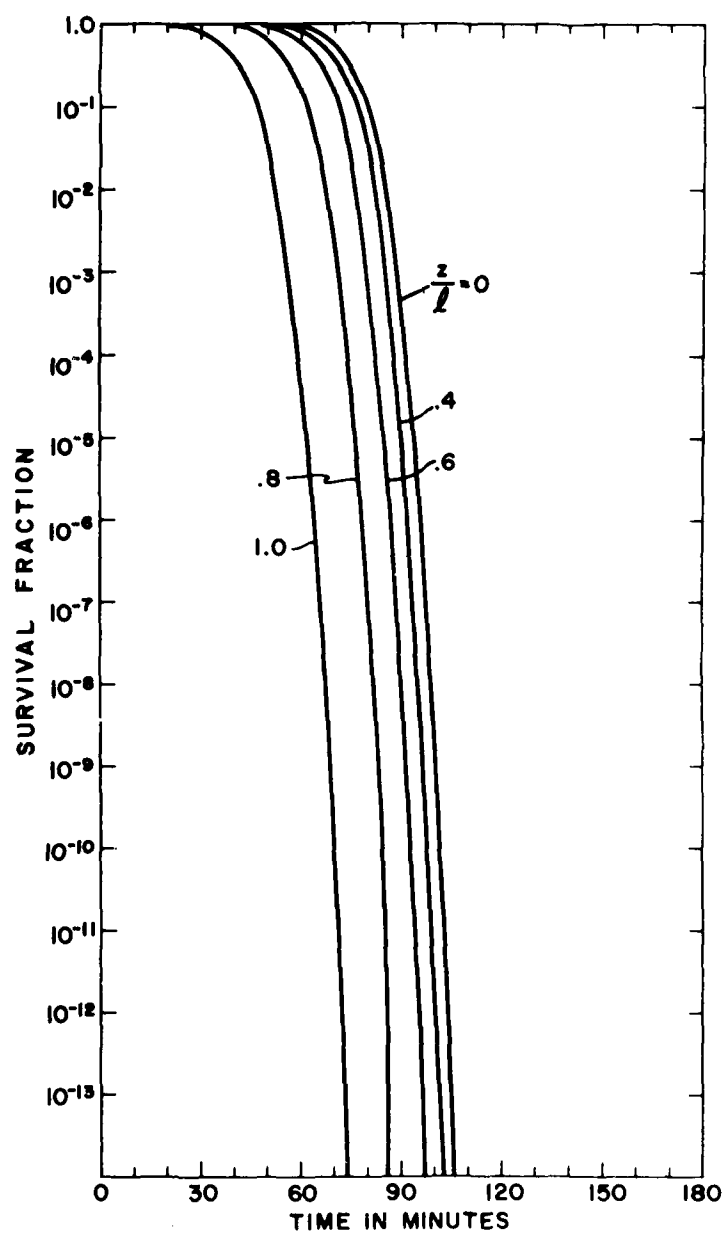
FIG. 2. INTEGRAL SURVIVAL CURVES FOR CL. BOTULINUM SPORES AT THE CENTER (r/a=0) OF
THE CROSS SECTIONAL PLANES z/ℓ = 0, 0.4, 0.6, 0.8, 1.0, OF A FINITE CYLINDER.

REFERENCES

1. Wang, C. P. and Brynjolfsson, A., "Heat Transfer and the Killing of Bacteria during Thermal Sterilization of Meat Rolls," *paper 78-WA/HT-56, Winter Annual Meeting of the American Society of Mechanical Engineers* in San Francisco, Dec. 10-15, 1978.

2. Carslow, H.S., and Jagger, J.C., *Conduction of Heat in Solids,* 2nd ed., Oxford University Press, 1959.

3. Schneider, P.J., *Conduction Heat Transfer,* Addison-Welsly Publishing Co., 1955.

4. Pflug, I. J., and Odlaug, T.E., "A Review of z and F Values Used to Ensure the Safety of Low-Acid Canned Food," *Food Technology,* 32, No. 6, June 1978, pp. 63-67.

5. Aiba, S., Humphrey, A. E., and Millis, Nancy F., *Biochemical Engineering,* 2nd ed., Academic Press, 1973.

6. "Overview – Symposia in Food Science and Technology," *Food Technology,* 32, No. 3, March 1978.

THE EXTENSION OF [Hg,Cd]Te DETECTOR TECHNOLOGY
TO THE NEAR-MILLIMETER SPECTRAL REGION

*BRUCE A. WEBER, PhD, AND STANLEY M. KULPA, PhD
U.S. ARMY ELECTRONICS RESEARCH AND DEVELOPMENT COMMAND
HARRY DIAMOND LABORATORIES
ADELPHI, MD   20783

We report the development of the first hot-electron photo-
conductive detector using crystals of the alloy semiconductor mercury-
cadmium-telluride, $[Hg_{1-x}, Cd_x]Te$ [1]. When the crystals were irradi-
ated with near-millimeter wave (NMMW) radiation, sensitivity was ob-
served throughout the 100 to 1000 GHz spectral region. These results
are significant because they suggest that the extensive [Hg,Cd]Te
technology base developed for FLIR systems may also be exploited for
the development of NMMW sensors. Such exploitation might lead to the
development of hybrid NMMW/IR sensors using only one detection element.

The need for semiconductors with a variable bandgap has led
to the study of various ternary compounds. Among these, [Hg,Cd]Te has
been developed for use in detectors [2] and lasers [3,4] in the 8 to
14 μm spectral region. Operation in the hot-electron photoconductive
mode extends the use of this material to the NMMW spectral region.
Applications include IR and NMMW heterodyne receivers for all-weather
surveillance and tracking systems, NMMW broadband video receivers for
spectroscopic studies of materials and atmospheric gases, and submilli-
meter heterodyne receivers for fusion plasma diagnostics.

BACKGROUND

When radiation is absorbed by a photoconductor, electronic
transitions are induced that produce a change in electrical conductiv-
ity. This process is distinguishable from bulk thermal effects that
raise the temperature of the semiconductor by the fact that the re-
sponse time of the photoconductive process is usually much shorter than
that for the bulk thermal effects.

Four types of electronic transitions can lead to photocon-
ductivity. Figure 1 pictorially describes these processes. The upper
half shows the electronic transitions while the lower half shows the
corresponding spectral response. The four processes are intrinsic,
extrinsic, hot-electron (free carrier), and hopping.
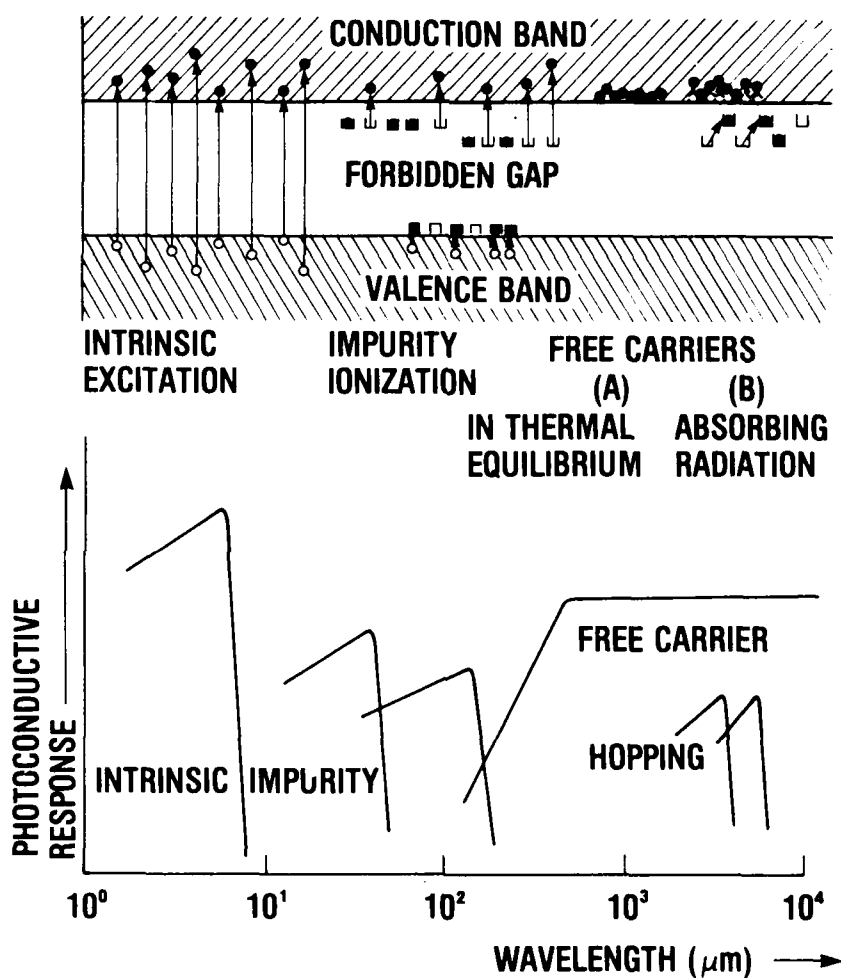
Figure 1. The photoconductive detector. Top
half shows electronic transitions.
Bottom half shows spectral response.

372

Intrinsic photoconductivity arises from electronic transitions between the valence and conduction bands of the semiconductor. Thus the concentration of both free electrons and holes is increased. This process occurs when the photon energy is greater than the energy difference between bands and thus has a long wavelength threshold corresponding to the energy gap. FLIR (8 to 12 µm) system detectors operate via the intrinsic absorption in [Hg,Cd]Te.

At longer wavelengths, impurities can be ionized to provide increased concentrations of electrons or holes. The ionization energy is smaller than the intrinsic energy gap, so that these transitions can be represented as originating at localized states within the gap. The threshold will be at a longer wavelength than the intrinsic threshold, and only one type of free carrier will be produced. This is impurity or extrinsic photoionization.

At still longer wavelengths, hot-electron photoconductivity due to radiation absorption by the free electrons is observed. At low temperatures (~ 4 K), the coupling of the electrons to the lattice is much weaker than at room temperature. Thus the electron temperature, which is the same as that of the lattice at room temperature, can be very much different from that of the lattice at low temperatures. This means that radiation absorbed by the electrons can raise the electron temperature above that of the lattice. This increase in electron temperature is observable by a change in the electron mobility and thus the photoconductivity. The process does not have a long wavelength threshold. The absorption, which can be described classically by Drude theory, varies as λ^2 for short wavelengths and becomes constant for wavelengths longer than a characteristic electron-electron interaction length. For NMMW operation the hot-electron mode dominates.

The fourth type of photoconductivity, hopping, is due to electronic tunneling transitions between impurity states. This long wavelength effect is only observed at very low temperatures where freeze-out of free electrons from the conduction band onto impurity sites occurs, thus diminishing the free-electron absorption contribution. Under these conditions, a hopping movement of electrons from donor site to donor site characterizes the observed photoconductivity. This tunneling of donor electrons is due to the small overlap of the electron wave function with that of an adjacent donor site. Thus activation into the conduction band is unnecessary.

Hot-electron photoconductivity in the NMMW spectral region was first observed by Putley [5] using the semiconductor InSb. Rollin [6] has shown that under constant current conditions the absorption is manifest by a change in the free carrier mobility, μ. The

373

voltage responsivity, R, is given by

$$R = dV/dP = -(V/\mu)(d\mu/dP),$$

where V is the voltage across the crystal and $d\mu/dP$ is the change in free carrier mobility with incident radiant power, P. Using Kogan's analysis [7] for R with the classical Drude theory of conductivity, it is easy to show that

$$R \propto \alpha \propto (1 + \omega^2 \tau_s^2)^{-1},$$

where α is the radiation frequency dependent absorption coefficient, ω is the radiation frequency, and τ_s is the electron scattering time. Thus at long wavelengths where $\omega\tau_s \ll 1$, R will be independent of wavelength, and for short wavelengths were $\omega\tau_s \gg 1$, R will vary as λ^2.

EXPERIMENT

Experiments were performed with n-type [Hg,Cd]Te crystals obtained from Cominco American. They were specified to have the IR absorption edge at a wavelength long enough to permit good absorption of CO_2 laser radiation (9 to 11 µm). In addition, the carrier concentration and mobility were selected so as to achieve favorable NMMW detectivity. To date, several samples have operated in the hot-electron photoconductive mode.

Figure 2 is a schematic diagram of the experimental configuration. The [Hg_{1-x}, Cd_x]Te sample used was single crystal n-type with a CdTe mole fraction x of 0.215 ($\lambda_g \approx 13$ µm at 4 K). Measurements at 77 K indicated a carrier concentration of 7.8×10^{14} cm^{-3} and a mobility of 1.2×10^5 $cm^2/V\cdot s$. The 6 x 6 x 0.5 mm sample was etch-polished on the 6 x 6 mm faces, and ohmic contacts were applied to two opposite 6 x 0.5 mm faces by using a high purity indium solder. The detector element was placed in a liquid helium cryostat at the end of a 10 mm diameter, 100 cm long, gold-coated waveguide. A filter was used to attenuate radiation of wavelengths less than 100 µm. The filter consisted of a 2 mm thick clear polyethylene window held at 300 K, a 0.14 mm thick black polyethylene window, and a Z-cut 1 mm thick crystalline quartz window held at 4 K. Radiation entered the circular waveguide from various sources including a 4.3 mm wavelength IMPATT diode, a 2.5 mm wavelength klystron, and optically pumped laser sources at 1.2 mm ($C^{13}H_3F$), 0.496 mm ($C^{12}H_3F$), 0.206 mm (CD_3F), and 0.119 mm (CH_3OH). This radiation was simultaneously monitored with a planar GaAs Schottky barrier diode (SBD) detector and a Scientech calorimeter. The SBD detector was used to monitor signal amplitude variations, while the Scientech calorimeter was used to measure the power entering the [Hg,Cd]Te detector waveguide. Losses due to transmission through the waveguide and filters were accounted for by a

separate measurements.

Figure 2.   Experimental Configuration

     The sensitivity of the detector was measured by using a PAR
HR-8 lock-in amplifier with an effective bandwidth of 3 Hz.   No other
signal amplification was used for the measurements.   The temporal
response of the detector was measured by pulsing the 2.5 mm wavelength
klystron.

RESULTS

     Figure 3 shows the relative detector response (λ = 2.5 mm)
versus crystal bias current, I_B, for three different incident radiant
powers.   The three curves yield, in order of increasing power, respon-
sivities of 2.5, 1.3, and 0.9 V/W.   The decrease in responsivity by
about a factor of 3 is believed to be due to saturation effects.

END

1.0

2.8   2.5

2.2

2.0

1.1   1.8

1.25   1.4   1.6

MICROCOPY RESOLUTION TEST CHART

separate measurements.

Figure 2. Experimental Configuration

The sensitivity of the detector was measured by using a PAR HR-8 lock-in amplifier with an effective bandwidth of 3 Hz. No other signal amplification was used for the measurements. The temporal response of the detector was measured by pulsing the 2.5 mm wavelength klystron.

RESULTS

Figure 3 shows the relative detector response (λ = 2.5 mm) versus crystal bias current, I_B, for three different incident radiant powers. The three curves yield, in order of increasing power, responsivities of 2.5, 1.3, and 0.9 V/W. The decrease in responsivity by about a factor of 3 is believed to be due to saturation effects.

375

Figure 3. Relative [Hg,Cd]Te detector response
at λ = 2.5 mm.

Figure 4 shows the detector spectral responsivity obtained
with incident source power averaging approximately 200 µW. A peak
responsivity of about 2.5 V/W is observed for wavelengths longer than
1 mm. For shorter wavelengths, the responsivity decreases approxi-

mately as λ^2, in accordance with the Drude theory. Since the responsivity is proportional to the conductivity, σ, the electron scattering time, τ_s, can be calculated from

$$R = R_{max}/(1 + \omega^2\tau_s^2).$$

From figure 4, $R = R_{max}/2$ when $\lambda = 370$ μm, thus yielding $\tau_s = 2 \times 10^{-13}$s. A calculation using data from Long [8] and $\tau_s = m*\mu/e$, where $m*$ is the electron effective mass and μ is the mobility, yields $\tau_s = 5 \times 10^{-13}$ s.
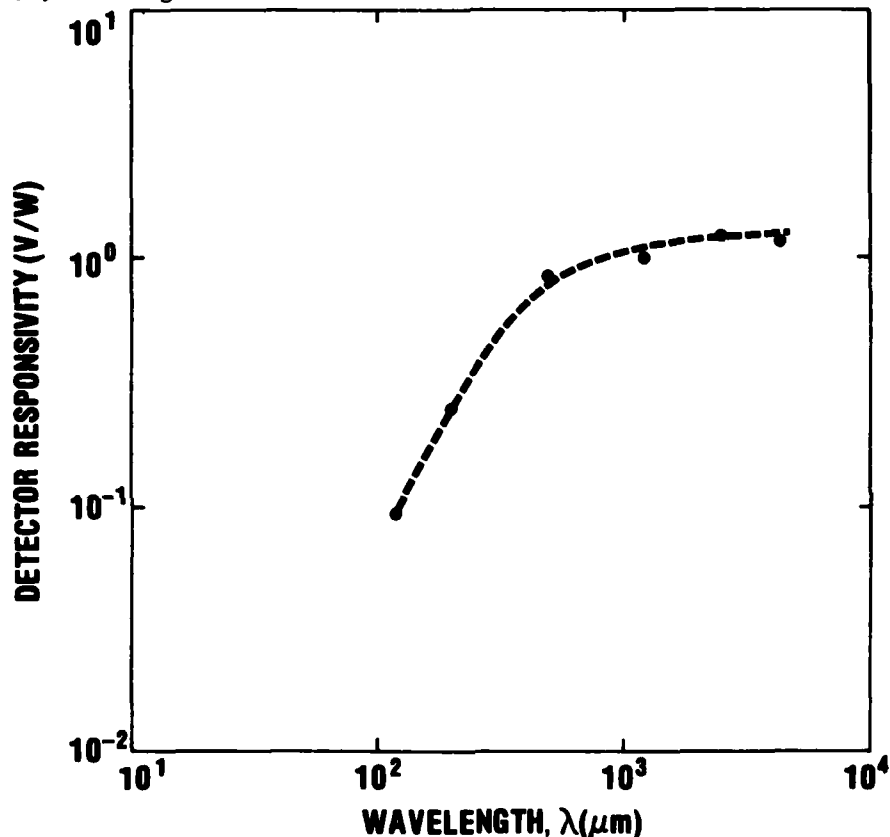
Figure 4. [Hg,Cd]Te spectral response

Figure 5 shows the detector response ($\lambda = 2.5$ mm) as a function of the pulse duration. Studies were made with pulse durations varying between 0.1 and 10 μs and rise times of approximately 20 ns. The high speed response rolloff yields an excess carrier lifetime of approximately 300 ns.

377
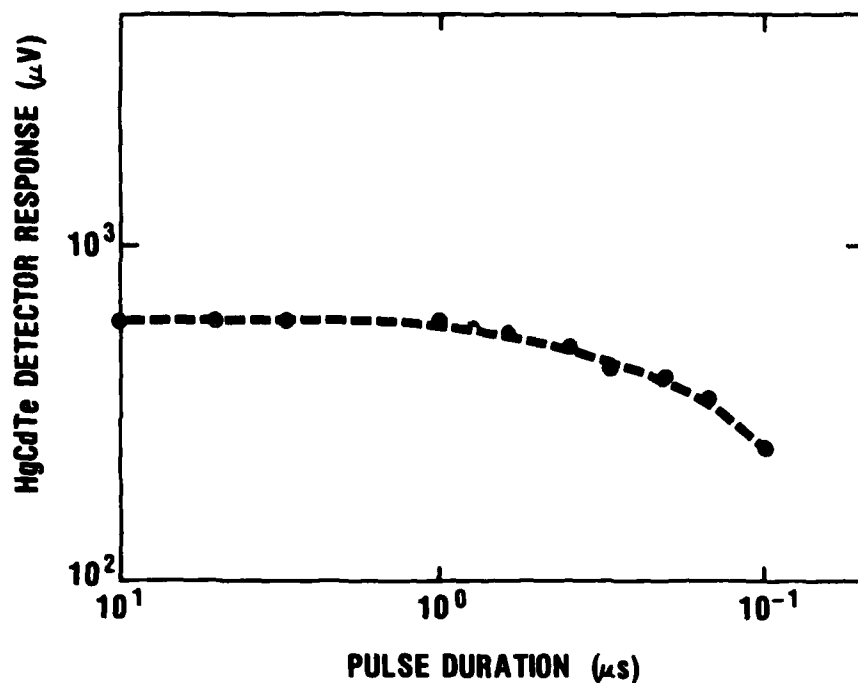
Figure 5. [Hg,Cd]Te temporal response
          at λ = 2.5 mm.

    Figure 6 shows a comparison of the response of a planar GaAs
Schottky barrier detector, a Scientech calorimeter, and the hot-
electron [Hg,Cd]Te detector to the attenuation of the output of a
2.5 mm wavelength klystron. For an attenuation of up to 30 dBm, the
[Hg,Cd]Te detector maintained a nearly linear response.
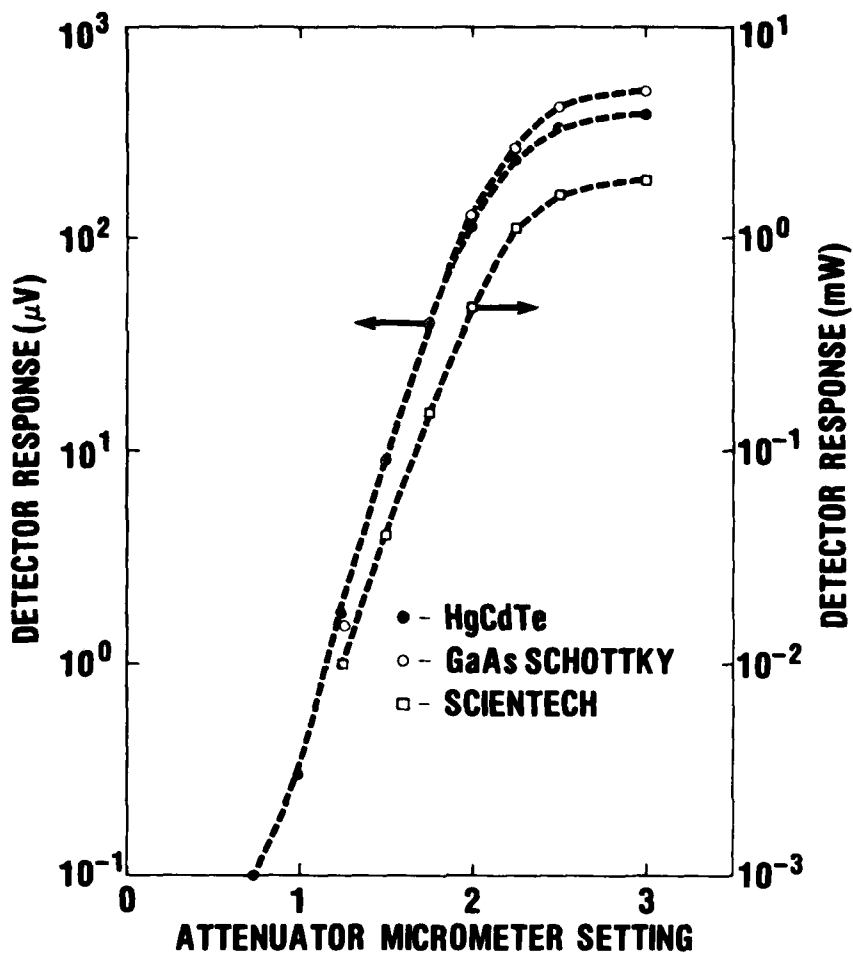
Figure 6. Comparative response of [Hg,Cd]Te detector
with Scientech calorimeter and planar GaAs
Schottky barrier diode detector.

Operation at 2.5 mm wavelength with optimum system parameters yields a noise equivalent power, NEP, of 2×10^{-10} W/$\sqrt{\text{Hz}}$. A comparative study with a sample of InSb in our dewar in place of the [Hg,Cd]Te crystal yielded an NEP of approximately 1×10^{-10} W/$\sqrt{\text{Hz}}$.

Our reported sensitivity for InSb is nearly a factor of 50 lower than that reported by Kinch and Rollin [9]. This difference is, at least in part, due to a loss in the coupling of the radiation to

379

the crystal and possibly to differences in crystal parameters (mobility and carrier concentration). Thus it is expected that refinements of coupling geometry and crystal parameters will yield similar improvements in the sensitivity for the [Hg,Cd]Te detector.

SUMMARY

We have observed hot-electron photoconductive detection of NMMW radiation in mercury-cadmium-telluride. Sensitivity is comparable to InSb throughout the NMMW spectral region. The sensitivity rolloff for [Hg,Cd]Te occurs at approximately 600 GHz (0.5 mm) as compared to 300 GHz (1 mm) for InSb, thus extending the useful range of these detectors to considerably shorter wavelengths. It is anticipated that NMMW applications for [Hg,Cd]Te will further the already extensive use of this ternary semiconductor in Army military systems.

REFERENCES

[1] B. A. Weber and S. M. Kulpa, Fourth International Conference on Infrared and Millimeter Waves and Their Applications, Miami Beach, Florida, 148, Dec. 1979.

[2] W. D. Lawson, S. Nielsen, E. H. Putley, and A. S. Young, J. Phys. Chem. Sol., Vol. 9, 325, 1959.

[3] I. Melngailis and A. J. Strauss, Appl. Phys. Lett., Vol 8, 179, 1966.

[4] B. A. Weber, J. P. Sattler, and J. Nemarich, Appl. Phys. Lett., Vol. 27, 93, 1975.

[5] E. H. Putley, J. Phys. Chem., Vol. 22, 241, 1961.

[6] B. V. Rollin, Proc. Phys. Soc. Cond., Vol. 77, 1102, 1961.

[7] S. M. Kogan, Sov. Phys. Sol. St., Vol. 4, 1812, 1963.

[8] D. Long, Phys. Rev., Vol. 176, 923, 1968.

[9] M. A. Kinch and R. V. Rollin, Brit. J. Appl. Phys., Vol. 14, 672, 1963.

PHYSIOLOGICAL WORK CAPACITY AND PERFORMANCE OF
SOLDIERS FOLLOWING TRANSATLANTIC DEPLOYMENT

*JAMES E. WRIGHT, CPT, MS, Ph.D., JAMES A. VOGEL, Ph.D.
JAMES B. SAMPSON, Ph.D., JOHN F. PATTON, Ph.D.,
WILLIAM L. DANIELS, CPT, MS, Ph.D., and JOSEPH J. KNAPIK, SP6, M.S.
US ARMY RESEARCH INSTITUTE OF
ENVIRONMENTAL MEDICINE
NATICK, MA   01760

Introduction

Current military threat analyses indicate a likelihood that
prior to future conflicts there will be an extremely limited period
for pre-deployment preparation and, furthermore, that following
deployment, replacements will be moved to the combat zone as rapidly
as possible (i.e., a "come-as-you-are" war). Such analyses have led
to U.S. military contingency plans which call for large scale troop
deployment by air. The capability to transport and deploy large
military forces over long distances by air, although a relatively
recent technological achievement, has significantly influenced both
international political philosophies and military strategies. Care-
ful consideration has been accorded the aircrews that operate the
now conventional super transport aircraft. However, it is
essential that equal consideration be given our ultimate weapon, the
individual soldier.

Soldiers traditionally have proven to be flexible, well-
motivated, and capable of great personal and group ingenuity and
adaptation in the face of a diverse variety of stresses. Such char-
acteristics have made for fighting forces able to go almost anywhere,
at any time, by any means, and remain operationally effective.

Certain human parameters of personal adjustment and adaptation
are, nevertheless, relatively slow and inflexible. Among these are
requirements for nourishment, rest, exercise, warmth, shelter, periods
of quiet, and physical and psychological support. Man does not adapt

immediately to sudden environmental changes, e.g., sea level to high altitude, equatorial to arctic, etc. The human response to such environmental alterations or deprivations, until accommodation occurs, covers a wide physiological and psychological range. These responses are to some extent understood and predictable. Irrespective of the mechanism(s) involved and whether the traveler is a soldier or civilian, the ultimate result seems to be a generalized reduction in the efficiency of the individual, particularly in mental and cognitive functions. From a military perspective, any advantages provided by advanced battlefield command and control/intelligence systems could be nullified by a stress which rendered data comprehension or decision making more difficult, or which can lead to malaise, fatigue, and a loss of physical ability or endurance in the individual soldier.

Rapid aerial deployment would necessarily entail not only the temporary desynchronization of normal circadian rhythms and geographic disorientation as in the case of a transatlantic deployment, but also a loss of sleep, possible food deprivation and dehydration, and exposure to aircraft noise and vibration (1). It is commonly believed that the symptomatology associated with jet-lag is sufficiently disruptive to interfere with the ability of athletes to perform maximally in a competitive event (2). Furthermore, it has been suggested that the effects of rapid translocation are likely different, and possibly more pronounced, in soldiers flying in troop configured transport aircraft than in business persons traveling commercially (1, 3). It is therefore not surprising that during deployment training exercises such as "Reforger", commanders have observed a general malaise and reduced performance of troops upon arrival in Germany.

In July 1977, the Commander in Chief of US Army Europe requested information on whether and, if so, to what extent, the effects of rapid transatlantic deployment would impair the health and operational effectiveness of troops. Information could be provided only on mental and cognitive functions which have been studied in commercial travelers and aircrew personnel (4-11). However, since no data were available on physical work performance capacities, the assistance of the Army Surgeon General was requested to define the scope and determine possible remedies for this critical combat readiness problem. Consequently, this laboratory was tasked to study the effects of translocation (jet-lag) on the ability of infantry soldiers to perform heavy physical work.

Methodology

Subjects for this investigation consisted of soldiers from rifle and headquarters companies of the 5th Battalion, 7th Brigade,

1st Cavalry Division that were being permanently transferred from
Ft. Hood, TX to West Germany. Ninety-four of the 97 soldiers who
were present for the informed consent briefing volunteered for the
study. Thirteen subjects were excluded from the study as a result of
a medical examination, leaving 81 as the starting sample. These 81
subjects were then randomly assigned to three groups for the purposes
of testing. In general terms, ninety percent held ranks between E-3
and E-5 with the majority having less than 5 years time in service.
Seventy percent were assigned to MOSs 11B or 11C, infantryman. Thir-
teen percent were medics, 91B. The sample was representative of the
Army wide enlisted population in age, height, weight and race (12).

The study employed a pre-post deployment test design. Subjects
underwent five days of testing one week prior to deployment and again
during the first 5 days after their arrival in Germany. The subjects
departed Ft. Hood on a DC-8 chartered commercial air craft at 0200 hrs
and arrived in Nuremberg at 2245 local Nuremberg time. With inter-
mediate stops in Philadelphia (1 hr) and Shannon, Ireland, (1/2 hr),
total in-transit time was 14-3/4 hours, over 6 time zones. From
Nuremberg, the subjects were moved by commercial bus to the test site,
Wildflecken Training Center, arriving there at 0115 hrs local time.
They were billeted by 0300 hrs, awakened at 0600 hrs, and reported
for testing at 0730 hrs, allowing for 8-3/4 hrs between flight touch-
down and commencement of testing.

Since the ability to carry out physically demanding tasks is
dependent upon motivation as well as the various physiological capa-
cities, this study was designed to examine both the physiological
(strength, anaerobic and aerobic) as well as behavioral aspects and
their integrated effects on task performance. Subjects were adminis-
tered behavioral (symptoms) questionnaires (13) twice daily but were
tested in only one fitness component each day as follows:

Day:	1	2	3	4	5
Group					
Red	A	P	S	A	P
Green	P	S	A	P	S
Yellow	S	A	P	S	A

A = aerobic power testing section
S = muscle strength testing section
P = task performance testing section

Aerobic power was determined by the most direct means - the determination of maximal oxygen uptake during uphill treadmill running, following the procedure of Mitchell et al.(14). In order to assess possible changes in the subject's own perception of his effort against actual work intensity, ratings of perceived exertion were recorded after each run using the Borg scale (15).

This is a psychophysical scale that is numbered from 6 to 20, with the uneven numbers anchored with descriptive terms, i.e., 9-very light, 13-somewhat hard, etc. Subjects were told to combine all sensations and feelings of physical stress, effort and fatigue and to thus concentrate on their total feeling or exertion.

Isometric strength of three muscle groups was measured with a device designed in our laboratory (16) and similar to that developed by Hermansen (17). The three muscle groups tested were: (a) the upper body (arm and shoulder), (b) legs and (c) back (trunk). Three contractions of each muscle group were performed, each 3-4 seconds. The force was registered on a spring-loaded force transducer connected to a bar against which the subject exerted force. In all cases the subject was instructed and encouraged to exert as much force as possible.

Dynamic muscular strength and endurance of two muscle groups, the arm flexors and knee extensors, were determined utilizing isokinetic (constant velocity) measuring equipment (Cybex II dynamometer, Lumex Corp., Cybex Div., Bay Shore, NY). The isokinetic device allows the subject to exert a maximal voluntary contraction at a constant velocity and thus allows the production and quantification of maximal force (torque) throughout the range of motion (18). Dynamic strength was assessed with two individual contractions for each muscle group at each of two contractile velocities, 36 and 180 degrees per second. Muscle endurance was quantified from a 60 second bout of repeated maximal contractions at 180 degrees per second.

In order to insure the successful execution of combat duties under any and all conditions, soldiers should be capable of performing the basic tasks of running, climbing, and carrying. A field task performance battery was therefore developed from events which reflect ability in basic military physical skills such as those which are essential both to personal safety and to effective combat operations. The tests selected were as follows: 6 meter rope climb; 110 m fireman carry of another soldier of similar body weight; 270 meter sprint; and a 2.8 km run. The performance criterion in each case was time.

The data were analyzed by means of one-way analysis of variance for repeated measures. The level of significance selected was p <0.05.

Results

The subjective symptomatology survey indicated that there was a significant increase in symptom reporting after arriving in Germany (Figure 1). Of these symptoms those which disappeared or were significantly diminished by the 5th day included: headache, light headedness, dry mouth, sore throat, blocked nose, trouble sleeping and tense and aching muscles. While the symptoms of running nose, tiredness, sleepiness and irritability were still high on day 5, none were statistically higher than baseline day 1 in Texas.
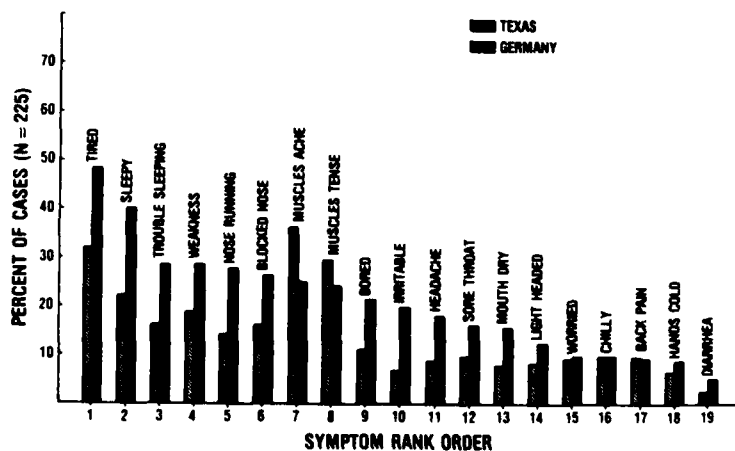
Figure 1. Rank order of symptoms based on percent reported during the five days in Germany. Number 1 through 6 and 9 through 12, were significantly higher (p <.05) following deployment.

A rough indicator of the importance of these symptoms was the number or percentage of individuals affected in Germany. Over 50% of the 45 men on whom complete data were collected reported problems with fatigue and trouble sleeping, more than 40% reported weakness and more than 30% reported problems with nasal congestion, aching muscles and irritability. Slightly more than 20% reported having headaches, light headedness, dry mouth and feeling bored. Approximately 10% reported having cold hands and feeling chilly. Less than 10% reported diarrhea and feeling worried. Since the sample is biased toward those who felt motivated and well enough to complete all questionnaires, the above results are, at best, underestimates of the true incidence of these symptoms (Figure 2).
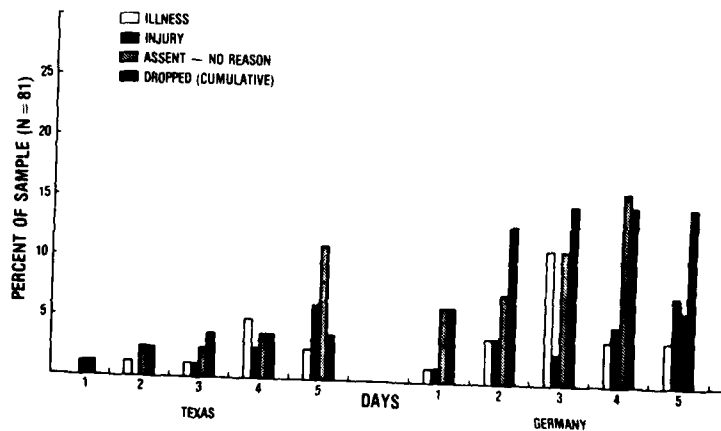
Figure 2.   Percent of sample (n = 81) not completing tests each day.

The results of the treadmill aerobic performance tests included evaluation of heart rate, ventilation, oxygen consumed, and relative perceived exertion at both submaximal and maximal workloads. Despite the symptomatology reported, no significant differences were noted in any of these parameters including perceived exertions with the

exception of a 5% increase in submaximal $\dot{V}O_2$ in one group on the third day in Germany (Table 1).

<hr>

Table 1. Aerobic Capacity Measures, Mean Values.

		Texas	Germany
1. Heart Rate (Beats/min)			
	a. Submaximal*	165	164
	b. Maximal	193	194
2. $\dot{V}_E$ (1/min, BTPS)			
	a. Submaximal*	73	75
	b. Maximal	130	132
3. $\dot{V}O_2$ (ml/kg/min)			
	a. Submaximal*	33.8	34.2
	b. Maximal	47.0	47.9
4. RPE			
	a. Submaximal*	11.1	9.6
	b. Maximal	16.0	15.7

*Submaximal refers to values recorded during the sixth minute of a run at 6 mph on a zero percent grade.

Changes in isometric strength following translocation were generally small, inconsistent and statistically insignificant (Figure 3). Dynamic arm strength was lower in every case following translocation (Figure 4). The percentage differences for test days one through five at a velocity of 36°/sec were 12.2, 4.0, 1.0, 3.2 and 7.8, respectively. The comparable differences at 180°/sec were 19.7, 5.7, 11.6, 11.3 and 6.0 percent. No strength scores recorded in Texas for a given group were statistically different from one another, nor were those recorded in Germany different from one another. If scores from each location for each group are combined to provide a single strength value for comparison, strength is found to be reduced significantly at both contractile velocities for all groups except the red group at the slower speed. For analysis of dynamic arm endurance, values of all groups were combined into single pre- and post-translocation scores (Figure 5). Analysis of variance indicated significant reductions in peak torque ($\bar{x}$:16.9%) for all contractions up through and including the thirty-third. Translocation thus appeared to have
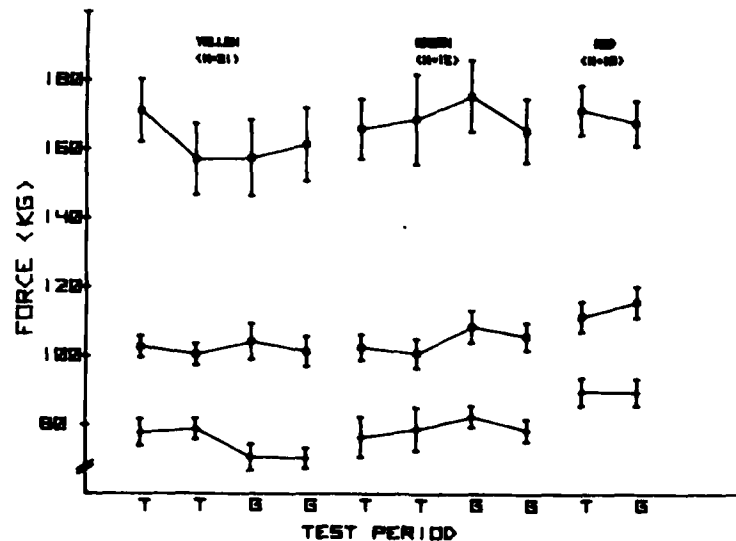
Figure 3. Isometric strength of legs, upper
torso, and trunk extensor muscles
(upper, middle and lower lines,
respectively). T:Pre-deployment
(Texas) values; G:Post-deployment
(Germany) values.

a detrimental effect on dynamic strength and endurance of the elbow
flexor muscles.

Dynamic leg strength scores are depicted in Figure 6. For
the yellow group a higher strength score was obtained in test period
1 than test periods 2, 3 and 4 at both velocities. There were no
other significant differences within this group. For the green group
at 36°/sec the only significant difference was between the two test
periods in Texas. For the green group at 180°/sec leg strength de-
clined significantly from the first test period to the second (in
Texas), but by the time of testing in Germany, values had risen signi-
ficantly to equal those obtained in the first period. The red group
demonstrated significantly higher strength in Germany than in Texas.

388
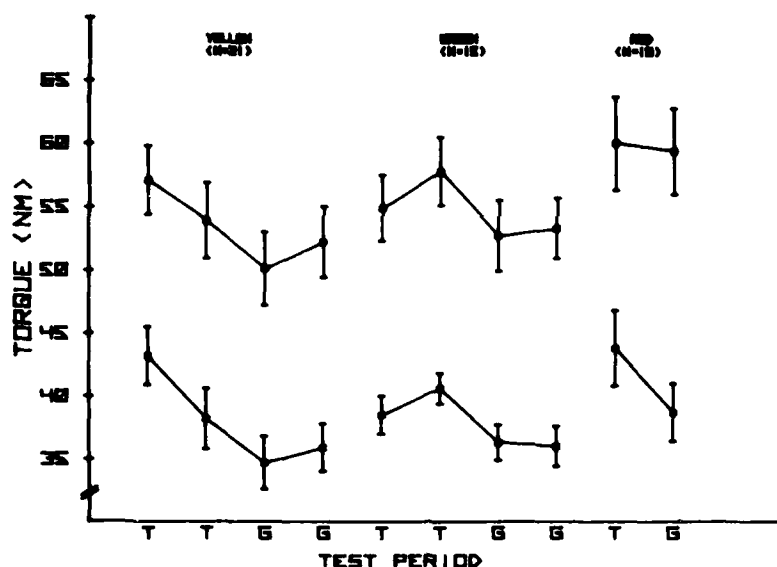
Figure 4. Peak strength (torque) exerted by
           elbow flexors at 36 (top) and 180
           (bottom line) degrees per second.
           T:Texas; G:Germany.

At both velocities a steady decline in dynamic leg strength
is seen from cest day 1 to test day 3. The mean scores for the
yellow group (strength tested on day 1 in both locations) are approxi-
mately the same as for a large sample of subjects from the 2d Infantry
Division tested on the same apparatus (19). By the second day the
green group shows a considerable and significant decline in strength
when compared to the yellow group. This is especially surprising
since the two groups are approximately equal on the other strength
parameters. Strength values of the red group, tested on the third
day, are below those of the green group. On most of the other strength
parameters the red group demonstrated higher values than the other two
groups. On day 4, the yellow group shows a further decline over their
previous score as does the green group on day 5.

This pattern of declining scores suggests a fatigue effect
due to the intense and repetitive pattern of testing. Both the
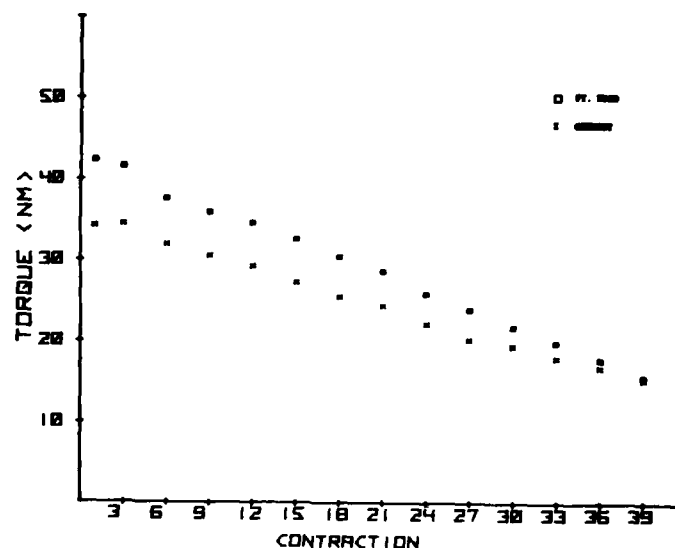
Figure 5. Dynamic arm endurance at 180°/sec for
all test groups combined. Differences
were statistically significant at all
contractions except 36 and 39.

aerobic power and field performance tests primarily stressed the
lower body and the relatively short recovery times (24 hrs) allowed
between test sessions may have adversely affected the dynamic leg
strength scores. This hypothesis is partially substantiated by the
subjects' evaluations of "muscle aches" on the symptoms questionnaire.
At Ft. Hood on day 1 only 13.3% of the individuals in the green group
reported "muscle aches" (15). But on day 2 following field perform-
ance and just prior to muscle strength testing, 46.7% of these sub-
jects reported aches. 57.1% of the red group reported muscle aches
on day 3 following treadmill and performance testing. In yellow and
green groups, 53.3% and 46.7% of the subjects reported aches on days
4 and 5, respectively, following the field performance testing. It
thus appears that the dynamic leg strength scores were to some extent
confounded by the fatigue of repetitive testing. That is, the fatigu-
ing effects of hard physical work outweigh or at least mask any
effects of translocation on laboratory measures of muscle strength.
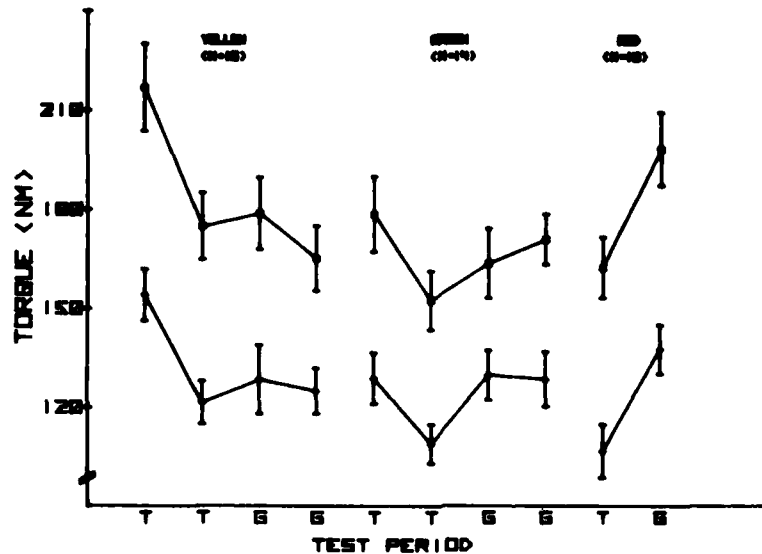
Figure 6. Peak strength (torque) exerted by
knee extensors at 36 (top) and 180
(bottom line) degrees per second.
T:Texas; G:Germany.

The pattern of scores for dynamic leg endurance mirrors the
results of the dynamic leg strength data. The yellow group shows the
least endurance decrement on all contractions in test period 1 in
Texas. The green group exhibits a larger decrement than the yellow
group in their initial test while the red group decrement was even
more marked than the other two groups on test 1. Further performance
depressions were seen on test 2 in Texas for the yellow and green
groups. As with dynamic leg strength, it is likely that fatigue from
the field performance and treadmill tests influenced the dynamic leg
endurance measures.

Performance on the four selected military physical tasks is
illustrated in Figure 7. No decrements were observed in the rope
climbs (testing overall upper body strength and coordination), man-
lift and carry (back and leg strength, anaerobic capacity and coordin-
ation), or 2.8 km run (cardiorespiratory function).

391
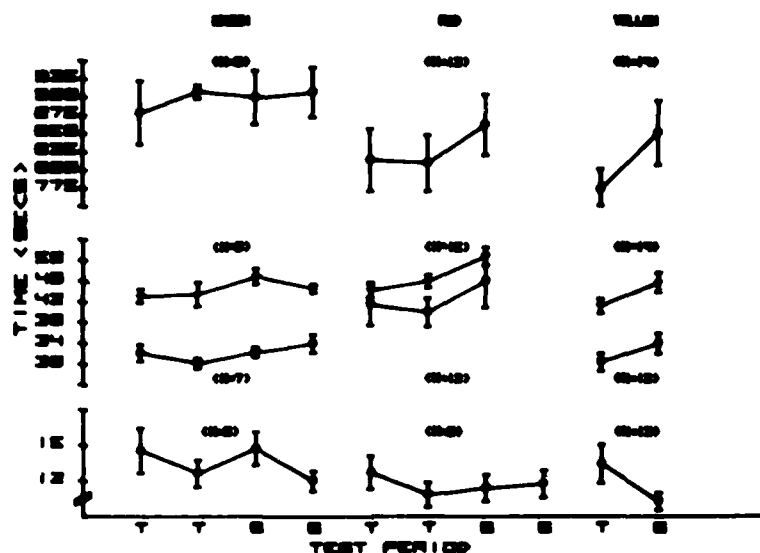
Figure 7. Performance times in military physical
tasks, top to bottom: 2.8 km run (top),
270 m rush, 110 m fireman carry, and
6 m rope climb (bottom).

The 270 m rush was included to assess leg muscle power, anaerobic
capacity and overall body coordination. Scores on this test were
variable but not statistically different within or among groups over
the five days of testing at Ft. Hood. Following arrival in Germany
however, average performance times increased in all groups. Perform-
ance decrements were recorded for 49 of the total of 52 soldiers
tested on the first three days in Germany. Analysis of the times of
each test group indicated that while neither the green nor the yellow
group experienced a statistically significant reduction in performance
following translocation, the red group completed the sprint on the
second day in Germany at a significantly slower pace than in Texas.
Two basic interpretations of this finding may be offered. One is the
possibility that the decrement resulted from an impairment or altera-
tion in some physiological function or process that influences anaero-
bic power capacity. A second interpretation is that the jet-lag (or
jet-lag plus testing) effects were on psychological parameters which,

392

in the case of one group, experted a significant negative influence on the motivation to perform work.

Discussion and Conclusions

Behavioral responses commonly reported for transatlantic travel were observed and confirmed in a majority of the subjects in this study: tiredness, sleepiness, weakness, headache and irritability. While most symptoms had disappeared or significantly diminished by the fifth day in Germany - tiredness, sleepiness and irritability still persisted at that time.

While static (isometric) strength of upper body, legs and trunk was unchanged, dynamic strength of arms was reduced after arrival in Germany in two out of three groups at the slow contraction speed and in all groups at the fast velocity. Dynamic leg strength appeared to be less affected by translocation than by the fatigue of repetitive testing. Measures of both arm and leg muscular endurance (anaerobic power) declined significantly after arrival in Germany. The finding was generally consistent in all test groups, although fatigue from other testing may again have confounded the leg endurance findings. Aerobic power was completely unaffected by translocation. Oxygen transport capacity and aerobic muscle metabolism for sustained whole body activity appears to be unaffected by the conditions experienced in this study.

Performance of military physical field tasks (rope climp, rush, lift and carry and run), which should reflect the culmination of both psychological and physiological affects on work ability, was essentially unaffected by translocation. Only one group exhibited an isolated significant decrement in one event (rush). Thus, the work task performance suggested that, if present, psychological and physiological alterations were not of sufficient magnitude to alter work performance during the five days following translocation as assessed in this study.

It is somewhat perplexing that decrements were found in muscular strength and endurance capacity without concomitant changes in task performance. Assuming that our measures of capacity in fact tested the same muscle groups that were employed in the task performance, one can only conclude that the tasks were either not performed to the point of taxing the maximal capacity of the physiological systems, or were inappropriate tasks for maximally taxing the physiological systems. If we can assume that the tasks selected sufficiently represent work performance required by the combat soldier, then we can

only conclude that physiological capacity changes are not of suffi-
cient magnitude to affect performance from a practical standpoint.

It is impossible to resolve from the present study whether
these observed alterations in muscular strength are due to the general
stress resulting from translocation or due to one single component,
such as biorhythm disruption or sleep loss. The stress of noise,
vibration and fear often included in the description of translocation
can be ruled out in this study since the movement was made in commer-
cial aircraft, by troops who for the most part previously deployed to
Germany and were adequately prepared for this permanent change of
station. Despite the comforts of commercial aircraft, sleep depriva-
tion was nevertheless a prominent finding upon arrival in Germany and
evident during the first days of testing. Halloway (3) has suggested
that sleep loss is likely a more dominant stress than the rhythm dis-
ruption. No studies have been found which have examined the effects
of sleep deprivation per se on muscle strength and endurance. Such
a study appears indicated. Aerobic power during sleep deprivation
has been studied in this laboratory (Gleser and Vogel, unpublished)
without any discernable effects.

In summary, the results of the study suggest that despite the
behavioral and isolated physiological changes, no significant decre-
ment in work task performance could be documented with transatlantic
deployment. It can be concluded that any decrements in willingness
to work or physiological capacity were insufficient to become apparent
in gross work ability as measured in this study.

References

1. Knapp, S.D. Problems of adaptation to long range large scale
   aerial troop deployments. USAARL Report No. 71-10, Sept. 1970.

2. Klafs, C.E. and D.D. Arnheim. Modern Principles of Athletic
   Training,(3rd Ed.). St. Louis:Mosby, 1974.

3. Memorandum for Psychiatric Consultant, USAMEDCOMEUR from A.C.
   Holloway, Dir., Div. of Neuropsychiatry, WRAIR, Subject: Bio-
   medical Stress and Long Range Troop Deployment, dated 18 Oct. 1977.

4. Crane, J.E. The time zone fatigue syndrome. Flying Physician 7:
   19-22, 1963.

5. Hanty, G.T. and T. Adams. Phase shifts of the human circadian
   system and performance deficits during periods of transition.
   II. West-east flight. Aerospace Med. 37:1027-1033, 1966.

6. Klein, K.E., H. Bruner, H. Haltman, H. Rehme, J. Stolze, W.D. Stein-
   hoff and H.M. Wegmann. Circadian rhythm of pilots efficiency and ef-
   fects of multiple time zone travel. Aerospace Med. 41:126-132, 1970.

*WRIGHT, VOGEL, SAMPSON, PATTON, DANIELS and KNAPIK

7. Klein, K.E., H.M. Wegmann, G. Athanassenas, H. Hohlweek and P. Kulkinski. Air operations and circadian performance rhythms. <u>Aviat. Space Environ. Med.</u> <u>47</u>:221-230, 1976.

8. Klein, K.E., H.M. Wegmann and H. Bruner. Circadian rhythm in indices of human performance, physical fitness and stress resistance. <u>Aerospace Med.</u> <u>39</u>:512-518, 1968.

9. Klein, K.E., H.M. Wegmann & B.I. Hunt. Desynchronization of body temperature and performance circadian rhythm as a result of outgoing and homegoing transmeridian flights. <u>Aerospace Med.</u><u>43</u>:119-132,19

10. Mohler, S.R., J.R. Dillie and H.L. Gibbons. The time zone and circadian rhythms in relation to aircraft occupants taking long distance flights. <u>Am. J. Pub. Health</u> <u>58</u>:1404-1409, 1968.

11. Siegal, P.V., S.J. Gerathewehl and S.R. Mohler. Time zone effects: disruption of circadian rhythms poses a stress on the long distance air traveler. <u>Science</u> <u>164</u>:1249-1255, 1969.

12. Vogel, J.A., J.B. Sampson, J.E. Wright, J.J. Knapik, J.F. Patton and W.L. Daniels. Effect of transatlantic troop deployment on physical work capacity and performance. <u>USARIEM Report No.T-3/79,</u> March 1979.

13. Kobrick, J.L. and J.B. Sampson. New inventory for the assessment of symptom occurrence and severity at high altitude. <u>Aviat. Space Environ. Med.</u> <u>50</u>:925-929, 1979.

14. Mitchell, J.H., J.Spourle and C.B. Chapman. The physiological meaning of maximal oxygen uptake test. <u>J.Clin.Invest.</u> <u>37</u>:538-547, 1957.

15. Borg, G. Perceived exertion: A note on "history" and methods. <u>Med. Sci. Sports</u> <u>5</u>:90-93, 1973.

16. Knapik, J., D.Kowal, P.Riley, J.Wright and M.Sacco. Development and description of a device for static strength measurements in the Arme Forces Examin tion and Entrance Station. <u>USARIEM Report No.T-2/79,</u> January 1979.

17. Hermansen, L. Individual Differences In: Fitness, Health and Work Capacity: International Standards for Assessment, L.A. Larson (editor). New York:MacMillan Pub. Co., 1974.

18. Moffroid, M., R.Whipple, J.Hofkosh, E.Lowman and H.Thistle. A study of isokinetic exercise. <u>Phys.Ther.</u> <u>49</u>:735-746, 1968.

19. Knapik, J.J. and M.U. Ramos. Isokinetic and isometric torque relationships in the human body. <u>Arch.Phys.Med.Rehab.</u> <u>61</u>:64-67, 1980.

PENETRATION WITH LONG RODS: A THEORETICAL FRAMEWORK
AND COMPARISON WITH INSTRUMENTED IMPACTS (U)

THOMAS W. WRIGHT, PhD
USA ARRADCOM, BALLISTIC RESEARCH LABORATORY
ABERDEEN PROVING GROUND, MARYLAND   21005

I. Introduction.

The eroding rod model for deep penetration(1,2) is attractive because of its simplicity and its ability to make qualitative predictions that appear to be useful for parametric studies. Nevertheless, it contains several obvious flaws. Chief among these is the use of the modified Bernoulli equation and of the oversimplified rigid/perfectly plastic material model, which is implied by that equation. A critical review of the model as it presently exists is presented in the next section.

In spite of its shortcomings the eroding rod model appears to be a good starting place for an experimental investigation of penetration, which in turn should lead to a more complete model. In the third section of this paper the theoretical framework for an experimental program is described. The theory of one dimensional wave propagation is used to show how data from instrumented long rods and targets may be fitted together to give a coherent picture of the time sequence of events during penetration. Data for one impact condition is then compared within the theoretical framework. In the final section the results to date are discussed.

II. Review of the Eroding Rod Model.

The eroding rod model(1,2) for deep penetration by long rods is based on three simple ideas. First, a long rod penetrator may be considered to be rigid and undeforming, except where it is in contact with the target. There the material erodes and flows at a constant

397

characteristic stress. Second, there is a constant characteristic flow stress in the target. Third, a modified Bernoulli equation holds, which includes the characteristic rod and target stresses. The rod stress, of course, acts to decelerate the intact rear end of the rod. The situation is shown in Fig. 1. The equations expressing these ideas are as follows(2).

Balance of Mass: $\quad \ell = \dot{p} - u$

Balance of Momentum: $\quad \rho_p \, \ell \, \dot{u} = - \Sigma$ $\qquad\qquad$ (1)

Modified Bernoulli: $\quad \Sigma + \tfrac{1}{2} \rho_p (u - \dot{p})^2 = T + \tfrac{1}{2} \rho_t \, \dot{p}^2$

$\qquad\qquad\qquad\qquad\qquad$ = stress at rod/target interface
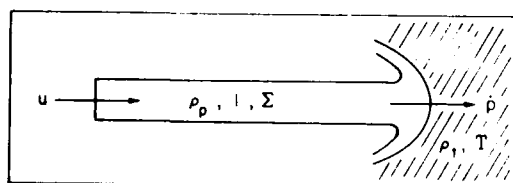
Figure 1. Long Rod Penetrating a Target

Here ℓ is the instantaneous length of intact rod and u is its instantaneous speed. The depth of penetration is p and the rate of penetration is $\dot{p}$. The densities of rod and target respectively are ρ_p and ρ_t. The characteristic stresses are Σ and T in the rod and target.

Equation $(1)_3$ is solved for $\dot{p}$ and substituted in $(1)_1$. This procedure gives three ordinary differential equations for ℓ, p, and u, which are to be solved simultaneously. The integration is not quite straight forward, however, because there are simple physical constraints on $\dot{p}$, namely

$$0 \le \dot{p} \le u. \qquad\qquad (2)$$

The lower limit is reouired since penetration can only open a hole in the target, never close one. The upper limit is required since it is assumed that penetrator and target are always in contact, but since the penetrator cannot increase in length, $\ell \le 0$ in $(1)_1$.

Now consider the two limiting cases in turn as was done by Tate(2). When $\dot{p} = 0$, there is no further penetration and no further flow of target material, so the stress in the target must be less than T. If the penetrator is still flowing, then the target stress at the interface from $(1)_3$ is given by

$$\tau = \Sigma + \tfrac{1}{2}\rho_p u^2 \le T \qquad\qquad (3)$$

Clearly this can only occur if

$$T > \Sigma$$

and

$$u \leq \left[2(T-\Sigma)/\rho_p\right]^{\frac{1}{2}} \tag{4}$$

Similarly, if $\dot{p} = u$, then $\dot{\ell} = 0$, there is no further flow of rod material, and, therefore, the stress in the rod must be less than Σ. If the target material is still flowing, from $(1)_3$ the rod stress at the interface is given by

$$\sigma = T + \tfrac{1}{2}\rho_t u^2 \leq \Sigma \tag{5}$$

This can only happen if

$$T < \Sigma$$

and $\tag{6}$

$$u \leq \left[2(\Sigma-T)/\rho_t\right]^{\frac{1}{2}}$$

It must be concluded that the material model implicit in the use of the modified Bernoulli equation is the highly idealized case of the rigid/perfectly plastic solid for both penetrator and target as shown in Fig. 2.
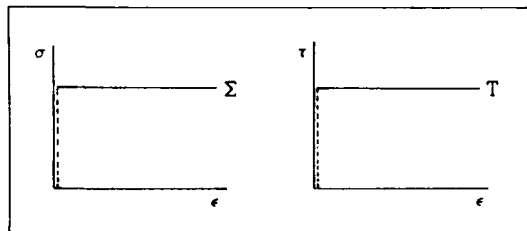
Figure 2.   Rigid/Perfectly Plastic Material

Equations (1) must be replaced by the following set of equations, which satisfy the restrictions outlined above.

$$\dot{\ell} = \dot{p} - u$$

$$\dot{u} = \begin{cases} - (T + \tfrac{1}{2}\rho_t u^2)/\rho_p \ell, & \text{if (6) holds} \\ - \Sigma/\rho_p \ell, & \text{in all other cases} \end{cases}$$

$$\dot{p} = \begin{cases} 0, & \text{if (4) holds} \\ u, & \text{if (6) holds} \\ \dfrac{1}{1- \dfrac{\rho_t}{\rho_p}} \left\{ u - \sqrt{\dfrac{\rho_t}{\rho_p}} \left[u^2 - 2\,\dfrac{\Sigma-T}{\rho_t}\, (1- \dfrac{\rho_t}{\rho_p}) \right]^{\frac{1}{2}} \right\}, & \text{in all other cases.} \end{cases} \tag{7}$$

399
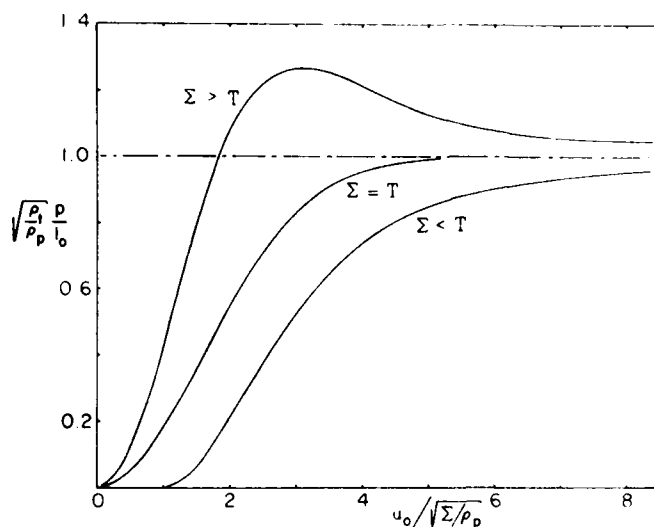
Figure 3.   Penetration as a Function of Impact Speed.

These equations are simple enough to be solved on a programmable hand calculator. Typical integrations of (7) giving depth of penetration as a function of impact speed in non-dimensional form are shown in Fig. 3. The results appear to be qualitatively correct, especially the characteristic S-curve for the case $T > \Sigma$, as shown by the experimental results of Stilp and Hohler(3) and Tate(4). Equations (7), therefore, have considerable intuitive appeal, combining as they do simplicity with qualitative accuracy, but they are difficult to use quantitatively because values for the characteristic stresses Σ and T are not readily available a priori. The usual procedure has been to choose the stresses so as to fit an experimental S-curve, and then to consider them as material constants. Due to the approximations inherent in the model, this procedure is unlikely to be satisfactory. The difficulties are threefold.

The first problem is in the origin of the modified Bernoulli equation itself. In the theory of perfect, incompressible fluids, the Bernoulli equation is obtained in steady flow by integration along a streamline. This gives

$$P + \tfrac{1}{2} \rho v^2 = \text{constant} \tag{8}$$

where P is pressure. Then by applying the result at a stagnation point and on the stagnation streamline far from the stagnation point in both penetrator and target, and by appealing to the idea of continuity of forces at the stagnation point, the Bernoulli equation as applied to jet interaction is derived(5).

$$\tfrac{1}{2} \rho_p v^2 = \tfrac{1}{2} \rho_t w^2 \tag{9}$$

The speeds v and w are measured with respect to the stagnation point.

Now apply the same ideas to the steady motion of a rigid/ perfectly plastic solid. With the z-axis and centerline of the rod coinciding in Fig. 1, the z-component of the momentum equation may be written

$$t_{zz,z} + t_{zy,y} + t_{zx,x} = \rho \, (u_{z,t} + u_x u_{z,x} + u_y u_{z,y} + u_z u_{z,z})$$

On the centerline $u_x = u_y = 0$ by symmetry, and for steady motion $u_{z,t} = 0$. Shear stresses also vanish on the centerline, but not their derivatives, so integration between points a and b yields

$$t_{zz}(b) - t_{zz}(a) = \int_a^b (t_{zy,y} + t_{zx,x}) \, dz \qquad (10)$$

$$= \tfrac{1}{2} \rho \left[u_z^2(b) - u_z^2(a) \right]$$

Equation (10) is similar to (8) with the important difference of the remaining integral. If equation (10) is to apply to the rod, point b could be fixed in the rod/target interface, and point a could be located at the rigid plastic boundary. The exact location of that boundary is unknown, but within the terms of the material model the stress there must be the constant flow stress, $t_{zz} = -\Sigma$, and the particle speed as it enters the region of steady flow must be the speed of the rigid rear end relative to the interface, $u-\dot{p}$. Similar considerations must apply to the target with the z-component of stress at the rigid/plastic boundary being $t_{zz} = -T$ and the particle speed relative to the interface being $\dot{p}$. Since stress must be continuous at the interface and since the stagnation velocities are zero, the modified Bernoulli equation should read

$$\Sigma + \tfrac{1}{2} \rho_p (u-\dot{p})^2 + I_p$$

$$= T + \tfrac{1}{2}\rho_t \, \dot{p}^2 + I_t \qquad (11)$$

$$\text{where } I = \int_a^b (t_{zy,y} + t_{zx,x}) \, dz$$

Thus, even within the limitations of the assumptions of a rigid/plastic material and steady flow, the modified Bernoulli equation cannot be strictly true.

The second problem concerns the validity of those assumptions; namely steady flow and a rigid/plastic material. Taken

overall, kinetic energy penetration is clearly an unsteady process, especially in the initiation and final stopping or breakout stages, but there may be parts of the process, localized in both space and time, that are nearly steady, as for example, a local interaction

region near the penetrator/target interface during the intermediate stages of penetration. In such a domain equation (11) should be valid, but even then there is no clear way to ᵣake an accurate estimate of the characteristic stresses. The stress/ strain curve of most real materials is not well approximated by the rigid/plastic assumption because of work hardening. For example, a typical curve is shown in Fig. 4. Because the failure processes are unknown there is no way a priori to choose the characteristic or average stress Σ either on the basis of energy equivalence or maximum stress or any other way. In the target the situation is even more muddled. For the rod it has been tacitly assumed that the state of stress is nearly uniaxial, but in the target the stress

Figure 4. Stress Strain Curve with Work Hardening and Rigid/Plastic Approximation.

will be triaxial with a substantial, but unknown spherical component. The matrix of components on the centerline may be represented by

$$
\begin{Bmatrix} T_1 & 0 & 0 \\ 0 & T_2 & 0 \\ 0 & 0 & T_3 \end{Bmatrix} = - \begin{Bmatrix} P & 0 & 0 \\ 0 & P & 0 \\ 0 & 0 & P \end{Bmatrix} + \begin{Bmatrix} -S & 0 & 0 \\ 0 & \tfrac{1}{2}S & 0 \\ 0 & 0 & \tfrac{1}{2}S \end{Bmatrix} \tag{12}
$$

The first matrix on the right contains the pressure and the second contains the deviatoric components, which are related to the instantaneous flow stress, F, in the usual theory of plasticity(6) by

$$
S = \frac{2}{3} F \tag{13}
$$

The target resistance stress T is given by

$$
T = -T_1 = P + \frac{2}{3} F \tag{14}
$$

402

Because of work hardening and unknown failure processes, the target flow stress is as ill defined as the rod stress, but in addition there is an unknown hydrostatic pressure, which may vary greatly during sequential stages of penetration. A final consequence of real, non-rigid material behavior is that there will be considerable plastic deformation at some distance from the quasi-steady interaction zone. In the rod this has the effect of slowing material down (relative to the rear end) before it reaches that zone so that the speed u to be used in (11) or $(1)_3$ is less than the speed of the rear end. How much less depends on the rate of work hardening. In the target, plastic deformation has the effect of increasing the spatial rate of penetration: that is to say, since real target materials can move ahead of the penetrator, the interface between penetrator and target will move farther in space than it would if the target were rigid in non-plastic regions. Furthermore, inertia will tend to increase the crater size even after the active driving forces have ceased.

The third problem is that the stress tending to decelerate the rod in $(1)_2$ is an average stress over the whole cross section, whereas the stress that enters into the modified Bernoulli equation is the local stress on the centerline. These may be somewhat different from each other.

In summary, then, it has been shown that:

(1) The modified Bernoulli equation cannot hold rigorously because of shear stress gradients in solids;

(2) The deformation processes are steady at most in a limited domain, but even then it is not possible to choose the characteristic stresses Σ and T a priori because of work hardening and unknown failure processes. Furthermore, plastic deformation will extend well outside the quasi-steady zone; and

(3) The local centerline stress is unequal to the average cross sectional stress.

For these reasons the eroding rod model is difficult to use quantitatively and gives only limited insight into the details of the actual rod/target interaction, but in spite of its shortcomings the model appears to contain the germ of a sound theory of penetration, as shown by the qualitative success of its predictions. The model probably averages over the forces and erosion processes in some way so as to achieve partial success.

III. Theoretical Framework for an Experimental Program.

An experimental program has been devised to begin probing the details of the interaction process. The program is based on the following assumptions and theoretical considerations. Penetration is controlled by flow and failure processes that occur at or near the penetrator/target interface. These processes will depend on the material properties of the particular materials involved, and therefore, they will depend only on the local stress and strain fields. These ideas are at least compatible with the formation of a region of steady flow at the interface. Since it is a local phenomenon, it seems reasonable to suppose that the steady conditions established will depend only on the local geometry and the mass flux through the region. In particular it should not depend at all on the length of the penetrator. This suggests that a long rod with strain gages attached could be used as a probe into the target interior. If the rod is long enough so that wave reflections from the rear cannot interfere with measurements, then the interpretation of the strain data will be considerably simplified. At the same time, any inferences concerning the forces, strains, or particle velocities at the impact end will be equally valid for shorter rods of the same material. In other words, it seems plausible that material characteristics will fix the boundary conditions locally at the impact end. It is the function of the experimental program to determine what those boundary conditions are.

In normal impact the motion of the rod is axi-symmetric. If the rod is treated as a one dimensional continuum where radial motions are ignored, the equations of motion may be written as follows:

$$\sigma_x = \rho u_t$$

$$u_x = \epsilon_t$$

(15)

In (15) σ is the axial stress in the rod (referred to the initial cross sectional area), ρ is the initial density, u is the particle velocity, and ϵ is the engineering strain. Subscripts denote partial differentiation where x is the material coordinate in the rod and t is time. The spatial location, x, of a material particle, X, is denoted

$$x = x(X,t) \tag{16}$$

We have

$$u = x_t, \quad \epsilon = x_X - 1 \tag{17}$$

WRIGHT

If strain gages are located at multiple stations along the rod in an impact experiment, then strain as a function of time can be recorded at each station, and by interpolation strain will also be known at all other stations as well. Instrumented rod experiments of this type have been conducted by Hauver over the past several years. He uses a light-gas gun where an evacuated target chamber and accurate alignment permit data of unusually high quality to be obtained. Complete experimental details are reported by him in other papers(7,8), but the experimental conditions, in brief, were as follows. A long steel rod, (S-7 tool steel, hardened to RC47), with length of 254mm and diameter of 8.13mm, impacts at normal incidence against a 25.4mm plate of rolled homogeneous armor at RC27. Speed of impact was nominally 1000 m/s for most tests, and 710 m/s in a few others. Strain was measured in the rod as a function of time, usually at stations 20, 40, 60, and 80mm from the impact end.

With ϵ-t data at hand, curves of constant strain may be plotted in X-t space. Along such a curve the slope, defined as c_p, the plastic wave speed, may be measured and related to derivatives of strain as follows.

$$d\epsilon = \epsilon_t \, dt + \epsilon_x dX = 0$$

$$\frac{dX}{dt} \equiv c_p = -\frac{\epsilon_t}{\epsilon_x} \tag{18}$$

These curves need not be straight lines, but if they are, as all experiments to date indicate, the analysis is greatly simplified because c_p then depends only on ϵ. Equations (15) may be integrated with respect to X along lines t = constant as was described by Kolski(9) and others. If the rod has speed u_o and zero stress and strain at any station before a wave arrives, we have

$$u(X,t) = u_o + \int_\infty^X \epsilon_t(X,t) \, dX$$

$$= u_o - \int_0^{\epsilon(X,t)} c_p(\epsilon) \, d\epsilon \tag{19}$$

$$\sigma(X,t) = \int_\infty^X \rho \, u_t(X,t) \, dX$$

$$= \int_0^{\epsilon(X,t)} \rho c_p^2(\epsilon) \, d\epsilon \tag{20}$$

405

Note that the stress has been obtained in (20) without recourse to any constitutive assumption. In fact, a dynamic stress-strain relation has been computed from the experimental data using only the simple one-dimensional equations of motion and compatibility.

Equations (19) and (20) determine the particle velocity and stress everywhere in the rod in principle. Thus, if the rate of rod erosion were known, these quantities would be known for the rod as it enters the quasi-steady region near the penetrator/target interface. The situation is shown in Fig. 5. The rays of constant strain are taken from Ref. 8.
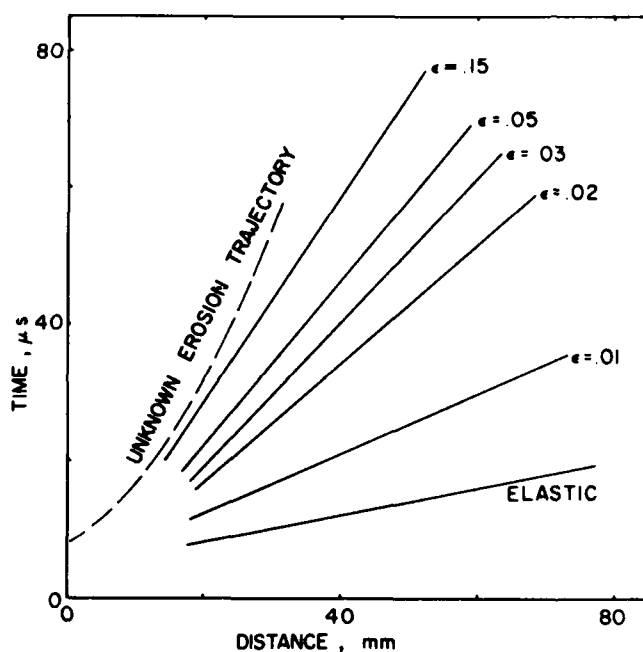
Figure 5. Lines of Constant Strain in X-t Space with Unknown Erosion Tra-jectory [after Hauver (8)].

The timing of gage failure cannot be used to establish the unknown erosion trajec-tory because gages are typically destroyed by ejecta before reaching the interface(8). Independent experiments by Netherwood have measured the rate of penetration into the target directly(10) for the same materials and impact conditions as in Hauver's experiments. Complete details are given in his paper, but essentially his tech-nique was to insert contact switches into the target block through holes drilled from the side. The timing of switch trig-gering then gives the trajectory of the penetrator/target interface in target material coordinates. Fig. 6 shows a compilation of data obtained by Netherwood(10). The unsteady entry region is clearly shown, followed by a steady intermediate region and an erratic, final, unsteady region.
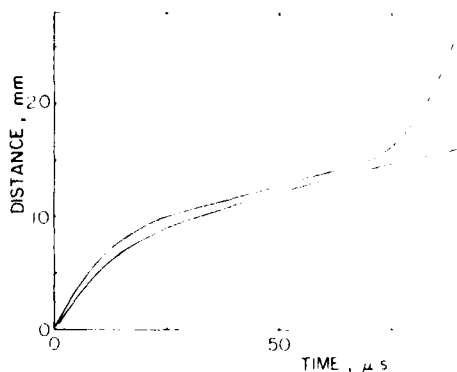
Figure 6. Envelopes of all Data Showing
Penetration vs. Time in Target
Coordinates from Ref. (10).

The final apparent increase in speed is probably due to pins shearing ahead of the penetrator as a small plug forms. The penetration trajectory may be compared with strain data, measured in material coordinates in the rod, if both sets of data can be transformed into a common coordinate system.

Fortunately, all data may be easily transformed, at least approximately, into laboratory coordinates. For the penetration data the transformation is a simple, time dependent translation. As penetration progresses the rear surface of the target bulges and finally fails by plugging. Netherwood has measured this motion of the rear surface with a streak camera(11). If deformation between switch pin and rear surface is neglected, then the translation of the pin in front of the penetrator is the same as that of the rear target surface. Target deformation remains completely unknown, but would contribute only a small correction compared to overall translation.

Rod data can also be transformed into laboratory coordinates. Since particle velocity is known as a function of position and time from (19), integration with respect to time will give trajectories in laboratory coordinates for each rod station. Hauver has computed some of these trajectories(8). It turns out to be more instructive to plot spatial trajectories of constant strain. From (16), with $X = X(t)$ being a curve of constant strain in material coordinates, differentiation yields the following equation.

$$\frac{dx}{dt} = \frac{\partial x}{\partial t} + \frac{\partial x}{\partial X} \frac{dX}{dt}$$

With the aid of (17), (18), and (19) this becomes

$$\frac{dx}{dt} = u_o - \int_o^\epsilon c_p \, d\epsilon + (1+\epsilon)c_p \qquad (21)$$

407

Several of these curves are plotted in Fig. 7. Both X and x are posi-
tive to the right, and u_o is positive, but both c_p and ε are negative
since strains are compressive, and plastic waves progress to the left
into the rod. Note that curves of constant strain are straight lines
in x-t space if they are straight in X-t space. Also shown in Fig. 7
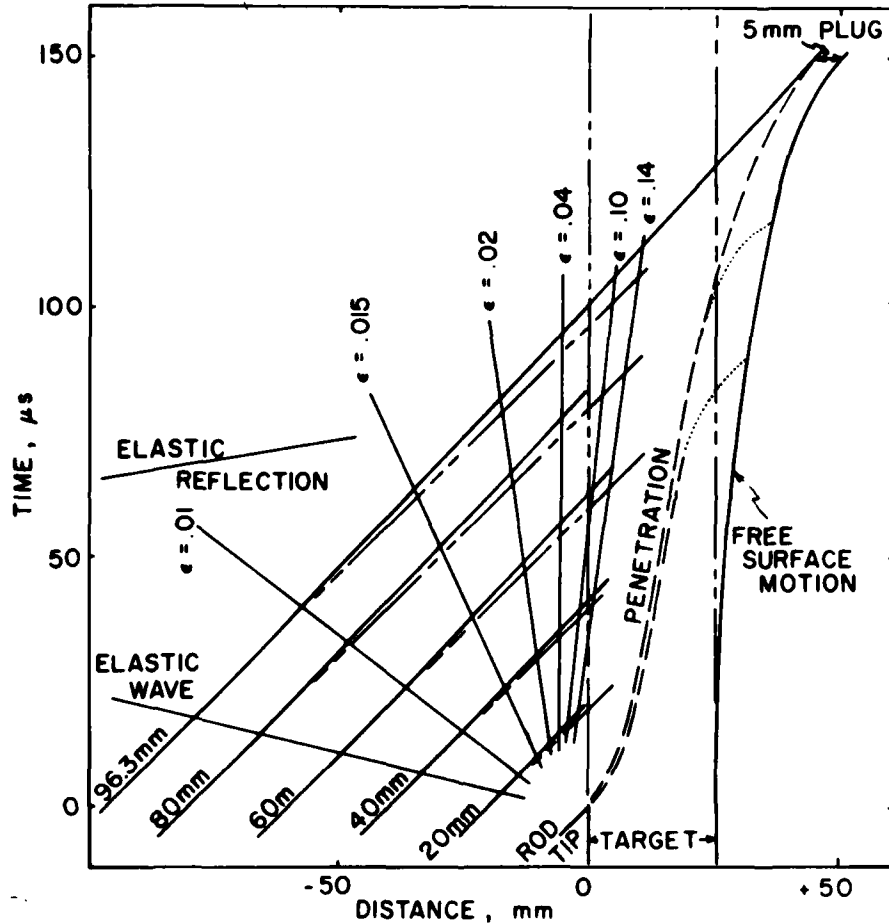
Figure 7. Trajectories in Laboratory Coordinates of Rod Stations,
Penetration, Target Free Surface, and Curves of
Constant Strain.

WRIGHT

is the back surface motion from Ref. (11) and the translated penetration trajectory. In some of his experiments Netherwood recovered the residual penetrator, whose initial, undeformed length was determined by weighing, and a small plug approximately 5mm thick. The trajectories of the leading station of the residual penetrator, labeled 96.3mm, and of the final plug are also shown.

IV. Discussion of Results.

Figures 6 and 7 contain a great deal of useful, albeit incomplete, information about the penetration process. In Fig. 6 the unsteady entry region seems to be about one penetrator diameter in width. The intermediate region shows a nearly constant speed of penetration, which is consistent with the idea of a zone of steady state deformation in penetrator and target.

There is no way of determining whether or not a switch triggers slightly before penetrator arrival in material coordinates, but since it could not be late, the measured arrival times are lower bounds. In any case, in the steady central section of penetration, it seems reasonable to assume that each switch is early by the same amount, on average, so that the true curve would be parallel to the one drawn in its middle section with corresponding minor adjustments in the unsteady end sections. The width of the breakout zone, about 9mm, is also approximately one penetrator diameter, although it is suspicious that one switch pin was usually located at the beginning of that zone and may have played a role in its initiation. Since the recovered plug was only about 5mm thick rather than 9mm, it seems clear that erosion of penetrator and target continues during plug formation and acceleration.

In Fig. 7 curves of constant strain, the penetration curve, back surface motion, and trajectories of selected rod stations are all shown in laboratory coordinates. There is actually considerable extrapolation of data here since strain gage records end near the target surface due to interference from ejecta(8), and the penetration curve ends at the start of plug formation. The free surface data do extend to 150µs, however, and serve to anchor the trajectory extrapolations for penetration and for the 96.3mm station. These three curves (i.e., free surface, penetration, and 96.3mm station) together with the known plug thickness give a remarkably coherent picture.

Strains higher than 14% were measured at one or two stations, but determination of c_p becomes unreliable so that trajectories for higher strains are not shown. Nevertheless, the figure clearly

409

suggests that the leading edge of the fan of constant strains might be roughly parallel to the penetration trajectory. If this were true, then equation (21) would give an estimate of rate of penetration possible for various levels of maximum strain. At the very least it will give a lower bound estimate for $\dot{p}$. This bound as a function of strain is plotted in Fig. 8 for the case considered. The measured value for $\dot{p}$, taken from Fig. 7, is about 190 m/s, which is not much greater than the maximum of the lower bound. Note that the bound, as given by equation (21), is linear in the impact speed u_o so that other cases may be considered simply by moving the horizontal axis up or down, provided the shape of the curve does not change too much with u_o.

Successful measurements have now been made of Σ, u, and $\dot{p}$ in equation (11). Another series of experiments to measure T directly for the same impact conditions are also under way by Pritchard at BRL. This leaves only the two terms I_p and I_t, which cannot be measured directly, but perhaps could be estimated analytically.

Figure 8. Particle Speed, u, and Speed of Strain Wave, dx/dt, vs. Strain, ϵ.

In future experimental work, the speed of impact, target thickness, and penetrator material will be varied. At the same time the analysis is being extended to include the effects of radial motion of rod material since the assumption of one-dimensional motion in equation (15) is probably not completely adequate.

The investigation of detailed interactions during penetration has been guided by a theoretical framework that is based on the one-dimensional theory of wave propagation. Although this work has

not yet led to a replacement for the eroding rod model, it has led to
an experimental description of events against which any successor
model may be evaluated.

REFERENCES

1. V. P. Alekseevskii, Penetration of a Rod into a Target at High
   Velocity, Comb., Expl., and Shock Waves, 2, 99-106 (1966).

2. A. Tate, A Theory for the Deceleration of Long Rods After Impact,
   J. Mech. Phys. Solids, 15, 387-399 (1967), and Further Results in
   the Theory of Long Rod Penetration, J. Mech. Phys. Solids, 17,
   141-150 (1969).

3. V. Hohler, and A. J. Stilp, Penetration of Steel and High Density
   Rods in Semi-Infinite Steel Targets, Third Int. Symp. Ballistics,
   Karlsruhe, Germany (1977).

4. A. Tate, K. E. B. Green, P. G. Chamberlain and R. G. Baker, Model
   Scale Experiments on Long Rod Penetration, Fourth Int. Symp.
   Ballistics, Monterey, CA (1978).

5. M. I. Gurevich, Theory of Jets in Ideal Fluids, Academic Press,
   New York and London (1965).

6. R. Hill, The Mathematical Theory of Plasticity, Oxford University
   Press, London (1950).

7. G. E. Hauver, Penetration with Instrumented Rods, Int. J. Eng.
   Sci., 16, 871-877 (1978).

8. G. E. Hauver, Experiments with Instrumented Long-Rod Penetrators,
   Fifth Int. Symp. Ballistics, Toulouse, France (1980).

9. H. Kolsky, Stress Waves in Solids, Dover Publications, New York
   (1963).

10. P. H. Netherwood, Rate of Penetration Measurements, ARBRL-MR-
    02978, Ballistic Research Laboratory, Aberdeen Proving Ground,
    MD, Dec. 1979.

11. P. H. Netherwood, private communication.

THE INITIAL BOUNDARY VALUE PROBLEM OF GUN DYNAMICS SOLVED BY
FINITE ELEMENT-UNCONSTRAINED VARIATIONAL FORMULATIONS (U)

JULIAN J. WU, PhD
US ARRADCOM, BENET WEAPONS LABORATORY, LCWSL
WATERVLIET, NY 12189

1. INTRODUCTION

The purpose of this paper is to introduce an efficient method, which is quite general and easy to use, to the solution of the gun dynamic problems, to describe some of the features associated with a finite element computer program, and to present some initial results.

The basic concept of unconstrained, adjoint variational formulation for linear problems was described in an earlier paper [1]. Its advantage over constrained methods in obtaining approximate solutions has been demonstrated for both conservative (self-adjoint) and unconservative (nonself-adjoint) problems [2]. In comparison with Galerkin procedure, the unconstrained, adjoint variational formulation has a further advantage in the freedom of selecting shape functions which have less requirement on differentiability and which are not required to satisfy any of the end conditions. The same concept was extended to solution formulation of initial value problems [3]. In view of the generality of this approach and its easy adaptability to finite element discretizations, it appears to be quite attractive in seeking solutions to the complicated problems associated with the dynamics of gun systems.

The basis of the present formulation for more general cases has been given in a previous paper [4]. The special problem of a uniform gun tube is treated here for demonstrated purposes. The differential equation and initial boundary conditions are given in Section 2. An unconstrained variational statement which is equivalent to the given governing equations is stated in Section 3. The details of some of the

413

special features on finite element discretization are described in Section 4. Finally some preliminary results are presented in Section 5.

2. GOVERNING EQUATIONS

The motion of a gun tube modeled by the lateral deflection of an Euler-Bernoulli beam is shown in Fig. 1. The differential equation in nondimensional form is

$$y'''' + (-\bar{P} + g \sin \alpha)[(1-x)y']' + \gamma^2 \ddot{y}$$

$$= -\bar{P}y''H(\bar{x}-x) - \gamma^2 m[\beta^2 t^2 y'' + 2\beta t \dot{y}' + \ddot{y}]\bar{\delta}(\bar{x}-x)$$

$$-(gm \cos \alpha)\bar{\delta}(\bar{x}-x)-g \cos \alpha \tag{1}$$

where

$\bar{P} = \pi R^2 p$
$y = y(x,t)$, the tube deflection
$x =$ spatial axis along the tube's length, $0 \leq x \leq 1$
$t =$ time axis, $0 < t \leq T$, T is the time limit of interest
$\alpha =$ elevation angle
$m =$ projectile mass
$\beta =$ acceleration of the projectile, assumed to be constant
$p =$ bore pressure, assumed to be constant
$g =$ gravitational acceleration
$\bar{x} = (1/2)\beta t^2$, projectile position
$H(x) =$ the Heavenside step function
$\bar{\delta}(x) =$ the Dirac delta function
$R =$ tube inner radius
$\gamma = c/T$

The constant c is defined by $(\rho A \ell^4/(EI))^{1/2}$ where ρ, E are density, Young's modulus of the tube material; ℓ, A, I, the length, area, and second moment of cross-section of tube, respectively (see Ref. [5]). Also in Eq. (1), a prime (') denotes a differentiation with respect to x and dot ($\cdot$), a differentiation with respect to t. The derivation of this equation and the end conditions which follow have been previously given [4,5] and will not be repeated here.

The initial condition, or more appropriately, the end conditions in time are

$$\dot{y}(x,0) = 0 \; ; \quad \dot{y}(x,1)[1 + m\bar{\delta}(\tfrac{1}{2} \beta-x)] + k_7[y(x,0) - Y(x)] = 0 \tag{2}$$

414
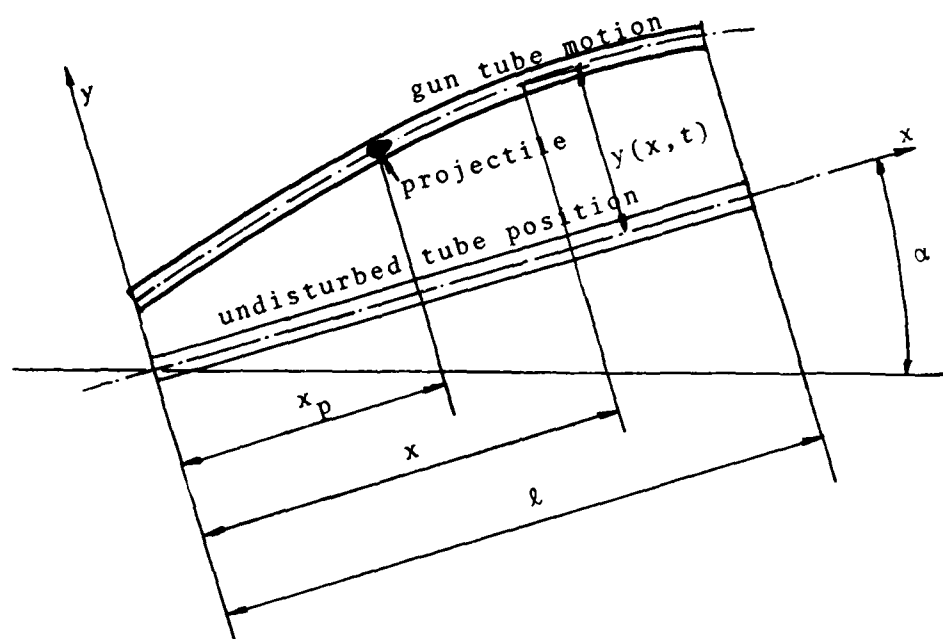
Fig. 1 A schematic drawing of the problem configuration

where the constant k_7 is introduced in conjunction with the unconstrained variational formulation (Section 3) so that if one takes k_7 to be infinite, the initial displacement $y(x,0)$ is forced to be identical to the prescribed shape $Y(x)$. Based on similar reasonings the boundary conditions have been shown to be the following:

$$y''(0,t) - k_2 y'(0,t) = 0 \tag{3a}$$

$$y''(1,t) + k_4 y'(1,t) = 0 \tag{3b}$$

$$y'''(0,t) + k_1 y(0,t) + (-\bar{P} + g \cos\ )y'(0,t)$$

$$+ \bar{P}y'(0,t)H(\tfrac{1}{2}\beta t^2) + m\beta^2 y'(0,t)\bar{\delta}(\tfrac{1}{2}\beta t^2) = 0 \tag{3c}$$

and

$$y'''(1,t) - k_3(1,t) + \bar{P}y'(1,t)H(\tfrac{1}{2}\beta t^2 - 1) + m\beta^2 y'(1,t)\bar{\delta}(\tfrac{1}{2}\beta t^2 - 1) = 0 \tag{3d}$$

where k_i, $i = 1, 2, 3, 4$, are the appropriate elastic spring constants at the supports.

415

3. UNCONSTRAINED VARIATIONAL STATEMENT

Through integrations-by-parts, it is straight forward to show that the following variational statement is equivalent to the differential equation and end conditions stated in Section 2.

$$\delta I = (\delta I)_y = \sum_{i=1}^{12} (\delta I_i)_y - \sum_{j=1}^{3} (\delta J_j) = 0 \qquad (4)$$

with

$$I_1 = \int_0^1 \int_0^1 y'' y^{*''} dx dt \; ; \; I_2 = (\bar{P} - g \sin \alpha) \int_0^1 \int_0^1 (1-x) y' y^{*'} dx dt$$

$$I_3 = -\gamma^2 \int_0^1 \int_0^1 \ddot{y} y^* dx dt \; ; \; I_4 = -\bar{P} \int_0^1 \int_0^1 y' y^{*'} H(\bar{x} - x) dx dt$$

$$I_5 = -\bar{P} \int_0^1 \int_0^1 y' y^{*'} \bar{\delta}(\bar{x} - x) dx dt \; ; \; I_6 = -m\beta^2 \gamma^2 \int_0^1 \int_0^1 t^2 y' y^{*'} \bar{\delta}(\bar{x} - x) dx dt$$

$$I_7 = -m\beta^2 \gamma^2 \int_0^1 \int_0^1 t y' y^{*'} \bar{\delta}'(\bar{x} - x) dx dt \; ; \; I_8 = 2m\beta\gamma^2 \int_0^1 \int_0^1 t y' y^* \bar{\delta}(\bar{x} - x) dx dt \quad (5)$$

$$I_9 = -m\gamma^2 \int_0^1 \int_0^1 \ddot{y} y^* \bar{\delta}(\bar{x} - x) dx dt \; ; \; I_{10} = -m\gamma^2 \int_0^1 \int_0^1 \dot{y} y^* \bar{\delta}(\bar{x} - x) dx dt$$

$$I_{11} = \int_0^1 \{ k_1 y(0,t) y^*(0,t) + k_2 y'(0,t) y^*(0,t)$$

$$+ k_3 y(1,t) y^*(1,t) + k_4 y'(1,t) y^{*'}(1,t) dt$$

$$I_{12} = k_7 \int_0^1 y(x,0) y^*(x,1) dx$$

and

$$J_1 = -g \cos \alpha \int_0^1 \int_0^1 y^* dx dt$$

$$J_2 = -gm \cos \alpha \int_0^1 \int_0^1 y^* \bar{\delta}(\bar{x} - x) dx dt \qquad (6)$$

$$J_3 = k_7 \int_0^1 Y(x) y^*(x,1) dx$$

416

The variational statement of Eq. (4) will serve as the basis of our finite element solutions.

4. FINITE ELEMENT DISCRETIZATION

The purpose of the discretization is to enable one to write the variational statement of Eq. (4), which is a functional of continuous functions y and y*, etc., in the form of a matrix equation

$$\delta \underset{\sim}{Y}^{*T} \underset{\sim}{K} \underset{\sim}{Y} = \delta \underset{\sim}{Y}^{*T} \underset{\sim}{F} \tag{7}$$

where $\underset{\sim}{Y}$, $\underset{\sim}{Y}^*$ are the "global" generalized coordinates vectors. $\underset{\sim}{K}$ is the "stiffness" matrix, and $\underset{\sim}{F}$ the "force" vector. These terminology are patented after the static structural analysis, but they do not necessarily have the physical meanings of those adjectives attached to them. Since the variational statement associated with Eq. (7) is unconstrained, the equation leads directly to

$$\underset{\sim}{K} \underset{\sim}{Y} = \underset{\sim}{F} \tag{8}$$

which can be solved for $\underset{\sim}{Y}$ if $\underset{\sim}{K}$ and $\underset{\sim}{F}$ are properly defined. The process by which $\underset{\sim}{K}$ and $\underset{\sim}{F}$ are assembled and the relation between $\underset{\sim}{Y}$ and the desired solution $y(x,t)$ will be described here in this section.

The first step is to write down the expressions in the variational statement in terms of the element variables. A grid scheme of elements is shown in Fig. 2. In this figure, the nondimensional length of the gun tube is divided into K equal segments and the time range of interest into L equal segments. The result is then a set of K x L rectangular elements. In the equations that follow n, the sub- or super-scripts m,n denote the association with the mth, n^{th} segments or the $(m,n)^{th}$ element. Define the relation between the local coordinates (ξ, η) of the $(m,n)^{th}$ element and the global coordinates (x,t) by

$$\xi = \xi^{(m)} = Kx - m + 1$$

$$\eta = \eta^{(n)} = Lt - n + 1 \tag{9}$$

Or,

$$x = \frac{1}{K} (\xi + m - 1) \quad ; \quad t = \frac{1}{L} (\eta + n - 1)$$

417
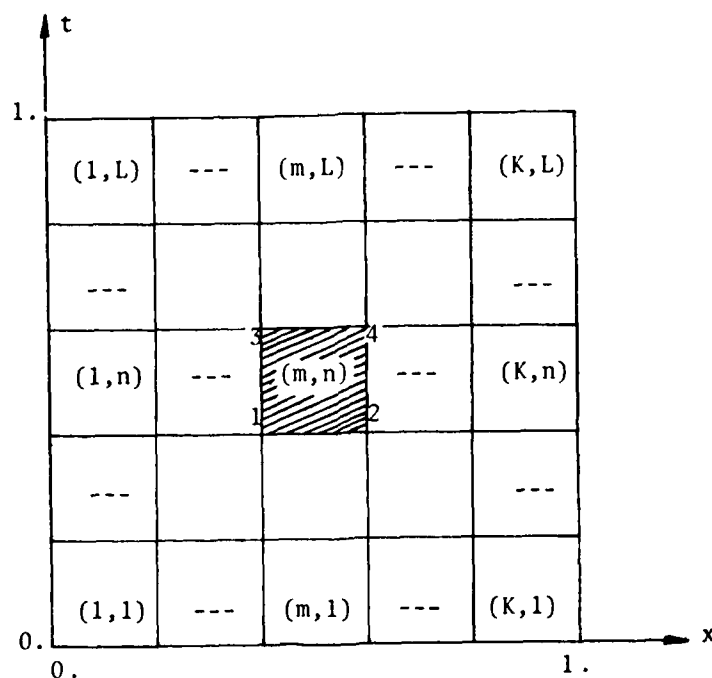
Fig. 2 Finite element grid scheme in space- and time-coordinates.
Also shown: node point ordering in a typical element (m,n).

One then can write from Eqs. (5) and (6)

$$\delta I_1 = \sum_{m=1}^{K} \sum_{n=1}^{L} \frac{K^3}{L} \int_0^1 \int_0^1 y''_{(m,n)} \delta y^{*''}_{(m,n)} d\xi d\eta$$

$$\delta I_2 = \sum\sum \frac{1}{L} (P-g \sin \alpha) \int_0^1 \int_0^1 [(K-m+1) - \xi] y'_{(m,n)} \delta y^{*'}_{(m,n)} d\xi d\eta$$

$$\delta I_3 = - \sum\sum \frac{L}{TK} \int_0^1 \int_0^1 \dot{y}_{(m,n)} \delta \dot{y}^{*}_{(m,n)} d\xi d\eta$$

$$\delta I_4 = - \sum\sum \frac{\bar{P}K}{L} \int_0^1 \int_0^1 y'_{(m,n)} \delta y^{*'}_{(m,n)} H_{(m,n)} (\bar{\xi}-\xi) d\xi d\eta$$

$$\delta I_5 = \sum\sum \frac{\bar{P}K}{L} \int_0^1 \int_0^1 y'_{(m,n)} \delta y^{*}_{(m,n)} \bar{\delta}_{(m,n)} (\bar{\xi}-\xi) d\xi d\eta \qquad (10a)$$

418

$$\delta I_6 = -\sum\sum \frac{m\beta^2 K\gamma^2}{L^3} \int_0^1 \int_0^1 [(m-1)^2 + 2(m-1)\eta + \eta^2] y'_{(m,n)} \delta y^{*\prime}_{(m,n)} \bar{\delta}_{(m,n)} (\bar{\xi}-\xi) d\xi d\eta$$

$$\delta I_7 = -\sum\sum \frac{m\beta^2 K\gamma^2}{L^3} \int_0^1 \int_0^1 [(m-1)^2 + 2(m-1)\eta + \eta^2] y'_{(m,n)} \delta y^{*\prime}_{(m,n)} \bar{\delta}'_{(m,n)} (\bar{\xi}-\xi) d\xi d\eta$$

$$\delta I_8 = \sum\sum \frac{2m\beta\gamma^2}{L} \int_0^1 \int_0^1 [(m-1)+\eta] y'_{(m,n)} \delta y^*_{(m,n)} \bar{\delta}_{(m,n)} (\bar{\xi}-\xi) d\xi d\eta$$

$$\delta I_9 = -\sum\sum \frac{mL\gamma^2}{K} \int_0^1 \int_0^1 \dot{y}_{(m,n)} \delta \dot{y}^*_{(m,n)} \bar{\delta}_{(m,n)} (\bar{\xi}-\xi) d\xi d\eta$$

$$\delta I_{10} = -\sum\sum \frac{mL\gamma^2}{K} \int_0^1 \int_0^1 \dot{y}_{(m,n)} \delta y^*_{(m,n)} \dot{\bar{\delta}}_{(m,n)} (\bar{\xi}-\xi) d\xi d\eta$$

$$\delta I_{11} = \sum_{n=1}^{L} \frac{1}{LK} \int_0^1 [k_1 y_{(1,n)} \delta y^*_{(1,n)} + k_2 K y'_{(1,n)} \delta y^{*\prime}_{(1,n)}$$

$$+ k_3 y_{(K,n)} \delta y^*_{(K,n)} + k_4 K y'_{(K,n)} \delta y^{*\prime}_{(K,n)}] d\eta$$

$$\delta I_{12} = \sum_{m=1}^{K} \frac{k_7}{K} \int_0^1 y_{(m,1)} \delta y^*_{(m,L)} d\xi \qquad (10b)$$

and

$$\delta J_1 = -\sum_{m=1}^{K} \sum_{n=1}^{L} \frac{\gamma^2 g \cos\alpha}{KL} \int_0^1 \int_0^1 \delta y^*_{(m,n)} d\xi d\eta$$

$$\delta J_2 = -\sum\sum \frac{\gamma^2 gm \cos\alpha}{L} \int_0^1 \int_0^1 \delta y^*_{(m,n)} \bar{\delta}_{(m,n)} (\bar{\xi}-\xi) d\xi d\eta \qquad (11)$$

$$\delta J_3 = \sum_{m=1}^{K} \frac{k_7}{K} \int_0^1 Y_{(m)}(\xi) \delta y^*_{(m,L)} d\xi$$

419

Now, the shape function vector $\underset{\sim}{a}(\xi,\eta)$ is introduced

$$y_{(m,n)}(\xi,\eta) = \underset{\sim}{a}^T(\xi,\eta)\underset{\sim}{Y}^{(m,n)}$$

$$y*_{(m,n)}(\xi,\eta) = \underset{\sim}{a}^T(\xi,\eta)Y*^{(m,n)} \qquad (12)$$

where $\underset{\sim}{Y}(m,n)$ and $\underset{\sim}{Y}*(m,n)$ are the generalized coordinates for the originaladjoint field variables. Thus, equations in the form of Eq. (7) and (8) are obtained in the usual manner of finite element formulation (see, for example, Ref. [5]).

5. NUMERICAL RESULTS

In actual computation, a simplified model of a M68-105 mm cannon tube is used. The source of data can be found in Reference [4]. For the cannon tube, we take

$$E = 3 \times 10^7 \text{ psi} \quad ; \quad \rho = 0.283 \text{ lb/in.}^3$$

$$\ell = 210 \text{ in.} \quad ; \quad A = 28.2 \text{ in.}^2 \quad ; \quad I = 123.6 \text{ in.}^4$$

and, for the projectile,

$$m_p = 20 \text{ lb} \quad ; \quad p \text{ (inbore pressure)} = 40,000 \text{ psi}$$

$$\beta \text{ (projectile acceleration)} = 6,000,000 \text{ in./sec}^2$$

$$v_{average} = 25,000 \text{ ft/sec} \quad ; \quad T = 0.008 \text{ sec}$$

Consequently,

$$c = (\rho A\ell^4/(EI))^{1/2} = 0.104 \text{ sec}$$

$$\ell/c = 2100 \text{ in./sec} \quad ; \quad \gamma = c/T = 13.00$$

In the finite element discretization, we have chosen a grid scheme of $5 \times 5 = 25$ elements as shown in Fig. 2. The shape functions used are cubic in x and linear in t. As an illustrative example, the support conditions are those of a cantilever. Thus k_1 and k_2 are infinite. In actual computations, they are taken to be very large numbers compared with unity (e.g., 10^8). The initial conditions are such that the tube has zero deflection and zero velocity at t = 0.

420

TABLE 1. DEFLECTION OF A GUN TUBE $[y(x,t)/\ell]$ x 10^4 AS THE
PROJECTILE MOVES THROUGH THE TUBE TILL EJECTION

t/T \ x/ℓ	0	0.2	0.4	0.6	0.8	1.0
0	0.0000	0.0000	0.0000	0.0000	0.0000	0.0000
0.25	0.0000	0.0151	0.0192	0.0182	0.0184	0.0281
0.50	0.0000	0.0413	0.0786	0.0735	0.0783	0.0986
0.75	0.0000	0.0724	0.1527	0.1768	0.1830	0.2156
1.00	0.0000	0.0905	0.2386	0.3245	0.3411	0.3362

TABLE 2. SLOPE OF A GUN TUBE $y'(x,t)$ x 10^4 AS THE PROJECTILE
MOVES THROUGH THE TUBE TILL EJECTION

t/T \ x/ℓ	0	0.2	0.4	0.6	0.8	1.0
0	0.0000	0.0000	0.0000	0.0000	0.0000	0.0000
0.25	0.0000	0.0511	-0.0079	-0.0121	0.0081	0.0710
0.50	0.0000	0.3132	0.0556	-0.0171	0.1021	-0.0936
0.75	0.0000	0.3758	0.2248	-0.0327	-0.0111	0.2647
1.00	0.0000	1.1419	0.7929	0.3932	0.3423	-0.2530

Fig. 3 Deflection
of a gun tube at
shot ejection.
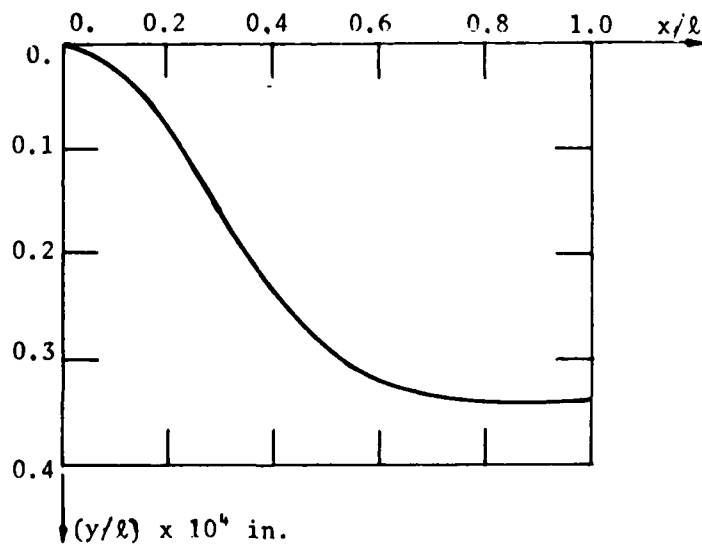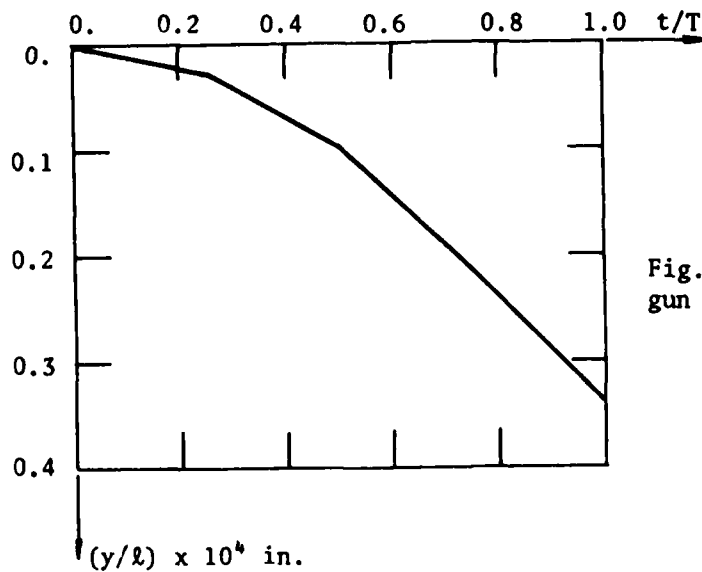
Fig. 4 Muzzle motion of a
gun tube during firing.

Tables 1 and 2 contain the results of tube deflection and
slope as the projectile moves down the tube from the breech end to
the muzzle. For example, at t = 0.5T, the deflection represents tube
deflection when the projectile is at a location of x = 0.25ℓ from the
breech end.

Figure 3 depicts the deflection curve of the gun tube at
projectile ejection and Figure 4 illustrates the muzzle motion as the
projectile moves down the tube.

From Tables 1 and 2 it is observed that the initial data
have been recovered for this present unconstrained variational formu-
lation. The data presented here are of the same order of magnitude
compared with other analysts [4]. Further verification of the compu-
tational results and a parametric study of the relative importance
of the various forces involved in the problem will follow in the
immediate future.

REFERENCES

1. Wu, J. J., "On Adjoint Operators Associated With Boundary Value Problems," <u>Journal of Sound and Vibration</u>, Vol. 39, 1975, pp. 195-206.

2. Wu, J. J., "On the Numerical Convergence of Matrix Eigenvalue Problems Due to Constraint Conditions," <u>Journal of Sound and Vibration</u>, Vol. 37, 1974, pp. 349-358.

3. Wu, J. J., "Solutions to Initial Value Problems by Use of Finite Elements - Unconstrained Variational Formulations," <u>Journal of Sound and Vibration</u>, Vol. 53, 1977, pp. 341-356.

4. Simkins, T. E., "Radial and Transverse Response of Gun Tubes by Finite Element Methods," <u>Proceedings of the First Conference on Dynamics of Precision Gun Weapons</u>, 1977, pp. 373-469.

5. Wu, J. J., "Gun Dynamics Analysis by the Use of Unconstrained, Adjoint Variational Formulations," <u>Proceedings of the Second U.S. Army Symposium on Gun Dynamics</u>, Watervliet, NY, September 1978, pp. II81-II99.

NEW CONCEPTS IN RECOIL MECHANISMS

RAO YALAMANCHILI, PhD
WEAPONS DIVISION
LARGE CALIBER WEAPON SYSTEMS LABORATORY
US ARMY ARMAMENT RESEARCH & DEVELOPMENT COMMAND
DOVER, NJ   07801

I   INTRODUCTION

The function of a recoil mechanism is to moderate the firing load on the supporting structure. This moderation is accomplished by prolonging the time of resistance to the reaction force caused by the action of the gun on the propellant gases. If no resistance is offered, the reaction force will be as great as the action force caused by the propellant gas. In other words, if the gun tube is rigidly fixed to the gun mount/carriage, the supporting structure is subjected to the full force of the propellant which, for large guns, may be 2- to 3- million pounds. To withstand such a force, the structure has to be not only strong and heavy but also wide-based to prevent tip over. As the gas pressure propels the projectile toward the muzzle, it exerts an equal and opposite force on the breech, which tends to drive the gun backward. The recoil mechanism suppresses this force gradually and also limits the rearward movement.

All guns, prior to about 1890, were mounted rigidly on a wheeled carriage which rolled backward to dissipate the recoil energy. The US first started to manufacture a gun with a recoil mechanism, the French 75mm field gun, during World War I. Since that time, the design of recoil mechanisms has been actively pursued.

The recoil mechanism is composed of three basic components: a recoil brake, a counterrecoil mechanism, and a buffer. The recoil brake normally consists of a hydraulic cylinder and a piston assembly. The counterrecoil mechanism consists of a recuperator and a counter-recoil cylinder assembly. These two subsystems (recuperator/counter-

recoil cylinder) can be either separate (independent recoil system) or combined (dependent recoil system). Sometimes, the counterrecoil mechanism and recuperator are used synonymously. The recuperator's function is to store part of the recoil energy in order to return the recoiling parts to the in-battery position, whereas the counterrecoil mechanism is used to return the recoiling parts to the in-battery position. The buffer's function is to absorb the counterrecoil energy as the weapon approaches the in-battery position, thereby assuring a smoothly controlled stop. The recoil brake may be either a hydraulic or a hydrospring type, whereas the recuperator may be either a hydropneumatic or a hydrospring type. Some examples of independent recoil mechanisms are the Schneider and Filloux types (1). In dependent recoil mechanisms, such as Puteaux and St. Chamond types (1), only the recoil piston rod is connected to and moves with the other recoiling parts and the fluid in the recoil brake directly influences the counterrecoil mechanism. All such mechanisms are single recoil systems (primary recoil systems). Sometimes, it is advantageous to have a secondary recoil system between the top and bottom carriages of heavy weapons (double recoil system). The Filloux and St. Chamond recoil mechanisms are variable recoil types (to accommodate changes in elevation), whereas the other two are constant recoil types.

Since these systems are all quite complex and contain several moving parts, their reliability is limited. As indicated later, the state of the art in the development of compressible hydraulic fluids is also quite limited. Today's artillery weapons may fire about one-quarter of the time and spend about another quarter of the time in moving about the battlefield. The remaining time is spent resolving RAM-D (reliability, availability, and maintainability-durability) problems. Various systems effectiveness studies indicate that the improvement which could be realized by doubling the RAM-D characteristics is significantly greater than that which could be realized by doubling the capability of weapon subsystem performance. There is nothing which can surmount this payoff potential of RAM-D improvements. In view of the multiple difficulties cited above, it is the object of this paper to discuss various recoil mechanism concepts having as few moving parts as possible, virtually unlimited compressibility, and transmitting the smallest amount of force to the supporting structure. These concepts are discussed in the following section. The development of a generalized mathematical model and the governing equations are given in section 3. The numerical results are presented in section 4 and the conclusions are stated in section 5

II CONCEPTS

A compressible fluid recoil mechanism presently under development uses a Dow Corning silicone fluid (DC 200-10CS). Although this fluid is considered compressible, its bulk modulus at 48°F (8.8°C) and at one atmosphere pressure is 141,200 psi (2). As temperature drops to -60°F and pressure increases to 4,000 psi, this fluid could have a bulk modulus as high as 260,300 psi. The ideal fluid should be highly compressible (low molecular weight), should possess a high flash point (low flammability) and its characteristics should be nearly independent of pressure and temperature. (A fluid's compressibility is the inverse of its bulk modulus). Artillery weapons are expected to function in a temperature range of -65°F to 120°F and with internal pressures ranging from 0 to 4,000 psi. Also, the temperature may rise approximately 1°F for each round fired unless adequate time is allowed for its heat dissipation between rounds or after a series of rounds. A perflourinated fluid (FC 75, 0.8 CS viscosity at 77°F) manufactured by 3M Company, and Freon E3 (1.3 CS viscosity at 77°F), currently no longer being manufactured by Dupont, may be up to 25% more compressible than the Dow Corning silicone fluid, although they still fall far short of the desired compressibility for recoil mechanisms.

It is not desirable to design flexibility into recoil mechanism test fixtures with the intent of boosting the compressibility of the total system beyond that of the fluid because the rate of loading of test fixture is so great (0 to 4,000 psi or higher within a few milliseconds) that the cylinder could buckle. Also, the oil seals between the moving and fixed members may make point contact rather than area contact thus causing leakage and permitting entrainment of the surrounding air. The air solubility for MIL-H-5606 is reported to be 0.109 (volume of air/volume of hydraulic fluid) whereas it is 0.168 to 0.19 for the Dow Corning silicone fluid at atmospheric conditions. Of course, the air content increases as the temperature drops and as the test fixture is actuated and could reach 1.3. Part of the entrained air may be undissolved. The dissolved and undissolved gases, collecting in pockets or foaming, can cause irregular motion and loss of control in recoil mechanisms. Magorien (3) discusses the behavior of air in hydraulic systems. However, the gas content increases the compressibility of the fluid and thus reduces the bulk modulus much beyond that for "liquids".

Consider, as an example, a liquid with a bulk modulus (B) in contact with an inert gas, such as N_2, with a specific heat ratio (r) of 1.4. The contents of the system may vary from 0 to 100% and may be separated by an elastic or floating member. The bulk modulus of a liquid is defined as

$$B = - \frac{v \, dp}{dv} \tag{2.1}$$

where p is the pressure and v is the volume. The bulk modulus is a function of pressure and temperature. However, the temperature variation of the fluid is small (such as one or two degrees) during any round of fire. The pressure, on the other hand, does vary nearly 3,000 psi. Therefore, the bulk modulus may be considered as a quadratic function of pressure $(a + b \, p + c \, p^2)$. In this instance, the integration of equation 2.1 yields

$$- \ln v = \frac{2}{\sqrt{q}} \tan^{-1} \left(\frac{2cp+b}{\sqrt{q}} \right) \text{ where } q = 4ac-b^2 \tag{2.2}$$

Sometimes, the pressure range is small and the bulk modulus can be considered as a linear function of pressure, p. Thus, the integration of equation 2.1 yields

$$\frac{v}{v^o} = \left(\frac{a+bp^o}{a+bp} \right)^{1/b} \tag{2.3}$$

where the superscript 'o' indicates initial conditions.

For concept evaluation or design purposes, such as, what will a combination of gas and liquid do as opposed to a liquid alone, or how to go about determining the compressibility of a given liquid, it may be advisable to consider the bulk modulus as independent of pressure at the desired temperature. In this case, the integration of equation 2.1 yields,

$$\frac{v}{v^o} = e^{(p^o-p)/B} \tag{2.4}$$

For example, a liquid (B = 120,000 psi p^o = 3,000 psi, p = 200 psi) undergoes a compression of about 2.33% because

$$\frac{v}{v^o} = e^{.0233} \simeq 1.0233$$

The equation of state for a gas may be written as

$$\frac{v_g}{v_g^o} = \left(\frac{p_g^o}{p_g} \right)^{\frac{1}{r}} \tag{2.5}$$

428

If a given liquid ($\bar{B}$) can do the job of a combination of some other liquid (B) and a gas, let it be called a super fluid and indicate its properties by a bar over the symbols. In order to make a fair comparison, let the total volumes and pressure ranges remain the same for both systems. By the use of equations (2.3) and (2.4), the super fluid's bulk moduli, respectively, become

$$\bar{B} = \frac{\dfrac{v_g^o}{v_h^o} \; (\dfrac{p^o}{p})\dfrac{1}{r} + (\dfrac{a+bp^o}{a+bp})^{1/b}}{\dfrac{1}{rp} \dfrac{v_g^o}{v_h^o} \; (\dfrac{p^o}{p})\dfrac{1}{r} + \dfrac{1}{a+bp} \; (\dfrac{a+bp^o}{a+bp})^{1/b}} \qquad (2.6)$$

$$\text{and } \bar{B} = \frac{(\dfrac{v_g^o}{v^o}) \; (\dfrac{p^o}{p})\dfrac{1}{r} + e^{-(p-p^o)/B}}{\dfrac{1}{rp} \dfrac{v_g^o}{v_h^o} \; (\dfrac{p^o}{p})\dfrac{1}{r} + \dfrac{1}{B} \; e^{-(p-p^o)/B}} \qquad (2.7)$$

The effective (or super fluid) bulk modulus is calculated at 3,000 psi for MIL-H-5606. This is shown in figure 1 as a function of nitrogen content. The bulk modulus is very sensitive to small changes of gas content when the percentage of gas is small. The bulk modulus of Dow Corning's expensive DC 200 silicone fluid is 168,607 psi at 3,000 psi and at 72°F. However, a better bulk modulus can be attained by combining inexpensive hydraulic fluid and gas.

A system with high RAM-D can be characterized as the one which is simple and contains few moving parts. Consider the M140 recoil mechanism mounted on the M60A1 tank. Although, this mechanism looks simple and has only three moving parts, its failure rate is high. Some of the failures are due to breakage (every few hundred cycles) of its giant mechanical spring, leakage of oil around the seals, failure to return to the battery position, inadequate replenisher, wear and tear of piston and sleeve, hang out of battery, breakage of the inertia valve, and either loosened or broken bolts. Most of these problems can be solved by elimination of the mechanical spring and the replenisher, and the utilization of only one moving part. Such concepts are shown in figures 2 through 5.

The bulk modulus of a fluid system as a function of the amount of nitrogen or air is shown in figure 1. Such a system is quite sensitive to the presence of small amounts of nitrogen and is

much less sensitive to larger amounts since the bulk modulus de-
creases significantly as nitrogen content is increased. The relation-
ship between bulk modulus and temperature is also shown in figure 1.
The bulk modulus varies drastically between -65°F and 120°F and drops
continuously as temperature increases. If the temperature is low at
a particular weapon's location, the bulk modulus increases; however,
increasing the gas content of the system will decrease the bulk mod-
ulus and thus compensate for the low ambient temperature. If the
temperature is higher at another operational location, the bulk mod-
ulus is lower; however, the gas content can be lowered to increase
the bulk modulus. Thus, the gas-oil mixture concept can accommodate
both compressibility and temperature compensation in lieu of the
separate mechanisms required in the past.

It was proposed by other investigators to use Dow Corning
DC 200 as a compressible fluid for new systems under development.
The cost of DC 200 silicone fluid is several times that of the hy-
draulic fluid used in many weapon systems. These inexpensive hydrau-
lic fluids can be used in the conceptual systems instead of the Dow
Corning fluid because the compressibility and temperature effects
are compensated for. Of course, the conceptual systems weigh less
than a pure liquid system.

With conventional recoil systems, the recoiling parts move
rearward upon initiation of the breech force, i.e., upon firing. The
rearward motion is resisted by the inertia of the recoiling parts,
friction, and the fluid pressure forces exerted inside the recoil
mechanism. The fluid pressure forces are a result of the throttling
of the fluid and compression due to the differential area of the
piston (a moving part) and its motion. However, if the recoiling
parts are put in motion in the direction of projectile travel
(forward run-up) and the breech force is not applied until these
parts have attained a predetermined forward velocity (equal to about
half of the recoil energy), lower resistance forces will result.
Such a principle is called "soft recoil". The development of this
technique began in the mid 1960's. The conventional versus soft
recoil principles are illustrated in figure 6. Since the resisting
force in a soft recoil mechanism is much smaller than in a convention-
al recoil mechanism, the time for application of this force is much
longer. To date, the soft recoil principle has been applied to the
M204, 105mm towed howitzer only.

Since the objective of any recoil mechanism is to design
the resisting force to be as small as possible (which can account for
all its breech force), and to have as few parts as possible, the

conceptual sketch shown in figure 2 was initially adopted. The initial position of the piston (the moving part) is shown. The hydraulic fluid, or DC 200, is at about 3,000 psi pressure and fills the entire recoil cylinder including the buffers.

The fluid pressure acts on all exposed surfaces. The pressurized fluid acting on the face (end) of the piston forces it to move (slide over the sleeve) in the forward direction, after it is unlatched. When it reaches a predetermined velocity, the firing (or initiation of breech force) takes place. Since this breech force overcomes the forward motion, the piston is brought to rest, momentarily, and then accelerates to the rear. Of course, there is an opposing force of pressurized fluid acting on the face of the piston. This opposing force continues to grow as the piston moves to the rear and compresses the fluid into a smaller volume. Eventually, the piston is brought to rest momentarily with or without the assistance of the rear buffer. (If the predetermined velocity of the piston is properly matched with the breech force, the piston stops without the aid of the rear buffer.) A sensor was developed to determine the velocity (4). Even when the velocity is accurately calculated and the sensor operates correctly, there may be occasions where the breech force cannot be applied at the correct time because of ignition delay or other considerations. In such situations, the actual velocity of the piston may be greater than the predetermined velocity and it may not be able to return to the latched (initial) position. It is desirable to utilize about 40% of the breech force to stop the forward (outward) motion of piston. This will cause the piston to enter approximately 2 inches into the rear buffer before its motion is stopped. The latch is reset by the piston near the end of its rearward motion. The pressurized fluid then forces the piston to move slightly forward to the latched (initial or in-battery) position.

Another purpose of the rear buffer is to check out the cook-off function. (Cook-off is the spontaneous firing of a round due to excessive heat or other cause.) The application of breech force to the piston takes place when the piston is in its initial position. The piston accelerates rearward because of the cook-off breech force. The pressure of the trapped fluid inside the buffer will be much higher than that of fluid outside the buffer. The design of the buffer should be such that the piston's rearward motion ceases before it slams into the rear end of the recoil cylinder and also such that the resisting force does not build to a point permitting weapon tip-over.

The front buffer is intended to control misfires. A misfire, or firing delay, may take place because of a bent firing pin or other malfunction. If no front buffer is provided, the piston may slam into the end of recoil cylinder. In the event of a misfire the piston enters the front buffer and traps the fluid inside the buffer raising its pressure much beyond the pressure inside the recoil cylinder. This sets up an opposing force to stop the forward motion of the piston. The design of the front buffer should be such that the piston velocity is reduced to a negligible value before it reaches the front end of the recoil cylinder and yet not permit cavitation inside either the cylinder or the buffer during any part of the cycle.

Some of the characteristics of this system are discussed in reference 5. However, in this reference the governing differential equations (coupled) were not simultaneously solved. The author solved these equations simultaneously and studied the system's operating characteristics. It was determined that the recoil cylinder would need to be about 8 feet long and cavitation would result if based upon the conceptual sketch of figure 2. The author modified the conceptual sketch as shown in figure 3. The normal run (without misfire and cook-off) characteristics remained the same. However, the handling of cook-off and misfire situations would be improved if cook-off and misfire chambers are as shown in figure 3. The storage chamber, in addition to the buffers, provides a shorter path and a better control of piston motion inside the buffers. The storage areas prevent a rapid rise and fall of buffer pressures and thus reduce the chances of weapon tip-over as well as cavitation inside the buffers.

To make the conceptual model as general as possible, to make the system lighter, to increase the compressibility of the system, to compensate for changes in temperature, and to use an inexpensive and small amount of oil (fluid), a gas, such as nitrogen, is introduced into the central part of the recoil cylinder and separated from the liquid by a polyurethane liner (dotted line). Since the pressures will remain the same on either side of the liner (because of its elasticity) it is expected that the operating pressures won't pose a problem. If the liner is not satisfactory, there is always the technique of the nineteen fifties, that of separation of gas and liquid by a floating piston.

It is recalled that the predetermined velocity chosen (about 50% of breech force) is somewhat less than the ideal because of ignition delay and other considerations. The piston enters the rear buffer approximately 2 inches (because of the slightly less than ideal soft recoil cycle) before it reverses its motion. Since the

piston could pick up significant velocity due to the high pressure
(more than 20 inch/sec by the time it reaches the latching position),
it may be difficult for a mechanical latch to function. In the event
of a cook-off, the   city of the piston just before latching will
exceed this speed. ᴸ₀ control the motion of the piston just before
it latches into the in-battery position, a combination of the middle
buffer and a step on the piston is provided as shown in figure 4.
In addition, a gas chamber is utilized as shown by the dotted line in
the figure.

The recoil cylinder will be about 6 feet long for a 155mm
weapon system. If a one-quarter-inch thick piston is chosen for any
of these concepts it may not be strong enough and induced vibration
or buckling could result. If a three-eighths-inch thick piston is
chosen, the effective area of the piston, due to its concentricity,
is about $16 in^2$. The effective piston area of existing weapons is
about $10 in^2$. However, the effective piston area can be controlled
by choosing either a multi-cylinder (nonconcentric) configuration or
a piston designed as shown in in figure 5. Thus, the effective area
is not a serious design problem.

The concept based on figure 4 is more general and, there-
fore, it is chosen for further evaluation. However, the concepts
based in figures 2 and 3 are special concepts based on figure 4.

III MATHEMATICAL MODEL OF HYDROPNEUMATIC
SOFT RECOIL MECHANISM

The hydropneumatic soft recoil concept is shown in figure 4.
This schematic figure is not drawn to a scale. This concept is a
concentric recoil mechanism and the piston, its only moving part, is
shown in its latched (in-battery) or initial position. First, fluid
fill-up takes place. Thus, nitrogen bottles can be attached to the
gas chambers for pressurization. The pressure inside the cylinder
will not exceed 3,000 psi, when the piston is in its latched posi-
tion. In a normal run, the piston is moved forward by the pressur-
ized fluid to a distance less than L2, returns past the latch by
virtue of breech force, and finally is pushed forward to the latch by
fluid pressure.

In figure 4, L indicates length, R indicates radius, and
P indicates pressure. The recoil cylinder consists of four chambers.
The cook-off chamber is inside the left end of the cylinder and the
misfire chamber is inside the right end of the cylinder. The latch-
ing chamber is next to the cook-off chamber. A two-ring piston is
used to control its motion just before latching. The normal chamber

is in front of the misfire chamber.

Mathematical models have been developed for both configurations (figures 3 and 4). However, because of space limitations, only the generalized model will be discussed. The application of Newton's second law yields the equation of motion for the piston:

$$\ddot{x} = (RP - HI * PBF \ (xx))/M_r - g \sin \theta \qquad (3.1)$$

$$\dot{x} = \int \ddot{x} \ dt \qquad (3.2)$$

$$x = L_3 + \int \dot{x} \ dt \qquad (3.3)$$

where x = location of piston, $\dot{x}$ = velocity, $\ddot{x}$ = acceleration, RP = rod pull, $PBF \ (xx)$ = breech force function, $HI=0$ or 1 to indicate inaction or action of breech force, M_r = mass of recoiling parts, g = gravity, θ = elevation of gun, and L_3 = length of rear (cook-off) chamber. The rod pull can be written as

$$RP = s * (1.345p_r + 2.97p_f) + p_r A_3 + p_m \ (A_7 - A_4) - p_f A_7$$

$$(3.4)$$

The first term indicates frictional force due to seals (5) and the subscripts r, m, and f signify the rear, middle or latching, and front chambers, respectively. Also $A_3 = \pi \ (R_3{}^2 - R_5{}^2)$, $A_4 = \pi \ (R_3{}^2 - R_4{}^2)$, $A_5 = \pi \ (R_4{}^2 - R_5{}^2)$, and $A_7 = \pi \ (R_7{}^2 - R_4{}^2)$.

The fluid volume (applicable to the driving force of the piston) at any time can be written as

$$v = v_g^o \ \left(\frac{p_2^o}{p_2}\right)^{1/r} + v_h^o \ e^{(p_2^o - p_2)/B} - (F^v{}_f + Jv_r + Mv_m)$$

$$(3.5)$$

where p_2 = pressure in the normal chamber,

$$v_f = v_f{}^o \ e^{(p_f^o - p_f)/B} - f \int_o^t Q_f \ dt \qquad (3.6)$$

$$v_r = v_r^o \; e^{(p_2^o - p_r)/B} - j \int_0^t Q_r \, dt \tag{3.7}$$

$$v_m = v_m^o \; e^{(p_2^o - p_m)/B} + j \int_0^t Q_r \, dt - m \int_0^t Q_m \, dt \tag{3.8}$$

$$v_f^o = v_{fs} + (A_7 + A_f)L_1, \quad v_{fs} = \pi L_1 (R_8^2 - R_1^2),$$
$$A_f = \pi (R_1^2 - R_7^2) \tag{3.9}$$

$$v_r^o = v_{rs} + (A_3 + A_r)L_3, \quad v_{rs} = \pi L_3 (R_8^2 - R_2^2),$$
$$A_r = \pi (R_2^2 - R_3^2) \tag{3.10}$$

$$v_m^o = v_{ms} + L_3 (A_7 + A_m), \quad v_{ms} = (L_5 - L_{4/2}) \; \pi$$
$$(R_8^2 - R_6^2), \quad A_m = \pi (R_6^2 - R_7^2) \tag{3.11}$$

$$v_2^o = v_{2s} + L_2 (A_7 + A_m), \quad v_{2s} = (L_2 + L_4/2) \; \pi$$
$$(A^2 - R_6^2) \tag{3.12}$$

$$Q_r = C_d A_r \left(\frac{2g \; P_r - P_m}{\rho} \right)^{1/2}, \quad Q_f = C_d \; A_f \left(\frac{2g |P_f - P_2|}{\rho} \right)^{1/2}$$

$$Q_m = C_d \; A_m \left(\frac{2g |P_2 - P_m|}{\rho} \right)^{1/2} \tag{3.13}$$

F, J, M, f, j, m, and s are all logical parameters and will be defined later. The symbols A, v, Q are used for area, volume, and flow discharge rates, respectively. The coefficient of discharge for fluid flow through the orifice is denoted as c_d. The physical volume based on solid boundaries can be written as

$$v = v_f^o + v_r^o + v_m^o + v_2^o - (F v_f + J v_r + M v_m) + A_5 (x - L_3) \tag{3.14}$$

One can obtain the following equation for p_2 by equating the rate of change of the two volumes described above:

$$p_2 = \left\{ -\left[A_5+F(A_7+A_f)-J(A_3+A_r)+M(A_4+A_r-A_m)\right] \dot{x} \right.$$

$$+F\left[v_f^o e^{(p_f^o-p_f)/B} \dot{p}_f/B+fQ_f\right] + J\left[v_r^o e^{(p_2^o-F_r)/B}\right.$$

$$\left. \dot{p}_r/B+jQ_r\right] +M\left[v_m^o e^{(p_2^o-p_m)/B}\dot{p}_m -j\ Q_r+mQ_m\right]\right\} \Bigg/$$

$$\left[\frac{v_g^o}{rp_2}\ (p_2^o/p_2)^{1/r}\ +e^{(p_2^o-p_2)/B}\ v_h^o/B\right] \qquad (3.15)$$

Similar treatment can be given for the rate of change of pressures inside the rear and front buffers. The volume of oil at any time in either buffer can be written as

$$v = F\ v_f + J\ v_r \qquad (3.16)$$

The physical volume based on boundaries is

$$v = F\left[v_{fs}+(A_7+A_f)(L-x)\right] +J\ v_{rs}+(A_3+A_r)\ x \qquad (3.17)$$

where $L = L_3+L_5+L_2+L_1$

The rate of change of pressure in either buffer can be derived by equating the rate of change of volumes and the result is given below.

$$\dot{p}_r\ or\ \dot{p}_f = \frac{\left[F(A_7+A_f)-J(A_3+A_r)\right]\dot{x}-(FfQ_f+JjQ_r)}{Fv_f^o/B\ e^{(p_f^o-p_f)/B}\ +Jv_r^o/B\ e^{(p_2^o-p_2)/B}}$$

$$(3.18)$$

Of course, these equations are valid for either $0 \leqslant L_3$ or $L_3+L_2 \leqslant L_3+L_2+L_1$.

A similar equation can be derived for pressure in the latching chamber. The volume of oil in the middle buffer is

$$v = M \left[v_m^o e^{(p_2^o - p_m)/B} + j \int_o^t Q_r \, dt - m \int_o^t Q_m \, dt \right] \quad (3.19)$$

The physical volume of the latching chamber can be expressed as

$$v = M \left[v_{ms} + (A_4 + A_r)(L_3 - x) + (A_7 + A_m) x \right] \quad (3.20)$$

The rate of change of pressure in the latching chamber can now be expressed as

$$\dot{p}_m = \frac{M \left[(A_4 + A_r - A_7 - A_m) \dot{x} + j Q_r - m Q_m \right]}{v_m^o / B \; e^{(p_2^o - p_m)/B}} \quad (3.21)$$

The logical parameters, for many of the equations in this section are given below:

$$s = 1 \text{ for } \dot{x} < 0, \quad s = -1 \text{ for } \dot{x} > 0$$

$$F = 1 \text{ for } x > L_2 + L_3; \quad F = 0, \; A_f = 0 \text{ for } x < L_2 + L_3$$

$$J = 1 \text{ for } x < L_3; \quad J = 0, \; A_r = 0, \; x > L_3$$

$$j = 1, \; f = 1 \text{ for } p_f \text{ or } p_r > p_2; \quad j = 1 \text{ for } p_r > p_m$$

$$j = -1, \; f = -1 \text{ for } p_f \text{ or } p_r < p_2; \quad j = -1 \text{ for } p_r < p_m$$

$$M = 1 \text{ for } L_3 - L_4 \le x \le L_3 \text{ and } M = 0, \text{ otherwise}$$

$$m = 1 \text{ for } p_m > p_2 \text{ and } m = -1 \text{ for } p_m < p_2 \quad (3.22)$$

The equations derived in this section, represent normal fire, cook-off and misfire conditions. The finite-element calculations as well as the one-dimensional analytical results of figure 2 indicate that the deflections of the recoil cylinder and sleeve are quite small and are within engineering or manufacturing tolerances. The governing equations for deflection of the recoil cylinder and the sleeve are second-order ordinary differential equations. The rate of change of pressure equations (3.15), (3.18), and (3.21) also will be different if deflections are taken into account. Since the deflections are small, the governing equations (with deflections) are not

given here. The equations derived above, represent a system of six
first-order ordinary differential equations. These are all coupled
to be solved simultaneously.

IV RESULTS

The hydropneumatic soft recoil conceptual sketch is shown
in figure 4. The mathematical model for its operational character-
istics is given in section 3. Since standard techniques can be util-
ized (the governing equations are not complex), the system of coupled
ordinary differential equations as well as logical parameters are
programmed for the CDC 6500/660 system and solved by Continuous
System Simulation Language (CSSL). The breech force (figure 7) is
computed for a zone 7 charge, 155mm weapon system. Due to a lack of
analytical functions, the tabular form of breech force is provided as
input and interpolation techniques are utilized during the course of
the calculations.

Following is the input data for a typical computer run:

L_1 = 20 in. $\qquad$ R_1 = 9.2684 in. $\qquad$ p^0 = 2,000 psi

L_2 = 30 in. $\qquad$ R_2 = 9.0484 in. $\qquad$ v_g^0/v_h^0 = 0.22

L_3 = 20 in. $\qquad$ R_3 = 9.0284 in. $\qquad$ θ = 0

L_4 = 8 in. $\qquad$ R_4 = 8.5 in. $\qquad$ M_r = 25.9 lbs

L_5 = 20 in. $\qquad$ R_5 = 8.125 in. $\qquad$ A = 11 in.

C_d = 0.9 $\qquad$ R_6 = 9.2684 in. $\qquad$ $X(0)$ = 20 in.

D = 8.125 in. $\qquad$ R_7 = 9.2484 in. $\qquad$ B = 150,000 psi

ρ = .033942 lbs-sec^2/in.^{4} $\qquad$ n = 1.3

The shape of the buffers are functions of x. These values are omit-
ted due to lack of space. Tabular data is input for these functions
and interpolation techniques are utilized.

Most of the firing, at least 99%, takes place in a normal
manner. Such firings are termed a "normal run" and the designs are
optimized for them. The free-run velocity of the piston before fir-
ing is given as 230 in/sec for the breech force shown in figure 7.
The velocity of the piston for a normal run is shown in figure 8.

The piston attained a velocity of 230 in/sec after traveling about 25 inches. Firing is initiated at this time. The piston's velocity is reduced to zero within one inch of travel. The piston reverses its motion and reaches a maximum velocity of 227 in/sec after traveling 5.8 inches. The piston continues its rearward coasting movement and attains a velocity of 57 in/sec upon arrival at its initial position. At this time the latch is reset. The piston travels slightly more than an inch into the rear buffer before its rearward velocity is reduced to zero. Finally, the piston is pushed forward by the pressurized fluid and reaches a speed of about 29 in/sec just before engagement of the latch.

The piston location, as a function of time, is also shown in figure 8. Forward travel requires 216 msec and rearward travel requires 177 msec. The piston completed its cycle in 423 msec.

The pressure, p_2, in the normal chamber, is the same as that in the misfire chamber and is shown in figure 9. The pressure drop is only 400 psi, although the piston (with a differential area of 19.6 in^2) travels about 25 inches due to the presence of gas in the system. The pressure inside the rear buffer is identical to the pressure in the normal chamber except for the short period of time that the piston is inside the buffer. During this period, there is a sharp rise in pressure to 2,504 psi followed by a fall-back to 1,647 psi. There is a similar behavior pattern for the pressure inside the latching chamber. In this instance, the pressure rises to 2,458 psi and falls back to 1,696 psi.

The rod pull is shown in figure 10. This has a low value during the free-run period, starting with a peak of 30,541 lbs and dropping slowly to 24,459 lbs. The initiation of breech force quickly raises the rod pull to 38,260 lbs at the time the piston reverses its direction. Thereafter, the rod pull rises slowly and reaches 47,800 lbs by the time the piston reaches its initial position. Finally, the rapid rise of pressure inside the buffer momentarily increases the rod pull to 78,018 lbs, which then drops back to a nominal value just before the piston is latched.

The following applies to a misfire simulation. The breech force is not applied although the piston velocity is 230 in/sec. The piston continues its forward travel and reaches a peak velocity of 250.15 in/sec just before it enters the front buffer. A braking force is applied by the misfire chamber and the piston's velocity is reduced to less than 1 in/sec by the time it travels 16 inches inside the buffer. At this point the piston begins to oscillate.

Whether or not an external or internal spring is used to stop this motion, it is not expected to create any damage to the mechanism because of its very low velocity and friction. The time required for the piston to reach a velocity of 0.6 in/sec, is 472 msec. The pressures in the cook-off, latching, and normal chambers are identical. These pressures vary from an initial pressure of 2,000 psi to 1,366 psi and then drop to a level similar to the normal chamber pressure in a normal run as shown in figure 9. All pressures would have been very small (indicating cavitation and a vacuum) if not for the presence of gas. The pressure inside the misfire chamber is the same as the pressure in the other chambers until the piston enters the misfire chamber. Because the buffer's design is not optimized, the misfire chamber pressure rises to 7,000 psi and then drops to 2,321 psi. (Bear in mind a misfire is not a normal firing condition for a howitzer.)

Following are the cook-off results. The breech force is applied while the piston is at rest at its initial position. As expected, the piston starts rearward and reaches a peak speed of 342.9 in/sec within 12 msec and travels a distance of 2.3 in. Finally, the piston's rearward velocity is reduced to zero within 38.7 msec after traveling a distance of 7.32 in. Obviously, the calculated distance and time are small and a need for redesign of the buffer is evident. The pressure in the cook-off chamber is as high as 10,000 psi. Outside the chamber it is 2,146 psi. Because of these high pressures (the latch is not expected to operate at this time), the piston starts forward reaching a velocity of 49 in/sec and dropping to a low of 5.79 in/sec before hovering at about 20 in/sec near the latching position. During this forward travel the pressure in the cook-off chamber is as low as 1,390 psi, is slightly higher than 2,000 psi in the normal chamber, and is between these extremes in the latching chamber. The elapsed time for the entire cook-off cycle is 380 msec. Cook-off is less likely to occur than misfire. Its operational cycle is less gentle than that for normal fire.

V SUMMARY

Various existing recoil mechanisms are reviewed and their drawbacks are discussed. The importance of RAM-D is stressed. Several new concepts are introduced having desirable characteristics such as: one moving part, highly compressible system much beyond the state of the art with liquids only, temperature compensating device, lower operating pressures with no cavitation or vaccuum, transmission of minimum forces to the supporting structure, ideal distribution of forces (symmetric and in line with the breech force), simplicity, and packaging of recoil and counterrecoil functions with-

in a single envelope (includes misfire and cook-off functions). All
such characteristics are incorporated into a new concentric hydropneu-
matic soft recoil mechanism shown in figure 4.

Mathematical models are developed by use of Newton's law of
motion, continuity equation, definition of bulk modulus for liquids,
perfect gas law, and Bernoulli's equation. Virtually unlimited com-
pressibility is proven and a method of compensating for temperature
variations is presented. The breech force data for a 155mm weapon
(including all propellant charge zones) is coupled to a system of six,
first-order, ordinary differential equations. These are programmed
for a digital computer and solved by CSSL. The operating character-
istics are obtained not only for normal fire but also for cook-off and
misfire. The deflections of the recoil cylinder and sleeve are found
to be negligible. The pressure in each chamber, the trunnion force,
and the location and velocity of the piston are obtained as a func-
tion of time. The concepts may not be feasible as "liquid only"
systems. Although a recoil mechanism without a latching chamber would
be short and light in weight, it would be very difficult to latch the
piston without damaging the latching mechanism. A recoil mechanism
having a latching chamber, a liquid-gas working medium, and employing
a partial or a complete soft recoil principle shows promise of suc-
cess. A parametric study is recommended after the buffers are rede-
signed. The objective of the redesign would be to raise the buffer
pressures to the desired level as quickly as possible and holding
these pressures constant until all motion ceases. As an alternative,
a conventional recoil mechanism, with fluidic control (no moving
parts) and sensor devices (currently being pursued), is recommended
as a means to obtain constant rod pull for all zones of fire.

REFERENCES

1. The Franklin Institute, "Carriages and Mounts Series Recoil
Systems", AMCP 706-342, Sept 1963.
2. Bornong, B.J., and Hong, V.Y.S., "Investigation of Compress-
ible Fluids for Use in Soft Recoil Mechanisms", ASD IR 3-77, ARRADCOM,
Dover, NJ (1977).
3. Magorien, V.C., "How Hydraulic Fluids Generate Air",
Hydraulics and Pneumatics, pp. 105-108, June 1969.
4. Courtney, W.J., Norikane, K., and Shaifer, T., "Development
of a Firing Device for a 155mm LCSR", Illinois Institute of Technol-
ogy Research Institute, Chicago, Illinois, April 1977.
5. Hoffgaard, B.L., "Analysis of a Compressible Fluid Soft
Recoil (CFSR) Concept Applied to a 155mm Howitzer", Technical Report
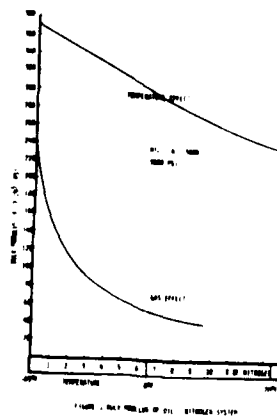ARLCD-TR-78026, US Army Armament Research & Development Command,
Dover, NJ, March 1979.
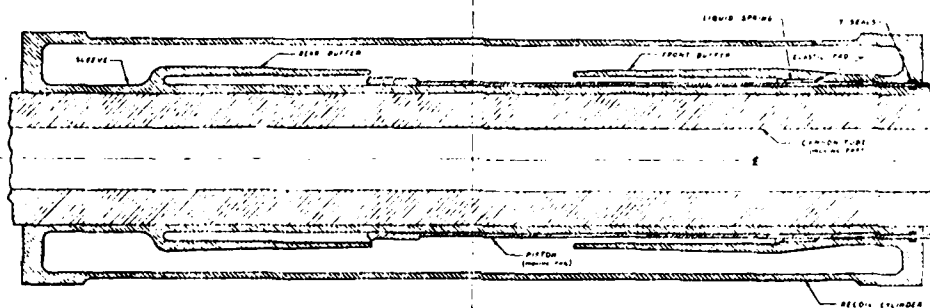
FIGURE 2. COMPRESSIBLE FLUID SOFT RECOIL CONCEPT
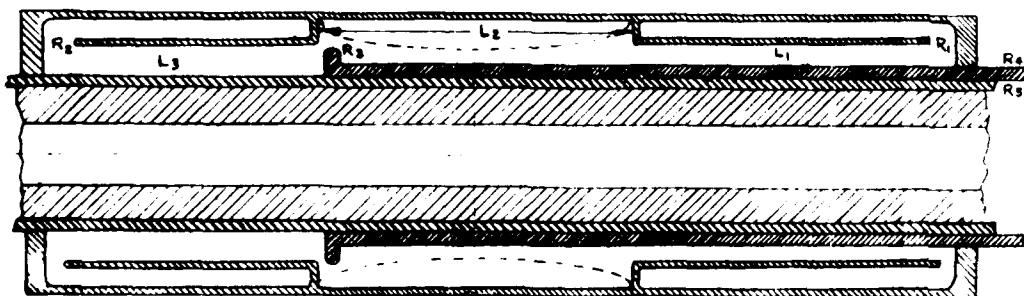

FIGURE 3 REVISED SOFT RECOIL CONCEPT
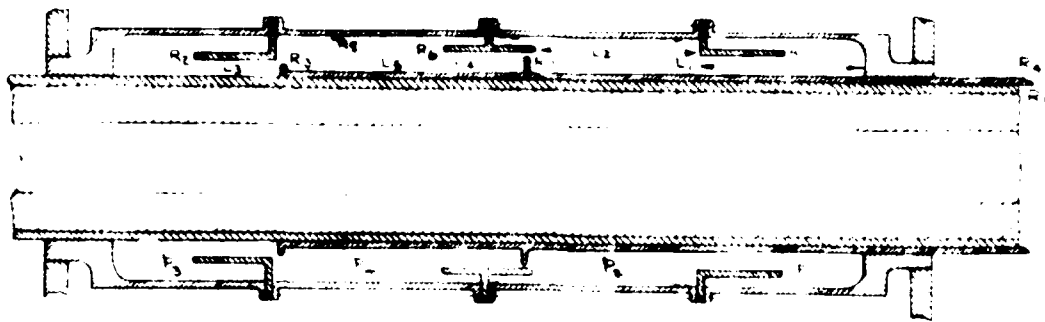
FIGURE 4 HYDROPNEUMATIC
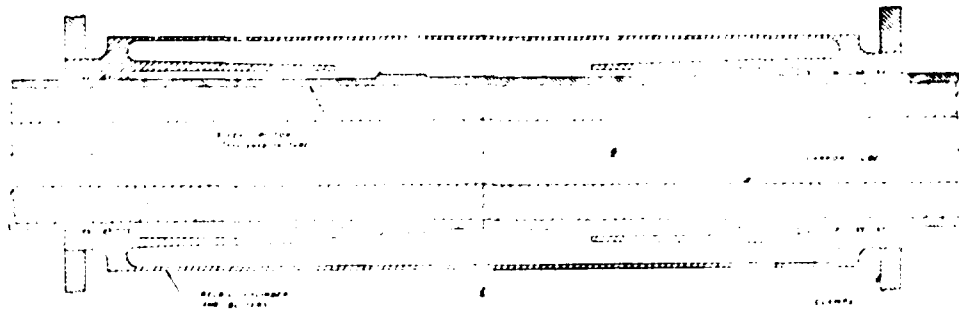
FIGURE 5 ALTERNATIVE PISTON DESIGN
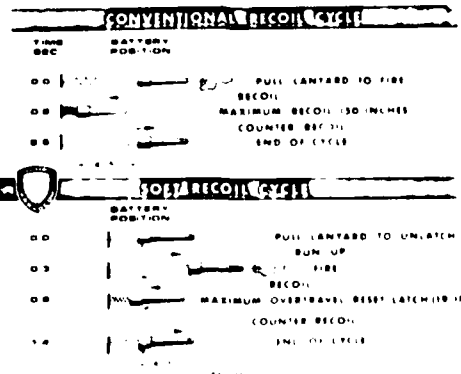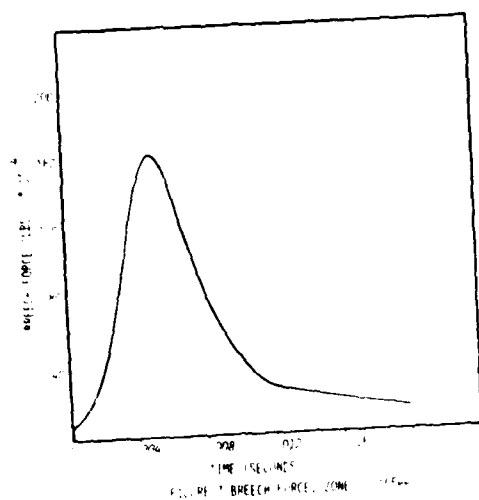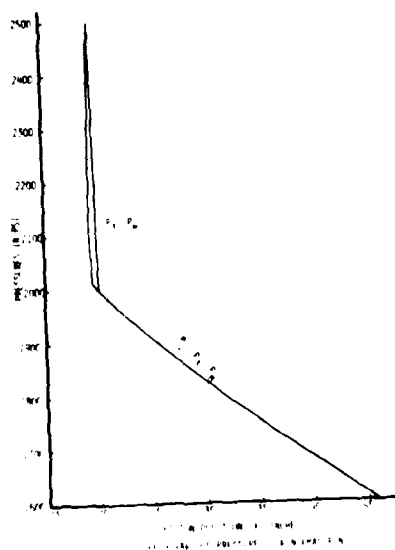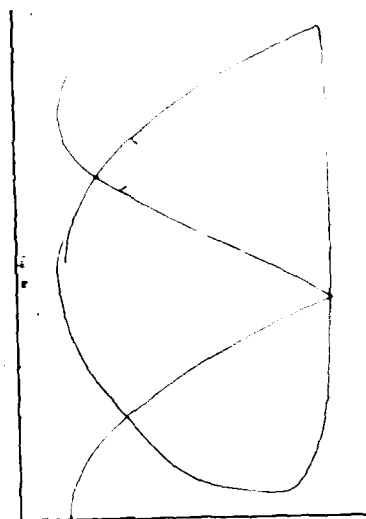
444
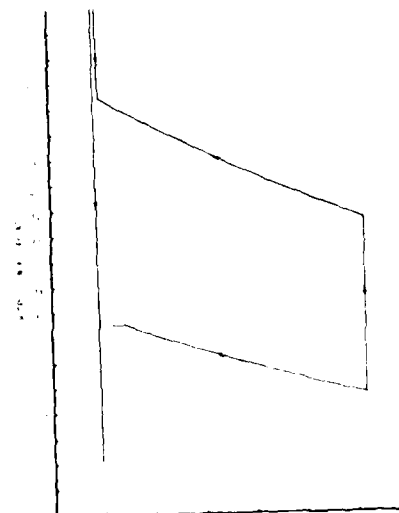
ION IMPLANTED GUIDED WAVE DEVICES
FOR ARMY FIRE CONTROL

*JOHN M. ZAVADA, DR.
HOWARD A. JENKINSON, MR.
THOMAS J. GAVANIS, MR.
Fire Control and Small Caliber
Weapon Systems Laboratory
ARRADCOM, Dover, NJ   07801

ROBERT G. HUNSPERGER, DR.
University of Delaware
Newark, DE   19711

DONALD C. LARSON, DR.
Drexel University
Philadelphia, PA   19104

JAMES COMAS, DR.
Naval Research Laboratory
Washington, DC   20375

I.   INTRODUCTION

In a recent review of the Army's Fire Control Technology
Base(1), several key issues were repeatedly emphasized. One of
these issues was that future fire control systems will have to
meet certain stringent requirements in order to permit the Army
to successfully engage hostile forces in anticipated combat scen-
arios. Prominent among these requirements are minimum acquisition/
reaction time, multiple target engagement capability, increased
first round hit probability, and 24 hour/all weather operation.
The first three requirements clearly indicated the need for sen-
sing and signal processing subsystems capable of handling large
amounts of digital and analog information and of processing this
information rapidly. In spite of the major advances that have
been made in the field of microelectronics, this need is still a

445

formidable challenge to Very Large Scale Integration (VLSI) circuits
and to Very High Speed Integrated Circuits (VHSIC). Another possible
solution to this problem lies in the development of fire control
systems incorporating guided wave components. Guided wave or opti-
cal devices are the analogs of the familiar electronic devices such
as cables, modulators, switches, sources and detectors, which rely
on the motion of electrons and their subbsequent deflection. How-
ever, optical devices guide an electromagnetic (EM) wave through a
material structure and function directly on the propagating wave.
Due to the higher carrier frequencies of optical waves, the infor-
mation that guided wave devices can process is nearly 10,000 times
greater than that of electronic devices. Also, these optical devices
are several orders of magnitude faster than their electronic coun-
terparts. Other advantages of guided wave devices include: lower
transmission losses, virtually complete immunity to EM interference
and countermeasures, and the elimination of use of strategic mate-
rials such as copper. Once these devices are integrated into optical
circuits, there are additional benefits of greater reliability and
durability.

The development of integrated optical circuits parallels very
closely the development of integrated electronic circuits. First
there was the use of discrete electronic elements such as trans-
istors, capacitors, and oscillators. This corresponds to the use of
discrete optical elements such as lenses, prisms, and lasers in cur-
rent optical systems. Later the discrete electronic devices were
assembled into circuit boards and, eventually, into monolithic
integrated circuits. Similarly, the goal of "Integrated Optics" is
to minimaturize and assemble the discrete optical elements and de-
vices into a monolithic circuit a few square millimeters in area.
This size reduction of optical systems is even more dramatic than
what has been accomplished in the electronics area.

While there has been considerable activity in both the military
and civilian sectors to utilize guided wave devices in communication
systems, such as telephone and television, the potential of this
technology for sensing and optical signal processing roles has been
largely untapped. The few military programs that are developing
guided wave components for these applications include the work on a
radio frequency (RF) spectrum analyzer(2), on optical correlators(3),
and on fiber optic sensors(4).

Due to the fourth requirement mentioned above for 24 hour/all
weather operation, the Army has been emphasizing systems which oper-
ate at longer wavelengths, in particular, at infrared and millimeter

446

wave (MMW) frequences. Active devices, such as carbon dioxide (CO_2) lasers and MMW transmitters, form a natural basis for additional applications of guided wave technology to Army Fire Control Systems. Typical systems which could utilize infrared optical circuits include CO_2 laser radars, Miss Distance Sensors (MDS) and sensors for smart munitions such as Smart Target Acquisition Fire and Forget (STAFF). These optical circuits could be used to perform various functions including phased array transmission, heteroyne detection, parallel processing and optical correlation.

Various methods have been used to fabricate optical waveguides and components. These include thin film deposition, epitaxial growth, filled channel techniques, ion diffusion and ion implantation. The latter method is a particularly interesting technique that offers a number of distinct advantages in comparison to the other methods. In ion implantation a beam of atoms is ionized, accelerated through a potential difference, and is directed at a suitable material target. The resulting damage in the material and the introduction of foreign atoms can produce electronic, chemical, and optical changes. In fact, ion implantation is one of the major production techniques used in the electronics industry for the manufacture of integrated electronic circuits. The primary advantage of this technique lies in the precise, external manner by which doping of materials can be controlled. Any ion species can be introduced into a given material and the dopant concentration is not limited by ordinary solubility considerations. The dosage can be monitored very accurately and the depth profile of the implanted ions can be controlled by adjusting the energy of the accelerator. This permits realization of dopant profiles that could not be achieved by diffusion or any other technique. Also, implantation of materials can be performed over a wide range of temperatures allowing for unique interactions of the implanted ions. This technique is a relatively simple procedure which is compatible with modern masking methods used to achieve special configurations of the doped regions. Additionally, there is the possibility that entire optical circuits can be "written" directly on a chip without the use of masks.

While ion implantation has been used to fabricate guided wave components at visible and near infrared wavelengths, little effort has been directed towards applying this technique to form guided wave devices in the far infrared. Lincoln Laboratories has made low loss waveguides at 10.6 microns through proton implantation of cadmium telluride(5). However, a drawback to this work is the very

447

high accelerating energies, over 1 MeV, that were required. Accelerating machines, capable of such large energy outputs, are not readily available and are very costly to operate. If it were possible to fabricate low loss infrared waveguides with moderate energy accelerators (less than 300 keV), then ion implantation would be established as a prime fabrication technique for integrated optics in this spectral region.

This is the task that we are addressing in our current research effort: to determine the feasibility of fabricating infrared waveguides in semiconductor materials using moderate energy ion implantation. Semiconductor materials were selected for this work because all of the major functions of an optical circuit, such as light generation, waveguiding, modulation and detection, can be achieved in these materials.

II. OPTICAL WAVEGUIDES

The basic component in an integrated optical circuit is the waveguide. This structure serves to confine the EM wave to a particular region and to specify the direction of propagation of this wave. Figure 1 illustrates the operation of a planar (two dimennsional) waveguide. In this figure, we assume that the EM wave has already been introduced into the waveguiding region. This can be accomplished through various methods including endfire coupling, or even light generation in the waveguide. The waveguide in this figure is formed by the middle region identified by its optical index of refraction, n_f. The regions above and below the waveguide are similarly labelled by their indices n_o and n_s. For the EM wave to be guided in the middle region, it is necessary that n_f be larger than either n_o or n_s. When this condition is satisfied, there exists an angle of incidence at each interface, called the critical angle, above which the incident wave will be totally reflected. The guided wave will then propagate in a zig-zag fashion undergoing total internal reflection at each interface. Upon each reflection the EM wave will experience a change in phase. For the wave to be propagated, these phase changes, in addition to the phase change resulting from the optical path difference, must add constructively. This leads to an eigenvalue equation, one for each polarization, which determines the propagating modes in the waveguide. For lossless media, the basic eigenvalue equation is (6) :

$$kn_f t \cos\Theta_f - \Phi_{fo} - \Phi_{fs} = j\pi$$

$$k = \frac{2\pi}{\lambda_o} \qquad j = 0, 1, 2, 3\dots \tag{1}$$

where t is the thickness of the waveguiding region, θ_f the angle of
propagation of the guided wave in the film, λ_o the wavelength of
the EM wave in free space, Φ_{fo} and Φ_{fs} the phase change due to
reflection at the respective f-o and f-s interface, and j is the
modal order. The phase changes can be calculated from the Fresnel
reflection coefficients for a planar interface and are given by:

$$tan\ \Phi_{fi} = \frac{(n_f^2 sin^2\Theta_f - n_i^2)^{\frac{1}{2}}}{n_f\ cos\ \Theta_f} \qquad (2)$$

for s polarization, and by:

$$tan\ \Phi_{fi} = \left(\frac{n_f}{n_i}\right)^2 \frac{(n_f^2\ sin^2\Theta_f - n_i^2)^{\frac{1}{2}}}{n_f\ cos\ \Theta_f} \qquad (3)$$

for p polarization. Here the subscript i refers to either the
region above the waveguiding layer (i = o) or to the region below
(i = s) depending upon the phase change under consideration. The
guided modes in a planar waveguide are usually denoted TE_j and
TM_j, where TE is transverse electric (parallel polarization) and TM
is transverse magnetic (perpendicular polarization). Once the opti-
cal indices are known, the eigenvalue equations can be solved to
determine the number of guided modes for a given value of the wave-
guide thickness. The resulting set of curves for a particular choice
of optical indices is shown in Figure 2. As can be seen in this
figure, curves corresponding to different modal orders are widely
separated as compared to curves of the same modal order but differ-
ent polarization. This means that the propagating modes of the same
order normally occur in doublets, one for each polarization, and are
distinct from the doublet for the next order.

The above equations can also be used to determine the optical
index and the thickness of the planar waveguide provided that the
waveguide can support at least two propagating modes and that the
optical indices n_o and n_s are known. Then, by measuring θ_f for
each mode, and by substituting this angle into Eq. (1) with the
appropriate expressions for the phase changes, a set of simultan-
eous, transcendental equations involving two unknowns can be ob-
tained. These equations can be solved numerically to yield the
parameters n_f and t of the waveguiding layer.

449

$n_f > n_s > n_o$

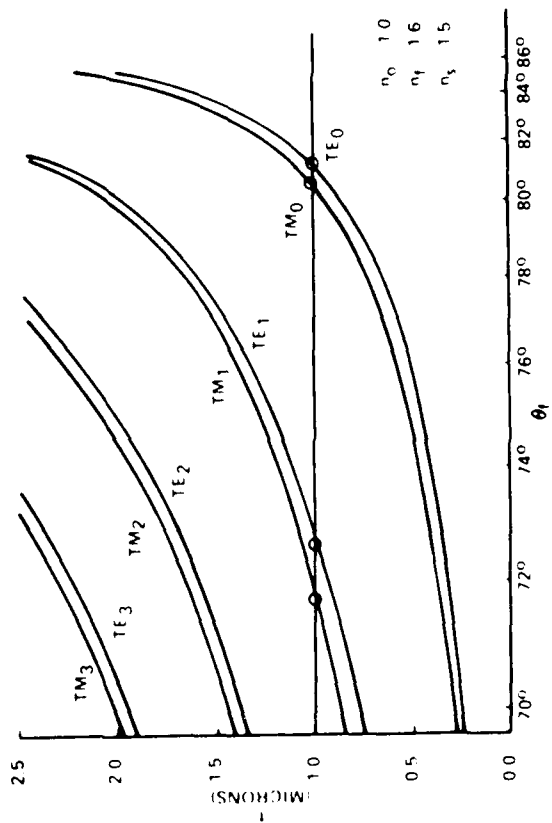**Figure 1. Planar Optical Waveguide**

Figure 2. Predicted Waveguide Modes

ZAVADA, JENKINSON, GAVANIS,
HUNSPERGER, LARSON & COMAS

During the current fiscal year, this method was used to determine the thickness and the refractive index of thin film aluminum oxide waveguides. These planar waveguides were prepared by evaporation of aluminum oxide onto glass substrates in Fire Control Division's thin film laboratory. In order to couple laser light into the waveguide and to measure the angles of propagation for the guided waves, an optical facility, sketched in Figure 3, was assembled. This facility consists of a helium neon (HeNe) laser source (0.6328 microns), a beam collimator, and a stage which holds both the planar waveguide and a high index glass prism (optical index 1.732). The prism is used to couple the laser light into the waveguide and the stage is mounted on a motorized rotary table. Figure 4 contains a schematic drawing of the prism coupling technique in which the collimated HeNe laser beam impinges on the glass prism at an incident angle θ, is refracted to the corner of the prism where, at certain distinct angles, it is coupled into the waveguide. The rotary table allows the incident angle to be varied until waveguiding is achieved, as indicated visually by the slide flashing with the red HeNe light. While the film was highly transparent at this wavelength it did contain inhomogeneities and surface roughness which resulted in light being scattered out of the waveguide. This scattering is responsible for the flame-like pattern in the slide during coupling. For a perfect film, the waveguided light would be visible only at the end of the film where light would be scattered back into the air. Measurements were made of the coupling angle for each polarization of the propagating modes. Once the coupling angle has been measured, the angle of propagation in the waveguide is determined by (7):

$$\sin \Theta_f = \frac{n_p}{n_f} \sin \left\{ \sin^{-1}\left(\frac{n_0}{n_p} \sin \Theta\right) + \Theta_c \right\} \qquad (4)$$

where θ_c is the corner angle of the prism and n_p is the prism's optical index. In order to couple light by this technique into every mode of the waveguide, it is necessary that $n_p > n_f$.

Results of this experiment for one of the thin film waveguides are contained in Table I. There, the incident coupling angle, the excited mode and the angle of propagation are listed. Below the table are stated the calculated values for the thickness and the
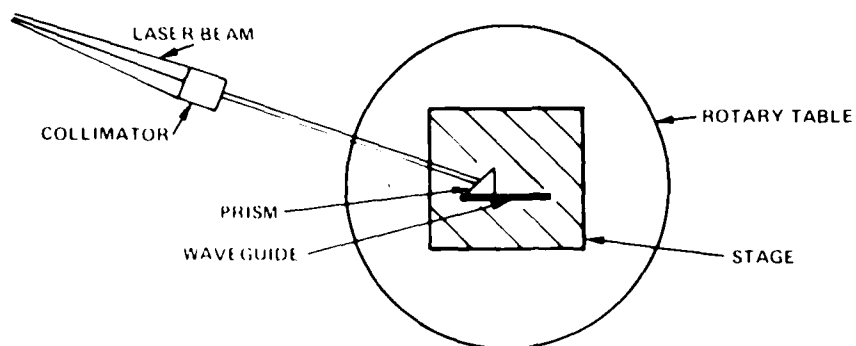
Figure 3. Experimental Facility
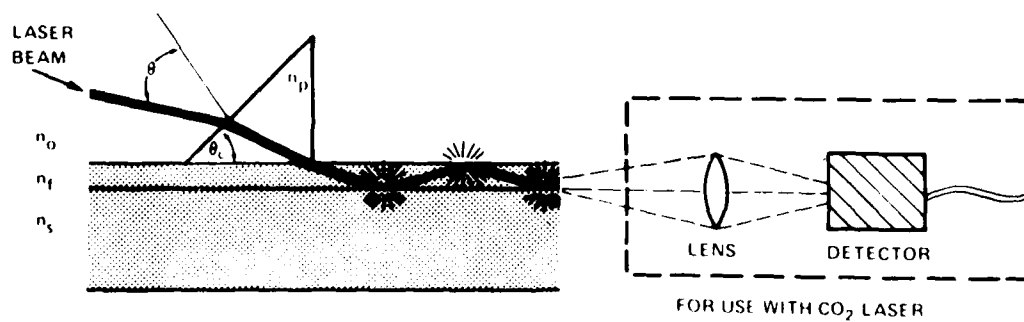
Figure 4. Prism Coupling Technique

452

TABLE I. Prism Coupling Parameters

θ	MODE	θ_f
48.75°	TE$_0$	82.27
48.50°	TM$_0$	82.01
39.75°	TE$_1$	74.50°
38.75°	TM$_1$	73.86°
29.75°	TE$_2$	67.46°

LASER WAVELENGTH	0.6328	MICRONS	
PRISM INDEX	1.732		
WAVEGUIDE INDEX	1.650	$\pm$.001	
WAVEGUIDE THICKNESS	1.18	$\pm$.015	MICRONS

ZAVADA, JENKINSON, GAVANIS,
HUNSPERGER, LARSON & COMAS

optical index based on this data. The experimental accuracy in
measuring the coupling angle is estimated to be $\pm$ 0.1° in this
method. This results in an error of $\pm$ 0.015 microns for the
thickness and of $\pm$ 0.001 for the optical index.

Channeled, or three dimensional, waveguides are the structures
that will be eventually required in integrated optical circuits. Ir
such circuits, the guided wave will have to be switched, coupled
into other waveguides, polarized, filtered, modulated, and converted
into electrical signals. This processing and conversion is more
efficient in channeled waveguides. While the description of modes
in a channeled waveguide is more complicated, the same concepts,
discussed above, of total internal reflection and constructive
interference apply. The guided modes in this case are specified
TE_{jk} and TM_{jk} with two modal numbers j and k now being
necessary. These modes are likewise determined by eigenvalue
equations similar in form to Eq. (1).

III. ION IMPLANTED WAVEGUIDES

In crystalline semiconductor materials, ion implantation can pro-
duce a change in the refractive index through various physical mech-
anisms. These mechanisms include: damage to the crystal lattice
resulting ultimately in an amorphous region; introduction of dopant
atoms into the lattice causing a change in the polarizability of the
unit cell; localized regions of stress in the lattice due to damage
and the presence of large numbers of dopant atoms in these regions;
and, the compensation of the free carrier of dopant atoms into the
lattice causing a change in the polarizability of the unit cell;
localized regions of stress in the lattice due to damage and the
presence of large numbers of dopant atoms in these regions; and, the
compensation of the free carrier concentration in suitably doped
materials. This last mechanism has been the primary method used to
form optical waveguides in semiconductor materials through ion
implantation(8). Naturally, in any actual implantation the above
mechanisms are interrelated and the change in the refractive index
of the implanted material is due to the total effect of these pro-
cesses. However, it is possible, by careful design of the experi-
mental conditions, to accentuate one of these mechanisms and to
minimize the effects of the others. The present research experiments
are centered on free carrier compensation since this mechanism
appears to afford the greatest flexibility in altering the optical
properties of the implanted regions.

ZAVADA, JENKINSON, GAVANIS,
HUNSPERGER, LARSON & COMAS

For a homogeneous, isotropic, n-type crystalline semiconductor, the relative dielectric constant K can be expressed as the sum of two contributions:

$$K = K_L + K_{FC} \qquad (5)$$

where K_L is the relative dielectric constant due to the atoms in the lattice and K_{FC} is the contribution from the free carriers. Usually, K is a complex quantity with the imaginary part being related to the absorption in the material. The refractive index is also a complex quantity and is given by:

$$n = \sqrt{K} = n_1 - in_2 \qquad (6)$$

Where n_1, is related to the phase of the EM wave in the material and n_2 is the extinction coefficient.

In the classical treatment of the free carriers as a plasma gas, the contribution to the dielectric constant is:

$$K_{FC} = \frac{-\omega_p^2}{\omega(\omega - i\gamma)} \; ; \; \omega_p^2 = \frac{e^2 N_c}{\epsilon_0 m^*} \; ; \; \gamma = \frac{e}{\mu m^*} \qquad (7)$$

Here ω_p is the plasma frequency, ω the angular frequency of the EM wave, g the damping coefficient, e the charge of the electron, N_c the density of free carriers, ϵ_0 the vacuum permittivity, m* the effective mass of the carriers and μ the mobility of the carriers.

During ion implantion of a doped semiconductor, the energetic ions produce displacements in the lattice which, in turn, trap some of the free carriers. This reduction of the carrier concentration results in an increase to the refractive index of a surface layer whose thickness is approximately equal to the penetration range of the implanted ions. Assuming complete compensation of the free carriers in this layer, the change in the dielectric constant is simply K_{FC}. For frequencies below that of the bandgap and for materials in which g is small, the change in the refractive index can be approximated by:

$$\Delta n \sim \frac{1}{2 n_1} \left(\frac{\omega_p}{\omega}\right)^2 \qquad (8)$$

provided that the damage produced in the lattice by implantation is minor. The optical index of the implanted region will be $n_1 + \Delta n$ which is larger than that of the unimplanted substrate, n_1. Then, if the thickness of this region is large enough for Eq. (1) to be satisfied with these values for the optical indices, the implanted layer will form an optical waveguide. As an example, for n-type GaAs with a carrier concentration of $1.1 \times 10^{18}/cm^3$, $\Delta n = 0.225$ at a wavelength of 10.6 microns and the implanted region must have a thickness of at least 2.25 microns in order that optical waveguiding can occur.

A difficulty with this carrier compensation technique is that the remaining free carriers in the substrate can lead to absorption losses. The formal solutions to Maxwell's equations for optical waveguiding show that even though there is total internal reflection at each interface a portion of the EM field extends into the surrounding regions. If the thickness of the waveguide is just above the minimum thickness, then the field in the substrate will be appreciable. Consequently, for low loss optical waveguides at 10.6 microns, the thickness of the waveguiding layer must be approximately 10 microns.

A study was made of various semiconductor materials that would be suitable for use as infrared waveguide substrates. Initially GaP, GaAs, ZnTe, ZnS, ZnSe, CdS and CdTe were considered because each of these materials has very promising optical and electrical characteristics. However, only GaAs, GaP and CdTe are commercially available in the required single crystal wafer form. It was decided to limit the present investigation to GaAs and GaP because CdTe is considerably more expensive and the processing technology for CdTe (polishing, etching, cleaning, heat treatment, etc.) is much more difficult. The wafers that were selected for implantation were <100> oriented substrates since these samples can be easily cleaved to the desired rectangular shape for waveguiding experiments.

Protons (H^+) were chosen as the initial ion species to be used in these implantation experiments in order to minimize the contributions to the optical properties arising from physical processes other than free carrier compensation. These ions produce the least amount of damage to the crystal and are very unlikely to occupy substitutional sites in the lattice. Furthermore, protons have the greatest projected range by direct energetic penetration without relying on any secondary or defect diffusion. In fact, protons are also a useful species for investigating such diffusion effects.

Since one of the basic objectives of this work is to produce
waveguides of sufficient thickness to support low loss propagation
at 10.6 microns while using a minimum implantation energy, 300 keV
was selected as the ion energy to be used. Practical considerations
make low energy very desirable because many electronics fabrication
facilities are equipped with ion accelerators of 300 keV or less,
while relatively few have units delivering greater than 300 KeV
acceleration.

With 300 keV protons, calculations indicate that optical wave-
guides, of approximately three microns thick, can be produced in
both GaAs and GaP provided that these materials have carrier con-
centrations on the order of $10^{18}/cm^3$. While such implanted
layers could support guided waves at 10.6 microns, lower losses
would be obtained if the thickness of these layers were increased.
Several experimental investigations(9) have noted that the waveguide
thickness is often increased beyond that produced by direct ener-
getic ion penetration if the substrate is heated during the implan-
tation process. This heating is expected to produce a diffusion of
implantation generated defects, resulting in carrier compensation to
a thickness as much as an order of magnitude greater than the pene-
tration depth of the ions (protons) themselves. Because the defect
diffusion process is not yet well characterized, the approach taken
in this work is to use a range of implant temperatures spread both
above and below room temperature by about 200 to 300°C to determine
the optimum temperature empirically. Ion dose should be at least
$5 \times 10^{13}/cm^2$ to produce adequate carrier compensation in the wave-
guide but, again, some samples should be implanted with doses as
high as $5 \times 10^{15}/cm^2$ to determine the optimum dose experimentally.
Polished wafers of n-type GaAs have been implanted with protons to
the required fluence levels and at the temperature ranges specified
by this approach. The implantation of the wafers was performed at
the Electronics Technology Division of the Naval Research Laboratory.

The next step in this investigation is to measure the optical
index and thickness of the implanted layers. These parameters can
be determined by the prism coupling method described in Section II.
However, since the implanted layers are being designed to function
at CO_2 laser wavelengths, an infrared detector is required to moni-
tor waveguiding and to measure of the coupling angle. The experi-
mental set up is illustrated by the insert in Figure 4. This in-
frared facility is presently being assembled and tested. Simulta-
neously, the optical properties of the implanted layers are being
investigated using capacitance-voltage (C-V) measurements and
ultraviolet/infrared reflectively techniques (10).

457

ZAVADA, JENKINSON, GAVANIS,
HUNSPERGER, LARSON & COMAS

IV. CONCLUSIONS

Theoretical calculations and prior experimental work indicate
the low loss infrared optical waveguides can be produced by 300 keV
proton implantation of GaAs and GaP. Samples of these materials have
been prepared and the resulting optical properties of the implanted
layers, as determined from C-V and reflectivity measurements, are
suitable for IR waveguiding. Once this is demonstrated and the re-
levant material and implantation parameters have been established,
this method can be used for the fabrication of more complex guided
wave structures such as channeled waveguides, directional couplers
and modulators. These components can then be integrated to form
infrared optical circuits for sensing and signal processing roles.
Furthermore, it appears quite certain that such integrated optical
circuits, with their greater bandwidth and faster operation, will
play an increasingly larger role in helping the Army meet its future
fire control requirements.

V. REFERENCES

1. "Army Fire Control Technology Base Plan (U), (6.1, 6.2.,
    6.3a), " Vol. I, U.S. Army DARCOM, (Conf.), 1978.

2. D. B. Anderson, "Integrated Optics RF Spectral Analyzer for
    Electronic Warfare", IEEE Spectrum, Vol. 15, No. 12, p 22
    (1978).

3. N. J. Berg, J. N. Lee, M. W. Casseday and B. J. Udelson,
    Appl. Opt., Vol. 18, No. 16, p 2767 (1979).

4. C. Davis and R. Einzig, "Fiber Optic Sensor System (FOSS)
    Technology Assessment (U)", Dynamic Systems, Inc., Report No.
    79-385-10-C, (Conf.), 1979.

5. D. L. Spears, "Integrated Optical Circuits Semiannual Tech-
    nology Summary", Lincoln Laboratory, M.I.T., Report No. ESD-
    TR-75-103, 1979.

6. See, for example, D. Marcuse, Theory of Dielectric Optical
    Waveguides, Academic Press, New York, 1974.

7. J. E. Goell, "Thin-Film Waveguide Fabrication and Testing
    Considerations", in Introduction to Integrated Optics, M. K.
    Barnoski, Ed., Plenum Press, New York, 1974.

458

ZAVADA, JENKINSON, GAVANIS,
HUNSPERGER, LARSON & COMAS

8. E. Garmire, "Semiconductor Components For Monolithic Applica-
    tions", in Integrated Optics, T. Tamir, Ed., Springer-Verlag,
    New York, 1975.

9. R. G. Hunsperger, O. J. Marsh, and C. A. Mead, Appl. Phys.
    Letters, Vol. 13, p 295 (1968); R. G. Hunsperger and O. J.
    Marsh, Metal. Trans. Vol. 1, p 603 (1970).

10. J. M. Zavada, H. A. Jenkinson, T. J. Gavanis, R. G. Hunsperger,
    M. A. Mentzer, D. C. Larson, and J. Comas, Proc. of SPIE, 24th
    Intl. Symp. 1980.

A SOLID STATE DARK ADAPTOMETER (U)

*HARRY ZWICK, PhD
SILMON L. BIGGS, MD
PETER A. O'MARA, PhD, MAJ, MS
CHARLES W. VAN SICE, MR
LETTERMAN ARMY INSTITUTE OF RESEARCH
PRESIDIO OF SAN FRANCISCO, CA   94129

INTRODUCTION

Many of the current field exercises conducted within the Army
involve extensive night maneuvers. Such exercises place large
numbers of personnel and millions of dollars of sophisticated
weaponry into a scenario. No accurate measurements have been made
assessing the ability of these troops to adapt to low-level light
or perform in night operations.

Recommendations have been made for the development and
wide-spread use of a device to screen recruits and active duty
military personnel for dark adaptation. It is estimated that
perhaps as many as 15 percent of the "normal" population has some
difficulty in altering light sensitivity in darkness. If the
military has within its ranks a similar percentage of adaptation
problems, there may be a platoon sargeant, company commander,
tank commander, or others in a night exercise with minimum ability
to adapt to the low-level light environment. Without actual intent,
this individual may jeopardize the lives of other military and
destroy friendly lives and equipment because either the individual
cannot adapt or has not realized that adaptation is a problem.

The subjective phenomenon of dark adaptation is familiar to us
as the initial inability to "see" hen entering a dark room from a
bright-light environment. The longer we stay in the darkness the
better we can see. The sensitivity of the fully dark-adapted human
eye is unsurpassed by even the most sensitive physical detection
systems. The functional relationship that describes this increase

461

in sensitivity with reduction in ambient light levels is known as
dark adaptation. Our purpose in this paper is to show how the
military can improve the measurement of dark adaptation in its
personnel.

The quantitative measurement of this process has traditionally
been a complex problem. The technique involves various light
sources, filters, optics, and graphic data reduction. A two-step
procedure is always involved. The visual system must brought to a
standard level of light adaptation and then, subsequently, the
temporal course of visual threshold in the dark-adapting eye can
then be measured over a subsequent 20 to 30 minutes of darkness.
The typical function measured in this manner for a large retinal
area with an unfiltered white light test source passes through an
initial plateau at about five minutes ("rod-cone break") before
achieving a final plateau 20 to 30 minutes after the termination
of light adaptation. The initial portion of dark adaptation measured
in this manner is attributed to the dominance of cone function over
rod function during the early minutes of dark adaptation. (The
cone system is the human photoreceptor system that mediates color
vision and visual acuity. The human rod photoreceptor system
mediates absolute visual sensitivity.) The final dark-adapted
threshold, occurring 20 to 30 minutes after light adaptation,
reflects the dominance of rod vision and the ability of the rods to
detect minimal light levels.

While conventional dark adaptometry has traditionally employed
a white light test stimulus and relatively intense light adaptation
exposure levels, other approaches to the separation of rod and cone
dark adaptation processes are possible. If dark adaptation functions
are measured with spectral (monochromatic) rather than white light
test sources, functions varying in steepness and rate of adaptation
are obtained as a function of spectral (monochromatic) location
(1,2). Functions measured with red light are generally more shallow
and rapid in adaptation. They appear much like functions measured
for central retinal regions that are dominated by cone photo-
receptors (3). Functions measured with green or blue-green lights
are steeper and require more time for full adaptation. Such
functions are more of a composite of both rod and cone processes.
By appropriate selection of test light wavelengths and retinal
location, such functions can be made to reflect specific local
retinal receptor processes.

Until recently, the measurement of spectral dark adaptation
functions of any kind has been even more complex than conventional
measurement of dark adaptation with white light sources. The

development of light emitting diodes (LED) that emit selectively
in the long (red) and in the intermediate (green) spectral regions
has changed this situation. In this paper, we will introduce a new
solid-state dark adaptometer recently developed at the Letterman
Army Institute of Research (LAIR) that uses red and green LED sources
to separate rod and cone function in a rapid and a simple automated
technique for spectral dark adaptometry (4).

METHODS

A schematic illustration of the LAIR dark adaptometer — its
principle of operation, pulse modulation; and its product, a sample
individual dark adaptation function — is presented in Figure 1. A
36-inch hemisphere, fitted with a chin and headrest, can be
indirectly illuminated to provide a constant uniform light
adaptation source of 110 candela/m^2.

Red and green LED sources are mounted inside the hemisphere and
are used in either of two display modes. In Display 1, five blocks
of LED red and green sources are mounted on a board. At their
widest points, they subtend an angle of 20 degrees at the retina
(Figure 1). This diode array was specifically designed to test
a large area of the retina without the use of any specific
fixation point. The subject is simply instructed to respond when
any test light is just visible. In Display 2, specific fixation
to a central fixation diode is required. Any retinal area over an
eight-degree region of the retina can be focalized by this
arrangement and local spectral dark adaptation of this retinal
region measured. If the proximal ring of diodes is chosen, the dark
adaptation measurement will reflect adaptation primarily in the
central retina (foveomacular dark adaptation). If the outermost
ring of diodes is chosen at eight degrees from fixation, then a
peripheral retinal dark adaptation function will be obtained. The
display contains two complete "crosses," one comprised of red and
the other comprised of green LED sources. Each display is a separate
modular unit. Changing modules from one to the other involves
plugging in the appropriate diode display board into the same control
socket.

Visual threshold measurement in this apparatus was made by a
pulse modulation procedure where pulse width varied from one to
10,000 µsec (duty cycle) at a pulse repetition frequency of 100 Hz,
a value above fusion flicker threshold. In this pulse domain,
average quantal flux rather than average power determines threshold
level. Thus, for a constant output power of the LED, the total
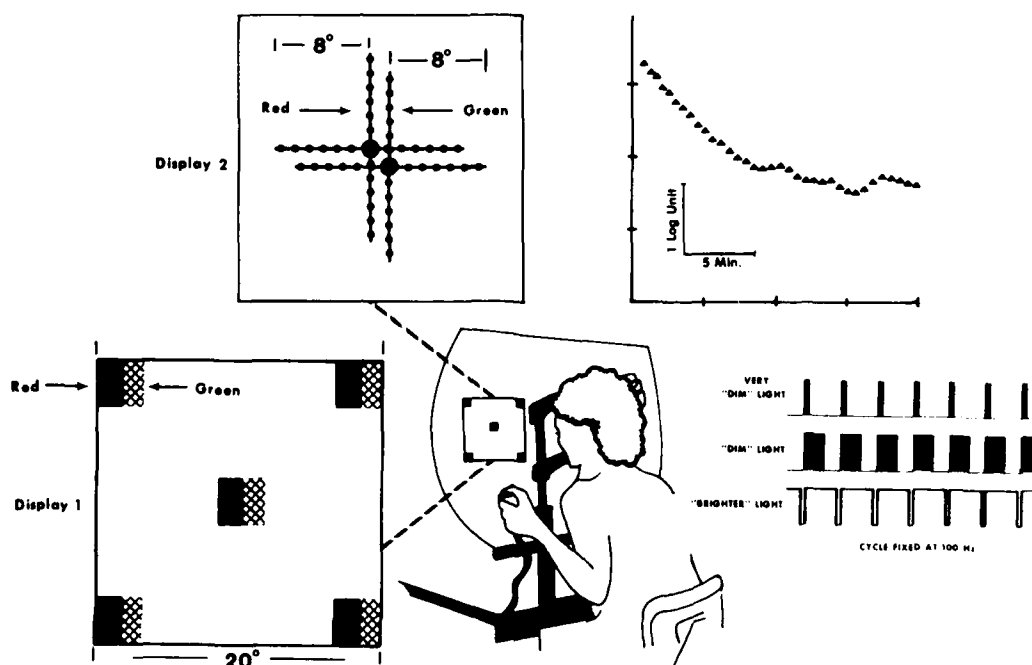average quantal flux required for threshold is directly manipulated

' Figure 1. A schematic illustration of the LAIR dark adaptometer with interchangeable display modules. In the upper right, a sample dark adaptation function as drawn under computer software control by the X-Y plotter is shown. The duty cycle or pulse width modulation for a dim light (late dark adaptation) as compared to that of a bright light (early dark adaptation) is shown in the lower right insert. Threshold pulse width decreases as dark adaptation increases.

464

by pulse width variation. (In independent experiments, the reciprocity between diode output power, i.e., light output, and pulse width modulation was unity over the pulse width range from one to 10,000 microseconds.)

The LAIR dark adaptometer is controlled by a low-cost microcomputer system and the function shown in Figure 1 is an on-line sample of the final output of this system. This computer system automatically calculates threshold pulse widths and prints them out as the subject is being tested. Presentation of different spectral LED sources is alternated and independent estimates of thresholds are calculated and alternately printed. The digital records of the threshold estimates of each subject are labeled and stored on a magnetic disk for later review or statistical analysis. An X-Y plotter provides the on-line copy of each dark adaptation function obtained for both spectral sources. When Display 2 is used, the computer operates the fixation LED and automatically adjusts its level to be a fixed constant pulse width increment above the threshold pulse width that is continuously being estimated by the computer.

For the data presented in this paper, the following protocol options were used. Light adaptation for five minutes at a hemispheric illumination level of 110 candela/m^2 was given to each subject before 20 minutes of darkness. During this time threshold estimates were continuously made for both spectral light sources. While computer software provided two options for the psychophysical test procedure, tracking and ascending limits, only the tracking procedure was used in the experiments reported in this paper. In the tracking procedure, the subject was required to depress the response button whenever a light was detected and not to release this button until the light was no longer detectable. Thresholds for both red and green LED sources were continuously tracked over the 20 minutes of darkness in this manner. When a fixation source was employed, the subject was carefully instructed not to depress the response button until light other than the fixation source was detectable. The computer automatically signaled the end of the test by displaying all of the LED sources at level above detection threshold for the dark-adapted eye.

A total of 21 human volunteers (average age 25; 3 women and 18 men) were tested. One of these volunteers was a referred patient (man, age 23 years); one was the human protanope (man, age 50 years).

RESULTS

Dark adaptation functions measured for 19 human volunteers for both the red and green LED sources are shown in Figure 2. These data were obtained by using LED Display 1 where thresholds were measured without fixation over a nonspecified 20 degree retinal area. Average threshold values were calculated at 1.25 minute intervals over the 20 minute dark adaptation period for both the red and green LED sources. The inner horizontal bars about each threshold point represent ±1 standard deviation, whereas the outer horizontal bars about each threshold point represent ±2 standard deviations about each mean threshold point. The variability of the curves is approximately ±0.5 log units over the entire 20 minute range of dark adaptation. The green LED function is slightly more variable at five minutes than at other times during the dark. (This variability may reflect individual differences in the rod/cone break of the dark adaptation function.)

The basic shapes of these functions are not similar. The dark adaptation function for the green LED covers nearly a two log unit range as compared to less than a log unit range for the red LED function. Dark adaptation is more rapid for the red LED source than it is for the green LED source. (This also reflects the possible operation of more than one photoreceptor system measured with the green LED.)

Data from a single volunteer are presented for comparison with the normal data (Figure 2). On the green LED for this subject, data points fall more than three standard deviations above normal values throughout most of the dark adaptation period. While he was closer to the norm for red LED function, his data were still more than 0.5 log units higher than threshold throughout the dark adaptation period. This subject was diagnosed as an individual with peripheral retinal disease; he had complained of his lack of being able to see at night. His vision under daylight condition was within normal limits as measured on standard tests of spatial vision (5).

Dark adaptation functions measured (Display 2) at three eccentricities from fixation are presented for one representative normal human subject (Figure 3). From this figure, one can compare the measurements at one degree eccentricity between the normal human volunteer and a human protanope (a person who has difficulty in making color discriminations in the red region of the visible spectrum). At an eccentricity of eight degrees, the red and green LED sources yield dark adaptation functions similar to those shown in Figure 2. However, as eccentricity from fixation is made more
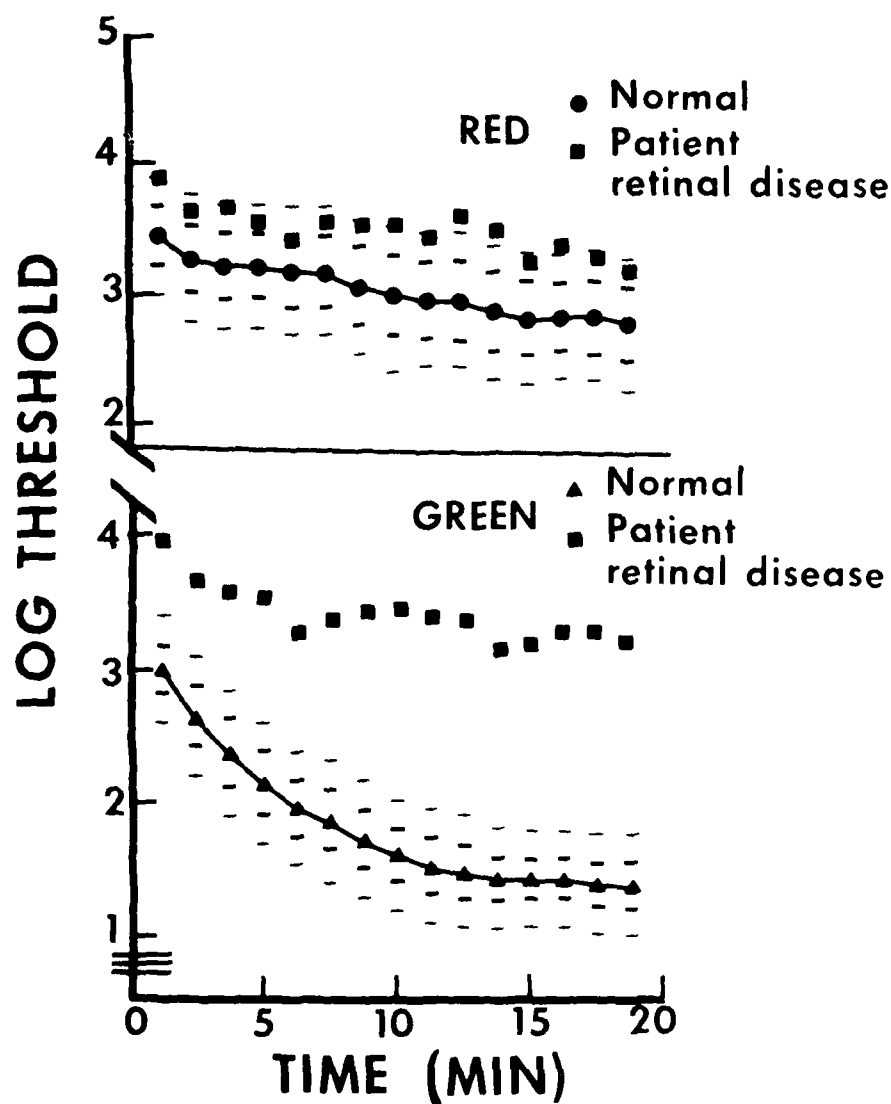
Figure 2. Average data from 19 human volunteers shown for both the red and green LED measured with Display 1. The inner horizontal bars represent ±1 standard deviation and the outer bars represent ±2 standard deviations about each mean threshold. Data from one volunteer patient with peripheral retinal disease are presented for both LED sources.
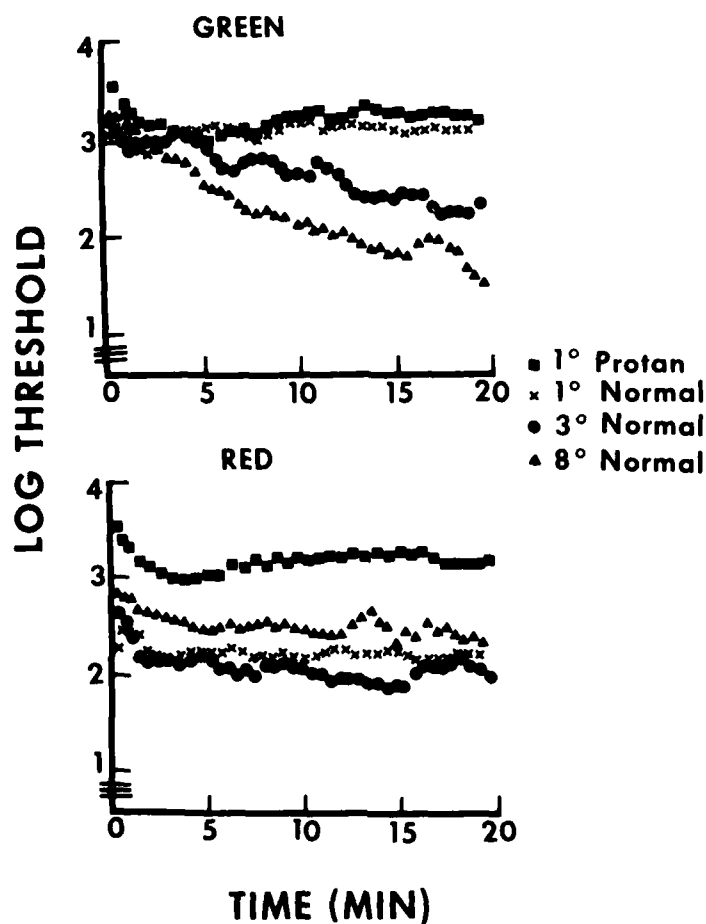
Figure 3. Data from one normal human volunteer measured at 8,3, and 1 degree eccentricity from fixation as well as data from one human protan (protanope) volunteer are presented. For the normal, threshold decreases in the red as eccentricity becomes more central and increases in the green with more central eccentricity. The protan at 1 degree is much higher on the red than the normal 1 degree function. In the green, the functions for normal and protan are identical.

central, dark adaptation for the green LED becomes more shallow and
an overall increase in threshold occurs. While the slope of the
function for the red LED changes little as threshold measurement
becomes more central, an overall increase in visual threshold for
the red LED occurs. Data from the human protanope relative to the
normal human at one degree eccentricity are considerably higher in
threshold for the red LED than for the green LED.

DISCUSSION

In this paper, we have introduced a new dark adaptometer, the
LAIR dark adaptometer, and data that validate its usage. Spectral
dark adaptation measurements in the red region of the spectrum should
be more rapid and shallow than measurements made in the green or
blue-green region of the spectrum. Our data for large peripheral
test fields with or without fixation support this finding (1,2).

Measurements of dark adaptation made within the central
retina should reflect more cone function and less rod function.
Anatomically, the density of cones increases towards the central
retina while that of the rods decreases (6). Such is the case,
as our red LED functions measured centrally are lower in threshold
than comparable functions measured peripherally. Thus, increasing
concentration of cone photoreceptors toward the central retina is
reflected. Conversely, the increase in thresholds obtained for the
green LED source reflects the general decrease in the concentration
of rods as the central retina is approached.

Data obtained from individual subjects with peripheral retinal
disease or congenital color vision deficiency involving long wave-
length color discrimination also support the validation of this
instrument. Traditional dark adaptometry made on the visual system
of individuals having peripheral retinal disease always reflects
greater loss in rod dark adaptation than cone dark adaptation. Our
dark adaptation data for one person with peripheral retinal disease
indicated more disruption in rod (green) adaptation measurements
than in cone (red) dark adaptation measurements. Similarly, the
one degree dark adaptation data of our single protanopic subject
reflected a greater departure from long wavelength cone dark
adaptation than shorter wavelength dark adaptation in normal and
congenitally color blind human subjects (2).

The variability obtained for our spectral dark adaptation
functions is quite similar to that obtained by Sloan (7) for conven-
tional apparatus utilizing a white light test source. As in her
study, 95% of the variability in our measurements of threshold equals

about ±0.5 log units over the entire course of dark adaptation.
Further comparison with the work of Sloan (7) is desirable, but
comparison between a broadbanded white light test source and a
spectral source is difficult. However, if her data are compared
with our peripheral green LED function, as both reflect rod and cone
function, the dynamic range over a comparable 20 minutes of dark
adaptation is quite similar. Comparison with more recent human
dark adaptation measurement made with green LED sources, where
current rather than pulse modulation was used to control threshold
detection, also yields a close agreement in overall dynamic range
for the first 20 minutes of dark adaptation (8). Both these
comparison studies measured dark adaptation out to 30 minutes and
thus obtained about another 0.25 log units of adaptation. In
several limited studies, we have obtained similar results, thereby
suggesting that we are in fact measuring close to the full dynamic
range obtained by Sloan (7) and others (8).

While the data presented here tend to support the usage of this
adaptometer, its application to military night vision problems needs
emphasis. Over the past two years, it has become increasingly
obvious to us that the most routine screening of individuals for
night vision military assignment can partial out individuals with
severe night vision problems with underlying retinal disease etiology.
While we have presented only a single case in this paper, we have
made similar observations in many individuals, some of whom have been
in critical positions during night vision military functions. The
routine use of dark adaptometry testing to screen such individuals
has obviously been greatly hampered by the complexity of the pro-
cedure and instrumentation typically associated with even the
simplest dark adaptometry measurement. The LAIR adaptometer
eliminates such complexity, as its computer-based format automatically
plots and stores data and provides the basic options of measurement
to the operator.

The associated problem of selection of those individuals that
may adapt most rapidly and achieve the lowest final thresholds is a
problem that can be more easily approached with an automated data
storage instrument. The more complex problem of determining exactly
what night vision functions are essential to overall night vision
performance can best be assessed with the use of an instrument that
will allow measurements of dark adaptation to be made in a varied
format that offers maximum complexity of visual measurement with
maximum flexibility in experimental design. The LAIR dark
adaptometer will greatly aid the applied visual scientist to resolve
the present problems of optimizing night vision performance. At the

same time, it will fill an important need for simple routine
capability to measure rod and cone dark adaptation in the military
population.

ACKNOWLEDGMENTS

*ZWICK, BIGGS, O'MARA, & VAN SICE

REFERENCES

1. KOHLRAUSCH, A. Untersuchungen mit farbigen Schwellpruflichtern über den dunkeladaptationsuerlauf des normalen auges. Pfluegers Arch Gesamte Physiol Menschen Tiere 196:113-117, 1922

2. CHAPANIS, A. The dark adaptation of the color anomalous measured with lights of different hues. J Gen Physiol 30:423-437, 1947

3. MOTE, F.A., and A.J. RIOPELLE. The effect of varying the intensity and the duration of pre-exposure upon foveal dark adaptation in the human eye. J Gen Physiol 34:657-674, 1951

4. BIGGS, S., S. LAYTON, H. ZWICK, C. PECK, and B.S. STUCK. Dark adaptometer prototype. Protocol: Project No. 3S762772A814, Work Unit 014, ST-4. San Francisco, California: Letterman Army Institute of Research, July 1977

5. ARDEN, J. The importance of measuring contrast sensitivity in cases of visual disturbance. Br J Ophthalmol 62:198-209, 1978

6. ØSTERBERG, G. (Topography of the layer of rods and cones in the human retina. Acta Ophthalmol 13 Suppl 6, 1935), as cited by H. Ripps and R.A. Weale. In: The Eye, Vol 2A. Visual Function in Man, edited by H. Davson. New York: Academic Press, 1976. p 11

7. SLOAN, L.L. Rate of dark adaptation and regional threshold gradient of the dark-adapted eye: Physiologic and clinical studies. Am J Ophthalmol 30:705-720, 1947

8. HENSON, D.B., and M.J. ALLEN. A new dark adaptometer. Am J Optom Physiol Opt 30:705-720, 1977